Study and design of 15 MW electrical generator structures for offshore wind power : dimensi*o*nment and *o*ptimisati*o*n

Amina Bensalah

Normandie Université

THESE

Pour obtenir le diplôme de doctorat

Spécialité Génie Électrique

Préparée au sein du « Groupe de Recherche en Électrotechnique et Automatique du Havre (EA3220) »

Étude et conception de structures de génératrices électriques de 15 MW pour l'éolien offshore : dimensionnement et optimization

Présentée et soutenue par
Amina BENSALAH

Thèse soutenue publiquement le 15/11/2022 devant le jury composé de		
Mr / Nicolas BERNARD	Maître de conférences HDR, Université de Nantes	Rapporteur
Mr / Noureddine TAKORABET	Professeur des universités, Université de Lorraine	Examinateur
Mr / Sami HLIOUI	Professeur des universités, Université CY Cergy Paris	Rapporteur
Mr / Mohammed Ali BENHAMIDA	Ingénieur, Somfy	Examinateur
Mr / Georges BARAKAT	Professeur des universités, Université Le Havre Normandie	Directeur de thèse
Mr / Yacine AMARA	Professeur des universités, Université Le Havre Normandie	Codirecteur de thèse

Thèse dirigée par Georges BARAKAT et Yacine AMARA, laboratoire GREAH

UNIVERSITÉ LE HAVRE NORMANDIE

ED PSIME

GREAH

Dedications

to my parents,

to my husband,

to my sisters and brothers,

to all people who supported me,

Acknowledgements

First and above all, I want to give thanks to Allah, the most gracious and merciful for providing me the courage and strength to accomplish this work.

I would like to express my deepest appreciation to my supervisor, Prof. Georges Barakat, for his continuous guidance throughout the development of this work. My gratitude extends to my co-supervisor, Prof. Yacine Amara, for his instructive advices.

I would like to thank to the Ph.D. examination committee, Dr. HDR Nicolas Bernard, associate Professor at University of Nantes, and Prof. Sami Hlioui, professor at CY Cergy Paris University, for accepting to chair the jury and for their constructive comments that helped me to improve the quality of my dissertation. I would like to extend my gratitude to the other two thesis committee members, Prof. Noureddine Takorabet, professor at University of Lorraine, and Dr. Mohammed Ali Benhamida, electric machine design engineer at Somfy, for their time to review my thesis and their insight comments.

Special gratitude goes to Normandy region for the financial support of this research work.

I would like to thank Dr. Mohammed Ali Benhamida and Dr. Salim Asfirane for their valuable support and advice for fulfilling this work.

Acknowledgement go to staff and engineer of GREAH and UFR-ST Université Le Havre Normandie, especially Mme. Julie Roger and M. Eric Lemains. I would like also to thank all my colleagues in GREAH LOMC for providing me a great environment for work.

My thanks also go to Sara Rachidi and Amel Fares, for their friendship and encouragement. I am thankful to my friends Louiza Oudni and Salima Imoudache for their sincere friendship and support. They have always been a source of comfort and confidence for me.

I would like to acknowledge the commitment, the sacrifice and the support of my parents. My sincere thanks also goes to my family, especially my lovely sisters, Asma and Nour el houda, and brothers, Ibrahim and Ilyes, for their support and love.

Last but not least, I am deeply grateful to my beloved husband, Tayeb, for his support, patience, tolerance and understanding.

Contents

List of Figures

List of Tables

General Introduction

This introductory section presents the background of the project.

Why Wind Turbines are Getting larger ?

To meet the rapid growth of the power generation, the current researches in wind energy are discussing the idea of upscaling the wind turbines. Large wind turbine leads to high net power rating and low average Levelized Cost Of Energy (LCOE)[5]. Indeed, with higher hub altitudes, the turbine captures stronger and more stable wind than the hubs in the small and medium turbines [42]. Furthermore, longer blades catch the wind more efficiently since the power generated by the wind turbine is proportional to the swept area. Then, the offshore wind turbine seems to be a good solution to increase the wind power exploitation with lower costs [43] [9].

What Are The New Challenges To Be Faced When Constructing Large Wind Turbines ?

Not surprisingly, the average size of offshore wind turbine is increasing over the last years. The increased interest in large wind turbine generates new technical and economical challenges. Upscaling a turbine without affecting the amount of material, including its mass, volume, and the construction's cost can prove quite challenging. In particular, the energy conversion system mass increases faster than the power rating; and thus, the drive train issues are of interest. Thus, it is interesting to consider the scaling effects on the nacelle, tower and foundations. In addition, while attempting to reduce the cost of the energy, multi-megawatts wind turbines must guarantee high availability, reliability and serviceability.

The cost of wind power is driven by technological advancements and consequently the world's policy addresses

[5]The LCOE is an indicator taking in consideration the capital cost, operation and maintenance costs (OM) and the annual energy production.

many technical and economic challenges in producing large wind turbines. The main challenges related to large wind generator:

- Upscaling the existing concepts of electrical machines might appear to be not beneficial. The resulting designs are too heavy and large, while the weight and size limits are a serious problem in the offshore transport and logistics. The cost of an electrical generator is directly related to its mass. Increasing the generator's diameter by 5 will rise the generator mass by 5^3, and that increases significantly the machine's cost (keeping all other parameters fixed).
- Rising the wind turbine generator power increases the complexity of their design, manufacturing, transportation and installation. In particular, mass raise of the rotor, nacelle and the tower present design challenge, especially in offshore environment, where many factors affects the deployment of wind turbine.
- In large turbine, the foundation must manage the dynamic movement and support of large and heavy tower, that dramatically increases the wind turbine cost especially in offshore.
- Therefore, new designs should be developed to address the challenges of marine conditions and reliability issues.

Why Direct-Drive Wind Turbines ?

The drive-train, which represents the direct link between the rotor shaft and the electrical generator, is subject of high dynamic loads (wind loads, electrical load). Therefore, considering the mechanical, structural and magnetic performances of the drive train is crucial in the design of reliable and efficient electrical generator [44] [45]. In the conventional wind turbines, most of the drive trains had gearbox and high-speed induction generator. In contrast, with the considerable increase on the average power of wind turbines, direct-drive low-speed generator are gaining increasing attention due to some technical and economic constraints.

As technology develops, offshore direct-drive large wind turbines (over 10 MW) are gaining popularity. Usually, gearboxes incur additional cost and potential failure. Despite the fact that gearbox failure is not the most common, it has high downtime [46] [47] [48]. Thus, a direct-coupled generator would improve the reliability and efficiency of wind turbine especially in the offshore environment. Although indirect-drive doubly-Fed-induction generator is the most common combination used in wind turbines, in large wind turbines over 10 MW, all the commercialized wind turbine are equipped with permanent magnet synchronous generator. Permanent magnet

synchronous machines offer low copper losses, and then high efficiency compared to the conventional induction machines (single/doubly-fed). The trends toward direct-drive permanent magnet synchronous generators are mainly due to their simplicity in terms of design and manufacturing and their capacity to enhance the heat removal. Indeed, large diameters of direct-drive machines allow the use of flat magnets, which simplify the manufacturing process. In addition, large diameters result on large cooling surface, so these machines can be built with natural cooling.

What Are The Challenges Related to Rare-Earth Permanent Magnets ?

The rare-earth elements (REE) permanent magnets, used in such huge electrical machines due to their superior magnetic performances, are considered to be one of the most resources critical raw materials. In 2019, the global rare-earth magnet production was estimated to be roughly 130.10^3 t, almost 95 per cent of this production was in China. This centralisation is mainly due to the lack of investment of the other countries, in the last decades. China has gained a monopoly position in the production of REE PM, and its difficult to compete with in a free market. The lack of supply chain diversity, the market competition, the flexibility against the supply shocks and supply chain transparency combined with the potential environmental and social impact of the extortion of these materials, induce significant price fluctuations of rare-earth materials. Hence, in order to address uncertainties in REE cost, reducing the use of these materials in the electrical machine is of primordial importance.

Thesis Goals and Objectives

Permanent magnet synchronous machines are considered a viable solution for ultra-large (over 10 MW) offshore wind turbines. To achieve high machine performances, considerable quantities of rare-earth permanent magnets with superior magnetic performance, such as Neodymium Iron Boron (NdFeB), are necessary. The significant price fluctuations of REE made reducing the use of magnets in the electrical machine of primordial importance. This could be done either by designing free-REE permanent magnet synchronous generator or by proposing some machine topologies that may reduce the mass of REE permanent magnet for the same power compared to the conventional generators. Therefore, it was of interest to examine other cheap, plentiful and more stable price permanent magnet materials such as Ferrite. Replacing NdFeB magnets by Ferrite magnets, having relatively poor magnetic properties, may require new rotor topologies. Indeed, the remanent flux of NdFeB

is good enough to give an acceptable flux density in the airgap with surface-mounted magnets, while Ferrites require a flux concentration to achieve acceptable airgap flux densities.

The aim of this work is to find the suitable generator for 15MW direct-drive wind turbine with high energy yield and low cost. In order to achieve that, the suitability assessment of some topologies and configurations was conducted. The different proposed generators are compared with a conventional surface mounted permanent magnet synchronous generator using NdFeb for the same power rating in terms of permanent magnet mass, machine mass, machine's cost, torque density and efficiency.

The objective of this thesis is to investigate a very broad spectrum of synchronous generators through optimal magneto-thermal design. In order to find the set of machine dimensions for the optimal configuration, inspecting a large design space with fast method is required. Then, multi-physic sizing tool for preliminary analysis of high-power low-speed permanent magnet synchronous generator was developed. Speeding up the first stages of electrical machines design with fairly accurate model has received substantial interest. In that stage, a compromise should be made between the computing time consumption and the accuracy of the models. However, reducing the design cycle time is an arduous computationally task since the relationships between the different parameters and the performances of the machine are mostly nonlinear and highly convoluted. In fact, satisfactory results could be obtained with less accurate model by making the appropriate assumptions.

Outline of the Thesis

This thesis consists of three distinctive parts and seven chapters. It is organized in the following manner:

General Introduction

Part I : Background & Literature Review The first part of this thesis is a literature review. It helps in evaluating the state-of-the-art in wind turbine generator technology and identifying opportunities for improvement.

Chapter 1 : Generator Systems for Wind Turbine

In this chapter the current state of wind energy technology is discussed, and an overview of the most common megawatts wind conversion system is provided. Several topologies and configurations of generators available commercially and those reported in literature are presented.

Chapter 2 : Electrical Generators for Large Wind Turbine: Trends and Challenges

This chapter reviews the state of the art of under-construction, existing and prototypes of drive-train and electrical generator used in large multi-megawatts wind turbine, it also discuses future development trends.

Part II : Multi-physic machine modelling The second part is concentrated on magneto-thermal modelling of electrical machines.

Chapter 3 : Assessment Criteria and Design Requirement of Direct Drive Wind Turbine Generators

The objective of this chapter is to select the suitable permanent magnet machine for high-power low-speed application. The main material choices and topology choices are presented. Further, the scaling laws that make it possible to estimate the size and the main geometrical dimensions of direct drive machine are given.

Chapter 4 : Magnetic Model

This chapter presents the electromagnetic modelling of the machine. To calculate the 2D magnetic field distribution two models were proposed (Analytical and semi-analytical one). Then, the results from both models are compared to finite element elements simulations for validation.

Chapter 5 : Thermal Model

In this chapter the lumped thermal model is developed. In order to validate the lumped model, 2D finite element models were created.

Part III : Optimization of Direct-drive Wind Turbine Generator

Chapter 6 : Design Optimization of Electrical Machine

This chapter discusses the basic principles of design optimization. The three important features that should be considered in electrical machines optimization process including optimization strategies, models and algorithms are presented and explained.

Chapter 7 : 15 MW Wind Generator Design - Optimization

This chapter aims to propose specific 15 MW generator to reduce the mass and cost of direct-drive wind turbine generators and improve their efficiencies.

Conclusions and Recommendations

This part concludes this thesis by summarizing the presented work. Recommendation and guidelines for further work are outlined.

Scientific Contributions

The main scientific contributions of this thesis are:

- Evaluating the state-of-the-art in wind turbine generator technology.
- Identifying opportunities for improvement (mass and cost) of high-power low-speed permanent magnet synchronous generator for large wind turbines.
- Integrating new optimization module in SIMUMSAP[6] software.

[6] An Analytical Design Tool for Permanent Magnet Electrical Machines already developed in GREAH laboratory [49].

Part I

BACKGROUND & LITERATURE REVIEW

Chapter 1

Generator Systems for Wind Turbine

1.1 Introduction

With the considerable growth of the global wind power capacity, several wind turbine concepts have been developed. This chapter provides an overview of drive-train configurations for megawatts wind turbines. In section 1.2, the current status of wind energy is presented. The section 1.3 covers the basis of wind energy power in order to establish a context for understanding the contemporary wind energy industry. The the last section 1.4, reviews the state of the art of the wind turbine drive-train technology.

1.2 Overview On The Global Wind Energy Development

Pushed by the energy crisis of 1970, the renewable energy sector became a major area of interest for both industrialized countries (China, US, Germany, etc.) and private companies. At the universal scale, the Paris agreement in November 2016, which aims to hold the increase of the global average temperature below $2°C$, started to affect the renewable energy targets by creating new global challenges. Therefore, other interlinked areas were impacted by this greatly step towards green power such as environment, economy and technical development, dealing with the collection of the energy, the cost of the conversion systems (Design, installation, maintenance, and supervision) and the conception of an optimal efficient systems. Then, many solutions were proposed to ensure a reliable decarbonized energy sector, that derived from natural processes, at the same time, secure and with affordable costs; through a seamless and successful energy transition.

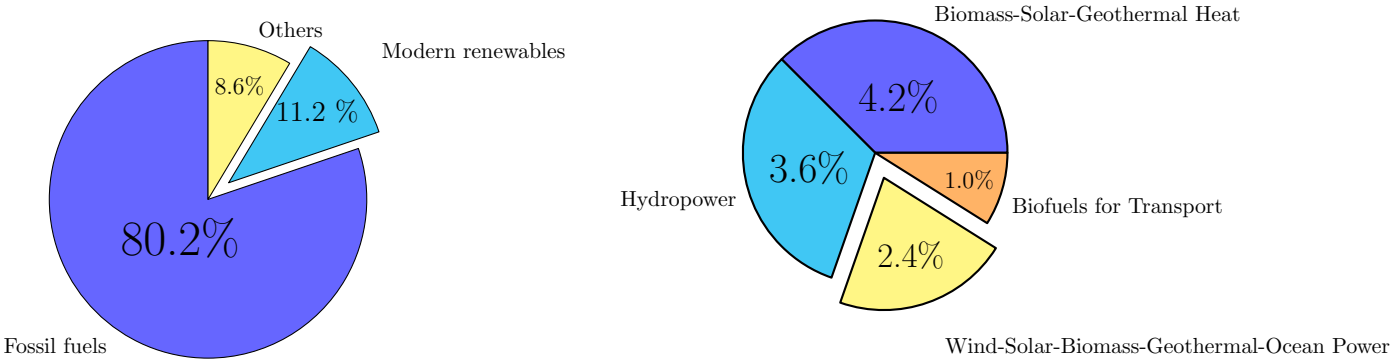

(a) Energy share of global final energy consumption in 2019

(b) Breakdown of modern renewables in the energy mix

Figure 1.1: Global share of renewable energy [1]

As it can be seen from the diagram in Fig. 1.1a, the fossil fuels energy consumption, which remained steady for many years, is the most common type of energy converted to final power in the world on 2019 with almost 80 per cent of the total final energy consumption. We can notice that the modern renewable energy (including: geothermal, solar heat, hydro-power, bio-fuels for transport, wind and solar) totaled 11.2 per cent in 2019, with slight increase from 2015. Despite all the governments and industrials efforts the oil, coal and natural gas remains the world's dominant final energy source. Nevertheless, by the end of 2050, renewable energy is estimated to produce more than the half of the world's electricity.

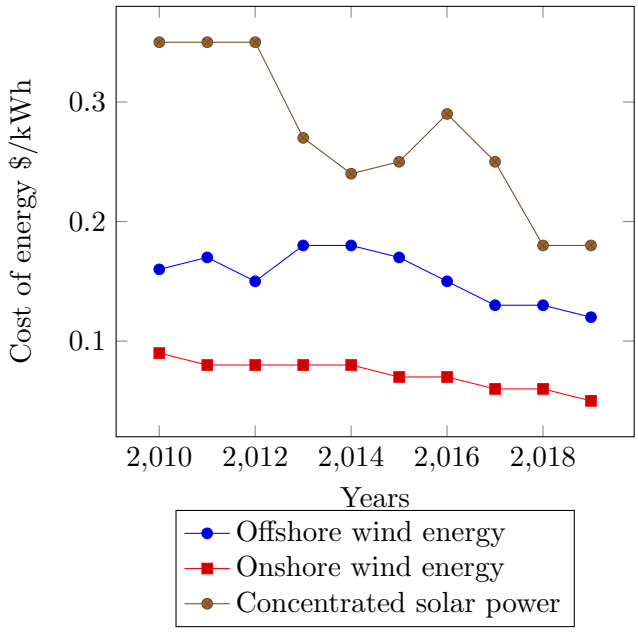

Figure 1.2: Levelized cost of electricity by technology[1] [2]

From 2015 to 2019, global renewable energy generation capacity was continuously increasing. The latest available data shows growth of 176 GW in 2019 [50]. At the end of 2020, the global annual renewable generation capacity reached nearly 2800 GW [51]. Although the hydro-power accounted for the largest installed renewable energy in 2020 with 20 GW rises compared to 2019 [51], the solar and wind energy continue to lead renewable generation capacity expansion with an augmentation of 126 GW and 111 GW, respectively [51]. The renewable energies are progressing significantly due to the reduction in costs, which is a normal consequence of the tremendous potential offered by those energies, and the ever-increasing awareness of the importance of such kind of energies (policy development, supporting mechanisms). Many countries try to widen geographical support of some renewable energies to meet the rapid rise on the electricity demand and moderate the cost of energy, wind energy seems to be the most competitive way to clean energy generation. Solar power faces limitation since it's linked to region's specifications. In addition, hydro-power energy is considered to be fully developed [52]. The wind power is the second largest renewable energy, behind hydro-power energy. Its market is increasing all over the world, it shows one of its largest annual increase in 2020 although the Covid-19 sanitary crisis. Further, over the last decade (2010—2019), the cost of the Kilowatt-hour (kWh) for onshore and offshore has declined about 40 per centand 30 per cent, respectively [53]. The global Levelized Cost Of Electricity (LCOE) from onshore wind has driven down by 10 per cent from the second half of 2018 to the same period in 2019, which is nearly 50 per cent lower than in the second half of 2009 (See Fig. 6.2) . For offshore wind, the global LCOE plunged by 60 per cent in 7 years, from nearly 230 $ per MWh on the second half of 2012 to 78$ per MWh in 2019 [2]. The LCOE depends not only on the project cost (e.g., costs of development, construction, equipment, operation and maintenance) but also on the wind resources, however, it varies greatly by country, by region and by farm. The improvements in wind turbine technology (e.g., higher capacity factor, higher efficiency, reduced cost of manufacturing, lower operations and maintenance costs) and the downward trend in the cost of the wind energy generated new wind markets. The statistics show that the biggest companies, that invest in renewable energy, concentrate on wind energy, Fig. 6.9 illustrates how investment in wind energy over the other renewable energy technologies.

The global new installed wind capacity expanded by 53 per cent growth in 2020 (86.9 GW in onshore and 6.1 GW in offshore) compared to 2019 [3] (See Fig. 6.11), and bringing the total installed capacity to 743 GW. Asia Pacific, as the largest regional market thanks to China, accounted for 60 per cent of the global new installations at the end of 2020 [3]. It is followed by North America, Europe, Latin America and Africa &

[1]Data source: UNEP, Frankfurst School-UNEP Centre, BloombergNEF
[2]Data source: UNEP, Frankfurst School-UNEP Centre, BloombergNEF

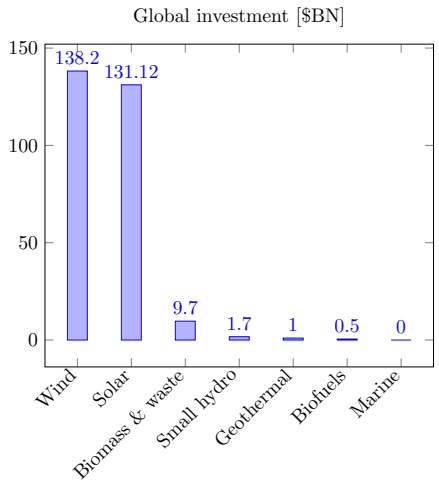

Figure 1.3: Global investment in renewable energy [2][2]

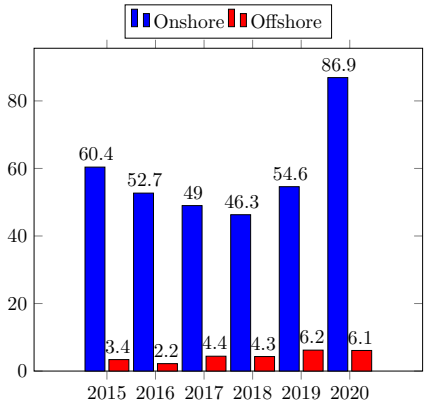

Figure 1.4: Global new installed wind power capacity [3]

middle East with 18 per cent, 16 per cent, 5 per cent, and 1 per cent of the additional wind capacity (See Fig. 6.10) [3], respectively.

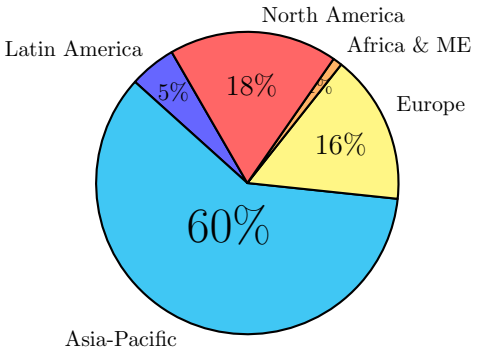

(a) By region

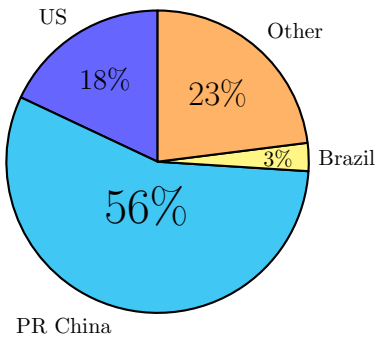

(b) By top markets

Figure 1.5: Global added wind energy capacity in 2020 [3]

1.2.1 Onshore

Sinking on prices of wind turbines have lessen the cost of the onshore energy, while up-scaling the wind conversion system has boosted the capacity factor[3] from 27 per cent (in 2010) to 36 per cent (in 2019) at the same time as operation and maintenance costs have fallen [53]. The global wind industry has been witnessing a growing in average wind turbine size. The largest averages power rating were in Morocco with 4.2 MW

[3]The capacity factor represents the energy output from a wind farm on an annual basis as a percentage of the farms maximum output and is predominantly determined by two factors: the quality of the wind resources where the wind farm is sited; and the turbine and balance-of-plant technology used.

followed by Finland and Norway with almost 4.2 MW and 3.8 MW respectively [54].

1.2.2 Offshore

Offshore wind power generation is one of the most promising technologies not only to rise the power generation with acceptable cost, but also to manage the public resistance due to the visual pollution. It is expected that offshore wind will keep expending in future years [55]. As the graph in Fig. 6.2 shows, although the considerable decrease on the price of the offshore wind energy, due to the fell on the installation cost (18 per cent from 2010 to 2019) and on the operation and cost of maintenance with the large power wind turbines, is still having higher costs than onshore wind. Nearshore technology could decrease considerable the price of the offshore wind energy, due to the facilities related to the depth, the distance to the connection point and the interventions [56]. Therefore, locating the wind farm in the nearshore up to 15 km off the coast could result in significant savings in the cost of wind energy [55]. The highest average per unit capacity of newly installed turbines in offshore were in Belgium and Portugal with 8.4 MW followed then by Denmark with 8.3 MW [54].

1.2.3 Wind power market by region: status and trends analysis

1.2.3.1 Asia

Over the last decade, Asia was the largest wind power regional market. Although slight marked reduction on the annual installed shared capacity in 2019 compared to 2018, it accounted more than 292 GW cumulative wind energy [54]. China, the huge market globally, which accounted for 42.8 per cent of the new wind installations in the world, remained its lead with more than 86 per cent of the Asian market. However, India, Turkey, Japan, and south Korea made some favorable signs on the horizon. By the supporting the research on the wind systems technologies (Smart control technology of wind turbine, key technologies of intelligent operation and maintenance of large-scale wind farm) China is expected to expand its cumulative wind energy.

1.2.3.2 Europe

Over the last decade, Europe was home to the largest offshore wind energy generation, with nearly three quarters of the global capacity. Also Europe, with the second spot in the world annual new capacity of wind energy, installed 14.7 GW in 2020 and bring its market share to 219.5 GW (194.5 GW onshore and 25 offshore)

[4]. However, approximately 71 per cent (10.5 GW) of this capacity were implemented on the European Union EU[4], specifically Netherlands added more than 13 per cent (1.9 GW) in the European wind capacity, which allowed it to reached more than 6.8 GW cumulative capacity, followed by Germany (1.6 GW), Norway (1.5 GW), Spain (1.4 GW) and France (1.3 GW) [4] (See Fig. 1.6b). Although the steep fall in the German annual added installations, it is largest market in terms of cumulative wind energy in EU with 63 GW, followed by Spain (27 GW), France (18 GW) and Italy (11 GW) (See Fig. 1.6a). Also, Germany joined the international competition with China and USA[5] as the first European leader in term of cumulative capacity [4].

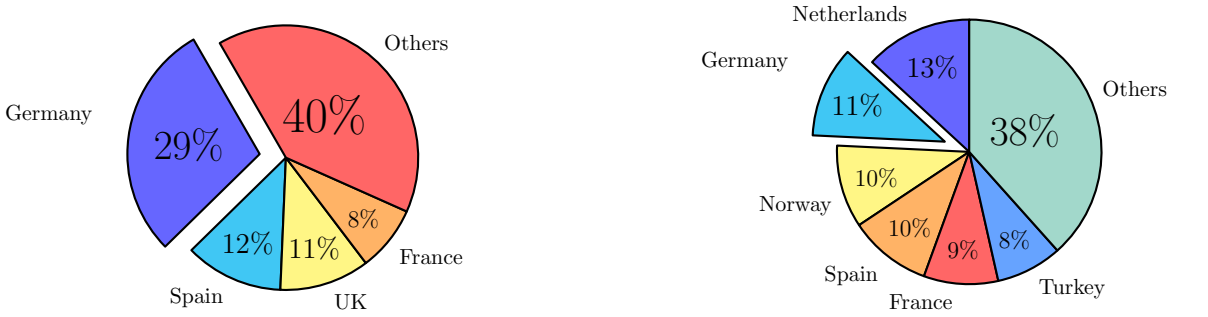

(a) Total installations

(b) New added installations

Figure 1.6: Wind energy capacity in Europe [4]

Furthermore, with the current wind energy production 417 TWh the wind energy covered 15 per cent of the EU's annual electricity consumption [4]. Although the wind German capacity is considerably higher than Danish one, but the later was, in 2020, is the EU's member with the highest penetration rate[6] (48 per cent) three times more than the European average (15 per cent). Thereby, with this elevated percentage, by 2021, wind power accounted for almost 50 per cent of Danish electricity market.

1.2.3.3 North and South America

The market of wind energy in the North America is completely different from that of the Latin America. While the North part (USA, Canada and Mexico) was in a stiff competition with Europe and Asia in the last five years, the south one is far from such considerations. By the end of 2020, American Wind energy capacity expanded 33.75 GW (21.75 GW onshore, 12 GW Offshore), bringing the total cumulative capacity to almost 211.75 GW. In 2020, more than 92 per cent of the American's wind capacity was spread across three countries the United States (164.27 GW), Brazil (17.75 GW) and Canada (13.58 GW) [3]. Thus, the USA

[4] 27 European Union countries UK
[5] Countries with cumulative wind power rate of more than 50 GW
[6] The percentage of demand covered by wind energy in a certain region normally on an annual basis

is the second largest market, after China, in the world in terms of wind power capacity, with 22 per cent. Moreover, according to the International Energy Agency IEA the USA department of Energy DOE is working in many projects to optimize wind design systems.

1.2.3.4 Middle east and Africa

According to the last report of GWEC global wind energy council. In 2020, the total new wind installation in Africa, Middle east was much lower than the global average with 0.8 GW, bringing the total regional capacity to 7.3 GW (South Africa (2.5 GW), Egypt (1.5 GW) and Morocco (1.3 GW) [54]. A significant majority (63 per cent [54]) of this capacity is added in South Africa. This capacity is nowhere near as experience as the others in Europe, Asia and America. Middle east and Africa are generally discussed for long time as ripe region to explore solar energy. Therefore, wind power does feature highly in the region's energy mix. In contrast, South of Africa and Morocco are embarking on a new era, by setting new and they are expected to expand their capacities by 3.2 GW over the next four years.

1.3 Wind Turbine Technologies

1.3.1 Aerodynamics of wind turbines

Wind turbines convert the kinetic energy first into rotational mechanical energy and then to electrical energy. A typical wind turbine is presented in Fig. 6.8. It could be divided into three main parts the tower, the rotor and the nacelle. The tower is the supporting structure of the wind turbine. The rotor, referring to the blades and the hub, transfers the mechanical energy to the nacelle. Depending on the rotor orientation, two types of wind turbines could be distinguished: Upwind and downwind (See Fig. 1.8). In the upwind machine, the rotor is facing the wind, whereas in the downwind machine, the rotor is placed on the lee side of the tower. The nacelle, which contains the electrical generator, the gearbox (if present), the controller and the brake, serve to convert the rotational energy form the rotor hub to the gearbox or the generator directly.

The total power delivered by the wind turbine differs with respect to wind speed and characteristic power performance curve of the wind turbine. The amount of the power extracted by the wind turbine is proportional to its swept area A $[m^2]$ ($A = \pi r^2$(r is the radius of the swept area and the blade's length)), the air density ρ_{air} (i.e. mass per unit of volume) in $[kg/m3]$ and to the cube of the wind velocity υ_{air} in $[m/s]$ reduced by

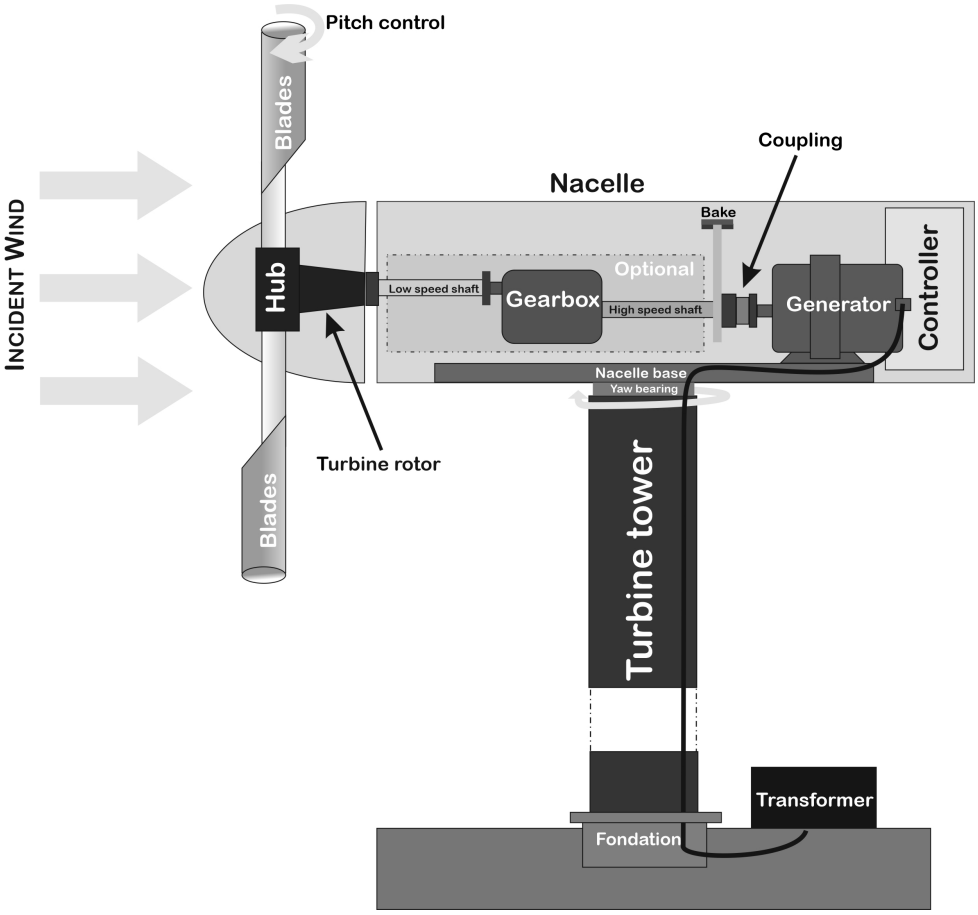

Figure 1.7: Wind turbine diagram

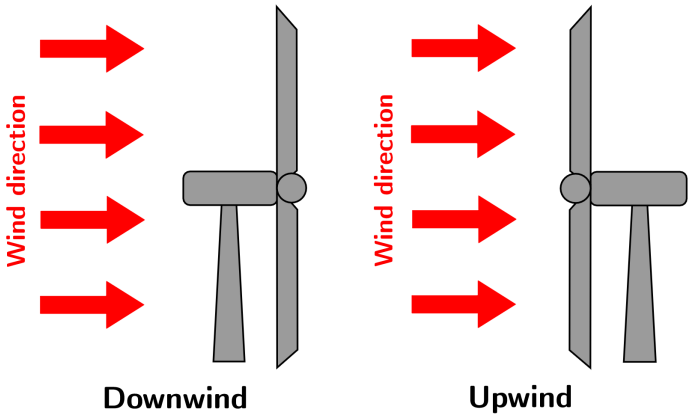

Figure 1.8: Upwind and downwind wind turbines

power coefficient C_p according to the formula

$$P_{turbine} = C_p(\beta, \lambda) \underbrace{\frac{1}{2}\rho_{air}(z) A v_{air}^3}_{P_{wind}} \tag{1.1}$$

where P_{wind} is the available power in wind $[W]$. It should be noted, that the air density varies as a function of temperature and pressure in compliance with perfect gas law. Since both pressure and temperature depend on the altitude above the sea level, the air density can be expressed by:

$$\rho_{air}(z) = \frac{P_0}{RT} e^{\frac{-gz}{RT}} \tag{1.2}$$

where P_0 standard sea level atmospheric density $(1.225 kg.m^{-3})$;

R specific gas constant for air $(287.05 J.kg^{-1}.K^{-1})$;

g gravity constant $(9.81 m.s^{-2})$;

T temperature (K);

z altitude above sea level (m).

The power coefficient represents the aerodynamic efficiency of the wind turbine, it is a measurement of how efficiently the wind turbine extracts the wind energy (in the airflow). This coefficient depends on the aerodynamic airfoil shape, chord length, blade length, and blade twist. Furthermore, the overall wind turbine efficiency depends on the aerodynamic, mechanical (gearbox, shaft bearing support) and electrical (generator, converter) efficiencies of the power conversion system.

The theoretical maximum value of this coefficient is defined by Betz's Law, which states that the maximum captured power by wind turbine could not exceed 16/27 (59.3 per cent) of the available wind power wind [57] (See Fig. 1.9), but usually C_p is less than 45 per cent due to the aerodynamic losses. This significant reduction in the power coefficient is due to the presence of aerodynamic losses in the wind turbine systems such as the blade tips, blade roots, and wake losses [58]. Due to advances in technology, modern wind turbine is operating near to the theoretical limit. Further, C_p could be expressed as function of the tip speed ratio λ and the pitch angle β, the curve relating those coefficients could be best obtained from direct measurements of the turbine in operation [59]. The tip speed ratio (TSR), refers to the ratio between the rotor tip speed (linear speed of the rotor tip) and the wind speed:

$$\lambda = \frac{\omega_r r}{\upsilon} = \frac{\upsilon_r}{\upsilon} \tag{1.3}$$

where υ_r ($\upsilon_r = 2$) is rotor tip angular velocity $[rad/s]$, f is the blades frequency $[Hz]$, and υ_r rotational speed of the blades (speed of the blades ends). It is therefore essential to calculate the optimal tip speed in order to maximize the turbine's efficiency [60]. The shape and the number of the rotor blades are important factors in the choice of the TSR. Fig. 1.9 shows rotor power coefficient with respect to the tip speed ratio of a range of common wind turbine types.

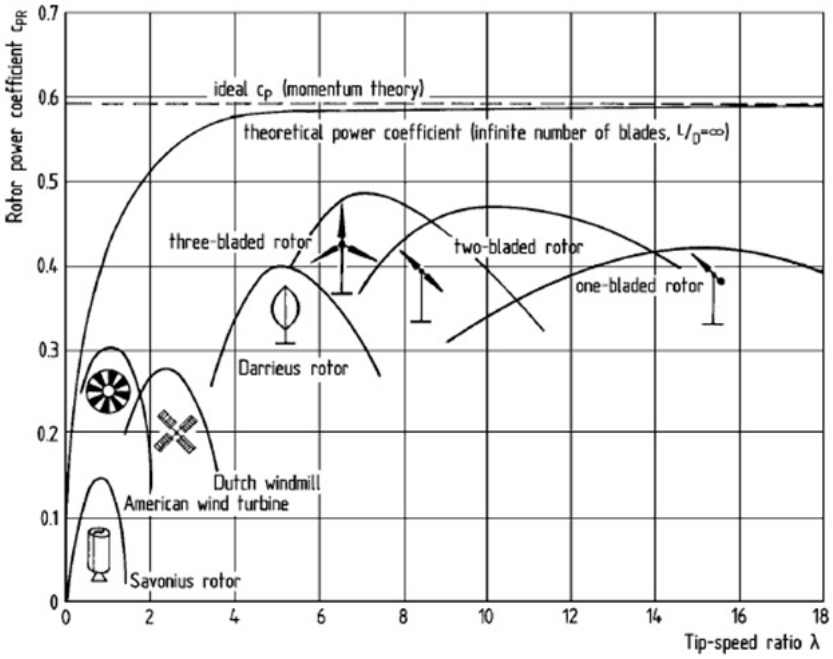

Figure 1.9: Power coefficient versus tip speed ratio of a class of wind turbine

In Fig. 6.12, an example of a power coefficient curve is shown ($600kW$ two blades upwind turbine, installed at national wind technology center in Golden (in Colorado) (Controls Advanced Research Turbine CART-2 installed in test site at the National Wind Technology Center (NWTC) in the US national renewable energy laboratory (NREL), this turbine was modified to be a state-of-the-art test for controls research [61]). The power coefficient depends on both the tip speed ratio and pitch angle; and thus, can be represented on three-dimensional surface. The characteristic surface in Fig. 6.12 illustrates the interrelationship between $C_{p-\lambda}$, for different values of pitch angle. For particular value of λ, the power coefficient increases with the decrease of β, and thus the maximum of the power coefficient is achieved for zero pitch angle (0 degree). However, Fig. 1.11 illustrates the power coefficient of (E-126 /7.5 MW) versus the wind speed for a given pitch angle, it can be

seen that the C_p increases with the increase in the tip speed ratio until it reaches its maximum at λ_{opt}, and then it starts to decline steadily with further increase in λ.

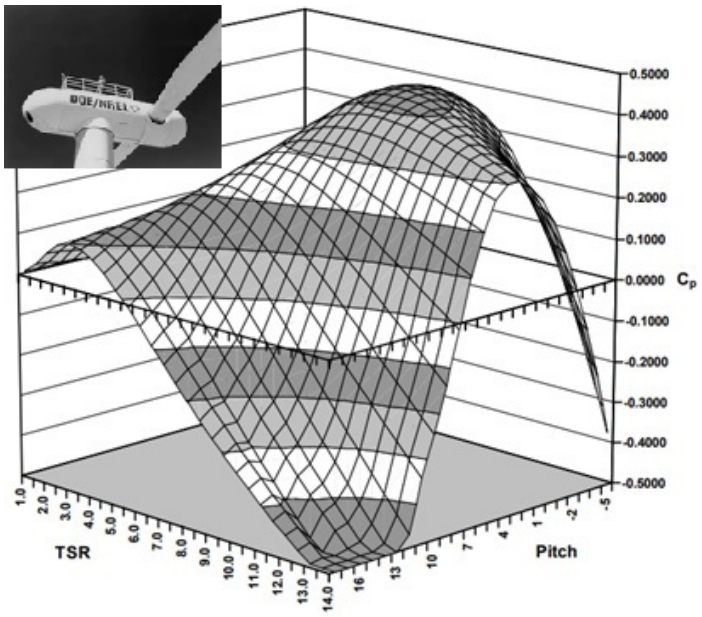

Figure 1.10: Power coefficient with respect to the pitch angle and tip speed ratio $C_p(\lambda, \beta)$ for two blades Horizontal-Axis Wind Turbine [5]

The efficiency of wind turbines depends on the wind speed, so it is not constant. Thus, the power curve could split into four operation regions with respect to the wind speed (See Fig. 1.11)

- Region I : when the wind speed is less than the threshold speed, the torque is insufficient to overcome the power loss (i.e. losses due to drag at the blade, frictions losses in the gearbox and in bearings, electrical losses with the generator); and thus no power is generated below the cut-in speed .

- Region II : (**variable speed region**) when the wind speed exceeds the cut-in speed (around 3-5 m/s depending the turbine design), there is a sufficient torque for rotation; and thus the turbine starts to generate electricity. In this operational mode, which accounted more than 50 per cent of the yearly energy capture for a typical modern wind turbine [62], the power produced by wind turbine increases proportional to the cubic power of the wind speed, as it is expected in Eq. 1.1. It could be noticed form Fig. 1.11 that the power curve reaches a peak around the so-called rated output speed (12-14 m/s). Above the rated output speed, the power generated remains unchanged at its permanently permissible maximum (known as rated power); it is kept almost constant by different control options. The pitch angle is usually controlled to keep the wind turbine operating at the peak of $C_{p_{TSR-Pitch}}$ surface [62],

and to limit the power when the speed exceeded the rated wind speed to avoid structural failure [63].

- Region III: (**constant speed region**) at which the wind speed is between rated speed and cut out speed (around 25 m/s). The rotor speed is held constant above the rated speed, by the regulation of the angle of attack. This ensures limited aerodynamic power in this region despite much more available wind energy.

- Region VI: when the wind speed exceeds the cut-out speed, the wind turbine is shut down.

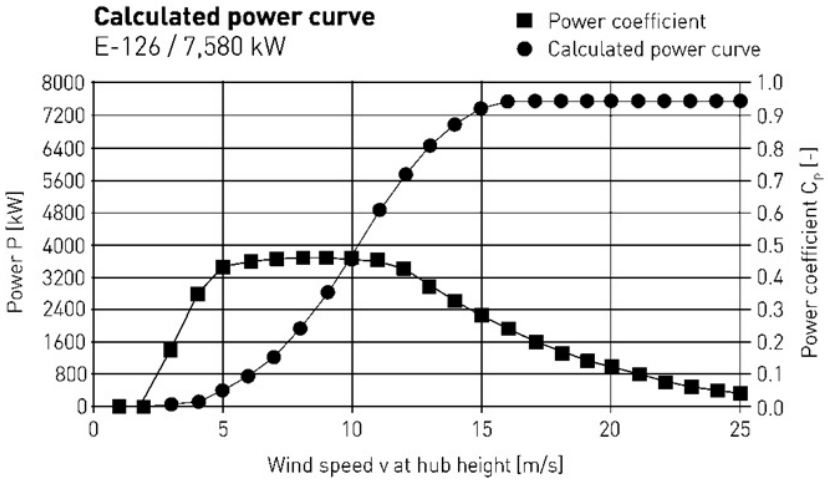

Figure 1.11: Power curve of $E-126/7.5MW$

1.3.2 Classification of wind turbines

Wind Turbine can be classified according to several criteria, the most common are shown in Fig. 1.12.

1.4 Wind Turbine Drive-train Technologies

The drive-train represents all rotating parts of wind turbine from the rotor hub to the generator, it included the gearbox, the generator and the power converter. The wind turbine drive-train convert the mechanical energy at rotor to electrical energy, and hence is subject of high dynamic loads (wind loads, electrical loads). Therefore, considering the mechanical, structural and magnetic performances of the drive train is crucial factor in the design of reliable and efficient electrical generator.

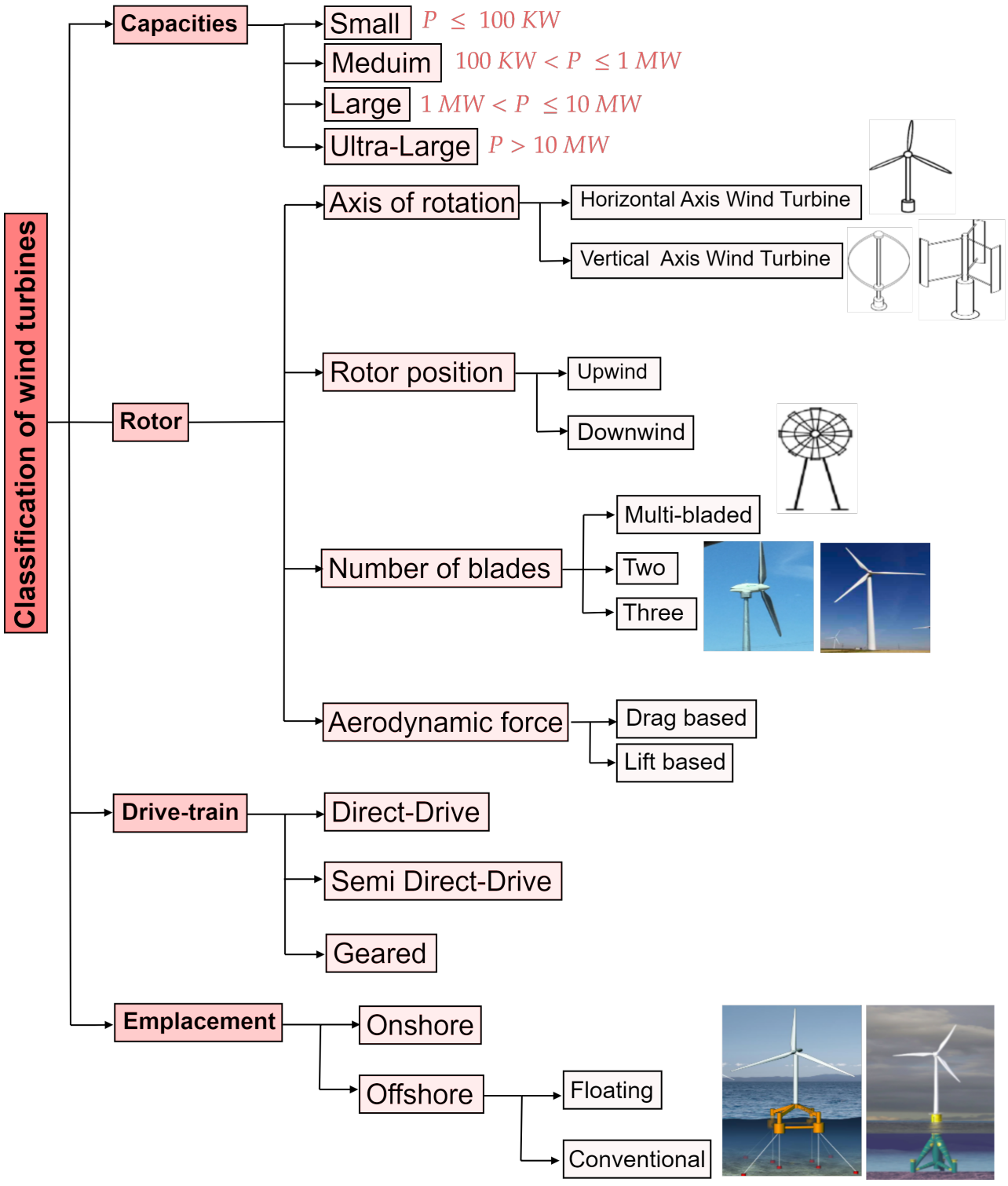

Figure 1.12: Classification of wind turbines

In the conventional wind turbines, most of the drive-trains had gearbox and high-speed induction generator. However, in recent years, direct-drive (without gearbox) have risen in popularity. According to the rotation speed, wind turbines can operate either at fixed or variable speed. While in fixed speed concept a multi-stage gearbox is often used, in variable speed concept the drive-train would either be geared (multi-stage or single-stage) or gearless (direct-drive). In the fixed-speed conversion speed, there is only one wind velocity on the turbine's power curve at which the tip-speed ratio is optimum. Therefore, unless the wind regime at particular site is highly peaked at that optimal wind speed, the wind turbine will generally be operating off of its optimum performance, and hence this system is aerodynamically less efficient. The variable speed drive-train can remedy this situation, since it operates over a wider range of wind speeds and can exhibit more efficient energy extraction at the lower wind speeds. Depending on turbine aerodynamics and wind regime, variable-speed wind turbine can collect up to $[10-15]$ per cent more annual energy and then, a considerable revenue increase over the lifetime of the turbine $[20-25]$ year. Each drive-train type is presented in this section with its specific advantages and disadvantages(efficiency, reliability, maintenance , etc.).

1.4.1 Fixed speed concept

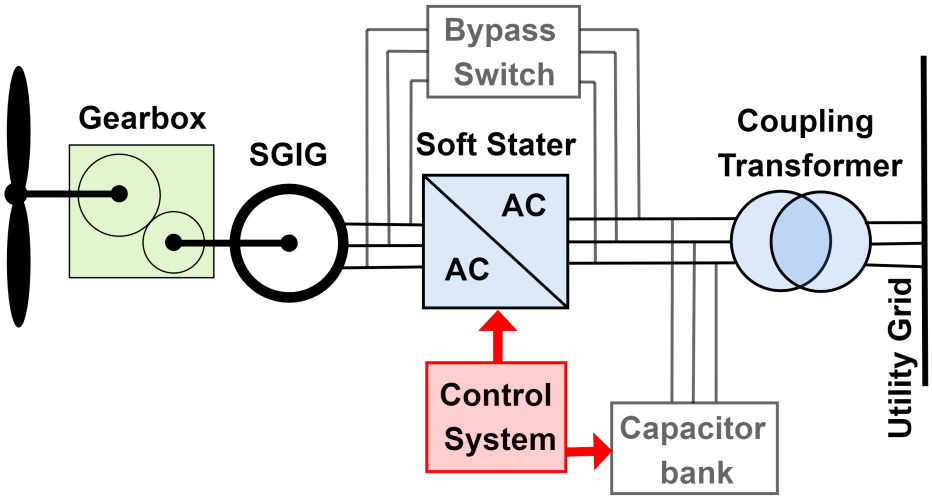

Figure 1.13: The block diagram of a constant-speed wind turbine using SGIG generator

Fixed-speed wind turbines, often also called Danish concept, were widely adopted in the early years of wind energy industry (1980-1990) due to their reliability, simplicity and low cost. In this configuration, a three-stage gearbox (the gear ratio is about 100) connected to a conventional squirrel-cage induction generator (operates often at around 1500 rpm [64]). Further, the generator is directly connected to the power network (50Hz or

60Hz) through a transformer (See Fig .6.14); and thus the wind turbine speed must be determined cautiously. The conversion system is designed so that the tip speed ratio is maximum around the average wind speed. The Squirrel Cage Induction Generator (SCIG) is the most suitable generator for this system. To enhance the performance of induction motor and limit the disturbances on the grid, a capacitor banks is introduced to compensate the reactive power consumed by the squirrel cage machine, while a soft starter is used to reduce the inrush starting current [65] [66]. Constant speed wind turbine operates at single imposed fixed speed, and that whatever the wind speed. This speed, which could vary slightly (1 per cent) [67], is function of the generator pole pairs number, the machine slip, and the gearbox ratio. When the wind speed increases beyond the level at which rated power was generated, power is limited aerodynamically either by stall or pitch control. Further, in this configuration, we usually have two fixed speeds; this could be achieved either by two generators with different ratings or by one generator with two winding configurations (pole-changeable squirrel cage induction generator) [68] [69].

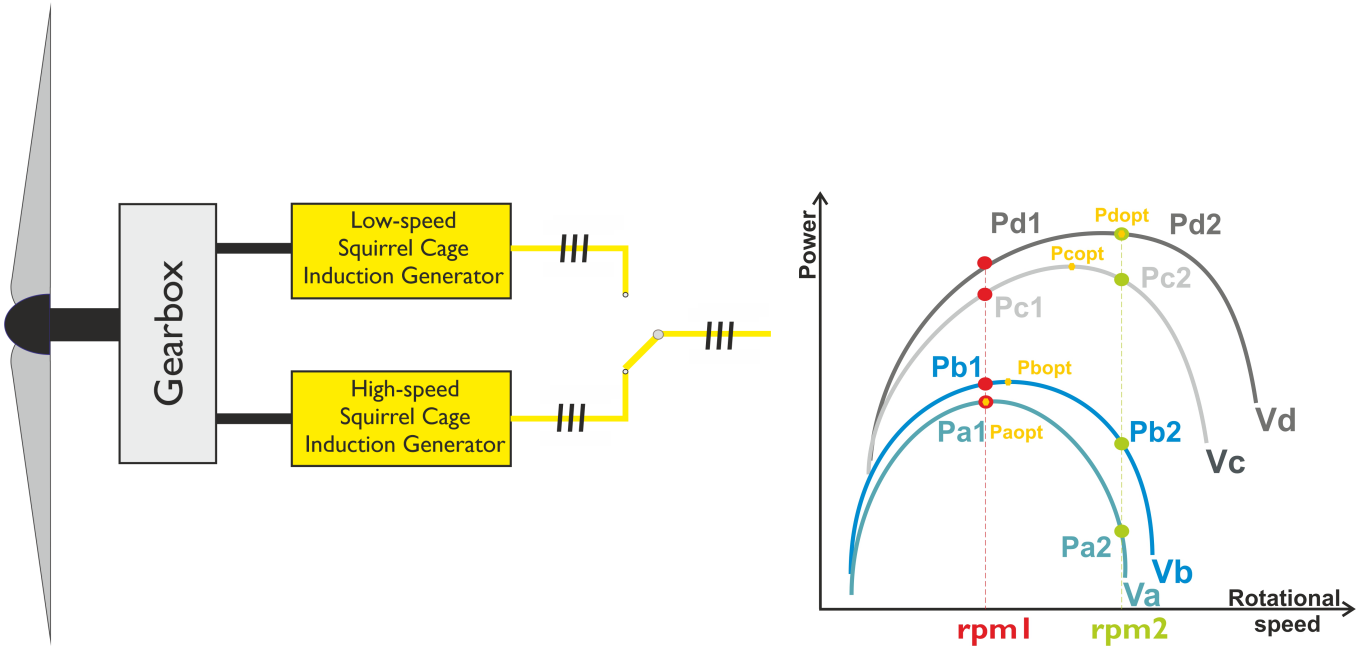

(a) Block diagram

(b) Power versus rotational speed

Figure 1.14: Dual-Speed Wind Turbine Generation

A wind turbine with fixed speed starts operating when the rotor's speed exceeded a certain rotational-speed threshold. However, by using two different induction generators (See Fig. 6.16), where the small generator operates around the rated power at low speed and the bigger one operates at higher speeds, the efficiency is improved at low power [68]. It can be seen in the power curve (see Fig. 6.15) that if the wind turbine is operated at high wind speed regions with relatively high rotational speed, it could operate near to its optimal power

coefficient C_p and hence maximize the energy conversion, but if it operates in low speeds ($< \Omega_1$) it is far from its maximal efficiency. However, using different generator sizes would higher the overall efficiency of the wind turbine. Unless the dual speed technology, the wind turbine will be often operating off its optimal performances due to the wind regime. The pole changeable technology is more common in wind power conversion system. Most of the wind turbine generators have four or six poles (1500/1000 rpm). Fig. 1.15 shows an example of dual-speed asynchronous generator (AGUA-400LX-64A, 600/150 kW, 4/6-poles with forced air-cooling).

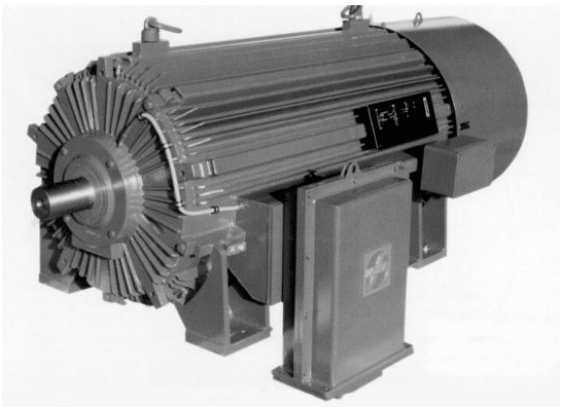

Figure 1.15: Flender two-speed asynchronous generator

The power is limited aerodynamically either by stall, active stall or by pitch control. Stall-control in combination with fixed-speed system is commonly used for small turbines, however with rated power over 1 MW an active-stall aerodynamic regulation is employed. Although pitch control is widely used with variable speed wind turbines, it is not common in constant speed one.

1.4.1.1 Advantages of the fixed speed concept

- Low initial price.
- Simple and robust.
- Reliable operation.

1.4.1.2 Limitation of the fixed speed concept

- Operate with maximum efficiency just four unique speed wind velocity on the turbine's power curve [70], corresponding to its designed TSR, so the wind turbine is usually operating off its optimum.

- Conversion efficiency cannot be optimized, just slight variations of the rotor shaft speed is allowed. The fixed speed wind conversion systems are around 10 percent less efficient than variable speed one.
- Turbulence of wind may cause torque pulsations, which affect not only the power quality but also the mechanical stress [71] [72]. The fluctuation on the transmitted power could reach 20 per cent of the nominal power [73].
- Low efficiency and reliability due to the presence of the gearbox.

1.4.1.3 Examples

Examples of fixed speed megawatts wind turbines are presented in Table **??**.

1.4.2 Limited variable speed concept

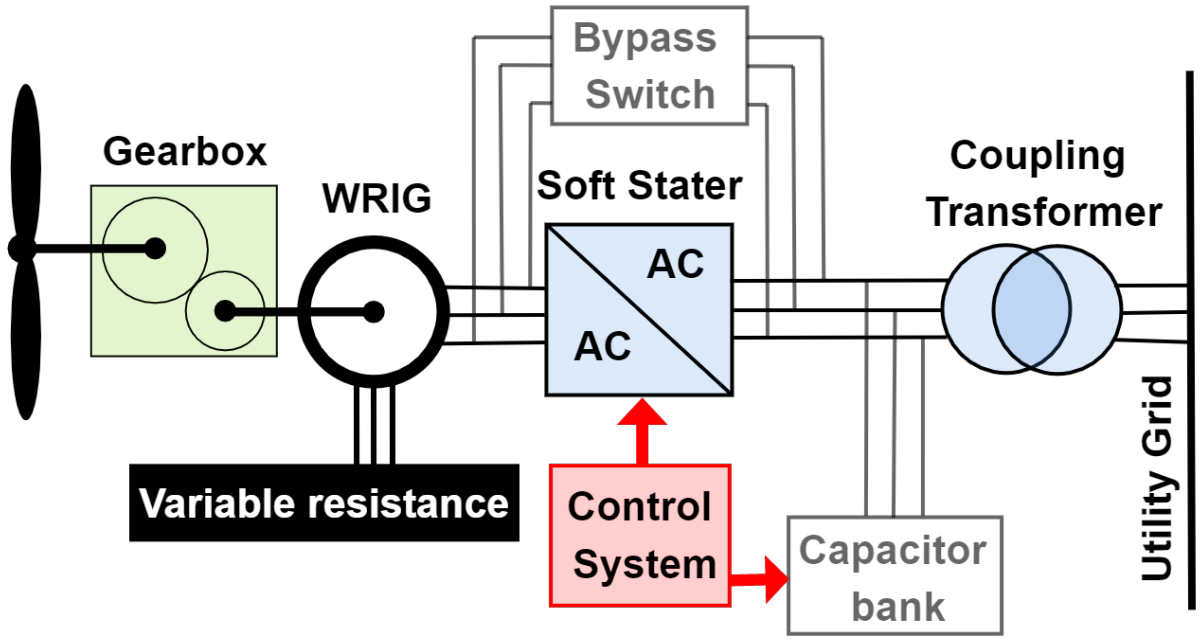

Figure 1.16: The block diagram of a limited variable-speed wind turbine using WRIG

The limited-variable speed wind turbine concept with variable rotor resistance (±10 per cent) conversion system, also known as variable-slip, OptiSlip, dynamic rotor resistance concept or partial-variable speed [74], is an ameliorate version of fixed-speed system. The wind turbine with such power conversion system can operate over a range of rotor speeds and hence it helps to counter the varying nature of the wind speed, this

can be done by using Rotor Current Controller (RCC). This configuration has been introduced the first time by the Danish manufacturer Vesta, it uses a wound rotor induction generator as presented in Fig. 6.17. While the stator of the generator is connected directly to the grid, the rotor windings are connected to variable resistance bank via brushes and slip rings. The resistor blank, controlled by power electronics, enables controlling the rotor's circulating current and therefore adjusting the generator speed. However, increasing the slip by rising the rotor's winding resistance, will increase the power extracted. Therefore, the variable speed range of the induction generator is limited by the size of the rotor resistors [71], it is possible to achieve a range of 0-10 per cent above the synchronous speed [75]. This concept not only offers a higher control flexibility but also allows to extract more energy compared to the fixed-speed concept. Nevertheless, there is still a lack of capacity regarding the electrical losses (heat in rotor resistance) and the power quality. In order to enhance the efficiency of the system and avoid the costly slip rings, optical coupling could be use [76].

1.4.2.1 Advantages of limited variable speed concept

- Higher efficiency compared with fixed-speed concept.
- Decrease the maintenance cost requirement.

1.4.2.2 Limitation of limited variable speed concept

- High electrical losses (heat in rotor resistance).
- limited speed operation ($\pm$10 per cent).

1.4.3 Variable speed concept

Variable speed concept enable the rotor blades to operate at its optimal TSR by adapting its rotation speed to the wind speed (See Fig. 6.4), so that more wind power is extracted. Further, adapting the rotation speed of the rotor to the wind speed not only increases the efficiency of the drive-train but also helps to absorb power fluctuation caused by the turbulence of the wind. The speed of the generator can be regulated by interposing a frequency converter between the generator and the grid. The speed range around the synchronous speed is nearly the same as the power through the converter. Therefore, variable speed wind turbine concept can be

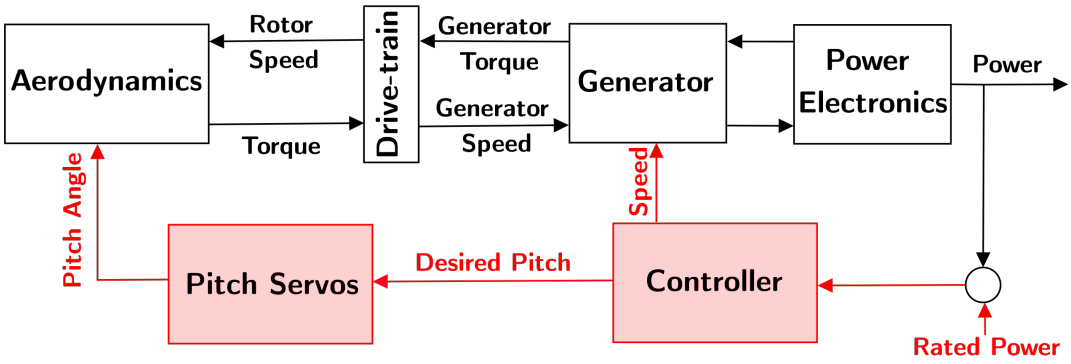

Figure 1.17: Flowchart of variable speed variable-pitch wind turbine

classified into two categories based on the power rating of the converter: the partially-rated converter-based system (limited range variable speed) and the fully-rated converter-based system (wide range variable speed).

1.4.3.1 Variable speed with partial scale frequency converter concept (± 30 per cent)

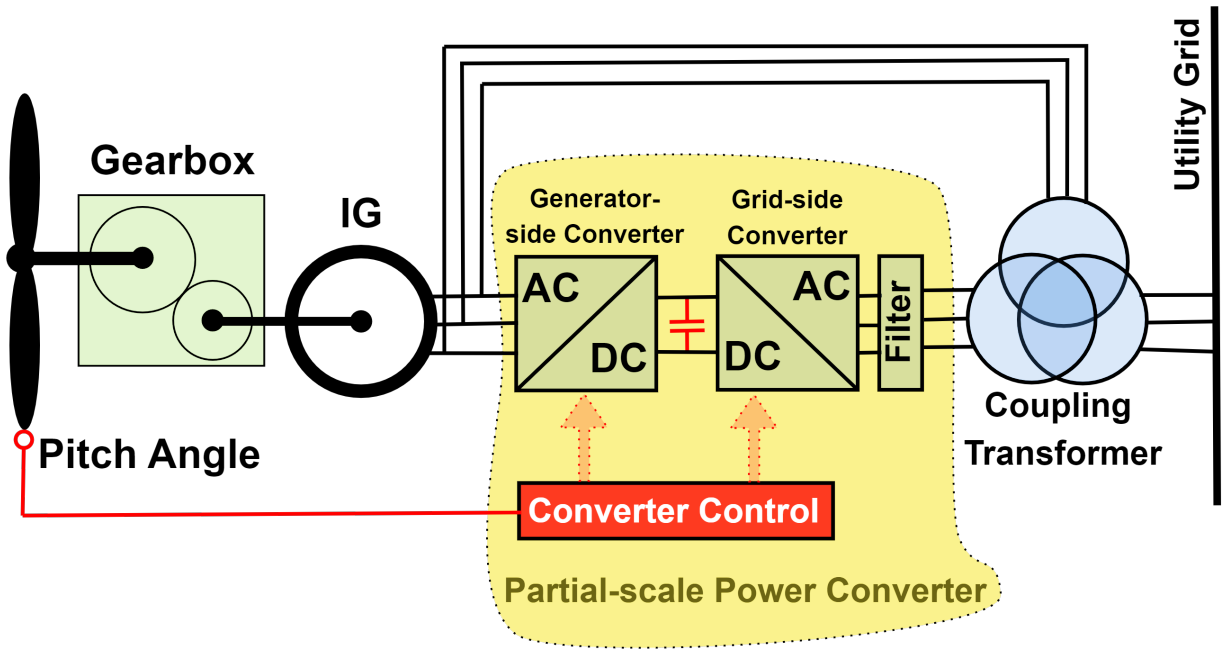

Figure 1.18: The block diagram of a variable-speed with partial scale converter wind turbine using IG

This configuration, known as the doubly fed induction generator (DFIG) concept, has become popular in commercial wind turbines and it is likely one of the dominant wind turbine systems. It consists on wound rotor induction machine coupled with a gearbox (three/four-stage) in one side and a partial scale frequency

Table 1.2: Example of multi-megawatt variable speed with partial scale frequency converter wind turbine concept

Wind Turbine		Gearbox		Generator	
Reference Manufacturer	Rated power [MW]	Stages	Gear ratio	Type	Voltage [V]
N149/4.5 Nordex	4.5	3	1:113.5	DFIG	660
SG 5.0-145 Siemens	5.0	3	1:128.7	DFIG	690
SL 6000/155 Sinovel	6	3		DFIG	6300
UP 6000/136 United Power	6			DFIG	6600
6.2M-152 Repower	6.2	3	1:116	DFIG	6600/660

converter in the other side. The DFIG generators deliver power to the grid through both the rotor and stator. While the stator of the induction generator is connected directly to the grid (50 Hz), the rotor is connected through slip rings and brushes to partial-scale converter (AC/DC/AC converter) and then to the grid, which controls the rotor speed and frequency. A common speed range of ±30 per cent [75], gives a power converter rated 30 per cent of generator power. The converter not only performs the reactive power compensation but also ensures smother grid connection. As it can be noticed, this configuration offers wider speed range compared with Optislip concept. Table 6.2 shows some examples of this concept in Megawatt wind turbines.

1.4.3.1.1 Advantages of the partial scale frequency converter concept

- Decoupled active and reactive output power control (due to the use of flux-vector control of the rotor current).
- Enhance the aerodynamic efficiency over a range of wind speeds compared to the fixed speed concept.
- Soft starter and reactive power compensator.
- Only a part of the power goes through the converter and hence small/cheap converter (with lower losses) is needed.
- Lower losses mainly due to the reduction on the stator losses (the stator current is nearly 30 per cent lower) since only two-third of the rated power passes through the stator.
- Less variation in the power output.

1.4.3.1.2 Limitation of the partial scale frequency converter concept

- Regular maintenance, audible noise and heat dissipation due to the presence of the gearbox.
- Complex converter control [77].
- Limited speed variation.
- Higher maintenance costs due to the present of slip rings and brushes (The average life time of DFIG brushes is $6 \sim 12$ months).
- High overall wind turbine cost due to the use of the gearbox (including both manufacturing and regular maintenance cost).

1.4.3.2 Variable speed with full scale frequency converter concept

While in constant-speed and semi-variable wind turbines the rotational speed of rotor is assumed to be constant or with slight variations for all wind speeds, in variable-speed concept, the rotor is allowed to rotate proportionally to wind speed. This speed flexibility helps to extract more power by optimal energy conversion system. In the full scale frequency converter concept (full variable speed) the wind turbine the converter, connecting the generator's stator to the grid, must handle all the energy supplied to the grid. Therefore, the power extracted is fully managed and transferred to the grid using the converter (speed range of up to $100-120$ per cent) and the conversion system is completely uncoupled from grid frequency. While the machine-side of the power converter can provide the generator torque and velocity control, the grid-side can perform reactive power delivered to the grid. There are two types of variable speed wind conversion system with full converter based on the rotation speed of the generator. In first concept the generator is connected to the shaft though a gearbox (high-speed), whereas in the second concept it is connected directly to the shaft (low-speed). For large scale wind turbines the direct drive-train is by far the most common commercialized concept, this configuration gets rid of the gearbox and use either Electrically Excited Synchronous Generator (EESG) or Permanent Magnet Synchronous Generator (PMSG).

1.4.3.2.1 Indirect drive-train (high-speed)

1.4.3.2.1.1 SCIG system with three-stage gearbox In 1990, stator-controlled SCIG had been introduced the first time in the wind energy conversion system by the US company Kenetech [6]. Unlike fixed-speed

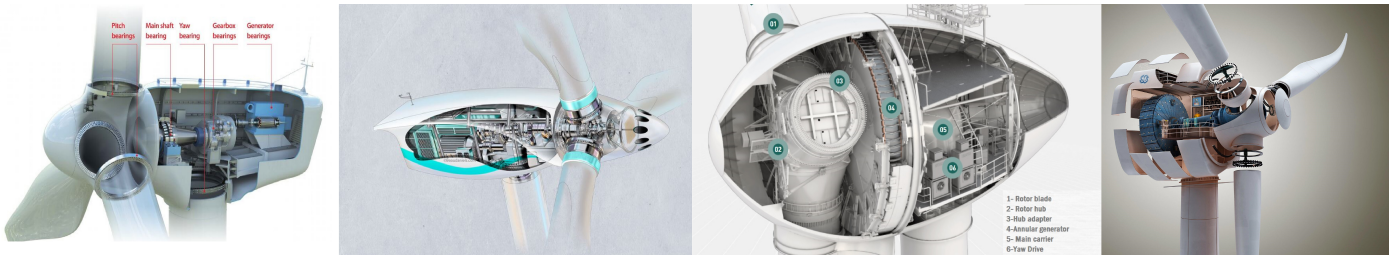

(a) Geared wind Turbine (b) Gearless wind Turbine

Figure 1.19: Comparison of indirect and direct drive-train wind turbine

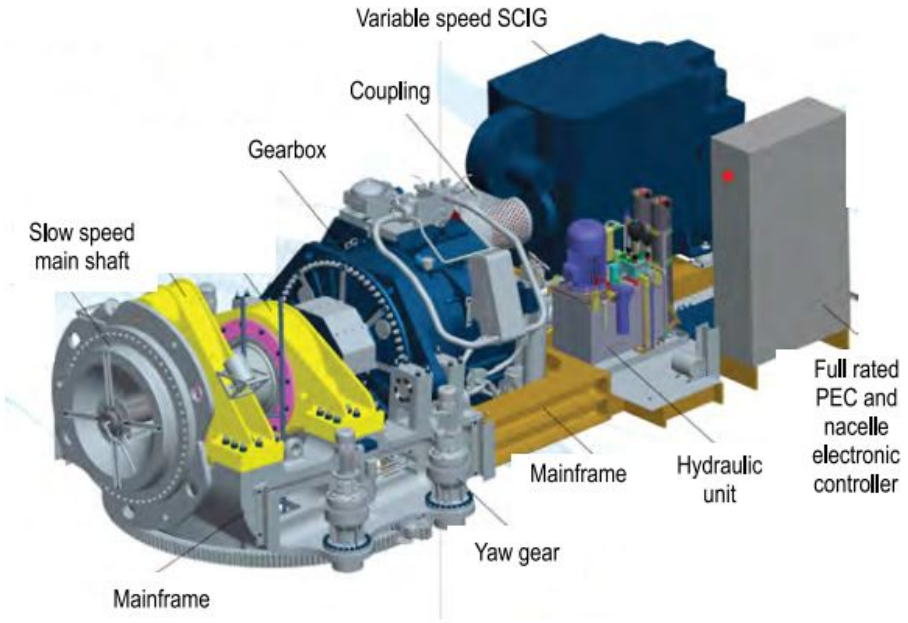

Figure 1.20: Variable-speed full scale converter SCIG-based drive-train driven by gearbox (PS-1800) [6]

SCIG the stator of the machine is connected to the grid through a converter. The converter decoupled the frequency between the machine and the grid, it has to be disgned for full load. An example for such concept was proposed by RRBEnergy for its PS-1800 (1.8 MW) wind turbine (Fig. 6.3) and an other by Siemens SWT-3.6-120 (3.6 MW) (more details are given in Table 6.3). The control of the SCIG can be achieved by simple scalar control, so that the converter is relatively simple. Nevertheless, the presence of full-scale converter causes extra losses and thereby decreasing the efficiency of the system.

1.4.3.2.1.2 PMSG/EESG system with three-stage gearbox In this configuration a high-speed Synchronous Generator SG) is connected to the grid through a frequency converter and hence the conversion system can operate at full speed range. The use of the three-stage gearbox can dramatically decrease the size

Table 1.3: Example of multi-megawatt variable speed with full scale frequency converter wind turbine concept (SCIG system with three-stage gearbox)

Wind Turbine		Gearbox		Generator	
Reference/Manufacturer	Rated power [MW]	Stages	Gear ratio	Type	Voltage [V]
PS-1800 RRB Energy	1.8	3	1:61	SCIG	690
SWT-3.6-120 Siemens	3.6	3	1:119	SCIG	690
V 126-3.45 MW Vestas	3.45	3	1:125.16	SCIG	750

of the synchronous machine comparing with machines used in direct-drive conversion system. The rotor's flux in synchronous machines is created by using either Permanent Magnets (PMSG) or field winding (Electrically excited EESG). Further, PMSGs are more popular due to their high efficiency. However, the price of rare-earth permanent magnet material fluctuates sharply which made PMSG less competitive in terms of manufacturing cost. Compared to geared DFIG system, the geared PMSG concept require larger converter. Then the full-rated power converter become more expensive and present higher losses. Over the last decade, both advances in power electronics and the significant fall in the prices of power converter made the development of such system very attractive. Table 1.4 presents examples of such concept.

Table 1.4: Example of multi-megawatt variable speed with full scale frequency converter wind turbine concept (PMSG/EESG system with three-stage gearbox)

Wind Turbine		Gearbox		Generator	
Reference Manufacturer	Rated power [MW]	Stages	Gear ratio	Type	Voltage [V]
HS139-5.5MW Hyosung	5.5	3	1:93.3	PMSG	3300
aM 5.0/139 Aerovide	5.0	3		PMSG	690-3300
PowerWind 100 PowerWind	2.5	3	1:114	PMSG	690
eno 126 EnoEnergy	3.5	3	1:119	EESG	690

1.4.3.2.2 Direct drive-train (low-speed) In the direct drive wind turbines, the generator is directly connected to the rotor hub. Hence, it operates at low rotating speeds. The gearless drive-train presents many advantages over the geared one. First, eliminating the gearbox will not only increase the global efficiency significantly by decreasing the losses of the gearbox, but also reduce the need for operator intervention, which is costly and take long downtime. For instance, it has been reported in [78], that it is required to replace the gearbox four times over the 20-year design lifetime of the wind turbine. A large reduction on the need

for maintenance leads to a low cost of energy. In addition, by avoiding the premature failure of gearboxes, longer lifetime for both the drive-train and the wind turbine can be ensured and then the reliability of direct-drive systems is higher compared to indirect ones. Furthermore, with fewer moving parts and without the mechanical gear system, both the noise and the weight can be decreased. The drive-train can be shorted by integrating the outer-rotor of the generator to the hub (See Fig. 1.21). In order to maintain the tip speed

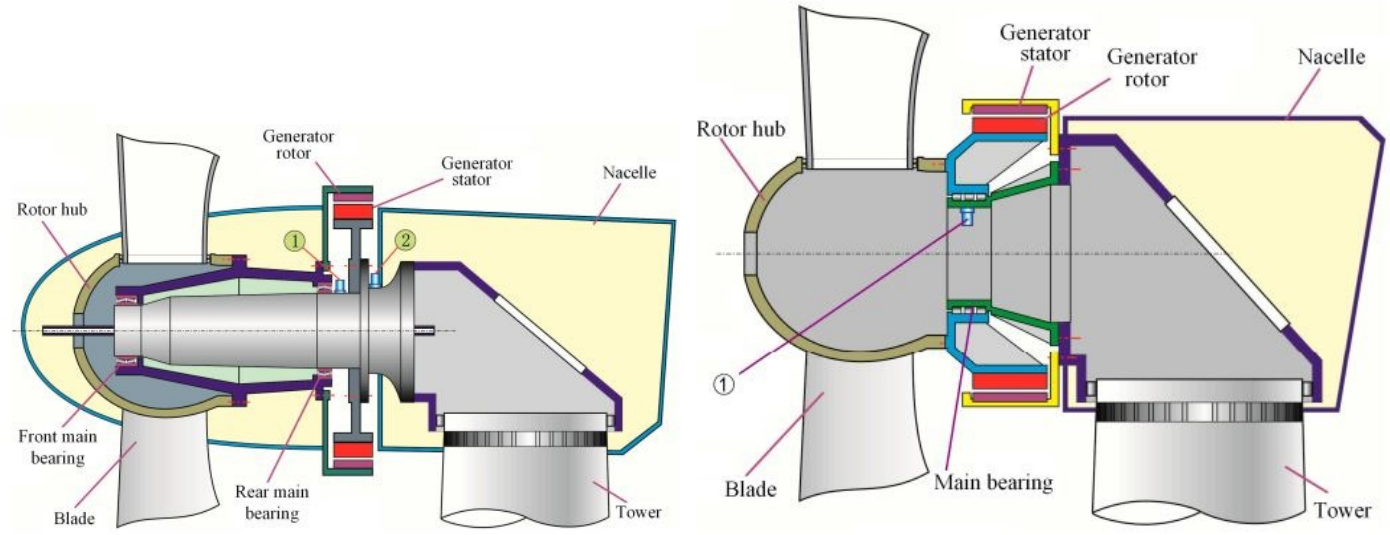

(a) external rotor (b) internal rotor

Figure 1.21: Comparison of wind turbine rotor concepts [79]

ratio at its optimum, continually adjustment of the rotational speed is required. Therefore, fully rated power converter is used to connect the generator to the utility grid. However, the design of high power converter is technologic and economical demanding task. Although additional losses introduced by the converter, the overall efficiency of the full-scaled converter direct-drive wind turbine is higher than the partial-scaled converter with induction generators. Even though direct-drive system present many advantages compared to the indirect-drive (simplicity, high overall efficiency, availability and reliability), the generator in this concept are usually larger, heavier and more expensive [80] [81] [16]. Various topologies of generators have been proposed for the direct-drive wind turbines. Each of them is discussed briefly in this section. A more detailed description of electrical machines (performances, topologies, etc) is presented in the next chapter, which is dedicated to low-speed high-power wind turbine drive-train .

1.4.3.2.2.1 Permanent-Magnet Synchronous Generator PMSG / Electrically Exited Synchronous Generator EESG Permanent-Magnet Synchronous Generator PMSG, with lower joule losses and reduced

mass compared to Electrically Exited Synchronous Generator EESG, are the most promising generators for multi-megawatt direct-drive wind turbines. In addition, the elimination of the external excitation and slip rings made the PMSGs more efficient and reliable than EESGs. By using PMSGs, small pitch poles may be allowed, and therefore PMSGs fitted to low-speed applications. On the other hand, EESGs do not require the use of permanent magnets, making this option really interesting if the price of the PM still unstable. Different topologies of PMSG have been investigated for large range of rated power.

Table 1.5: Example of multi-megawatt variable speed with full scale frequency converter direct-drive wind turbine concept (PMSG/EESG)

Wind Turbine		Generator	
Reference / Manufacturer	Rated Power [MW]	Type	Voltage [V]
Haliade-X GE	12	PMSG	3220
SG 10.0-200DD Siemens	11	PMSG	820
GW 171/6450 GoldWind	6.45	PMSG	720
E-126 Enercon	7.58	EESG	690
TWT 1.65-77 M.Torres	1.65	EESG	690

1.4.3.2.3 Semi-direct drive-train (mid-speed/Multibrid) In the semi-direct concept only single stage planetary gearbox (sometimes two-stages) is used with medium-speed PMSG, this configuration combines advantages of both geared and gear-less wind turbine conversion system. In this concept, the gear ratio is about only 10. A single-stage gearbox is lighter and more reliable than multi-stage one. In addition, unlike PMSG in direct-drive wind turbine, which require rather a large diameter generator, the PMSG in multibrid system is relatively smaller and cheaper. Both the generator and the gearbox have approximately the same size leading to more balanced drive-train arrangement [82]. Consequently, improved performances, structural economy and higher efficiency could be achieved.

1.4.3.2.3.1 PMSG/EESG system with single-stage This arrangement was first introduced by Areva and further promoted by Vestas, WinWinD, Adwen, Aerodyn and Guangdong Mingyang. Although most of large wind turbine manufacturers adopted medium-speed PMSG (See Table 6.3), Aerodyn with its SCD 8.0MW used an electrically exited synchronous generator (See Fig. 1.22). Table 6.3 shows examples of Semi-direct variable-speed Megawatt wind turbine.

(a) Areva Multibrid M5000 (5MW)

(b) Areva Multibrid M5000 (5MW) nacelle

(c) Adwen AD8-180 (8MW) Nacelle

(d) Adwen AD8-180 (8MW) gearbox

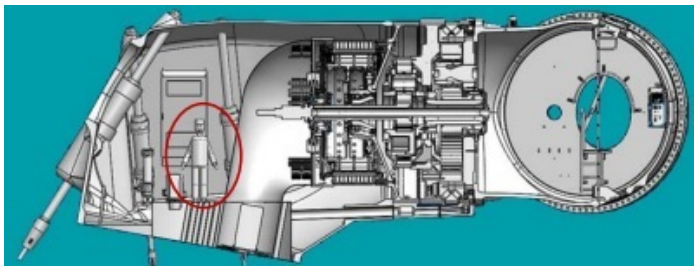

(e) SCD drive-train technology (8MW) Aerodyn

Figure 1.22: Multibrid wind turbines

Table 1.6: Example of multi-megawatt variable speed with full scale frequency converter wind turbine concept (PMS-G/EESG system with one/two-stage gearbox)

Wind Turbine		Gearbox		Generator	
Reference Manufacturer	Rated Power [MW]	Stages	Gear ratio	Type	Voltage [V]
M5000-116/135 Areva	5	1	1:10	PMSG	3300
WWD-3 D120 WinWinD	3	2		PMSG	690
G128/5000 Gamesa	5	2	1:41	PMSG	690
HTW5.2-136 Hitachi	5.2	2	1:40 (Approx.)	PMSG	33000
AD 8-180 Adwen	8	2	1:41	PMSG	6600
SCD 8.0MW Aerodyn	8	2	1:27	EESG	-
MySE7.25-158 Guangdong Mingyang	7.25	2	1:23.18	PMSG	690
V164-10MW Vestas	10	2	1:40.8	PMSG	730

1.4.3.2.3.2 PMSG multiple generator-based concept (Liberty/Clipper Wind Power concept)

The price of gearboxes per Kilowatt (kW) increases with the increase on the rated power, hence distributed drive-train with several generators can help to achieve high power density with competitive cost [83] [84]. The Clipper concept is based on splitting the drive path from the wind's rotor to drive multiple parallel generator [84]. Therefore, when one generator/converter fails (under repair), the rest generators/converters continue to

produce the electric power hence this concept offers effective fault-tolerant operation. A commercial conversion system of 2.5 MW with special quantum drive-train[7] (See Fig. 1.23), four PMSGs and four converters (Clipper Windpower) was developed by Clipper wind (See Fig. 1.23b). Although this configuration offers a number of technical and economic advantages, it has a drawback of complicated gear-set.

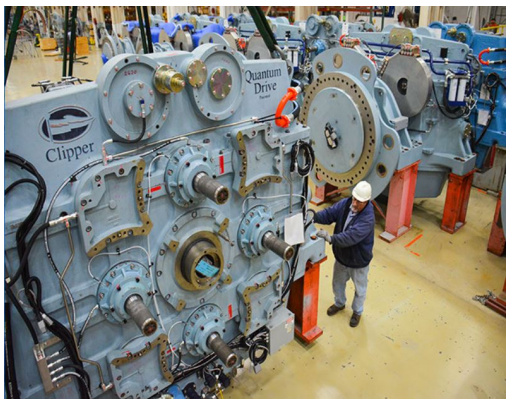

(a) Distributed drive

(b) Nacelle

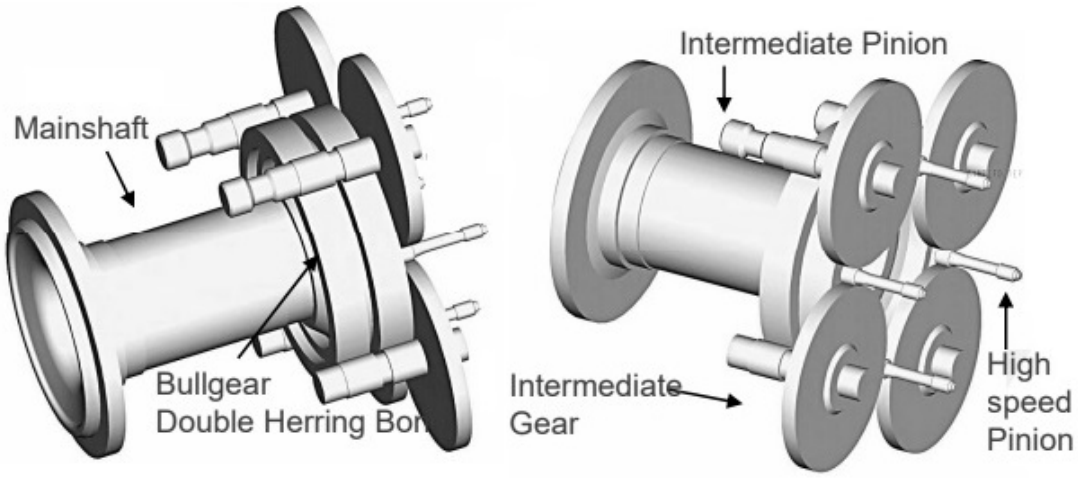

(c) Clipper Liberty quantum gearbox

Figure 1.23: Clipper Liberty 2.5 MW drive-train concept

1.4.3.2.4 Advantages of the full scale frequency converter concept

- Extract more power from the wind.
- Reduced fluctuations and flicker on the grid output.
- Lower audible noise emission at low-speed Lower mechanical loads on the wind turbine components

[7] Not a conventional gearbox with planetary design, but new patented design.

during rotor torque transients.

- Wide range control capability.

1.4.3.2.5 Limitation of the full scale frequency converter concept

- Power conversion system incorporates advanced power electronic component, which may increase the cost of the turbine [70].

1.5 Conclusion

Fives types of wind energy drive-train configurations have been presented and analysed in this chapter. Wind turbines drive-train concepts can be broadly divided into three types: fixed speed concept, limited-speed concept and variable speed concept. While in the former concepts, fixed- and limited- speed, induction generators are often used, in variable-speed concept synchronous generators are by far the most common. In megawatts power ranges, it can be concluded that variable-speed permanent magnet synchronous generators with full-scale converter are gaining the market share, they are becoming more popular than doubly fed induction generator with partial-scale converter. The permanent magnet synchronous machine present their high efficiency, better thermal characteristics (no excitation field losses), high reliability (absence of slip rings) and high torque to weight ratio. The next chapter deals with ultra-large wind turbine generator technology.

Chapter 2

Electrical Generators for Large Wind Turbine: Trends and Challenges

2.1 Introduction

This chapter reviews the state of the art of under-construction, existing and prototypes of drivetrain and electrical generator used in large multi-megawatts wind turbine, it also discuses future development trends. Section 5.1 discusses the main driving factors for ultra-large wind turbines. Section 2.3 presents the current status of megawatts turbines and the following section 2.4 introduces the challenges related to such huge constructions in terms test, size, cost, weight and transport. Then, in section 5.8 the largest wind turbine manufacturers are presented. Section 2.6 reviews drivetrain technologies used in large wind turbines, focus will be on direct drive permanent magnet synchronous machine. Advantages and drawbacks of direct-drive generator are provided. Then, different possibilities to overcome the drawbacks of direct-drive wind turbines are examined.

2.2 Motivation For Large Wind Turbine

Not surprisingly, the average size of the new installed wind turbines, for both onshore and offshore, continued to rise toward double-digit megawatts ($>$ 10 MW) structures Fig. 2.1. Sinking on prices of wind turbines have lessen the cost of the energy, while up-scaling the wind conversion system has boosted the capacity factor

at the same time the operation and maintenance costs have fallen [53]. Increasing the swept area helps to improve the capacity factor for a given site area, by capturing more energy per area land use, wind turbines with 10-12 MW are promising capacity factors over 50 per cent [85]).

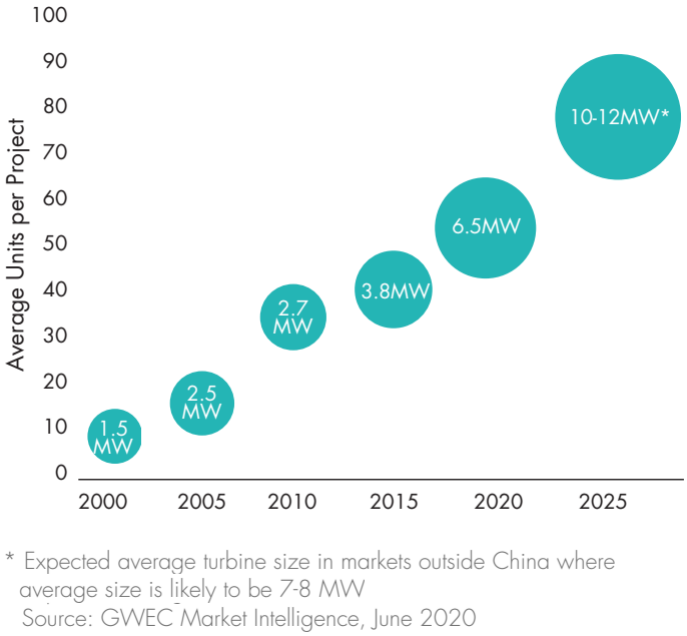

Figure 2.1: Evolution of offshore wind turbine size [7].

2.3 Global Market Status

According to the Fraunhofer IEE[1], roughly a quarter of new installed offshore wind turbines have more than 5 MW, and approximately three-quarter range between 3 MW and 5 MW. Fig. 2.2 shows that pace of growth of new installed large wind turbines ($>$ 5 MW) has increased gradually from 1.67 per cent to 23.41 per cent of the totalled cumulative number installed in 2010 and 2018, respectively. The global average size of installed turbines was about 2.76 MW, in 2019 (with 2.6 MW for onshore and about 5.7 MW for offshore). In the same year, in Europe, the average size for new installation reached 7.2 MW. The highest average per unit capacity of newly installed turbines in offshore were in Belgium and Portugal with 8.4 MW followed then by Denmark with 8.3 MW. According to WindEurope, in the first quarter of 2017, the power range of ordered offshore wind turbines were between 7 MW and 9 MW [86]. Thus, the average growth on the size of new installed offshore

[1]Fraunhofer Institute for Energy Economics and Energy System Technology

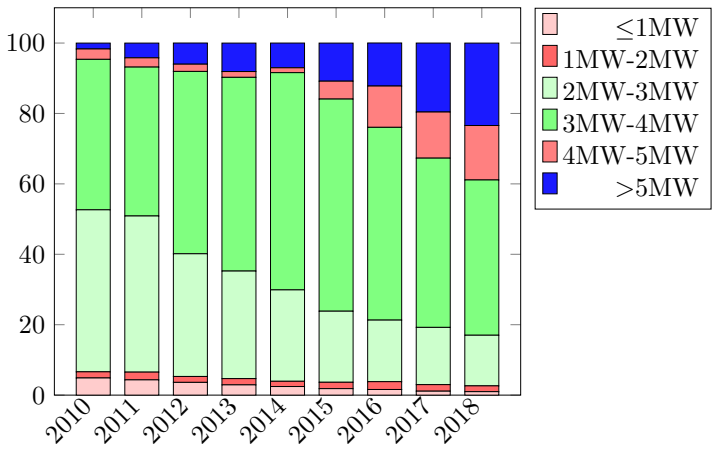

Figure 2.2: The market share of offshore wind turbine capacities on the cumulative number of wind turbines

turbines in Europe rate more than 35 per cent from approximately 6 MW in 2017 to around 8.2 MW in 2020 [87]. Furthermore, Europe, with 83 per cent of the global floating wind capacity, is the world leader in floating wind energy generation [87]). The largest averages of onshore wind turbine size were in Morocco with 4.2 MW followed by Finland and Norway with alomost 4.2 MW and 3.8 MW, respectively [1]. Table 5.2 provides an example of commercially available large wind turbine.

The most powerful available wind turbine to date is Haliade-X (General Electric GE) Fig. 6.12.a, it features 12 MW (or 13 MW and 14 MW in boosted mode). Currently, Haliade-X 12 MW prototypes (the first one was installed in Netherlands (Port of Rotterdam) and the second one in France (Saint-Nazaire)) are undergoing an advanced testing program. Haliade-X is three blades horizontal-axis, upwind and pitch-controlled wind turbine, with 138/260 m hub height, 220 m rotor diameter, the capacity factor of Haliade could reach 64 per cent [94]. Further, SGRE (Siemens Gamesa Renewable Energy) has lunched 10 MW (SGE 10.0 -193 DD) wind turbine, provisional type certificate has been awarded to this model (Østerild (Denmark)) and it is expected to be commercialized by the end of 2022 [95]. Almost all large-scale wind turbines built today are horizontal-axis three-bladed, Seawind, a Netherlands company, patented 6MW and 12MW two-bladed floating offshore wind turbines Fig. 2.3.b [96]. The adoption of such technology makes the wind turbine much simpler, lighter and with few moving parts. A full-scale demonstrator of Seawind 6 MW (Seawind 6-126) was installed in the European marine energy center in Scotland, it is planned to be followed by upscaled models with 12 MW capacity (Seawind 12-225), which will be tested in 2022 [97]. The commercial version for these turbines will

Table 2.1: An Example of commercially available large wind turbine

Manufacturer	Wind Turbine	Power Rating [MW]	Wind Farms (Example)		
			Farms	Number of turbines	Total Capacity [MW]
MHI-Vestas	V164-9.5 (offshore)	9.5	Northwester II (Belgium) [88]	23	219
			Kincardine II (United Kingdom) [89]	5	48
			Borssele 3&4 (Netherlands) [87]	76	722
			Borssele 5 (Netherlands) [87]	2	19
	V164-8.4 (offshore)	8.4	Windfloat Atlantic (Portugal) [87]	2	17
	V150-5.6 (onshore)	5.6	Paskoonharju 2 (Finland)	21	117.6
Siemens Gamesa	SG 8.0-167 DD (offshore)	8	Kaskasi II (Germany) [87]	38	342
			Le Tréport (France) [90]	62	496
			Noirmoutier (France) [91]	62	496
			Hornsea II (UK) [92]	165	1320
			Borssele 1&2 (Netherlands) [87]	94	752
	SG 8.4-167 DD (offshore)	8.4	Seamade (Belgium) [87]	58	487
			Kriegers Flak (Denmark) [87]	72	604
	E-126 7.580 (onshore)	7.5	Estinnes (Belgium) [93]	11	81
General Electric	Cypress 5.5-158 (onshore)	5.5	Oitis (Brazil)	103	567
			Metsälamminkangas (Finland)	240	132
NORDEX	N163/5.X	5.X	Stakraft - Ventos de Santa Eugenia (Brazil)	91	518.3

be available in 2023 and 2024 [97], respectively. Another 2-bladed offshore wind turbine was developed by the German manufacturer Aerodyn Engineering GmbH, offering light weighted turbine for 8 MW and 6 MW with 110m and 100 m rotor diameter respectively. The same company in collaboration with EnBW (Energie Baden-Württemberg) tested scaled-down (1:10) version of a novel floating foundation technology (Nezzy^2) in the Baltic Sea (See Fig. 6.12.c), after extensively test in Japanese inland waters. The full-scale demonstrator of 15 MW multi-rotor two-bladed concept including two SCD[2] 7.5 MW (Aerodyn) supported by a partially submerged floating foundation (Nezzy^2) is expected to be tested in 2021/2022 [87]. The first French floating wind turbine concept was patented by Eolink [98]. Cooperation agreement with Centrale Nantes have been concluded to install a down-scaled demonstrator (5MW) with respect to the full- scale design (12 MW) in SEM-REV[3] Test Field.

[2]Super Compact Drive.
[3]The first European site for multi-technology offshore testing that is connected to the grid [99].

(a) Haliade-X prototype [94]

(b) Seawind 6 MW demonstrator [96]

(c) SG 11.0-193 DD prototype [95]

(d) Nezzy^2 prototype (scale 1:10) [100]

Figure 2.3: Examples of large wind turbines

2.4 Challenges For Large Wind Turbines (Key issues in design of large wind turbine)

The cost of wind power is driven by technological advancements and consequently the world's policy addresses many technical and economic challenges in producing large wind turbines. Up-scaling such structures increases the complexity of their design, manufacturing, transportation and installation. In particular, mass raise of the rotor, nacelle and the tower present design challenge, because upscaling the existing concepts might appear to be not beneficial. Besides, there are many key factors affecting the deployment of offshore wind. New designs should be developed to address the challenge of marine conditions, corrosion and reliability issues. The development of testing facilities is a crucial issue. Thus, many projects were supported to tackle these challenges in different disciplines:

- INNWIND (Alumni), vision: High-performance innovative design of a beyond-state-of-the-art 10-20MW offshore wind turbine and hardware demonstrators of some of the critical components [101].

- SUMR (Segmented Ultralight Morphing Rotor), mission: to conceptualize, design and demonstrate morphing technologies for 50-megawatt wind turbines that can reduce offshore levelized cost of energy by as much as 50 per cent by 2025 [102].

- HiPRWind (High Power, High Reliability Offshore Wind Technology), the project aims to unlock new deep-water areas for wind power by enabling research on floating systems. It is dedicated to create and test, at the megawatt scale novel, some cost effective approaches of floating offshore wind turbines [103].

- COREWIND, the project aims at achieving significant cost reductions and enhancing performance of floating wind technology through the optimization of mooring/anchoring systems and dynamic cables [104]).

- FLOTANT, aims to develop an innovative and integrated floating offshore wind solution, optimized for deep waters (100-600m) capable to host a 10 MW wind turbine generator [105].

2.5 Manufactures Of Operational Large Wind Turbine

Several wind turbines manufacturers introduced large turbines with rating power from 7 MW to 13 MW. Due to the rise on the deployment of offshore wind turbines with capacity greater than 4 MW, the power average of offshore the wind turbine reached 4.8 MW in 2016. As can be seen from Fig. 2.7, Siemens manufactures nearly 83 per cent of the global wind turbines with capacities more than 5 MW [8] followed by Enercon and GE Wind with 9.7 per cent and 4.3 per cent respectively.

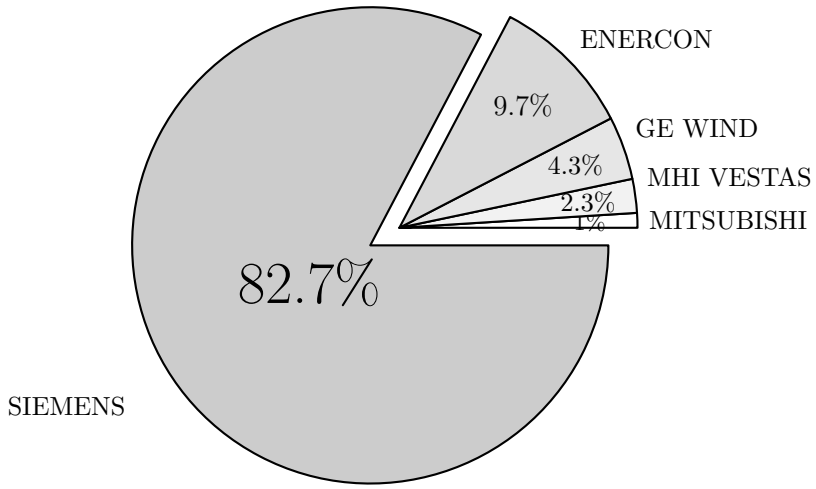

Figure 2.4: The total capacity of the top five suppliers of large wind turbines greater than 5 MW in 2016 (Own representation with information from: [8])

2.6 Large wind Turbine Drive-train Technology

The drive-train, which represents the direct link between the rotor shaft and the electrical generator, is subject of high dynamic loads (wind loads, electrical load). Therefore, considering the mechanical, structural and magnetic performances of the drive-train is crucial factor in the design of reliable and efficient electrical generator. In the conventional wind turbines, most of the drive trains had gearbox and high-speed induction generator. In contrast, with the considerable increase on the average power of wind turbines, direct-drive technology is constantly gaining market share. Avoiding the gearbox helps to increase the reliability and efficiency of the power drive system. For instance, the EU-28[4] market share of gearless drive-train expand by

[4]Abbreviation of European Union (EU) which consists a group of 28 countries.

more than 10 per cent from 2010 to 2018, bringing its regional share to 35 per cent in 2018 [97]. According to the rotation speed, wind turbines can operate either at fixed or variable speed. While in fixed speed concept a multistage gearbox is often used, in variable speed concept the drive-train would either be geared (multistage or single-stage) or gearless (also called direct-drive). All multi-megawatts wind turbines are designed to operate over large range of variable-speeds.

2.6.1 Direct-drive wind turbine (Low speed generators)

The gearbox is considered the largest contributor to turbine downtime per failure [47], and they usually do not achieve their 20-year design life [106] [78] [107]. This is especially true with offshore installations where it is too expensive to repair/exchange it [108] [107]. The gearbox increases the rotational speed of the rotor blades by step-up ratio. This ratio is equal to the electrical generator speed divided by the turbine rotor blades speed. Due to the size, efficiency and availability requirements, most of commercially-available large wind turbines are gear-less. Further, in direct Drive Wind Turbine (DDWT), the electrical generator is directly connected to the rotor hub, and thereby it operates at low rotating speeds. Large scale wind turbines are designed to spin at relatively low speeds in order to maximize the turbine's efficiency by maintaining the optimal tip speed and this with respect to specific limitations related to the rotational speed of the blades. Indeed, due to aerodynamic noise restrictions the control tends to lower the tip speed. In contrast to the small wind turbines were the mechanical noise ((e.g., from gearbox, generator, or bearing [109]) is considered to be the main source of noise, in large wind turbines the aerodynamic noise(due to high tip speed) is dominant [110]. For example, the generators of GE 12 MW offshore wind turbine HALIADE-X, SG 11.0-200 DD (Siemens), SG 8.0-167 DD (Siemens) and GW 171/6450 (Goldwind) operate at rated speed 7.81 rpm, 8.6-9.1 rpm, 10.3 rpm and 10.7 rpm, respectively. Therefore, such generators are not standard and it remains a technical challenge to design low-speed/high-torque electrical generator. The size and the weight of the low-speed generator need to be further investigated. Despite this rapid growth on the low-speed generator structure, the heavy and large generator could take advantage of supporting the turbine rotor [111]. Furthermore, synchronous generator are widely used in direct-drive power conversion systems. Whereas the cost, the weight and the losses of conventional high-speed induction generators are relatively low compared to low-speed permanent magnet generator, the direct drive permanent magnet generator seems reach the most interesting compromise between the energy yield and the losses with acceptable cost [112] [113]. DDWT configuration is most widely used with variable-speed synchronous machine. In the grid side, the generator is connected to the grid through a full-scaled power

electronic converter.

2.6.2 Advantages of direct-drive wind turbine

The gearless drive-train presents several advantages over the geared one, they came mainly from avoiding failure issues and the downtime effects associated to the gearbox. First, eliminating the gearbox will not only increase the global efficiency (e.g.; no belt friction, no gearbox friction) but also lower the maintenance cost [114] [81] and replacement requirements (e.g.; oil have to be replaced regularly in the gearbox). Second, with few moving parts, directly driven power systems present an improved reliability [114] [80] [81]. Although electrical and electronic sub-systems present higher failure rate than mechanical one (e.g., gearbox) is relatively low, the downtime of mechanical equipment is longer, which results in high maintenance cost [47], especially in hard-to-reach offshore environment. Third, the gearless drive-train was found to be less noisy (audible noise) than the geared one, the noise is mainly caused by the high rotational speeds [112]. By avoiding the gearbox vibration, less stress and noise are applied to turbine tower and foundations. This lessen the overall noise emission from the wind turbine. Finally, the full-scaled converter, which offers high operation flexibility over large wind speed range [115] [116] by decoupling the control of the machine-side and grid-side[5] [117] [120] converter, helps to enhance the performance of the wind energy conversion system and increase the energy yield [112].

2.6.3 Proposed generator types for direct-drive wind turbine

In the last couple of decades, low-speed multipole synchronous generators have increasingly gained popularity amongst modern direct-drive wind generator manufacturers (e.g.; Siemens, Adwen, General Electric). In this concept, the generator directly coupled to the turbine's rotor, which operates at the optimal speed, can rotate at the variable speed of the rotor independently to the grid frequency. Therefore, the energy extracted from the wind increases. Depending on the type of the excitation, the synchronous generator can be either magnetically excited (Permanent Magnet Synchronous Generator (PMSG)) or electrically excited (Electrically Excited Synchronous Generator (EESG)).

[5]The power converter in directly driven permanent magnet synchronous generator can be divided into a machine-side converter and grid-side converter interconnected by a DC-link capacitor. Whereas the control of the machine-side converter is designed to achieve the maximum power point tracking (MPPT) by adjusting the synchronous permanent magnet generator's speed to the change in the wind speed [117] [118], the grid-side inverter helps in achieving the grid requirements in terms of voltage level (regulates the DC-link voltage), frequency, active and reactive power flow to the grid [119].

2.6.3.1 Direct-Drive Electrically Excited Synchronous Generator (DD-EESG)

Although EESG are not as popular as PMSG in large diameter generator, the German manufacturer Enercon proposed an annular 12 rpm EESG (as shown in Fig. 2.5) for its 7.5 MW directly driven wind turbine (E-126). It is upscaled version of E-112 4.5 MW, with 10 m diameter generator with a weight of 220 tones [121]. DD-EESG was adopted by many wind turbine manufactures for rated powers (100 kW-3 MW) such as Lagerwey (e.g.; LW58/750kW) and M.Torres (e.g.; TWT 1.65 MW/82) but up-scaling those machines makes their manufacturing process complicated and expensive, this has prevented manufactures from considering electrically exited generator as an option for high-power low-speed applications. Gearless EESG are built with wound rotor excited by direct current source using slip rings and brushes[6], that increases the maintenance requirement and lead to additional resistive heat losses due to the DC current supply. Brush-less exciter with rotating rectifier could be used in such machine, but it is not common for wind turbine generators [122]. Furthermore, the excitation field in the rotor rotates at the synchronous speed, and thus high number of poles is required. However, EESG are not suitable for direct-drive applications because they are limited by pitch pole, that must be large enough to house the rotor winding. Thus the volume and weight get larger when designing high-power high-torque wound rotor machine. Moreover, the field winding leads to additional copper losses, which reduce significantly the efficiency of the generator. Consequently, by managing those thermal losses the cooling system become more complex. For instance, the DD-EESG proposed by Enercon (the initial model E-66/2 MW and its adapted versions E-70/2-2.3 MW, E-87/2-2.3-3 MW and E-92/2.3 MW) rated up to 3 MW for wind turbines have rotor air cooling system, whereas, with the same outer diameter and increased axial length, Enercon proposed for areas with high wind conditions (E-82/3 MW E4 (IIA[7]) and E-82/3 MW E3 (IA)[8]) water-cooled generator [124]. In fact, the modern DD-EESG proposed by Enercon (e.g.; E-101, E-151/2.9-4.2 MW) are water-cooled [124]. Also, the converter capacity must be larger than the generator nominal power due to the reactive power. This results large and expensive converter with extra losses. Additionally, EESG offers an opportunity of adjustable excitation current, and hence control the Elector-Motive Force (EMF[9]), but this may not be critical for DD-EESGs since they are connected to the grid through electronic converter [16]. Finally, EESG might be structurally demanding due to the weight of the machine's active parts. For instance, the

[6]The most common type for wind turbine generators [122].
[7]Referring to the IEC wind classes, II designates medium wind conditions and A refers to high turbulence site characteristics [123].
[8]Referring to the IEC wind classes, I designates high wind conditions and A refers to high turbulence site characteristics [123].
[9]No-load voltage.

(a) Stator assembly of E-126 [125] [126]

(b) E-126 annular EESG [127]

Figure 2.5: Enercon E-126 7.5 MW wind turbine

On the whole, although DD-EESGs are robust, simple to construct and easy to assemble (due the absence of permanent magnet), it has been demonstrated in [80], that for 3 MW wind turbine operating at 15 rpm DD-EESG is the most expensive and heaviest generator compared with other configurations (Direct-drive PMSG, single-stage geared PMSG & DFIG and three-stage geared DFIG).

2.6.3.2 Direct-Drive Permanent Magnet Synchronous Generator (DD-PMSG)

The PMSG would present an attractive alternative for direct-drive low-speed application, then it is widely used by wind turbines suppliers (e.g.; General Electric (GE) Energy, Siemens Gamesa (SG) Renewable Energy). The rotor excitation is made by permanent magnet, therefore no slip rings and external excitation is needed. The elimination of the slip rings will increase the reliability of the generator and brought down the maintenance cost, whereas the absence of the external energy source result in lower overall copper losses and thus DD-PMSGs feature a higher efficiency compared to EESG [80]. PMSGs offer considerable active weight (The active part of machine is the part that participate to the torque production) reduction and energy yield advantages [122], the high torque to weight ratio could be explained by the use of relatively small pole pitches [128] [16]. Indeed, PMSGs are well-adapted to low-speed applications, the higher the pole number the lighter is the magnetic

circuit. For the same flux density, low flux is produced by one pole when high number of poles is considered and thus thinner back-iron is required to carry this flux [129]. Although the circulation of eddy currents in permanent magnet induces losses, they are much lower than the copper losses in EESG [16], thereby resulting in improved thermal characteristics. In particular, the iron losses[10] are highly influenced by the pole/slot combination. As illustrated in eq. 2.1, the frequency f is proportional to the rotor speed n and to the number of poles p, for a large pole number at low speeds will keep relatively low frequencies and then the iron losses are low compared to the copper resistive losses. The iron losses increase considerably when the frequency goes up (the frequency is proportional to the pole pairs number p), but this expansion is limited when the iron core (stator yoke and rotor yoke) decreases. As the rotor speed is determined by the application, the frequency, therefore, must be carefully assessed.

$$N = \frac{60 \times f}{p} \tag{2.1}$$

The use of PM excitation allows design flexibility in the placement, size, orientation and shape of the permanent magnet [16]. Rare Earth Element (REE), such as samarium cobalt (SmCo) or neodymium iron boron (NdFeB), are required in the manufacture of high performances PMSG. Most of the PMSGs use NdFeB magnets due their magnetic properties (high remanent flux density and high coercivity). Table 2.2 gives some specific characteristics of those permanent magnets. Apart from the technological advances in the power converter systems, the fall in the REE prices a 15 years ago play an important role in the use of such permanent magnet in most commercial ultra-large wind turbines. Table 2.3 lists some MW-scale DD-PSMG in operational wind farms.

Table 2.2: Main characteristics of permanent magnets

	Remanence B_r $[T]$ [130]	Energy Product $(B-H)_{max}$ $[Kj/m^3]$ [130]	Maximal Temperature T $[°C]$ [131]	Price [132]
Ferrites	0.20-0.46	6.4-41.8	300	Cheap
SmCo	0.87-1.19	143-251	250-350	Medium
NdFeB	1.08-1.49	220-430	150	Expensive

As explained in the previous section, the permanent magnets allow a great deal of design flexibility, with various shapes, several sizes, varied topologies and flux orientations. According to [133], depending on the

[10]Including Hysteresis and eddy current losses

Table 2.3: List of ultra-large operational direct drive permanent magnet synchronous generators

Wind Turbine	Rated Power [MW]	Manu-facturer	Rotor Diameter [m]	Hub Height [m]	Electric Generator						Power Converter
					Manu-facturer	Rated Power [MW]	Rated Speed [rpm]	Rated Ferquency [Hz]	Rated Current [A] / Voltage [V]	Insulation Class	Rated Current [A] / Rated Voltage [V]
Haliade-X (Offshore)	12	GE Renewable Energy	220	138	GE	12.79	7.81	7.81	2x1455 / 3220	F	
SG 11.0-200 DD (Offshore)	11	Siemens Gamesa	200	140	Siemens Gamesa	11-12	8.6-9.1	14-15	2x4900-5000 / 820	H	6000 / 690
SG 8.0-167 DD	8	Siemens Gamesa	167	119	Siemens Gamesa	8.4-9.4	10.3-10.8	12-13	2x4000 / 820	F	4250 / 690
SWT-7.0-154	7	Siemens Gamesa	154	120	Siemens Gamesa	7-7.35	10.3-10.8	12-13	1x3400 / 750	F	2x4000 / 690
GW 171/6450	6.45	Goldwind	171	109	Xingjiang Goldwind	6.9	10.7-12.84	10.7	1560 / 720	F	5941/690

magnetic flux direction in the stator core, PMSGs can be categorized into : longitudinal and transverse flux machine [134] . The direction of the flux is parallel to the direction of the rotation in longitudinal flux machines, whereas, it is perpendicular to the direction of rotation in transverse flux machine (See Fig. 2.6). Further, based on the direction of magnetic flux crossing the airgap, PMSG can be either radial flux (RF) or axial flux (AF) machine. It is also possible to classify them in iron-cored and in air-cored depending on the presence

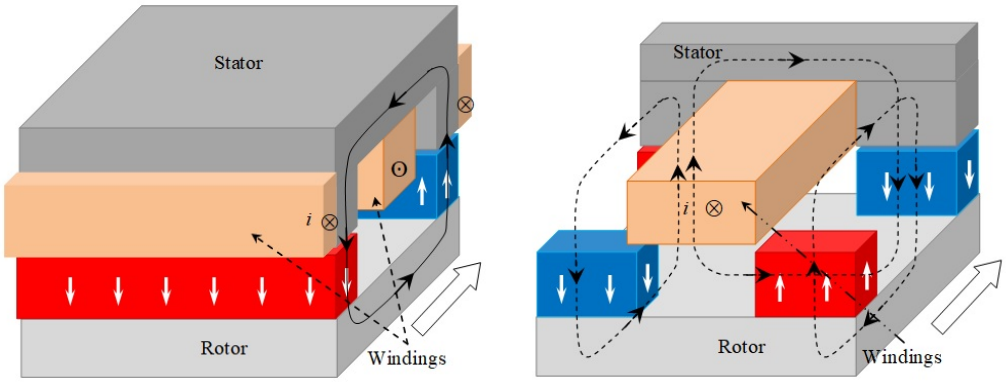

(a) Longitudinal (b) Transverse

Figure 2.6: Flux path in one pole pair of longitudinal and transverse PMSG [9]

or the absence of the iron in stator's core [135], whereas based on the stator's core design the machine can be slotted of slotless. The different PMSG suitable for direct-drive low-speed wind turbine applications are describe. Their characteristics are discussed below.

2.6.3.2.1 Radial Flux Permanent Magnet Synchronous Generators (RF-PMSG) Due to economic consideration, the RF-PMSG, with surface mounted permanent magnet, is the most common commercialized topology for direct-drive multi-megawatt wind turbines [81] [136], it is also the most mature technology in terms of manufacturing process. This topology offers not only robust design but also structural stability [137]. In RF machine, while the magnetic flux flows radially, the current flows axially. The global leader of offshore wind turbine, Siemens, has already commercialized many DD-RF-PMSG large wind turbines such as SG 11.0-200 DD (11 MW) and have at present 14 MW DD-RF-PMSG under development. Also, in the current year, the DNV-GL certified the Haliade-X 12 MW GE (Fig. 2.7) offshore wind turbine with RFPM, it has shown a high capacity factor of $60 - 64$ per cent [94] and high performance in terms of reliability and efficiency. Different configurations of RF-PMSG have been discussed in literature.

The RF machine may be divided into many categories based on the placement of the permanent magnet, the rotor design, the rotor position, the stator core and the winding distribution (See Fig. 6.18). The permanent magnet can be surface mounted, inserted of buried. In surface mounted PMSG the permanent magnets are glued to the surface of the rotor, however, to provide acceptable flux density in the airgap it is necessary to use high energy magnets (e.g.; Alnico, NbFeB), while in buried PMSG with flux concentration the flux density in the airgap is higher than the remanent flux density of the permanent magnet. The eq. 2.2 and

(a) Haliade-X 12MW [94]

(b) Haliade-X 12MW nacelle

Figure 2.7: Haliade-X 12 MW wind turbine

eq. 2.3, estimate the airgap's flux density for a surface mounted PMSG and a concentration flux PMSG [138], respectively. Notice that in order to have the usual range of induction in large machines ($[0.8T - 1.1T]$) the remanence flux density should be at least $1T$ for the surface mounted topology, whereas for the flux concentration PMSG, with convenient choice of the permanent magnet dimensions, it is possible to have high flux density with low cost permanent magnet like ferrite (with $B_r \cong [0.20 - 0.46]T$).

$$B_{gsm} = \frac{B_R t_{PM}}{t_{PM} + \mu_r g} \tag{2.2}$$

$$B_{gcf}{}^{11} = \frac{B_R}{\frac{h_{yoke}}{h_{PM}} + 2\mu_r \frac{g}{t_{PM}}} \tag{2.3}$$

where B_r is the permanent magnet remanence, g is the airgap thickness, t_{PM} is the magnet thickness, h_{yoke} is rotor yoke thickness, h_{PM} is the magnet height and μ_r is the magnet permeability.

Although low cost magnet may be used in such structure, no mass reduction is expected. In fact, due to the need of large amount of weak magnets (such as ferrit) the machine mass will increase. Thus no mass saving is expected with this geometry. Buried and concentrated flux rotors of PMSGs offer a better retainment of the magnets, which is an attractive point in high-speed applications, but in gearless wind turbine, PMSG operates at low speeds so the centrifugal force is not a big concern. Regarding the cost and the better retainment of the

[11] Neglecting the effects of stator slots and leakage within the rotor

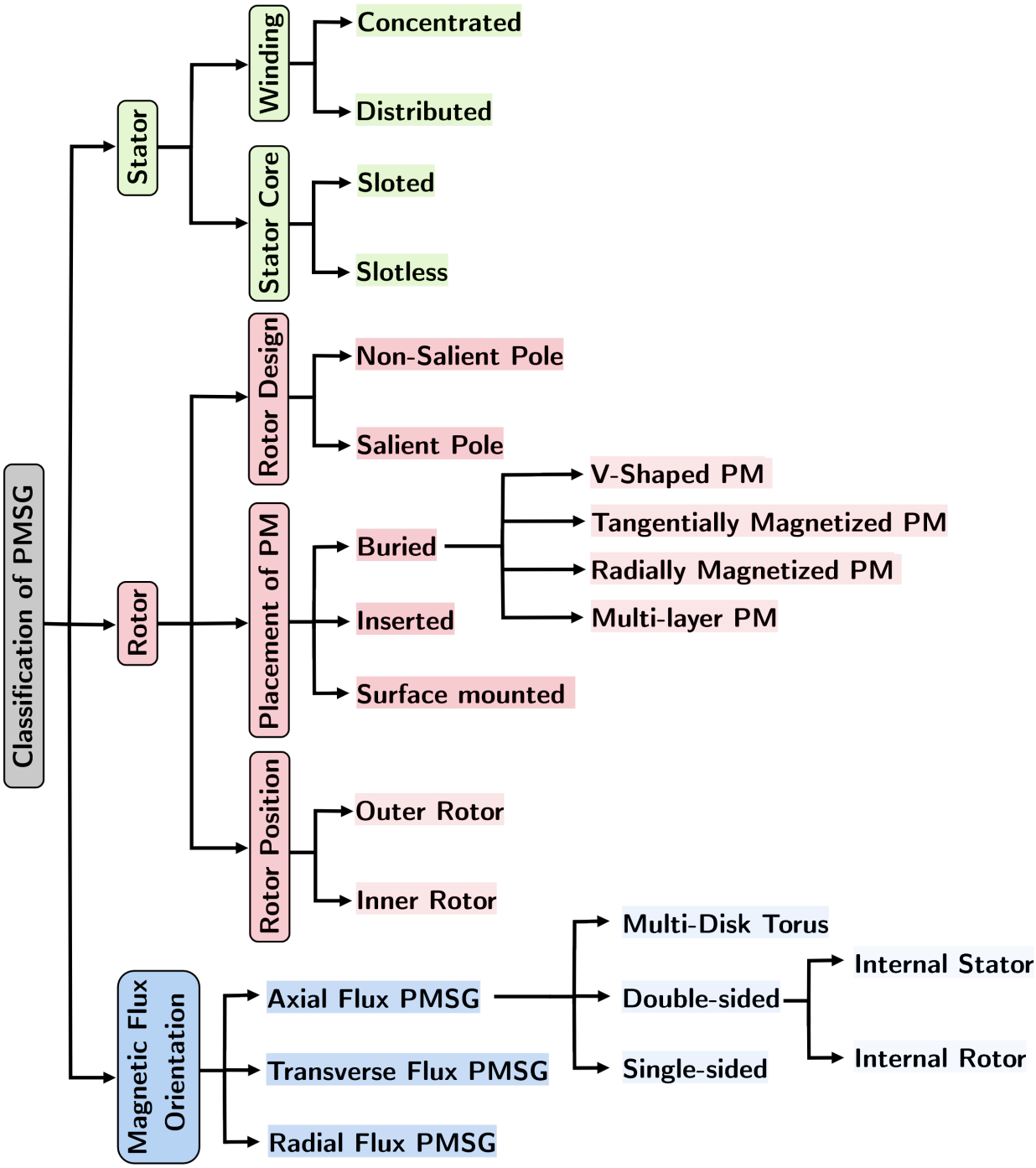

Figure 2.8: Classification of PMSGs

magnets, the machine is heavy and with complex manufacturing issues (Burying magnets) [137]. Further, in insert surface mounted and buried configurations the flux leakage is high, which might reduces the power factor and the efficiency of the machine. That is why the insert and buried PMSG are not common on direct-drive wind application. However, to reduce the effect of the leakage flux, an additional magnet could be added to

the rotor [139]. A comparative study has been conducted in [44], for a 6 MW DD-PMSG. The results show that flux-concentrating ferrite PMSG weighs (considering the active and the structural mass) nearly twice as much as surface-mounted NdFeB PMSG. Even though the price of the NdFeB magnets were to double, the later allows significant energy cost savings comparing to flux-concentrating ferrite PMSG.

2.6.3.2.1.1 Inner-Rotor or Outer-Rotor The stator surrounds the rotor in conventional electric machine, however, in outer-rotor RF-PMSG the rotor is in the outside of the generator. Then, for the same machine's external diameter, the outer-rotor configuration offers a higher rotor's radius compared to stator one, and thus higher number of poles is allowed. In addition, in this configuration the centrifugal force exert pressure to the rotor core, so acting is way that prevented the magnet detachment (in the case of inner circumference placed permanent magnet) [140]. Further, the outer rotor placed in contact to the wind improve the cooling of the magnet, so decrease the risk of demagnetization. On the other hand, inner-stator have no natural cooling (exposing the stator to the wind helps on the cooling of the winding), so forced cooling system should be considered, that introduces reliability issues and additional maintenance cost [137]. However, the rise of the temperature made the stator subject to deflection [45]. This configuration requires a stiffer supporting structures, then the total mass of the drive-train get bigger [137]. Although this structure is not common on high-power low-speed generator, it has been used by Bergey for their 7.5 kW wind turbine.

2.6.3.2.2 Axial Flux Permanent Magnet Synchronous Generators (AF-PMSG) In axial flux machines, the permanent magnet produces a flux in axial direction across the airgap while the current in the slot flows in the radial direction. AF-PMSGs offer a high torque density, a simple winding and a large diameter machine with much smaller axial length compared to radial flux machine [141] [142] [136] [143]. To minimize the weight of machine, especially the supporting structures, a 10 MW iron-less axial flux permanent magnet generators was investigated [144] for offshore wind turbines. Despite the fact that, moving from slotted (iron-cored) to slotless (air-cored) machine reduces considerably the active part's mass and simplify the stator production [16], the airgap will be larger in slotless topology and hence the flux density falls for the same quantity of the magnet, this construction also conducted to winding retention issues and structural instability [136]. Air-cored machine have low iron losses due to the fact that they are toothless, this is especially interesting in the case of high-speed generators. However, in directly drive AF-PMSG, iron losses is not seen as an significant problem [16].

This structure has been widely investigated by scientists for small and medium wind turbines (5 kW- 350 kW) [145] [146] [147] [148], such as single sided slotted stator (1.6 kW) generator [10] (the machine is illustrated in Fig. 2.9). A fundamental issue for this single sided structures is their magnetic attraction force between the permanent magnet disc and the stator disc. Commonly, to balance the forces and prevent the displacement of the rotor or stator, double-sided machine(putting rotor between two stator or vice versa) or multi-stage machine are used [149] [150] [10]. The most prevalent machine configuration in low-speed applications is the Torus machine [124], where the stator with toroidal winding is placed between two permanent magnet based rotor, if the permanent magnet are placed opposite to each other on the two rotor discs it is called TORUS NS type; otherwise it is TORUS NN type. TOURS machine offers compact lightweight generator with good stator's cooling and negligible cogging torque. Although the benefits of TOURS concept, the absence of teeth create an additional aigap, and thus TORUS configuration requires more magnet weight. However, with an increase of the power rating, the airgap become larger due to the magnet and the winding. Hence, this configuration is more suitable for small wind turbines [151]. Although Multi-stage TORUS machine could be used to compensate the attraction force in case of an imbalance airgaps, the amelioration of the flux density should be considered for high-power application.

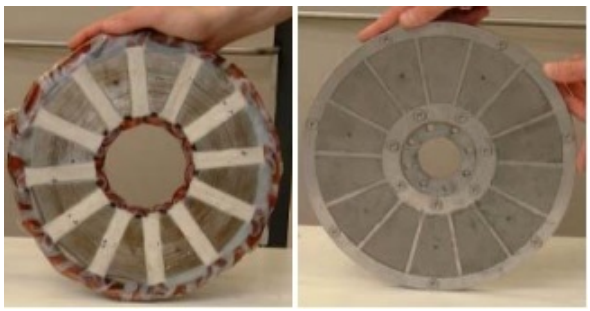

Figure 2.9: The stator and the rotor of the prototype of AF-PMSG for 1.6 kW wind turbine [10])

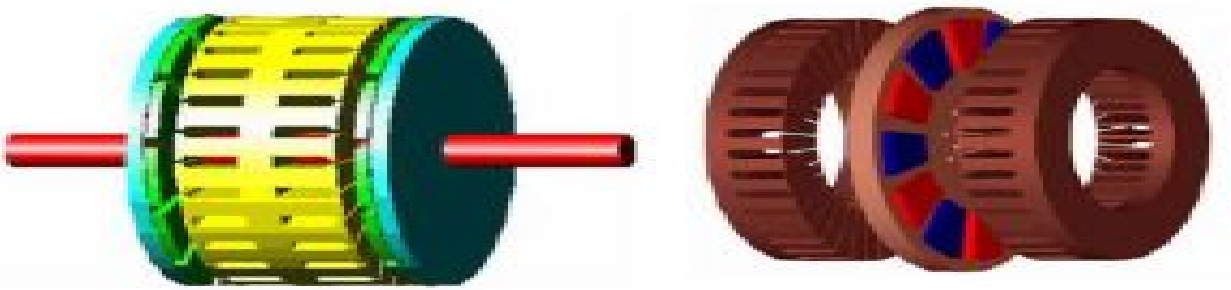

(a) One-stator and two-rotor [150])

(b) One-rotor and two-stator [10]

Figure 2.10: A slotted surface-mounted AF-PMSG

Another topology were proposed in [152], it consist on slotless C-core AF-PMSG, more details could be found in [137]. Low-speed 1 MW C-core AF-PMSG generator (See Fig. 2.11) was commercialized by NGenTec [11], the machine is designed to reach high power ranges ($\geq$ 6 MW).

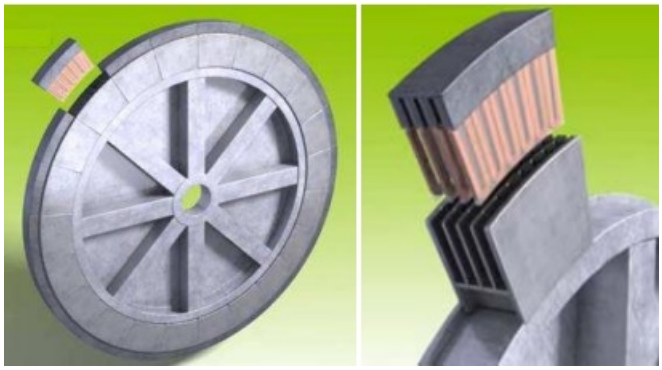

Figure 2.11: C-core AF-PMSG model of the 1MW prototype [11]

Jeumont Industry installed their first prototype of an axial flux permanent magnet machine J48/750 (0.75 MW) in 2009 at the French wind farm Widehem [153]. In Fig. 2.12, one can observe considerable reduction on the axial length due to the elimination of the voluminous gearbox. This model is not currently available. No large wind turbines equipped with AF-PMSG generators are installed.

Figure 2.12: Jeumont J48/750 direct-drive AFPMSG wind turbine

2.6.3.2.3 Transverse Flux Permanent Magnet Synchronous Generators (TF-PMSG) TF-PMSG generators produce flux which is perpendicular to the direction of rotor rotation (See Fig. 2.13), while compared to radial flux machine, in the TF-PMSG the electric and magnetic circuit are decoupled. Unlike conventional machines with longitudinal stator, the space available for conductor in transverse flux machine does not depend on the pole pitch [16] (See Fig. 2.14). Usually, the filling factor in TF-PMSGs is much larger than in longitudinal machines (See Fig. 2.15). Therefore, it is possible to obtain high current loading (up to 300 kAm^{-1} [154]) in with short pole pitch . Consequently, TF-PMSGs offer high power densities (up to 150 kNm^{-2} [154])[12] [155].

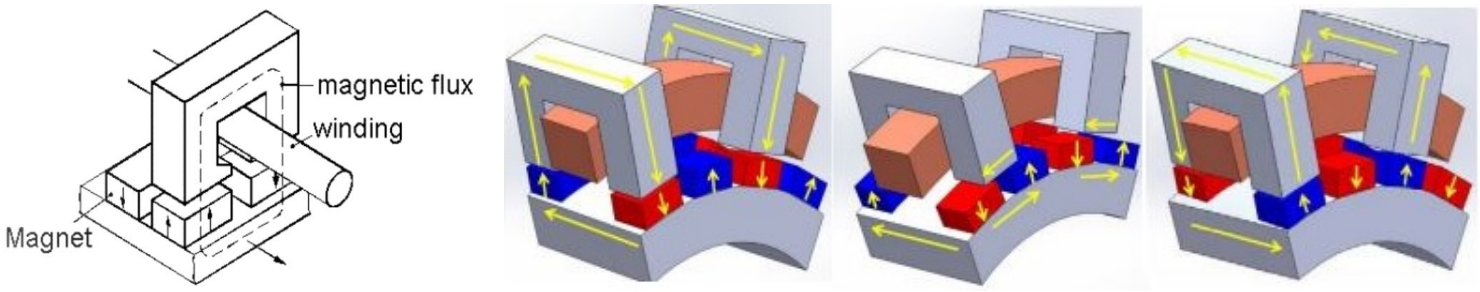

(a) Topology [156] (b) Flux path [157]

Figure 2.13: Surface-Mounted transverse Flux Permanent Magnet Synchronous Generators

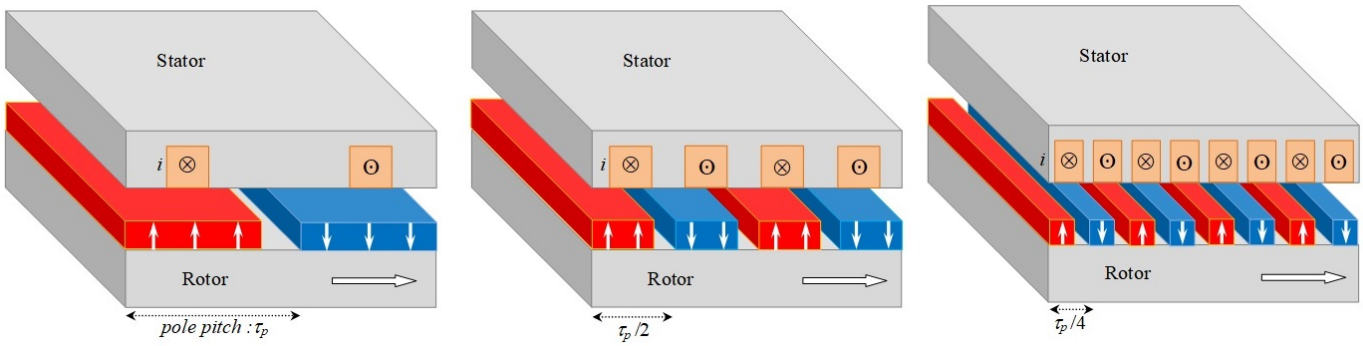

(a) Longitudinal PMSG

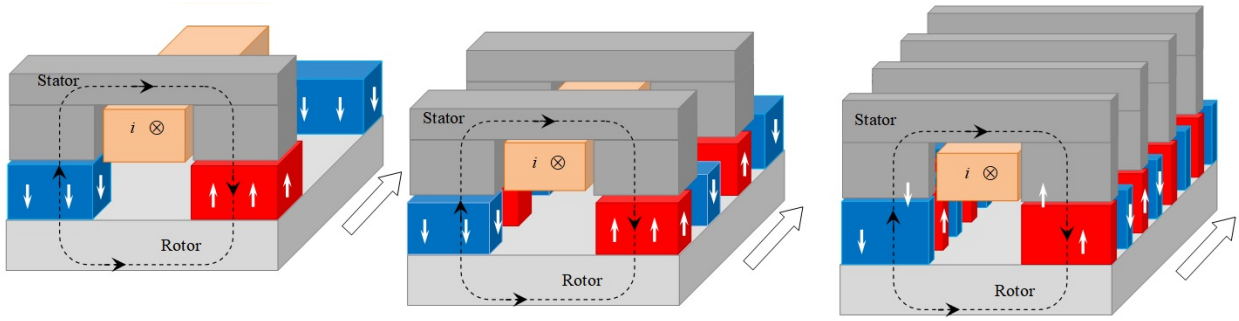

(b) Transverse Flux PMSG

Figure 2.14: The influence of the pole-pitch reduction on PMSG's force density [9]

Besides their high torque density (three to five times compared to conventional machines [12]), TF-PMSGs offer low copper losses, modular structure, fault tolerance and simple winding [158]. In contrast, the construction such machines is complicated (e.g.; 3D flux path makes lamination difficult) and costly. TF-PMSGs suffer from low power factor (between 0.35 - 0.55) [159] [160] and high cogging torque [161]. Indeed, the poor power factor is due to the high armature leakage[12] and the ineffective use of the magnetic flux[13] [163], however, even with flux concentration TF-PMSG or iron bridge the power factor is in range of 0.7. Power factor improvement is

[12]The portion of the flux that is not crossing the airgap [162].
[13]The flux crossing the airgap in the opposite direction.

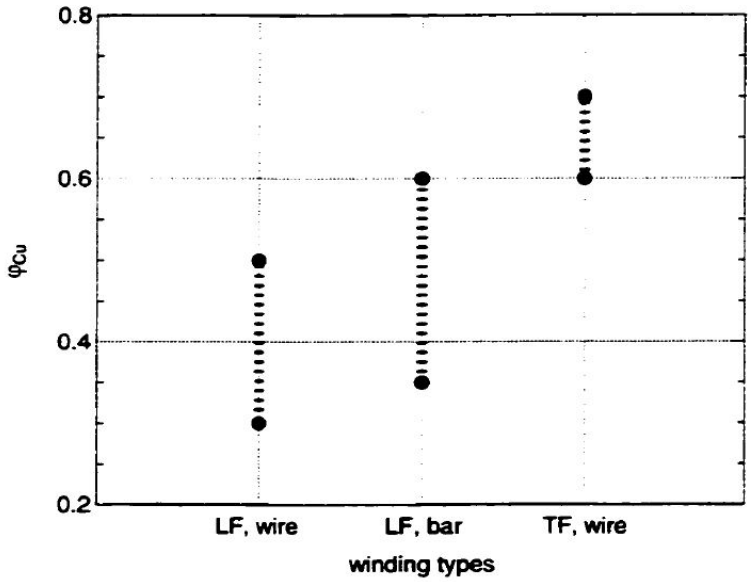

Figure 2.15: Comparison between filling factor for longitudinal and transverse flux machine [12]

possible by either an active current control of the converter or by optimizing the magnetic circuit to minimize the leakage [163] [160] [164]. TF-PMSGs with large air gap seems to be no more attractive because its force density is a little high or even low compared to RFPM machines [165]. The influence of the airgap thickness on the cost to torque ratio has been investigated in [165], it could be concluded that for direct-drive drive-train TF-PMSG are only beneficial with thin airgap, in such case the mechanical design should be considered. Then, air-cored TF-PMSGs were rapidly excluded, not only due to their large airgap but also the need of the iron core is required to create flux lines lying in the transversal plane to the direction of movement [137]. In [13], four different topologies of TF-PMSGs has been investigated (see Fig. 2.16), the authors found that inner-rotor topologies are lighter and cheaper than outer-rotor ones.

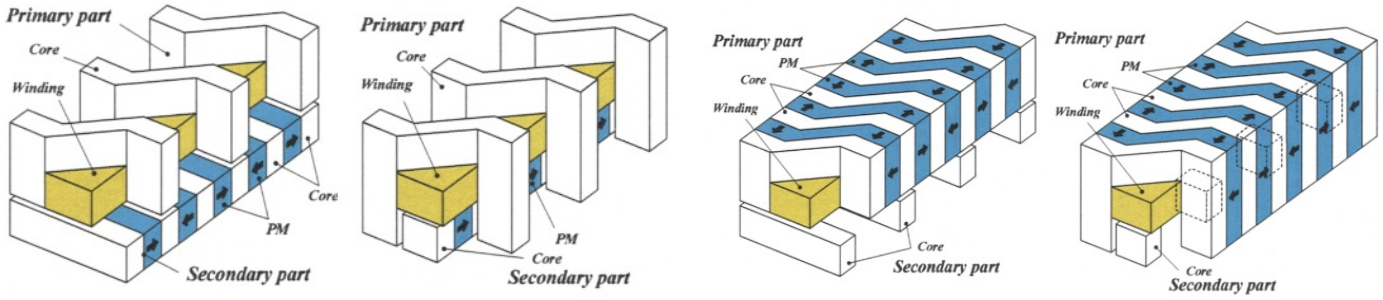

(a) Inner-rotor (b) Outer-rotor

Figure 2.16: Transverse flux permanent magnet synchronous generators [13]

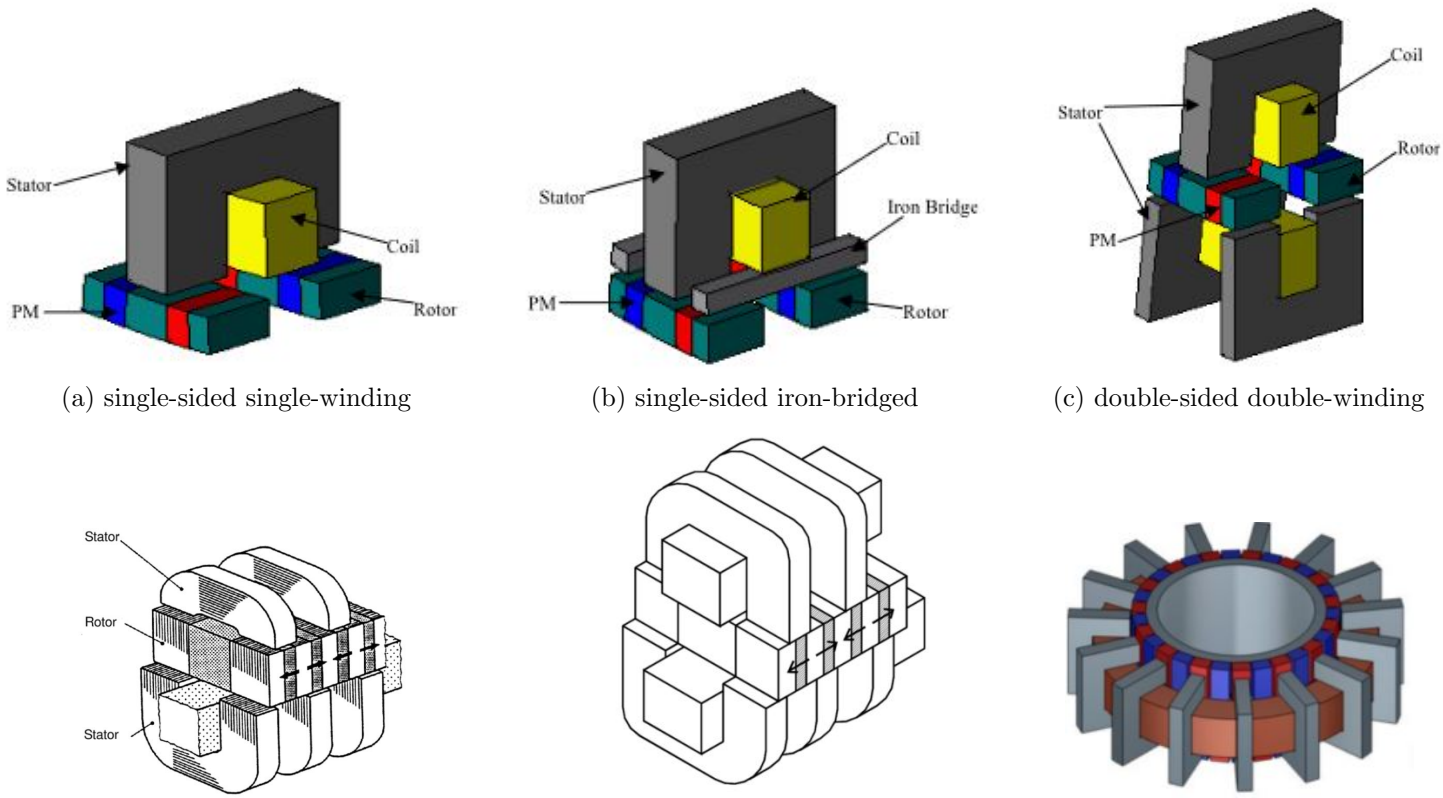

(a) single-sided single-winding (b) single-sided iron-bridged (c) double-sided double-winding

(d) double-sided single-winding (e) double-sided double-winding (f) Single-phase 3D vue

Figure 2.17: U-Core flux-concentrating transverse flux permanent magnet synchronous generators topologies [14] [15] [16]

Due to their high performances compared to surface-mounted permanent magnet machines, many flux-concentrating TF-PMSG have been reported in literature. They could be either single- or double- sided, with- or without-iron bridges, single- or double- winding and with passive or active rotor (see Fig. 2.17). The stator cores can take various shapes C-core, U-core and E-core (See. Fig. 2.18). The iron bridges, placed between the stator cores, are used to reduce the fluxes generated by the unused permanent magnets. Different topologies of TF-PMSG for direct-drive wind turbine have been assessed with diverse criteria including mass, losses, cost and power density [13] [137] [166].

TFPM generators with a broader range of output power have been investigated. In [167], Svechkarenko has studied TF-PMSG generators rated between (3-12) MW for Offshore Wind Turbines. In [168], a lightweight 10 MW direct-drive TF-PMSG was designed, resulting on generator with 60 per cent of mass reduction compared with RFPM. Despite several advantages of TF-PMSGs for direct-drive applications, they still branded as low factor machine with high manufacturing and assembling complexity. Therefore, No large wind turbines

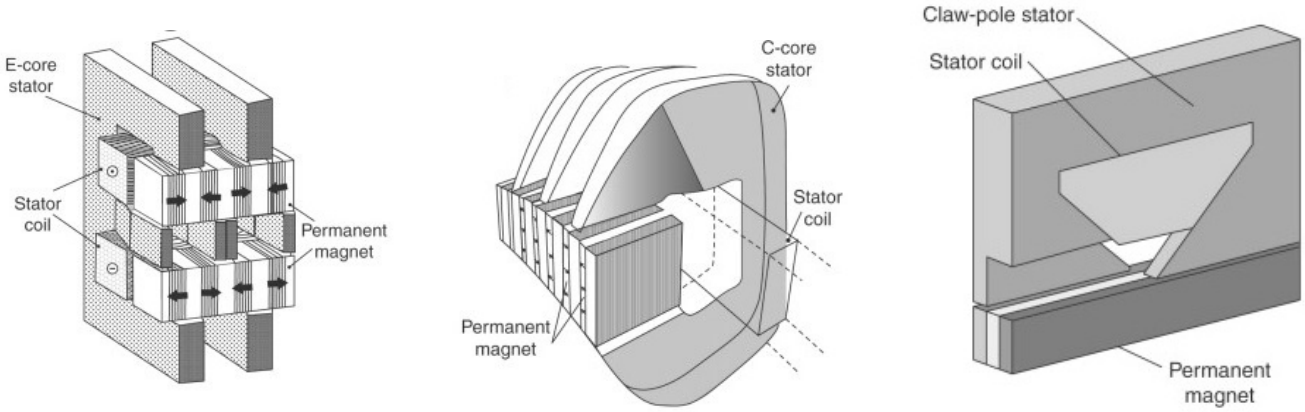

(a) E-shaped core (b) C-shaped core (c) Claw-pole core

Figure 2.18: Suggested stator-cores of TF-PMSG topologies in direct-drive wind turbines[17] [18]

equipped with TF-PMSG generators are installed.

2.6.4 Drawbacks of direct-drive wind turbine

2.6.4.1 Risks associated to the weight and diameter

Decreasing the rotating velocity at a high power levels in the directly driven generators, will induce a rise on the torque. Therefore, as mentioned before such machines are special and not conventional. The generator power could be defined:

$$P = 2\overbrace{\underbrace{\times\pi \times R_g^2 \times l_s}_{V_{rotor}} \times\sigma_{Fd}}^{\Gamma} \times\omega_m \tag{2.4}$$

where: σ_{Fd} is the tangential force density, R_g the radius of the machine, l_s the axial length, ω_m and the mechanical angular speed. It follows that, the torque is proportional to the air gap diameter squared, to the axial length and to the tangential force density [169]. Therefore, to increase the torque we could either rise the axial length or the airgap diameter of the machine. Hence, directly driven generator have large diameter with high tangential force [112], so a high number of pole pairs is required. That will result on heavy mass with considerable rise on the construction cost. Moreover, a heavy structural support is necessary to maintain a small air gap, which must be kept within a few millimeters to maximize the flux density. Achieving such high precision with large and heavy electromagnetic structure would be a real manufacturing challenge[170]. The structural and electromagnetic scaling laws for such special machine are presented in [171]. However, to ensure the feasibility of the low-speed high-torque machine, the mass of the generator and structural should be

considered. Several methods have been proposed in order to lower the DD-PMSG mass and volume, namely:

2.6.4.1.1 Increasing the flux density In order to reduce the mass of the volume of the large machine, it is possible to increase the tangential force density (eq. 2.5), which represent the average airgap shear stress resulting from the interaction of the machine's magnetic filed and the stator current density. Indeed we should either increase the current density or the airgap flux density due to the magnet, as illustrated in eq. 2.5 [172]. Transverse-flux PMSGs could be used due their high shear stress [122]. Nevertheless, as explained in the previous section those structures are not well adapted to our application and present crucial manufacturing issues.

$$F_d \approx \frac{1}{2}.\hat{B}_g.\hat{J}_g.cos(\delta)^{14} \tag{2.5}$$

where $\hat{B}_g$ is the fundamental's amplitude of the airgap flux density from the magnet, $\hat{J}_g$ is the fundamental's amplitude of the stator's surface current density and δ is the angle between the peak of the $\hat{B}_g$ and $\hat{J}_g$. It could be concluded from the eq. 2.5, that the torque is maximal when the $\hat{B}_g$ and $\hat{J}_g$ are in phase. However, the $\hat{B}_g$ is limited by the stator teeth saturation and the linear current density is limited by thermal constraints, which are imposed by the insulation materials, the characteristic of the magnet and the cooling techniques. The eq. 2.6 illustrates peaks of both the air-gap flux density and the current loading:

$$\begin{cases} B_p = 1.2 \underbrace{B_{sat}.k_{Fe}.\dfrac{w_t}{w_s + w_t}}_{B_{max}} \\ J_p = \sqrt{2}.J_s.K_{Cu}.(h_s - 2h_i)\frac{w_t - 2h_i}{w_s + w_t} \end{cases} \tag{2.6}$$

where B_{sat} is the saturation flux density, k_{Fe} is the copper fill factor in the coil, w_t, w_s are the width of the tooth and the slot, respectively, h_s is the depth of the slot and the h_i is the slot insulation thickness. The maximum allowable current density in DD-PMSG air-cooled machine is around $3 - 4A/mm^2$ [173]. Hence, by enhancing the cooling system (forced-air cooling, water cooling or mixed cooling), higher values of temperature and densities could be reached. In fact, replacing the air-cooling with direct water-cooling will slightly influence the total mass of the generator[15]. Although air-cooling systems are a bit more efficient that water-cooling ones,

[14] Assuming that the flux density due to the magnet and the linear current loading forom the stator sinusoidally distributed around the stator

[15] The mass of the liquid-to-liquid cooling system is around 50 kg [174]

they are heavy and bulky [122]. Another possible solution is using superconducting generators [175] [176] [177] [178].

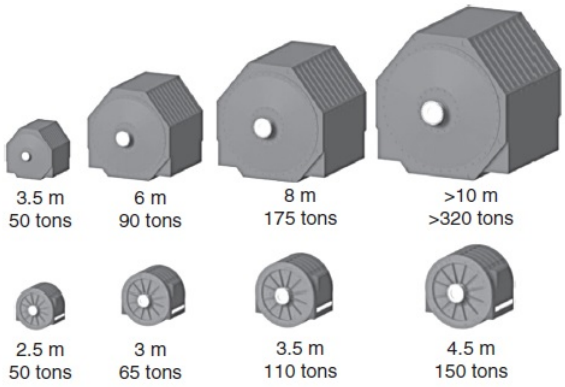

Figure 2.19: Size and mass comparison between DD-PMSF and DD-HTSG [19]

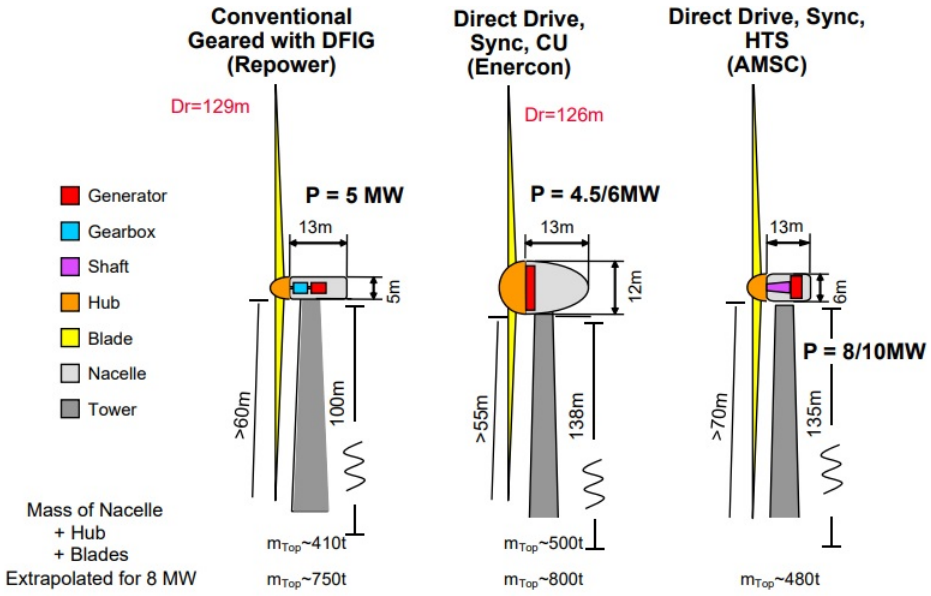

Figure 2.20: Size comparison between wind turbines with conventional and superconducting generators [20]

2.6.4.1.2 High Temperature Superconducting Generators (HTSG) With the progress in high temperature superconducting wire, High Temperature Superconducting Generators (HTSG) looks promising solution to increase power densities and avoid the rare-earths, while offering a high efficiency and a reduced weight compared to the conventional generators (See Fig. 2.20). Many generators were proposed for large capacities in wind turbine using the superconductivity [177] [178] [179] [180]. In [181], 10 MW MgB2 superconducting generator for offshore was designed and compared with conventional PMSG, weight reduction was noticed in both generator and tower, with 26 per cent and 11 per cent, respectively. Furthermore, in [182],

an electromechanical feasibility of a 10 MW HTSG class wind turbine was investigated. As well as, in [183], the minimization of the amount and the cost of HTS field coils was discussed. Moreover, in [184], an other optimisation of 10 MW HTSG wind generator based on its weight, its volume and the length of the HTS wire was discussed. Resulting on machine with almost the half of the weight compared with PMSG for the same capacity. However, in [185], 12 MW offshore wind turbine was proposed but with Low Temperature Superconductors field LTS winding. Besides, the academic community, where the HTS emerge as a promising solution for the large scale generators in the wind turbines, many prototypes were proposed by the industrials such as AMSC SeaTitan 10 MW, GE [21] [186] [187] and AML [188]. Recently, the first full-scale gearless high temperature superconducting wind turbine generator had been tested [189].

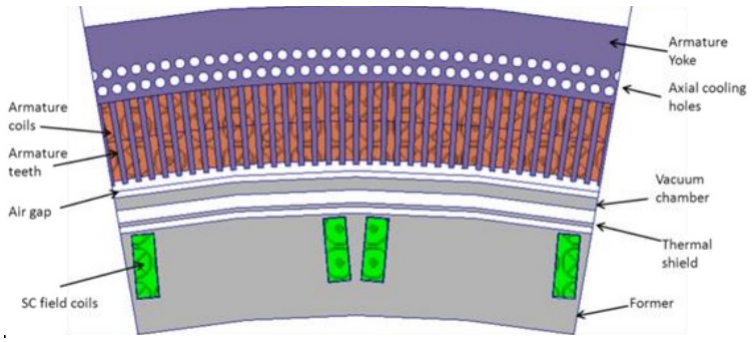

Figure 2.21: Cross-sectional view of the 10 MW HTSG [21]

2.6.4.1.3 Using a single/two-stage gearbox (Semi-Direct Drive Wind Turbine (Mid speed generators)) Hybrid system (Multibrid concept) of conversion has been introduced in the wind turbines in order to decrease the mass and the volume of the DD-PMSG [190]. It has been proposed to use a single-stage gearbox (with a gear ratio in the order of 6 or higher) coupled to a permanent-magnet generator. I has been introduced the first time by Multibrid for 5 MW. It aims to avoid the drawbacks of both geared and gearless drivetrain, by coupling permanent magnet machine with gearbox having a reduced number of stages. Hence, that conducted to high efficiency and lighter mass compared to the conventional generators. This technology is not widely used nowadays. Here are some examples:

- **Vestas** with *V164-8.0*[16] (8.0 MW).
- **Vestas** with *V174-9.5* (9.5 MW) two stage gearbox.

[16]Named Best Offshore Turbine 2014 by Windpower Monthly Magazine.

- **Areva** with *M5000-116* (6 MW) gear ratio (1:10).
- **Guangdong Mingyang** with *MYSE7.0-158* (7.0 MW) two stage gearbox.
- **M5000(116/135)** (5 MW) of *Areva* using step-planetary gear helical with ratio of 9.92 and PMSG.
- **WWD-3 DX** (3 MW) of *WinWinD* the rotor is connected to a low speed permanent magnet generator through two stages planetary gearbox.
- **HTW5.2-136** (5.2 MW) of *HITACHI* gear ratio (1:40).

2.6.4.1.4 Using lighter material Using material such as aluminum alloys and carbon fiber may offer a light but expensive structural support compared to steel support [191] [192].

2.6.4.1.5 Using iron-less machine A more promising solution was investigated in [193] [194]. It consists on the use of iron-less PM generator Fig. 2.22, which are lighter than the iron cored PM generators (a mass typically 20 per cent to 30 per cent of equivalent designs based on iron-cored magnetic circuits) with efficiency over 90 per cent. In contrast, because of its large diameter this structure could be aerodynamically inefficient [191]. Furthermore, another original idea was proposed in [195], it is based on putting a generator bearings adjacent to the air-gap and supporting them with rails, Fig. 2.23, in order to reduce the stiffness requirements of the rotor and the stator, leading to large mass reduction. Also, in [191], a new concept using magnetic bearing and mechanical bearing was investigated, it allowed to reduce 5 MW rotor's mass from 50 t (conventional rotor) to 28 t .

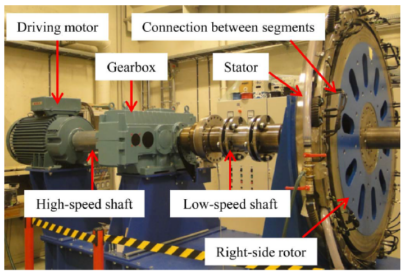

Figure 2.22: Experimental setup of a two-rotor conventional-array axial-flux generator

2.6.4.1.6 Using modular machine Using modular concept (physical modularity of functional modularity) on the conception of the machine could help in reducing the mass of the machine by avoiding wasted

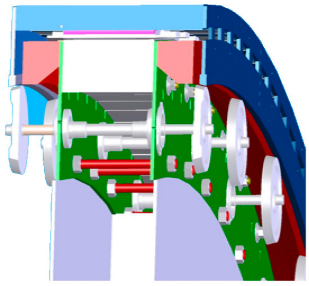

Figure 2.23: NewGen generator design with rail-way technology

material [196] [197] [198]. Besides, physical modularity offers simple stator lamination with assembly facilities, especially for large airgap diameter (easy to add and remove modules) [197]. The functional modularity (winding with to multiple parallel circuits) would be an interesting option to enhance the fault tolerence of the machine. Even though modular machines present many advantages, experiments shows that they present high leakage inductance, which impose complex power conditioning unit [73]. Further, the arrangement of modules can lead to mechanical instability, and thus audible noise and fatigue may be generated [73]. Also, using modular concentrated winding would induce large space harmonics, that lessen the efficiency of the machine. Fig. 2.24 illustrates an example segmented stator core.

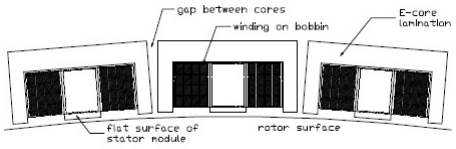

Figure 2.24: Segmented stator core [22]

2.6.4.2 Risks associated to the price of rare-earth elements

The amount of PM required for PMSG is proportional to the size of the machine, and inverse proportional to its speed [199]. As discussed above, the permanent magnets were adopted to reduce the mass of direct-drive wind turbine generator. PMSGs are attractive than the induction generator and electrically excited generator for low-speed high -power wind turbines. Unfortunately, the price of rare-earth elements (**REE**) has been proven to be very unstable [200], so PMSG is not economically viable solution. Furthermore, the control of the global market is concentrated geographically in Asia especially China, so a serious risk is associated to the REEs price. In addition, the extraction of this materials could have a bad impact on the environment.

2.6.4.2.1 Replacing the rare-earth material in wind turbine generators Researchers tried to tackle this problem, by seeking for alternative free REE generators, especially for the large wind turbine. The flux concentration allows the use of magnet materials with low energy density (ferrite) avoiding REE (NdFeB) [138] [201]. Inserting Ferrites magents between pole shoes, will reinforce the rotor magnetic flux. Therefore, one can get rid of the need for PM with high energy production. In [41], a 6 MW PMSG for direct-drive wind turbin, using only ferrite magnet, was exposed. Furthermore, a valuable comparison was conducted between two 6 MW PMSG topologies, a conventional surface mounted NdFeB generator and an alternative topology with flux concentrating ferrite magnet, both machines have the same stator. Authors proved that despite the fact that the generator with free REE heavier (119.6 t versus 42.3 t) with high inertia (156783 kg.m^2 versus 898587 kg.m^2), the cost of energy for both machines was almost the same. Therefore, with an appropriate optimization the ferrite PMSG could be one of the most appropriate option if the price of the NdFeB magnets will continue to increase. Nevertheless, when considering the structural support the energy cost of the free rare-earth magnets machine surged by more than 90 per cent [44]. Also, Halbach arrays could be used to concentrate the magnetic flux [202]. Another solution was patented in 2015, exploiting new design of magnetic circuit, allows the use rare-earth free permanent magnet with low coercivity (AlNiCo, FeCoW) to ameliorate the performance on the PMSG [203].

2.6.4.2.2 Using doubly-excited machine Unlike PMSG, doubly-excited machine use permanent magnets and excitation coils. This aims to avoid drawbacks of both electrically exited synchronous generator and permanent magnet synchronous generators.

2.6.4.3 Transportation and logistics limitations

Transporting and assembling direct-drive generator for large wind turbine over 10 MW can became a real challenge. Logistics and construction technology limited the external diameter if the electrical generator to 8 m [174]. Moreover, the cranes used in wind turbines assembling are limited to lifting a maximum of 100 t to a height of just over 100 m.

2.7 Conclusion

To meet the rapid growth of the power generation with lower cost its recommended to build larger wind turbines. Indeed, increasing the size of the wind turbine leads to high net power rating and low average levelized cost of energy. In addition, stronger and more stable wind can be captured at high hub altitude. Furthermore, longer blades catch the wind more efficiently. Nevertheless, upscaling a wind turbine without affecting the mass, the volume, and the construction's cost can prove quite challenging. In order to identify the suitable generator with improve cost and high efficiency, a comparison was conducted between different generators. It can be concluded that, due to the elimination of the gearbox, the direct drive systems offer better performances compared to geared ones, including low maintenance cost, higher reliability, reduced noise and higher efficiency. Direct-drive wind turbines with high power range require generators with high torque levels and low rotational speed. This chapter identified the challenges of low-speed generator in direct-drive wind turbines in terms of size, weight and cost. Different solutions has been exterminated to overcome the drawbacks associated to such machines.

From the review it can be can concluded that:

1. Radial flux generator seems to be a better option for direct drive wind turbines.
2. In low speed wind turbine the mass of the supporting structure becomes dominant in the total drive-train mass.
3. Electrically excited synchronous generator are not suitable for small pole pitch machine (high pole number).
4. The size and cost reduction of generators are of particular interest. There are two main drawbacks of DD-PMSG :
    - Risks associated to diameter and size. Opportunities for improvement:
        - Size reduction (increasing the flux density, enhancing the cooling, using high-temperature superconductors, adding single stage gearbox, using modular generator, using large diameter magnetic bearing).
        - Mass reduction (using iron-less machine, using lighter materials (e.g., aluminium alloys)).
    - Risks associated to the price of rare-earth permanent magnet. Opportunities for improvement:

  - Replacing rare-earth permanent magnet.
  - Doubly excitation.
  - using superconductor.

- Transportation and logistic limitations (related to the size and the mass of the machine).

Part II

MULTI-PHYSICS MACHINE MODELING

Chapter 3

Assessment Criteria and Design Requirement of Direct Drive Wind Turbine Generators

3.1 Introduction

The rated speed influences the size and the weight of electrical machine. Depending on the power, the rotational speed of the direct-drive wind turbine generator varies between 7 and 15 rpm. Direct-drive high-power generators in wind turbines (over 10 MW) need to attain high torque levels. When the torque rating increases and the speed decreases, the machine is getting bigger and heavier. Therefore, it is necessary to consider a machine with high torque density (ratio of torque capability to volume) in order to minimize the size, the price and masses of both the electrical machine and the supporting structure. Further, when selecting a generator topology for offshore application, which is the case of most ultra-large wind turbine, reliability of the machine should be taken into account. The conventional high-speed induction generators, with poor power factor and low torque density compared to synchronous generator, were rapidly excluded for such application. Indeed, increasing the pole numbers will increase the leakage inductance and then reduce the power factor of induction generators [204]. The stator winding in induction generator carries both the active power issued from the conversion and the reactive power used in the rotor's excitation. This require large copper cross-section and then induces high stator losses. Therefore, synchronous generator market for wind turbine has

been growing rapidly in the last decade. Our study focuses exclusively on PMSGs. The cost of the generator depends not only on the price of materials used (size) but also on the complexity of construction. However, the gearless conversion system needs to meet many requirements (weight, price, complexity of construction, grid connection, installation, transport, etc.).

The objective of this chapter is to discuss the electromagnetic design of 15 MW direct drive generators for renewable energy generation. In section 6.2, the above-mentioned requirements are discussed in details. Then, the existing technologies of direct drive machines are reviewed, merits and demerits relative to them are discussed in order to select the suitable permanent magnet machine for such high-power low-speed application. The main material choices and topology choices are presented. In section 3.3, the scaling laws that make it possible to estimate the size and the main geometrical dimensions of direct drive machine are given. Finally, a preliminary machine sizing of 15 MW 7.5 rpm machine is set. The presented sizing parameters will be used as base for the optimization design process.

3.2 Design Consideration for a Direct-Drive Wind Power Generator

3.2.1 Assessment criteria and design requirement of direct drive wind turbine generators

The wind power conversion system has to meet many requirements, including manufacture, grid connection, transport and installation. In direct-drive wind turbine the synchronous generator is connected to the grid via a variable frequency power converter, which separated the stator windings from the grid and allowed a full control of the stator current. As discussed in the previous chapter, the manufacturer of generator for gearless large wind turbine need to address several practical aspects related to their transport and installation. Multimegawatt wind turbines are often installed in offshore wind farms for their higher energy resource potential, and then this highly complex environment should be considered. The different components of the generation system should be compatible with the present transportation capacities and construction techniques. The installation and the lifting operations of such large and heavy system require heavy-lift cranes with good capacities. Therefore, most of conventional offshore vessels are not adapted to multimegawatt wind turbine [205], especially lifting heavier loads of up 100 t to heights of up 100 m. For example, the maximum lifting capacity of a large currently available Liebherr crane (HLC 295000) is 200 t for 150 m lifting height [206]. Thus, having an electrical generator with more than 200 t is not always practical for wind turbine manufacturers. An alternative approach would be to

use segmented machine (modular), that helps on the manufacturing, transportation and maintenance of the nacelle.

The design of direct-drive wind turbine generator has proven to be arduous task that has to account for the interaction between many disciplines and the presence of diverse constraints which may usually be contrasting design requirements. Our study focuses only on electromagnetic and thermal design requirements. Various criteria, including torque density, efficiency, cost, power density, outer diameter, active material weight and power factor have been introduced to assess the relevance and feasibility of electrical machine for high-power wind turbine applications. The most important design criterion in such low-speed applications is the generator's torque density. The torque density must be improved to address two specific generator issues, namely the weight and size. The cogging torque should be kept low enough to enable the self-start ability of the generator at low power levels, prevent possible mechanical vibration and reduce the audible noise [207] [173]. The frequency of the power converter is determined by the required rotational speed of the electrical generator, n, and its pole pairs number, p,

$$f = \frac{p \times n}{60} \tag{3.1}$$

where the rotational speed n is in rpm. The electrical frequency should be kept high enough ($>$ 10 Hz) in order to avoid additional cyclic temperature stress on transistors of the power converter, and then prevent over-dimensioned IGBTs [208] [209]. Therefore, according to the Eq. 3.1, with low rotational speeds the use of large number of poles is necessary. Increasing the pole number reduces the stator iron losses and the amount of lamination materials needed for stator yoke. Nevertheless, the pole number is limited by the pole pitch, which should be large enough to arrange the bar-shaped conductor in the stator slots.

3.2.2 Forces in electrical machines

Maintaining small airgap clearance could be a big challenge in the case of direct-drive wind turbine. Electrical generators under operational loading are subject to several forces including Maxwell's stress, centripetal force, thermal expansion and gravitational force. Those operational loads might be structurally demanding, due to the non-conventional structure of low-speed high-torque generators [210] [45]. Indeed, the larger the rotor surface (large diameters), the higher forces acting on it [210]. The support structure need to be robust and stiff enough to not only maintain the airgap clearance between the rotor and the stator against the structural forces, but also keep the machine's active part in place against the attraction forces and gravity [137]. The

main forces acting within an electrical generator are presented and discussed in this section.

3.2.2.1 Stress in the airgap

In electrical machines, the force applied to one part of the magnetic circuit can be obtained by integrating the Maxwell's stress tensor, σ_F along an airgap closed surface, S that surrounds the rotor and enclosing thus magnetic part. Using the Maxwell's stress tensor, the resulting torque acting on the rotor surface could be written in a scalar form as

$$T = \oint_S r \times \sigma_F dS \tag{3.2}$$

The airgap is assumed to be small enough to be negligible compared to the rotor radius. The stress created on the object surface can be defined as

$$\sigma_F == \begin{cases} \sigma_{F_n} = \frac{1}{2}\mu_0(H_n^2 - H_t^2) \\ \sigma_{F_t} = \mu_0 H_n H_t \end{cases} \tag{3.3}$$

μ_0 is the vacuum permeability, H_n and H_t represent the normal and the tangential magnetic field strength, respectively. Taking into account the relationship between the flux density,B, and the magnetic field strength,H, in the airgap, the stress created on the surface of the rotor can be expressed by

$$\sigma_F = \begin{cases} \sigma_{F_n} = \frac{1}{2\mu_0}B_n^2 - \frac{\mu_0}{2}H_t \\ \sigma_{F_t} = B_n H_t \end{cases} \tag{3.4}$$

where B_n is the radial airgap flux density (in the middle of the airgap, if desired.). However, only the tangential stress component σ_{F_t} contributes on the torque's production .

3.2.2.1.1 Tangential stress The tangential component of the airgap stress, also called shear stress or force density, is a useful concept in electric machine design (See Fig. 5.7). It represents the average tangential force F_d per unit of swept airgap surface area A_g, it is expressed as

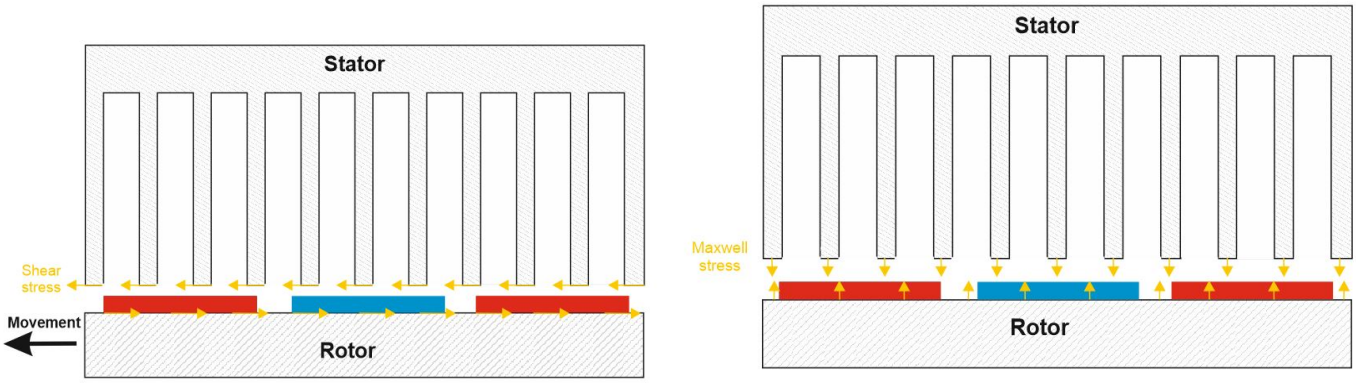

(a) Shear stress (Tangential stress)

(b) Maxwell stress (Normal stress)

Figure 3.1: Airgap stress in radial flux machine

$$\sigma_{F_t} = \frac{F_d}{A_g} \tag{3.5}$$

For radial flux machine with airgap radius R_g and axial length L_{act}, the torque can be calculated by

$$T = F_d \times R_g \tag{3.6}$$

Substituting Eq. 3.5 in Eq. 3.6 gives

$$T = \sigma_{F_t} A_g R_g = 2\sigma_{F_t} \underbrace{\pi R_g^2 L_{ax}}_{V_g} = 2\sigma_{F_t} V_g \tag{3.7}$$

The Eq. 3.7 shows that the rated torque of an electric machine is proportional to its rotor volume (square of the airgap diameter and length of the machine) and shear stress. Moreover, the shear stress, given in Eq. 3.4, represent the product of the radial airgap flux density and the tangential magnetic field. The linear current density around the airgap circumference A produces the main part of the tangential magnetic field, Eq. 3.4 became

$$\sigma_{F_t} = B_n A = BA \tag{3.8}$$

B and A are also know as the magnetic and electric loading, respectively. While the magnetic loading is a measure of the maximum permissible airgap flux density, the electric loading represents the maximum allowable current in the machine. In PMSG the magnetic loading is contained by both steel and permanent magnet

proprieties. Indeed, the teeth flux density must be limited to about $B_{max} = 2\,T$, else core losses may became excessive, that excluded airgap flux densities higher than $B_{n_{max}} = 1\,T$. Permitted values of airgap flux density are given in Table 3.1.

Table 3.1: Typical values of radial airgap flux density magnitude for synchronous machines [31]

	Salient pole	Non-Salient pole
$B_{g_{max}}$ [T]	0.85 - 1.05	0.8 - 1.05

Further, in practice, for fixed slot area the electric loading is limited by the cooling technology. It could lie between $A = 30 - 80\,kAm^{-1}$ for air-cooled machine, and could reach $A = 200\,kAm^{-1}$ with direct water cooling [211]. Typical values of shear stress are provided in Table 3.2. It is important to notice that transverse-flux machines have high torque density compared to longitudinal-flux machines. Indeed, in TF-PMSGs the electric and magnetic loading are decoupled. Furthermore, the shear stress is rather constant for different generators, it could lie between $\sigma_{F_t} = 30 - 60kN/m^2$ for direct-drive air-cooled machine [173].

Table 3.2: Typical values of magnetic shear stress for different machine types [32][12]

Machine type	Shear stress $[kN/m^2]$
Small totally-enclosed motors (Ferrite PM)	7 - 14
Totally-enclosed motors (Rare Earth PM)	14 - 42
Totally-enclosed motors (Bonded Neodymium-Iron-Boron PM)	20
High-performance servomotors	15 - 50
Aerospace machines	30 - 75
Large liquid-cooled machines	100 - 250
Transverse flux machine with active rotor	80 - 200
Transverse flux machine with passive rotor	80 - 200
Transverse flux machine reluctance	20 - 40

3.2.2.1.2 Normal stress The Normal stress, also called Maxwell stress, in the airgap represents the magnetic attraction force between the permanent magnets in the rotor and the stator iron, it may cause radial vibration and noise in the machine structure (See Fig.5.7). The normal stress deforms the magnetic circuit to minimize the airgap length and reduce the reluctance of the airgap [212], then it trends to pull stator awards rotor. This force is considered to be the largest force within an electrical machine. For a high airgap flux densities, the normal stress can be about ten times than that of tangential stress [45]. Based on the continuity theorem of normal component flux density and magnetic strength field in the interface between airgap and

stator iron surface, in front of theeth, and with the absence of current density, one can write that

$$\begin{cases} B_{n_{air}} = B_{n_{iron}} \\ H_{t_{air}} = H_{t_{iron}} \Rightarrow \dfrac{B_{t_{air}}}{\mu_0} = \dfrac{B_{t_{iron}}}{\mu_r \mu_0} \Rightarrow B_{t_{air}} = \dfrac{B_{t_{iron}}}{\mu_r} \approx 0 \end{cases} \tag{3.9}$$

By substituting the relation between the magnetic filed strength and the flux density ($B = \mu H$) in equation. 3.4, and by neglecting saturation effects, the normal stress became

$$\sigma_{F_n} \approx \frac{1}{2\mu_0} B_n^2 \tag{3.10}$$

To facilitate computations, when evaluating radial stress, it is common to neglect the tangential airgap flux density [213] [214]. As seen in equation 3.10, the normal airgap stress component is proportional to the square of the airgap flux density. The higher is the airgap length, the lower is the flux density and the radial stress force. Slotless synchronous machine, with large magnetic gap, exhibits lower magnetic attraction compared to slotted machines. Hence, to maintain the required airgap between the stator and rotor in iron cored low-speed high-power machines, heavier and larger structural support is needed. In addition, because of their non-conventional structure, long tooth with thin stator yoke, the tangential stress in direct-drive PMSG generates radial deflection, that may be intensified due to the the tooth bending motion [215] [23]. Fig 3.2 illustrates an example of radial deflection caused by tangential forces in a stator of 12 slots. Consequently, that might add structural challenges to the direct-drive electrical generators.

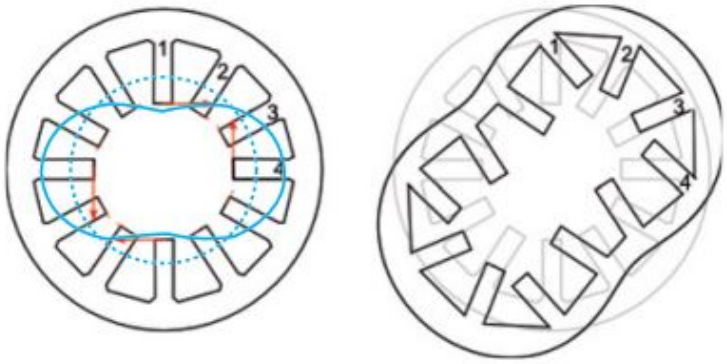

Figure 3.2: Deformation of the stator core caused by the tangential pressure [23](order 2[1]).

[1] order of radial magnetic forces[214]

3.2.2.2 Gravitational force

The weight of the Direct-drive electrical generator might be an important load to be considered. It could cause deflections of the support structure [126].

3.2.2.3 Thermal expansion

Losses in electrical generators generate considerable amount of heat, which leads to a temperature rise in different parts of machine. Usually, the stator is the main source of heating in electrical machines, that causes unequal thermal expansion (See Fig. 3.3) of stator and rotor and that might alter the airgap clearance [45][126] (closing the airgap in the outer-rotor machine, and widening airgap in inner-rotor machine [126]). The amount of the expansion is given by [45]

$$\Delta L = L_0 \alpha \Delta T \tag{3.11}$$

where ΔL is the change in dimension, L_0 is the original dimension, α is the thermal coefficient of expansion of the material and ΔT is the temperature rise. In our study, thermal expansion is not considered because we assumed that the generator cooling is adequate, and the stator expansion is very large compared to the rotor one.

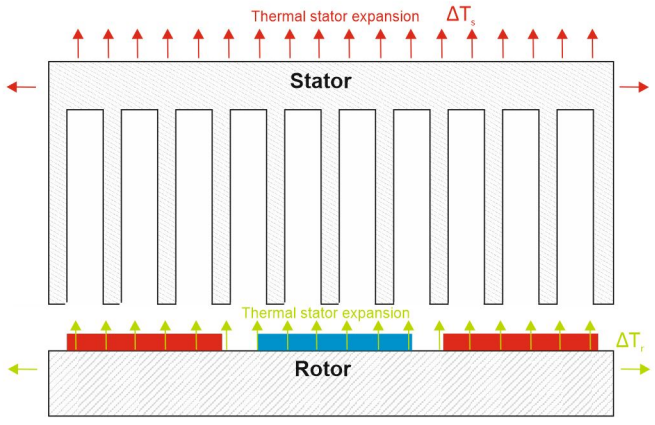

Figure 3.3: Thermal expansion effects in radial-flux machine (Cross-section)

3.2.2.4 Centripetal force

Torsional deflection of generator support structure may be caused by the angular acceleration of the generator rotor. The centripetal force is proportional to the diameter and rotational of the electrical generator. The magnitude of the force exerted on the rotating mass is given by

$$F = R\omega^2 m = \frac{m\upsilon^2}{R} \tag{3.12}$$

where R, υ, m and ω are the radius, peripheral velocity, mass of the object and is its rotational velocity, respectively. The rotation of the object causes a force in the direction of the centre. For ring radius the deflection is given by

$$\Delta R = \frac{\rho R^3 \omega^2}{E} \tag{3.13}$$

where E is Young's modulus and ρ is the mass density of the steel. For radial-flux machine with a fixed $L_{act}/2R$ ratio, the acceleration decreases as the generator gets larger. Then, for direct-drive generators operating at low speeds the centripetal force can be neglected [45] [126].

3.2.3 Preliminary machine sizing

This section presents a concept study of 15 MW low-speed generator.

3.2.3.1 Materials

3.2.3.1.1 Permanent Magnet Materials As explained in previous chapter, in high-power low-speed machine for wind energy, the permanent magnet electrical machines are gaining popularity as a good alternative to electrically-excited machine. This is mainly due to their high efficiency and high torque density. The magnetic behavior of permanent magnets can be characterized by:

- Remanent flux density (remanence), B_r, is the residual magnetization remaining in a permanent magnet material after the magnetizing field is removed.
- Maximum energy product, BH_{max}, indicates the maximum energy that the permanent magnet material can store.

- Coercivity, H_c, is the negative field strength necessary to bring the remanence to zero in material previously magnetized.
- Hysteresis cycle and more particularly second quadrant of the hysteresis loop.
- Resistivity

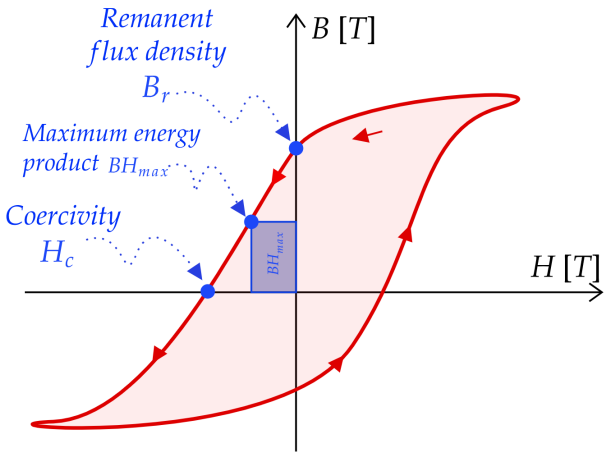

Figure 3.4: B-H loop of a permanent magnet

Figure 3.4 presents a typical BH curve of a permanent magnet. A good permanent magnet should produce a large magnetic flux with small mass and has the ability to withstand high demagnetizing field. These desirable properties can be stated in terms of remanent flux density and coercive field.

The development of permanent magnet materials has been considerable in the last century, the historical development throughout this period is shown in Fig. 3.5. This figure shows the improvement of the energy product form the beginning of the twentieth century. Excluding the natural magnet, and earlier K.S. steel (Honda steel) and M.S. steel, the modern history of permanent magnet began with Alnico (Aluminium-nickel-cobalt) in the 1930s. The Alnico magnets, based on iron and other metals, have an energy product between 10-83 kJ/m^3. They are resistant to temperature, so usually used in applications where the temperature exceed 300 ^{o}C [216]. Although these magnets offer high remanent flux density, their high risk of demagnetization (low coercivity) and high price (complex manufacturing process) [217], make them financially and magnetically unattractive for high power density machines. Therefore, Alnico magnets were rapidly replaced by Ferrite (mainly iron) in the late 1950s. Although Ferrite magnets do not have desirable values in energy products and are not suitable for very high temperature applications, it still widely used in electrical machine nowadays since

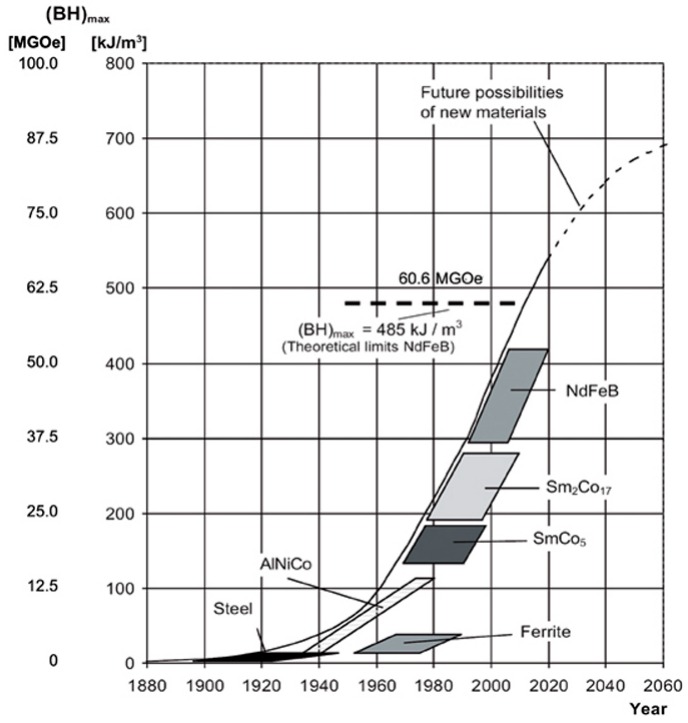

Figure 3.5: Historical development of permanent magnets [24]

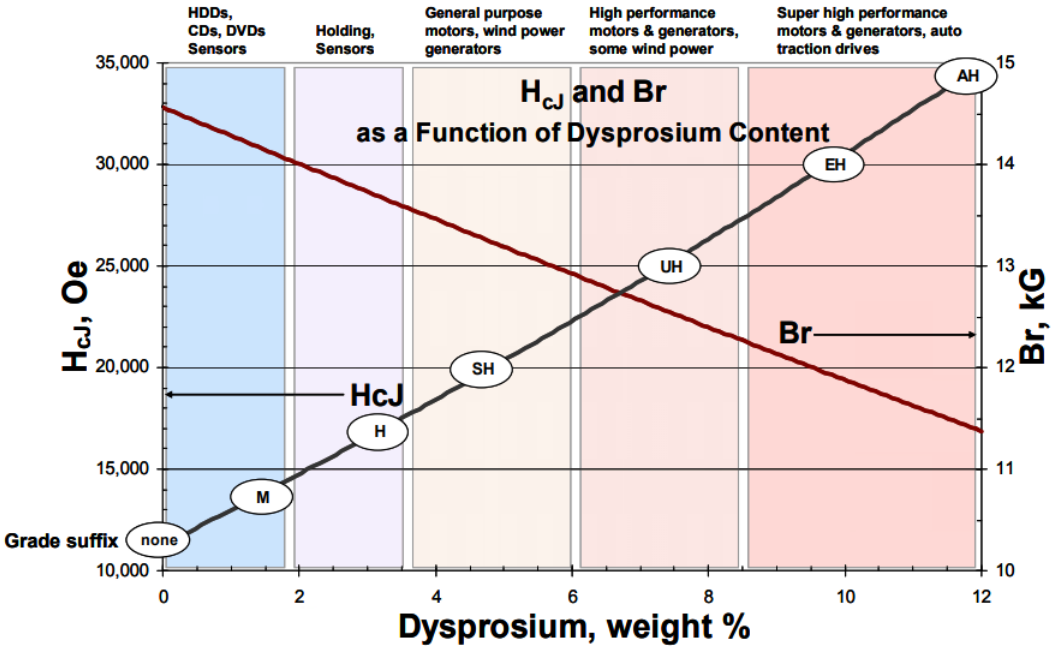

Figure 3.6: The Coercivity and remanence of NdFeB as a function of Dysprosium content [25]

it is made of cheap, plentiful and non strategic raw materials (Iron oxide, Fe_2O_3, and barium, Br, or strontium, Sr). Furthermore, Ferrites are popular for use in complex shapes. The next considerable step forward was

with the discovery of rare-earth metals in 1960s. Rare-Earth Cobalt magnets (RECo) were introduced in the early 1970s, they are made of rare-earth metals, mainly Samarium, Sm, and cobalt, Co. The most important RECo were $SmCo_5$ and Sm_2Co_{17}. The maximum energy product of the SmCo varies from 143 kJ/m^3 to 250.7 kJ/m^3. Although their high remanent flux density (0.87-1.16 T) and energy product, these magnets showed limited commercial success due to their cost and availability [37]. After that, in 1983, the Neodymium Iron Boron (NdFeB) magnets were developed by General Motors and Sumimoto. In this type of magnet, the rare samarium and cobalt were replaced by relatively more common metals: neodymium and iron. NdFeB became widely used in electrical machines, for their high energy (200 kJ/m^3 - 415 kJ/m^3) capability, relatively low cost and better mechanical properties for processing complex shapes compared to SmCo [37]. However, NdFeB are sensitive to changes in temperature [216]. NdFeB consists of nearly 67 per cent[2] of iron, 1 per cent of boron and 32 per cent of rare-earth materials. In wind turbine generators, besides Nd, small but important amount of other REEs is used in NdFeB-based permanent magnet machines (e.g.; dysprosium (Dy), terbium (Tb) and praseodymium (Pr)) [218]. In practice, in wind turbine's generator, Dy is more commonly used than Tb and Pr. Adding Dy help to achieve a better stability of the magnet at high temperatures (See Table 3.3) with relatively half the price of Tb. Table 3.3, shows that NdFeB permanent magnet contains about 30–32 per cent of REEs (mainly 21.5–29.5 per cent (Nd &Pr) and 0–11 per cent of Dy plus small amounts of others REEs). Dy is also added to enhance the magnetic properties of the NdFeB (See Fig. 3.6).

Table 3.3: Maximum operating temperature function of the Dysprosium content of NdFeB magnet grades [33]

Suffix	-	M	H	SH	UH	EH	AH
Max operating temperature	80	100	120	150	180	200	220
Dy content [%]	< 0.5	1.4	2.8	4.2	6.5	8.5-11	8.5-11
Nd&Pr content [%]	29.5	28.6	28.2	25.8	24.5	19-21.5	19-21.5

The rare earth metals (17 elements) can be classified depending on their abundance. They are often distinguished as either light REE (LREE) or heavy REE (HREE). The HREEs have higher economic importance and are less abundant than the light elements, then they tend to be more expensive [219]. It is worth noting that Dy is considered to be the most critical HREE (See Fig. 3.7) by U.S. Department of energy (DOE) [202].

The main application fields of NdFeB permanent magnet by grades are presented in Table 3.4. Usually, permanent magnets for wind turbine application are SH-grade.

[2]All the percentage given are weight percentage.

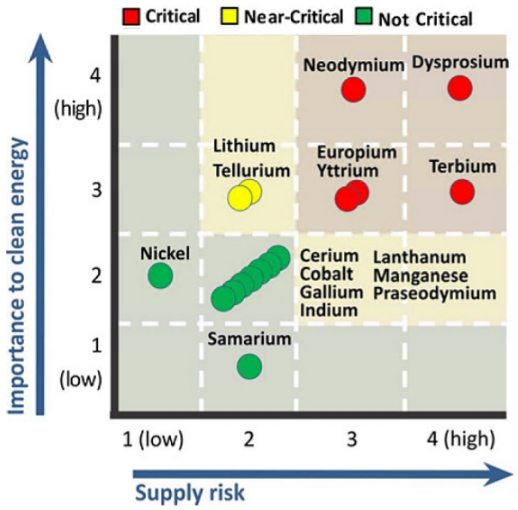

Figure 3.7: Medium-term (2015-2025) criticality matrix [25]

Table 3.4: List of main application fields of NdFeB grades

Suffix	Max. Working Temperature [^{o}C]	Temperature coefficient of the remanent flux density [%/^{o}C]	Applications
-	80	-0.12	Toys, latches, advertising, etc.
M	100	-0.12	Hard disk drives, CD/DVD, sensors, etc.
H	120	-0.11	Magnetic separations, gauges, etc.
SH	150	-0.1	Wind power generators, electric bicycles, energy storage systems, magnetic braking, magnetically levitated transportation, etc.
UH	180	-0.19	Commercial and industrial generators
EH/AH	200	-0.085_0.08	Hybrid and electric traction drives, high temperature machines, etc.

Figure 3.8 shows an example of REE share on the NdFeB permanent magnet used in wind turbines. As it can be notice, Nd account for almost one third of the material used in the REE NdFeB permanent magnet. A small quantity of Dy is added, depending on the application as explained before, to increase operating temperature. Often, magnets with more Dy contain less Nd [220]. Some typical properties of some commonly used magnets in electrical machines are shown in Table 3.6.

Nowadays, most of the existing large-power low-speed PMSG in wind turbines are NdFeB based. The wind turbine production is projected to double in this decade. Due to the recent sharp fluctuations in the price of such rare-earth permanent magnet (in the last ten years, See Fig. 3.9), the electrical machine manufacturers

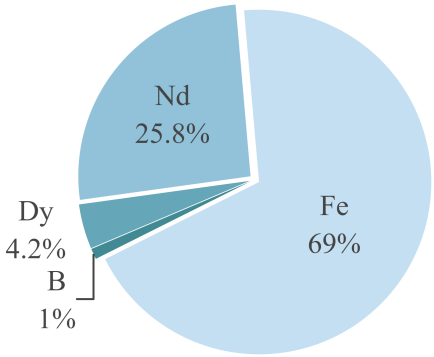

Figure 3.8: Share of rare-earth elements in the NdFeB permanent magnets used in wind turbines

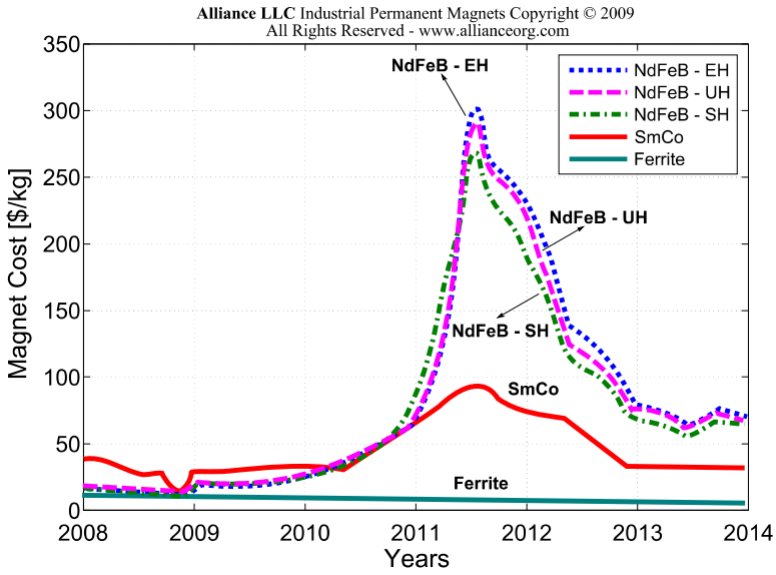

Figure 3.9: Permanent magnet price trend (EH, UH, SH are series of NdFeB)

are working on reducing the wind turbine industry's dependency on the rare-earth metals by suggesting alternative designs (e.g.; Less/No rare-earth magnets, recycle rare-earth magnets, etc). Then, it would be interesting to investigate other cheap, plentiful and more stable price permanent magnet materials such as Ferrite. Replacing NdFeB magnets by Ferrite magnets, having poor magnetic properties, may require new rotor topologies. Indeed, the remanent flux of NdFeB is good enough to give an acceptable flux density in the airgap with surface-mounted magnets, while Ferrites require a flux concentration to achieve acceptable airgap flux densities. Although direct-drive synchronous machines with Ferrites are heavier, they still lighter than asynchronous machines combined with gearbox. Then, the Ferrite magnets can be a better compromise between the machine's weight and the machine's cost.

In this thesis, two grades of Ferrite and two of NdFeB were found suitable. The neodymium magnet grades are usually labelled in form NxxYY, where N stands for neodymium, xx refers to the maximum energy product in Mega-Gauss Oersteds (MGOe)[3] and the letter (two letters, lack of letter), YY, following the number is related to the temperature rating. The NdFeB grades without suffix letter, YY, has maximum operating temperature 80^{o}C. However, the highest grade of N52 and N55 only work at 60^{o}C [33].

The properties of these magnets are provided in Table 3.5.

Table 3.5: Magnetic properties of the selected magnets

Magnet material	Name	Supplier	Remanence T	Coercivity $[kA/m]$	Resistivity [Ω m]	Mass density $[Kg/\mathrm{m}^3]$	$\mathrm{T}_C(\mathrm{B}_r)$ $[\%/^oC]$
NdFeB	N40SH [221] (T_{max} = 150^{o}C)	Arnold Magnetic	1.20	959	1.5-1.3 $\times 10^{-6}$	7600	-0.12
	N48SH [222] (T_{max} = 150^{o}C)	Arnold Magnetic	1.39	1032	1.5-1.3 $\times 10^{-6}$	7600	-0.12
Ferrite	Y30[4](C5[5]or HF26/18[6]) [223] [224] (T_{max} = 250^{o}C)	Eclipse Magnetics	0.4	240	1×10^5	5000	-0.2
	NMF-15G[7][225]	Hitachi Magntic	0.49	350	100	5000	- 0.21

[3] 1 $\mathrm{MGOe}_{cgs_{units}}$ = 7958 J/m^3
[7] Chinese Standard – Commonly used globally, especially in UK and EU [226].
[7] American Standard (still in use but limited range) [226].
[7] European Standard (still in use but rarely outside mainland Europe) [226].
[7] The highest grade ferrite magnets in the market [227].

Table 3.6: Typical properties of different permanent magnet materials [34][35]

Magnet material		Units	Alnico	Ferrite	SmCo	NdFeB
Composition		-	Fe, Co, Ni, Al, etc.	Fe_2O_3, Br, Sr, etc.	Sm, Co, Fe, Cu, etc.	Nd, Fe, B, etc.
Mass density	ρ	kg/m^3	5000 - 7200	3500 - 5000	8400	7500 - 7800
Energy product	$(BH)_{max}$	kJ/m^3	10.74 - 83.55	6.36 - 34.37	143 - 250.7	222 - 430
Remanence	B_r	T	0.66 - 1.32	0.2 - 0.41	0.87 - 1.19	1.08 - 1.49
Coercivity	H_c	kA/m	37.8 - 117	125 - 318	653 - 867	875 - $2.7e^3$
Permeability	μ	N/A^2	1.5 - 5.0	1.1 - 1.2	1.05 - 1.09	1.03 - 1.08
Maximum operating temperature	T_w	^oC	450 - 500	250	250 - 550	80 - 230
Curie temperature	T_c	^oC	760 - 860	450	750 - 840	310 - 350
Temperature coefficient of the remanent flux density	$T_C(B_r)$	$\%/K$	-0.02	-0.2	-0.03 - -0.04	-0.11 - -0.13
Temperature coefficient of the coercivity	$T_C(H_c)$	$\%/K$	-0.07 - 0.03	0.2 - 0.5	-0.15 - -0.30	-0.55 - -0.65

3.2.3.1.2 Steel Lamination Material The selection of the stator and rotor core materials is based on the magnetic, thermal, and mechanical properties of materials, as well as the material cost. The selection of the core materials involves a trade-off between material properties (e.g., permeability, saturation flux density, density, and tensile strength), cost, core losses and fabrication processes [37]. For instance, the lamination material of the stator has higher requirement for electromagnetic properties, while the rotor materials has higher requirement for mechanical properties since it is a subject of large centrifugal force as it rotates. Usually, the electrical steel used in electrical machines are characterized by the saturation flux density and the core losses. The saturation flux density needs to be as high as possible to give higher possible tangential force density [173]. Generally, laminations with a higher saturation level have a lower percentage of silicon and higher iron losses, so there is a trade-off between saturation flux density and losses. The machine frequency is so low in direct-drive wind turbine that at rated load the iron losses are much smaller compared to the copper losses. Table 3.7 shows a list of suitable steel grades for different types of applications. In our study, M350-50A is found suitable for low-speed high-torque multi-megawatts generators.

Table 3.7: Examples of suitable Cogent grades for various applications [36]

	M235-35A – M330-35A M250-50A– M350-50A M330-65A – M350-65A	M400-50A M700-50A M400-65A M700-65A	M800-50A M940-50A M800-65A M1000-65A
Large size rotating machines	✓		
Medium size rotating machines	✓	✓	
Small size rotating machines			✓
Hermetic motors		✓	✓
Small power transformers	✓		

3.2.3.1.3 Conductor Material The stator windings are made up of copper coils inserted into stator slots. Investigate the impact of using alternative conductor materials, such as aluminium could be of interest to the electrical equipment manufacturers in order to reduce the mass and the cost of generators in large wind turbines. The main properties of the copper and aluminium are given in Table 3.8.

Table 3.8: Comparison between properties of copper and aluminium [37]

	Units	Copper	Aluminum
Density	kg/m^3	8900-8940	2700
Thermal conductivity	W/m.K	391	96.2
Melting temperature	^oC	1083	660

3.2.3.2 Proposed Generator Topology

3.2.3.2.1 Electrical vs. permanent magnet excitation Depending on the rotor's excitation method, the synchronous machine can be excited either electrically or by permanent magnets. However, passive rotor can be used in Switched Reluctance Machine (SRM), in which a single excitation is placed in the stator. According to [169], SRM topology gives torque density and cost to torque ratio comparable to the RF-PMSG for diameters below 1 m. This difference became larger with increasing diameter. For instance, for the same equivalent diameter (4.2 m) the torque density is nearly 50 per cent higher in SRM than in RF-PMSG; however, SRM leads to four times higher cost to torque ratio [169]. Consequently, SRM is not promising candidate for large-diameter wind turbine generators. Despite the simplicity and robustness of the EESG, PMSG are more suitable for direct-drive large wind turbine. In fact, the need of DC excitation, slip rings and brushes might reduces dramatically the overall efficiency and reliability of the power generation system, which might be critical for large wind turbine. Apart from this, increasing pole number and decreasing pole pitch is very challenging in the design of EESG. To illustrate this, the ratio of the coil material hight to the permanent magnet hight required for the same airgap flux density is considered and can be calculated as in [16]

$$h_r = \frac{h_{Cu}}{h_{PM}} = \frac{2B_{sat}(B_r - B_g)}{\mu_0 J_r k_{fill} \tau_p (B_{sat} - B_g)} \tag{3.14}$$

where h_{Cu} and h_{PM} are the copper and the permanent magnet height, respectively. B_{sat} and B_g are the iron saturation flux density and airgap flux density, respectively. J_r is the rotor current density, k_{fill} is the rotor slot filling factor. Let as consider, for example, an iron saturation flux density of $B_{sat} = 1.8\,T$, a remanent flux density of $B_r(NdFeB) = 1.2\,T$, a rotor slot filling factor of $K_{fill} = 0.7$ and a current density $J_r = 2e6\,A.m^{-1}$. In such case, for a given airgap flux density, the ratio of the copper height to the permanent magnet height increases with the decreasing pole pitch (See Fig. 3.10). Consequently, EESGs are more bulky, and heavier compared to PMSGs. It can be concluded that, despite the fluctuation on REE specific cost (5 to 14 times the price of the copper and laminated steel), PMSGs with NdFeB may become cheaper than EESGs for small pole pitches less than $\tau_p = 8\,cm$.

In [166], the overall mass of different direct-drive generators has been estimated, the author concluded that the EESG Enercon concept, with $m/T = 66.5\,kg\,kN^{-1}m^{-1}$ (mass to torque ratio), is the heaviest and the most expensive system configuration compared to three PMSG including Zephyros concept, theoretical concept and

[8] Data source: FRED, Federal Reserve Economic Data [228]

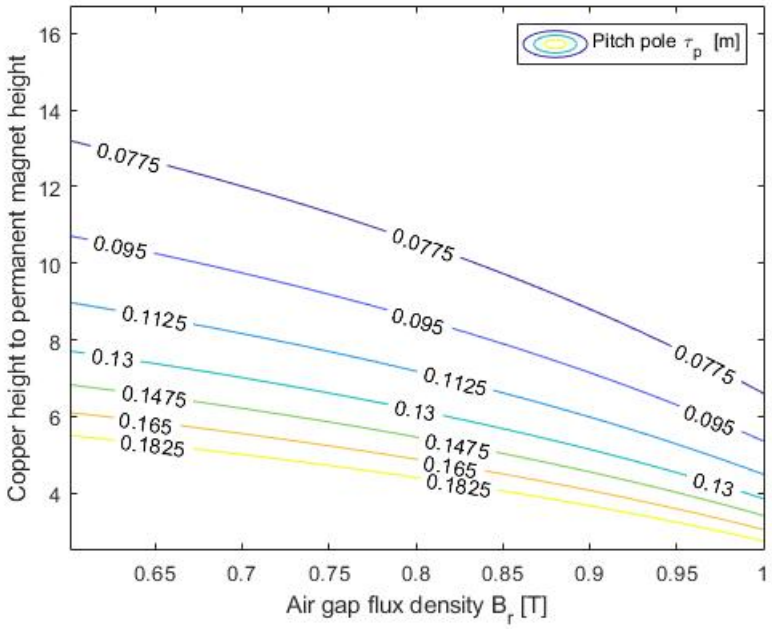

Figure 3.10: The copper thickness to the permanent magnet thickness for equivalent airgap flux density

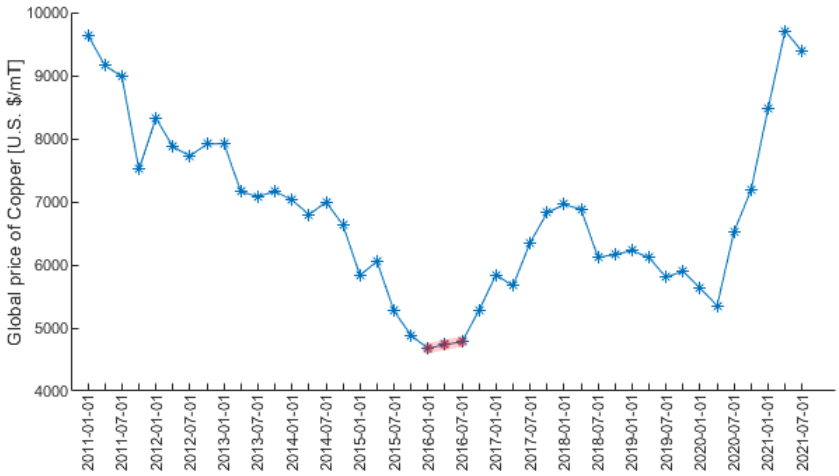

Figure 3.11: The copper global price over the last ten years [8]

NewGen concept. In [229], a comparison between 10 MW synchronous generators shows that despite the fact that the EESG ($\tau_p = 18.23\,cm$) have more than three times the mass of PMSG ($\tau_p = 9.98\,cm$) (almost four times the mass of PMSG including inactive parts) it was the cheapest option. There was a significant variation in the copper specific cost over the last ten years. After, it hits a low of $4781\,\$/mt$ in 2016 (See. Fig. 3.11), the reference year of the price estimation, the copper cost increased significantly four years later. Then, the

EESG may not be a promising topology when large amount of copper is used.

Moreover, EESG offers controllable current excitation. Indeed, by reducing the excitation current for low wind speeds, losses decrease which may enable low cut-in wind speeds [173]. Furthermore, by adjusting the voltage for high wind speeds, the power converters might do not have to be overrated [173] [169]. This is not very important parameters to be considered in large-power direct-drive systems, where the generator is connected to the grid via power electronic converter. As presented earlier, PMSGs in direct-drive wind turbines, with large number of pole pairs, may offer reduction of both the mass and the cost of the machine [169] [80].

3.2.3.2.2 Stator core orientation: Longitudinal- vs. transverse- flux machine As explained in the previous section, the construction of ultra-large TF-PMSG for direct-drive wind turbine would be a challenging task. In [166], four different topologies of 10 MW TF-PMSG and surface mounted RF-PMSG has been investigated, authors conclude that in spite their high force density, 65-71 kNm^{-2}, TF-PMSGs seem to have high mass to torque ratio compared to RF-PMSG, with 41 kNm^{-2}. Further, increasing the airgap diameter (larger airgap), above 1 m, degrades the performances of TF-PMSG [16]. Therefore, transverse flux will not be considered for further investigation in this thesis.

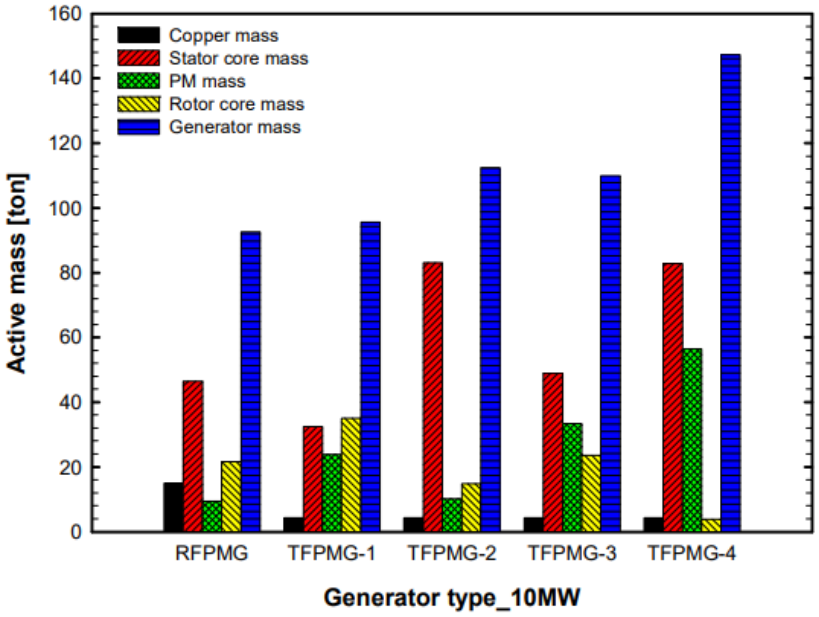

Figure 3.12: Active mass comparison of TF-PMSG and RF-PMSG

3.2.3.2.3 Air gap orientation: Radial-flux vs. axial flux machine For high-torque low-speed applications, axial flux machines seem to be heavier than radial and transverse flux machines [166]. A proper analysis of the slotted axial-flux permanent magnet machine allows highlighting the challenges faced by manufactures when is comes to such machine. The potential difficulty with AF-PMSGs is the production of the stator core, since the slot pitch varies on stator laminations for different radii [166]. In addition, maintaining of the airgap of such special large diameter machines is particularly challenging. Despite the fact that, AF-PMSGs have short axial length and high torque to volume ratio, it seems that they have low torque to mass ratio and present structural instability. Furthermore, thermal expansion does not affect the airgap of axial flux machine contrary to that of radial flux machine, but usually in machines with large diameters the heat evacuation area is increased and then the thermal expansion is not major problem. Finally, due to their structural stability and mass to torque ratio, RF-PMSGs were selected in this thesis.

3.2.3.2.4 Permanent magnet integration in the rotor: surface mounted vs. buried/inserted magnet According to the integration of the magnets in the rotor, the radial-flux PMSM can be divided in three categories: surface mounted, inset and buried PMSGs. In the surface mounted PMSGs (SM-PMSG), the magnets are glued to the surface of the rotor (See Fig. 3.13). One of the main advantages of this topology is its simplicity and then its low price.

Inserted PMSGs (I-PMSG), in which the magnets are glued inside rotor's slots (See Fig. 3.14), are nowadays widely considered due to attractive features, including high efficiency, well protection against demagnetization and mechanical stress, wide constant power speed range and production of reluctance torque due to the saliency of the machine and robustness [230] [231].

In buried PMSGs (B-PMSG), the magnets are inserted inside the rotor. A high airgap flux density can be achieved using the B-PMSG configuration that employs flux concentration with tangential magnetization topology[9] (See Fig. 3.15) [232] [233]. ST-PMSG, with high poles number, seems to be an attractive solution to reduce the mass of rare-earth PMs. Nevertheless, comparing to other I-PMSG, ST-PMSG machines exhibit important drawbacks that are summarized in a limited flux-weakening capability, lower saliency ratio and lower demagnetization strength [234] [232] [235]. Thus, while designing a spoke-type machine it is important [236]:

[9] It is also called spoke-type PMSG (ST-PMSG).

- to prevent irreversible demagnetization resulting from the low coercivity if using ferrite magnets.
- to prevent rotor stress resulting from inserting large size magnets into the rotor.

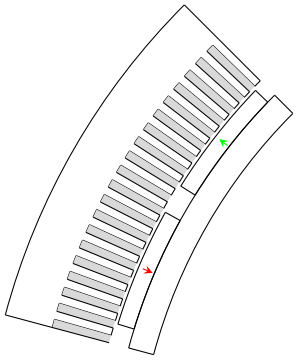

Figure 3.13: SM-PMSG with orthoradially magnetised PMs

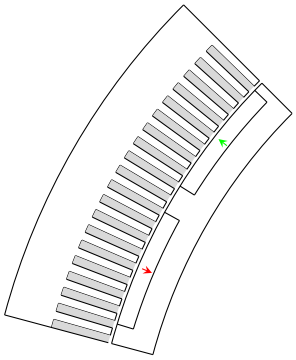

Figure 3.14: I-PMSG with radially magnetized PMs

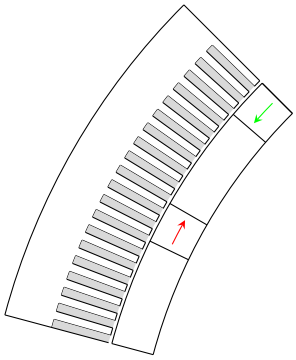

Figure 3.15: ST-PMSG with radially magnetized PMs

A comparative design of RF-PMSG and ST-PMSG for 15MW direct-drive wind turbine will be discussed to assess different configurations of the PMSGs based on the rare-earth permanent magnet mass, machine's mass and losses. The geometric parameters of the initial designs of the selected machines will be discussed in the section 3.3.

3.2.3.2.5 Permanent magnet orientation: radial vs. ortho-radial orientation Permanent magnet with ortho-radial (tangential) orientation (See Fig. 3.13 and Fig. 3.14) differs from the radial one by the direction of magnetization of the magnets (See Fig. 3.15).

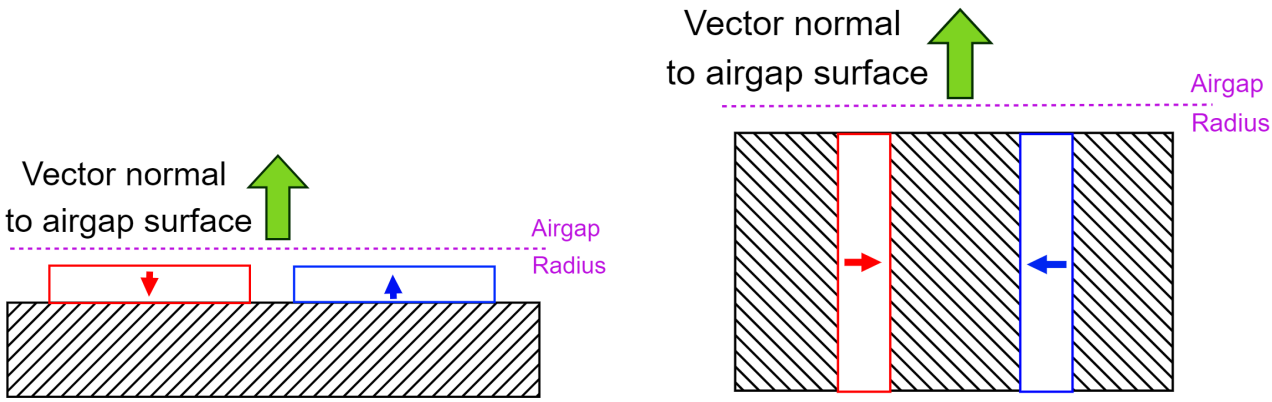

(a) radial orientation

(b) ortho-radial orientation

Figure 3.16: Permanent magnet orientation with respect to airgap

3.2.3.2.6 Combination of pole pair number and stator slot number As explained in section 3.2.1, PMSG with large number of pole pairs is preferable in direct-drive applications.

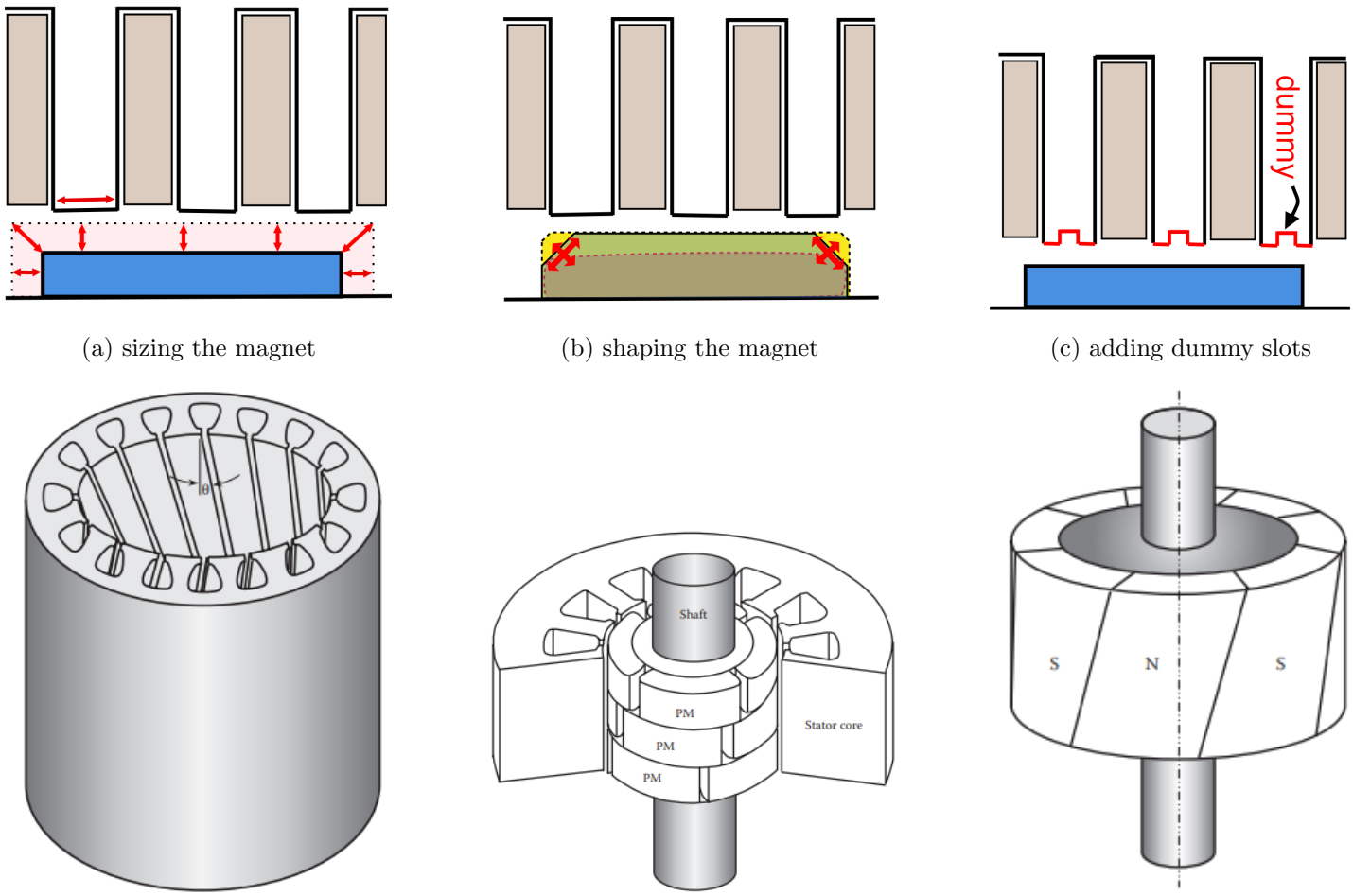

(a) sizing the magnet (b) shaping the magnet (c) adding dummy slots

(d) skewing the stator by θ [237] (e) step-skewing for segmented PM [237] (f) whole-skewing PM [237]

Figure 3.17: Techniques used to reduce the cogging torque

One of the main drawbacks of PMSGs is the cogging torque, especially in low-speed high-torque machines with open slots. It is caused by the air-gap permeance variation due to slotting effect, and represents the required force to break the attraction when the rotor's poles line up with the stator's teeth. This torque is an unwanted parasitic torque, which can lead to mechanical vibrations and noise production. Reducing cogging torque is of great importance in the design of large PMSGs. Several techniques have been used to reduce cogging torque including shaping or sizing the magnet (See Fig. 3.17.a and Fig. 3.17.b) in order to produce a more sinusoidal flux density, adding dummy stator slots (See Fig. 3.17.c), skewing either the stator (See Fig. 3.17.d) or the rotor (as illustrated in Fig. 3.17.e and Fig. 3.17.f), and modulating drive current waveform in a way to cancel the pulsations [238] [239] [240].

Although skewing is the most common technique used to reduce the cogging torque, it has been considered only for one investigated topology. Indeed, in large direct-drive machine while the stator skewing may cause manufacturing problems, the rotor skewing requires PMs with special shapes, which is hard to manufacture, difficult to be magnetized and can make rotor core very expensive.

An effective way to reduce the cogging torque, is to consider a combination of slot and pole numbers having a large least common multiple (LCM). The cogging torque is periodic and can be expressed as

$$T_{cog} = \sum_{k=1}^{n} \alpha_k sin(LCM(N_s, 2\,p)\,k\,\theta) \tag{3.15}$$

where α_k is the Fourier coefficient, $LCM(N_s, 2\,p)$ is least common multiple of the number of slots, N_s, and the number of pole pairs, p, and θ is the position of the rotor. As it can be seen form the Eq. 3.15, the $LCM(N_s, 2\,p)$ represents the number of cogging torque periods per mechanical revolution of the rotor. Higher LCM yields lower cogging torque. The closer the number of poles to number of slots, the higher their LCM. On the other hand, the greatest common divisor of N_s and p (GCD) defines the magnetic period of the machine and therefore combination of low $GCD(N_s,\, p)$ and high $LCM(N_s, 2\,p)$ helps in reducing the cogging torque. A part from this, the combination of slot and pole numbers is not only selected to obtain a low cogging torque, but also high fundamental winding factor, many symmetries in the winding layout, low amplitude and low number of sub-harmonics in the MMF distribution.

Torque ripple are quite small in PMSMs with concentrated windings compared to those with distributed windings [241] [209]. Thus, in this thesis, a correct choice of pole/slot combination will be considered enough to have an acceptable ripple in non overlapping windings. However, skewing the stator by slot pitch angle is considered to reduce the cogging torque for the investigated machines with distributed windings.

3.2.3.2.7 Position of the rotor: inner vs. outer rotor The inner-rotor configuration is often used in large DD-PMSG due of its suitability. RF-PMSG with outer-rotor allows a larger airgap diameter compared to RF-PMSG with inner rotor for the same external diameter [242] [243] [244]. This permit a larger number of magnetic poles, and then may increase the machine's efficiency [245]. In contrast, the cooling of the stator windings is less efficient in inner-stator PMSG. The main heat sources in large direct-drive PMSG is in the stator windings and thus complex cooling systems such as liquid cooling are necessary. That introduces additional reliability issues and maintenance cost. For these reasons, most of DD-PMSGs are air cooled [174].

Considering these aspects, an inner-rotor configuration was chosen for our application.

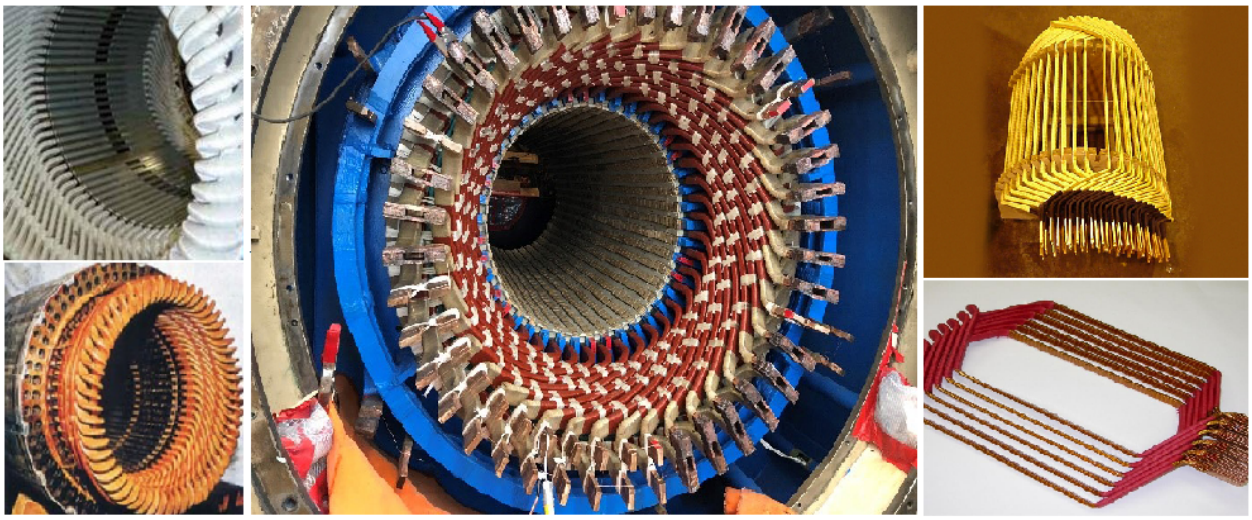

Figure 3.18: Generator's with form-wound coils

3.2.3.2.8 Winding Technology Various types of windings are used in electrical machines manufacture. According to the conductor type, the winding can be divided into: random-wound stator coils[10] or form-wound stator coils[11] (See Fig. 3.18 and Fig. 3.19). The selection of the winding conductor depends on many aspects such us the application, the supply voltage and the fill factor. Random-wound coils are used in stator operating at voltages less than 1 kV [26]. However, in high-voltage machines (> 3 kV) usually prefabricated rectangular coils made of form-wound copper coil are layered uniformly in the stator slot. With their rectangular form, slot's filling factor up to 65 per cent can be achieved with bar-wounds. In addition, form-wound coils allow a better conductance of losses, easier modelling of eddy currents and offer robust structure of end-winding compared to random-wound winding [246] [247]. Nevertheless, due to their large size bar-conductors are more sensitive to skin effect when compared to random-wound conductors (See section 6.3 for more details.). In addition, bars are difficult to assemble and sold in much smaller quantities, which may lead to higher cost per kW and difficulties in acquiring replacement parts [246].

The form-wound stators could be either made from multi-turn coil (two legs with full loop) or single turn bars (half-turn coils 'Roebel bar') (See Fig. 4.12). Indeed, due to the difficulties related to the profile wire of high-width to thickness ratio, several wires in parallel may make one turn, usually with dedicated insulation

[10] Also called wire-wound.
[11] Also called bar-wound.

Figure 3.19: Generator's with random-wound coils

Figure 3.20: Multi-turn pre-formed stator coils (left) and single-turn stator bars (right)

whereas single turn bars do not. Individual turns are arranged in precise location with respect to each other. That is, turn one is always next to turn two, and so on (See Fig. 3.21).

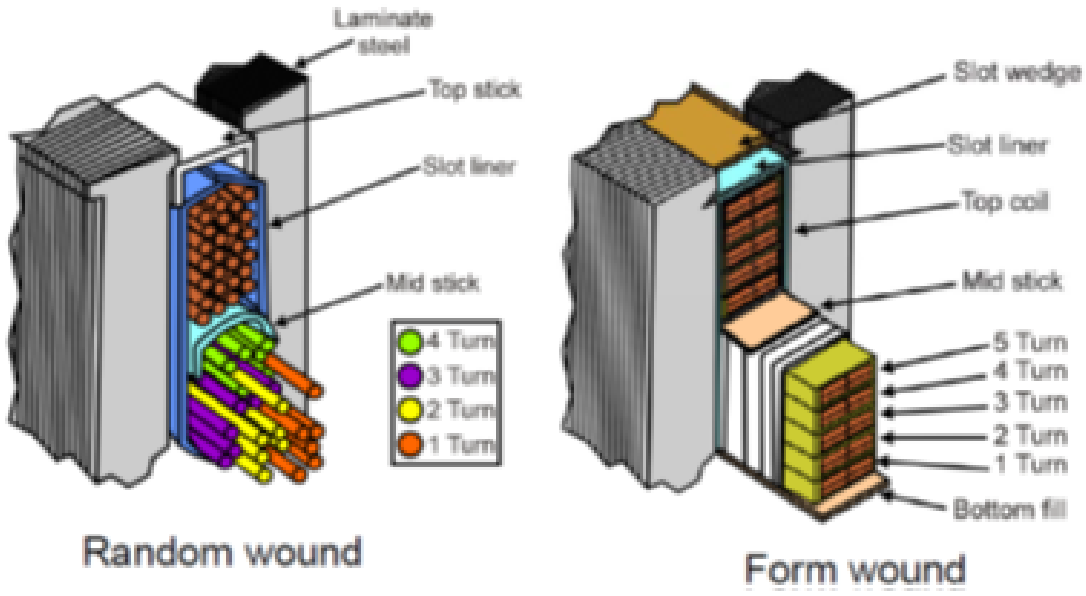

Figure 3.21: Random wound versus form wound

A bar-wound design was considered in our application. Indeed, it provided a better turn-to-turn insulation, which results in a more reliable machine with acceptable cost [246].

3.2.3.2.9 Winding housing: slotted vs. slotless The stator lamination can be made either with or without teeth. The stator teeth are used to carry the magnetic flux. In slotted stator the airgap is not affected by the winding, while in the case of slotless stator, the coils are placed at the airgap, leading to larger magnetic gap. To minimize the weight of machine, especially the supporting structures, ironless permanent magnet generators was investigated. Despite the fact that, moving from slotted to slotless machine decreases significantly the active part's mass and make the stator production simple, the airgap will be larger in slotless generators and then the flux density falls for the same quantity of the magnet, this construction may conduct to winding retention issues and structural instability [136].

3.2.3.2.10 Slot In order to facilitate the insertion of the prefabricated bar coil, the stator slots are assumed to be open and rectangular. In fact, the bar winding are inserted radially in such large machines, so the stator slot need to be wide enough (See Fig. 3.22).

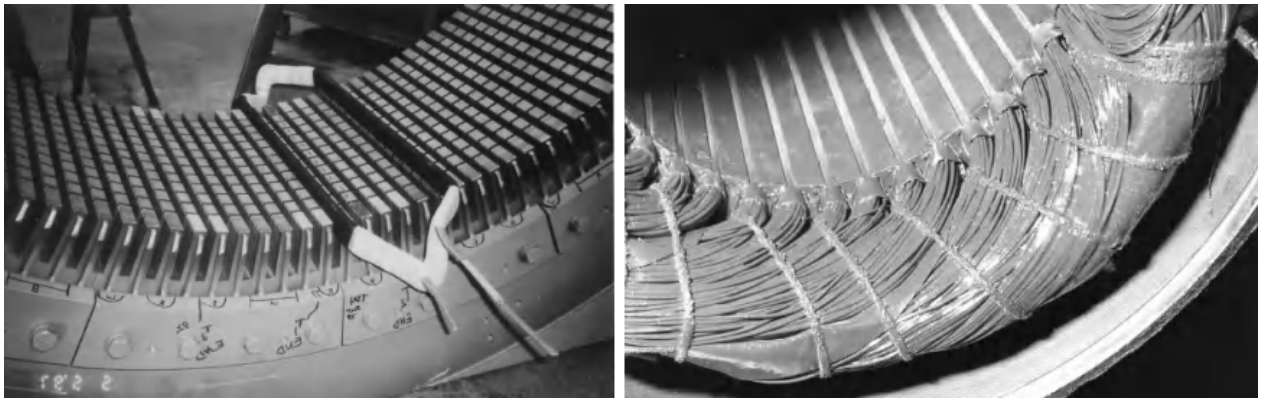

Figure 3.22: Open stator slots with form coils (left), semi-closed slots with random windings have small openings (right) [26]

3.2.3.2.10.1 Stator Cooling In low-speed PMSG machines, the main source of heat is the power losses in the stator windings (Joule losses). The temperature rise alters both the performances of the permanent magnets and the torque density. In the stator windings, high temperatures may cause degradation of copper wires and the coatings which is caused by quick oxidation of the coatings. The cooling system defines the amount of the heat that can be removed and then sets the electric loading limits. Multi-megawatt electrical generators are designed for high torque density. To achieve such densities effective cooling system is needed. The cooling systems in electrical machine depend on the cooling target. Fig. 3.23 presents the different cooling methods available in literature. In the simplest stator core cooling scenario of radial flux machines, the heat

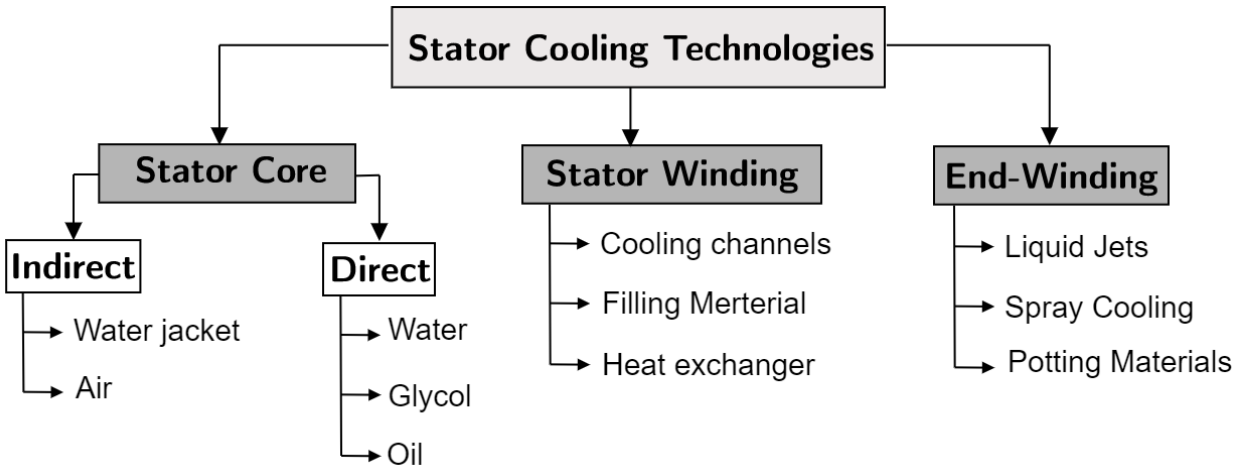

Figure 3.23: Stator cooling technologies depending on the cooling target

produced in the coil is transferred to the stator core, which is then radially carried to the frame followed by natural convection to the ambient air. The cooling could be enhanced by rising the transfer surface using fins

on the frame or tubes for air/water jacket cooling.

In low-speed large-power generators, it is usually essential to bundle several single conductors that are insulated against one another to form a conductor bar. The insulation between the conductor bar and stator core is defined as the principal insulation. Indeed, the thermal resistance for stator windings in the axial direction differs significantly from the radial one. While the copper or aluminium conductor has high thermal conductivity around 360 W/m.K and 200 W/m.K, respectively, insulation conductivity is ranged from 0.3 to 0.5 W/m.K. As results, the thermal resistance differs considerably in the axial and radial directions for stator windings. In the axial direction, the heat flow more freely, whereas out of the conductor and through the insulation, heat flow is considerably less. Further, an effective way to rise the heat dissipation efficiency in large power direct-drive synchronous generator is to provide the direct liquid cooling to their windings (See Fig. 3.24). A hollow conductors may be used, through which liquid coolant passes directly during the application of current in order to increase the convective heat transfer capabilities and reduce the generator mass.

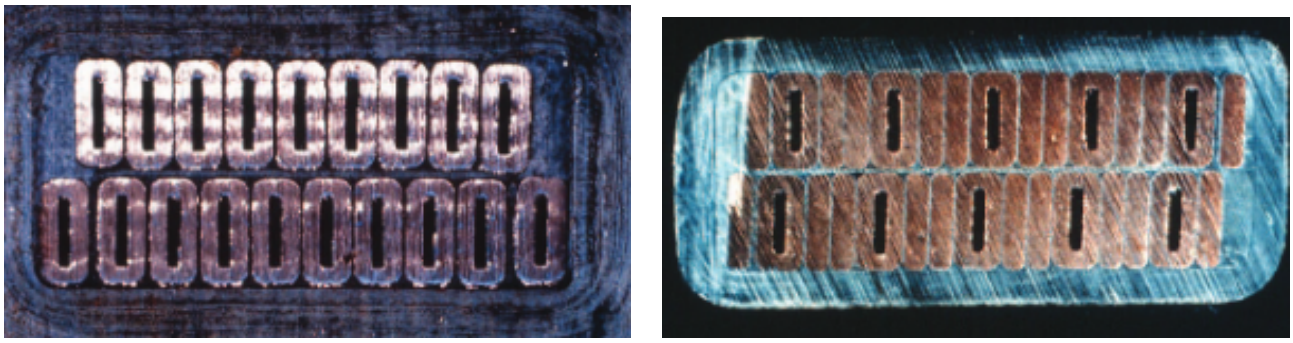

(a) All-hollow-strands (b) Mixed-strands

Figure 3.24: Direct water-cooled Roebel stator bar [27]

3.2.3.2.11 Concentrated winding vs distributed winding Direct-drive PMSGs are characterized by a large number of poles, and low number of slot per pole per phase. Several types winding arrangements exists, the choice of the type of winding depends on the size of the machine, the rated voltage/current, the slot geometry and the pole number. Two Different winding configurations will be investigated: distributed windings with fractional/integer plot pitch and superior to 1 slot per pole per phase and concentrated windings with a fractional slot pitch and inferior to 1 slot per pole per phase. Although distributed winding is the most common used configuration for large power electrical machines, concentrated windings can be good alternative. In concentrated winding (tooth coil winding) each coil is wound around a single tooth. For low-speed high-power PMSG, non-overlapping winding is attractive due to its simplicity, shorter and less-complex end-winding,

good fault tolerant capability and good adaptation to segmented stator [248] [249] [250]. Further, with shorter end-windings, the copper volume can be significantly reduced, and then lower masses and less losses are expected compared to distributed windings. For low frequencies (low-speed machines), copper losses are much higher compared to core losses, and it is important to lower them as much as possible in order to improve the efficiency of the machine. However, the main issues with concentrated winding is low winding factor, some combination of pole and slots might produce unbalanced magnetic forces due to space harmonics [251].

Both winding techniques were investigated in this thesis. The concentrated windings were used with machines having a number of slots close to the number of poles, while the distributed windings were used in the opposite case.

3.2.3.2.12 Number of layers: single-layered vs double-layered The selection of the number of layers is driven by the application. In concentrated windings, single-layer windings (See Fig. 3.25.a) provide good fault tolerance capacities since the winding phases are electrically and thermally isolated, it also had very low mutual inductance and high self-inductance, which insures the magnetic insulation and limits the prospective short-circuit current respectively. Alternatively, double-layer windings (See Fig. 3.25.b) are used to limit the losses and torque ripple. Furthermore, there are more possible combinations of pole and slot numbers to choose between with double-layer windings than with single-layer windings. In distributed winding with double-layered windings, it is possible to short pitch the winding in order to reduce harmonics in the machine. Consequently, double-layered windings were adopted for both investigated machines (with concentrated and distributed windings).

3.3 Selection of Permanent Magnet Synchronous Types for 15 MW Direct-Drive Wind Turbines

The following five PM generators were selected for the comparative design :

- SM-PMSG: Surface Mounted RFPM generator with single/double layered - concentrated/distributed windings.
- I-PMSG: Inserted RFPM generator with double layered distributed windings.

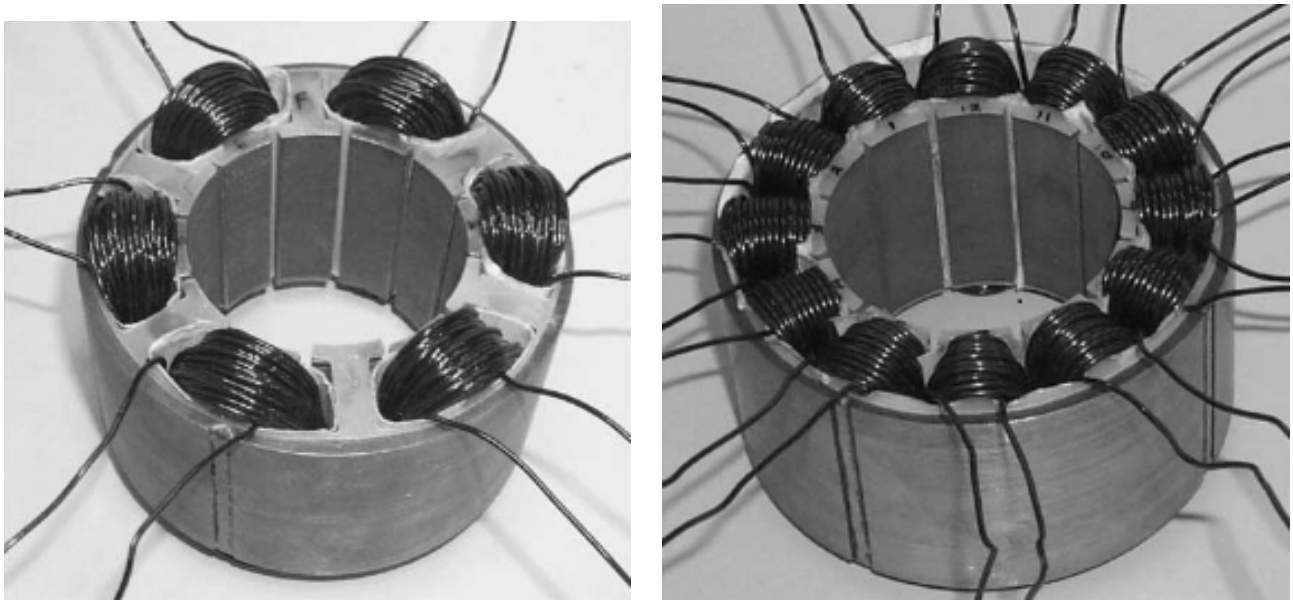

(a) Single-layered [252] (b) Double-layered [252]

Figure 3.25: Single and double-layer concentrated windings

- ST-PMSG: Spoke-Type RFPM generator with single/double layered - concentrated/distributed windings.

3.3.1 Main dimensions of the 15 MW PMSG

The design process starts with the definition of the constraints and the requirement of machine. The main dimensions of the radial flux PMSG are discussed in this section.

3.3.1.1 Generator power

The mechanical power in electrical generator can be expressed as a product of the torque, T, by the rotational speed, ω, as in

$$P_{mec} = T\,\omega \tag{3.16}$$

The required power, P, should be greater than $15\,MW$ if we considered the mechanical losses.

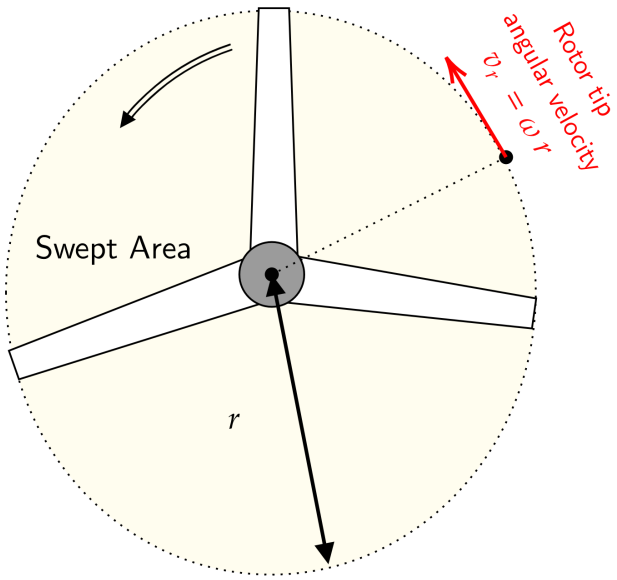

Figure 3.26: Wind turbine tip Speed

3.3.1.2 Generator speed

The rotational speed of the machine is determined by the tip speed ratio. As explain in Eq. 1.1, in a wind turbine, the mechanical power is proportional to the swept area of the wind turbine

$$P \propto A \quad \Rightarrow \quad P \propto r^2 \tag{3.17}$$

where r is the radius of the turbine rotor blades (See Fig .3.26) (equal to the length of one blade).

The power is constrained by a maximum rotor blade tip speed. When scaling up the wind turbine, the rotor diameters increases and the rotational speed must decrease considering the tip speed limitation.

$$\omega \propto \frac{1}{r} \tag{3.18}$$

In this thesis, it is assumed that the generator rotates at

$$\Omega = [7 - 8]\, rpm$$

The developed torque is then equal to

$$T = [20.49 - 17.92]\, MNm$$

3.3.1.3 Airgap diameter

As can be seen in Eq. 3.7, the machine's torque is proportional to its volume and shear stress. Then, for given aspect ratio, $K_{rad} = \dfrac{L_{act}}{2\,R_g}$, the Eq. 3.7 gives

$$T = 4\pi\,\sigma_{F_t}\,R_g^3\,\frac{L_{act}}{2\,R_g} = 4\pi\,\sigma_{F_t}\,R_g^3\,K_{rad} \tag{3.19}$$

where R_g and L_{act} are the airgap diameter and the axial length of the machine. For fixed values of K_{rad} and σ_{F_t}, the torque is proportional to the cube of the rotor radius.

$$T \propto R_g^3 \tag{3.20}$$

The airgap diameter, D_g, can be determined as

$$D_g = \sqrt[3]{\frac{2\,T}{\pi\,K_{rad}\,\sigma_{F_t}}} \tag{3.21}$$

The shear stress is rather constant over a wide range of power machine. As mentioned in Table 3.2, for totally-enclosed rare-earth machine, the tangential force density varies between 14 kN/m^2 and 42 kN/m^2. In our case, the machine is supposed to be naturally cooled on the stator outer surface. A force density of 40 kN/m^2 is assumed [172] [253] [254]. Further, an optimization including the supporting structures is possible to define the optimal K_{rad} and find the lighter machine. In this study, the aspect ratio, K_{rad}, is assumed to be between 0.15 and 0.35. Then the airgap radius (stator bore radius) is in the range of

$$D_g = [\,9.33 - 12.95\,]\,m \Rightarrow R_g = [\,4.66 - 6.47\,]\,m$$

3.3.1.4 Axial stack length

The axial length of the machine is calculated by choosing the value of the aspect ratio, K_{rad}. According to the K_{rad} rage adopted above,the axial length of the machine can vary between 1.40 m and 3.23 m.

$$L_{act} = [\,1.40 \; - \; 3.23\,]\,m$$

3.3.1.5 Airgap length

The mechanical stiffness and the thermal expansion of the generators limit the minimum airgap length [126], e_g, to

$$e_g \; = \; D_g/1000 \tag{3.22}$$

Then, the airgap length can vary between 9.33 mm and 12.95 mm

$$e_g \; = \; [\,9.33 \times 10^{-3} \; - \; 12.95 \times 10^{-3}\,]\,m$$

3.3.1.6 Pole pitch and pole pair number

As explained in section 3.2.1, the electrical frequency depends on the pole pairs (See Eq. 3.1). The electrical frequency should be kept high enough (>10 Hz) in order to prevent over-size IGBTs. For this purpose, the pole pair number, p, varies between 75 and 192 (corresponding to 10 Hz and 24 Hz).

$$p \; = \; [\,75 \; - \; 192\,]$$

Direct-drive PMSGs are usually designed with small pole pitches (around 0.1 [254]), which would help to decrease the stator and the rotor yoke height and reduce the end-winding losses [81]. The rotor pole pitch, τ_p, can be expressed as function of the number of pole pairs

$$\tau_p = \frac{\pi\,(R_g - e_g)}{p} \tag{3.23}$$

Then, the pole pitch is in the range of

$$\tau_p = [\,0.08 \; - \; 0.26\,]\,m$$

3.3.1.7 Slot's dimensions

The number of the stator slots, N_s, can be given by

$$N_s = 2\,p\,q\,m \tag{3.24}$$

where q and m are the number of slots per pole per phase and the number of phase, respectively. In this thesis, we investigated two types of machines :

1. Three-phase distributed winding with $q = 1$, one slot per pole per phase, the number of slots is in the range of

$$N_{s_1} = [\,450 \; - \; 1026\,]$$

2. Concentrated windings with $q < 1$. As explained previously, in this type of machines the number of slots is close to the number of poles ($q \sim Q$). For three-phase machine with $q = 1/3$, the number of slots is in the range of

$$N_{s_2} = [\,175 \; - \; 350\,]$$

The slot pitch, τ_s, is given by

$$\tau_s = \frac{2\pi R_g}{N_s} = w_s \; + \; w_t \tag{3.25}$$

where w_s and w_t denote the slot and the tooth width, respectively. The slot pitch, τ_{s_1}, τ_{s_2} corresponding to the machines that contain N_{s_1} and N_{s_2}slots respectively are

$$\begin{cases} \tau_{s_1} = [\,0.03 \; - \; 0.06\,]\,m \\ \tau_{s_2} = [\,0.11 \; - \; 0.16\,]\,m \end{cases} \tag{3.26}$$

Assuming that the slot width is $45 - 50$ per cent of the slot's pitch

$$\begin{cases} w_{s_1} = [\,13.5 \times 10^{-3} \; - \; 30 \times 10^{-3}\,]\,m \\ w_{s_2} = [\,50 \times 10^{-3} \; - \; 80 \times 10^{-3}\,]\,m \end{cases}$$

The ratio of slot's height, h_s, to slot's width, w_s, is limited over the range of 4-10, which prevent excessive tooth mechanical vibration occurring

$$\begin{cases} h_{s_1} = [\,54 \times 10^{-3} \; - \; 300 \times 10^{-3}\,]\,m \\ h_{s_2} = [\,200 \times 10^{-3} \; - \; 500 \times 10^{-3}\,]\,m \end{cases}$$

3.3.1.8 Permanent magnet dimensions

Assuming a rectangular shape of the flux density above the magnet and neglecting flux leakage, the fundamental space harmonic of the magnetic flux density in the air gap due to the magnets can be calculated as in

$$\hat{B}_g = \frac{4}{\pi}\, B_g \, sin\left(\frac{\pi\, w_{PM}}{2\,\tau_p}\right) \tag{3.27}$$

where w_{PM} is the magnet width and B_g is magnetic flux density above the magnet, which can be given by

$$B_g = B_{r_{PM}} \frac{1}{1 + \mu_{r_{PM}} \dfrac{e_{g_{eff}}}{h_{PM}}} \tag{3.28}$$

where h_{PM}, $B_{r_{PM}}$ and $\mu_{r_{PM}}$ are the magnet length, the remanent flux density of the magnet and the relative permeability of the magnet. The $e_{g_{eff}}$ is the effective airgap including the effect of the stator slotting, it can be expressed in

$$e_{g_{eff}} = K_c \left(e_g \; + \; \frac{h_{PM}}{\mu_{r_{PM}}}\right) \tag{3.29}$$

where K_c is the Carter factor, it is given by [173]

$$K_c = \frac{\tau_s}{\tau_s - \dfrac{4}{\pi}\left(\dfrac{w_s}{2\,e_1}\arctan\left(\dfrac{w_s}{2\,e_1}\right) \; - \; log\sqrt{1 + \dfrac{w_s}{2\,e_1}}\right) \times \; e_1} \tag{3.30}$$

with $e_1 = e + \dfrac{h_{PM}}{\mu_{r_{PM}}}$.

By substituting Eq. 5.6 in Eq. 3.27, the permanent magnet thikness can be expressed as

$$h_{PM} = \frac{\mu_{r_{PM}}\, e_{g_{eff}}}{\dfrac{4\, B_{r_{PM}}\, sin\left(\dfrac{\pi\, w_{PM}}{2\,\tau_p}\right)}{\hat{B}_g \pi} - 1} \tag{3.31}$$

Let's keep the width of the permanent magnet between 60 and 90 per cent of the pitch pole (taking into account the inter-pole flux leakage)

$$w_{PM} = [\, 48 \times 10^{-3} - 234 \times 10^{-3}\,]\, m$$

3.3.1.9 Stator and rotor yoke

In a PMSG, the flux density in the different parts of the machine, varies between 1.2 – 1.8 T. The stator and rotor back iron flux density $\hat{B}_{sy}$ and $\hat{B}_{ry}$ respectively, can be approximated by [81]

$$\begin{cases} \hat{B}_{sy} = \dfrac{\hat{B}_g\, w_{PM}\, L_{act_c}}{2\, k_{Fes}\, L_{act}\, h_{ys}} \\ \hat{B}_{ry} = \dfrac{\hat{B}_g\, w_{PM}\, L_{act_c}}{2\, L_{act}\, h_{yr}} \end{cases} \tag{3.32}$$

where L_{act_c}, $L_{act_c} = L_{act} + 2 \times e_g$, represents the corrected stator core length (considering the fringing from the edge field at the machine end) and k_{Fes} is the iron filling factor that accounts for the insulation layer between core laminations. Then, the stator yoke height, h_{ys}, and the rotor yoke height, h_{yr}, can be determined by

$$\begin{cases} h_{ys} = \dfrac{\hat{B}_g\, w_{PM}\, L_{act_c}}{2\, k_{Fes}\, L_{act}\, \hat{B}_{sy}} \\ h_{yr} = \dfrac{\hat{B}_g\, w_{PM}\, L_{act_c}}{2\, L_{act}\, \hat{B}_{sy}} \end{cases} \tag{3.33}$$

Assuming a peak magnetic flux density in the electric steel of the rotor and stator yoke of 1.8 T and a peak flux density in the airgap of 1.2 T, the Eq. 3.33 gives

$$\begin{cases} h_{ys} = [\,22.81 \times 10^{-3} \; - \; 106.36 \times 10^{-3}\,]\,m \\ h_{yr} = [\,14.45 \times 10^{-3} \; - \; 70.23 \times 10^{-3}\,]\,m \end{cases}$$

3.3.2 The selected machine designs

Considering the main dimensions of the machine defined in section 3.3, and the design considerations discussed in section 3.2.1, three initial designs of RF-PMSG were selected, these machines will serve as a reference for further comparisons. The main dimensions are determined in Table 3.9.

Table 3.9: Parameters and dimensions of the selected machines

		Units	**Machine A**	**Machine B**	**Machine C**
Rated power	P	MW	15	15	15
Rated torque	T	MNm	19.78	19.92	20.05
Rated speed	Ω	rpm	7.5	7.5	7.5
Nominal frequency	f	Hz	11.25	12.5	23.62
Geometrical parameters of the machine					
Stack length	L_{act}	mm	2400	2170	1666
Airgap mean radius	R_g	mm	5726	5047	6390
Number of pole pairs	p	-	90	100	189
Number of slots	N_s	-	684	240	1134
Airgap length	e_g	mm	12	10.16	16
Stator slot width	w_s	mm	25.38	60	15.6
Stator slot height	h_s	mm	80	150	132
Stator yoke height	h_{ys}	mm	50	60	45
Rotor yoke height	h_{yr}	mm	40	60	45.2
Magnet width	w_{PM}	mm	159	126.3	79.3
Magnet height	h_{PM}	mm	20	25	16.3
Physical properties of the materials					
Permanent magnet	PM		NdFeB (N40H)		
Magnet remanence (at 20^oC)	$R_{r_{PM}}$	T	1.2	1.2	1.2

Magnet relative permeability	$\mu_{r_{PM}}$	-	1	1	1
Current density	J_s	A/m^2	3 $\times 10^{-3}$	2.5 $\times 10^{-3}$	3 $\times 10^{-3}$
Conductors packing factor	k_f	-	0.66	0.66	0.66
Windings					
Number of phases		-	3	3	3
Number of coils per phase windings			12	4	1
Number of winding layer			2	2	1
Winding configuration			Distributed	Concentrated	Distributed

3.3.2.1 Winding configurations

As explained before, the slots are considered to have rectangular shape, as well as the conductors in the windings. The winding configurations of machine A, B and C are represented in Table 3.10, Table 3.11 and Table 3.12, respectively. The winding configuration patterns are typically repeated GCD(Ns,2p) times to represent the stator winding.

Table 3.10: Winding layout for machine A

a_{12}^+	a_2^+	b_1^+	b_2^+	a_2^-	c_3^+	b_2^-	b_4^-	c_3^-	c_4^-	b_4^+	a_5^-	c_4^+	c_6^+	a_5^+	a_6^+	c_6^-	b_7^+	a_6^-
a_1^+	c_1^-	c_2^-	a_1^-	a_3^-	c_2^+	b_3^-	a_3^+	a_4^+	b_3^+	b_5^+	a_4^-	c_5^+	b_5^-	b_6^-	c_5^-	c_7^-	b_6^+	a_7^-
1	2	3	4	5	6	7	8	9	10	11	12	13	14	15	16	17	18	19

a_8^-	b_7^-	b_8^-	a_8^+	c_9^-	b_8^+	b_{10}^+	c_9^+	c_{10}^+	b_{10}^-	a_{11}^+	c_{10}^-	c_{12}^-	a_{11}^-	a_{12}^-	c_{12}^+	b_1^-
c_7^+	c_8^+	a_7^+	a_9^+	c_8^-	b_9^+	a_9^-	a_{10}^-	b_9^-	b_{11}^-	a_{10}^+	c_{11}^-	c_{11}^+	b_{12}^+	c_{11}^+	c_1^+	b_{12}^-
20	21	22	23	24	25	26	27	28	29	30	31	32	33	34	35	36

Table 3.11: Winding layout for machine B

c_4^-	a_1^-	a_2^+	b_1^+	b_2^-	c_1^-	c_2^+	a_3^+	a_4^-	b_3^-	b_4^+	c_3^+
a_1^+	a_2^-	b_1^-	b_2^+	c_1^+	c_2^-	a_3^-	a_4^+	b_3^+	b_4^-	c_3^-	c_4^+
1	2	3	4	5	6	7	8	9	10	11	12

Table 3.12: Winding layout for machine C

a_1^+	c_1^-	b_1^+	a_1^-	c_1^+	b_1^-
1	2	3	4	5	6

3.4 Conclusion

This chapter presents the electromagnetic design procedure of 15 MW direct drive permanent magnet synchronous generator. After presenting the requirement of such large structures, the preliminary parameters of generator design have been set. That may help in the preparation for the optimization design by setting the lower and the upper limits for the optimization parameters. It can be conclude that:

- It is preferable in certain circumstances, such as for large direct drive generators to use well-known technologies (windings, topology, materials, etc.). With well-established technologies, the electrical machines are usually more robust, more efficient and cheaper.
- Although air-cored machines help to avoid the large attractive forces between stator and rotor, this option was discarded because it may conduct to winding retention issues and structural instability.
- Radial flux machine is used because it has simple generator structure and allow a good use of the active materials. Further, this topology make it easy to manufacture slotted stator.
- The main design requirements for high-power low-speed PMSG are
    1. Simple construction,
    2. Lighter machine,
    3. Small cogging torque,
    4. Low cost,

- Although distributed winding is the most common configuration in large DD-PMSG it was of interest to investigate the use of concentrated windings. Concentrated winding help in

    1. Simplifying the machine's assemble and machine's segmentation,
    2. Reducing the manufacturing and assembly cost,
    3. making the end windings simple and shorter, and then lowering the mass of the copper and the Joule losses.

Chapter 4

Magnetic Model

4.1 Introduction

In order to find the set of machine dimensions for optimal configuration, inspecting a large design space with fast method is fundamental. The pre-design phase is therefore challenging task, however, speed up the first stages of electrical machines design with fairly accurate model, has received substantial interest.Indeed, a compromise should be made between the computing time consumption and the accuracy of the models.

Reducing the design cycle time is an arduous computationally task since the relationships between the different parameters and the performances of the machine are mostly non-linear and highly convoluted. In fact, satisfactory results could be obtained with less accurate model by making the appropriate assumptions. In the last decade a large number of methods has been proposed for the prediction the magnetic field in electric machines [255] [256], they could be categorized into analytical models, hybrid (semi-analytical) model and numerical models.

In the analytical model, the magneto-static/magneto-dynamic Maxwell equations are solved in low permeability regions under many assumptions such linearity of the material characteristics and periodicity [257] [258]. It consists in expressing the magnetic field quantities as a Fourier series, where the harmonic coefficients are calculated by satisfying the boundary conditions between the multiple regions of the machine. First, this method consists in dividing the machine's geometry into different regions in non-periodic direction, then the boundary values are deduced. Further, the separation of the variable technique and the superposition of the harmonics allow to write the governing equation to predict the electro-magnetic field distribution in the

machine. Despite its accuracy and rapidity, this method only suited for machines with simple geometry. Unfortunately, its major drawback is the non-consideration of the magnetic saturation. To overcome this problem, semi-numerical or numerical methods could be used. The Finite Element Method (FEM) is the most precise numerical method used in the computation of the magnetic field in the electric machines. In spite of its ability to include the magnetic saturation, complex geometries and anisotropic materials, the FEM models are too-time consuming especially for finer mesh-elements or in 3D problems. In addition, they are not able to explain the influence of the geometrical parameters on the machine performances. The semi-numerical models such as the reluctance network models are considered as an adequate solution comparing to analytical model and FEM models [259] [260] [261]. Reluctance network model not only takes into account the non-linearity of the materials properties, but also is more refined than analytical model and more intuitive compared to the FEM.

This chapter describes two techniques used for modelling and analysis of the magnetic field distribution in electrical machines. In section 4.2, an analytical model based on the formal solution of Maxwell equations is detailed. In section4.3, a semi-analytical model lumped magnetic parameters and its formulation in magneto-static case is described. The value of the permeances are presented in section 4.3.3.2.2 and 4.3.3.3. The developed model make it possible to consider the nonlinear behaviour of soft-magnetic materials. The modelling of the nonlinear materials was introduced in section 4.3.3.4. Finally results using analytical model and reluctance network model will be compared to those obtained by FEM (Flux2D) in order to justify the use of this type of methods for future design optimization.

4.2 Analytical Model

This section is devoted to the description of analytical magnetic modelling of electrical machines based on the analytical solution of the Maxwell equations thanks to the separation of variables method. In fact, for first stages design of electrical machines, engineers need a fast and reasonably accurate model helping to explore design potentialities and to define the main dimensions of the machine prototype to be refined in the next design steps. Among the different analytical magnetic models, approaches based on the formal solution of Maxwell equations have proven their effectiveness to give a satisfying computation time to accuracy ratio for the first stages of the design procedure where trends exploration are very helpful to the designer. Formal solution of Maxwell equations provide valuable information on the local distribution of the magnetic field in

different regions of an electrical machine helping to compute relatively accurately common global quantities like magnetic fluxes, induced voltages, strength and torque as well as delicate global quantities like cogging strength and torque or eddy current loss [262][263].

However, formal solution of Maxwell equations approach encounters some limits superimposed mainly by the potential complexity of the machine geometry, the non-linearity of material properties and the numerical stability of series expansion. More clearly, analytical solution of Maxwell equations could not exist for geometries where the boundaries are not parallel to the axes of the chosen coordinate system. As a consequence, analytical models based on a formal solution of Maxwell equations are suitable for geometries having high symmetries (like Cartesian symmetries, cylindrical symmetries, spherical symmetries, etc.). For instance, formal solution of Maxwell equations could not be used in the modelling of electrical machines having complex rotor geometries (variable reluctance machine) or/and complex slot geometries [264]. Fortunately, the large dimensions machines studied in this thesis have high symmetry geometries allowing the development of adequate analytical magnetic models based of the formal solution of Maxwell equations. However, as it could be expected with a large number of analytical methods, it is very hard even impossible to take intrinsically into account the non linear B-H curve of magnetic material in the formal solution of Maxwell equations. Despite this drawback, there is some remedial solution consisting in increasing the airgap length multiplying it by a saturation coefficient in the same way than the Carter coefficient. Saturation coefficient could be determined based on a small expert reluctance network which could help to evaluate the saturation impact on the airgap fluxes. Both Maxwell analytical model and the expert reluctance network could be coupled and executed sequentially helping by the way to consider magnetic saturation. Also, for numerical concerns, the series expansion inherent to the separation of variables technique used in the establishment of the formal solution of Maxwell equations could lead to a lack of convergence face to some combinations of machine geometrical dimensions. In fact, the boundary conditions exploitation sometimes results in a badly conditioned matrix of coefficients which could deteriorate the model accuracy. Despite all the mentioned drawbacks, analytical models based on Maxwell equations constitute a very interesting tool for the sizing and optimisation of electrical machines for the first steps of the design process. In the following sections, a brief description of the main stages of the Maxwell type analytical models construction will be given.

4.2.1 Machine geometries and analytical modelling assumptions

The classical assumptions adopted in the development of analytical models focus on idealised ferromagnetic materials. The steel laminated magnetic circuit is considered to have either an infinite permeability or a constant relative permeability in some cases and zero conductivity. The permanent magnets are assumed to have a linear B-H curve. Analytical modelling was applied to linear machines, radial flux machines and axial flux machines [265] [266] [267] [268] [269]. Figure 4.1 gives some common radial flux machines geometries for which it is possible to develop a Maxwell type analytical model. The geometries of such machines are illustrated in Fig. 4.1.

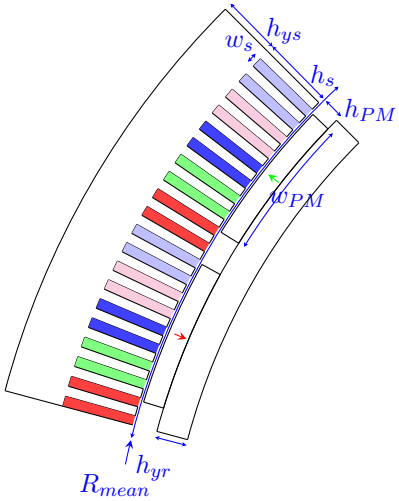

(a) SM-PMSG

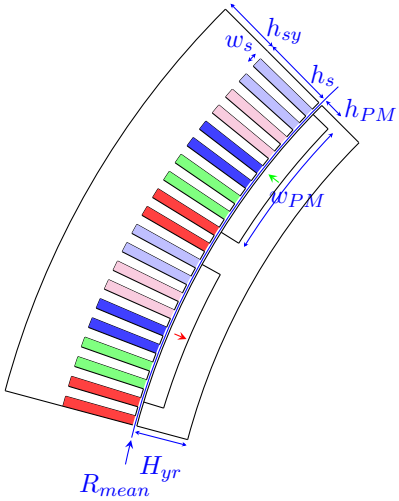

(b) I-PMSG

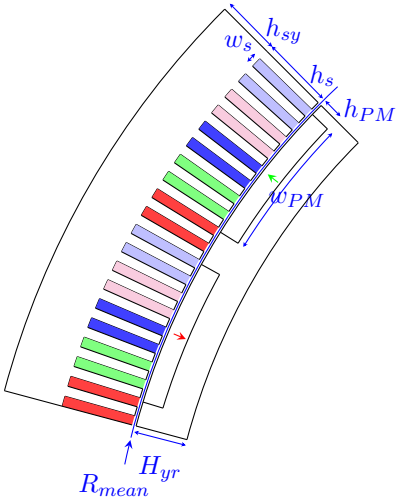

(c) ST-PMSG

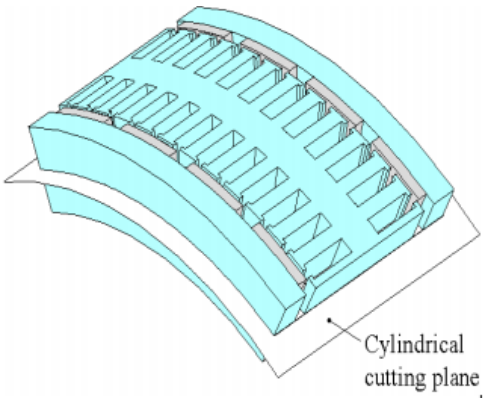

(d) Axial flux SM-PMSG

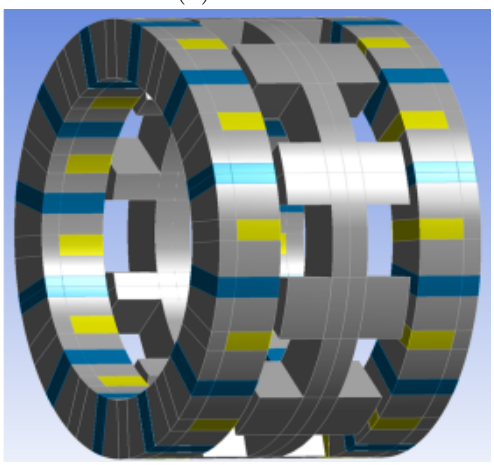

(e) Axial Switching Flux PMSG

Figure 4.1: Different electrical machine geometries suitable for formal solution of Maxwell equations

For low frequency problems, the electromagnetic field in electrical machines is governed by the laws of Maxwell-

Ampere, Maxwell-Faraday and the magnetic field conservation law

$$\vec{\nabla} \times \vec{H} = \vec{J} \tag{4.1}$$

$$\vec{\nabla} \times \vec{E} = -\frac{\partial \vec{B}}{\partial t} \tag{4.2}$$

$$\vec{\nabla}.\vec{B} = 0 \tag{4.3}$$

These partial derivative equations are associated to the B-H relationship and the Ohm law written in the following form

$$\vec{B} = \mu_0 \mu_r \vec{H} + \vec{B}_R \tag{4.4}$$

$$\vec{J} = \gamma \vec{E} \tag{4.5}$$

where is μ_0 the permeability of the empty space, μ_r is the relative permeability considered constant for all the studied magnetic materials, γ is the conductivity and $\vec{B}_R$ is the remanence. The introduction of the magnetic vector potential which derives from the conservation law Eq. 4.3 ($\vec{B} = \vec{\nabla} \times \vec{A}$) in the B-H relationship Eq. 4.4, helps to generate the **magnetic formulation in vector potential**

$$\Delta \vec{A} + \mu_0 \mu_r \vec{J} + \vec{\nabla} \times \vec{B}_R = 0 \tag{4.6}$$

by using the Coulomb gauge ($\vec{\nabla}.\vec{A} = 0$). The partial derivatives formulation in Eq. 4.6 could be used to compute vector potential in the case of magneto-static problems where the current density and remanence distribution are given sources and also in the case of magneto-dynamic problems. For the latter, the induced current density is due to the electromotive field ($\vec{E} = -\partial \vec{A}/\partial t$) derived from the Maxwell-Faraday law in Eq. 4.2 and involving Ohm law in Eq. 4.6 gives the **magneto-dynamic formulation in vector potential**

$$\Delta \vec{A} - \mu_0 \mu_r \gamma \frac{\partial \vec{A}}{\partial t} + \vec{\nabla} \times \vec{B}_R = 0 \tag{4.7}$$

In some cases, in regions free of current density, one can introduce the magnetic scalar potential by $\vec{H} = -\vec{\nabla}\,\varphi$ derived from the Maxwell-Ampere law. As a consequence, the combination of the conservation law in Eq. 4.3 and the B-H relationship in Eq. 4.4 leads to the following **magneto-static formulation in magnetic scalar**

potential

$$\Delta\varphi - \frac{1}{\mu_0\mu_r}\vec{\nabla}.\vec{B}_R = 0 \tag{4.8}$$

Partial derivative equations resulting from the projection of the above formulations on the coordinate system axes can be solved analytically using the separation of variables technique for geometries where all the subregions have boundaries parallel to the coordinate system axes. In the following, the main steps for the construction of such an analytical modelling will be briefly presented in the case of a radial flux machine.

4.2.2 2D analytical solution of the magneto-static field distribution for radial flux machines

In the case of radial flux machines, a common assumption is to consider the invariance of physical quantities in the axial direction. As a consequence, the magnetic vector potential is taken parallel to the rotational axis and depending only on the x and y coordinates in a Cartesian coordinate system. The studied domain is then bi-dimensional and the magneto-static formulation in Eq. 4.6 becomes scalar and can be written in cylindrical coordinates as

$$\frac{\partial^2 A_z}{\partial r^2} + \frac{1}{r}\frac{\partial A_z}{\partial r} + \frac{1}{r^2}\frac{\partial^2 A_z}{\partial \varphi^2} = -\mu_0\mu_r J - \frac{1}{r}\left(\frac{\partial (rB_{R_\phi})}{\partial r} - \frac{\partial B_{R_r}}{\partial \varphi}\right) \tag{4.9}$$

where B_{R_r} and B_{R_ϕ} are respectively the radial and the circumferential components of the remanence. The right hand side of Eq. 4.9 is obviously equal to zero in the air regions. In the slot region, the current density is usually uniformly distributed on the slot section by considering the filling factor. The magnetic vector potential solution of the homogeneous part of Eq. 4.9 is then derived thanks to the separation of variables technique and can be written as follows

$$\begin{aligned} A_{z,hom} = {} & a_0 + a_1 \ln r + a_2\,\varphi + a_3\,\varphi \ln r \\ & - \sum_{k=1}^{+\infty} \frac{1}{k}\left[\left(C_k.r^k + D_k.r^{-k}\right)\left(E_k.cos(k\varphi) + F_k.sin(k\varphi)\right)\right] \end{aligned} \tag{4.10}$$

where the coefficients are to be determined considering the boundary conditions of each subregion of the

domain. To the homogeneous solution in Eq. 4.10, one has to add the particular solution for each subregion depending on the present source distribution.

4.2.2.1 Case of the surface mounted permanent magnet synchronous machine

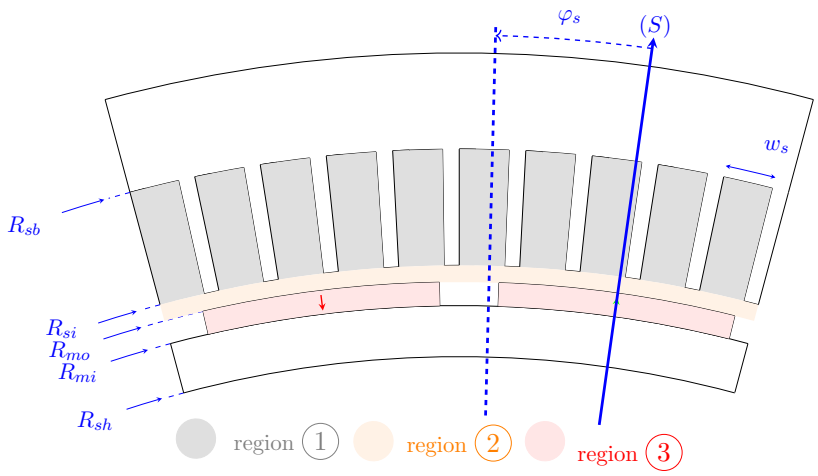

Figure 4.2: Radial flux surface mounted permanent magnet open slot synchronous machine

For illustration, in this section, the Maxwell type analytical modelling is applied to the case of the radial flux surface mounted open slot permanent magnet synchronous machine divided into three regions (See Fig. 4.2): slot region (1), airgap region (2) and permanent magnet region (3). In the following developments, the iron laminations are considered to be non conductive and to have very high permeability leading to negligible magnetic field strength in the stator and the rotor magnetic circuits.

4.2.2.1.1 Solution in the slot region Boundary conditions in the slots yield to

$$\begin{cases} H_r^{(1l)}(r, \varphi_{(1l)}) = 0 \\ H_r^{(1l)}(r, \varphi_{(1l)} + w_s) = 0 \\ H_\varphi^{(1l)}(R_{sb}, \varphi) = 0 \end{cases} \tag{4.11}$$

where $l = 1, ..., N_{sp}$ is the indices of slots on a magnetic period of the machine. Handling the abode boundary conditions and considering the presence of a current density uniform distribution, the vector potential solution in the slot region can be written as

$$A_z^{(1l)}(r,\varphi) = a_0^{(1l)} + \frac{\mu_0 J^{(l)}}{2}\left(R_{sb}^2 \ln r - \frac{r^2}{2}\right) - \sum_{m=1}^{+\infty} \frac{R_{sb}\, w_s}{m\pi} f_m^{(1l)} \left(\left(\frac{r}{R_{sb}}\right)^{\frac{m\pi}{w_s}} + \left(\frac{r}{R_{sb}}\right)^{-\frac{m\pi}{w_s}}\right) . \sin\left(\frac{m\pi}{w_s}(\varphi - \varphi_{1l})\right) \tag{4.12}$$

and the magnetic flux density components are given

$$B_r^{(1l)}(r,\varphi) = \sum_{m=1}^{+\infty} f_m^{(1l)} \left(\left(\frac{r}{R_{sb}}\right)^{\frac{m\pi}{w_s - 1}} + \left(\frac{r}{R_{sb}}\right)^{-\frac{m\pi}{w_s - 1}}\right) sin\left(\frac{m\pi}{w_s}(\varphi - \varphi_{1l})\right) \tag{4.13}$$

$$B_\varphi^{(1l)}(r,\varphi) = \sum_{m=1}^{+\infty} f_m^{(1l)} \left(\left(\frac{r}{R_{sb}}\right)^{\frac{m\pi}{w_s - 1}} - \left(\frac{r}{R_{sb}}\right)^{-\frac{m\pi}{w_s - 1}}\right) cos\left(\frac{m\pi}{w_s}(\varphi - \varphi_{1l})\right) - \frac{\mu_0 J^{(l)}}{2}\left(\frac{R_{sb}^2}{r} - r\right) \tag{4.14}$$

4.2.2.1.2 Solution in the airgap region Considering the periodicity of radial machines over a magnetic period in the circumferential direction in the airgap region, the vector potential solution in the airgap is written as

$$A_z^{(2)}(r,\varphi) = a_0^{(2)} + \sum_{k=1}^{+\infty} \frac{1}{k\lambda_p} \left(\left(C_k^{(2)}\left(\frac{r}{R_{si}}\right)^{k\lambda_p} + D_k^{(2)}\left(\frac{r}{R_{si}}\right)^{-k\lambda_p}\right)\cos\left(k\lambda_p\varphi\right) + \left(E_k^{(2)}\left(\frac{r}{R_{si}}\right)^{k\lambda_p} + F_k^{(2)}\left(\frac{r}{R_{si}}\right)^{-k\lambda_p}\right)\sin\left(k\lambda_p\varphi\right)\right) \tag{4.15}$$

where p and N_s are the pole pair number and slot's number respectively. The λ_p is the $GCD(p, N_s)$. The airgap flux density components are then

$$B_r^{(2)}(r,\varphi) = \sum_{k=1}^{+\infty} \left(C_k^{(2)} \left(\frac{r}{R_{si}} \right)^{k\lambda_p - 1} + D_k^{(2)} \left(\frac{r}{R_{si}} \right)^{-k\lambda_p - 1} \right) \sin\left(k\lambda_p \varphi\right) - \left(E_k^{(2)} \left(\frac{r}{R_{si}} \right)^{k\lambda_p - 1} + F_k^{(2)} \left(\frac{r}{R_{si}} \right)^{-k\lambda_p - 1} \right) \cos\left(k\lambda_p \varphi\right) \tag{4.16}$$

$$B_\varphi^{(2)}(r,\varphi) = \sum_{k=1}^{+\infty} \left(C_k^{(2)} \left(\frac{r}{R_{si}} \right)^{k\lambda_p - 1} - D_k^{(2)} \left(\frac{r}{R_{si}} \right)^{-k\lambda_p - 1} \right) \cos\left(k\lambda_p \varphi\right) + \left(E_k^{(2)} \left(\frac{r}{R_{si}} \right)^{k\lambda_p - 1} - F_k^{(2)} \left(\frac{r}{R_{si}} \right)^{-k\lambda_p - 1} \right) \sin\left(k\lambda_p \varphi\right) \tag{4.17}$$

4.2.2.1.3 Solution in the permanent magnet region In order to consider different type of remanence distribution, the radial and circumferential components of remanence is written in Fourier series form

$$\begin{cases} B_{R_r}(\varphi_r) = \sum_{k=1}^{+\infty} E_k^M . \cos(k\lambda_p \varphi_r) + F_k^M . \sin(k\lambda_p \varphi_r) \\ B_{R_\varphi}(\varphi_r) = \sum_{k=1}^{+\infty} C_k^M . \cos(k\lambda_p \varphi_r) + D_k^M . \sin(k\lambda_p \varphi_r) \end{cases} \tag{4.18}$$

The only boundary condition in this region is the nullity of the magnetic field strength circumferential component at the rotor magnetic circuit surface

$$H_\varphi^{(3)}(R_{mi}, \varphi) = 0 \tag{4.19}$$

Handling the above boundary condition and considering the same periodicity in the permanent magnet region as in the airgap region, the vector potential solution is consequently given by

$$
\begin{aligned}
A_z^{(3)}(r,\varphi_r) = a_0^{(3)} + \sum_{k=1,\lambda_p\neq 1}^{+\infty} \Bigg[& \left(\frac{R_{mo}}{k\lambda_p} C_k^{(3)} . \left(\left(\frac{r}{R_{mo}} \right)^{k\lambda_p} + \left(\frac{R_{mi}}{R_{mo}} \right)^{2k\lambda_p} . \left(\frac{r}{R_{mo}} \right)^{-k\lambda_p} \right) \right. \\
& \left. - \frac{R_{mo}}{k\lambda_p} \left(\frac{k\lambda_p F_k^M - C_k^M}{1-k^2\lambda_p^2} + C_k^M \right) \left(\frac{R_{mi}}{R_{mo}} \right)^{k\lambda_p+1} . \left(\frac{r}{R_{mo}} \right)^{-k\lambda_p} - \left(\frac{k\lambda_p F_k^M - C_k^M}{1-k^2\lambda_p^2} \right) .r \right) . \cos(k\lambda_p \varphi_r) \\
& + \left(\frac{R_{mo}}{k\lambda_p} E_k^{(3)} . \left(\left(\frac{r}{R_{mo}} \right)^{k\lambda_p} + \left(\frac{R_{mi}}{R_{mo}} \right)^{2k\lambda_p} . \left(\frac{r}{R_{mo}} \right)^{-k\lambda_p} \right) \right. \\
& \left. + \frac{R_{mo}}{k\lambda_p} \left(\frac{k\lambda_p F_k^M + D_k^M}{1-k^2\lambda_p^2} - D_k^M \right) \left(\frac{R_{mi}}{R_{mo}} \right)^{k\lambda_p+1} . \left(\frac{r}{R_{mo}} \right)^{-k\lambda_p} + \left(\frac{k\lambda_p E_k^M + D_k^M}{1-k^2\lambda_p^2} \right) .r \right) . \sin(k\lambda_p \varphi_r) \Bigg]
\end{aligned}
\tag{4.20}
$$

The above solution is made for λ_p. Then an adapted form is possible for the case $\lambda_p = 1$ and $k = 1$ which is not given here in order to lighten the presentation. The magnetic flux density components are then given by

$$
\begin{aligned}
B_r^{(3)}(r,\varphi_r) = \sum_{k=1,\lambda_p\neq 1}^{+\infty} \Bigg[& \left(C_k^{(3)} . \left(\left(\frac{r}{R_{mo}} \right)^{k\lambda_p-1} + \left(\frac{R_{mi}}{R_{mo}} \right)^{2k\lambda_p} . \left(\frac{r}{R_{mo}} \right)^{-k\lambda_p-1} \right) \right. \\
& \left. - \left(\frac{k\lambda_p F_k^M - C_k^M}{1-k^2\lambda_p^2} + C_k^M \right) \left(\frac{R_{mi}}{R_{mo}} \right)^{k\lambda_p+1} . \left(\frac{r}{R_{mo}} \right)^{-k\lambda_p-1} - k\lambda_p \left(\frac{k\lambda_p F_k^M - C_k^M}{1-k^2\lambda_p^2} \right) \right) . \sin(k\lambda_p \varphi_r) \\
& + \left(E_k^{(3)} . \left(\left(\frac{r}{R_{mo}} \right)^{k\lambda_p-1} + \left(\frac{R_{mi}}{R_{mo}} \right)^{2k\lambda_p} . \left(\frac{r}{R_{mo}} \right)^{-k\lambda_p-1} \right) \right. \\
& \left. + \left(\frac{k\lambda_p F_k^M + D_k^M}{1-k^2\lambda_p^2} - D_k^M \right) \left(\frac{R_{mi}}{R_{mo}} \right)^{k\lambda_p+1} . \left(\frac{r}{R_{mo}} \right)^{-k\lambda_p-1} + k\lambda_p \left(\frac{k\lambda_p E_k^M + D_k^M}{1-k^2\lambda_p^2} \right) \right) . \cos(k\lambda_p \varphi_r) \Bigg]
\end{aligned}
\tag{4.21}
$$

$$
\begin{aligned}
B_\varphi^{(3)}(r,\varphi_r) = \sum_{k=1,\lambda_p\neq 1}^{+\infty} \Bigg[& \left(C_k^{(3)} . \left(\left(\frac{r}{R_{mo}} \right)^{k\lambda_p-1} - \left(\frac{R_{mi}}{R_{mo}} \right)^{2k\lambda_p} . \left(\frac{r}{R_{mo}} \right)^{-k\lambda_p-1} \right) \right. \\
& \left. + \left(\frac{k\lambda_p F_k^M - C_k^M}{1-k^2\lambda_p^2} + C_k^M \right) \left(\frac{R_{mi}}{R_{mo}} \right)^{k\lambda_p+1} . \left(\frac{r}{R_{mo}} \right)^{-k\lambda_p-1} - \left(\frac{k\lambda_p F_k^M - C_k^M}{1-k^2\lambda_p^2} \right) \right) . \cos(k\lambda_p \varphi_r) \\
& + \left(E_k^{(3)} . \left(\left(\frac{r}{R_{mo}} \right)^{k\lambda_p-1} - \left(\frac{R_{mi}}{R_{mo}} \right)^{2k\lambda_p} . \left(\frac{r}{R_{mo}} \right)^{-k\lambda_p-1} \right) \right. \\
& \left. - \left(\frac{k\lambda_p F_k^M + D_k^M}{1-k^2\lambda_p^2} - D_k^M \right) \left(\frac{R_{mi}}{R_{mo}} \right)^{k\lambda_p+1} . \left(\frac{r}{R_{mo}} \right)^{-k\lambda_p-1} + \left(\frac{k\lambda_p E_k^M + D_k^M}{1-k^2\lambda_p^2} \right) \right) . \sin(k\lambda_p \varphi_r) \Bigg]
\end{aligned}
\tag{4.22}
$$

Considering the periodicity of such machines in the circumferential direction, In the permanent magnet regions, the remanence allowing by the way the development of a 2D solution the vector potential is parallel to the rotational axis.

4.2.2.1.4 Boundary conditions between slot regions and airgap region At the boundary between the slot region and the airgap region, the continuity of the flux density normal component and the magnetic field strength tangential component lead to the following expressions

$$\left.\begin{aligned} B_r^{(1l)}(R_{si},\varphi_r) &= B_r^{(2)}(R_{si},\varphi_r) \\ H_\varphi^{(1l)}(R_{si},\varphi_r) &= H_\varphi^{(2)}(R_{si},\varphi_r) \end{aligned}\right\} \text{for} \quad \varphi_{1,l} \leq \varphi \leq \varphi_{1,l} + w_s \quad \& \quad l = 0, ..., N_s - 1 \tag{4.23}$$

and

$$H_\varphi^{(2)}(R_{si},\varphi) = 0 \quad \text{for} \quad \varphi_{1,l} + w_s \leq \varphi \leq \varphi_{1,l+1} \tag{4.24}$$

where $\varphi_{1,l} = \dfrac{-w_s}{2} + l.\dfrac{2\pi}{N_s}$ with $l = 0, ..., N_s - 1$. Expressions in Eq. 4.13, Eq. 4.14, Eq. 7.13a and Eq. 4.17 have to be involved in Eq. 4.23 and Eq. 4.24 given relationships between the coefficients of regions (I) and (II). Using Fourier integrals, two algebraic relations between coefficients can be derived as follows

$$\begin{aligned} C_k^{(2)} - D_k^{(2)} = &-\frac{\mu_0}{k\pi}\left(\frac{R_{sb}^2}{R_{si}} - R_{si}\right)\sin\left(k\lambda_p\frac{w_s}{2}\right)\sum_{l=0}^{N_{sp}-1} J^{(l)}.\cos\left(k\lambda_p l\frac{2\pi}{N_s}\right) + \\ &\frac{\lambda_p w_s}{2\pi}\sum_{l=0}^{N_{sp}-1}\sum_{m=1}^{+\infty} f_m^{(1l)}\frac{R_{sb}}{R_{si}}.\mathcal{M}\left(R_{si}, R_{sb}, \frac{m\pi}{w_s}\right)\left(\frac{1}{m\pi + k\lambda_p w_s} - \frac{1}{m\pi - k\lambda_p w_s}\right) \\ &\times\left[(-1)^m\sin\left(k\lambda_p\left(\frac{w_s}{2} + l.\frac{2\pi}{N_s}\right)\right) - \sin\left(k\lambda_p\left(-\frac{w_s}{2} + l.\frac{2\pi}{N_s}\right)\right)\right] \end{aligned} \tag{4.25}$$

$$\begin{aligned} E_k^{(2)} - F_k^{(2)} = &-\frac{\mu_0}{k\pi}\left(\frac{R_{sb}^2}{R_{si}} - R_{si}\right)\sin\left(k\lambda_p\frac{w_s}{2}\right)\sum_{l=0}^{N_{sp}-1} J^{(l)}.\sin\left(k\lambda_p l\frac{2\pi}{N_s}\right) + \\ &\frac{\lambda_p w_s}{2\pi}\sum_{l=0}^{N_{sp}-1}\sum_{m=1}^{+\infty} f_m^{(1l)}\frac{R_{sb}}{R_{si}}.\mathcal{M}\left(R_{si}, R_{sb}, \frac{m\pi}{w_s}\right)\left(\frac{1}{m\pi + k\lambda_p w_s} - \frac{1}{m\pi - k\lambda_p w_s}\right) \\ &\left[\cos\left(k\lambda_p\left(-\frac{w_s}{2} + l.\frac{2\pi}{N_s}\right)\right) - (-1)^m\cos\left(k\lambda_p\left(\frac{w_s}{2} + l.\frac{2\pi}{N_s}\right)\right)\right] \end{aligned} \tag{4.26}$$

$$\sum_{l=0}^{N_{sp}-1} f_m^{(1l)} \frac{R_{sb}}{R_{si}} . \mathcal{P}\left(R_{si}, R_{sb}, \frac{m\pi}{w_s}\right) . \left[\cos\left(k\lambda_p\left(-\frac{w_s}{2}+l.\frac{2\pi}{N_s}\right)\right) - (-1)^m \cos\left(k\lambda_p\left(\frac{w_s}{2}+l.\frac{2\pi}{N_s}\right)\right)\right]$$
$$- N_{sp} \sum_{\substack{n\neq 0 \\ n+k=\rho N_{sp}}} \left(E_n^{(2)}+F_n^{(2)}\right)\left(\frac{1}{m\pi-n\lambda_p w_s}+\frac{1}{m\pi+n\lambda_p w_s}\right)\left[cos\left((n+k)\frac{\lambda_p w_s}{2}\right) - (-1)^m cos\left((n-k)\frac{\lambda_p w_s}{2}\right)\right]$$
$$- N_{sp} \sum_{\substack{n\neq 0 \\ n-k=\rho N_{sp}}} \left(E_n^{(2)}+F_n^{(2)}\right)\left(\frac{1}{m\pi-n\lambda_p w_s}+\frac{1}{m\pi+n\lambda_p w_s}\right)\left[cos\left((n-k)\frac{\lambda_p w_s}{2}\right) - (-1)^m cos\left((n+k)\frac{\lambda_p w_s}{2}\right)\right] \quad (4.27)$$

$$\sum_{l=0}^{N_{sp}-1} f_m^{(1l)} \frac{R_{sb}}{R_{si}} . \mathcal{P}\left(R_{si}, R_{sb}, \frac{m\pi}{w_s}\right) . \left[\sin\left(k\lambda_p\left(-\frac{w_s}{2}+l.\frac{2\pi}{N_s}\right)\right) - (-1)^m \sin\left(k\lambda_p\left(\frac{w_s}{2}+l.\frac{2\pi}{N_s}\right)\right)\right]$$
$$- N_{sp} \sum_{\substack{n\neq 0 \\ n+k=\rho N_{sp}}} \left(C_n^{(2)}+D_n^{(2)}\right)\left(\frac{1}{m\pi-n\lambda_p w_s}+\frac{1}{m\pi+n\lambda_p w_s}\right)\left[cos\left((n+k)\frac{\lambda_p w_s}{2}\right) - (-1)^m cos\left((n-k)\frac{\lambda_p w_s}{2}\right)\right]$$
$$+ N_{sp} \sum_{\substack{n\neq 0 \\ n-k=\rho N_{sp}}} \left(C_n^{(2)}+D_n^{(2)}\right)\left(\frac{1}{m\pi-n\lambda_p w_s}+\frac{1}{m\pi+n\lambda_p w_s}\right)\left[cos\left((n-k)\frac{\lambda_p w_s}{2}\right) - (-1)^m cos\left((n+k)\frac{\lambda_p w_s}{2}\right)\right] \quad (4.28)$$

4.2.2.1.5 Boundary conditions between airgap region and permanent magnet region As done before, boundary conditions between airgap region and permanent magnet region are expressed in the following manner

$$\begin{cases} B_r^{(2)}(R_{mo}, \varphi_s) = B_r^{(3)}(R_{mo}, \varphi_s - \theta) \\ H_\varphi^{(2)}(R_{mo}, \varphi_s) = H_\varphi^{(3)}(R_{mo}, \varphi_s - \theta) \end{cases} \quad (4.29)$$

where θ is the angular position between the stator reference frame and the rotor reference frame. Involving expressions in Eq. 7.13a, Eq. 4.17, Eq. 4.21 and Eq. 4.22 in Eq. 4.29 and using the Fourier integrals lead to the new following algebraic relationships between the coefficients of regions (II) and (III)

$$C_k^{(2)} = \left(\frac{R_{mo}}{R_{si}}\right)^{-k\lambda_p+1} . \left(C_k^{(3)}\cos(k\lambda_p\theta) - E_k^{(3)}\sin(k\lambda_p\theta)\right)$$
$$+ \frac{1}{2}.\frac{k\lambda_p}{1-k\lambda_p}.\left(\frac{R_{mo}}{R_{si}}\right)^{-k\lambda_p+1}\left[\left(C_k^M\cos(k\lambda_p\theta) - D_k^M\sin(k\lambda_p\theta)\right) - \left(E_k^M\sin(k\lambda_p\theta) + F_k^M\cos(k\lambda_p\theta)\right)\right] \quad (4.30)$$

$$
\begin{aligned}
D_k^{(2)} = & \left(\frac{R_{mo}}{R_{si}}\right)^{k\lambda_p+1}\left(\frac{R_{mi}}{R_{mo}}\right)^{2k\lambda_p}.\left(C_k^{(3)}\cos(k\lambda_p\theta)-E_k^{(3)}\sin(k\lambda_p\theta)\right) \\
& +\frac{1}{2}.\frac{k\lambda_p}{1-k^2\lambda_p^2}.\left(\frac{R_{mo}}{R_{si}}\right)^{k\lambda_p+1}\left(2k\lambda_p\left(\frac{R_{mi}}{R_{mo}}\right)^{k\lambda_p+1}-k\lambda_p+1\right)\left(C_k^M\cos(k\lambda_p\theta)-D_k^M\sin(k\lambda_p\theta)\right) \\
& -\frac{1}{2}.\frac{k\lambda_p}{1-k^2\lambda_p^2}.\left(\frac{R_{mo}}{R_{si}}\right)^{k\lambda_p+1}\left(2\left(\frac{R_{mi}}{R_{mo}}\right)^{k\lambda_p+1}+k\lambda_p-1\right)\left(E_k^M\sin(k\lambda_p\theta)+F_k^M\cos(k\lambda_p\theta)\right)
\end{aligned}
\tag{4.31}
$$

$$
\begin{aligned}
E_k^{(2)} = & \left(\frac{R_{mo}}{R_{si}}\right)^{-k\lambda_p+1}.\left(C_k^{(3)}\sin(k\lambda_p\theta)-E_k^{(3)}\cos(k\lambda_p\theta)\right) \\
& +\frac{1}{2}.\frac{k\lambda_p}{1-k\lambda_p}.\left(\frac{R_{mo}}{R_{si}}\right)^{-k\lambda_p+1}\left[\left(C_k^M\sin(k\lambda_p\theta)+D_k^M\cos(k\lambda_p\theta)\right)-\left(E_k^M(k\lambda_p\theta)-F_k^M\sin(k\lambda_p\theta)\right)\right]
\end{aligned}
\tag{4.32}
$$

$$
\begin{aligned}
D_k^{(2)} = & \left(\frac{R_{mo}}{R_{si}}\right)^{k\lambda_p+1}\left(\frac{R_{mi}}{R_{mo}}\right)^{2k\lambda_p}.\left(C_k^{(3)}\sin(k\lambda_p\theta)-E_k^{(3)}\cos(k\lambda_p\theta)\right) \\
& +\frac{1}{2}.\frac{k\lambda_p}{1-k^2\lambda_p^2}.\left(\frac{R_{mo}}{R_{si}}\right)^{k\lambda_p+1}\left(2k\lambda_p\left(\frac{R_{mi}}{R_{mo}}\right)^{k\lambda_p+1}-k\lambda_p+1\right)\left(C_k^M(k\lambda_p\theta)+D_k^M\cos(k\lambda_p\theta)\right) \\
& -\frac{1}{2}.\frac{k\lambda_p}{1-k^2\lambda_p^2}.\left(\frac{R_{mo}}{R_{si}}\right)^{k\lambda_p+1}\left(2\left(\frac{R_{mi}}{R_{mo}}\right)^{k\lambda_p+1}+k\lambda_p-1\right)\left(E_k^M\cos(k\lambda_p\theta)-F_k^M\sin(k\lambda_p\theta)\right)
\end{aligned}
\tag{4.33}
$$

4.2.2.1.6 Linear algebraic system in terms of airgap region coefficients The different algebraic relationships between coefficients in Eq. 4.25, Eq. 4.26, Eq. 4.27, Eq. 4.28, Eq. 4.30, Eq. 4.31, Eq. 4.32 and Eq. 4.33 issued from the exploitation of boundary conditions between regions are handled to eliminate the coefficients of regions (I) and (III) in order to the following algebraic equations involving coefficients and of

the airgap region

$$
\begin{aligned}
&\left(1-\left(\frac{R_{mi}}{R_{si}}\right)^{2k\lambda_p}\right).C_k^{(2)}-\sum_{n\neq 0}\left(1+\left(\frac{R_{mi}}{R_{si}}\right)^{2n\lambda_p}\right).C_n^{(2)}.\alpha(n,k)= \\
&-\frac{\mu_0}{k\pi}\left(\frac{R_{sb}^2}{R_{si}}-R_{si}\right)\sin\left(k\lambda_p\frac{w_s}{2}\right)\sum_{l=0}^{N_s-1}J^{(l)}\cos\left(k\lambda_p l\frac{2\pi}{N_s}\right) \\
&+\frac{1}{2}.\frac{k\lambda_p}{1-k^2\lambda_p^2}.\left(\frac{R_{mo}}{R_{si}}\right)^{k\lambda_p+1}\left(1-k\lambda_p+2k\lambda_p\left(\frac{R_{mi}}{R_{mo}}\right)^{k\lambda_p+1}-(1+k\lambda_p).\left(\frac{R_{mi}}{R_{mo}}\right)^{2k\lambda_p}\right)\left(C_k^M\cos(k\lambda_p\theta)-D_k^M\sin(k\lambda_p\theta)\right) \\
&+\sum_{n\neq 0}\frac{1}{2}.\frac{k\lambda_p}{1-k^2\lambda_p^2}.\left(\frac{R_{mo}}{R_{si}}\right)^{k\lambda_p+1}\left(1-n\lambda_p+2n\lambda_p\left(\frac{R_{mi}}{R_{mo}}\right)^{n\lambda_p+1}-(1+n\lambda_p).\left(\frac{R_{mi}}{R_{mo}}\right)^{2n\lambda_p}\right)\left(C_n^M\cos(n\lambda_p\theta)-D_n^M\sin(n\lambda_p\theta)\right)\times\alpha(n,k) \\
&+\frac{1}{2}.\frac{k\lambda_p}{1-k^2\lambda_p^2}.\left(\frac{R_{mo}}{R_{si}}\right)^{k\lambda_p+1}\left(1-k\lambda_p+2\left(\frac{R_{mi}}{R_{mo}}\right)^{k\lambda_p+1}+(1+k\lambda_p).\left(\frac{R_{mi}}{R_{mo}}\right)^{2k\lambda_p}\right)\left(E_k^M\sin(k\lambda_p\theta)+F_k^M\cos(k\lambda_p\theta)\right) \\
&+\sum_{n\neq 0}\frac{1}{2}.\frac{k\lambda_p}{1-k^2\lambda_p^2}.\left(\frac{R_{mo}}{R_{si}}\right)^{k\lambda_p+1}\left(1-n\lambda_p+2n\lambda_p\left(\frac{R_{mi}}{R_{mo}}\right)^{n\lambda_p+1}+(1+n\lambda_p).\left(\frac{R_{mi}}{R_{mo}}\right)^{2n\lambda_p}\right)\left(E_n^M\sin(n\lambda_p\theta)+F_n^M\cos(n\lambda_p\theta)\right)\times\alpha(n,k)
\end{aligned}
\tag{4.34}
$$

$$
\begin{aligned}
&\left(1-\left(\frac{R_{mi}}{R_{si}}\right)^{2k\lambda_p}\right).E_k^{(2)}-\sum_{n\neq 0}E_n^{(2)}\left(1+\left(\frac{R_{mi}}{R_{si}}\right)^{2n\lambda_p}\right).\beta(n,k)= \\
&-\frac{\mu_0}{k\pi}\left(\frac{R_{sb}^2}{R_{si}}-R_{si}\right)\sin\left(k\lambda_p\frac{w_s}{2}\right)\sum_{l=0}^{N_s-1}J^{(l)}\sin\left(k\lambda_p l\frac{2\pi}{N_s}\right) \\
&+\frac{1}{2}.\frac{k\lambda_p}{1-k^2\lambda_p^2}.\left(\frac{R_{mo}}{R_{si}}\right)^{k\lambda_p+1}\left(1-k\lambda_p+2k\lambda_p\left(\frac{R_{mi}}{R_{mo}}\right)^{k\lambda_p+1}-(1+k\lambda_p).\left(\frac{R_{mi}}{R_{mo}}\right)^{2k\lambda_p}\right)\left(C_k^M\sin(k\lambda_p\theta)+D_k^M\cos(k\lambda_p\theta)\right) \\
&-\sum_{n\neq 0}\frac{1}{2}.\frac{k\lambda_p}{1-k^2\lambda_p^2}.\left(\frac{R_{mo}}{R_{si}}\right)^{k\lambda_p+1}\left(1-n\lambda_p+2n\lambda_p\left(\frac{R_{mi}}{R_{mo}}\right)^{n\lambda_p+1}-(1+n\lambda_p).\left(\frac{R_{mi}}{R_{mo}}\right)^{2n\lambda_p}\right)\left(C_n^M\sin(n\lambda_p\theta)+D_n^M\cos(n\lambda_p\theta)\right)\times\beta(n,k) \\
&-\frac{1}{2}.\frac{k\lambda_p}{1-k^2\lambda_p^2}.\left(\frac{R_{mo}}{R_{si}}\right)^{k\lambda_p+1}\left(1-k\lambda_p+2\left(\frac{R_{mi}}{R_{mo}}\right)^{k\lambda_p+1}+(1+k\lambda_p).\left(\frac{R_{mi}}{R_{mo}}\right)^{2k\lambda_p}\right)\left(E_k^M\cos(k\lambda_p\theta)-F_k^M\sin(k\lambda_p\theta)\right) \\
&+\sum_{n\neq 0}\frac{1}{2}.\frac{k\lambda_p}{1-k^2\lambda_p^2}.\left(\frac{R_{mo}}{R_{si}}\right)^{k\lambda_p+1}\left(1-n\lambda_p+2n\lambda_p\left(\frac{R_{mi}}{R_{mo}}\right)^{n\lambda_p+1}+(1+n\lambda_p).\left(\frac{R_{mi}}{R_{mo}}\right)^{2n\lambda_p}\right)\left(E_n^M\cos(n\lambda_p\theta)-F_n^M\sin(n\lambda_p\theta)\right)\times\beta(n,k)
\end{aligned}
\tag{4.35}
$$

were function $\alpha(n,k)$ and $\beta(n,k)$ can be written as :

$$
\begin{cases}
\alpha(n,k)=f(n,k)-g(n,k) \\
\beta(n,k)=f(n,k)+g(n,k)
\end{cases}
$$

$$f(n,k) = \frac{N_s w_s}{2\pi} \sum_{m\neq 0} \frac{\mathcal{M}\left(R_{si}, R_{sb}, \frac{m\pi}{w_s}\right)}{\mathcal{P}\left(R_{si}, R_{sb}, \frac{m\pi}{w_s}\right)} \cdot \left(\frac{1}{m\pi + k\lambda_p w_s} - \frac{1}{m\pi - k\lambda_p w_s}\right)\left(\frac{1}{m\pi - n\lambda_p w_s} - \frac{1}{m\pi + n\lambda_p w_s}\right)$$
$$\times \left(\cos\left((n+k)\frac{\lambda_p w_s}{2}\right) - (-1)^m \cos\left((n-k)\frac{\lambda_p w_s}{2}\right)\right) \quad \text{if} \quad n + k = \rho N_s/\lambda_p$$
$$f(n,k) = 0 \qquad \text{otherwise} \tag{4.36}$$

$$g(n,k) = \frac{N_s w_s}{2\pi} \sum_{m\neq 0} \frac{\mathcal{M}\left(R_{si}, R_{sb}, \frac{m\pi}{w_s}\right)}{\mathcal{P}\left(R_{si}, R_{sb}, \frac{m\pi}{w_s}\right)} \cdot \left(\frac{1}{m\pi + k\lambda_p w_s} - \frac{1}{m\pi - k\lambda_p w_s}\right)\left(\frac{1}{m\pi - n\lambda_p w_s} - \frac{1}{m\pi + n\lambda_p w_s}\right)$$
$$\times \left(\cos\left((n-k)\frac{\lambda_p w_s}{2}\right) - (-1)^m \cos\left((n+k)\frac{\lambda_p w_s}{2}\right)\right) \quad \text{if} \quad n - k = \rho N_s/\lambda_p$$
$$g(n,k) = 0 \qquad \text{otherwise} \tag{4.37}$$

Equations Eq. 4.31 and Eq. 4.32 can be written in a vector-matrix form constituting a linear algebraic system of which the solution gives the unknown coefficients $C_k^{(2)}$ and $E_k^{(2)}$ of the airgap region

$$\begin{bmatrix} [M_{C_2}] & [0] \\ [0] & [M_{E_2}] \end{bmatrix} \cdot \begin{bmatrix} [C^{(2)}] \\ [E^{(2)}] \end{bmatrix} = \begin{bmatrix} [U_1] \\ [U_2] \end{bmatrix} \tag{4.38}$$

$D_k^{(2)}$ and $F_k^{(2)}$ coefficients are derived from $C_k^{(2)}$ and $E_k^{(2)}$ coefficients using boundary conditions relationships. In the same manner, the slot region and permanent region coefficients are deduced from the airgap region coefficients.

4.2.2.1.7 Global quantities computation Having the vector potential distribution in slots, the magnetic flux through stator phases could be computed by means of the average of vector potential over each coil section in slots. For 2D problems, the magnetic flux through a coil is then written as

$$\phi_c = N_{sp} \oint_{\breve{C}} \vec{A}.d\vec{r} = n_{sp} L_{ax} (A_{avg}^{(1l_r)} - A_{avg}^{(1l_a)}) \tag{4.39}$$

where N_{sp} is the coil turn number, L_{ax} the machine active length $A_{avg}^{(1l_r)}$ and $A_{avg}^{(1l_a)}$ are the spatial average of vector potential of the forward and return coil sides respectively. Stator phase flux can also be computed using the airgap flux density thanks to the winding distribution functions technique. Stator phase 'k' flux is then deduced by summing the fluxes over the N_{BOB} phase coils

$$\phi_{Sk}(\theta) = \sum_{j=1}^{N_{BOB}} \phi_{cj}(\theta) \tag{4.40}$$

The stator phase 'k' electromotive force is computed by deriving the stator phase flux at no-load by the rotor position for a given rotational speed

$$e_k = \Omega \frac{d\phi_{Sk}}{d\theta} \tag{4.41}$$

where Ω is the rotational speed. The electromagnetic torque is computed thanks to the Maxwell tensor as follows

$$\Gamma_{elm} = \frac{\lambda_p L_{ax} R_{mo}^2}{\mu_0} \times \int_0^{2\pi/\lambda_p} B_r^{(2)}(R_{mo}, \varphi_s) B_\varphi^{(2)}(R_{mo}, \varphi_s) d\varphi_s \tag{4.42}$$

The integral in Eq. 4.42 can be computed in terms of the airgap region coefficients yielding to the following torque expression

$$\Gamma_{elm} = \frac{2\pi L_{ax} R_{si}^2}{\mu_0} \times \sum_{k \neq 0} \left(-C_k^{(2)} F_k^{(2)} + D_k^{(2)} E_k^{(2)} \right) \tag{4.43}$$

4.2.2.1.8 Numerical considerations As it can be seen in the torque expression Eq. 4.43, the airgap region coefficients of the vector potential solution play an important role in the accuracy determination of the electromagnetic torque developed by the machine. The same comment can be given for the stator phase fluxes computation. So, a well-conditioned matrix of the algebraic system in Eq. 4.38 is necessary to obtain accurate computation of local and global quantities. This aspect appears to be particularly sensitive in the computation task of cogging torque. However, as it can be seen in equations Eq. 4.31 and Eq. 4.32, the diagonal elements of the system matrix in Eq. 4.38 depend on ratios between machine radii which are powered by the element indices and one can have positive power and negative power in the same time for some geometries (it is not the case for the actual studied machine). Depending on machine dimensions, it is not always possible to maintain these ratios between radii closed to one in order to guarantee a well-conditioned matrix. A way of matrix conditioning improvement is to limit the considered harmonic number which could result in a loss of precision for some quantities.

4.3 Reluctance Network Model

Reluctance network model[1], in which an analogy is made with electrical circuits, is one of the most frequently used techniques in the description of the magnetic field in electrical machines [270] [271] [272] [273]. It offers a compromise between the FEM and analytical models. It consist of subdividing the electromagnetic structure of the studied domain into a network of simplified flux tubes. The resulting network together with sources is transformed into an equivalent reluctances/permeance network, for which the flux through the tube and the scalar potential at the nodes can be solved by applying Kirchhoff's laws [274] [275]. When it incorporates the nonlinear ferromagnetic materials proprieties, the reluctance block distribution yields a nonlinear system of equations. In that case, an iterative nonlinear solving algorithm, such as Newton-Raphson and fixed-point, can be implemented to solve the system.

Before addressing the construction of the RNM, a brief description of the flux tube concept is outlined in short in the next subsection.

Table 4.1: Equivalent between electric and magnetic circuits

Field	
Electric	Magnetic
Potential difference U	Magnetic potential U
Electric current I	Magnetic flux ϕ
Resistance R	Reluctance $\mathcal{R}$
Current density $\overrightarrow{J}$	Flux density $\overrightarrow{B}$
Electric field $\overrightarrow{E}$	Magnetic field $\overrightarrow{H}$
Electric conductivity σ	Magnetic Permeability μ

4.3.1 Flux tube fundamentals

As explain before, the reluctance network model theory is based upon flux tubes (See Fig. 4.3). A flux tube is defined as space with quasi-stationary magnetic field (i.e. time independent), in which :

- the magnetic flux is confined to flowing in one direction,
- No flux penetrates the longitudinal faces (no leakage occurs at longitudinal faces),

[1] Also known as Magnetic Equivalent Circuit (MEC).

- the magnetic flux lines are parallel and have the same amplitude,
- the magnetic flux is perpendicular (normal) to the transversal faces where it enters and leaves the tube,
- a uniform flux density throughout the cross-section of the tube is assumed.

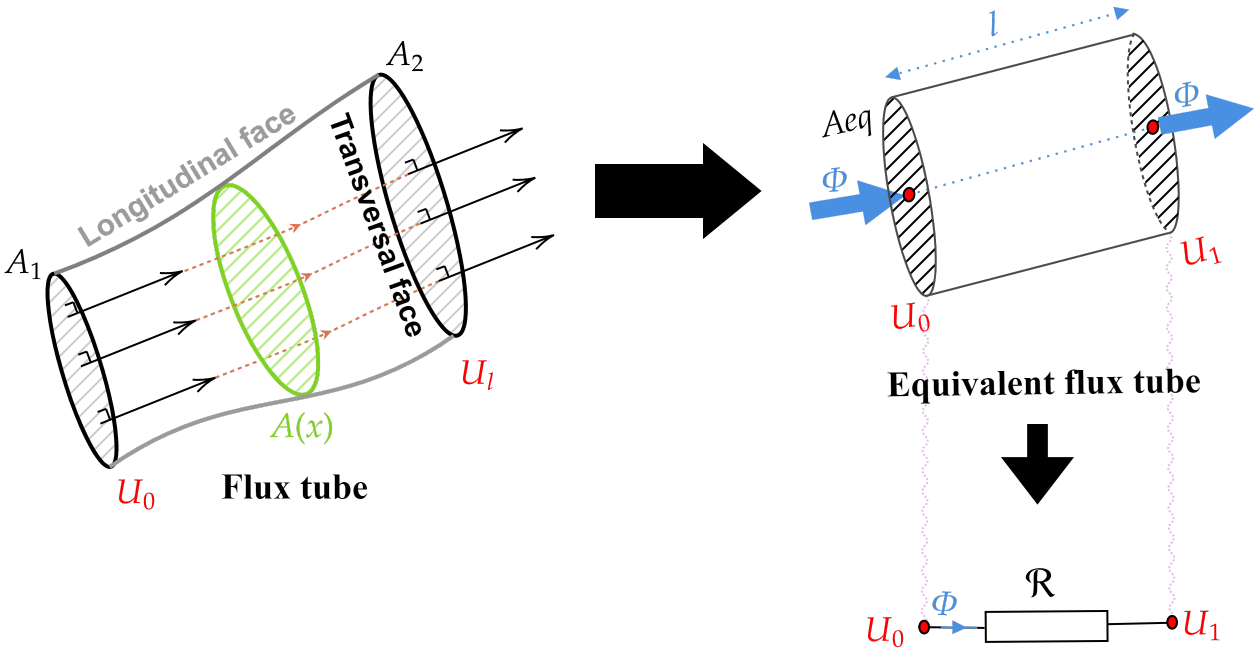

Figure 4.3: Flux tube and its corresponding reluctance

Under these assumption, the flux tube can be represented by equivalent flux tube, in which the potential distribution is uniform on every surface perpendicular to the magnetic flux vector. Fig. 4.3 illustrates a flux tube together with magnetic flux lines, equipotential surfaces and the equivalent flux tube. In that case, the magnetic flux, ϕ, can be expressed as a function of the magnetic scalar potential, U, as follow

$$\Delta U = U_1 - U_0 = \mathcal{R} \times \phi = \frac{\phi}{\mathcal{P}} \tag{4.44}$$

where $\mathcal{R}$ is the reluctance and $\mathcal{P}$ the permeance of the flux tube. The reluctance of the flux tube can be expressed as a a function on its geometrical dimensions and material proprieties. Its expression is achieved through the simplification of Maxwell's equations with taking into account the previously defined simplifying assumptions [275] [276] [277]

$$\mathcal{R} = \int_l \frac{1}{\iint_A \mu(x,s)\, ds}\, dx \tag{4.45}$$

where l is the length of the flux tube, μ is its magnetic permeability and A its cross-sectional area. In almost all the cases, one can assume that the magnetic permeability does not depend on the flux tube geometry, the Eq. 4.45 becomes

$$\mathcal{R} = \int_{l} \frac{dx}{\mu_r(x)\,\mu_0\,A(x)} \tag{4.46}$$

where μ_r and μ_0 are the relative and vacuum permeability respectively. The saturation effects can be taking into account by solving the nonlinear network with an iterative algorithm. Referring to Eq. 4.46, the permeance is a function of the geometry and the magnetic proprieties of the flux tube. According to [271], there are three types of magnetic permeances: constant, inherently non-linear and parametric non-linear.

- **Constant Permeance (CP)**

  In constant permeances, the geometry and the permeability are constant and never change during the machine operation. CPs are assigned to the machine's part in which the geometry and the relative permeability does not change during the operation of the device. Slots (copper), permanent magnets and unsaturated parts of the magnetic device will have constant permeance [271] [277]. In this case, the Eq. 4.46 can be integrated as

$$\mathcal{P}_{CP} = \frac{1}{\int_{0}^{l} \frac{dx}{\mu_r\,\mu_0\,A}} \tag{4.47}$$

- **Inherently Non-linear Permeance (INP)**

  In inherently non-linear permeances, the influence of the magnetic saturation effect, which means that the permeability of the iron core part is not a constant value but varies as the function of the passing magnetic flux or the instantaneous magnetic field density. INPs are assigned to machine parts composed of ferromagnetic material [271] [277]. In this case, the Eq. 4.46 can be integrated as

$$\mathcal{P}_{INP} = \frac{1}{\int_{0}^{l} \frac{dx}{\mu_r(x)\,\mu_0\,A}} \tag{4.48}$$

- **Parametric Non-linear Permeance (PNP)**

  Parametric non-linear permeance represents the flux tubes whose dimensions are variable. Usually, in electric machines, it refers to the moving part (airgap) permeance [271] [277]. In this case, the Eq. 4.46 can be integrated as

$$\mathcal{P}_{PNP} = \frac{1}{\int_0^l \frac{dx}{\mu_r \, \mu_0 \, A(x)}} \tag{4.49}$$

4.3.2 experience-based/mesh-based reluctance network model

Despite the fact that the magnetic field is acting in all directions, in pre-design stage, it is common to apply a 2D modeling to predict the magnetic field in electrical machine. This domain's reduction allows considerable calculation time saving. One can consider that at this design stage, a sufficiently accurate prediction of the magnetic field quantities is obtained by using 2D modeling.

4.3.2.1 Experience-based Reluctance Network Model

In this method, to construct the reluctance network, a prior knowledge of the flux distribution is required. Then, an experience-based division of the studied domain into elementary flux tubes is done. Indeed, the presence of high-permeable materials, the preferred direction of the magnetic flux could be defined. Although a good reliability are obtained for some topologies, this accuracy might be lost due to parameter variation or relative motion (stator-rotor) especially in the airgap region (e.g., leakage flux path) [277].

4.3.2.2 Mesh-based Reluctance Network Model

As explain before, the experience-based RNM has few limitations: require a prior knowledge of flux distributions (had to resort to other modeling techniques to define the main flux path) and present a high sensitivity to variations on the parameters (especially in the airgap and with relative motion (stator-rotor)) [277]. To overcome these limitations mesh-based model has been introduced. The later does not require prior knowledge of the main flux path, which permit arbitrary magnetic field behaviour inside the studied domain. In addition, it offers the possibility to adapt the mesh with parameters variations. The elements appeared in the RNM may be either passive or active. The active ones are referred to the magnetic sources (Magento-Motive Force (MMF) sources) whereas the passive ones are referred to reluctances in branches that represent the opposition to the magnetic flux.

An example of passive reluctance elementary blocks is schematically shown in Fig. 4.4 and Fig. 4.5. While

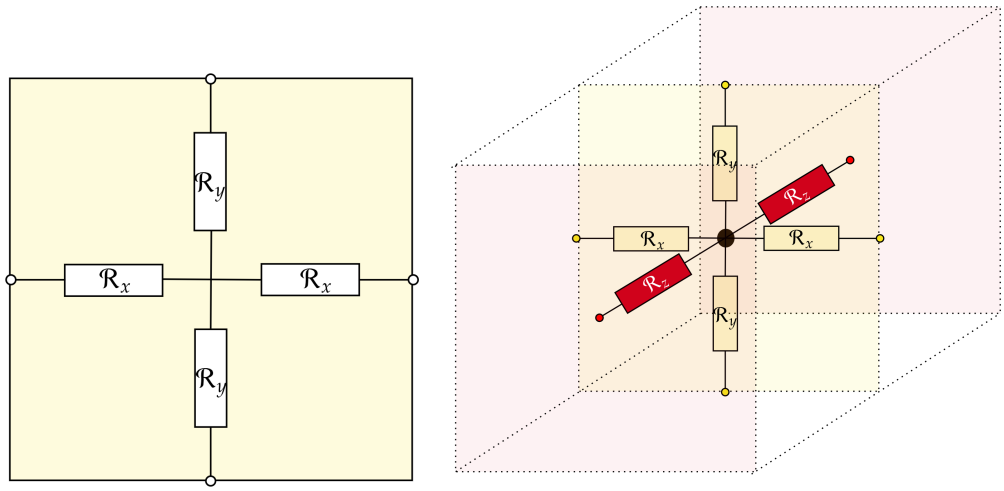

(a) 2D (b) 3D

Figure 4.4: Representation of RNM rectangular shape passive elementary block in Cartesian coordinate system

in Fig. 4.4 the discretization of the machine's geometry is done with rectangular mesh element in Cartesian coordinate frame, in Fig. 4.5 it is done with cylindrical polar mesh element in cylindrical coordinate frame. Each mesh element has a center node and four(2D)/three(3D) reluctances connecting it to the adjacent mesh elements.

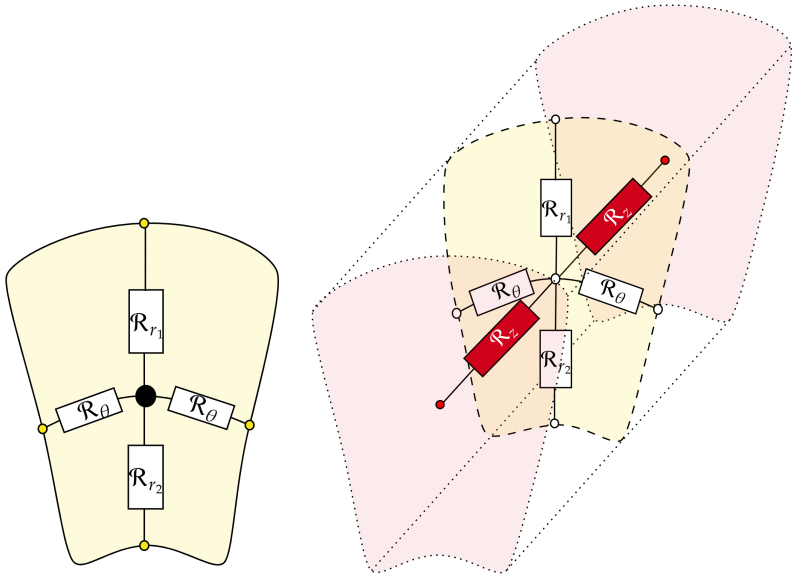

(a) 2D (b) 3D

Figure 4.5: Representation of RNM circular shape passive elementary block in Cylindrical coordinate system

Fig. 4.6 presents an example of active element, where the F_{ab} denotes the MMF source that depends on the coil current or permanent magnet section and characteristics.

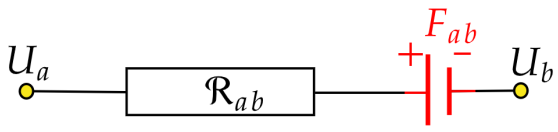

Figure 4.6: An example of active reluctance element

4.3.3 Reluctance network model building

4.3.3.1 Permeance network equations

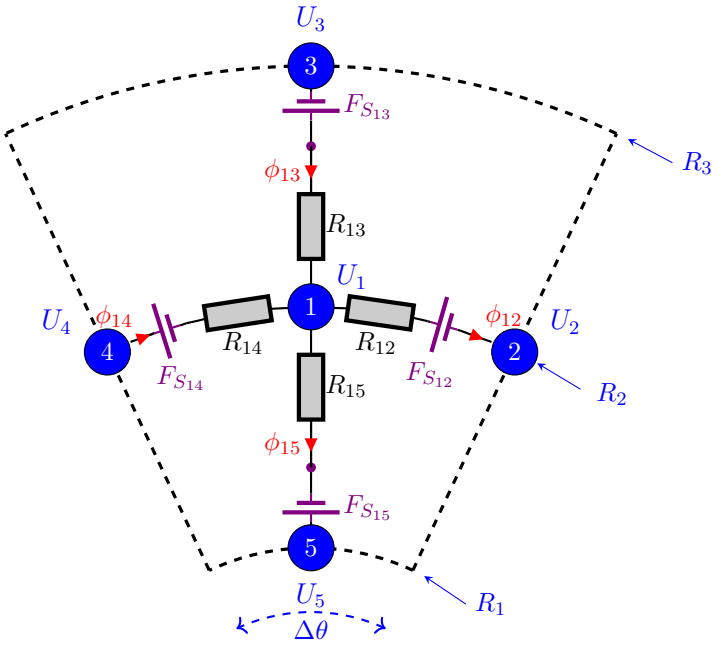

Figure 4.7: 2D reluctance elementary block in cylindrical coordinates

Despite the fact that the electromagnetic fields in electrical machine is a three-dimensional phenomenon, in nature, a translation to a two-dimensional modeling is commonly made. This simplification allow a reduction in the computational complexity and time, helps in speeding up the preliminary design stage. A magnetic 2D mesh-based RNM was adopted in this design optimization process, Fig. 4.7 shows a reference elementary block (sector layer) used in the construction of radial-flux machine model. The elementary block has a central node, (1), and four branches with their corresponding reluctances, $\{R_{12}, R_{13}, R_{14}$ and $R_{15}\}$, connecting it to the adjacent blocks. To model either conductors currying current or permanent magnets, the magnetic sources, $\{F_{12}, F_{13}, F_{14}$ and $F_{15}\}$, can be added to each branch . The magnetic sources could be represented either by flux source placed in parallel with the branch reluctance (See Fig. 4.8.a) or by MMF source placed in series with the branch reluctance (See Fig. 4.8.b).

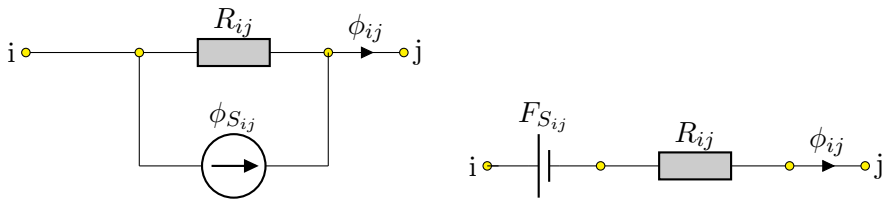

(a) Flux source (b) MMF source

Figure 4.8: Equivalent reluctance circuit including magnetic source

The Gauss'law for magnetism is applied to the central node (equivalent to Kirchhoff's current law), (1), of elementary block presented in Fig. 4.7, it considers that the sum of the flux entering to the node equals to those leaving this node

$$\sum_{j=2}^{5} \phi_{1j} = 0 \tag{4.50}$$

where ϕ_{1j} is the magnetic flux travelling through the branch connecting the (1) node to the (j) node.

The branch flux, ϕ_{ij}, can be expressed in terms of the scalar magnetic potentials of the boundary nodes, U_i and U_j, and the permeance connecting them, P_{ij} as (See Fig. 4.8.b)

$$(U_i - U_j) = R_{ij}\phi_{ij} + F_{S_{ij}} \Longleftrightarrow \phi_{ij} = \frac{U_i - U_j}{R_{ij}} - \frac{F_{S_{ij}}}{R_{ij}} \tag{4.51}$$

Substituting the expressions of the branch fluxes Eq. 4.51 into Eq. 4.50 and by replacing the reluctances, R_{ij}, by permanences, P_{ij}, the governing equation of the central node can be written as

$$(U_1 - U_2)P_{12} + (U_1 - U_3)P_{13} + (U_1 - U_4)P_{14} + (U_1 - U_5)P_{14} = F_{S_{12}}P_{12} + F_{S_{13}}P_{13} - F_{S_{14}}P_{14} - F_{S_{15}}P_{15} \tag{4.52}$$

The governing equation in Eq. 4.52 can be simplified into

$$\left(\sum_{k=2}^{5} P_{1k}\right) U_1 - \sum_{k=2}^{5} P_{1k}\, U_k = \sum_{k=1}^{5} \phi_{S1k} \tag{4.53}$$

In general, for a node (i) the Eq. 4.53 can be expressed as

$$\left(\sum_{k=k_1}^{k_2} P_{ik}\right) U_i - \sum_{k=k_1}^{k_2} P_{ik} U_k = \underbrace{\sum_{k=k_1}^{k_2} \phi_{Sik}}_{\Phi_i} \tag{4.54}$$

where Φ is the sum of the flux source connected to the (i) node.

The nodes potential of the global system can be describe in more compact expression

$$[P][U] = [\Phi] \tag{4.55}$$

where, $[P]$ is the permeance matrix $(n-m \times n)$ (The m missing equation in the matrix system will be provided by the air gap modeling method), $[\Phi]$ is the flux source vector $(n \times 1)$ and $[U]$ is the magnetic scalar potential (unknown vector) $(n \times 1)$. n is the number of the nodes and m is the number of the nodes located in the sliding surface positioned in the air-gap, which will be detailed in the next section.

As shown in Fig. 4.7, the elementary mesh block is delimited by two radii, R_1 and R_2, an arc, of an angle $\Delta\theta$, lying between these two radii. The radial and circumferential permeance components (P_r and P_θ) can be expressed using cylindrical coordinates by integrating Eq. 4.46 along the radial and circumferential direction, respectively [277] [278]

$$P_r : \begin{cases} P_{15} = \mu_r \, \mu_0 \, L_{act} \, \dfrac{\Delta\theta}{log\dfrac{R_2}{R_1}} \\ P_{13} = \mu_r \, \mu_0 \, L_{act} \, \dfrac{\Delta\theta}{log\dfrac{R_3}{R_2}} \end{cases} \tag{4.56}$$

$$P_\theta : \begin{cases} P_{14} = P_{12} = 2\mu_r \, \mu_0 \, L_{act} \, \dfrac{log\dfrac{R_3}{R_1}}{\Delta\theta} \end{cases} \tag{4.57}$$

where L_{act} and R_2 denote the the machine's active length and the mean value of the elementary block outer and inner radii $\left(\dfrac{R_1 + R_2}{2}\right)$, respectively. More details about the coupling of the elementary blocks with theirs adjacent blocks in RNM is provided in [277]. In the circumferential direction, it is assumed that the flux tube cover half of the element and then the values of the permeances P_{14} and P_{12} are equal.

4.3.3.2 Magnetic sources

4.3.3.2.1 Permanent magnet Fig. 4.9 illustrates a mesh element of cylindrical permanent magnet and its equivalent reluctant circuit. The magnet was modeled by flux sources connected to reluctance with constant

permeability. The value of the flux source given by the magnet, ϕ_{PM}, is given by

$$\phi_{PM} = B_R \, S_{PM} \tag{4.58}$$

where B_r and S_{PM} represent respectively the remanent flux density and the section of permanent magnet.

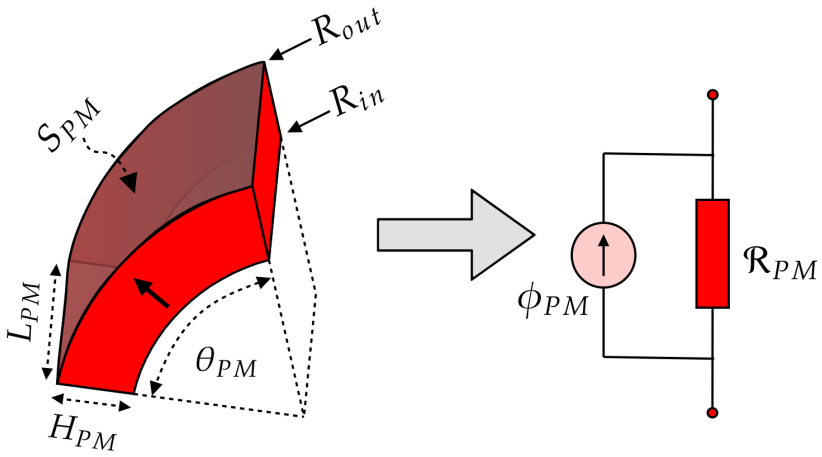

Figure 4.9: Equivalent reluctant circuit of a permanent magnet

4.3.3.2.2 Windings The current in windings is modeled by an MMF source. The maximum value of the magentomotive force due to winding can be written as

$$F_J = I_s \, N \tag{4.59}$$

where I_s is the phase current and N is number of turns. Unlike the MMF related to permanent magnet which only exist in the elementary blocks where the magnet is present, the one related to the current forms contours within and outside the winding regions. The distribution of the MMF should guarantee the fulfillment of Ampere's law for any arbitrary closed contour. A more detailed description of the arrangements that can meet this law is provided in [277].

4.3.3.3 Airgap modeling and incorporation of motion

The airgap modeling is quite difficult task to be achieved, since permeances attributed to the airgap will depend on the relative position of the rotor/stator, the rotor's discretization is different from that of the stator [279] and the presence of fringing effect results on an additional complexity. Furthermore, multi-megawatt

wind turbine generators have rather big airgap which might lead to rise the calculation errors. The air-gap permeances are considered as the parametric nonlinear permeances. The calculation of the airgap permeances can be performed using several approaches [279] [280], including hybrid analytical model [281] [282] [283] [284], variable reluctance network and node interpolation in the sliding region.

In the Hybrid Analytical Modeling (HAM) technique, a combination of a AM based on the formal solution of Maxwell's equations and a meshed-based RNM is made. The coupling between both models is obtained by assuring the magnetic flux and magnetic scalar potential continuity at the transition surfaces: airgap/stator and airgap/rotor. This method help to combine the advantages of both AM and RNM. It might help to reduce the calculation time as compared with the FEM [283] [282]. Although hybrid approach is rather simple and allows an accurate prediction of the performances of electrical machines [284], it suffers from badly scaled matrix. It results on a less sparse matrix which leads to time expensive model. In theory, an infinite number of harmonics can be considered. In reality, the maximum number of Fourier harmonics in AM is limited by the computer performances. It depends strongly on the machine's geometry such as the machine mean radius and number of magnetic repetition for a mechanical period [280].

In Variable Reluctance Network (VRN) approach a PNP are used (full reluctance network model). Indeed, the permeances in the airgap are function of the relative position between the rotating armature and the fixed one [271]. The magnetic field in the airgap have to be calculated to estimate the airgap permeances. Further, the number of the airgap nodes will change according to the rotor relative position and then the size of the scalar potential vector will change. This variation impacts the global matrix, making problems for post-processing. To avoid that, the airgap matrix is stored at each step in the memory, that will slow the program on one hand and necessitate more memory on the other [280]. VRN might may suffer from numerical issues. Indeed, the permeance connecting the stator block to the rotor one will considerably increase when the the exchange surface between these two blocks is small. Therefore, the matrix stability and thus the results accuracy will be disturbed [280].

In this thesis, node interpolation in the sliding region was used. In this approach, the air-gap is modeled by nodal interpolation functions, which take into consideration the continuity of the magnetic scalar potential and the magnetic flux density at the surface of the sliding region (the surface separating the moving parts from the static one) [275] [285].

Let's assume a rotor node located in the sliding surface is sandwiched between two nodes associated to the

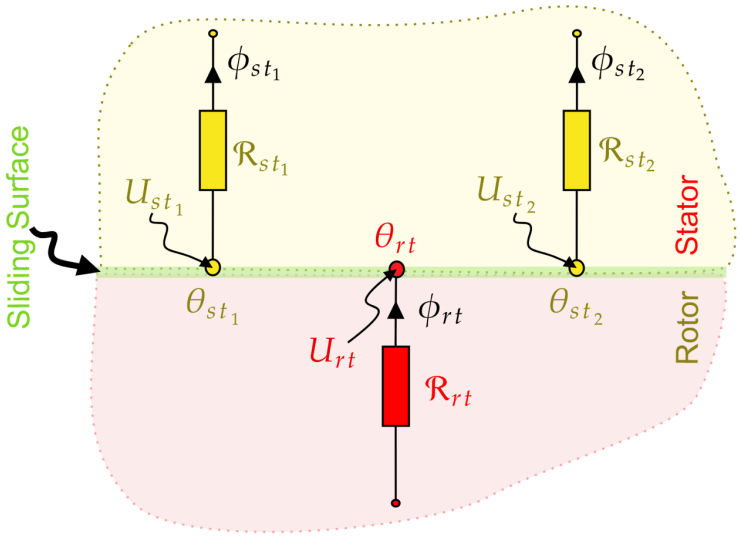

Figure 4.10: Magnetic scalar potential interpolation in the interface between the stator and the rotor

stator having θ_{rt},θ_{st_1} and θ_{st_2} as circumferential coordinates and U_{rt},U_{st_1} and U_{st_2} as nodal scalar potential respectively (See Fig. 4.11). The potential located in the rotor can be written in function of the two placed in the stator by using first order Lagrange interpolation as in

$$U_{rt} = \frac{\theta_{rt} - \theta_{st_1}}{\theta_{st_2} - \theta_{st_1}} U_{st_2} + \frac{\theta_{rt} - \theta_{st_2}}{\theta_{st_1} - \theta_{st_2}} U_{st_1} \tag{4.60}$$

With the previous equation, we assume that the potential has a linear shape between two successive nodes. This assures the equality of the scalar potential at the sliding surface, which will provide the m missing equations for the rotor. The previous equation can be generalized and written in the following format

$$[U_{rt}] - [M_{interp_{strt}}][U_{st}] = 0 \tag{4.61}$$

where $[U_{rt}]$ and $[U_{st}]$ are the vector containing the potentials corresponding to the nodes located at the sliding surfaces, and $[M_{interp_{strt}}]$ is the interpolation matrix.

To satisfy the second interface condition; which is the continuity of the magnetic flux density, and provide the missing equation for the stator, the magnetic flux density continuity between the two reluctance networks will be assured by using the same interpolation method employed previously resulting in

$$B_{st} = \frac{\theta_{st} - \theta_{rt_1}}{\theta_{rt_2} - \theta_{rt_1}} B_{rt_2} + \frac{\theta_{st} - \theta_{rt_2}}{\theta_{rt_1} - \theta_{rt_2}} B_{rt_1} \tag{4.62}$$

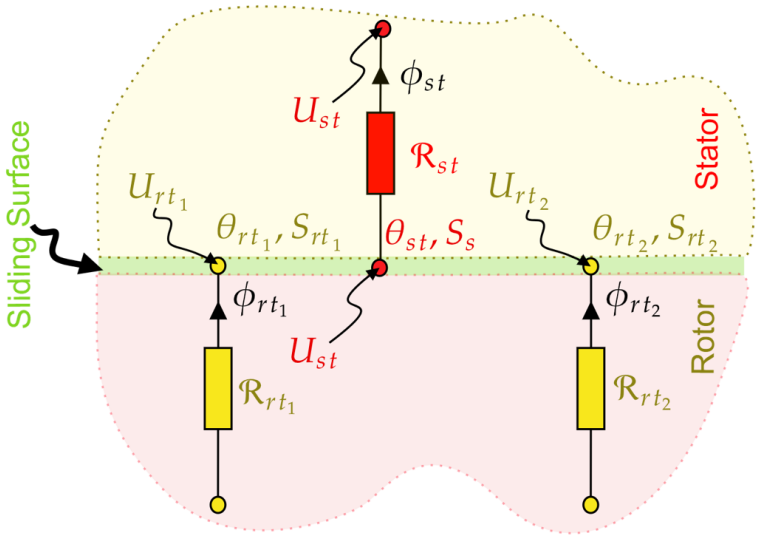

Figure 4.11: Magnetic flux density interpolation in the interface between the stator and the rotor

Using the relation between the magnetic flux density and the scalar potential, which is the scalar potential difference multiplied by the permeance and divided by its cross section, given in

$$B_{st} = \frac{\theta_{st} - \theta_{rt_1}}{\theta_{rt_2} - \theta_{rt_1}} \frac{\Delta U_{rt_2}}{R_{rt_2} S_{rt_2}} + \frac{\theta_{st} - \theta_{rt_2}}{\theta_{rt_1} - \theta_{rt_2}} \frac{\Delta U_{rt_1}}{R_{rt1} S_{rt_1}} \tag{4.63}$$

The previous equation can be transformed into matricial system as follow

$$[M_1][U_{st_1}] - [M_1][U_{st_2}] - [M_{interp_{rtst}}][U_{rt_1}] - [M_{interp_{rtst}}][U_{rt_2}] = 0 \tag{4.64}$$

where $[U_{st_1}]$, $[U_{rt_1}]$ are the vectors containing rotor and stator corresponding to the nodes located at the sliding surface, and $[U_{rt_2}]$, $[U_{rt_2}]$ contain the rotor and stator first scalar potential located below/above the sliding surface. $[M_{interp_{rtst}}]$ and $[M_1]$ are the modified interpolation matrix, in which every element is divided by the reluctance and its cross section and the the matrix contenting the permeance of the element divided by the cross section for each element.

It is clear that, in this technique, the motion can be taken into consideration easily, since the number of nodes is fix and it is only a question of interpolating the scalar potential and the magnetic flux density at the sliding surface for each new rotor position. In addition, the same technique can be used to model the air-gap for thermal simulation by replacing the magnetic scalar potential by temperature and magnetic flux density by

heat flux density.

4.3.3.4 Incorporation of the saturation

Nonlinear material properties can be handled by solving the set of nonlinear algebraic equations through an iterative nonlinear algorithm, for instance Newton-Raphson method [286] [274] [287], fixed-point method [287] [278] and Gauss-Siedel method [288] [289]. In fact, permeances in the iron core parts might be affected by the magnetic saturation and this will be reflected in their permeability. Therefore, the magnetic permeability values are no longer constant and are function of the magnetic flux density $\mu_r(H)$ or the magnetic field $\mu_r(B)$.

The Eq. 4.55 can be written in the following form

$$R(U) = [P][U] - [\Phi] = 0 \tag{4.65}$$

In iterative method, once the set of the algebraic equations defined in Eq. 4.55 is determined, the Eq. 4.65 need to be solved (first assuming a fixed permeability in all the permeances). Then, the branches magentic field are calculated, and the permeances are updated based on upon the present solution and the B-H curve of the material (several approaches has been already used to model the B-H curve [271], See Section. 4.3.3.4.1). The system is then resolved using the new updated permeances, and the error is computed. The iterative process is carried on until a certain termination criteria is satisfied, either the maximum number of iteration or by error criteria.

The Newton-Raphson method gives a relatively good quadratic convergence and could be very attractive to be used in system with high nonlinearity [286]. Nevertheless, it requires an initial guess and the computation of the Jacobian matrix, in which the elements are the partial derivative of reluctance with respect to flux (more details are provided in [290]). The system's convergence depends highly on the Jacobian matrix. Indeed, although the Jacobian matrix may be numerically computed, it could be a source of numerical issues and then may cause the divergence of the system. For instance, it has been observed that for the nodal formulation, the one adopted in this thesis, an exact evaluation of the Jacobian leads to a highly ill-conditioned system [274].

Assume the iron follows a nonlinear B-H curve, in this thesis M350-50A B-H was used, its curve is shown in Fig .4.12. In order to solve the nonlinear system in Eq. 4.55, the fixed-point method was applied. The error

checked in each iteration, $k+1$, can be given by

$$\left\| \frac{\mu^{k+1} - \mu^k}{\mu^k} \right\|_\infty \leqslant \varepsilon \tag{4.66}$$

Eq. 4.66 means that the maximum local error of the permeability,μ, between two consecutive iterations, $k+1$ and k, is smaller than the imposed tolerance ε.

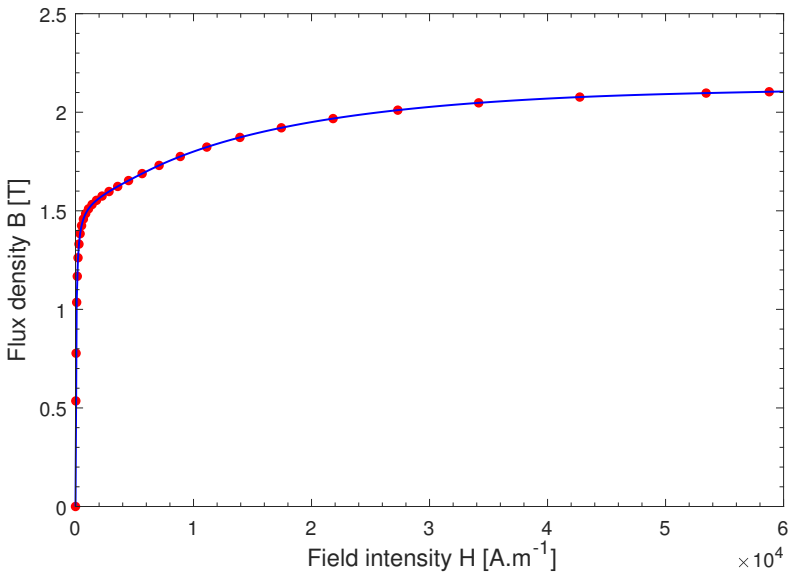

Figure 4.12: B-H curve of the M400-50A

4.3.3.4.1 Modeling of the Magnetic Materials Ferromagnetic materials have a strongly nonlinear material curve. They are commonly characterized by the hysteresis loops, however, this characteristic may be very complex. Therefore there was a need for simplification and the hysteretic characteristic can be reduced to a single-valued characteristic. Further, using approximated mathematical B-H curve helps the designer in accelerating the preliminary stage of electrical machine. When integrating such models into the computation of the RNM permeances, they should be very accurate and fast to compute. Several model forms of B-H curves have been already developed [291] [292] [292] [293]. They can be broadly divided into two groups [294]: smooth approaches [295] and piecewise approaches [296]. The choice of an approximation function depends mainly on the range, in which the machine is operating.

- Smooth approach

  In smooth approaches attempts to find a single analytical approximation by explicit expressions to fit the

B-H curve over the whole useful range. The proposed function have small number of fixed parameters, which are smooth over $\mathbb{R}^+$. Many representations has been proposed such as: representation by power series, representation by transcendental functions and representation by hyperbolas. Table. 4.3 shows some analytical expressions used for the single-valued representation of a B-H curve over the whole useful range, more details about the advantages and drawbacks of each representation is provided in [297]. Although these function forms have the desirable characteristic of both interpolating and extrapolating the B–H data set, but a good fit is hardly obtained by a single function.

Table 4.3: Examples of analytical expressions used for the single-valued representation of a B-H curve (smooth approach)

Proposed Function	Examples	Coefficients computation
Power series	$B = \alpha H^n$ [298]	Curve fitting
	$\alpha H = bB + (bB)^{2n+1}$ [298]	
	$H = \alpha_0 + a_1 B + \alpha_n B^n + \alpha_m B^m$ [298]	
Hyperbola	$B = \frac{H}{\alpha + \beta H}$ [298]	Curve fitting
	$B = \alpha_0 + \alpha_1 H - \frac{\alpha_2}{H}$ [298]	
	$B = \frac{H}{\alpha + \beta H} + \mu_0 H$ [295]	
Transcendental	$B = e^{\frac{H}{\alpha + \beta H}}$ [298]	Curve fitting
	$\beta H = sinh(\frac{B}{\alpha})$ [298]	
	$B = \alpha tan^{-1}(bH) + cH$ [298]	
	$H = (k_1\, e^{k_2 B^2} + k_3)\, B$ (Brauer) [295]	
Fourrier series	$H = \sum_{k=1}^{n} a_k cos(k\alpha)$ [298]	Curve fitting
	$H = \sum_{k=1}^{n} a_k sin(k\alpha)$ [298]	
Rational fraction	$H = \frac{\alpha_0 + \alpha_1 H + \alpha_2 H^2}{1 + \beta_1 H + b_2 H^2}$ [299]	Curve fitting
Exponential / Exponential series	$B = k_1(1 - e^{-k_2 H})$	Iterative process
	$B = k_1(1 - e^{-k_2 H}) + k_3(1 - e^{-k_4 H}) + ... + \mu H$ [300]	

- Piecewise approaches

In this approach piecewise-polynomial approximations and interpolations are used [301] [302] [303]. Usually this approach provide a better approximation than the smooth one. When using iterative methods to consider the nonlinearity of soft materials, such as Newton-Raphson algorithm, the model should satisfy the continuity of the first derivative at least such as cubic interpolation (Spline) and make sure that the curve is as smooth as possible. In our model, a piecewise cubic B-H curve representation was used.

4.4 Model Validation

Two permanent magnet synchronous machines, with two different topologies, will be used to validate the developed model. The electromagnetic performances obtained by using the RNM and AM including electromagnetic torque and the magnetic flux densities in the middle of the airgap will be compared with those obtained with FEM (FLUX2D). The electromagnetic torque was computed at the sliding surface and using maximum torque angle and Maxwell's stress tensor.

4.4.1 9.5 rpm - 15 MW PMSG (Machine C)

Table 4.5 contains the key design parameters used to validate the magnetic behavior of the studied machines.

Table 4.5: Key design parameters and thermal simulation conditions of (9.5 rpm - 15 MW) PMSG

Generator power	9.5 rpm-15 MW PMSG (p = 189, N_s = 1134, e_g =16 mm)
Winding topology	3-phases one-layer Distributed winding
Permanent magnet	N48SH (B_r=1.4 T)
ST-PMSG	[R_g[m], L_{act}[m],θ_s[%], h_s[m], θ_{PM}[%], h_{PM}[m], J_s[A/m^2], h_{ys} [m]] = [6.39, 1.27, 0.44, 0.123, 0.458, 0.044, 3.40e6, 0.044]
SM-PMSG	[R_g[m], L_{act}[m],θ_s[%], h_s[m], θ_{PM}[%], h_{PM}[m], J_s[A/m^2], h_{ys} [m], h_{yr} [m]] = [5.97, 1.50, 0.44, 0.140, 0.642, 0.020, 3.06e6, 0.045,0.045]

As can be seen from Fig. 4.13, Fig. 4.14 a good agreement is shown between results obtained from the developed AM and RNM and those derived from FEM analysis.

Table 4.7: Magnetic model results validation (SM-PMSG)

	Γ_{mean} [M.N.m]	[Γ_{min} , Γ_{max}] [M.N.m]	Error
AM	-16.2	[-1.73 , -1.62]	0.537 %
RNM	-16.82	[-1.74 , -1.61]	0.417 %
FEM	-16.75	[-1.73 , -1.60]	Reference

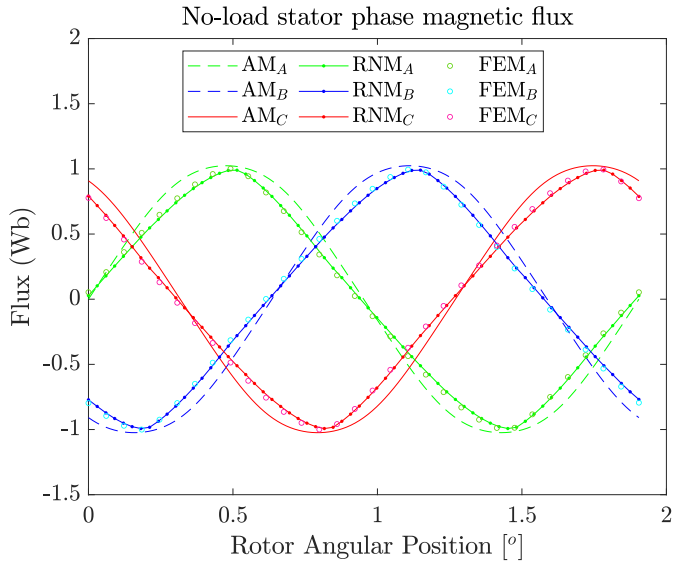

(a) Magnetic flux comparison

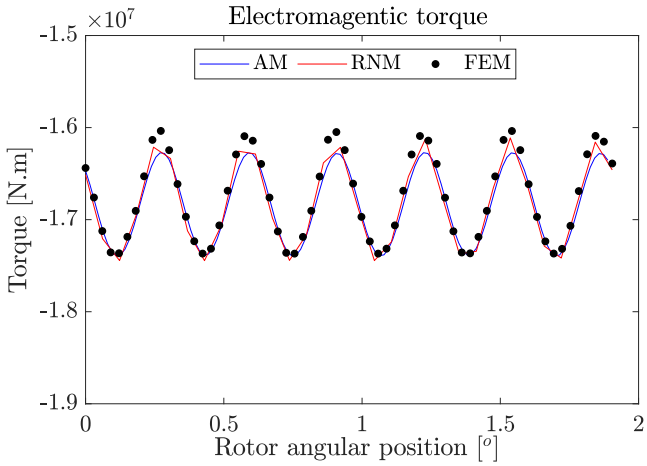

(b) Electromagnetic torque comparison

Figure 4.13: SM-PMSG Machine C results

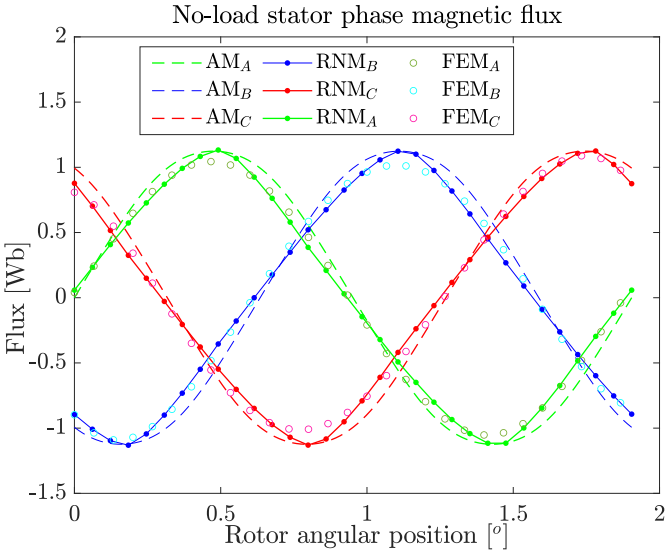

(a) Magnetic flux comparison

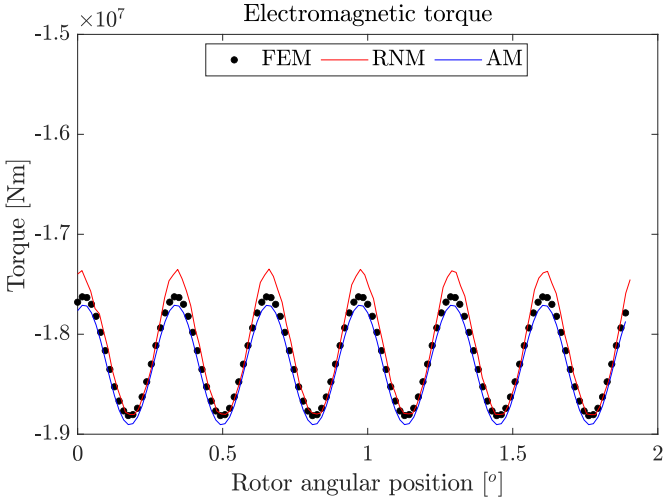

(b) Electromagnetic torque comparison

Figure 4.14: ST-PMSG Machine C results

Table 4.8: Magnetic model results validation (ST-PMSG)

	Γ_{mean} [M.N.m]	[Γ_{min} , Γ_{max}] [M.N.m]	Error
AM	-18.31	[-1.89 , -1.77]	0.438 %
RNM	-18.18	[-18.88 , -17.35]	0.274 %
FEM	-18.23	[-18.81 , -1.76]	Reference

It can be seen in Table 4.7 and Table 4.8 that AM and RNM, with maximum error $e_{max_{\%}} = 0.537\%$ (corresponding to $e_{max} = 0.55$ MNm), give a very accurate torque prediction for preliminary design stage.

4.5 Conclusion

Accelerating the design optimization process of electrical machines remains an important goal for engineers and researchers. In this chapter, a magnetic model is proposed for the design-optimization of large Permanent Magnet Generator. The magnetic design is performed thanks to two types of models: a linear analytical model based on the formal solution of Maxwell's equations solution in low permeability regions of the machine, by the separation of variables technique and a non-linear meshed-based reluctance network model. The Analytical Model is issued from solving Maxwell's equations in terms of the magnetic vector potential in low permeability regions using the separation of variables technique. In Reluctance Network Model, the magnetic structure of studied domain is subdivided into a network of simplified flux tubes. In 2D, each elementary subdivision is represented with 4 reluctances. The resulting network together with sources is transformed into an equivalent reluctances network, for which the flux through the tube and the scalar potential at the nodes can be solved by applying Kirchhoff's laws. The value of the reluctances are calculated according to the set of formula defined in section 4.3.3.2.2 and 4.3.3.3. Once constructed, the nonlinear algebraic set of equation was solved using fixed-point method. Validation of the models is performed using FEM. It can be concluded that :

- With Analytical model, the airgap region coefficients of the vector potential solution play an important role in the accuracy of the electromagnetic torque developed by the machine. So, a well-conditioned matrix of the algebraic system in Eq. 4.38 is necessary to obtain accurate computation of local and global quantities.
- With Analytical model, the number of the harmonics was limited in such very large machines in order to don't loss the precision of some quantities.
- Although analytical method based on Fourier analysis is fast, it suffers from the lack of its genericity and can be easily trapped by numerical problems.
- Both methods give an accurate results, proving their reliability and efficiency.
- The comparison shows a strong agreement of the developed models and FEM simulations, a maximum

error of 0.5 % on torque mean value. The investigated machine are not highly saturated which may explain the good accuracy of linear analytical model when compared to non-linear finite element models.

- It would be of special interest to compare the two developed modelling approaches AM and RNM, in term of computation time when integrated into optimization process. In the last chapter of this thesis, both models were combined with genetic algorithm in order to optimize the mass of the generator and that of permanent magnets. The Pareto fronts were compared and analysis.

Chapter 5

Thermal Model

5.1 Introduction

The electrical machine analysis is thermally dependent. Indeed, properties of materials such as the permanent magnet flux and winding resistance are strongly depending on the temperature. The temperature tolerance of materials such as permanent magnets, glue used to attach those magnets and winding insulation, set the thermal limits, and then the safe operating conditions of electrical machine. Going beyond those limits will reduce considerably the machine life expectancy, for instance each 10 added over the maximum allowed temperature decreases by 50% winding's life time [304]. PMs may be irreversibly demagnetized under high temperature, the demagnetization effects may then appear either locally or globally [305]. Nevertheless, by operating far from those limits, the machine may lose some of its potential. Further, a more homogeneous temperature distribution, include avoiding hot-spot temperature in the winding, could be achieved by taking into account the thermal constraints at the pre-design stage optimization. Additionally, estimating the temperature distribution in an early stage can help in the development of an efficient cooling system which may be cost saving. Overall, thermal behavior analysis of the machine plays a vital role in the improvement of its overall design in terms of efficiency, reliability, durability, performances (torque density, overload time capability) and cooling requirement.

In order to estimate the heat distribution accurately, much attention should be paid to three elements, including heat transfer, heat storage and heat generation. In section 6.2, the heat transfer mechanisms in electrical machine are described and the related equations are given. Then in section 6.3, the heat sources originated

from internal losses are presented. In the last part of the chapter, the determination of the critical parameters in lumped parameter thermal network are discussed. Further, a steady state thermal analysis based on lumped parameter thermal network is developed for the investigated topologies. The main focus is on the air gap's and the winding's thermal distribution. Finally, thermal FEM (Flux2D) model is used to validate the developed model and justify further use in the optimization process.

5.2 Thermal Modeling In Electrical Machines

The thermal modeling is about describing the thermal behavior of an electrical machine employing mathematical means. It should combine the heat transfer and the fluid mechanics, that made electrical machine complex system to design. Two approaches are used to predict the temperature distribution within electric machine: analytical lumped parameters model and numerical methods. The analytical approach, based on lumped parameter thermal network (LPTN)[1], is claimed to be a quick method with satisfactory results. In addition, it allow swift sensitivity analysis. Numerical approaches, including thermal finite elements method (FEM) (2D/3D) and computational fluid dynamics (CFD), are known to be more accurate to capture the thermal dynamics of electric machines, but they are time consuming compared to LPTN. The FEM and LPTN can only be used to analysis the conduction heat transfer in solid domains. For convective and radiative heat transfer, FEM and LPTN use boundary conditions based on analytical expressions or empirical correlation, already available in literature [306][307]. In the contrary, with CFD it is possible to perform simulations in order to predict the fluid flow characteristics (especially in complex region such as end-winding [308]), thus there is no need to use empirical or experimental data which may require costly test facilities. Although CFD is the most accurate method used in the prediction of the temperature's distribution, it is excluded in early stage design because its time consuming [309]. The computational cost is bought forward as the the most important criteria in design optimization context, hence LPTN seems to be the most suitable technique for relatively simple topologies at early-stage stage.

[1] Also called thermal equivalent circuit method (TEC)

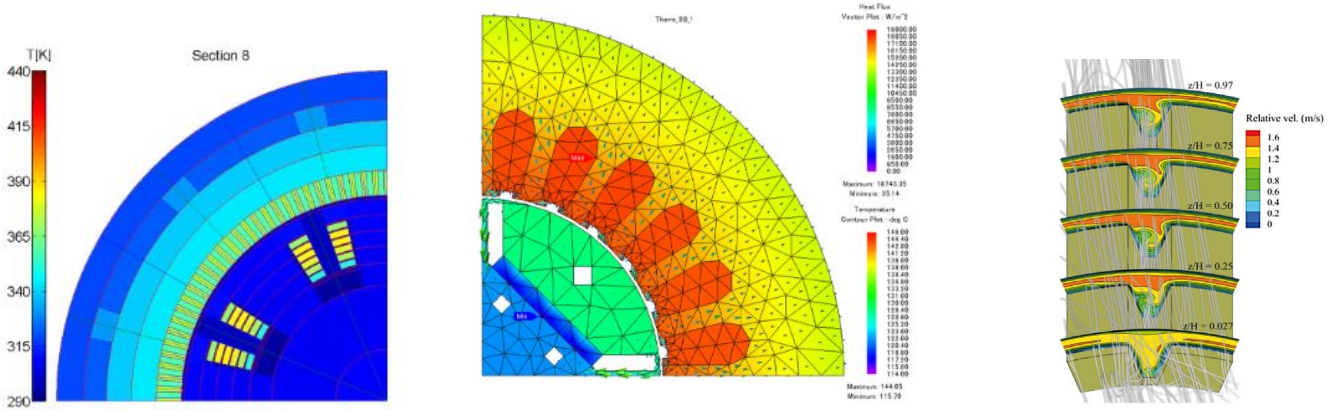

(a) Temperature LPTM [307] (b) Loss density distribution FEA [310] (c) Loss density distribution CFD [311]

Figure 5.1: Techniques used in the thermal modeling of electrical machines

5.3 Lumped Parameter Thermal Network

In lumped parameter thermal network[2], an equivalence is made between the thermal model and the electric circuit, in which the temperature $T\,[K]$, the heat flow rate $\dot{Q}\,[W]([J/s])$, heat flux density $q\,[W.m^{-2}](q = \dot{Q}/A$ (A is the heat transfer area).), thermal resistance $R_{th}\,[K.W^{-1}]$ and capacitance $C_{th}\,[J.K^{-1}]$ are analogous to the voltage $V\,[V]$, the current $I\,[A]$ the current density $J\,[A.m^{-2}]$, electrical resistance $R\,[\Omega]$ and capacitance $C\,[F]$ respectively.

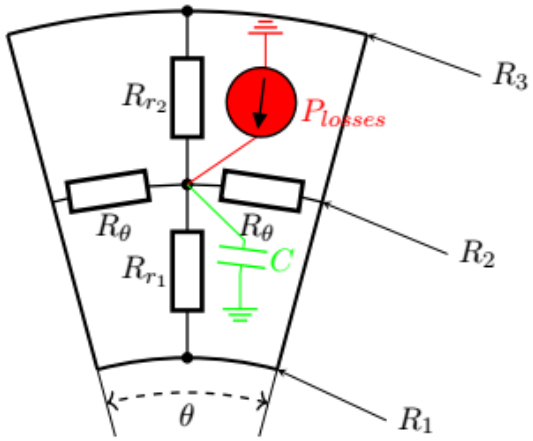

Figure 5.2: Representation of a sub-element block of a hollow cylinder in thermal lumped model

LPTN involves subdividing the machine geometry into many basic elements (volumes) that are assumed to have

[2]Also called Nodal Network Model.

physical and thermal uniformity [312] (Temperature and heat flow within the elements, material proprieties and convection condition) (See Fig. 5.2). Each element is represented by node. Nodes are connected to each other via thermal resistances, that depend on the element's geometry, material and transfer mode, through which heat can flow (See Fig. 5.2). In transient analyses, thermal capacitors C are attached to nodes. The thermal capacitance estimation is very important especially for short time heat transfer.

Figure 5.3 shows the thermal transfer paths in an electric machine. In fact, for solid-solid connections, the thermal resistances are based on the conductive resistance between the solids in question (red arrows in Fig. 5.3). Whereas, for solid-fluid connections, the thermal resistances are based on the convective resistance of the fluids (green arrows in Fig. 5.3). The thermal radiation is the heat dissipation through electromagnetic waves, it can occur regardless of solid or fluids (purple arrows in Fig. 5.3). The resistances associated to each heat transfer mechanisms will be detailed in the next subsection.

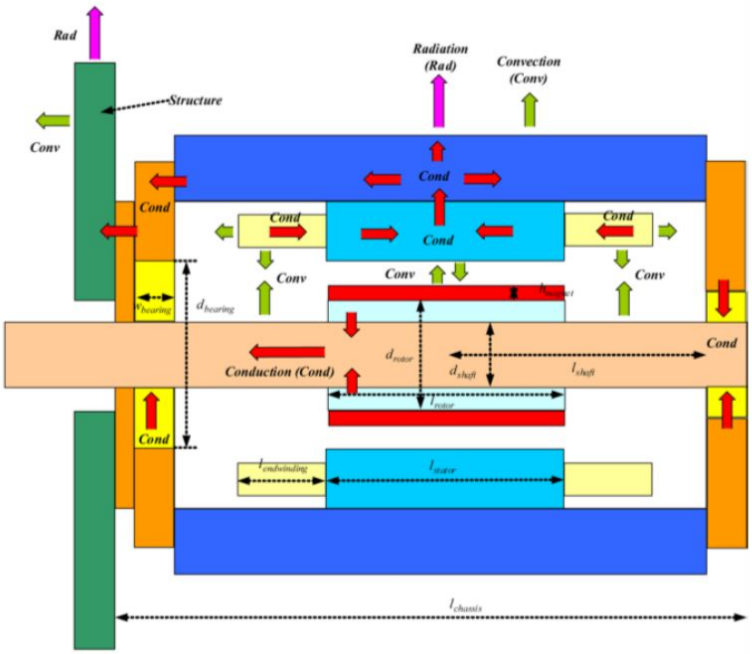

Figure 5.3: Thermal transfer paths in an electric machine [28]

5.3.1 Thermal resistance

The thermal energy is transferred from a higher temperature region to a lower one. There three modes by which the heat is transferred in electrical machine, including conduction, convection and radiation. The conduction heat transfer occurs inside a body (e.g., steel, copper, permanent magnet and insulation) by the interaction

of adjacent particles. Although it is the only process that take place in solid, it could take place in fluid as well. The convection occurs in case of a moving fluid (e.g., air and cooling fluid) over a solid surface. Both heat transfers are linear and proportional to the temperature difference between two adjacent nodes ΔT and the thermal conductance G_{th}, the heat flow rate can be described by

$$\dot{Q} = G_{th}\,\Delta T = \frac{\Delta T}{R_{th}} \tag{5.1}$$

However, heat transfer may happens without contact like in radiation, where the body emits photons, carrying energy, depending on the its temperature and emissivity. The radiation is often neglected in electrical machine due to the relatively low temperature gradient inside electrical machine [313].

5.3.1.1 Thermal conduction resistance

The heat flux density, q, in an isotropic[3] region can be written as (Fourier's Law)

$$\vec{q} = -\lambda\,\nabla T = \begin{cases} \underbrace{-\lambda\frac{\partial T}{\partial x}}_{q_x}\vec{i}\underbrace{-\lambda\frac{\partial T}{\partial y}}_{q_y}\vec{j}\underbrace{-\lambda\frac{\partial T}{\partial z}}_{q_z}\vec{k} & \text{(Cartesian coordinates)} \\ \underbrace{-\lambda\frac{\partial T}{\partial r}}_{q_r}\vec{i}\underbrace{-\lambda\frac{\partial T}{r\partial \phi}}_{q_\phi}\vec{j}\underbrace{-\lambda\frac{\partial T}{\partial z}}_{q_z}\vec{k} & \text{(Cylindrical coordinates)} \end{cases} \tag{5.2}$$

where λ is the thermal conductivity in $[W.m^{-1}.K^{-1}]$, $A\,[m^2]$ is the heat transfer area perpendicular to direction of heat flow and ∇T is temperature gradient.

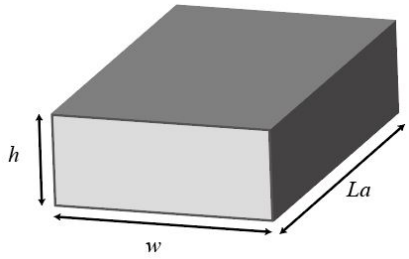

Figure 5.4: Heat transfer across plane wall

[3]Materials whose properties remain the same when tested in different directions.

The Fourier's law for one-dimensional steady-state system Eq. 5.3 can be simplified

$$q_x \approx -\lambda \frac{dT}{dx} \Rightarrow \dot{Q}_x \approx -\lambda\, A. \frac{dT}{dx} \tag{5.3}$$

Then, the thermal resistance between two nodes is calculated with respect to the heat flow (See Fig. 5.4) as in

$$\begin{cases} R_{th_x} = \frac{h}{\lambda A} = \frac{h}{\lambda L_a w} \\ R_{th_y} = \frac{w}{\lambda A} = \frac{w}{\lambda L_a h} \end{cases} \tag{5.4}$$

where L_a is the distance between the two nodes and A is the effective area through which the heat is transferred.

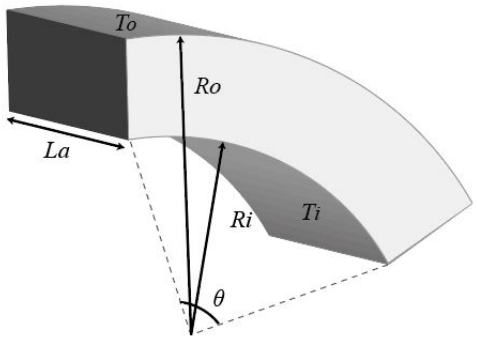

Figure 5.5: Heat transfer across hollow cylindrical

In the cylindrical case the thermal resistances are given by (See Fig. 5.5) :

$$\begin{cases} R_r = \frac{ln(R_o/R_i)}{\lambda L_a \theta} \\ R_\theta = \frac{\theta}{\lambda ln(R_o/R_i) L_a} \end{cases} \tag{5.5}$$

5.3.1.2 Thermal convection resistance

The rate of convection heat transfer is given by Newton's Law of cooling by

$$\begin{cases} q = h\,(T_{\text{inf}} - T_A) = h\,\Delta T \\ \dot{Q} = h\,(T_{\text{inf}} - T_A) = h\,A\,\Delta T \end{cases} \tag{5.6}$$

Table 5.1: Thermal material proprieties at $20\,°C$ [38]

Material	Thermal conductivity $[W.m^{-1}.K^{-1}]$	Heat capacity $[J.kg^{-1}.K^{-1}]$	Density $kg.m^{-3}$	Resistivity $n\Omega.m$
Air	0.025	1007	1.204	1.3e25
Water	0.0153	4180	997.4	2e10
Epoxy	0.15-0.30	1100	1150	10^{15}-10^{23}
Silicon Steel	20-30	490	7700	300-500
Aluminium	220	900	2700	28
Copper	360	380	8950	17.2
NdFeB magnet	9	420	7400	1600
Ferrite magnet	4.5	800	4900	1e5

where h is the convective heat transfer coefficient in $[W.m^{-2}.K^{-1}]$, A and T_{inf} are respectively the convection exchange area and its temperature, and T_A is the fluid temperature. Then, the thermal convection resistance R_{th} between a solid surface and fluid can be written as

$$R_{th} = \frac{1}{h\,A} \tag{5.7}$$

In electrical machine this can occur in the air-gap, between stator and rotor, or between stator and external medium. The calculation of the convective coefficient is challenging. As mentioned above, CFD can be used to simulate the air flow in the machine, although its high accuracy it is has been excluded in our study case. The investigated machine topologies are relatively simple, and hence the different thermal parameters can be accurately estimated.

5.3.2 Thermal capacitance

The thermal capacitance represent the ability of an object to store thermal energy for a given temperature's change, and it is added to the correspond node in transient modeling. The capacitance $C_{th}\,[J.K^{-1}]$ is function of the material's mass m and capacity $c_p\,[J.kg^{-1}.K^{-1}]$, it is given by

$$C_{th} = m\,c_p \tag{5.8}$$

Typical thermal proprieties of some selected materials used in electrical machines are shown in Table. 6.1.

5.3.3 Thermal equivalent circuit

Based on the thermal energy balance, the equation governing the heat diffusion in domain Ω, is written as

$$\rho c_p \frac{\partial T}{\partial t} = \vec{\nabla}.(\lambda \vec{\nabla} T) - \vec{v}.\vec{\nabla} T + q_v \tag{5.9}$$

where $T[K]$ is the temperature of the material, $c_p[J.kg^{-1}.K^{-1}]$ is the specific heat capacity, $\rho[kg.m^{-3}]$ is the density, $\lambda[W.m^{-1}.K^{-1}]$ is the thermal conductivity, $v[m.s^{-1}]$ is the velocity field of the fluid and $q_v[W.m^{-3}]$ is the heat production density (per unit volume of the medium). Assuming constant thermal conductivity and $v = 0$, results in

$$\frac{1}{\alpha}\frac{\partial T}{\partial t} = \nabla^2 T + \frac{q_v}{\lambda} \tag{5.10}$$

$\alpha = \lambda/\rho c_p[m^2.s^{-1}]$ denotes the thermal diffusivity of the material. Further, in steady-state regime, the heat diffusion Eq. 5.10 is reduces to the Poisson differential equation:

$$\nabla^2 T = -\frac{q_v}{\lambda} \tag{5.11}$$

where for radial flux machine and in 2D cylindrical coordinates

$$\nabla^2 T = \frac{1}{r}\frac{\partial}{\partial r}\left(r\frac{\partial T}{\partial r}\right) + \frac{1}{r^2}\frac{\partial^2 T}{\partial \theta^2} + \frac{\partial^2 T}{\partial z^2} \tag{5.12}$$

The heat equation is associated to boundary and initial conditions to obtain a complete solution for the temperature field within the system. It can be done either by specifying the boundary temperatures at the surface of the system (Dirichlet boundary condition) (e.g. $T(r_{limit}) = T_{inf}$) or by imposing heat fluxes through boundary surface (Neumann boundary) (e.g. $\lambda\vec{\nabla}T.\vec{n} = \dot{Q}$, $\lambda\vec{\nabla}T\vec{n} = h(T_{inf} - T) + \varepsilon\sigma(T_{inf}^4 - T^4)$ (convection and radiation) where ε is the surface emissivity, σ is the Stefan–Boltzmann constant and T_{inf} is the ambient temperature).

Assuming rigid, homogeneous and isothermal sub-volume through which heat is produced uniformly, the thermal energy balance for node i (See Fig. 5.6) can be written as (Kirchhoff's current law)

$$\overbrace{(\rho_i c_{p_i})\, V_i}^{C_i} \frac{\partial T_i}{\partial t} = \sum_k \phi_{cond_{ik}} + \sum_n \phi_{conv_{in}} + \cancelto{0}{\sum_m \phi_{rad_{im}}} + \phi_{ext_i} \qquad with \sum_{j,j\neq i}^{n} \phi_{ij} = 0 \tag{5.13}$$

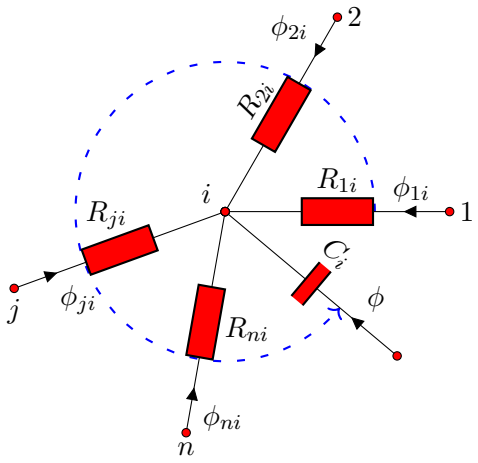

Figure 5.6: Schematic of a general node i in a lumped thermal model

Therefore, a system of N ordinary differential equations can be obtained

$$C_i\frac{\partial T_i}{\partial t} = -\sum_{j,j\neq i}^{n}\frac{1}{R_{ij}}(T_i - T_j) + \phi_{ext_i} = \sum_{j,j\neq i}^{n} G_{ij}(T_j - T_i) + \phi_{ext_i} = \sum_{j,j\neq i}^{n} G_{ij}T_j - (\sum_{j,j\neq i}^{n} G_{ij})T_i + \phi_{ext_i} \quad (5.14)$$

where G_{ij} and R_{ij} are the thermal conductance and resistance between two adjacent nodes, i and j, respectively. The previous equation may be expressed in matrix form as

$$-[C]\frac{\partial[T]}{\partial t} = [G][T] - [\phi_{ext}] \quad (5.15)$$

$$C = \begin{pmatrix} C_1 & 0 & \dots & & 0 \\ 0 & \ddots & & & \\ \vdots & & C_i & & \vdots \\ \vdots & & & \ddots & 0 \\ 0 & & \dots & 0 & C_N \end{pmatrix} \quad T = \begin{pmatrix} T_1 \\ \vdots \\ T_i \\ \vdots \\ T_N \end{pmatrix} \quad \phi_{ext} = \begin{pmatrix} \phi_{ext1} \\ \vdots \\ \phi_{exti} \\ \vdots \\ \phi_{extN} \end{pmatrix} \quad G = \begin{pmatrix} \sum_2^N G_{1j} & \dots & & \dots & G_{1N} \\ \vdots & \ddots & & & \vdots \\ G_{i1} & & \sum_{1,j\neq i}^N G_{ij} & & \\ \vdots & & & \ddots & \vdots \\ G_{N1} & \dots & & \dots & \sum_{1,j\neq N}^N G_{Nj} \end{pmatrix}$$

$[C](N \times N)$ denotes the thermal capacity and $[G](N - m \times N)$ is the thermal conductance matrix, where the diagonal elements represent the sums of the conductance connected to the node i and the other elements represent the thermal conductances connecting the i node to the j node. The $[T](N \times 1)$ and $[\phi_{ext}](N \times 1)$ represent the unknown temperature and the known heat source vector at each node. The m missing equations in the conductance matrix represent the nodes located in the airgap sliding surface, it will be provided by the airgap modeling technique, discussed in the next section.

In the steady-state case, Eq. 5.15 can be reduced to

$$[G][T] = [\phi_{ext}] \tag{5.16}$$

However, in the steady-state case, the equation with no-heat generation, like in the airgap, became

$$[G][T] = 0 \tag{5.17}$$

The temperature rise of each element in the thermal model is computed by the previous matrix equation system,

5.4 Heat Sources (Losses Modeling)

In order to obtain an accurate estimation of the efficiency and the thermal behavior of electrical generator, particular attention should be paid to the evaluation of losses. Losses incurred on an electric machine (magnetic circuit, electrical circuit and mechanical circuit) are distributed in heat form, that give rise to temperature. Hence, losses in machine constitute the heat sources. They can be categorized into electrical or mechanical losses. Further, the main heat sources in an electric machine are stator iron losses, stator copper losses and rotor eddy current losses and mechanical losses. Total losses can be calculated with:

$$P_{losses} = P_{mech} + P_{iron} + P_{Joule} + P_{additional} \tag{5.18}$$

where $P_{mech}[W]$, $P_{iron}[W]$, $P_{Joule}[W]$ and $P_{additional}[W]$ are the mechanical losses, iron losses, Joule losses and additional load losses, respectively.

Losses depend on the load. Nevertheless, the electrical generator in wind turbine is usually operating at lower speed and torque compared to the ratings. Thus, in the developed model, the generator is supposed to operate under rated conditions, it means that thermal estimations are performed at the rated operating point, so that high performance will be guarantee. Several types of losses are shortly presented in this section.

5.4.1 Mechanical losses

Mechanical loss in electric generators can be divided into windage and friction losses. Friction losses are due the relative motion in bearings, while windage losses[4] represent the power absorbed by the air around the rotor as a result of the relative motion between the rotor and the stator. Mechanical losses in the bearings can be calculated as:

$$P_{bearing} = C_0 \omega D_{bearing}^3 \tag{5.19}$$

where C_0 is the bearing coefficient, which is determined by empirical formula [314], $\omega[rad.s^{-1}]$angular rotation speed and $D_m[m]$ is the average diameter of bearing.

The windage losses for a smooth cylinder rotating within concentric cylinder, can be estimated analytically using the equations [315]:

$$P_{windage} = k\pi\rho_v C_d R^4 \omega^3 L \tag{5.20}$$

where C_d denotes the skin friction coefficient, which is determined by empirical formula [316][315], depend on the airgap structure and rotor surface condition , $\mu[kg.m^{-1}.s^{-1}]$ is the dynamic velocity of cooling fluid, $\rho_v[kg.m^{-3}]$ is the density of the fluid, $\omega[rad.s^{-1}]$ is the mechanical angular velocity, $R[m]$ is the rotor's radius, $L[m]$ is the rotor's length, $e[m]$ is the airgap length and k is the roughness coefficient, which varies from 1.0 to 2.5 for smooth and axially slotted surface [316].

The heat loss distribution in low-speed generator is rather different from that in high-speed generator. As shown in Eq. 6.4 and Eq. 6.5, friction and windage losses are proportional roughly to the angular velocity, so they become significant as the machine speed increases. Therefore, for direct-drive applications mechanical losses are ignored, either those depending on the rotational speed or those caused by high-frequency, due to their negligible effect on the winding and permanent magnet temperature.

5.4.2 Core losses

The alternating magnetic field in the iron causes core losses[5], which includes eddy-current and hysteresis losses. A formulation of iron losses which depends on the frequency $f[Hz]$, the maximum flux density $\hat{B}$,

[4] Also called air friction losses.
[5] Also called iron losses.

the steel sheet $d[m]$, the electrical conductivity of the material and its density $\sigma_t[\Omega^{-1}m^{-1}]$ and $m_v[kg.m^{-3}]$, respectively, and a coefficient for hysteresis losses C_{hyst} as in [317]:

$$P_{core} = \underbrace{C_{hyst} f \hat{B}^2}_{P_{Hysteresis}} + \underbrace{\frac{(\pi d)^2 \sigma_t}{6\rho_v} f^2 \hat{B}^2}_{P_{eddy-current}} + P_{excess} \tag{5.21}$$

The eddy-currents losses (dynamic) are caused by the electromotive force induced in laminated parts of the machine and are proportional to the square of both the frequency and the peak flux density. However, hysteresis losses (static) are caused by the continuously varying magnetic flux, both in value and direction, and are proportional to the frequency and the peak flux density. Consequently, iron losses are more significant at higher frequencies, their contribution is neglected compared to Joule losses in such relatively low-speed application. In addition, for the same open-circuit airgap flux density, the one-pole flux is inversely proportional to the number of poles and thereby for high pole pair number thinner stator and rotor yokes are required. Further, thinner yoke dimensions means lower iron losses. For instance, copper losses in a 4 MW DD-PMSG stator, can easily be four to seven times the iron losses [174]. The stator core losses are relatively low and may can be neglected in the steady-state thermal calculations.

5.4.3 Joule losses

In low-speed direct-drive PMSG, stator windings are subjected to a large amount of heat; therefore, Joule losses[6] constitute a considerable part of the total losses. Hence, only the copper losses will be considered in this study. These losses occur due to resistance in the winding coil (e.g. copper coil, Aluminum), and are proportional to the square of the phase current $I_{ph_{rms}}[A]$ and winding resistance $R_{ph}[\Omega]$. For m phase machine, Resistive losses are defined by the Joule's first law as follows:

$$P_{copper} = m R_{ph} I_{ph_{rms}}^2 \tag{5.22}$$

The winding resistance is affected not only by the copper's temperature but also by skin effect. It can be

[6] Also called copper losses or Resistive losses.

evaluated for each phase by:

$$R_{ph} = \underbrace{\rho_e \frac{N_{ph} L_{N_{ph}}}{N_p A_c}}_{R_{DC}} + R_{skin}(f) = k_{skin} R_{DC} \tag{5.23}$$

where $\rho_e[\Omega.m]$ is the electrical resistivity of the conductor material, N_{ph} is the turns number, R_{skin} is the phase skin resistance, R_{DC} is the DC resistance, N_p is the number of parallel conductor, $A_c[m^2]$ is the conductor cross-sectional area and $L_{Nph}[m]$ is the average length of conductor in coil.

In fact, skin effects depend on the current frequency, for rectangular conductor the average skin effect coefficient over the slot is given by [211]:

$$k_{skin} = \varphi(\xi(f)) + \frac{1}{3}(N_h - 1)\psi(\xi(f)) \qquad \begin{cases} \varphi(\xi(f)) = \xi(f)\frac{sinh(2\xi(f)) + sin(2\xi(f))}{cosh(2\xi(f)) - cos(2\xi(f))} \\ \psi(\xi(f)) = \xi(f)\frac{sinh(\xi(f)) - sin(\xi(f))}{cosh(\xi(f)) + cos(\xi(f))} \end{cases} \tag{5.24}$$

where N_h is the number of the electric conductor per slot arranged above each other, and ξ is the reduced conductor height. For rectangular conductor arrange above each other, the reduced high is defined as [211]:

$$\xi(f) = h_c \sqrt{\frac{\pi f \mu_0}{\rho_e} \frac{w_c}{w_s}} \tag{5.25}$$

where $h_c[m]$ and $w_c[m]$ are the height and the width of each conductor, w_s is the slot's width, $\mu_0[m.kg.s^{-2}.A^{-2}]$ is the permeability of vacuum. It is obvious from Eq. 5.25 that the for low operating frequency limiting the conductor skin effect. Despite the fact that large bars, used in low-speed high-power generator winding, allow higher filling factor and better thermal conductance, they are more sensitive to skin effect compared to pull-in winding. This creates non-uniformly current density distribution in slot bars, which is mainly due to the large size of the conductor Eq. 5.25. Then, the R_{DC} will be increased by skin effect coefficient[7], representing the alternative current resistance (R_{AC}). It has been shown in [29], that for $8MW$ liquid cooling DD-PMSG at $f = 11Hz$ and $I = 1110A$, the skin effect coefficient varies along the slot's height from $k_{skin} = 1$ in the bottom of the slot to $k_{skin} = 4.63$ in the top of the slots. Indeed, although the real part of the current density is constant in the radial direction over the conductor cross section, the imaginary part (eddy-current) is curved distributed. The skin effect will be considered in calculation of the active part of coil (inside the stator's slot), whereas it is neglected in the end-winding region.

[7] Also known as resistance factor [211], which represents the ratio between the winding resistance at frequency f to that at $0Hz$

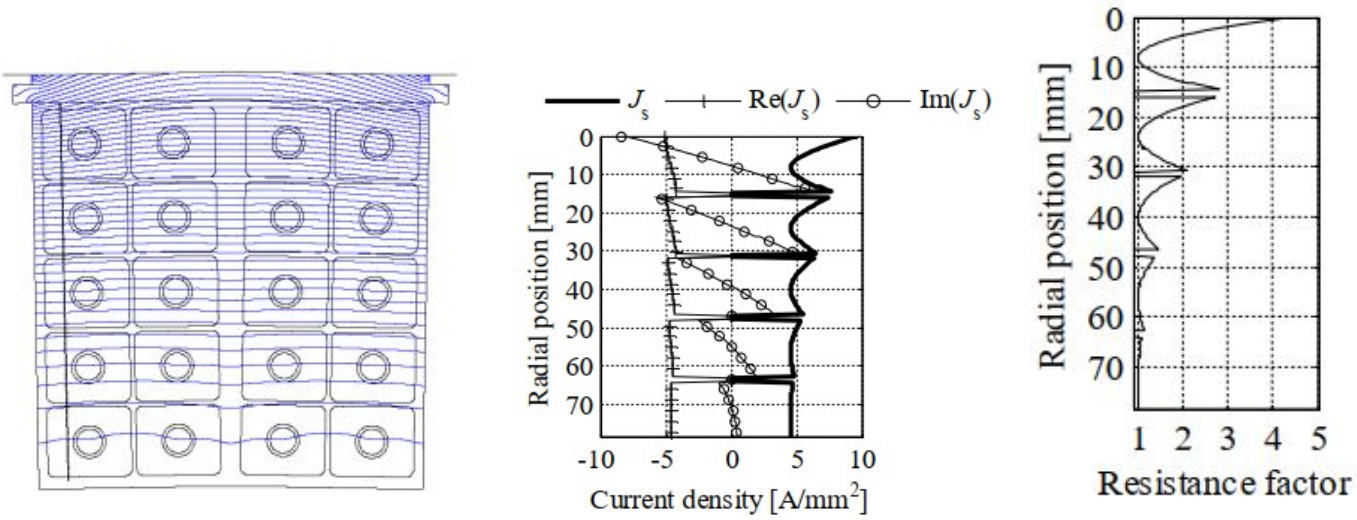

(a) Flux distribution (b) Current density distribution (c) Skin effect coefficient

Figure 5.7: The skin effect along the stator slot height in 8MW liquid cooling DD-PMSG with rectangular-form hollow copper conductor winding [29]

Further, the average length of coil turn in high-voltages [8] large machines with prefabricated winding can be approximated by [211]:

$$L_{N_{ph}} \approx 2L_{ax} + 2L_{end} = 2L_{ax} + \underbrace{2.9W + 0.3}_{\text{average legnth of the end-winding}} \tag{5.26}$$

where $L_{ax}[m]$ is the machine stack length, L_{end} is the average length of the end-winding and $W[m]$ is the average coil span. It is important to emphasize that short-end windings reduce winding resistance, and hence the Joule losses generated in the end-winding, which may represent considerable part of the total losses. Further, the winding resistance, and as results, the resistive losses rise with temperature rises. Depending on the conductor material, the resistivity ρ is function of the temperature as:

$$\rho(T) = \rho_0(T_0)\left[1 + \alpha_{T_0}(T - T_0)\right] \tag{5.27}$$

where α_{T_0}, and ρ_0 are the temperature coefficient and the material resistivity at particular temperature T_0, respectively. The temperature coefficient for copper and aluminum are $\alpha_{T_{Cu}} = 1.7e-8\,°C^{-1}$, $\alpha_{T_{Al}} = 2.82e-8\,°C^{-1}$, respectively. Besides rising the coil resistance, higher temperature may induce mechanical stress. Indeed, the differences in thermal expansion ratios and thermal distributions between slot materials including

[8] High-voltages between $6kV$ and $11kV$.

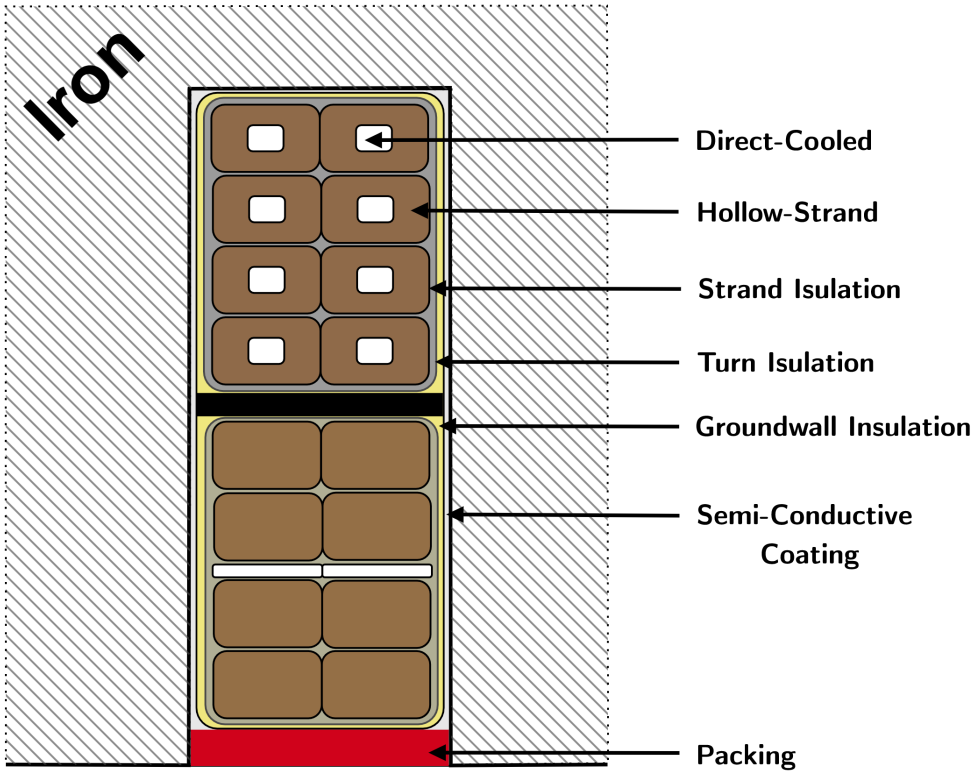

Figure 5.8: Typical stator bar cross section (for large-power generator)

groundwall insulation, winding coating and copper, creates a thermomechanical stress in the interfaces between materials due to the expansion or contraction of the winding coil. For instance, the copper, with its thermal high expansion coefficient, expanded speedily in the axial direction compared to the thermal lag in the insulation and its contact with the still cool core constrains the insulation from moving with the copper [318]. Further, the mechanical stress is a source of fatigue which may cause premature failures of the generator [319][320]. In wind turbines, operating large-power generator under faulty conditions causes significant economic impact, either by reducing the efficiency and shorten the life expectancy of the machine or by stopping the generator, which has one of the highest donwtime failure in wind turbine components [321]. In contrast, we consider that the linear expansion is compensated by the surface expansion (See Fig. 5.9) so the thermal expansion does not affect the winding resistance (define in Eq. 5.23).

The conductor cross section A_c can be calculated as:

$$A_c = k_f \frac{pq}{N_s} A_{slot} = k_f \frac{pq}{N_s} \left(\frac{\pi(R_{bst}^2 - R_{tst}^2)}{S} \theta_{st} \right) \tag{5.28}$$

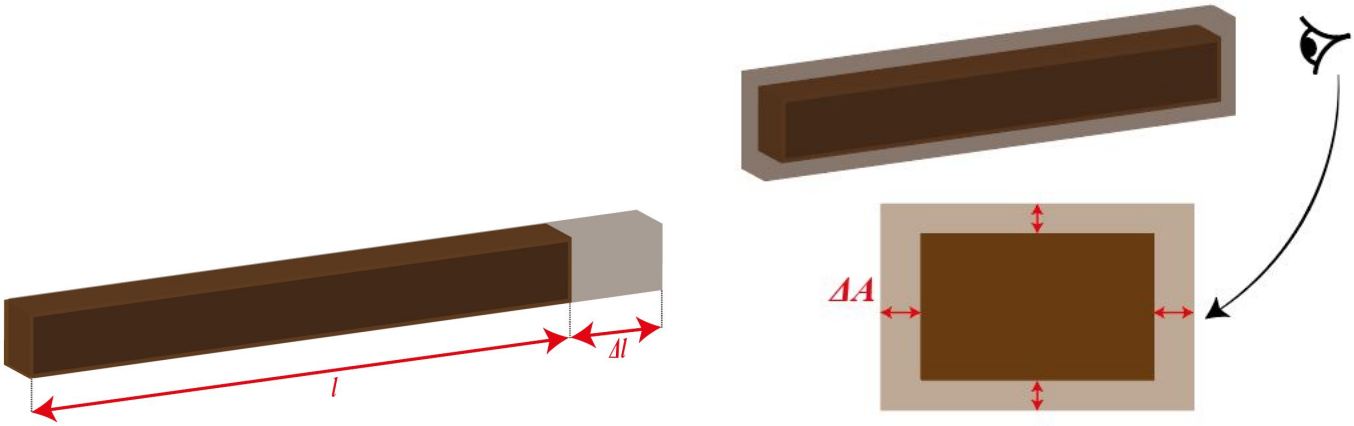

(a) Linear thermal expansion

(b) Surface thermal expansion

Figure 5.9: Thermal expansion in copper-bar winding

where k_f is the stator filling factor, p the number of pole pairs, q is the number of slots per pole per phase, N_{ph} is the number of stator turns in series per phase, S is the number of slots, R_{bst} and R_{tst} are the slot bottom radius and top radius, respectively, and $\theta_{\%st}$ is the ratio of slot opening to stator slot pitch.

5.5 Critical Parameters in the Thermal Lumped Model

5.5.1 Equivalent thermal conductivity of winding

The slot's winding temperature plays crucial role in the durability and reliability of the electric machine. Excessive winding temperatures may cause a insulation damage, which may shorten dramatically the life time of the machine and cause the machine fails due to a electric fault (short circuit). The critical temperature is known to occur in the winding insulation and the maximum operating temperature in machine is determined by the its insulation class. Table 5.2 shows electric machines insulation classes, according to the IEC 60085 classification.

Table 5.2: Thermal class assignment (IEC 60085) [39]

Thermal Class	Maximum allowed temperature [$^{\circ}C$]
A	105
B	130
F	155
H	180

An accurate estimation of the winding temperature is crucial in the design of electric machines. Unfortunately, the stator slots present many challenges in terms of thermal modeling. The major challenges are related to the heterogeneous nature of the slot's composition and the heat generation partition inside. Unlike the copper, which have high thermal conductivity, the residual air, the insulation (between the stator teeth and the winding) and the impregnation in slot present low conduction factor. The slot's thermal resistance in the axial direction is relativity the same as that of the winding, whereas in the radial direction is dominated by several materials with lower conductivity. Usually, the heat path cannot be defined precisely and a full representation of the individual wires is avoided due to its complexity. In pre-design iterative design optimization, predicting the temperature distribution accurately would not necessarily require to model each individual conductor [322], even when using form-wound windings [323]. The thermal analysis of electrical machines make use of several techniques, with varying complexity, for representing the winding region. Some of the existing methods are represented in Fig. 5.10. There are two main categorizes of approaches commonly used winding modeling. The first one involves the thermal homogenization of the winding region; this is done by considering the conductor and the impregnation in the slot as one bulk material with equivalent thermal conductivity (See Fig. 5.10.a and Fig. 5.10.b Fig. 5.10.a). While the equivalent copper conductor is put in the center of the slot, equivalent insulation is placed outside the equivalent conductors. The determination of such conductivity can be performed by using analytical formula [324] [325] [326] [327] [323], empirical correlations [328] or via numerical analysis [306]. Due to its lower computation time, the slot's equivalent conduction technique is well suited for iterative pre-design optimization process using LPTN model. The second approach includes multi-layers structure (copper and impregnation layers) used to analysis the thermal behavior of the stator slot (See Fig. 5.10.c). In this method, conductor that have roughly equal temperature are expected to be a similar distance from the lamination, so they are lumped together as layer. Losses are then injected into the copper layer considering the layer volume. The number of layers, which allows correct predictions of the hot-spot location, can be determined using analytical formulas [329]. It depends not only on the number and the size of the conductors but also on the slot's filling factor. This approach allows a better estimation of the temperature distribution within slot.

In iterative process, such as in pre-design optimization, the homogenization of the winding region (composite thermal conductivity of the system winding implementation and insulation) seems to be a good choice. The thermal resistance between the winding and the stator, $R_{cu,ir}$, is function of the equivalent thermal conductivity coefficient of the air and all insulation material in the slot, $k_{cu,ir}$, the interior slot's area, A_{slot} ($A_{slot} = l_{sp} \times L_s$,

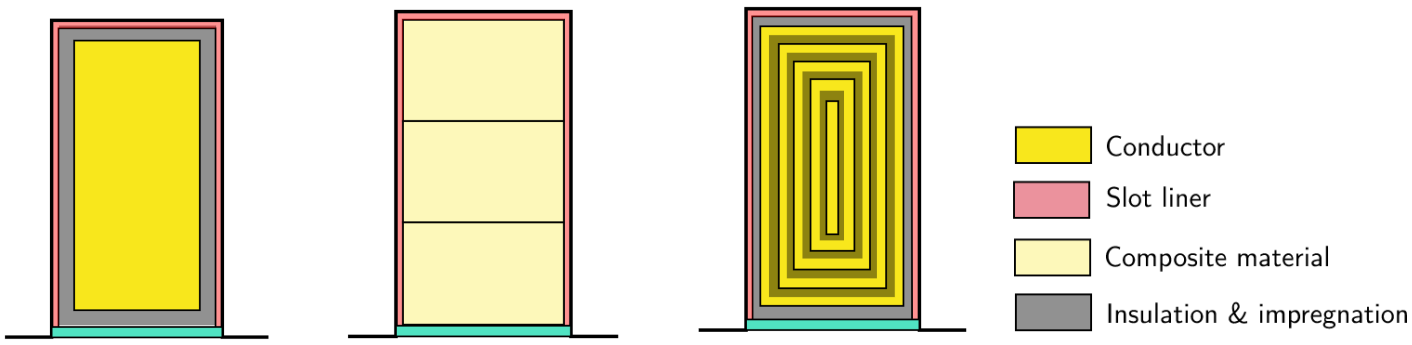

(a) Homogenised model (b) Equivalent material model (c) Layered model

Figure 5.10: Different winding representations used in thermal analysis of electric machines

the stator slot perimeter times the axial core length) , and the equivalent thickness made out of the insulating materials and the insulation residual air, t_{eq}. The equivalent thermal resistance in the radial direction can be written as

$$R_{eq} = \frac{t_{eq}}{k_{Cu,ir} A_{slot}} \tag{5.29}$$

To estimate the composite thermal conductivity two formulation were used. The first formulation was introduced in [323] and further validated in [278] and [330], in which the radial equivalent thermal conductivity and the thickness of the insulating material can be expressed as [323]

$$k_{Cu,ir} = 0.1076\, k_f + 0.029967 \tag{5.30}$$

$$t_{eq} = \frac{S_{slot} - S_{Cu}}{l_{sp}} = \frac{(1 - k_f) \times S_{slot}}{l_{sp}} \tag{5.31}$$

where k_f the slot's filling factor, S_{slot} the slot's surface and S_{Cu} is the copper surface in the stator slot. This formulation was found to be not adapted to large diameter machines, over 4.5 m of machine's radius. It was used in the thermal model dedicated to semi-direct drive generators (15 MW at 100 rpm). It was developed in the context of two-materials component, so it neglects the conductor insulation, and applied only on relatively small radius machines. Indeed, for fairly accurate model, it is important to consider the conductor insulation in high-power low-speed synchronous generator. A three-component formula can be used, in which the radial equivalent thermal conductivity is given by

$$k_{Cu,ir} = \frac{(2\lambda_{res} + \lambda_{Cu})(k_2 \times (2\lambda_{res} + \lambda_{var} + 3k_3.\lambda_{var}) + 3k_1 \times \lambda_{Cu} \times (2\lambda_{res} + \lambda_{var}))}{k_2 \times (2\lambda_{res} + \lambda_{Cu})(2\lambda_{res} + \lambda_{var}) + 3\lambda_{res} \times (k_1 \times (2\lambda_{res} + \lambda_{var}) + k_3 \times (2\lambda_{res} + \lambda_{Cu}))} \tag{5.32}$$

where λ_{var}, λ_{Cu} and λ_{res} are the varnish, copper and resin thermal conductivities respectively. k_1, k_2 and k_3 are the ratio of the volume of copper, resin and varnish in the slot to the total volume of the slot.

5.5.2 Convection heat transfer

The convection coefficient is evaluated in the contact surfaces between the air gap and both the fixed stator and rotating rotor. It can be set by numerically by CFD or Finite Element Analysis or empirically by data tests. Although the high accuracy of the CFD analysis; it is excluded in this design stage due to its high computation cost. A combination of dimensionless numbers (e.g., Reynolds number, Taylor number, Nusselt number) is introduced to define the convection transfer nature. Those numbers rely mainly on the fluid properties: size, velocity, temperature, and gravity [331] [306]. To evaluate the heat transfer coefficient in the air-gap rapidly, the empirical correlation in [278] [327] will be used. The convection coefficient can be expressed as:

$$h = \frac{\lambda_{air} N_u}{2\,L} \tag{5.33}$$

where λ_{air} is the air thermal conductivity, N_u is the Nusselt number, and L is the characteristic length. The Nusselt number can be defined as in [10]:

$$\begin{cases} N_u = 0.064\, T_{am}^{0.367} & 1800 \leq T_{am} \leq 10^4 \\ N_u = 0.205\, T_{am}^{0.241} & 10^4 \leq T_{am} \leq 4.10^6 \end{cases} \tag{5.34}$$

Doing so, modified Taylor's number Tam should be first computed in order to determine the airflow mode in the airgap (stable, transient, or turbulent). The T_{am} can be defined as in :

$$\begin{cases} T_{am} = \frac{T_a}{\pi^4 X} \left(1697(0.0056 + 0.05571\, X^2)\,(1 - e/R_{mean})\right) \\ X = (2\,R_{mean} - 2.304\,e)\,(2\,R_{mean} - e)^{-1} \\ T_a = \left(\rho_{air}^2 \omega^2 R_{mean} e^3\right) \upsilon^{-2} \end{cases} \tag{5.35}$$

where R_{mean} is the mean radius of the airgap (middle of the airgap), ω is the angular speed, ρ_{air} is the air density, e is the airgap length, and the υ is the dynamic viscosity of the air.

5.5.3 Airgap modelling

The same technique described in section 4.3.3.3, used in the magnetic reluctance network model, can be used to model the airgap for thermal simulation, in which the magnetic scalar potential is replaced by temperature and magnetic flux density by heat flux density (See [278] for more details).

5.5.4 Thermal behaviour of copper

A convenient thermal model requires an accurate evaluation of losses. The copper losses cover a large part of total losses in high-power low-speed synchronous generators, while the iron losses are neglected in such low-frequency applications. Therefore, it is essential to consider the variation of the copper electrical resistivity with the temperature [278]. In [332], it has been reported that, the resistivity of the winding copper increases linearly with the raise of the winding temperature. This raise can be defined as

$$\rho_{Cu}(T) = \rho_{Cu_{20}}(1 + \alpha_{Cu}(T - 20)) \tag{5.36}$$

where $\rho_{Cu_{20}}$ is the copper resistivity at 20 $[^oC]$, and the α_{Cu} is the electrical resistivity expansion coefficient. This formula is true only for operating points between 20 $[^oC]$ to 200 $[^oC]$, which is acceptable temperature range in our application. The losses are first estimated using the resistivity at 20 $[^oC]$ and the temperature distribution is computed. Then, the losses are corrected at each iteration through the computed temperature.

5.6 Model Validation

In order to validated the thermal model, the results obtained with lumped parameters thermal model (LPTN) are compared to those obtained with FEM (Flux2D). Two machines were tested in this validation process. The first one is 100 rpm - 15 MW ST-PMSG used in semi-direct drive-train wind turbine and the second one is 7.5 rpm - 15 MW PMSG (both SM- and -ST) used in direct-drive drive-train wind turbine. Some modelling assumptions were considered:

- The windings are formed with copper coils covered by insulation material.
- The thermal conductivity of the winding insulation was taking 0.3 $W.m^{-1}.K^{-1}$.

- The stator was assumed to be cooled through fluid with mean temperature of 35 [^{o}C].
- The radiation heat transfer is not considered.
- The equivalent conductivity of the slot was checked through FEM before the validation process.
- As explained in the previous section, the two-component equivalent thermal conductivity was used in the first machine (reduced radius $<$ 4.5 m) and the three-component equivalent thermal conductivity was used in the second machine (radius $>$ 4.5 m).
- As explained in the previous section, Joule losses are calculated at 20 [^oC] first and the slot's temperature distribution is estimated. Then, the slot's mean temperature is used to corrected the losses, the processes iterates until the temperature change is under 1 %.
- End windings losses are estimated and then inserted into the slot.

Table 5.3 and Table 5.5 summarized the main parameters of both machines and the simulation conditions.

5.6.1 7.5 rpm - 15 MW PMSG (Machine C)

Table 5.3: Key design parameters and thermal simulation conditions of (7.5 rpm - 15 MW) PMSG

Generator power	7.5 rpm-15 MW PMSG (p = 189, N_s = 1134, e_g =16mm)	
Winding topology	3-phases one-layer Distributed winding	
Permanent magnet	N48SH (B_r=1.4 T)	
ST-PMSG	[R_g[m], L_{act}[m],θ_s[%], h_s[m], θ_{PM}[%], h_{PM}[m], J_s[A/m^2], h_{ys} [m]] = [6.39, 1.27, 0.44, 0.123, 0.458, 0.044, 3.40e6, 0.044]	
SM-PMSG	[R_g[m], L_{act}[m],θ_s[%], h_s[m], θ_{PM}[%], h_{PM}[m], J_s[A/m^2], h_{ys} [m], h_{yr} [m]] = [5.97, 1.50, 0.44, 0.140, 0.642, 0.020, 3.06e6, 0.045,0.045]	
Thermal simulation conditions	Cooling fluid temperature [^{o}C]	35
	Convection heat coefficient stator/ cooling fluid [W.K^{-1}.m^{-2}]	1000

The steady state of the machine C (defined in chapter 3 and summarized in Table 5.3) was investigated. Figure 5.11 and Fig. 5.12 present the temperature distribution within surface-mounted and spoke-type permanent magnet synchronous generators. It was found that the highest temperature is reached in the machine windings (around 124 ^{o}C). The rotor temperature remains relatively low (around 70-80 ^{o}C).

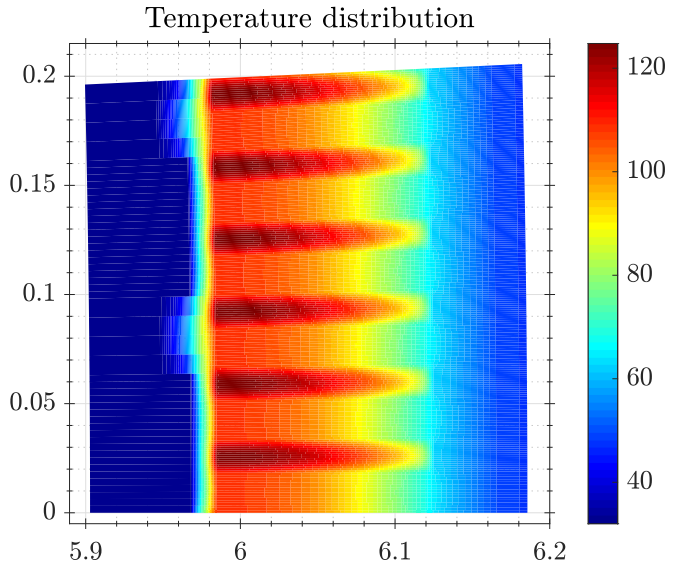

Figure 5.11: Temperature distribution within 7.5 rpm -15 MW surface mounted synchronous machine

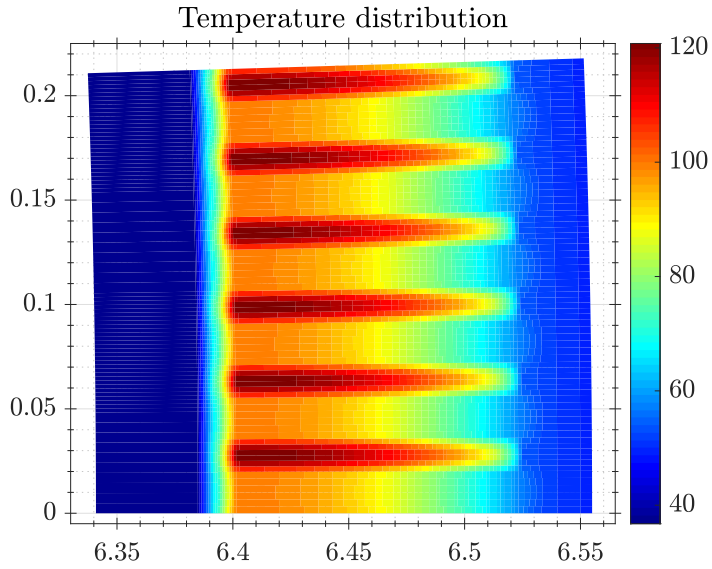

Figure 5.12: Temperature distribution within 7.5 rpm -15 MW spoke-type synchronous machine

Table 5.4: Thermal model results validation

	$T_{max_{PM}}[^o$ C]			$T_{max_{slot}}[^o$ C]		
	LPTN	FEM	Error	LPTM	FEM	Error
SM-PMSG	87.60	85.23	2.78 %	124.93	125.20	0.21 %
ST-PMSG	74.01	73.50	0.69 %	120.76	121.78	0.83 %

5.6.2 100 rpm - 15 MW ST-PMSG

Table 5.5: Key design parameters and thermal simulation conditions of (100 rpm - 15 MW) ST-PMSG

Generator power	100 rpm-15 MW PMSG (p = 21, N_s = 420, e_g =20mm)	
Winding topology	5-phases one-layer Distributed winding	
Permanent magnet	N40SH (B_r=1.2 T)	
ST-PMSG	[R_g[m], L_{act}[m],θ_s[%], h_s[m], θ_{PM}[%], h_{PM}[m], J_s[A/m^2], h_{ys} [m]] = [2.26, 1,11, 0.50, 0.136, 0.17, 0.062, 2.8e6, 0.045]	
Thermal simulation conditions	Cooling fluid temperature [^{o}C]	35
	Convection heat coefficient stator/ cooling fluid [W.K^{-1}.m^{-2}]	1000

The steady state of the machine defined in Table 5.5 was investigated. Figure 5.13 depicts the temperature distribution within the machine.

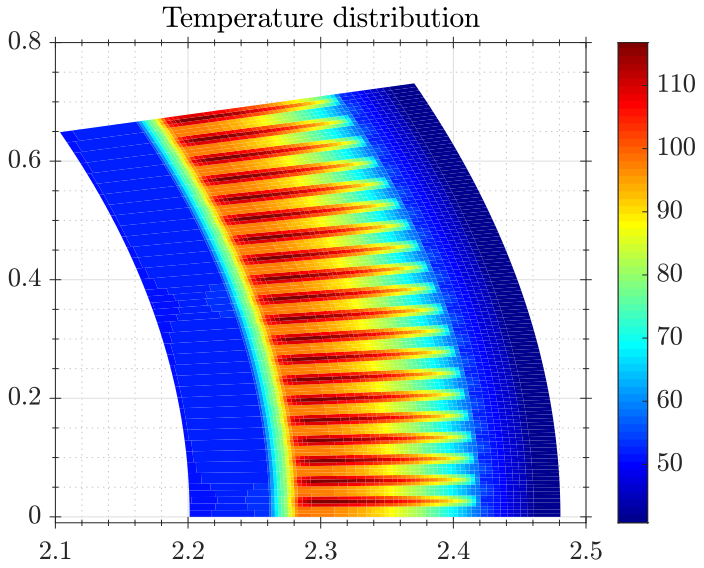

Figure 5.13: Temperature distribution within 100 rpm - 15 MW spoke-type synchronous machine

Table 5.6: Thermal model results validation

	$T_{max_{PM}}$ [^{o}C]			$T_{max_{slot}}$ [^{o}C]		
	LPTN	FEM	Error	LPTN	FEM	Error
ST-PMSG	77.46	77.89	0.55 %	116.79	115.20	1.38 %

Table 5.6 and Table 5.4 illustrates the accuracy of the proposed LPTN by comparing its results to FEM one.

5.7 Conclusion

In this chapter a two-dimensional steady-state lumped parameters thermal network of permanent magnet synchronous generator was developed. It can be conclided that:

1. For a large wind turbine generators, steady state can be reached in many hours (around ten hours). Although the steady state is not enough in wind turbine generator due to the non-constant load, the unsteady state (transient) thermal was not found necessary in pre-design stage since it required a lot of resources and CFD is usually indispensable.

2. The developed LPTN was based on the representation of heat sources and generators materials by a heat generator and a thermal resistances respectively. Since Joule loss is the major loss component in such machines, only copper losses were considered in this model.

3. It should be noticed that the FEM was used in the determination of some winding parameters in LPTN.

4. The axial diffusion term was neglected because the gradients in the axial direction was relatively small compared to the radial gradients, then two-dimensional model would be deemed sufficient in preliminary design optimization. The developed model was validated by FEM model developed in the commercial software Flux2D. The temperature distribution from LPTN model strongly correlated to that from FEM model within 0.21 % - 2.78 % error on the maximum magnet and slot temperature.

5. The 2-D steady-state LPTN will integrated into an optimization routine, where the electromagnetic performances and thermal performance will be optimized at the same time.

Part III

OPTIMIZATION OF DIRECT-DRIVE WIND TURBINE GENERATOR

Chapter 6

Design Optimization of Electrical Machine

6.1 Introduction

Design optimization is the application of numerical algorithms and techniques to engineering systems in order give assistance to the engineers and ensure the performances of the final design. It plays crucial role in the performance enhancement of the electrical machines. In electrical machine the constraints and the objectives often contain electromagnetic performances such as cogging torque, efficiency, induced voltage, power factor and power density. Usually, these requirements, which should be considered simultaneously, are in contradiction to each other. In addition, designing electric machine involves a combination of electromagnetic, thermal and mechanical analysis. The relationship between these different domains is complicated and most phenomena in machine are nonlinear in nature. Therefore, the performances and the design are strongly coupled which made it complex to design/optimize an electric machine. Further, the optimisation routine has to be defined carefully in such global optimization problems. The design optimization of electrical machine includes two stages, design and optimization. The objective of the design stage is to establish an initial machine for a given application based on expert knowledge, whereas the aim of the optimization stage is to find the optimal design of the machine, already proposed in the design stage, though optimization methods. Three important features need to be considered in the optimization process including optimization strategies, models and algorithms [333]. The full process will be described in this chapter. In section 6.2, a literature survey is conducted about the design optimization techniques used in electrical devices. Then in section 6.3, recent developments on the design optimization of electrical machines are presented. Finally, in section 6.4 the formulation of optimization

problem is described the optimization procedure is exposed.

Note that, for all illustrations in multi-objective optimization problem, a bi-objective minimization problem is taken.

6.2 Methods and Techniques Of Optimization

Although the principle of operation of machines is based on electromagnetic theory, taking into account the thermal and structural aspects is crucial in the design optimization of electric machines. Indeed, the design optimization aims to find the optimal solution, through a multi-physics process, considering the electromagnetic characteristics, thermal constraints and structural limitations. Usually, heuristic techniques are used to solve such complex multi-disciplinary problem. The optimization models can be classified according to many different criteria such as constraints, nature of design variables, structure of the problem and nature of the equations involved. These classifications are briefly discussed in this section.

6.2.1 Optimization methods (structural optimization)

Most of optimization methods have been originally developed for mechanical applications, and was further extended to electromagnetic applications such as electrical machine [334] [335], electrostatic device [336] and microwave devices [337]. Then, the proposed models for structural optimization of mechanical devices can be applied to solve electromagnetic geometry optimization problem in electric machine although the differences in physical context. Indeed, in mechanical structure optimization the objective is to reduce the structure mass taking into account the imposed mechanical constraints; while in electromagnetic structure optimization it is desired to have magnetically optimal structure with respect to certain magnetic field, forces, flux densities, etc. In addition, the nonlinearity nature of the ferromagnetic materials should be considered in electromagnetic devices, however, such effects are not present in mechanical applications. The phenomena are not desirable for the optimization algorithm convergence [338], especially in the magnetic saturation case where the topology might be altered [339]. Further, contrary to the mechanical devices which are often needed to be static stationary while resisting to a specific load, the movement in electrical machines should be addressed.

Considering the design variables used in the definition of the magnetic topology, the design optimization methods can be classified into three types, namely, sizing optimization, shape optimization, and topology opti-

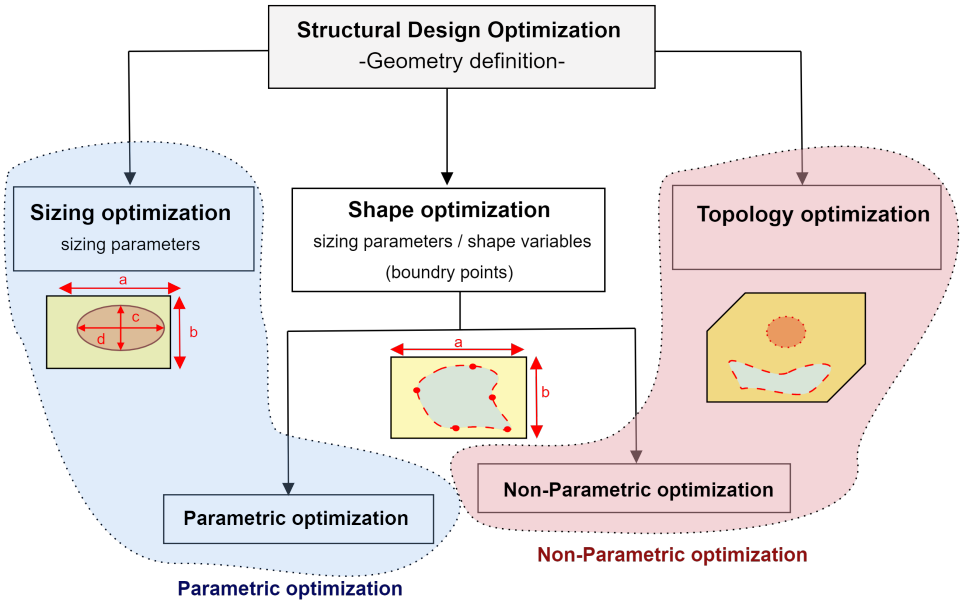

Figure 6.1: Structural design optimization

mization. These methods can be combined for better design performance [340]. Analytical, semi-analytical or numerical models used in the design optimization of electrical machines require an initial geometric template, in which dimensions parameters are controlled by the optimization. Such parametric-based methods including sizing and parametric shape optimization are time consuming due to the evaluation of large number of variables combinations. In addition, such design parameters are not truly independent [341]. Nonparametric-based methods including topology and non-parametric shape optimization offer an alternative to the classical parametric one. While in the shape optimization only the boundaries between regions are deformable which limited the design space to the initial geometry and may end up with a local minima [342], in topology optimization the optimal solution within the solution space is obtain by freely distributing the materials in the design space. Each method will be discussed in the next subsections.

6.2.1.1 Sizing optimization

The goal of the sizing optimization is to find the optimum design by varying some size parameters, (e.g., the rotor mean radius, the slot's opening, the slot's height, the permanent magnet thickness, the permanent magnet opening or the air gap length). However, the topology and the shape of the machine are predefined in the initial design. The research space is delimited by the variables bounds and/or the imposed constraints [343].

This method has several limitations. First, the preselection of the machine's geometry restricts the solution space which restrain the freedom of the optimization and hence limited the performance improvement [344]. Second, it requires an expert knowledge to define the solution space limitation and preselect the appropriate topology of the electrical machine [344]. Finally, the representation of electrical machine necessitates a large number of parameters, resulting in high dimension of design optimization problem with huge computation burden. This optimization has been widely used in the design of electrical machine [345].

6.2.1.2 Shape optimization

The shape optimization aims to find the optimal layout of the machine by smooth variation of the boundary or of the material interface [346] [347]. Considering the geometry's definition, the shape optimization can be divided into two distinct types : parametric and non-parametric shape optimization. In parametric shape optimization, the optimization is linked to the CAD (Computer Aided Design) geometry though parameters, which represents the dimensions or the orientations of the object[1] [346] [348]. To prevent boundaries' ripples, the design parametrization of the boundaries may be done by using polynomial or rational representations [349] (e.g., Basis-splines (B-spline) [350] [351], Bezier curves and Non-Uniformal Rational B-Splines curves (NURBS)) or by surface, the control points representing such curves and surfaces serve as optimization variables [347]. This method suffers from a number of disadvantages. For instance, it does not provide any explicit information of the geometry or the topology of the boundary [352]. The finite number of parameters results on limitation on the possible designs [346]. Furthermore, the selection of the boundary points is usually based on experience or analytical calculation which rise the difficulty of the realization. It has already been applied for electric machines [353] [354] [355].

In the nonparametric shape optimization (also called free-form shape optimization), the design space consists of implicit parameters defined by the nodal coordinates of FEM design elements [356]. On each of the design points, a displacement vector is placed [348]. In the set of design nodes, each node could be modified by the optimization algorithm with respect to the domain boundaries defined by the constraints. This represents one of the main advantages of non-parametric shape optimization compared to parametric optimization [357] [348]. Nevertheless, this method is computationally expensive due to the new meshing required each time the geometry changes, in order to prevent deteriorated mesh and numerical instability [348]. The remeshing process may be avoided by adaptive refinement of the mesh [348] [358]. For more details [359]. It has already

[1] Also known as computer-aided geometric design (CAGD).

been applied in electric machine [360].

6.2.1.3 Topology optimization

This method aims to find the optimal layout of the machine's geometry for a given optimization design problem without a predefining of any parameters, hence no prior knowledge about the structure is needed. It proceeds by changing the distribution material (densities) within the design domain. Compared to parametric approaches, topology optimization has higher degree of freedom. The design variables represent the connectivity of the domain. Despite the fact that its non—parametric geometry definition method, topology optimization process required some parameters for defining structure of the assembly [344]. The non-parametric shape optimization, which, contrarily to the non-parametric topology optimization where the node position is fixed, proceeds by changing node location. Indeed, the optimization process attempts to reduce the weight without affecting the node location [361]. Various techniques have been used in the topology optimization, the most common approaches are homogenization [362] [363], phase-Field [364] [365], density-based [366], level set [367], topological derivative [368], derivative-free [369], Interrelations [370] and On/Off method (Also called Sensitivity with respect to material coefficient) [371]. The development of the topology optimization in the electrical machine still limited due to the design complexity such devices (e.g., Heterogeneous materials, magnetic Nonlinearity, constraints terms are highly coupled).

6.2.2 Optimization model

6.2.2.1 Objective function

The formulation of optimization problem may be classed depending upon whether it have scalar or vector objective functions. Multi-objective optimization problems are typically formulated with vector objective functions, while the scalar formulation is generally used for single objective optimization. The design optimization problem of electric machine is a non-linear multi-objective problem. Typical objectives in electrical machine are high torque density, high efficiency, low cost, and reduced mass.

6.2.2.1.1 Single/mono-objective In single-objective optimization, there is only one objective function to be optimized. Considering a mono-objective optimization problem with (l+m) constraints the mathematical

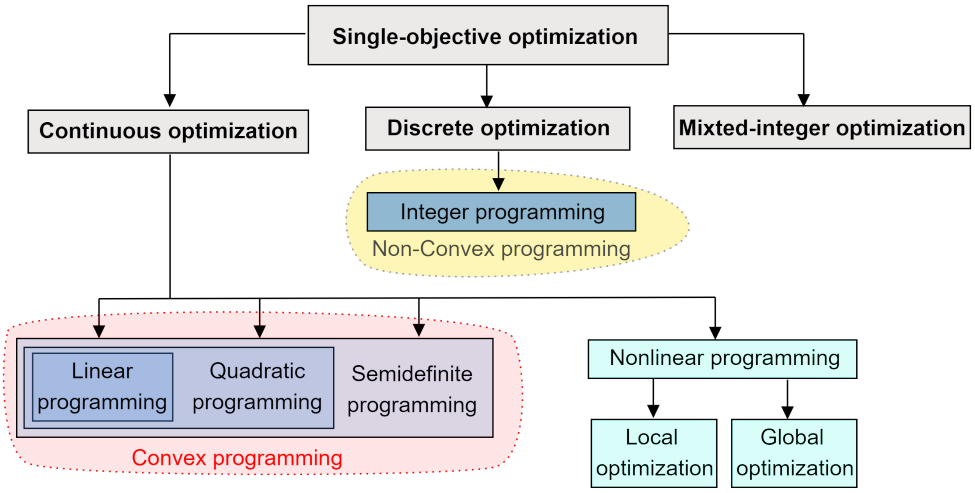

Figure 6.2: Classification of mono-objective optimization

formulation can be defined as follow :

$$\begin{cases} min \quad f(X) \\ s.b. \quad g_i(X) \leq 0 \qquad i = 1, ..., m \\ \qquad\quad h_j(X) = 0 \qquad j = 1, ..., l \\ X = [X_1, X_2, X_3, ..., X_n] \qquad X_L \leq X \leq X_U \end{cases} \tag{6.1}$$

where X is the vector of the design optimization variables, X_L and X_U is the lower and the upper bounds of X, f is the objective function, g and h are the vectors of the non-equality and equality constrains, respectively.

According to [372], the mono-objective optimisation may be either combinatorial or continues optimization. It is possible to combine both optimization variables, continues and integer, leading to mixed-integer optimization.

6.2.2.1.1.1 Continuous Optimization Continuous optimization treats problems dealing with continuous design variables, it could be divided broadly into linear and non-linear programming. In linear programming (LP) both the constraints and the objective functions are linear, while non-linear programming (NLP) present nonlinear equation. The later may leads either to local or global minimum. Contrary to local optimization, which gives the optimal solution around the neighbourhood of the initial starting point, global optimization converges to the global optimum in the presence of multiple local optima. The global optimization is time consuming, in fact, the computation time rises exponentially with the number of variables and/or constraints

[373] [374] [375].

6.2.2.1.1.2 Discrete optimization (Combinatorial) Combinatorial optimization treats discrete, integer and binary variables. In electrical machines, that may represent the pole pair number, the slots number, and winding layer in slot. In such optimization problem, it is possible to explore all the solutions in moderate time. Although, the number of solutions is large but it is limited by the number of variables (2^n).

6.2.2.1.1.3 Mixed-integer optimization The design optimization of the electrical machines is generally a mixed-integer optimization. Such optimization deals with various types of optimization variables.

6.2.2.1.2 Constraints Based on the presence or the absence of the constraints, the optimization problem can be either unconstrained or constrained. In unconstrained problems the optimization finds the optimal solution under the assumption that the parameters can take on any possible value. Nevertheless, most of engineering systems are constrained problems, especially electrical machines which are highly nonlinear and strongly constrained. Unconstrained problems are generally easier to deal with than constrained ones. If the design variables satisfy a given constraints, it is called feasible design. The following subsections presented the conversion of equality and inequality constrained problem to unconstrained optimization problem.

6.2.2.1.2.1 Equality constrained problem Considering the optimization problem define in Eq.6.1 with only equality constraints $h_i(X)$, it may be transformed to unconstrained optimization problem by introducing Lagrange multipliers, λ_i, as follow [372]:

$$\begin{cases} min\, L(X) \\ L(X,\lambda) = f(X) + \sum_{j=1}^{l} \lambda_i h_i(X) \\ X = [X_1, X_2, X_3, ..., X_n] \qquad X_L \leq X \leq X_U \end{cases} \tag{6.2}$$

Lagrange coefficients introduce the equality constraints into the optimality condition. For more details, see [372].

6.2.2.1.2.2 Inequality constrained problem Considering the optimization problem defined in Eq.6.1 with only inequality constraints $g_i(X)$, it may be transformed to unconstrained optimization problem by adding

j slack variables, z_j, and by using Lagrangian function. It can be expressed as follow [372]:

$$\begin{cases} min\, L(X) \\ L(X,z,\lambda) = f(X) + \sum_{j=1}^{m} \beta_j (g_j(X) + z_j^2) \\ X = [X_1, X_2, X_3, ..., X_n] \qquad X_L \leq X \leq X_U \end{cases} \tag{6.3}$$

where β_j represents the Lagrangian coefficient associated with the optimization problem.

6.2.2.1.3 Multi-objective In multi-objective optimization problems, there is no single objective function but a vector of objectives. In systems engineering, these multiple objectives, which are usually conflicting, are required to be optimized simultaneously. The multi-objective optimization (MOO) problem can be expressed as :

$$\begin{cases} min \quad F(X) = [f_1(X) f_2(X) ... f_n(X)]' \\ s.b. \qquad g_i(X) \leq 0 \qquad i = 1, ..., m \\ \qquad\quad\; h_j(X) = 0 \qquad j = 1, ..., l \\ X = [X_1, X_2, X_3, ..., X_n] \qquad X_L \leq X \leq X_U \end{cases} \tag{6.4}$$

where n ($n \geqslant 2$) is the number of objective functions $f : \mathbb{R}^n \longrightarrow \mathbb{R}$. In MOO a trade-off must be made between conflicting objectives. The solution that simultaneously optimizes all objectives almost never exists. Therefore, the MOO give rise to a set of Pareto optimality solutions, since there is no scalar concept of optimality. Let us consider a n-objective optimization problem, we say that the vector v_1 dominates the vector v_2 when conditions in Eq.6.5 are satisfied.

$$\begin{cases} f_i(v_1) \leq f_i(v_2) \quad \forall i \in [1, 2, ..., n] \\ f_i(v_1) < f_i(v_2) \quad \exists i \in [1, 2, ..., n] \end{cases} \tag{6.5}$$

When neither v_1 dominates v_2 nor v_2 dominates v_1, the two solutions v_1 and v_2 are incomparable. Therefore, in given a set of solutions, all solutions which are not dominated by any other solution of that set, are called the non-dominated solutions (Also called non-inferior and efficient points). Non-dominated solutions together they make up a non-domination front called Pareto-optimal solution (Also called Pareto efficient frontier or Pareto front) (See Fig. 6.3). Therefore, any amelioration in one objective results results on the worsening of at least one other objective. Furthermore, the shape of the Pareto front gives an indication about the nature of trade-off between the objectives. Fig. 6.3 illustrates a typical Pareto front of a two objective minimizing

MOO in objective space.

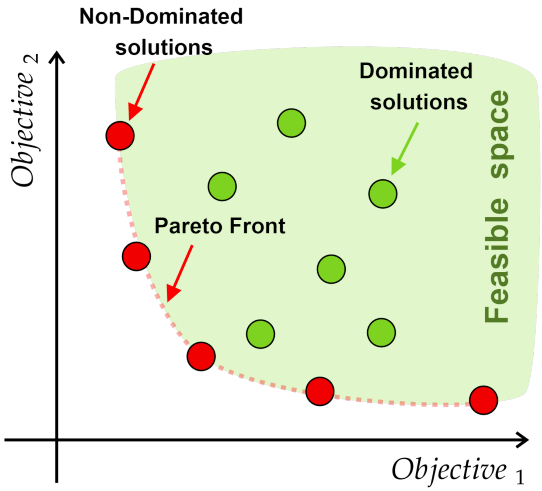

Figure 6.3: Notion of dominance and Pareto optimality

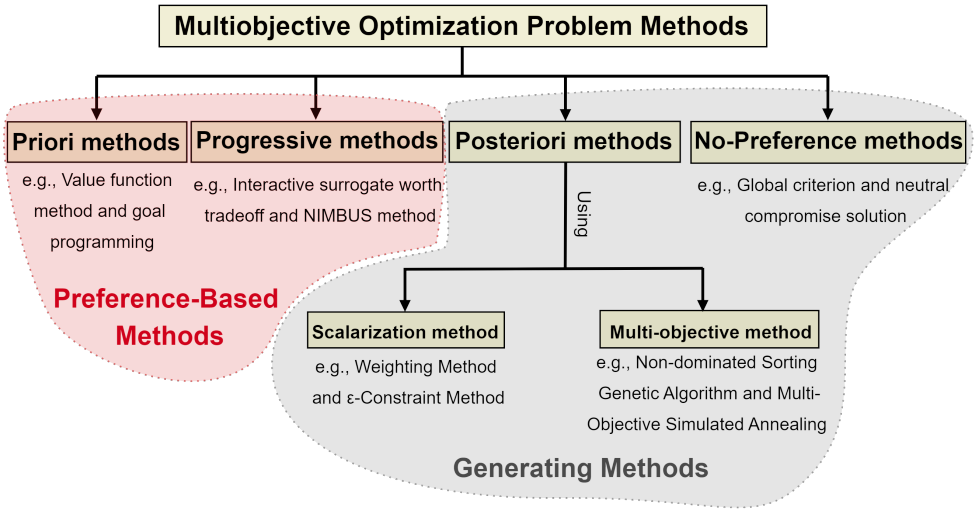

Figure 6.4: A classification of multi-objective optimization methods

The main difficulty in MOO lies is how the choose the suitable method to solve the problem. Two approaches can be used to to find the Pareto points: Scalarization techniques and Pareto technique. Unlike the former approach, where the MOO problem is transformed into many single-objective problems; in the latter one, the problem is solved more directly using the Pareto dominance notions. According to the role of the decision maker in the solution process, the methods used for generating Pareto optimal solutions can be divided into three categories (See Fig. 6.4) [376] [377]: no preference method, a posteriori methods, a priori methods and

progressive methods (See [378] for more details about advantages and drawbacks of each method). MOO methods can be either preference-based methods or generating methods. As shown in Fig. 6.5, in preference-based methods use the preferences specified by the decision maker, whereas in generating methods the optimization generates Pareto front solutions without any information from the decision maker [378] [376].

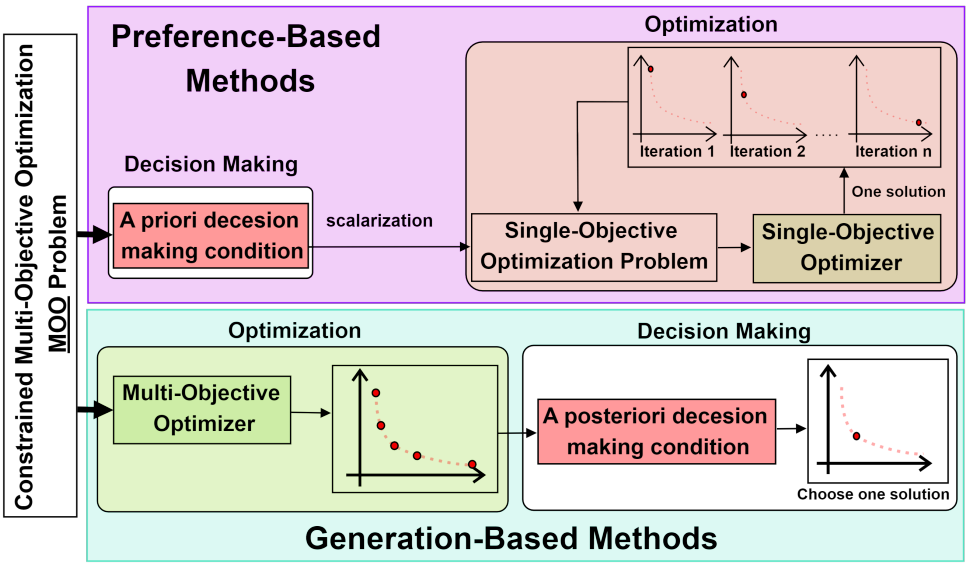

Figure 6.5: A classification of multi-objective optimization methods

Multi-objective optimization methods :

1. **Priori methods**

   The preference information is given by the decision maker before solving the optimization problem [379] [380].

2. **Posteriori methods**

   These methods are used to determine the complete set or only subset of non-dominated solutions. From the identified subset, the decision maker chooses the most suitable solution. Then, the trade-off information is received after the determination of non-dominated solutions subset [381] [377].

3. **Progressive methods**

   The progressive methods (Also called iterative or interactive methods) rely on the progressive definition of the decision maker's preferences along with the exploitation of the search space [381]. Indeed, it guided the decision maker a new Pareto optimal point from an existing one.

4. **No-Preference methods**

   In this class of methods, no preference information is given by the decision maker.

6.2.2.1.3.1 Scalarization-based approaches (Also called aggregation approaches) In scalarization approaches, the objective vector is transformed into a scalar function, such that the problem can be written as in Eq.6.1. Once scalarized, the problem is solved by the classical methods applied to single-objective functions. The most commonly used transformation methods in electrical machine are presented in this subsection.

- **Weighting method**

  Weighting methods belong to a posteriori methods using the scalarization approach (See Fig. 6.4). It

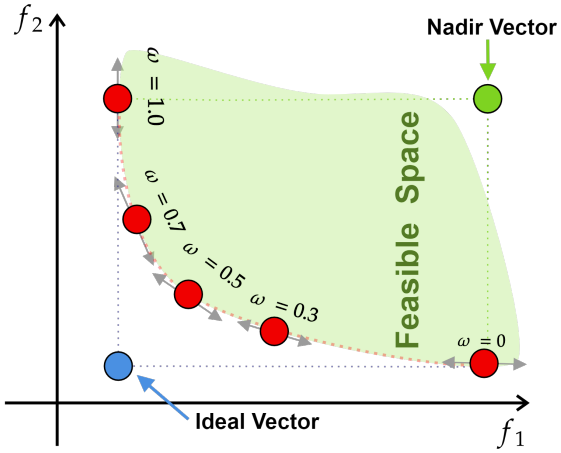

Figure 6.6: Generating different solutions with the weighted-sum method

was introduced by Cohon in 1978 [382]. In this technique, weights are assigned to each objective function ω_i, then the mono-objective optimization problem is obtained by minimizing the weighted sum of the objectives. We then solve :

$$\begin{cases} min & \sum_{i=1}^{n} \omega_i f_i(X) \\ s.b. & g_i(X) \leq 0 \qquad i = 1, ..., m \\ & h_j(X) = 0 \qquad j = 1, ..., l \\ X = [X_1, X_2, X_3, ..., X_n] & \qquad X_L \leq X \leq X_U \end{cases} \tag{6.6}$$

where $\omega_i \in \mathbb{R}$ ($\omega_i \geq 0 \quad \forall i \in [1, ..., n]$ and it is usually supposed that $\sum_{i=1}^{n} \omega_i = 1$) is the weight of the i^{th} objective. Obviously, this method depends on the relative values of the weights, which may be static of

dynamic [383]. To define the relative importance of objectives, often it is required first to normalized objectives [384]. For example, for bi-objective optimization problem, the normalized weighted sum can be expressed as:

$$min \quad \omega \frac{f_1(X) - f_1^*}{f_1^N - f_1^*} + (1 - \omega) \frac{f_2(X) - f_2^*}{f_2^N - f_2^*} \tag{6.7}$$

where the superscript * and ^{N} refer to the ideal[2] and the nadir objective vector[3]. In problem in Eq.6.8, when varying the value of the weight values between 0 and 1 the Pareto optimal front is obtained (See Fig. 6.6).

- **$\epsilon-$constraint method**

  This method was introduced by Haimes et al. in 1971 [386], it is the most common Scalarization method

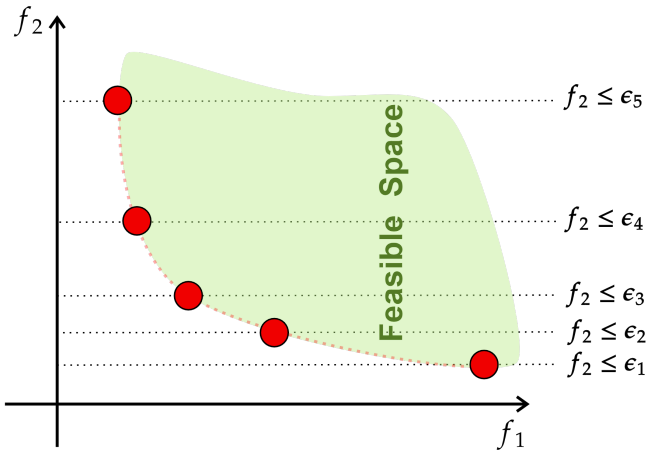

Figure 6.7: Generating different solutions with the $\epsilon-$constraint method

used in the generation of front Pareto [380]. In this approach the MOO is transformed into a series of mono-objective optimization problems. The idea is to keep only one of the objective functions whereas each of the others is turned into an inequality constraint until the Pareto front is found. The optimization

[2]Ideal point is contracted from the best objective values over the search space [385].
[3]Nadir point represents the vector composed of the worst objective values of Pareto optimal solution [385].

problem takes the following form :

$$\begin{cases} min \quad f_r \\ s.b. \quad f_k(X) \leq \epsilon_k \qquad k = 1, ..., n; k \neq r \\ \qquad\quad g_i(X) \leq 0 \qquad i = 1, ..., m \\ \qquad\quad h_j(X) = 0 \qquad j = 1, ..., l \\ X = [X_1, X_2, X_3, ..., X_n] \qquad X_L \leq X \leq X_U \end{cases} \tag{6.8}$$

An illustration of this method is shown in Fig. 6.7 for bi-objective optimization problem.

6.2.2.1.3.2 Pareto-based approaches The Pareto front can be generated either by scalarization methods, as explain in the previous section, or by stochastic methods. Details about multi-objective evolutionary algorithms are provided in the next sections.

6.2.2.1.3.3 Level-based approaches Multi-level programming is another method used to solve MOO problems, it aims to find one optimal point in the entire Pareto surface. Multi-level programming orders the n objectives according to a hierarchy.

6.2.2.2 Optimization Level

To overcome the computational burden of classical sequential design approaches for complex design problems, Multidisciplinary Design Optimization (MDO) has been introduced. The MDO method, in which engineers attempts to decompose the complex system into smaller, more manageable and interrelated subsystems, provides greater efficiency than a classical methods [387] [388]. While the classical disciplinary optimization approaches performed with sequential methods, MDO methods guarantee the interactions between the disciplines is by using the multi-disciplinary analysis (MDA) (See Fig. 6.8). Further, solving each discipline separately does not ensure the global optimality. The subsystems can be design with numerical or analytically models. Using sensitivity analysis, the multi-level optimization allows the division of the high dimensional system into several subsystems. The design variables with high sensitivities will be optimized before those with low sensitivities, therefore, a considerable reduction of total computation time is reduces considerably. Other methods could be used in the parameter significance analysis such as local sensitivity analysis (LSA), global sensitivity analysis (GSA), sizing equation, and analysis of variance (ANOVA). In [389], these four methods was used to perform

a multilevel optimization of Permanent magnet motor.

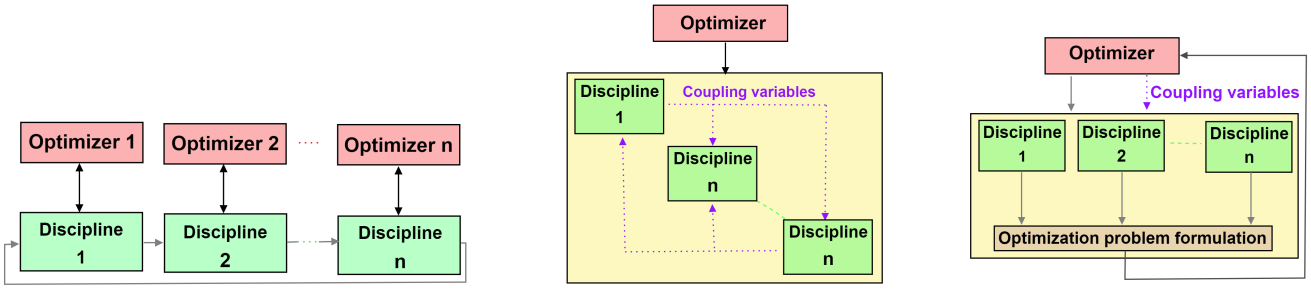

(a) Classical design approaches (b) Coupled MDA (c) Decoupled MDA

Figure 6.8: Design analysis approaches

MDO can be divided into two categories according to the number of optimizes: mono-level and multi-level optimization. In mono-level optimization design only one optimizer is used to solve the MDO problem, while in multi-level optimization, many optimizers are integrated in order to distribute the complexity of the problem over different disciplines [390]. The couplings are handled through coupling variables (See Fig. 6.8). Further, two approaches has been developed to manage the interdisciplinary in the MDA. In deterministic MDO, problem formulations is based either on coupled or decoupled formulations [391]. In the coupled approaches the a multidisciplinary analysis is performed at each system-level iteration, all along the optimization process, to guarantee the multidisciplinary interactions, whereas in decoupled formulation the interdisciplinary consistency is ensured only at the convergence of the optimization problem [391]. As can be seen in Fig. 6.8b and Fig. 6.8c, in decoupled methods the optimizer handles the design and coupling variables and is subjected to additional coupling constraints. Indeed, the decoupled formulation relaxes the coupling constraints during the optimization, and then need less computation cost compared to the coupled formulation, which became prohibitive in the case of complex engineering systems. Nevertheless, decoupled approaches are not efficient because of the inactivity of the processors running the inexpensive analyses and optimization which is waiting for the updates from the other processors.

6.2.2.2.1 Mono-level optimization Mono-level optimization [4] includes all kinds of optimization that deal with problems having a mono-level structure, the optimization is used at only one level (the system level). The problem formulation of system-level allows parallel analyses of the disciplines (subsystems). It could be either mono-objective or multi-objective. Further, it may deal with different types of design variables including integer/binary integer (zero-one), continues/discontinues and discrete variables. Many methods was proposed

[4] Also called system-level optimization.

to solve such optimization such as Multi-Discipline Feasible (MDF), Individual Discipline Feasible (IDF), All At Once (AAO) [392] [393] [394].

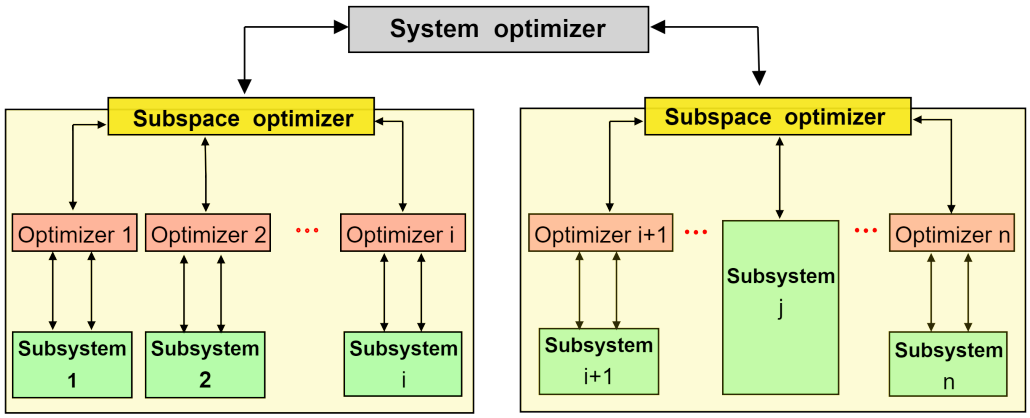

Figure 6.9: Multi-level optimization structure

6.2.2.2.2 Multi-level optimization The design optimization of electrical machines is a complex process that involves magnetic, electrical and mechanical sub-systems. The interaction between these sub-systems should be taken into account in order to avoid a sub-optimal system. Representing the machine as a whole may be challenging due to the large number of the variables and the strong interaction between them. The multi-level optimization has been introduced to avoid centralization of the mono-level approaches, which may require excessive computation time due to the data communication [392] [390]. Multi-level approaches use local decisions, and then reduce the communication requirement within the optimization process. As can be seen Fig. 6.9, the local variables will be no more transmitted to the system optimizer. The role of the system optimizer is limited to management of the optimization process. Many approaches have been developed to overcome these challenges such as Collaborative Optimization (CO), Bi-Level Integrated System Synthesis (BLISS), Concurrent Sub-Space Optimization (CSSO), Analytical Target Cascading (ATC).

6.2.2.2.3 Hybrid Strategies It is possible to combine both optimization strategies (See Fig. 6.11), mono-level and multi-level optimization by some subsystems with own optimizer and other without.

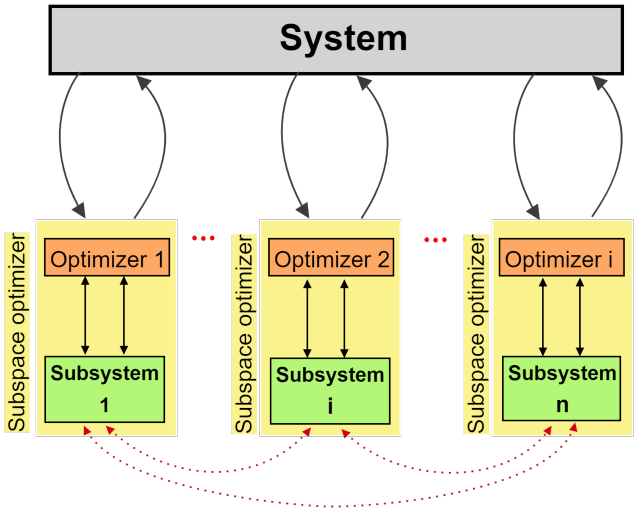

Figure 6.10: Collaborative optimization

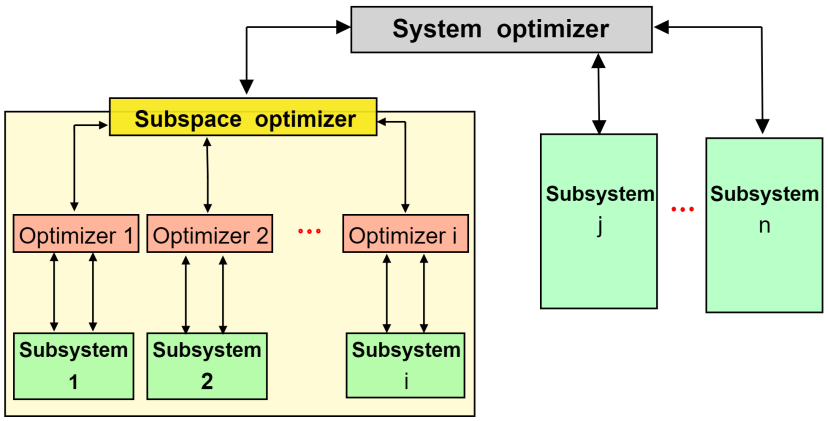

Figure 6.11: An example of a hybrid multi-level optimization

6.2.3 Optimization algorithms

Optimization algorithms have a key role to play in finding the global optimum design. The efficiency of the final solution depends broadly on the choice of the optimization algorithm. With recent advances in computational intelligence, optimization is become a part of computed-aided design process. Optimization algorithms can be classified into two distinct categories : deterministic and stochastic methods. The former finds the optimum solution algorithmically, while the stochastic methods conduct a random exploration of the solution space. No algorithm outperforms other algorithms in any specific problem, however, in practice, certain algorithm are more efficient in certain cases. In this section we will briefly present the advantages and disadvantages of the

different optimizer in the context of electrical machines design optimization.

6.2.3.1 Deterministic optimization

Deterministic optimization methods represent the the classical optimization search techniques, they are generally local optimization approaches. It is useful to distinguish between three categories of deterministic algorithms. Depending on information of the problem being used to create a new iteration, the deterministic algorithms may be :

1. **Zero-order algorithms (Derivative-Free algorithms)** Use only the values of objective functions and constraints.
2. **First-order algorithms** Exploit the gradient (first derivative) with respect to all the variables to be computed.
3. **Second-order algorithms** Exploit the Hessian (second derivative) matrix.

Gradient methods have the capacity to process a large number of design variables and constraints. They also help to speed up the process of finding a constrained optimum. Further, the Karush–Kuhn–Tucker conditions provide a criterion of convergence in order to use these optimization algorithm effectively. If correctly rightly configured, such methods can converge rapidly to local optimum [344]. However, deterministic methods are often unsuitable for optimization problem with multi-modal characteristics [344]. In addition, the use of such methods requires an exact information about the objective and the constraints functions and its derivatives in order to orient the search direction in each iteration. Further, the calculation of the gradient, when it is possible, is usually resource intensive. Moreover, the deterministic optimization algorithms will converge to the same optimum via the same path, then they are not appropriate in the characterization of random behaviors.

In [357], finite element model coupled respectively to Sequential Quadratric Program (SQP) and standard Particle Swarm Optimization (PSO) technique for the purpose of shape designing PMSG. The authors concluded that standard SQP outperforms PSO by two order magnitude. Although SQP uses gradient calculation, it find the optimum in fewer iterations compared to stochastic methods. Consequently, deterministic methods should be considered for such class of optimization problem. Some gradient based algorithm do not support constrained problem like Sequential Unconstrained Minimization Technique (SUMT). To overcome these drawbacks many solutions have been introduced [357]. Deterministic methods had been applied many time in the

design optimization of electrical machine, such as SQP [395] [396] [397] [357], an ameliorate version of Branch and Bound [398], IBBA (based on Branch and bound) [399], Hooke and Jeeves [400], and SUMT [401] [402].

To sum up, the drawbacks of deterministic approaches made it difficult to design electrical machines with many constraints and local optimums. Therefore, using heuristic algorithms is far more suitable for searching a global optimum in the electric machines.

6.2.3.2 Stochastic optimization

The stochastic algorithms ensure a diversity in the exploration of the search space, in principle, they allow to escape the local optimums. Indeed, the successive executions of the algorithm for the same initial conditions may lead to different solutions. Consequentially, stochastic programming is typically used for global optimality purposes. However, stochastic method may fail to detect the best search directions, that mainly due to their random nature, which made them time consuming optimization approaches.

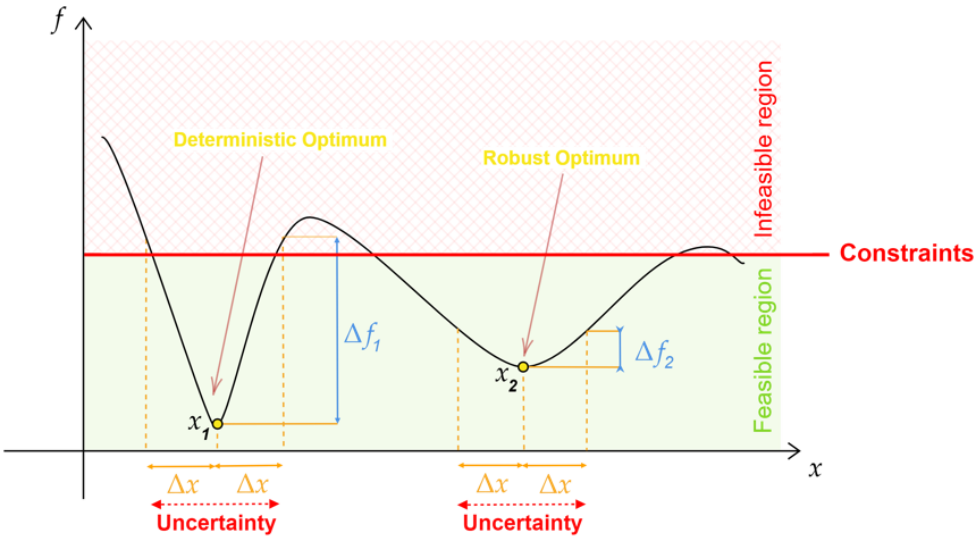

Figure 6.12: Robust design optimization concept

In electrical machines, there are several manufacturing variations and uncertainties in the practical production process [333], this is due to manufacturing tolerances (See Fig. 6.13a) (magnetic behavior law and iron losses), assembling inaccuracy (See Fig. 6.13b) and material diversities (See Fig. 6.13c) [403] [404] [405]. These uncertainties could be incorporated in stochastic optimization [406] [407] [408], in order to avoid the performance deterioration of the machine. As shown in Fig. 6.12, when optimizing the function $f(x)$, deterministic optimization algorithms trends to converge to global optimum x_1 which may results in large fluctuations of

the objective function ,when the design parameter varies Δx. These fluctuations could make the design non-feasible. Despite the fact that x_2 is local optimum, it offers design with superior robustness compared to x_1. The robust design optimization is challenging task in electrical machine.

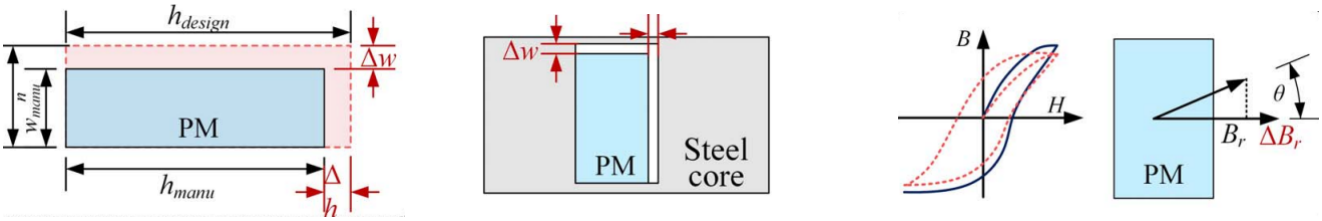

(a) Manufacturing error (b) Assembly inaccuracy (c) Material diversity

Figure 6.13: Uncertainties in electrical machines

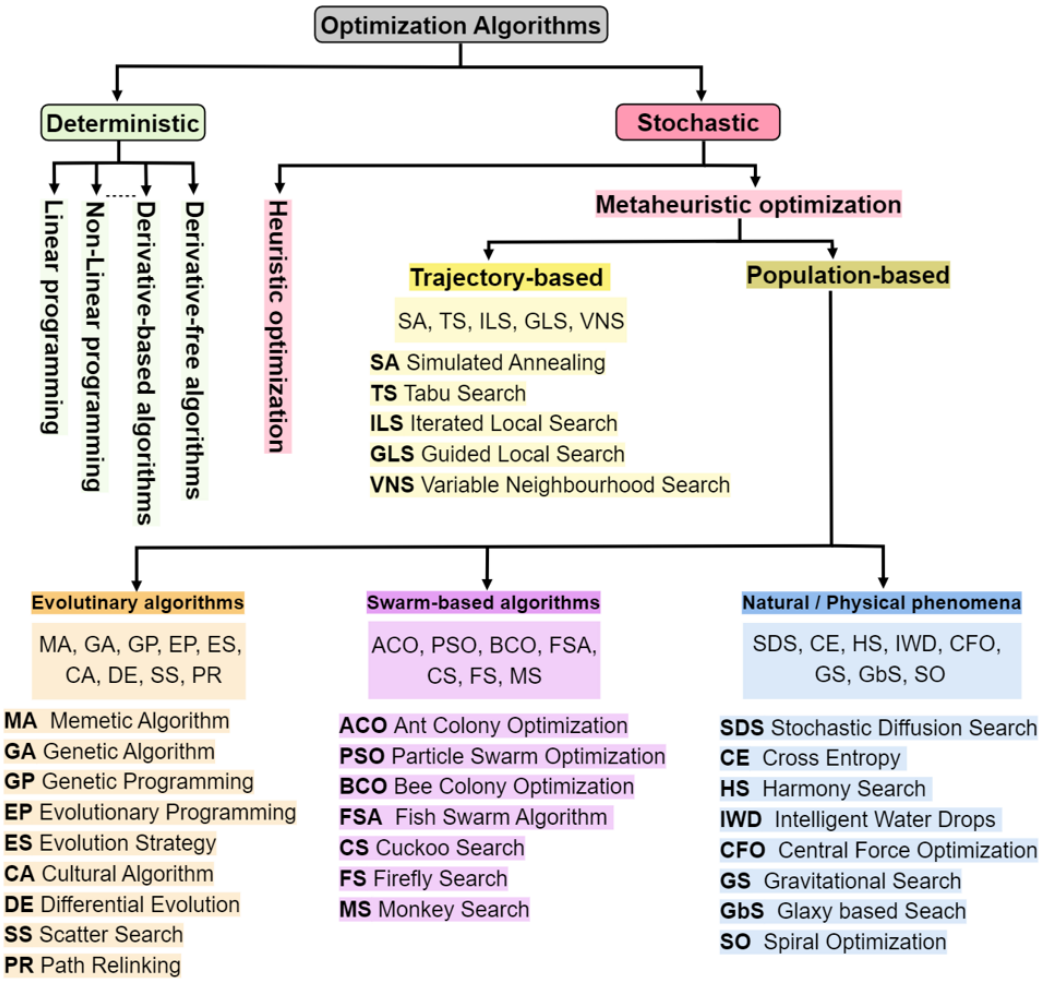

Figure 6.14: Stochastic optimization algorithms

The stochastic optimization could be either trajectory-based or population-based method. Fig. 6.14 presents some existing stochastic algorithms. The most commonly used in the design optimization of electrical machines

will be presented in this section.

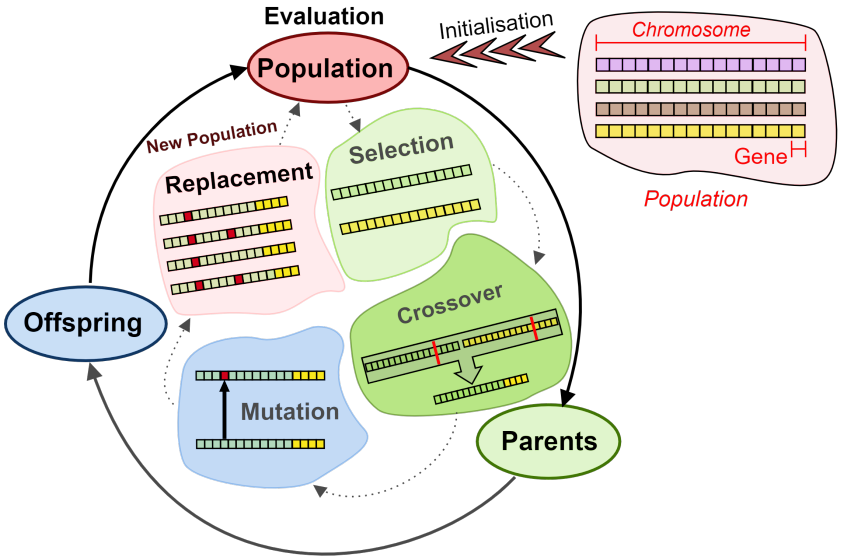

Figure 6.15: Reproduction operators in genetic algorithm

6.2.3.2.1 Genetic algorithms GA Genetic algorithms are the most popular evolutionary algorithms, they are designed to find global optimum for complex optimization problems [409]. It was first introduced by John Holland in 1975 [409], since then, many variant of genetic algorithms have been developed. GAs are inspired by Darwin's theory in which only the fittest survive [375] [410]. The Algorithm imitates the biological evolution process of species and the concept of natural selection. This is mainly performed through three operators; selection, crossover, and mutation. Selection is a process in which the parents are selected for mating based on their objective function values (See Fig. 6.15). Then children are created by crossover and mutation operations to form the new population (See Fig. 6.15). One generation represents one iteration of creating a new population. The flowchart in Fig. 6.16 illustrates the general schematic of GA.

6.2.3.2.1.1 Genetic operators

1. **Selection operators** Selection is the most important operator in GA, it allows not only the parets' selection but also the creation of the next generation.

   (a) **Selection**

   GA implement the optimization strategies by simulating biological evolution through natural selection [411]. Individuals who take part in the reproduction of the next generation are designated

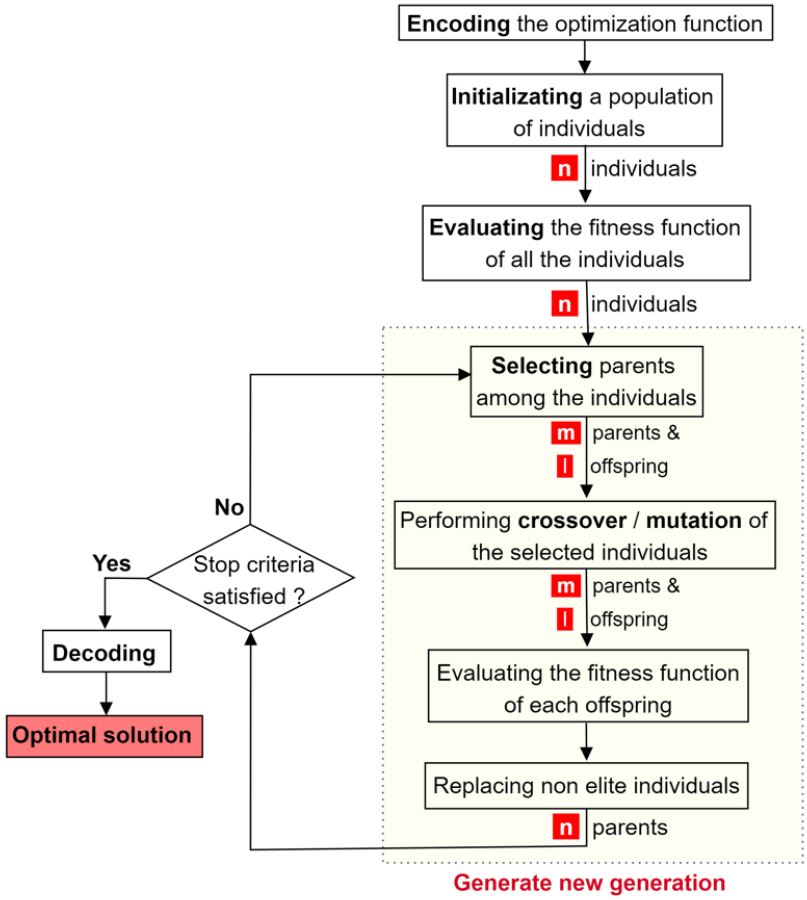

Figure 6.16: Flowchart illustrating the genetic algorithm

in the selection phase (mating pool), based on their survival probability, which is proportional to fitness function. It aims to enhance the quality of solutions by maintaining only the most suitable individuals and discarding poor solutions. There different techniques to implement selection in GA.

(b) **Selection for replacement (Replacement)**

Replacement selects which individuals will have to disappear from the population in each generation in order to maintain a constant population' size.

2. **Variation operators**

The variation operators manipulate the selected individuals to create the new generation by crossover and mutation.

(a) **Crossover**

The crossover operation creates offspring from mating pool parents. The two parents are mated

randomly. It is carried out if only a randomly generated number in the range 0 to 1 is less than or equal to the probability of crossover P_c, which is usually between 0.5 and 1 [412]. Higher crossover rates help to introduce quickly new structures in the population, while maintaining low values might stagnated the search. If the crossover is not performed, then two parents will be copied. In contrary, if the crossover does take place, then two offspring are created by exchanging segments of the parent genes. Indeed, the individuals are divided into many segments, depending the number of cross points, before the exchange of variables. Considering the number of cross points, the most commonly used crossover operators in GA are: n-point crossover, uniform crossover [413] [414] [415]. In n-point crossover, a n random points are chosen (between 1 and the length of the chromosome), then parents are split along those points and the offspring are created by alternating between parents with respect to the cross points; whereas in uniform crossover, the offspring genes are created by copying the corresponding gene from one of the two parents, a random mask is generated, the parity of each bit of that mask decides which parent will provide a bit to the corresponding position in a offspring.

(b) **Mutation**

The mutation operation involves a random alteration of each gene in the chromosome independently with a probability P_m. The mutation probability is usually small ($P_m \approx 1/populationsize$ [416]). It is used to maintain diversity of the population, prevent sub-optimal solution and early convergence.

GAs has been widely and successfully used in the design optimization of electrical machines, some particular examples are given in Table 6.1.

Table 6.1: Some GA applications in electrical machines

Electrical Machine Type	Objective Function	Number of Design Parameters	Model
RF-SM-PM-BLDC[5] [417]	Material cost	8	AM
RF-SM-PMSM[6] [418]	PM cost	8 / 5	AM / FEM
RF-I-PMSM[7] [419]	Motor efficiency	7	RN
AF-SM-PMSG[8] [420]	Active material cost	4	AM
RF-OR-BLDC[9] (Shape optimization) [421]	Cogging torque	5/3	RN
RF-OR-SM-PMSM[10] (Shape optimization) [422]	Cogging torque	3/4/8	AM

6.2.3.2.2 Particle swarm optimization PSO The PSO algorithm is an evolutionary algorithm inspired by the movement of birds within a flock. It was first introduced, in 1995, by Kenney and Eberhart [423] [424]. Particles (individuals) in PSO move to the optimum through search space, where the position is each particle within the warm (population) is adjusted by using a combination of two rules. The first rule is the attraction of the individual by its best position already found and memorized, and the second rule is the attraction of the particle to the best solution find in its neighborhood [425] [426]. The search behavior of the individuals is then affected by their experiences and that of the group. The position of the particle i, x_i, is updated by adding its current velocity v_i [426]:

$$x_i(t+1) = x_i(t) + v_i(t+1) \tag{6.9}$$

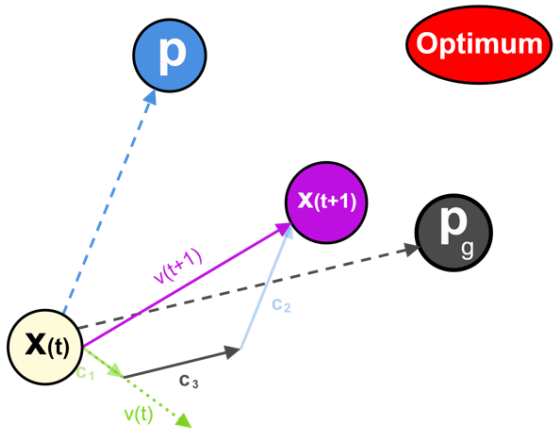

Figure 6.17: Velocity and position updates in PSO algorithm

It is the velocity term that drives the optimization process, and reflects both the experiential knowledge of the particle an socially exchanged information from the particle's neighborhood (See Fig. 6.17). The velocity is generated by [426]:

$$v_i(t+1) = k_{1_i}\, v_i(t) + k_{2_i}\, r_1\, (p_i - x_i(t)) + k_{3_i}\, r_2\, (p_{g_i} - x_i(t)) \tag{6.10}$$

where k_1, k_2 and k_3 are adjustable social factor representing the tendency to follow its own way, the tendency to reconsider its steps and the tendency to follow the best neighbor, respectively. p_i and p_{g_i} are the best position of the particle and the global best vector, respectively. r_1 and r_2 are random number between 0 and 1.

[5]Radial Flux Surface Mounted Permanent Magnet Brushless Direct Current
[6]Radial Flux Surface Mounted Permanent Magnet Synchronous Motor
[7]Radial Flux Surface Mounted Permanent Magnet Synchronous Motor
[8]Axial Flux Surface Mounted Permanent Magnet Synchronous Generator
[9]Radial Flux Outer Rotor Brushless Direct Current
[10]Radial Flux Outer Rotor Surface Mounted Permanent Magnet Synchronous Machine

Fig. 6.18 shows the flowchart of the PSO algorithm. PSO has been successfully used in the design optimization

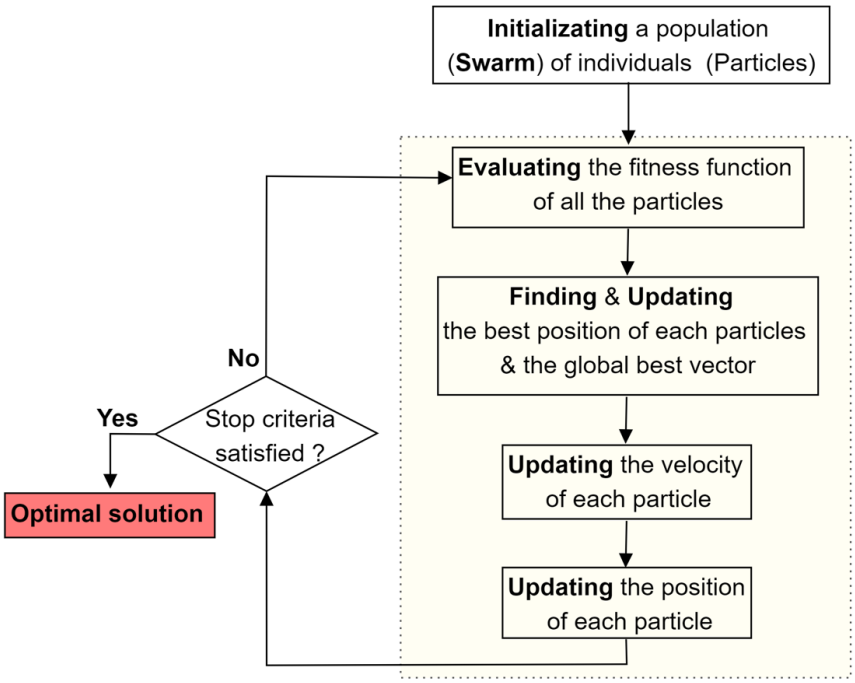

Figure 6.18: Flowchart illustrating the particle swarm optimization algorithm

of electrical machines, some particular examples are given in Table 6.2.

Table 6.2: Some PSO applications in electrical machines

Electrical Machine Type	Objective Function	Number of Design Parameters	Model
SS-LIM[11] [427]	Combination of power factor efficiency, weight and LEE[12] intensity	8	RN
I-PMSM[13] [428]	Power	4	FEM
I-PMSM [429] [430]	THD[14] of the B-EMF[15]	9/6	FEM
SynRM[16] [431]	Combination of torque ripple, total losses and torque average	3	AN

6.2.3.2.3 Ant colony optimization ACO Ant colony optimization algorithm is metaheuristic global optimization algorithm inspired by the foraging behavior of ants [432]. It was introduced in the early 1990s, by Marco Dorigo [433] [434]. Ants explore stochastically the area surrounding to find the shortest path between

[11] Single-Sided Linear Induction Motors
[12] The Longitudinal End Effect
[13] Interior Permanent Magnet Synchronous Machine
[14] Total Harmonic Distortion
[15] Back-ElectroMotive Force
[16] Synchronous Reluctance Motor

food and nest. After evaluation the quantity and the quality of the food, the ants lay pheromone trails to remember their path and guide the other ants to the food. Further, the more ants follow this path, the trail is reinforced, and more likely ants are to follow it [435]. In contrast, over time, pheromones start evaporated [433]. Then, the longer the path, the faster pheromones evaporated, the less likely ants are to follow it.

Contrary to a natural ant, an artificial ant (agent) has a memory and can help in broadening the search area surrounding the agent. The probability, p_{ij}, that an ant k in node i moves towards the node j can be given by [433] [432]:

$$p_{ij}^{k}(t) = \frac{[\tau_{ij}(t)]^{\alpha}[\eta_{ij}(t)]^{\beta}}{\sum_{k \in N_i^k}[\tau_{ik}(t)]^{\alpha}[\eta_{ik}(t)]^{\beta}} \tag{6.11}$$

where η_{ij} is the heuristic information (Also called visibility or attraction), which is computed from prior knowledge often it is represented by the inverse of the distance between the two points i and j ($\eta_{ij} = 1/d_{ij}$), τ_{ij} is the quantity of pheromone, $N_i(k)$ is the feasible neighborhood of ant k, α and β are two parameters weighting the relative importance of pheromone value and heuristic information, respectively, and k is all the positions that are permitted.

After each iteration of algorithm, and when each ant has constructed its new solution, the pheromone trail is updated (evaporation and reinforcement). The pheromone trail is updated in the following way [433]:

$$\tau_{ij}(t+1) = \rho\tau_{ij}(t) + \underbrace{\Sigma_{k=1}^{m}\Delta\tau_{ij}^{k}}_{\Delta\tau_{ij}} \tag{6.12}$$

where ρ ($0 \leq \rho < 1$) is the trail persistence ($1 - \rho$ is the evaporation constant) and $\Sigma_{k=1}^{m}\Delta\tau_{ij}^{k}$ is the amount of pheromone adds by m ants to each pheromone trail.

The τ_{ij}^{k} is the quantity of pheromone per unit of length of trail, it can be expressed as in [433] [432]:

$$\begin{cases} \Delta\tau_{ij}^{k} = \frac{Q}{L_k} & \text{if the } k^{th} \text{ ant uses edge (i,j) in its tour between } t \text{ and } t+1 \\ 0 & \text{otherwise} \end{cases} \tag{6.13}$$

where Q is a constant and L_k is the tour length of the k^{th} ant.

Fig. 6.19 shows the flowchart of the PSO algorithm.

ACO has been used in the design optimization of electrical machines, some particular examples are given in

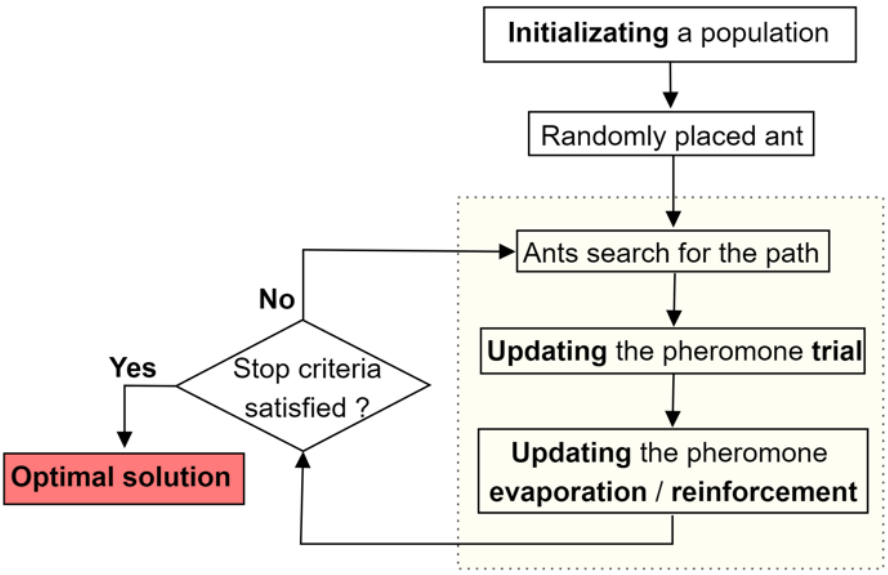

Figure 6.19: Flowchart illustrating the ant colony optimization algorithm

Table 6.3.

Table 6.3: Some ACO applications in electrical machines

Electrical Machine Type	Objective Function	Number of Design Parameters	Model
SRMs[17] [436]	Combination of average torque and efficiency	5	AN
IM[18] [437]	Combination of efficiency, starting torque, active material cost and temperature rise	7	AN

6.2.3.3 Multi-Objective Optimization Algorithms

The main difference between mono-objective and multi-objective optimization problems is presence of diverse multiple conflicting objectives. In the lest few years, there has been a growing interest in evolutionary multi-objective optimization algorithms. These algorithms combine the advantages of two major disciplines: evolutionary computation and the multi-criteria decision making [438]. Fig. 6.20 shows the classification of algorithms used in MOO. The first class of these algorithm, based on scalarization approach, was been developed in previous section. In this section, the evolutionary algorithms in MOO will be discussed. The main

[17]Switched Reluctance Motors
[18]Induction Motor

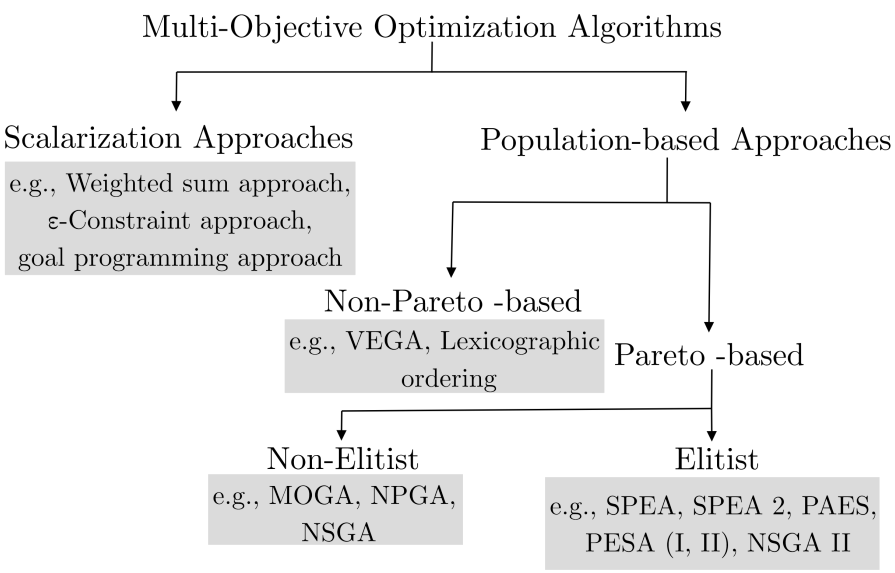

Figure 6.20: Classification of multi-objective optimization algorithms

goal of MOO is to find a good approximation of the Pareto optimal front while satisfying [438]:

- a good distribution of solutions
- a widespread solution set

The use of evolutionary algorithm to solve complex MOO problem, such as electrical machine, is motivated by the population-based nature of such algorithms [439]. In population-based multi-objective evolutionary algorithms (MOEAs), such as Vector Evaluation Genetic Algorithm **VEGA** (1984) [440] [441], Multi-objectives Genetic Algorithm **MOGA**(1993) [442], Niched Pareto Genetic Algorithm **NPGA** (1994) [443] [444], Non-dominated Sorting Genetic Algorithm NSGA (1994) [445], Pareto Archived Evolution Strategy **PAES** (2000) [446] [447], Non-dominated Sorting Genetic Algorithm II **NSGA-II** (2002) [448], Strength Pareto Evolutionary Algorithm **SPEA & SPEA2** (1999) [449] and Multiobjective Messy Genetic Algorithm **MOMGA** (2001) [450], a population of optimum are generated in single run. In addition, as metaheuristic algorithms, MOEAs have very large search spaces and they don't require prior knowledge from the problem. Furthermore, they are robust, less vulnerable to the shape and discontinuity of Pareto front, easy to implement and can run efficiently on a parallel [438] [451] [408]. More details of this algorithms may be found in [452] [453] [451]. Some example of MOEAs applied to electrical machines are presented in Table 6.4.

Table 6.4: Some examples of MOEAs in the design optimization of electrical machines

Electrical Machine Type	MOEA	Objective Function	Number of Design Parameters	Model
ML-PMSM[19] [454]	NSGA II	1. Average Torque 2. Total loss 3. Total mass	8	FEM
SM-PMSG/ST-PMSG[20] [278]	NSGA II	1. PM mass 2. Active part mass	8/9	RN
SM-PMSG[455]	MOGA	1. Machine mass 2. Machine cost 3. AEO[21]	8	AN
PMFSG[22] [456]	MOPSO	1. Induced voltage 2. THD 3. Machine mass 4. Machine cost	5	AN

One of the most important characteristics of MOA is their selection process. In order to generate the Pareto front in MOEA, ordering technique is required before the selection process. Raking methods sort individuals in objective function space. Then, a rank is associated to each possible point in objective function space before the selection. The dominance-based raking methods can be categorized into three groups (See Fig. 6.21)

1. Dominance rank: It is related to the number of solutions, in the population, that dominates the considered solution [457](e.g., MOGA and NPGA).

2. Dominance depth (Sort): It related to the rank of the considered solution in the non-dominated sorted population. Most of receltly developed algorithm are based on this technique [457](e.g., NSGA and NSGA II).

3. Dominance count : It is related to the number of solutions, in the population, that are dominated by the considered solution [457] (e.g., SPEA and SPEA II).

The most commonly used MOEA in electrical machine are presented in this section :

- **VEGA** VEGA was developed, in 1984, by Schaffer [440] [441]. It is an evolutionary algorithm where the Pareto dominance is not directly incorporated into the selection process. Indeed, in could be presented

[19] Multi-Layer Permanent Magnet Synchronous Machines
[20] Surface Mounted/Spoke-Type Permanent Magnet Synchronous Generator
[21] The annual Energy Output
[22] Permanent magnet flux switching generator

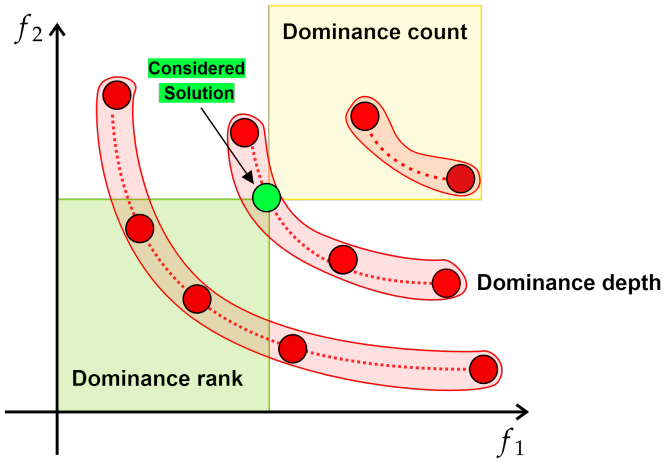

Figure 6.21: Techniques for dominance-based ranking

as GA with a particular selection mechanism. Suppose a given MOO problem with k objective functions, the idea of this algorithm is to divide the population into k equal sub-populations, which are selected by performing s selection according to each objective function, after that the sub-populations are reproduced separately. Finally, variation operators, including crossover and mutation, are applied to the whole population until the termination conditions are reached. Obviously, by using such selection process, which opposed to the concept of Pareto dominance, the algorithm will converge to the extremes and ignore the comprise solution [438]. In addition, non-convex Pareto sets can not be obtained with VEGA [372]. Further, many variations of VEGA has been introduced to enhance the performances of this method [438].

- **MOGA** MOGA was proposed by Fonseca and Fleming in 1993 [442], is the first MOEAs that uses the notion of Pareto dominance. Such algorithm aims to converge to the Pareto front, while maintaining as diverse a distribution as possible. In this method, a rank is associated to each individual. The rank of individual depends on the number of individuals that dominate it (See Fig. 6.22). Then, a fitness assignment is performed. For instance, rank 1 is associated to the non dominated individuals, high fitness values are assigned to these individuals. For more details about the fitness assignment see [458]. It has been used in the design optimization of synchronous reluctance motor (SyR), FEM was adopted to design the multiple flux barriers rotor. MOGA trends to perform well when compared to other MOO algorithms. However, it has been noticed that it produces poorly distributed solutions.

- **NSGA & NPGA** NSGA and NPGA has been proposed to overcome the drawbacks of MOGA, especially

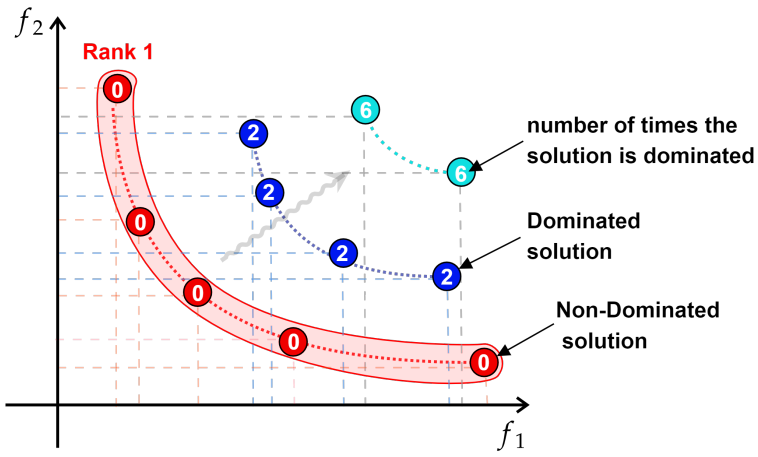

Figure 6.22: Pareto ranking in MOGA

the diversity of solutions. The NSGA is based upon the MOGA. The main difference is the the ranking procedure (computation of the efficiency of the individuals). As explain before, NSGA uses the dominance depth raking strategy, where the population individuals are ranked on the basis of non domination. All non-dominate individuals are grouped in one block, a dummy fitness function is associated to each individual (Sharing process), that is proportional to the population size and inversely proportional to the Pareto rank (sharing distance parameter σ_{share}). Then, this group is extracted from the whole population, the remaining indidivuals are reclassified. This process is repeated until ranking all the initial population individuals. Sharing allows the distribution of the population along the Pareto front in NSGA. Although its efficiency compared to MOGA, NSGA suffer from its lack of elitism and its dependence on the sharing distance parameter σ_{share}.

The NPGA is based upon the NSGA. The main difference is its new selection operator based on Pareto dominance, called tournament selection [443] [444]. In NSGA selection process, two individuals are compared. On the contrary, a subset of individuals, usually ten, is used to determine dominance. If one of the individuals in the subset is dominated and the other is not, then the non-dominated individual is selected. If both individuals are either dominated or non-dominated, we use fitness sharing [459]. See [443] [459] for more details about this selection methods. NPGA is easy to implement and efficient since it is applied only on a subset of population. However, its efficiency depend on the number of individuals in the subset, the sharing factor and tournament size.

- **NSGA II & SPEA2**

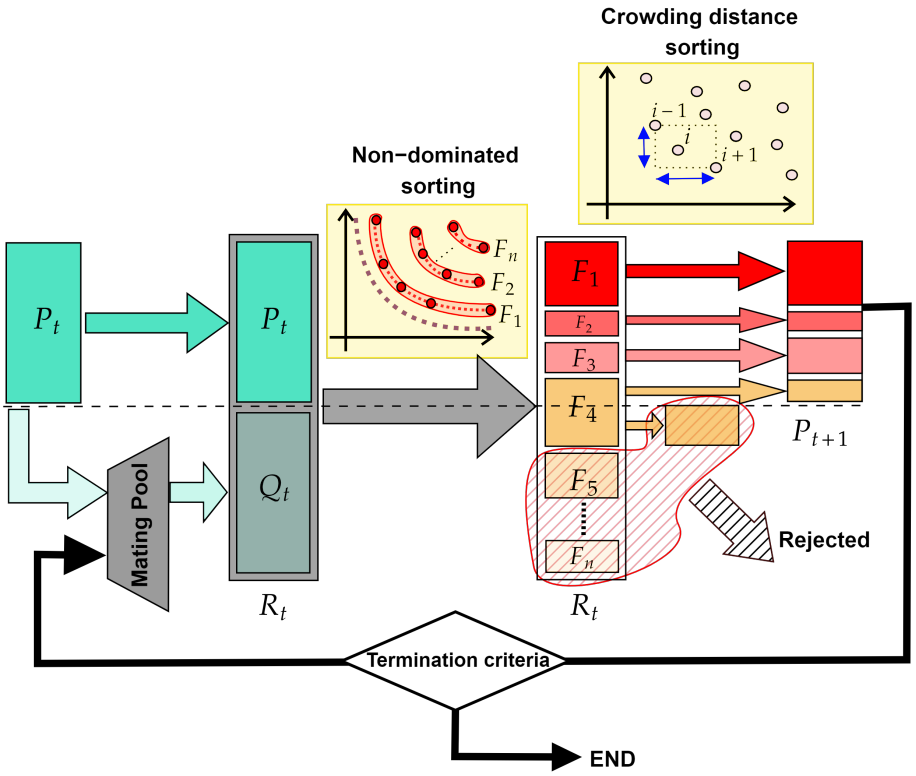

Figure 6.23: NSGA II procedure

NSGA II, introduced in 2002 [448], is an ameliorate version of NSGA, which has a better storing algorithm, integrate elitism [23] without specifying any priori parameters. NSGA II used the dominance depth ranking strategy, the population is then stored based on non dominance into several front. The following are the steps of the NSGA II algorithm (See Fig. 6.23):

1. **Generate a random initial population** P_0
2. **Initialize population the current population** $P_t = P_0$
3. **Create a mating pool of parents.**
4. **Create offspring population** Q_t.

   The offspring individuals are created using the initial population P_t, with N parents, and the previously defined genetic operator (selection, crossover). The two population are then combined to obtain population R_t of size $2N$.

5. **Sorting**

   The population R_t is classified using non dominated storing.

[23] Elitism is the process of preserving previous high performance solutions from one generation to the next [460].

⑥ **Create the new population P_{t+1}**

The parent population is replaced by the best selected individuals, in term of dominance and diversity. The filling of the new population P_{t+1} starts with the best non-dominated front F_1 and continues with solutions of the followed non-dominated fronts F_i, until the population P_{t+1} size reach N. The diversity is preserved by using a crowding approach [448] [459] (See Fig. 6.23). The rest of fronts are deleted.

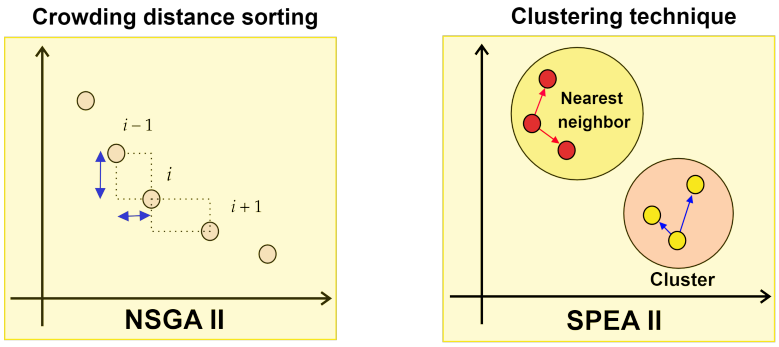

Figure 6.24: Comparison between fitness assignment in NSGA II (Crowding) and SPEA2 (Clustering)

The SPEA2 is similar to NSGA II. The main difference is in the fitness assignment process. While the diversity preserving mechanisms in NSGA II is based on crowding sort approach, in SPEA2 truncation approach ($k-$nearest neighbor approach) is adopted. Additionally, in NSGA II the individuals are stored into different front based on non domination, then an rank is assigned to each individual; whereas in SPEA2 a raw fitness, calculated based on the strength value of solutions who dominate it (clusters), is assigned to each individual [449] (See Fig. 6.24).

6.3 Recent Developments On The Design Optimization Of Electrical Machines

There has been numerous studies in the design optimization of electrical machine, in this section a review of recent works is presented (See Table **??**).

Table 6.5: Recent developments on the design optimization of electrical machines

Electrical Machine Type	MOEA	Objective Function	Number of Design Parameters	Model
FS-PMBM[24] [461]	PSO	$f(k_e, k_w) = C_e(1-k_e) + C_w k_w + p_f$ k_E is the efficiency, is the active weight, C_e is the weighting factor of efficiency, C_w is the weighting factor of the active weight, p_f is the penalty function (magnetic saturation)	4	2D AN
SM-PMSG [462]	PSO	$f(T_{cog}) = min(T_{cog})\ T_{cog}$ Cogging torque	4	2D AN
AF-PMSG [463]	GA	$f(T_{av}) = max(T_{av})\ T_{av}$ Average torque & $f(EMF) = min(B - EMF)$ B-EMF Back-EMF	5	RN
SM-PMSG [464]	PSO	$f(T_{av}) = max(T_{av})\ T_{av}$ Average torque $f(N_{elc}) = min(N_{ele})\ N_{elc}$ Electromagnetic noise	5	RN (magnetic, thermal, electrical) AN (vibro-acoustic, mechanical)
PMa-BSynRM[25] [465]	NSGA II	1. $f_1(T_r) = min(T_r)\ T_r$ Torque ripple 2. $f_2(F_r) = min(F_r)\ F_r$ Suspension force ripple 3. $f_3(PF) = P_f - P_f^*\ P_f$ Guarantee specified power factor	11	FEM
HESM[26] [466]	NSGA II	1. $f_1(er_{HR}) = min(er_{HR})\ HR$ Guarantee specified hybridization Ratio 2. $f_2(m_{cost}) = min(m_{cost})\ m_{cost}$ Machine's cost	8	RN
Vernier Machine [467]	NSGA II	1. $f_1(T_{av}) = max(T_{av})$ 2. $f_2(T_r) = min(T_r)$ 3. $f_3(\nu) = max(\nu)\ \nu$ Machine's efficiency	6	AN
D-PMM[27] [468]	NSGA II	1. $f_1(T_{av}) = max(T_{av})$ 2. $f_2(T_r) = min(T_r)$ 3. $f_3(T_{cog}) = min(T_{cog})$	9	FEM (Kriging surrogate)
BSRMs[28] [469]	MOPSO / NSGA II/ MOGPSO[29]	1. $f_1(T_{av}) = max(T_{av})$ 2. $f_2(\nu) = max(\nu)$ 3. $f_3(m_{weight}) = min(m_{weight})\ m_{weight}$ Machine's weight	4	AN
C-PMLSM[30] [470]	DE[31]	$f(x_w, x_{loss}, x_{rip}) = C_1 x_w + C_2 x_{loss} + C_3 x_{rip} + p_f$ x_w is the motor weight, x_{loss} is the loss, x_{rip} the thrust ripple on the basis of the average thrust, C_i are the weighting factors p_f is the penalty function	5	3D AN

[25] Permanent Magnet assisted Bearingless Synchronous Reluctance Motor
[26] Hybrid Excitation Synchronous Machine
[27] Double Permanent Magnet Machine
[28] Bearingless Switched Reluctance Motors
[29] MOGPSO novel Multi-Objective Genetic Particle Swarm Optimizer
[30] Coreless PM Linear Synchronous Motors
[31] Differential Evolution

6.4 Optimization Procedure

① **Set the specifications from the application**

Define the requirements of the application such as the operational speed, the rated torque, the machine's power, efficiency, weight, size, thermal and mechanical properties, etc.

② **Choose the initial design**

At this stage the initial design is selected considering machine type, topology, dimensions and materials. The analytical models presented in the previous chapters are useful to calculate the parameters and performance for a given topology and varied design parameters, that may serve as good starting points for a few initial dimensions that can fulfill the given machine requirements.

③ **Implement multi-physics model**

The multi-physics model is used to evaluate the performances of the initial design.

④ **Formulating the optimization problem according to the deign optimization**

In this step, objective functions are set, constraints are defined and design variables are selected.

⑤ **Objective functions**

⑥ **Perform optimization**

⑦ **Validate the optimization**

6.5 Conclusion

This chapter presented a review of electrical machine design optimization. Several optimization structures, model and algorithms were covered and compared. Given the multi-objectives and multi-constraints typically required in the pre-design optimization of electrical machines, one can concluded that:

- **Coupled multi-disciplinary analysis based** on the developed magneto-thermal model have been judged suitable in this design stage.
  - Although the decoupled formulation relaxes the coupling constraints during the optimization and so less computation cost is needed compared to the coupled formulation, it became prohibitive in the case of complex engineering systems.

    - Decoupled formulation are not efficient because of the inactivity of the processors running the inexpensive analyses and optimization which is waiting for the updates from the other processors.

- **Sizing optimization** can be a promising option in preliminary design stage when combined with suitable search algorithms.
- **Mono-level optimization** is suitable option in early stage optimization. The multi-level design optimization methods are known to be fairly simple to implement. However, the computational cost is usually very high since the optimization problems of the electrical machines are nonlinear and multidimensional.
- **NSGA-II** would be suitable in the case with large number optimization parameters problems.

Chapter 7

15 MW Wind Generator Design - Optimization

7.1 Introduction

The design optimization of electrical generator is a non-linear multi-objective problem. Although, the main aim of this thesis is to reduce the use of rare-earth permanent magnets in large wind turbine generators, several objectives such as highest efficiency, lowest cost and minimum mass of active materials should be simultaneously met.

As explained in section 3.2.3, there are several generator types that are possible to use in DD-PMSG. Only three topologies were selected for further investigation. Considering the goal of this thesis, which is the reduction of the use of rare-earth permanent magnet in large PMSG, many other criteria for the comparison of these machines were set. In this chapter, a design optimization of the selected PMSGs, for 15 MW direct-drive wind turbine, is conducted by solving an optimization problem using NSGA II algorithm. The goal is to minimize the mass of the machine and fulfil certain non-linear inequality constraints that guarantee the required thermal and magnetic behaviours. The surface-mounted radial-flux machine is used as a reference in the comparisons.

Although FEM and RNM are capable of providing accurate results for the optimization design, they are time-consuming taking several days or even weeks. The main contribution of this thesis is to develop a multiphysics model for radial PMSGs, which when integrated in optimization process provides the

different optimal performances with reasonable computation time in the preliminary design stages. The aim of this work is to find the suitable electrical machine for ultra-large wind turbine in terms of rare-earth PM use, machine's mass and efficiency. In the first section, the optimization methodology is presented. Then, a comparative study between two optimization designs is conducted, one based on linear AM and an other on nonlinear RNM for the magnetic design, both models are coupled with LPTM for the prediction of the thermal behaviour of the machine. The validity of the analytical model will be confirmed by FEM. In the last section, a comparative design of different permanent magnet synchronous generators for 15 MW wind turbines will be discussed.

7.2 Optimization Procedure and Specifications of 15 MW Permanent Magnet Synchronous Generator for Wind Turbine

The optimization for electric machines design is highly nonlinear, high dimensional and strongly constrained problem, then the conventional optimization are not affective in finding the optimum design. As was foreshadowed in the previous chapter, stochastic population-based algorithms such as evolutionary and swarm-based algorithms including memetic algorithm, genetic algorithm, genetic programming, evolutionary programming, evolution strategy, cultural algorithm, differential evolution, scatter search, path relinking, Ant colony optimization, particle swarm optimization, bee colony optimization, fish swarm algorithm, firefly search and monkey search seem to be suitable for such optimization problem. One of the most efficient algorithm applied in multi-objective engineering optimization problems is the NSGA II.

7.2.1 Criteria for the comparison between the proposed machines

Considering the goal of this thesis, which is the investigation of the active material mass and permanent magnet mass reduction, the criteria used for comparison between the different investigated topologies are torque density, airgap radius, losses, total volume and efficiency.

7.2.2 Objective function

When designing electrical machines, engineers attempt to maximize the performances of the machines while keeping as small as possible the quantity of materials used (copper, steel, permanent magnet, etc)

especially in high-torque low-speed applications. As explained in section 3.2.1, as the wind turbine size grow, the design requirements could become more stringent in terms of the tower's top weight ans size, this is mainly due to limitation associated with the transportation, assembly and installation [471]. In addition, the instability of the rare-earth permanent magnet made the optimization of permanent magnet use in PMSG mandatory. To sum up, direct-drive PMSG have very large size machines, which makes them expensive, heavy and difficult to build, transport and install. Two objective functions were chosen in this thesis, the active weight of the machine, m_{act}, and the permanent magnet mass, m_{PM}, which have to be minimized.

The general scheme of the design-optimization approach of ST-PMSG is shown in Figure 7.1.

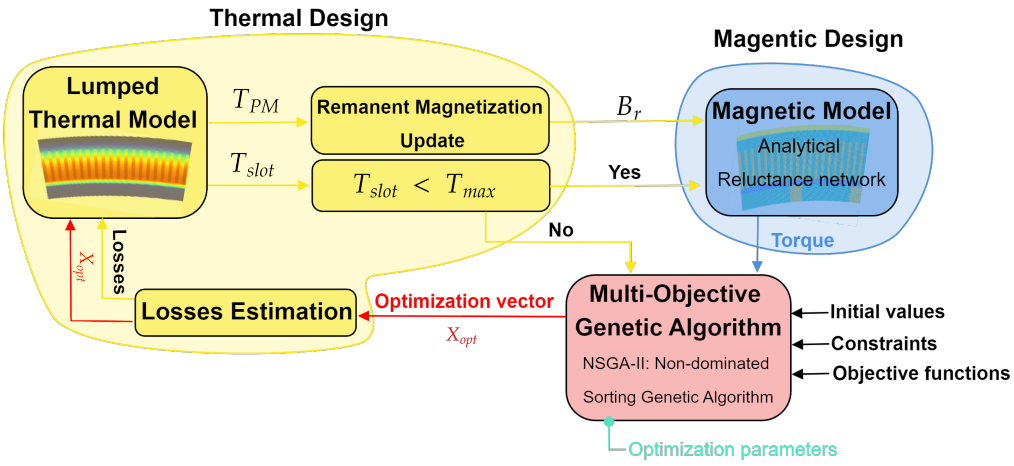

Figure 7.1: Design optimization approach of ST-PMSG

7.2.3 Optimization variables

The sizing model of PMSGs were coupled with multi-objective genetic algorithm NSGA II in order to evaluate the influence of some design parameters on the PMSG machine, and determine the feasible design corresponding to the smallest possible value of objective functions while respecting design specification and constraints. There are various design variables related to the geometry and the configuration of the PMSGs. In order to get convenient results for the preliminary design process, it is important to reduce the number of design variables and diminish the amount of computations. Based on literature survey and the some industrial products, some independent variables were chosen as a key variables for the optimization process. The selected set of independent variables, X_{opt}, which specify the search space of

the proposed machine optimization, is: $X_{opt} = [R_g, L_{act}, h_s, \theta_s, h_{PM}, \theta_{PM}, J_s, h_{ys}, h_{yr}]$

1. Mean airgap radius R_g (the mid airgap radius)
2. Stack length L_{act}
3. Stator slot height h_s
4. Stator slot opening θ_s (the stator slot width to the stator slot pitch)
5. Permanent magnet height h_{PM}
6. Permanent magnet opening θ_{PM} (the permanent magnet width to the pole pitch)
7. Slot's current density J_s
8. Stator yoke height h_{ys}
9. Rotor yoke height h_{yr} (used only in SM-PMSG and I-PMSG)

7.2.3.1 variables boundary

Because of the electromagnetic and mechanical limitations, some constraints should be considered for the optimization design variables.

7.2.3.1.1 Mean airgap radius and stack length The minimum airgap diameter is limited by the torque requirement while the maximum depends on some mechanical and logistic considerations. The mechanical strength of materials, vibrations, thermal expansions, transportation and manufacturing facility limit the generator radius. However, the axial length of low-speed high torque machines depends on may limiting factors such as the length of the cooling paths, torsional stress in shaft, rotor eccentricity etc.

7.2.3.1.2 Stator slot dimensions The minimum slot area should be provided to place the coils in the slots, however, for mechanical reason, the ratio of slot height to slot width, α_s, is limited to 4 - 10.

$$4 < \alpha_s = \frac{h_s}{w_s} < 10 \tag{7.1}$$

The rms value of the linear current density around the airgap circumference, A, defined in Eq. 3.8 can

be expressed as follow

$$A = \frac{J.A_{Cu}}{2.\pi.(R_g + e/2)} = \frac{n_s.I_s}{2.\pi.(R_g + e/2)} \tag{7.2}$$

where n_s is the number of coil turns, I_s is the rms value of the conductor current, A_{Cu} is the bare copper area in the slot ($A_{Cu} = A_{bare} \times n_s = k_f \times A_{slot}$) and J is the current density.

The expression in Eq. 7.2 shows that the linear current density is proportional to the number of turns and inversely proportional to the stator bore diameter. Additionally, the stator synchronous inductance is proportional to the squared number of turns. For instance, in SM-PMSG the direct (L_d) and quadrature (L_q) axes synchronous inductances are quite similar sine the permeability of the magnets is almost the same as that of air. Synchronous inductance, L_s ($L_s \simeq L_d \simeq L_q$), consists of magnetising inductance, L_m, and stator leakage inductance, L_σ, so that

$$L_s = L_m + L_\sigma \propto n_s^2 \tag{7.3}$$

On the one hand, it should be noted that if the diameter is decrease, it is difficult to use large slots, because otherwise, the teeth will become smaller resulting in high magnetic saturation level. On the other hand, rising the slot's height leads to large leakage inductance values. That's why a high values of electric loading leads to a high value of the stator synchronous inductance, resulting on reactive voltage drop of the machine and then considerable increase on the the cost of the converter [172].

7.2.3.1.3 Permanent magnet dimensions The permanent magnet volume should be large enough to produce the required rated torque. The lower limits on the magnet width are usually set to reduce the airgap tangential fringing flux. In SM-PMSG, this is could be set to three times the airgap length. Further, the upper limits of the magnets width are set to lower the leakage flux between two adjacent magnets. The permanent magnet height should be higher enough to prevent the demagnetization. However, over certain limits the flux density in the airgap might become large enough causing the steel saturation, and then reduce considerably the machine performances. The aim of the proposed optimization is to minimize the mass of the permanent magnet in order to reduce the weight, size and cost of the machine.

7.2.3.1.4 Slot's current density To prevent excessive cooling requirement and enhance the reliability of the machine, the slot's current density is limited over the range of 2.5 - 6 A/mm^2. As explained before, in direct-drive PMSG, large diameters are required to attain high power rating. Then the surface area available for heat dissipation is bigger, and the passive heat transfer is enhanced. All the selected machines are supposed to operate under forced air-cooling conditions. The windings are assumed to be cooled indirectly; by forced air flowing over the outer surface of the machine. In enclosed machines, this can be done by mounting a cooling fan on the generator shaft, or at the end of the machine. A passive cooling is supposed in the rotor since the the rotor losses in PMSG are small.

7.2.3.1.5 Stator and rotor yoke height Low-speed machines with high number of poles have a small magnet pitch and a low magnetic flux through the stator and rotor yokes. Then, the yokes in this particular machines may be relatively thin < 50 mm. The maximum flux density of the teeth is the most important constraint and the critical parameter to monitor the saturation phenomena. Considering the flux paths and the continuity of flux, the stator and rotor yoke height must be 1.5 times larger that the tooth width.

The range limits of the design variables will be further presented before each optimization scenario.

7.2.4 Fixed values, assumptions and constraints

In the design optimization process, some values are chosen to be fixed and there are also some restrictions that must be fulfilled. The number of poles, the airgap length, the filling factor, the number of slots, the number of turns per slot and number of phases are chosen to be fixed. The filling factor, k_f, is set to 0.66, which is practically fair considering bar-wound machines.

Concerning the stator, the chosen winding technology impacts the machine main characteristics, namely, the pair pole number, the slot number, the Joule losses and the thermal behaviour, the efficiency, the machine volume, etc. Taking into account the turbine nominal speed (7.5 rpm), the generator frequency is low (between 10 Hz and 15 Hz) comparing to the grid frequency (50 Hz in France). However, the electrical frequency should be kept high enough (> 10 Hz) in order to avoid additional cyclic temperature stress on the transistors of the power converter, then prevent over-dimensioned IGBTs. Lower frequencies necessitate very high number of pole pairs which make the feasibility of the generator very complex when it is not impossible and impose that the copper volume of the stator windings becomes the major source

of losses in the machine. In fact, the presence of a rectifier and an inverter between the generator and the grid reduces the constraints on the stator current and voltage harmonic contents. In this context, it seems that the modular winding technology could a good alternative to reach the different goals in the early design wind generator. So, both winding configuration, distributed and concentrated, was investigated in this thesis.

The cogging torque is undesirable component especially at low speeds. In order to reduce the cogging torque ($< 0.2\%$ of nominal torque), an effective way is to consider a combination of pole pair number and stator slots number having a high least common multiple, their greatest common divisor defining the magnetic period of the machine (the rank of the fundamental components of rotor and stator airgap flux densities which are involved in the main interaction between stator and rotor and giving the main electromagnetic torque). As there is an important number of combinations, it is not always obvious to discriminate the different possible combinations. One way to choose a combination is to focus on the combinations having a large value of least common multiple (The LCM represent the value of the first harmonic of the cogging toque, so high LCM traduces very low cogging) and a greatest common divisor helping to guarantee the desired value of the stator phase voltage (usually 6.6 kV in large generators), the phase windings, each per magnetic period of the machine, being connected in parallel. One efficient way to get large LCM is to select a slot's number close to number of poles. Furthermore, the cogging torque is caused by the attraction between permanent magnets on the rotor and the steel teeth on the stator, then it depends on other design parameters such as the slot opening, magnet width, skewing, etc. Controlling these parameters may help to reduce the cogging torque although the combination of pole and slot numbers is not advantageous. Finally, a low cogging torque does not often warranty a low torque ripple at load conditions.

7.2.4.1 Constraints

The machine designs are subject to two major constraints, one related to the maximum permissible temperature in the winding and an other one on the minimal rated torque to achieve the required power. To simplify the transportation, the site location may impose other constraints.

7.2.4.1.1 Maximum winding temperature We use F class high voltage insulation materials, the allowable maximum winding temperature would be 155 ^{o}C. As shown in Fig. 7.2, the maximum operating

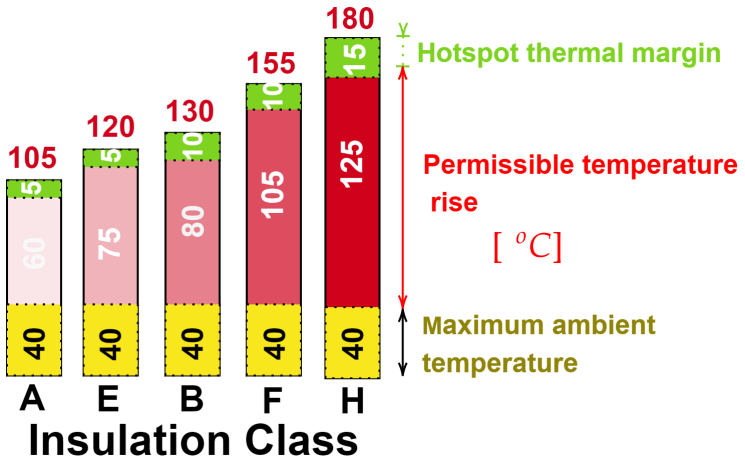

Figure 7.2: Temperature limits in accordance with standard design practices IEC 60034-1

temperature is reached by adding up the machine's ambient temperature (usually 40 ^{o}C), the permissible temperature rise, and the hotspot thermal margin (often between 5-15 ^{o}C). Electrical machines are usually designed with an average temperature below the rated hot-spot temperature to allow for acceptable life. Then, an average of 125 ^{o}C is used to allow margins for local hotspot. Often, insulation does not fail when reaching hotspot operating temperature, but useful operating life declines quickly. The standards in Table 7.1 refers to the classification of materials and insulation systems.

Table 7.1: Electrical machine thermal classes and insulation materials (IEC 60085 [40])

Insulation class NEMA [472]	Maximum permissible temperature	Materials
A	105 [^{o}C]	Cotton, silk, paper, synthetic fibers, vinyl acetate, etc. (impregnated with natural resin, cellulose esters, insulation oils, etc.)
E	120 [^{o}C]	Synthetic resins, enameled wires, cellulose, etc.
B	130 [^{o}C]	Mica, glass fibre, asbestos, shellac, bitumen, silk, polyesters, etc.
F	155 [^{o}C]	Mica, glass fibre, asbestos, epoxy, polyamides, silicone, etc. (materials with binders capable of higher thermal stability)
H	180 [^{o}C]	Silicone elastomer, epoxy, silicone combination of mica, glass fibre, asbestos, etc.

The thermal model is used not only to estimate the maximum winding temperature but also to correct the remanent flux density, that is related to the maximum temperature in the PM.

7.2.4.1.2 Required Torque The machines must respect an other constraint, the rated torque to achieve the requested rated power.

7.3 Design Optimization Validation of Semi-Drive Permanent Magnet Synchronous Generator

This section presents a design optimization of semi-direct (90rpm) 15 MW penta-phased single-layered ST-PMSG, SM-PMSG and I-PMSG in order to analyse the level of accuracy and time effectiveness of analytical model in the pre-design stages. In this context, the already developed magnetic models for PMSGs, linear AM and non-linear RNM, are combined respectively to a thermal lumped parameter model and then coupled to NSGA II in order to optimize the mass of both rare-earth magnets and generator's active materials. The optimization results will be illustrated for each model. Then, the design is verified using FEM.

In Table 7.2, a parametric design optimization is described in which minimizing the PM mass and active part of the machine is achieved by varying nine geometric variables. The multi-physic sizing model of PMSGs is coupled NSGA II in order to evaluate the maximum torque delivered and the hottest slot's spot, to provide the required power and prevent the overheating, respectively. As explained in the section 3.2.3.1, the temperature of the permanent magnets has an influence on remanent flux density, then the remanent flux density is corrected according to the resulting permanent magnet temperature. At a preliminary design stage and based on limits imposed by the mechanical stiffness and the thermal expansions 20 mm airgap has been chosen.

Table 7.2: Optimization problem of 100rpm-15MW PMSGs: key design parameters, bounds and constraints

<table>
<tr><th colspan="3">Fixed parameters</th><th>Constraints</th><th>Objectives functions</th></tr>
<tr><td>PMSG</td><td>SM-</td><td>I-</td><td rowspan="7">$T_{max} \leq 125\ ^{o}C$
$\Gamma_{max} \geq 1.6MNm$</td><td rowspan="7">$f_{Obj_1} = \min(m_{PM})$
$f_{Obj_2} = \min(m_{act})$</td></tr>
<tr><td>Nominal speed [rpm]</td><td colspan="2">100</td></tr>
<tr><td>Number of pole pairs</td><td colspan="2">26</td></tr>
<tr><td>Number of slots</td><td colspan="2">520</td></tr>
<tr><td>Winding topology</td><td colspan="2">Penta-Distributed</td></tr>
<tr><td>Permanent magnet</td><td colspan="2">N40SH (B_r=1.2 T)</td></tr>
<tr><td>Airgap [mm]</td><td colspan="2">20</td></tr>
<tr><td>Bounds</td><td colspan="4">LB/UB =
[R_g[m], L_{act}[m], θ_s[%], h_s[m], θ_{PM}[%], h_{PM}[m], J_s[A/m^2], h_{ys}[m],h_{yr}[m]]</td></tr>
</table>

SM-PMSG	LB	[1.00, 1.00, 0.40, 0.05, 0.70, 0.01, 2.5e6, 0.03, 0.03]
	UB	[3.50, 2.50, 0.55, 0.20, 0.95, 0.04, 5.0e6, 0.07, 0.07]
I-PMSG	LB	[1.00, 1.00, 0.40, 0.05, 0.70, 0.01, 2.5e6, 0.03, 0.03]
	UB	[3.50, 2.50, 0.55, 0.20, 0.95, 0.04, 5.0e6, 0.07, 0.07]

During the simulations, the optimization algorithm NSGA II was tuned as it is indicated in Table 7.3.

Table 7.3: Optimization Option of 100 rpm-15 MW PMSGs

Parameters	Value
Population size	150
Maximum generation	400
Crossover probability	0.8
Termination tolerance on the fucntion value	1.10^{-8}

7.3.1 Results and Discussion

7.3.1.1 Evaluating Analytical Model Accuracy

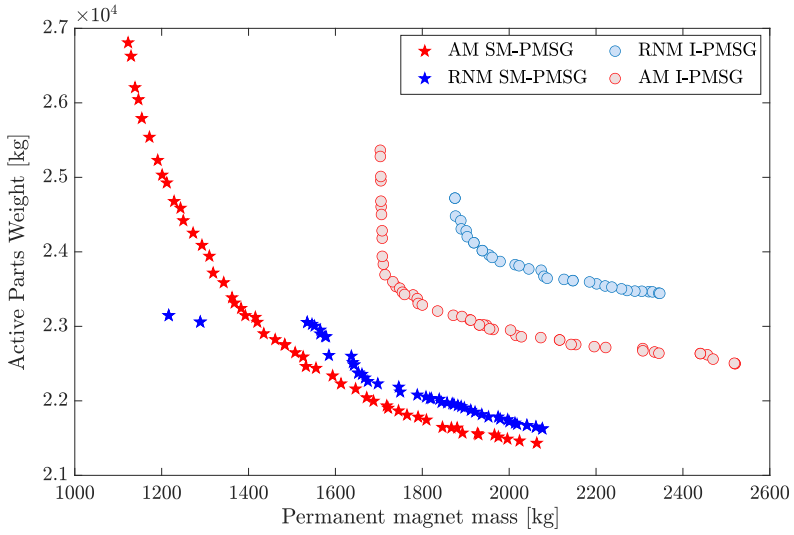

Figure 7.3: Pareto optimality of 15 MW-90 rpm SM-PMSG & I-PMSG with NdFeB N40SH (B_r = 1.2 T)

7.3.1.1.1 Results

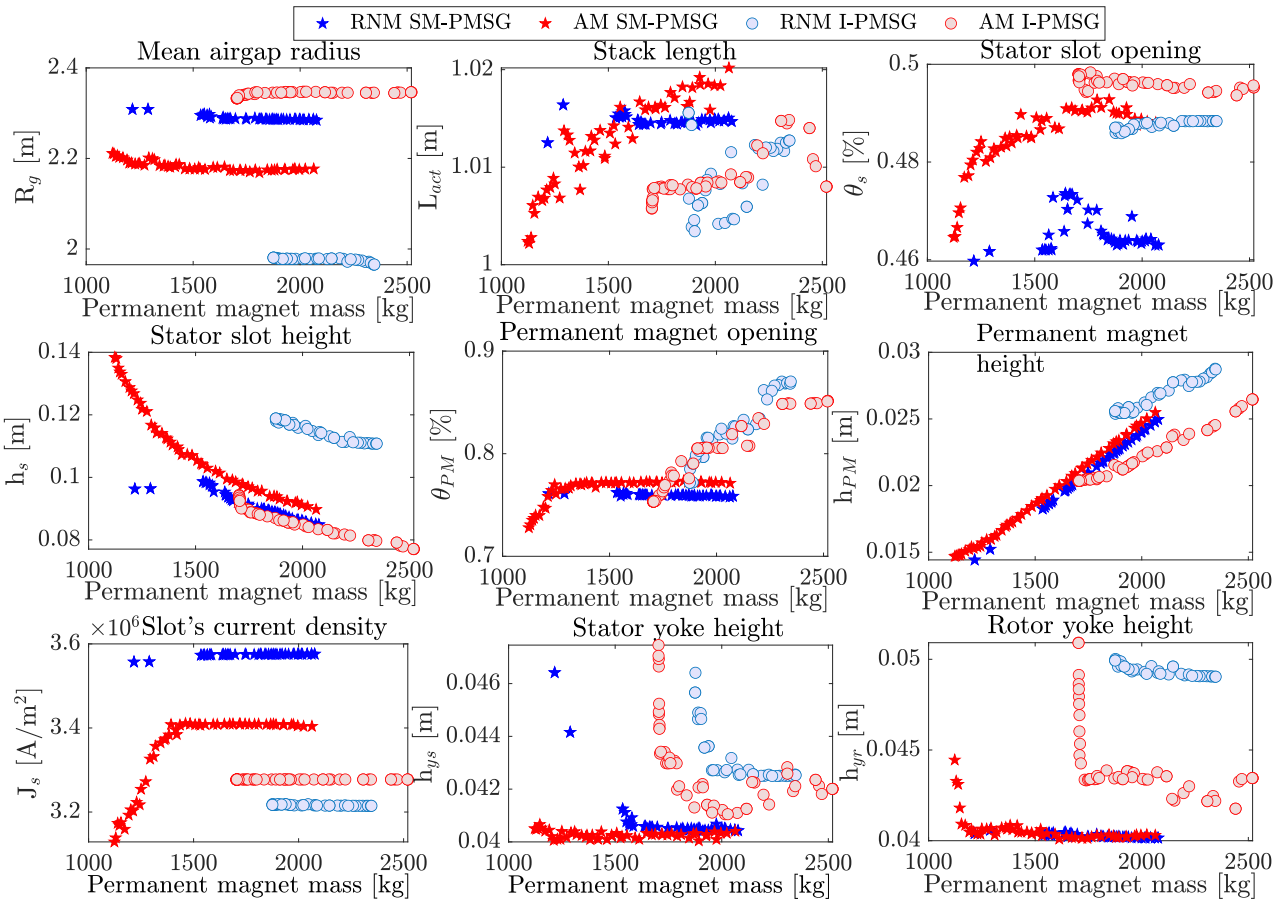

Figure 7.4: Variation trends of optimized machine parameters (p=26 & N_s=520 with NdFeB N40SH (B_r = 1.2 T))

7.3.1.1.2 Discussion Fig. 7.3 shows the Pareto front "machine's active parts mass vs. permanent magnet mass" obtained with the AM and RNM for two different topologies. In order to evaluate the accuracy of analytical model, it is necessary to compare the effect of each optimization variable on the machine (comparing topologies is not the objective of this section). The effects of stator, rotor, and PM dimensions on the produced torque are studied. The results of every single geometrical and physical parameter are presented in Fig. 7.4, the optimization variables from the design optimization process based on linear analytical model are compared with those from an optimization process based on nonlinear reluctance network model. The main conclusions that can be drawn from this study are :

- The Pareto fronts in Fig. 7.3 confirm the relationship between the machine's mass and permanent magnet mass, an increase on the mass of the permanent magnet help to reduce the generator active parts weight.
- Pareto optimal machines found by using RNM are heavier compared to those found by using AM

for the tested topologies. The gap between the two Pareto fronts depend on the machine's topology and its magnetic saturation. In Fig. 7.3, it can be noticed that the largest gap between the Pareto fronts is for the I-PMSG. This could be explained by the consequent saturation of the machine iron parts. Indeed, the magnetic model trends to increase the dimensions of the slots to enhance the machine's efficiency, due to non consideration of the magnetic saturation the linear model tries to open the slot more than the nonlinear model (θ_{s_L} = 0.485 % - $\theta_{s_{NL}}$ = 0.465 % for SM-PMSG and θ_{s_L} = 0.496 - $\theta_{s_{NL}}$ = 0.486 % for I-PMSG), and then to compensate the reduction of magnetomotive force the non-linear model either increases the airgap radius or the slot's height.

* In the case of the I-PMSG, the RNM results on machines with lower airgap radius (See Fig. 7.4) (around $R_{g_{NL}}$= 1.97 m - R_{g_L}= 2.34 m) but the slot's height is 25 per cent larger ($_{s_L}$ = 0.085 m - $h_{s_{NL}}$ = 0.114 m))compared to AM. The mean axial length is almost the same for the two models (L_{act_NL} = 1.0090 m for SM-PMSG and L_{act_L}= 1.0091 m for I-PMSG).
* In the case of the SM-PMSG, the RNM results on machines with larger airgap radius (See Fig. 7.4) (around $R_{g_{NL}}$= 2.29 m - R_{g_L}= 2.18 m), while the slot's height is nearly the same for both models (h_{s_L} = 0.108 m - $h_{s_{NL}}$ = 0.091 m), while approximately the same mean axial length is obtained with the two models (L_{act_NL} = 1.016 m for SM-PMSG and L_{act_L}= 1.018 m for I-PMSG).

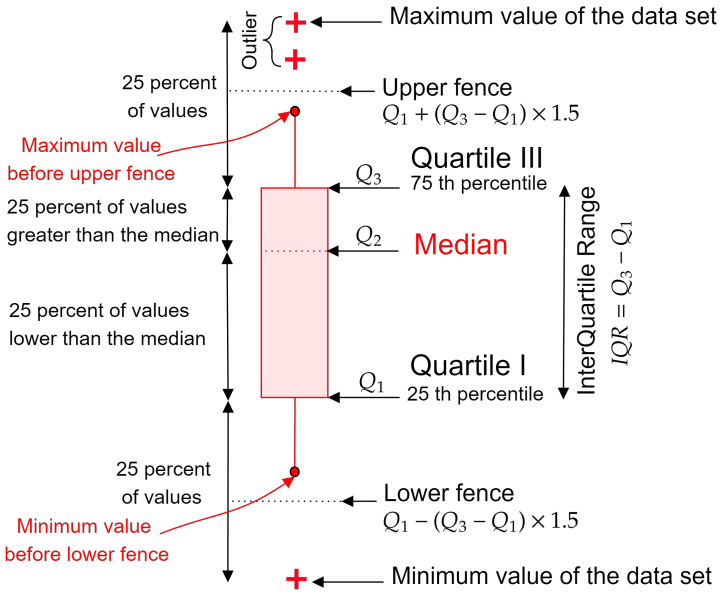

Figure 7.5: Interpreting box plot

– To visualise the differences in the distribution of the optimization variables, the variables were represented in a box plot (See Fig. 7.5). The boxplot analysis, also known as 5-number summary (Q_1, Q_2, Q_3, lower and upper fence), it gives an graphical information about the location, the dispersion and the skewness of a data set. As shown in Fig. 7.5, the interquartile range (IQR), which is difference between the lower and upper quartiles (represented by the lengths of the box), measures the spread of the middle 50 per cent of the data. The larger the box is, the more widely spread out from the mean the data are. The median, represented by the line that divided the box, marks the middle value of the data set (half the scores are greater than or equal to this value and half are less). Then, the larger the median, the larger the variable average.

Fig. 7.8 and Fig. 7.9 display the multiple boxplot of the 9 variables of SM-PMSG and I-PMSG, respectively. Table 7.4 gives a statistical descriptive of maximum value, minimum value and mean value of each optimization variable.

Table 7.4: Maximum, minimum and mean values of the optimization variables (SM-PMSG & I-PMSG)

Variables	Units	Min				Max				Mean			
		SM-PMSG		I-PMSG		SM-PMSG		I-PMSG		SM-PMSG		I-PMSG	
		L	NL	L	NL	L	NL	L	NL	L	NL	L	NL
R_g	m	2.169	2.285	2.333	1.965	2.211	2.308	2.347	1.981	2.184	2.909	2.343	1.977
L_{act}	m	1.002	1.013	1.006	1.003	1.020	1.016	1.015	1.016	1.013	1.015	1.009	1.009
θ_s	^{o}	0.322	0.318	0.341	0.336	0.341	0.327	0.345	0.338	0.336	0.323	0.343	0.337
h_s	m	0.089	0.084	0.077	0.111	0.138	0.098	0.094	0.118	0.108	0.091	0.086	0.115
θ_{PM}	^{o}	5.039	5.248	5.215	5.341	5.354	5.277	5.895	6.025	5.301	5.259	5.523	5.708
h_{PM}	m	0.015	0.014	0.020	0.025	0.025	0.024	0.026	0.029	0.019	0.021	0.022	0.027
J_s	A/mm^2	3.129	3.557	3.276	3.215	3.411	3.576	3.277	3.219	3.348	3.574	3.277	3.216
h_{ys}	m	0.040	0.040	0.041	0.424	0.041	0.046	0.047	0.046	0.040	0.041	0.042	0.043
h_{yr}	m	0.040	0.040	0.041	0.490	0.041	0.044	0.050	0.050	0.040	0.041	0.044	0.049

∗ For the SM-PMSG, it can be noticed that the boxplots of RNM are relatively short compared to the AM ones, and then the optimization variables are more spread out in AM. Optimization variables resulting from RNM expect the stators slots dimensions and the opening of the permanent magnet have often greater median than AM. This is mainly due to the non consideration of the saturation, with reduced volume (See Fig. 7.6), AM tries to increase the shear stress by increasing either the magnetic or the electric loading. The electric loading is related to the current density, so with the same cooling technology and insulation materials increasing the slot's opening and height enhance the electrical loading. Further, the magnetic loading is related to the airgap flux density, so boosting the magnetic loading is possible by varying the permanent

magnet dimensions. While with nonlinear RNM the magnetic flux density developed is limited by the characteristics of the iron used, with AM the it varies more freely. The Fig. 7.6 and Fig. 7.7 confirmed that the AM require less machine volume than RNM, and then shear stress is higher for AM.

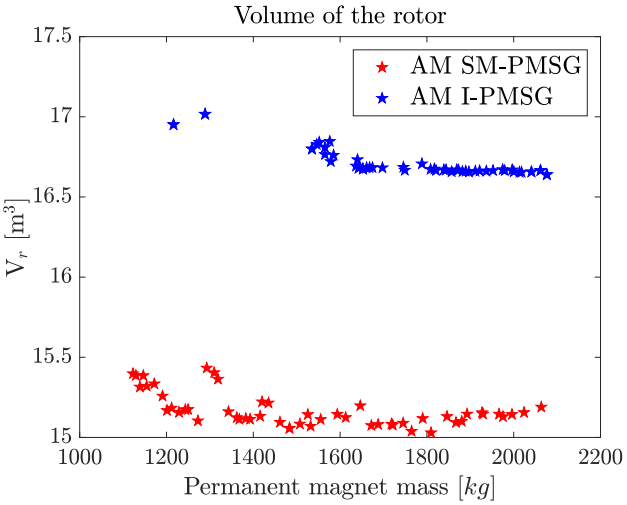

Figure 7.6: Rotor volume of the SM-PMSG

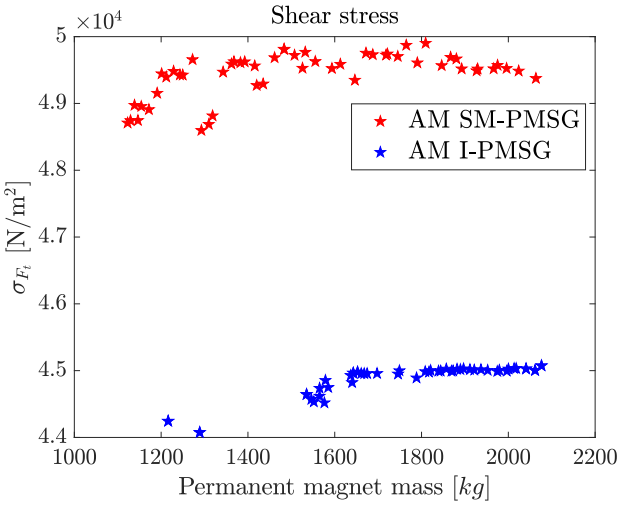

Figure 7.7: Shear stress of the SM-PMSG

∗ For the I-PMSG, it can be noticed also that the boxplots of RNM are relatively short compared to the AM ones, so the optimization variables are more spread out in AM. Contrary to what had been seen with SM-PMSG, in I-PMSG the median airgap radius is much higher in AM while the slot and permanent magnet dimensions are smaller with AM optimization results when compared to RNM ones.

7.3.1.2 Evaluating Analytical Model Rapidity

In this section, a comparison is conducted between the optimization design models in terms of computation time. ST-PMSG was taking as an example. In Table 7.5, a parametric design optimization is described in which minimizing the PM mass and active part of the machine is achieved by varying eight geometric variables.

Table 7.5: Optimization problem of 90rpm-15MW ST-PMSG: key design parameters, bounds and constraints

Fixed parameters		Constraints	Objectives functions
PMSG	ST-PMSG		

$T_{max} \leq 125\ ^o$C $\quad$ $f_{Obj_1} = \min(m_{PM})$

Nominal speed [rpm]		90
Number of pole pairs		21
Number of slots		420
Winding topology		Penta-Distributed
Permanent magnet		N40SH (B_r=1.2 T)
Airgap [mm]		20
Bounds		LB/UB =[R_g[m], L_{act}[m], θ_s[%], h_s[m], θ_{PM}[%], h_{PM}[m], J_s[A/m^2], h_{ys}[m]]
ST-PMSG	LB	[1.00, 1.00, 0.35, 0.05, 0.15, 0.02, 2.0e6, 0.03]
	UB	[3.5, 2.5, 0.55, 0.20, 0.50, 0.10, 5.0e6, 0.07]

7.3.1.2.1 Results The results in Fig. 7.10, confirm that there is a compromise between the permanent magnets mass and the machine's active mass. To countervail the reduction on the mass of permanent magnets, we should raise the copper volume to balance the magneto-motive force, which leads on a heavier machines. Further, for the ST-PMSG generators, the impact of the magnetic saturation is clearly visible in the gap between the linear and the non-linear Pareto fronts.

Table 7.6: Computation time comparison between AM and RNM

	Analytical model -Linear-	Reluctance Network model -Nonlinear-
Computation time [min]	65 (60 harmonics)	1153.2
Total number of function evaluations	37501	45001
Number of generations	250	300
Machine characteristics	MATLAB 2019b on a 64-bits Windows 10 operating system PC with Intel(R) Xeon(R) Platinum 8160 CPU @2.10GHz (24x2 cores and 48x2 threads)	

Table 7.6 shows that the AM-based optimization use much less computational effort, almost 18 times faster, compared to RNM-based optimization. The optimization run takes 65 min with AM compared to 19 h 13 min with RNM (The characteristics of the machine used in the simulation are given in Table 7.6). The NSGA II gives results after a few hundred generations. Both optimization design are compatible with parallelization. To measure time saved by using parallel processing, the optimization design based on analytical model has been run serially and in parallel (in the machine described in Table 7.6). With

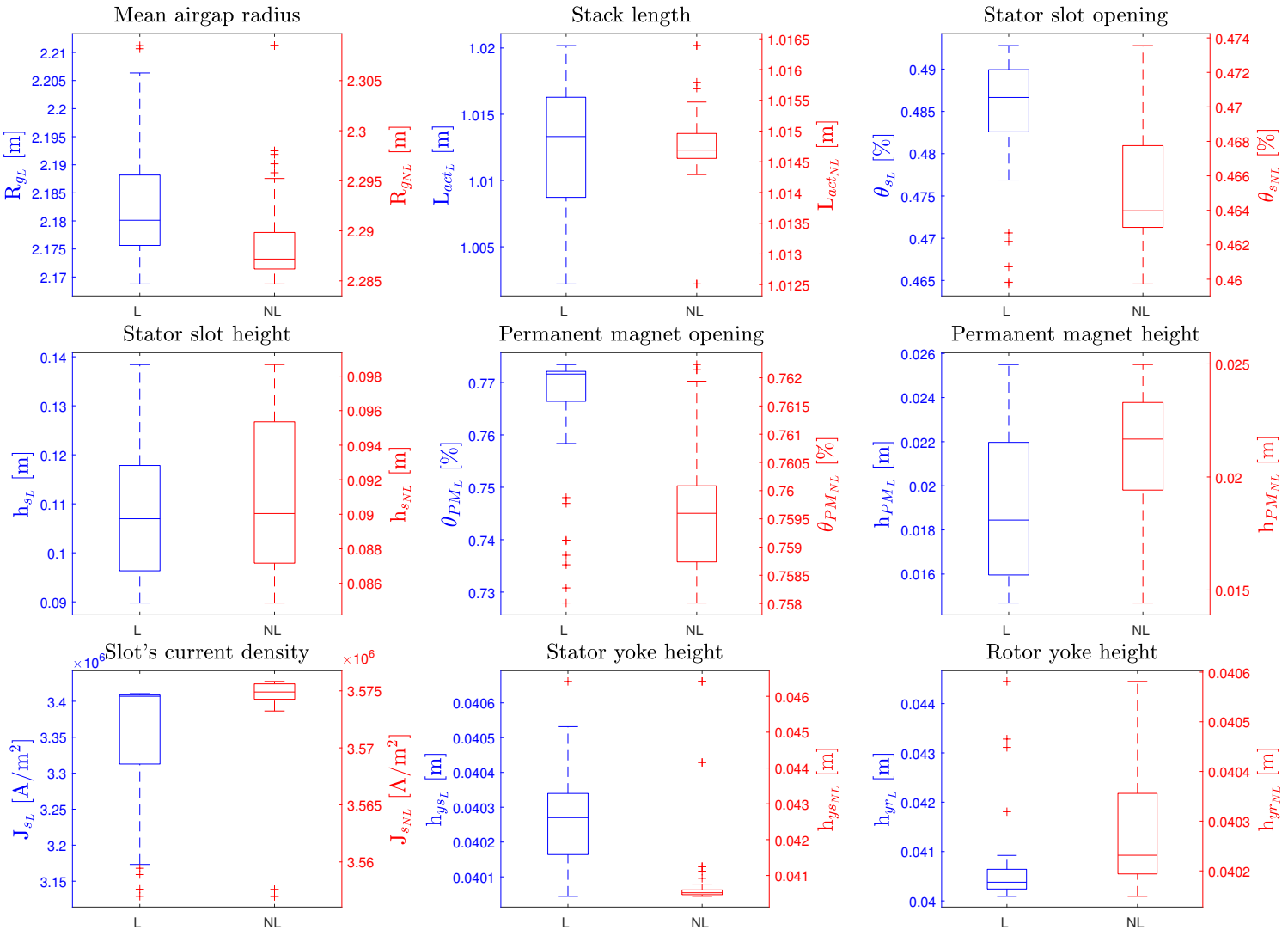

Figure 7.8: Boxplot comparison of optimization design models for SM-PMSG ('L' stands for linear and 'NL' stands for nonlinear)

serial calculation (single CPU[1] or single computer environment), the time required for the optimization to converge was 18 h 23 min 30s min, while the total time was 65 min with parallel processing. Consequently, parallel computing accelerated optimization by up to 16 times (the precise increase in speed depends on the the number of workers, the optimization algorithm and the topology of the machine used).

Table 7.7 provides a comparison between the torque obtained by the FEM, RNM and AM.

The machine AM-based optimization is validated through finite element analysis. As shown in Fig. 7.10, two distinct machines, A_{AM} and B_{AM}, were chosen from the AM Pareto front for validation (See Fig. 7.11).

[1]CPU : Central Processing Unit.

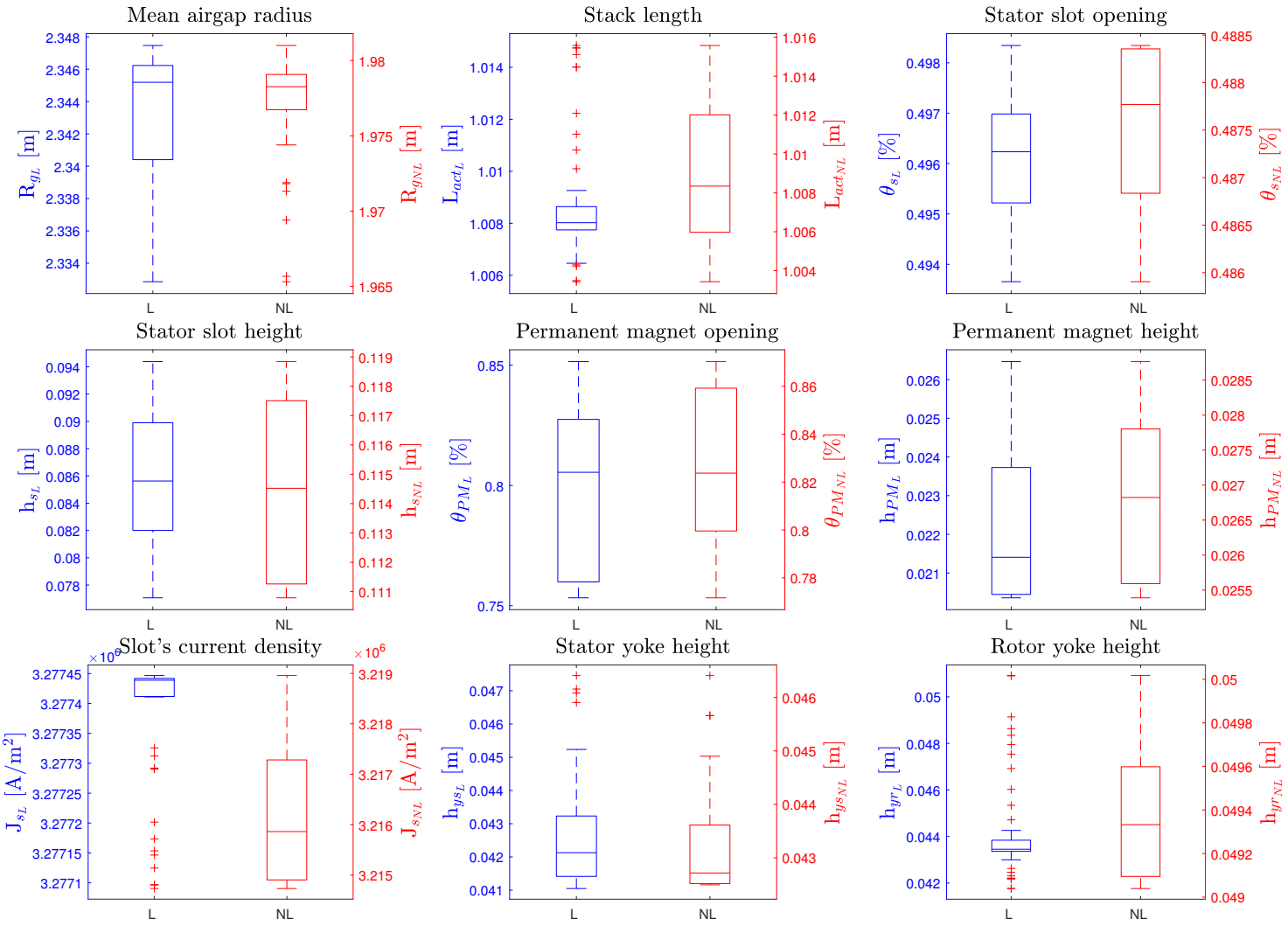

Figure 7.9: Boxplot comparison of optimization design models for I-PMSG ('L' stands for linear and 'NL' stands for nonlinear)

Table 7.7: Comparison between FEM, RNM and AM results

$\Gamma_{mean}[MNm]$	Analytical model AM	Reluctance Network model RNM	Finite element model FEM
Machine A_{AM}	1.80	1.71	1.72
Machine B_{AM}	1.81	1.68	1.73
Machine A_{RNM}	1.98	1.81	1.83
Machine B_{RNM}	1.94	1.80	1.81

7.3.1.2.2 Discussion In order to explain the gap between the two models, the evolution of each design variable on Pareto front, resulting from the parametric-optimization minimizing the mass of the permanent magnet and the ST-PMSG, was investigated. Explaining the design parameters trends is not

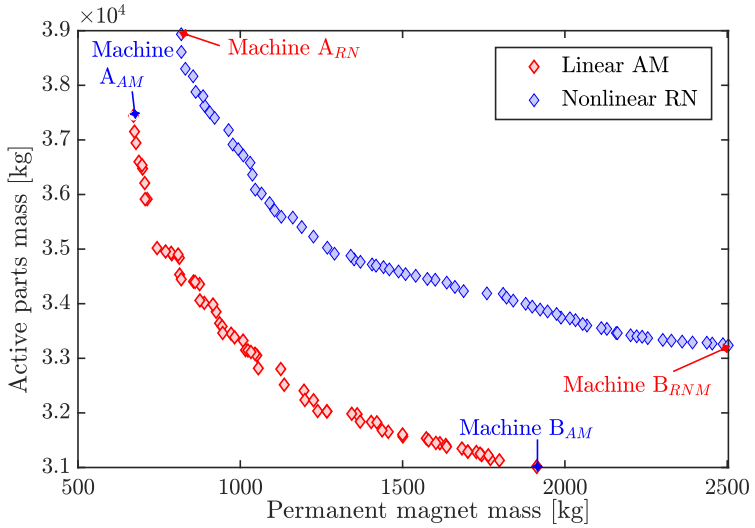

Figure 7.10: Pareto optimality of 15MW-90rpm ST-PMSG with NdFeB N40SH (B_r = 1.2 T)

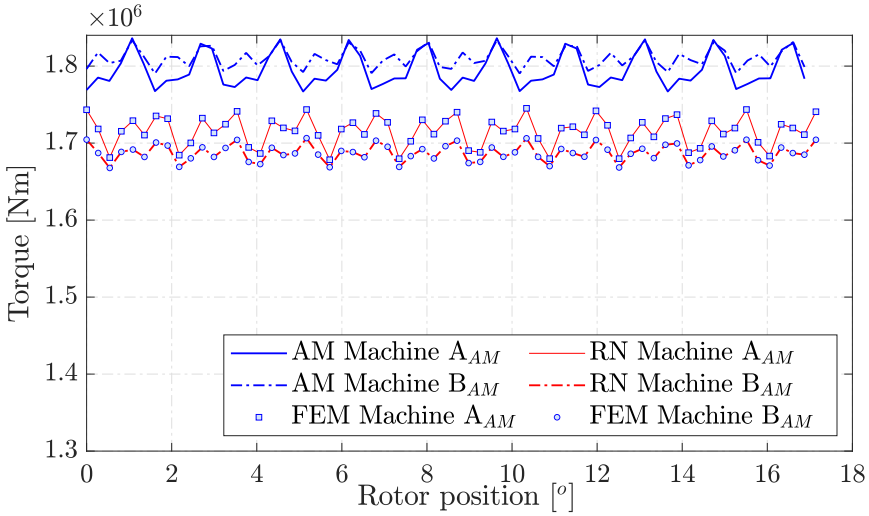

Figure 7.11: Results validation

clearly evident in many cases, since each optimization variables depend on the interaction between the objective functions as well as between other optimization variables. The main conclusions that can be drawn from this study are:

– As shown Fig. 7.12, with AM the air gap radius is in the range of 2.25-2.40 m compared to 2.40-2.58 m with RNM. The axial length of the machine is varying from almost 1.00 m to 1.04 m with AM compared to 1.00 m to 1.15 m with RNM. It is clear that the torque is proportional to the rotor's volume, so increasing the rotor external radius would help to attain the required performance. In contrast, the larger the mean air gap radius, the more materials are needful to create the high

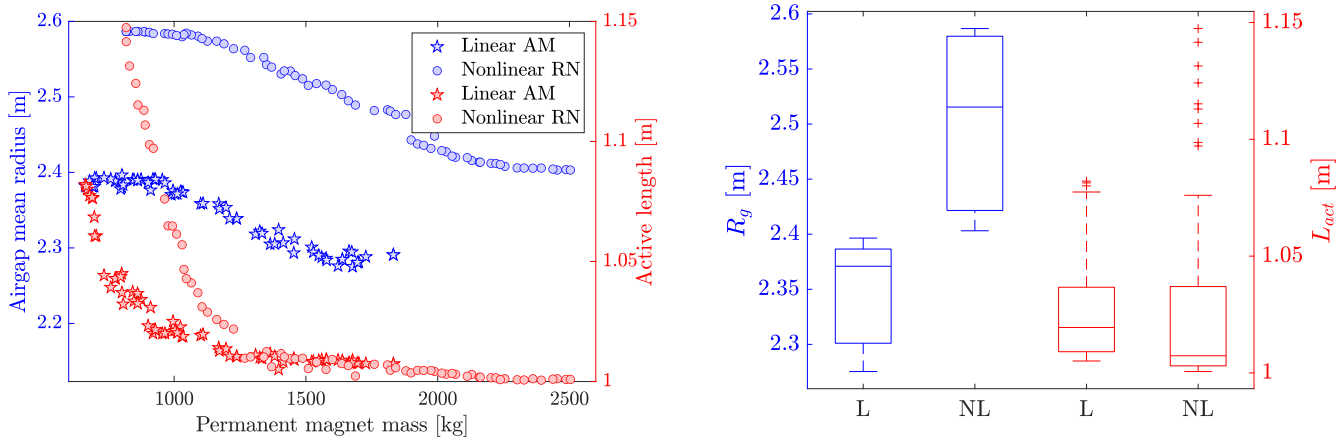

(a) R_g versus permanent magnet mass

(b) Boxplot Diagrams of R_g and L_{act}

Figure 7.12: Variation trends of machine's mean airgap radius and active length

flux density in the airgap (PM, Copper, Iron), leading to heavier machine. From the short review above, it was expected that to meet the required torque nonlinear RNM results in larger and heavier machines when compared with AM.

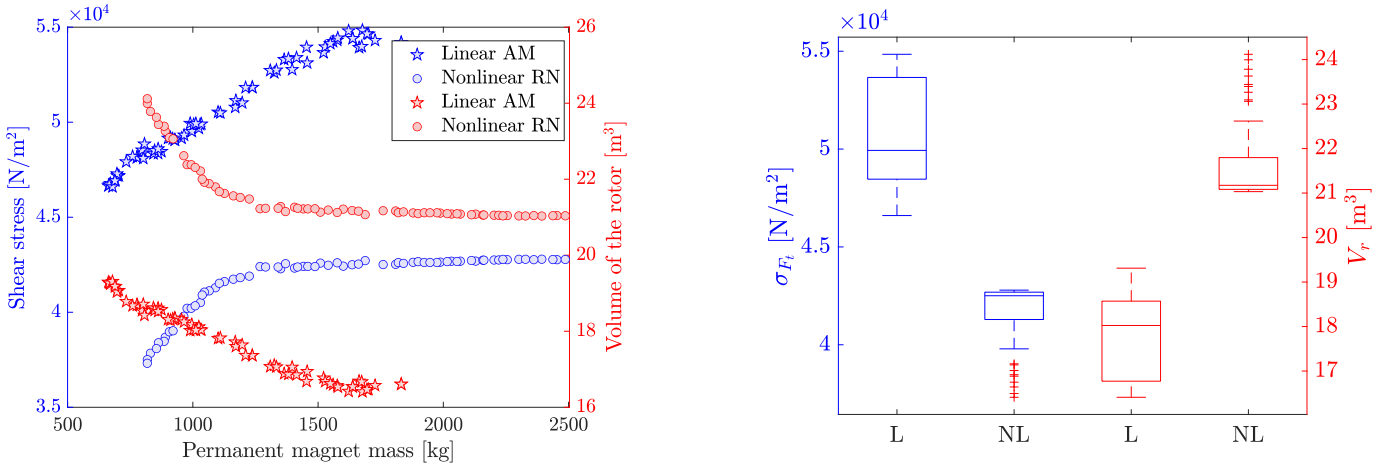

(a) σ_{F_t} and V_r versus permanent magnet mass

(b) Boxplot Diagrams of σ_{F_t} and V_r

Figure 7.13: Variation trends of machine's shear stress and rotor's volume

– As it can be noticed from Fig. 7.13 that the nonlinear model requires larger rotor compared to linear model (See Fig. 7.13b). Indeed, the consideration of the saturation in the RNM model constrains the magnetic loading, which leads to limited force density (See Fig. 7.13a). Therefore, the machines obtain by the analytical model have high force densities [48-55] kN.m^{-2}, while with nonlinear RNM model it varies between [40-43] kN.m^{-2}.

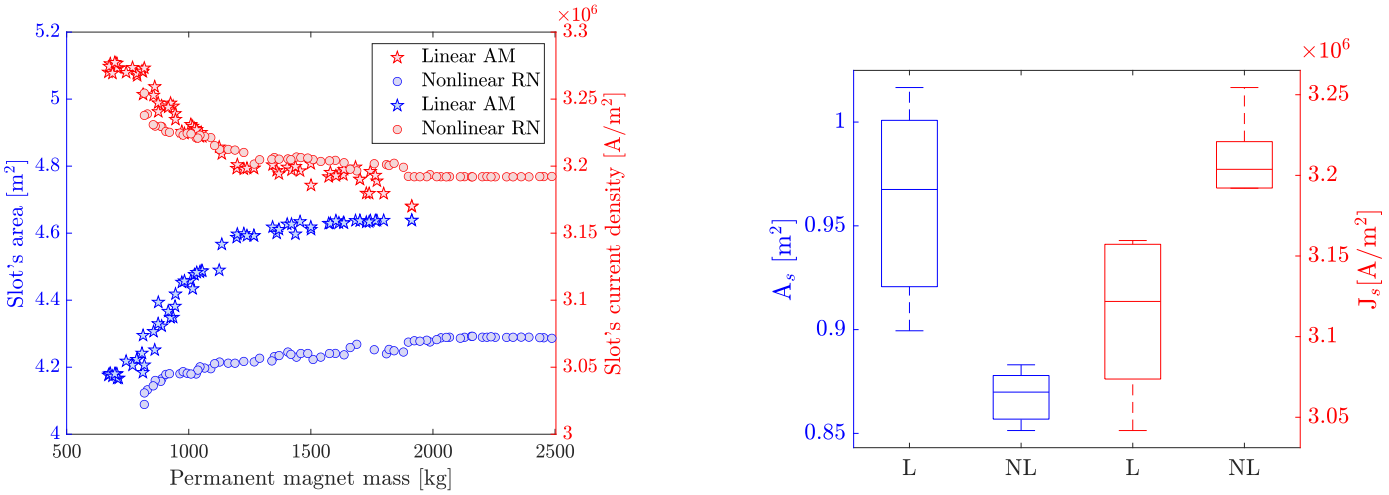

(a) A_s and J_s versus permanent magnet mass

(b) Boxplot Diagrams of A_s and J_s

Figure 7.14: Variation trends of slot's area and current density

– To recover the reduction of the PM volume, the optimization algorithm tries to boost the magnetic and the electric loading by changing the ratio of the slot's opening to the tooth opening and by increasing the slot's depth, respectively. Otherwise, the flux density is limited by the saturation of the stator teeth, and the current density presents restrictions related to the thermal conditions (cooling the winding). Fig. 7.14 shows that the slot's area is larger in linear then in nonlinear model, this could be explain by relatively small airgap radius in the linear model. The analytical model increases the copper volume by increasing the slot's area, however, this might help in winding cooling and then increasing the slot's current density.

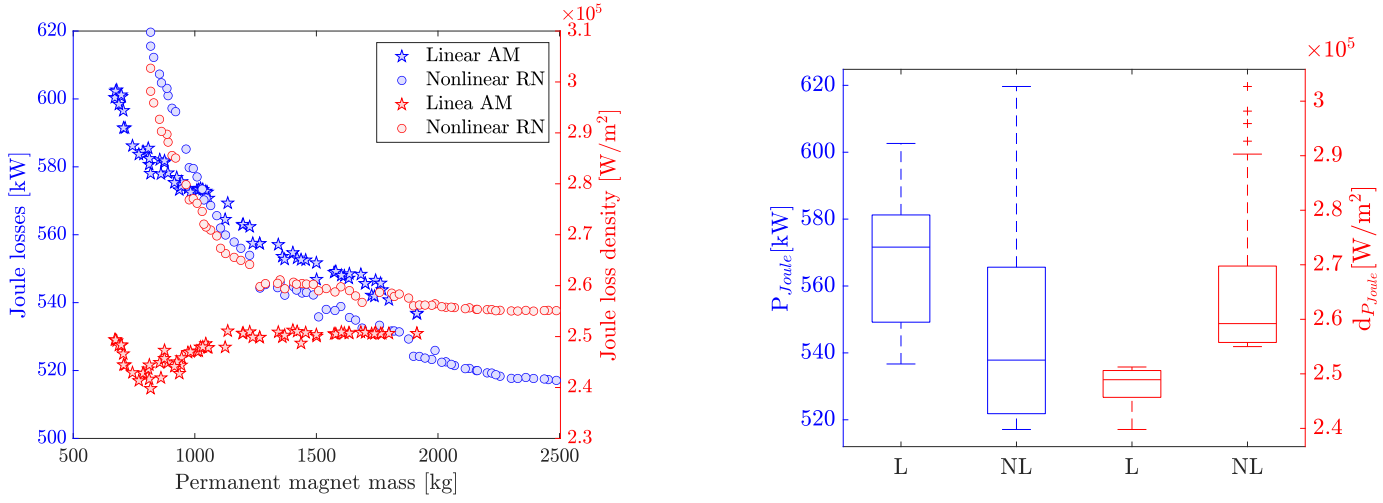

(a) P_{Joule} and $d_{P_{Joule}}$ versus permanent magnet mass

(b) Boxplot Diagrams of P_{Joule} and $d_{P_{Joule}}$

Figure 7.15: Variation trends of slot's area and current density

– As can be seen in Fig. 7.15, the Joule losses are inversely proportional to the permanent magnet mass. Although the significant difference on the slot's area between the two models, the copper losses and their density are slightly the same for the two models.

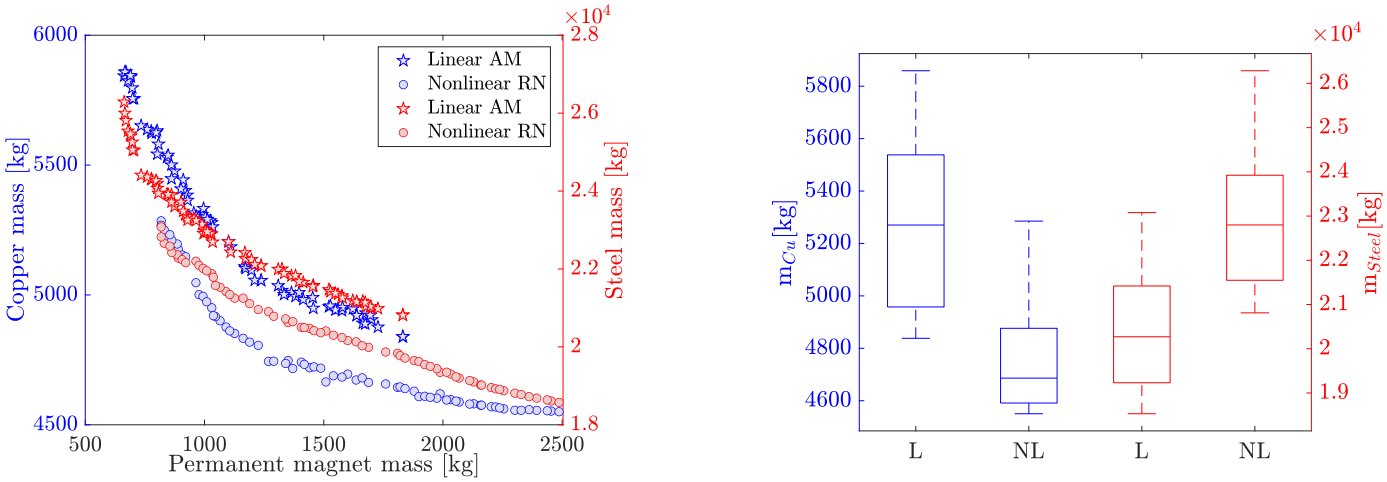

(a) m_{Cu} and m_{Steel} versus permanent magnet mass

(b) Boxplot Diagrams of m_{Cu} and m_{Steel}

Figure 7.16: Variation trends of copper and steel masses

– The relationship and the interaction between the copper mass, the steel mass and the permanent magnet mass can be seen in Fig. 7.16. The figure illustrates how the active parts mass, including copper and active steel, varies with the permanent magnet mass. The results from RNM-based optimization seem to follow the same trend as AM-based optimization. More precisely, the machines resulting from using linear AM required 11%-14% (See Fig. 7.16b) less electrical steel compared to those resulting from Non-linear RNM. Indeed, while the dimensions of the stator yoke, rotor yoke and stator teeth in RNM are determined to avoid the magnetic saturation, in AM they has to be minimized without considering the iron saturation. Hence, for given power rating, linear AM leads to lighter and smaller machines.

7.3.1.2.3 Three objectives optimization problem To refine the design, a three-objective parametric-optimization was carried (only with linear analytical model), in which the efficiency was added as an objective function. Using NSGAII, the simulation takes nearly 1235 min, which still small compared to the two objective RNM-based optimization. It can be noticed that by adding more objectives or constraints the design may be refined. Fig. 7.17 shows the 3D view Pareto frontiers. The projections of the Pareto in each direction are presented in Fig. 7.18a, Fig. 7.18b and Fig. 7.18c (The third objective

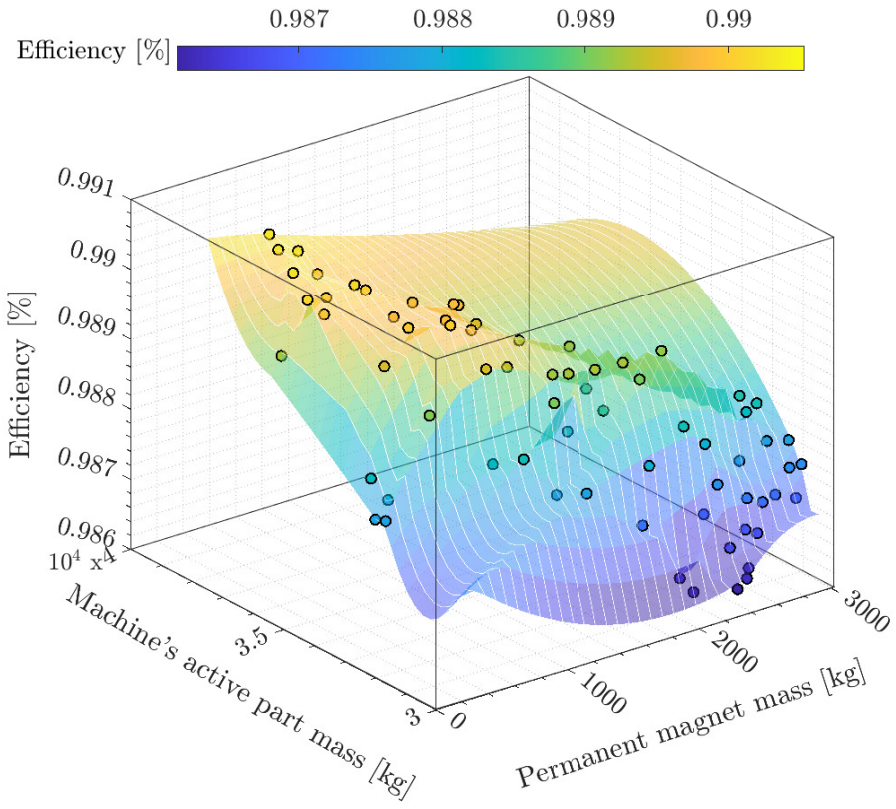

Figure 7.17: Optimization results: 3D view of Pareto frontiers

in the 2D projections is depicted by the marker gradient color.). It can be seen that the mass and the efficiency of the machine are fairly conflicting goals.

By adding the efficiency as an objective to maximize, the optimization attempts to reduce the machine losses. It could be noticed that when considering the efficiency, the losses density varies in the interval [1.6-2.2] W/m^2, while it varies between [2.4-2.5] W/m^2 when the efficiency is not considered (See Figure 7.17). Further, for a given permanent magnet mass, the efficiency of the machine increases with an increase in machine's mass/volume as illustared in Fig. 7.18a and Fig. 7.18b. Heavier machines consume less permanent magnet mass and have better efficiency than machines with low masses.

7.3.2 Conclusion

The two optimization models share a common trend in the optimization variables. Both optimization methods results on similar sized machines with the parameters agreeing within 1.04 - 18 % on most variables. The machine resulting from AM-based optimization have lower volume but higher shear

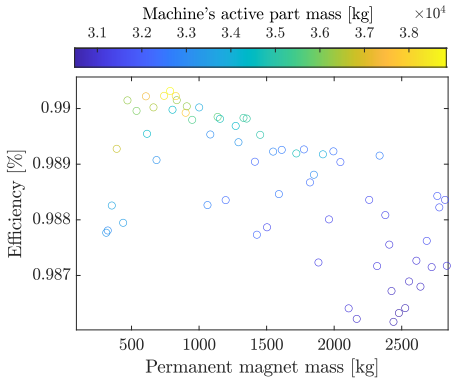

(a) Efficiency of the machine versus permanent magnet mass

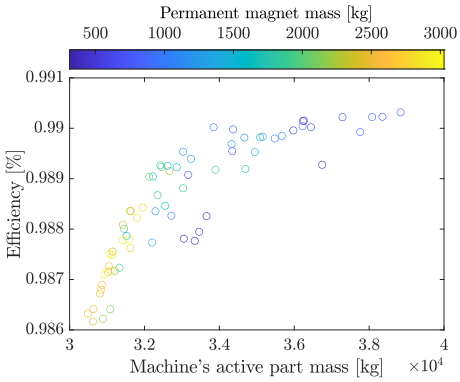

(b) Efficiency of the machine versus machine mass

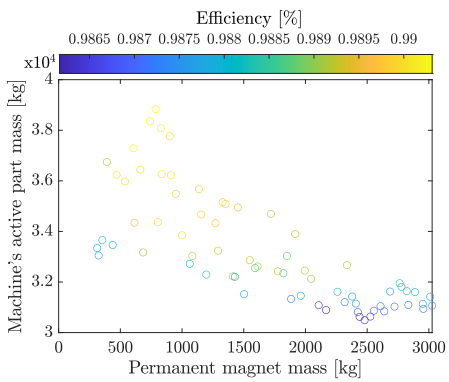

(c) Machine's mass versus permanent magnet mass

Figure 7.18: 2D view of Pareto frontiers: projections of 3D Pareto frontiers

stress and larger slots compared with RN-based optimization. The main cause of this difference is the consideration of saturation on the nonlinear RNM. The effect of each parameter on the optimization have been analysed. Although RN-based optimization is time consuming but it has relatively high accuracy.

7.4 Design Optimization of Direct-drive Permanent Magnet Synchronous Generator

In order to design the optimum machine, performances and the capabilities of selected PMSGs will investigated for direct-drive 15 MW wind turbine. The effect of each optimization parameters on the machine performances and the objective functions will be analysed separately. This section aims to compare permanent magnet generators using Ferrite with those using NdFeB in terms of different criteria such as permanent magnet mass, the machine mass, the machine cost and the the cogging torque.

In order to investigate the effect of magnet grade on the performances of the machine, many permanent magnets were selected for this study. The main criteria when selecting magnets were high maximum energy product, high remanence flux density and acceptable operating temperature. SH grade neodymium magnets were chosen (N40SH and N48SH) for their high operating temperature 120-150 ^{o}C (compared to 80 ^{o}C for the regular magnets) [33]. Thermal simulations were conducted and it has been noticed that without forced cooling (adding fans and heat exchanger) it would be difficult to ensure safe operation of regular permanent magnets.

The price of the selected magnets was difficult to obtain. In addition, the instability and the steep rise

of the price of rare earth magnets in the last few years (See Fig. 7.19), especially after the COVID-19 sanitary crisis, made it complex to fix reliable price for our study. In 2022, the prices of the REE increased dramatically (Dysprosium (571.97 € per kg [473]), Neodymium (185.84 € per kg [473]), Praseodymium (188.75 € per kg [473]) and Terbium (3827.96 € per kg [473])).

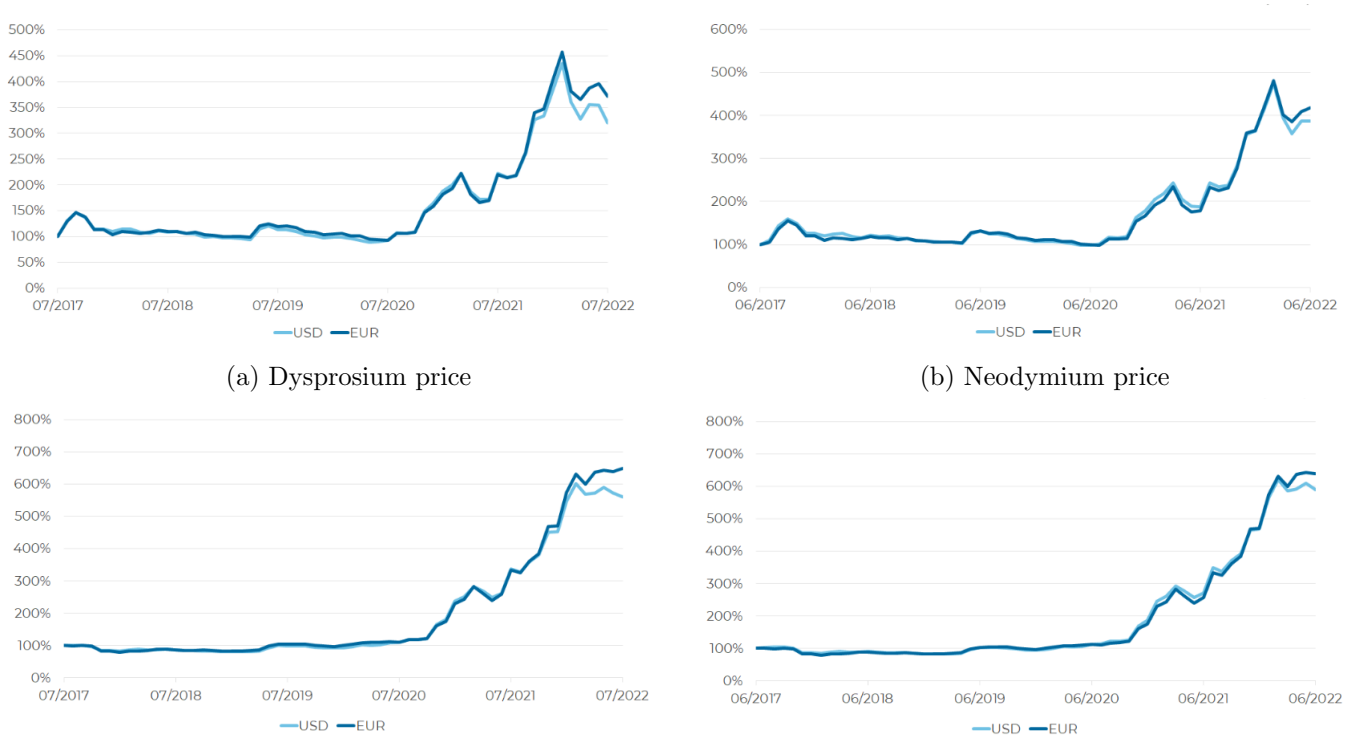

(a) Dysprosium price

(b) Neodymium price

(c) Praseodymium price

(d) Terbium price

Figure 7.19: Rare Earth Elements Prices

Table 7.8: The cost per kg of the main materials used in the machine [41]

Material	Electrical steel		Copper	NdFeB		Ferrite	
	Stator laminations	Rotor core iron		N40SH	N48SH	Y30	NMF-15G
Cost (euro/kg)	3	2.5	16	60	70	4	10

The indicated cost of the selected magnet in Table 7.8 are inferior when compared to their current prices, although it would be premature to say that this REE crisis (related to the COVID) is over, but we assume that it will only get better. This high price volatility increases riskiness of manufacturing permanent magnet synchronous generator based of REE with acceptable price. Thus, the prices were indexed on the basis of the average price of REE over a period of five year (2015-2020) before the present crisis. The relative cost of the H grade NdFeB was deduced from the formula presented in Fig. 7.20. Additionally, the cost of the permanent magnets depends on the magnet volume, the rate of segmentation and the

skewing (Segmented core is 10 per cent more expansive than unsegmented one and skewed rotor is 1.3 times more than skewed one.) [474].

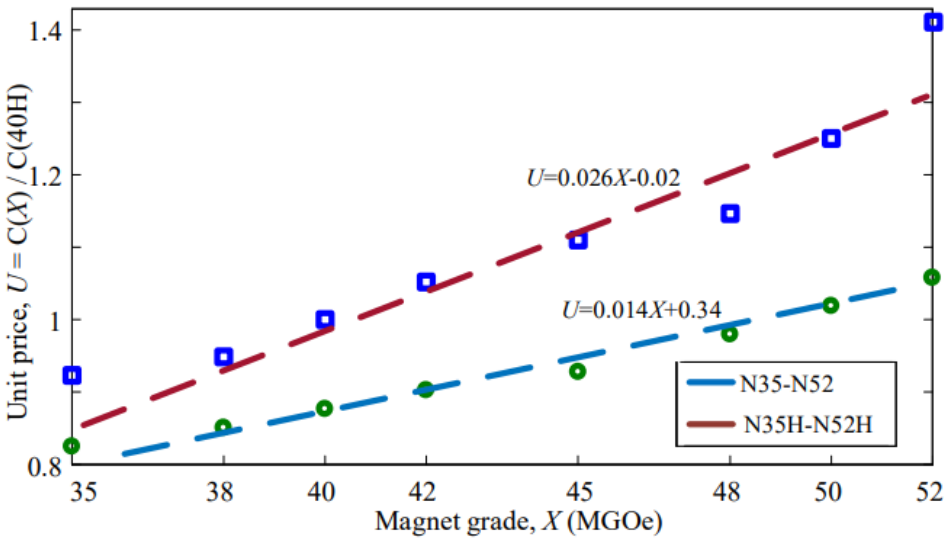

Figure 7.20: Specific cost of NdFeB magnet grades (relative to N40H (60euro/kg)) (X represents the maximum energy product) [30]

7.4.1 Optimization parameters

All the optimization scenarios for the proposed electrical machines were carried out based on the parameters defined in Table 7.9.

Table 7.9: The main parameters of NSGA II

Parameters	Values
Population size	300
Maximum generation	600
Crossover probability	0.8
Termination tolerance on the function value	1.10^{-8}

The constraints are used to limit machine dimensions so that the resulting machine has a physical meaning. The optimization problems with the design parameters and constraints are presented in Table 7.10, Table 7.11 and Table 7.12 for machine A, B and C, respectively.

7.4.2 Results and Discussion

Each optimized results will be presented in eight figures:

- The first set of sub-figures, represented by (1), (2) and (3), depicts the active parts weight versus the magnets mass, airgap radius and axial length respectively.
- The second set of sub-figures, represented by (4) and (5), depicts the variation trends of optimization variables with respect to magnet mass and statistical analysis of the those variables.
- The third set of sub-figures, represented by (6), (7) and (8), depicts the comparative analysis of the proposed topologies.

7.4.2.1 Machine A (90 pole-pairs and 648 slots)

Table 7.10: Optimization problem of Machine A: key design parameters, bounds and constraints

<table>
<tr><td colspan="5">Fixed parameters</td><td>Constraints</td><td>Objective functions</td></tr>
<tr><td>PMSG</td><td colspan="2">ST-</td><td colspan="2">SM-</td><td rowspan="5">$T_{max} \leq 125\ ^{o}$C
$\Gamma_{max} \geq 20$MNm</td><td rowspan="5">$f_{Obj_1} = \min(m_{PM})$
$f_{Obj_2} = \min(m_{act})$</td></tr>
<tr><td>Nominal speed [rpm]</td><td colspan="2">7.5</td><td colspan="2">7.5</td></tr>
<tr><td>Winding topology</td><td colspan="4">3-phases 2-layers
Distributed winding</td></tr>
<tr><td>Permanent magnet</td><td>N40SH</td><td>N48SH</td><td>Y30</td><td>NMF-15G</td></tr>
<tr><td>Airgap</td><td colspan="4">12</td></tr>
<tr><td colspan="7">Lower and upper bounds
LB/UB$_{ST-PMSG}$ =[R$_g$[m], L$_{act}$[m], θ_s[%], h$_s$[m], θ_{PM}[%], h$_{PM}$[m], J$_s$[A/m^2], h$_{ys}$[m]]
LB/UB$_{SM-PMSG}$ =[R$_g$[m], L$_{act}$[m], θ_s[%], h$_s$[m], θ_{PM}[%], h$_{PM}$[m], J$_s$[A/m^2], h$_{ys}$[m], h$_{yr}$[m]]</td></tr>
<tr><td>ST-PMSG$_{NdFeB}$</td><td colspan="6">LB = [3.0, 1.0, 0.30, 0.05, 0.15, 0.02, 2.5e6, 0.04]
UB = [7.0, 4.0, 0.55, 0.50, 0.50, 0.10, 5.5e6, 0.10]</td></tr>
<tr><td>ST-PMSG$_{Ferrite}$</td><td colspan="6">LB = [3.0, 1.0, 0.30, 0.05, 0.15, 0.02, 2.5e6, 0.04]
UB = [9.0, 5.0, 0.55, 0.50, 0.50, 0.10, 5.5e6, 0.10]</td></tr>
<tr><td>SM-PMSG$_{NdFeB}$</td><td colspan="6">LB = [2.7, 2.0, 0.30, 0.07, 0.50, 0.01, 2.5e6, 0.04, 0.045]
UB = [7.0, 4.0, 0.55, 0.50, 0.90, 0.10, 5.5e6, 0.30, 0.20]</td></tr>
<tr><td>SM-PMSG$_{Ferrite}$</td><td colspan="6">LB = [2.7, 2.0, 0.30, 0.07, 0.50, 0.01, 2.5e6, 0.04, 0.045]
UB = [9.0, 5.0, 0.55, 0.50, 0.90, 0.20, 5.5e6, 0.30, 0.20]</td></tr>
</table>

A) **Machine A (with NdFeB)**

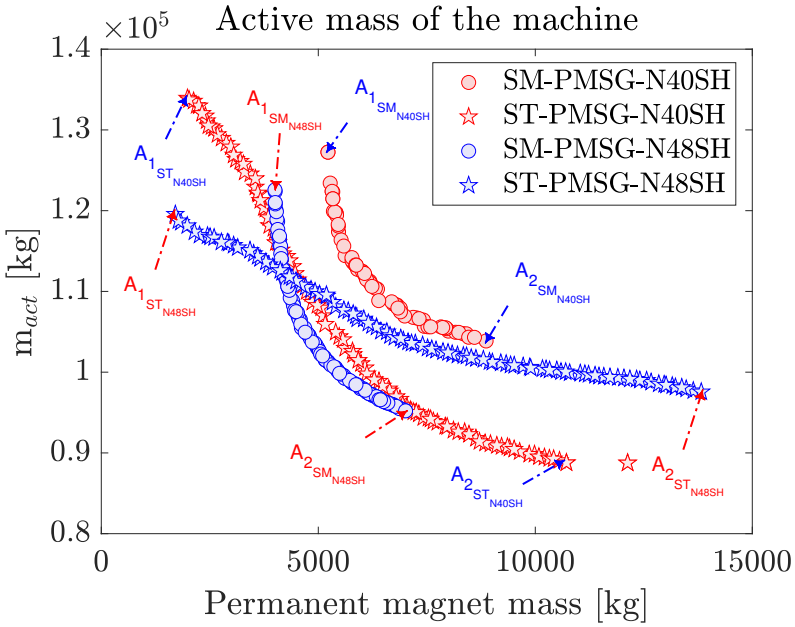

Figure 7.21: Pareto optimality of machine A (p=90 & N_s=648) with NdFeB N40SH (B_r = 1.21 T) & N48SH (B_r = 1.39 T)

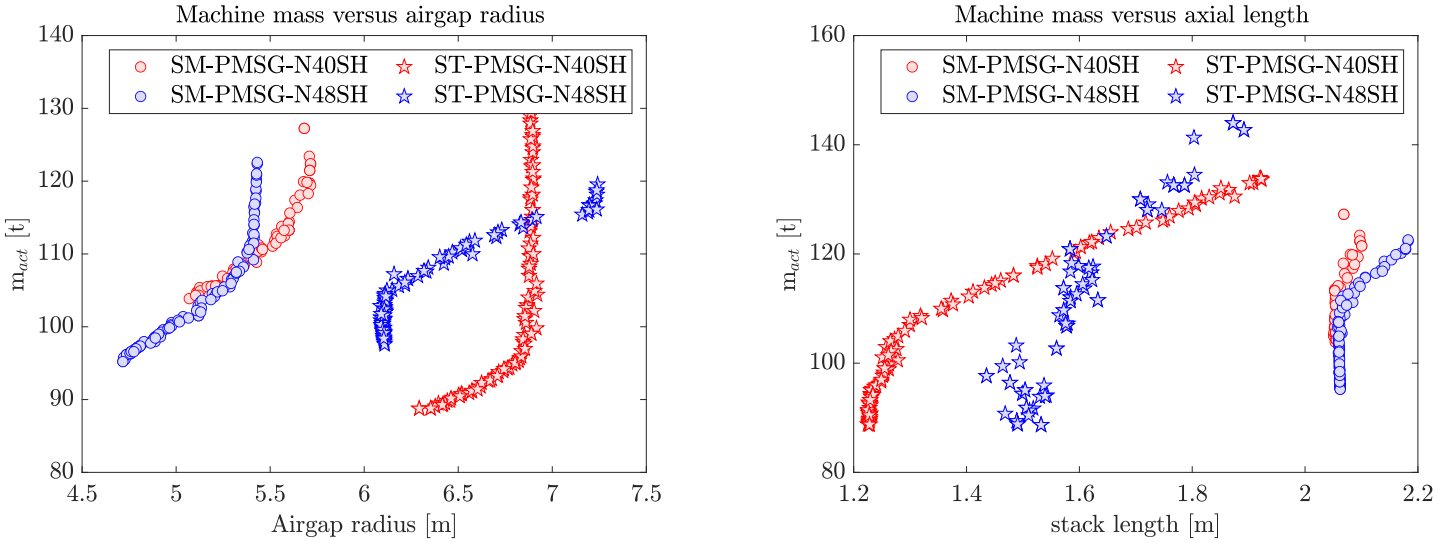

(a) Machine's mass versus airgap radius

(b) Machine's mass versus axial length

Figure 7.22: Mass of machine A versus its airgap radius and axial length

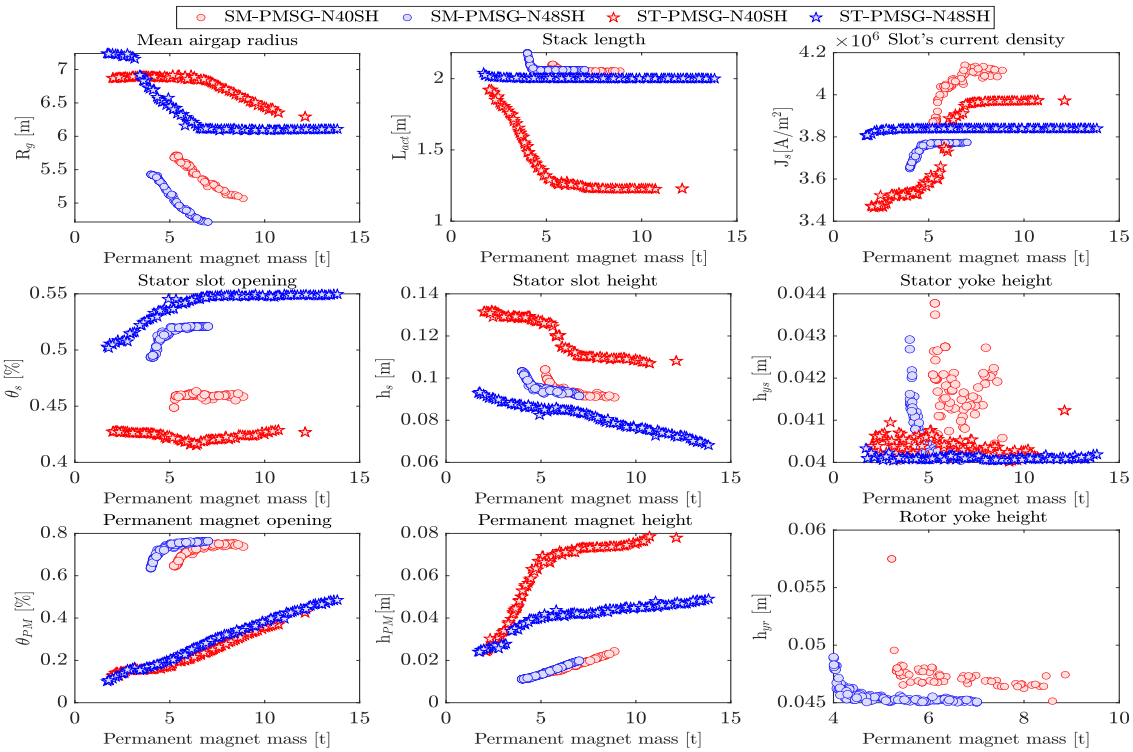

Figure 7.23: Variation trends of optimization parameters with respect to permanent magnet mass - machine A with NdFeB

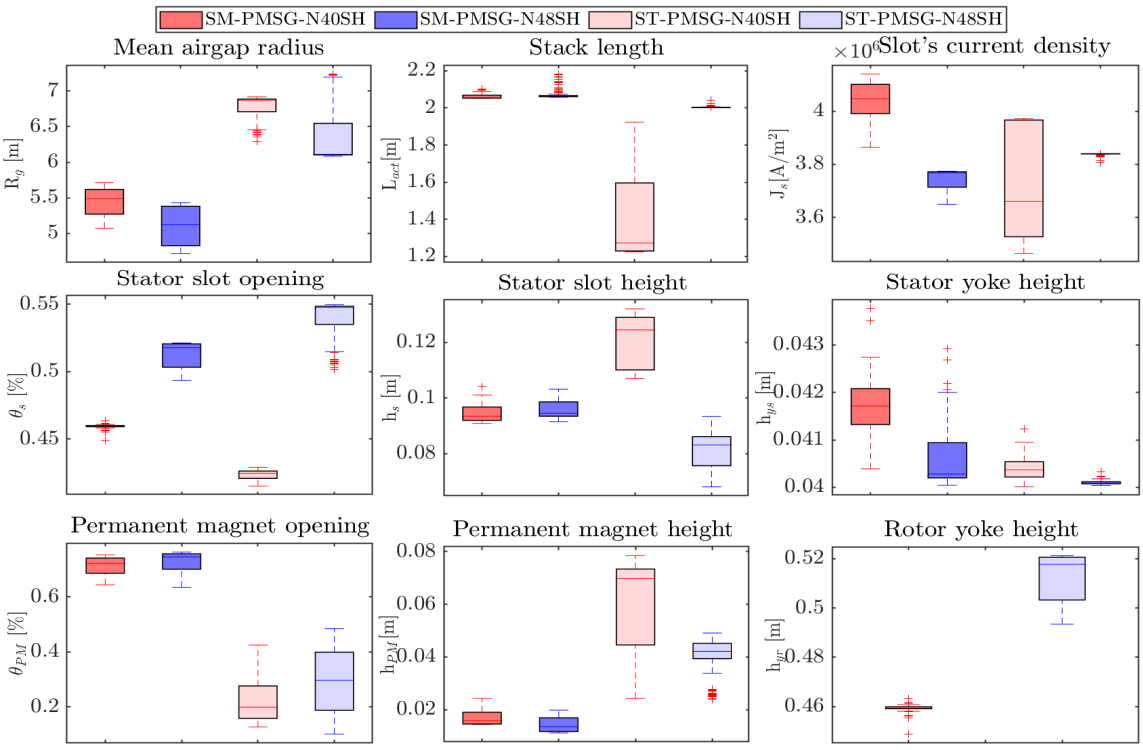

Figure 7.24: Statistical analysis of optimization parameters - machine A with NdFeB

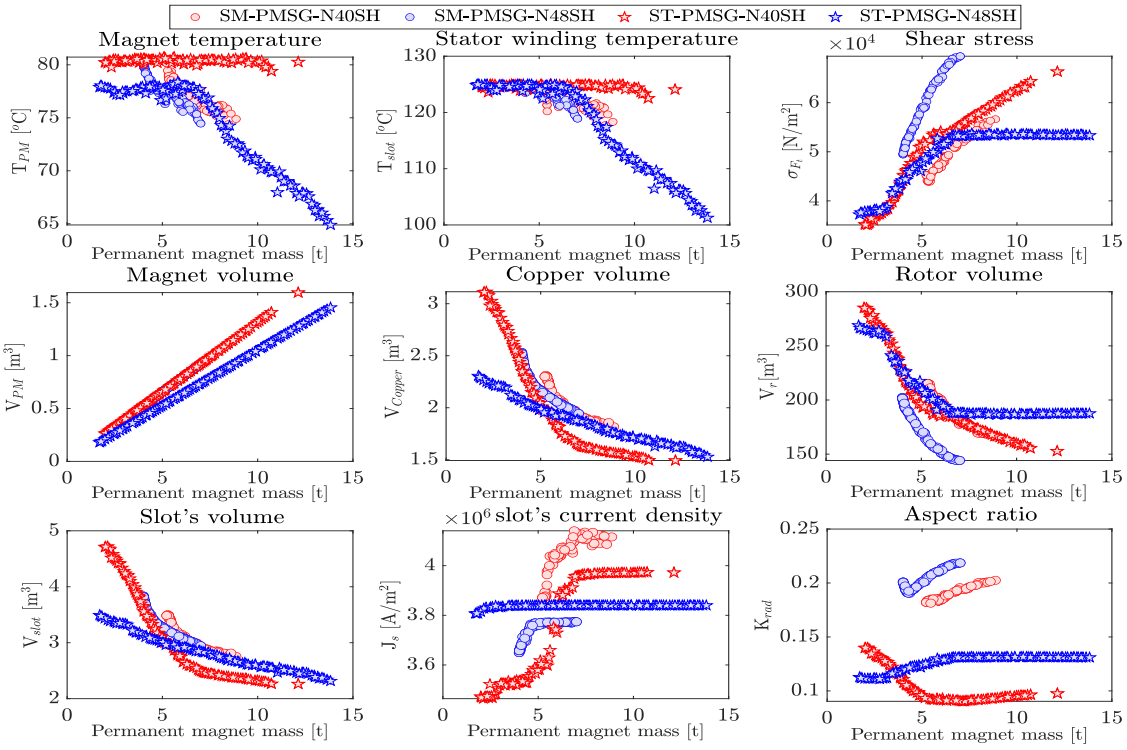

Figure 7.25: Comparative Analysis of machine A -with NdFeB- characteristics I

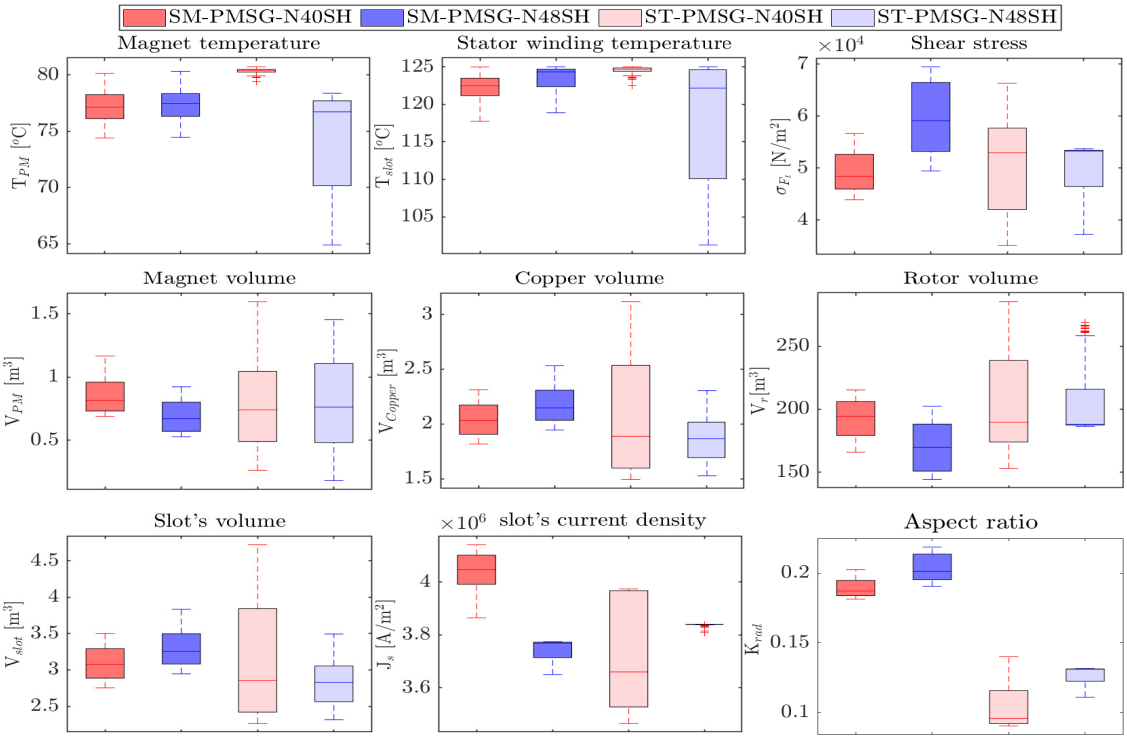

Figure 7.26: Statistical analysis of machine A -with NdFeB- characteristics I

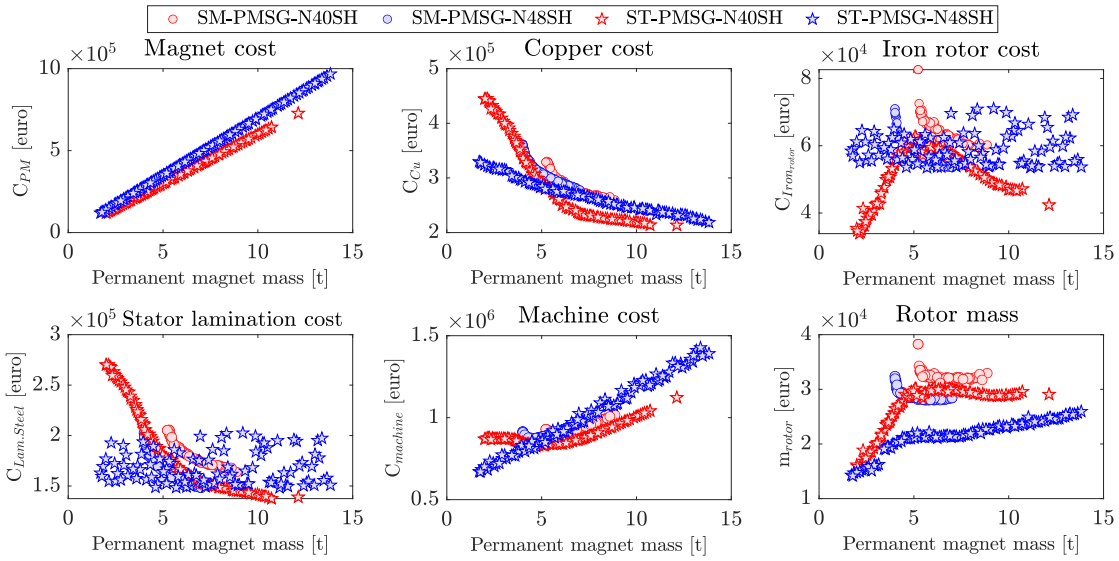

Figure 7.27: Comparative Analysis of machine A -with NdFeB- characteristics II

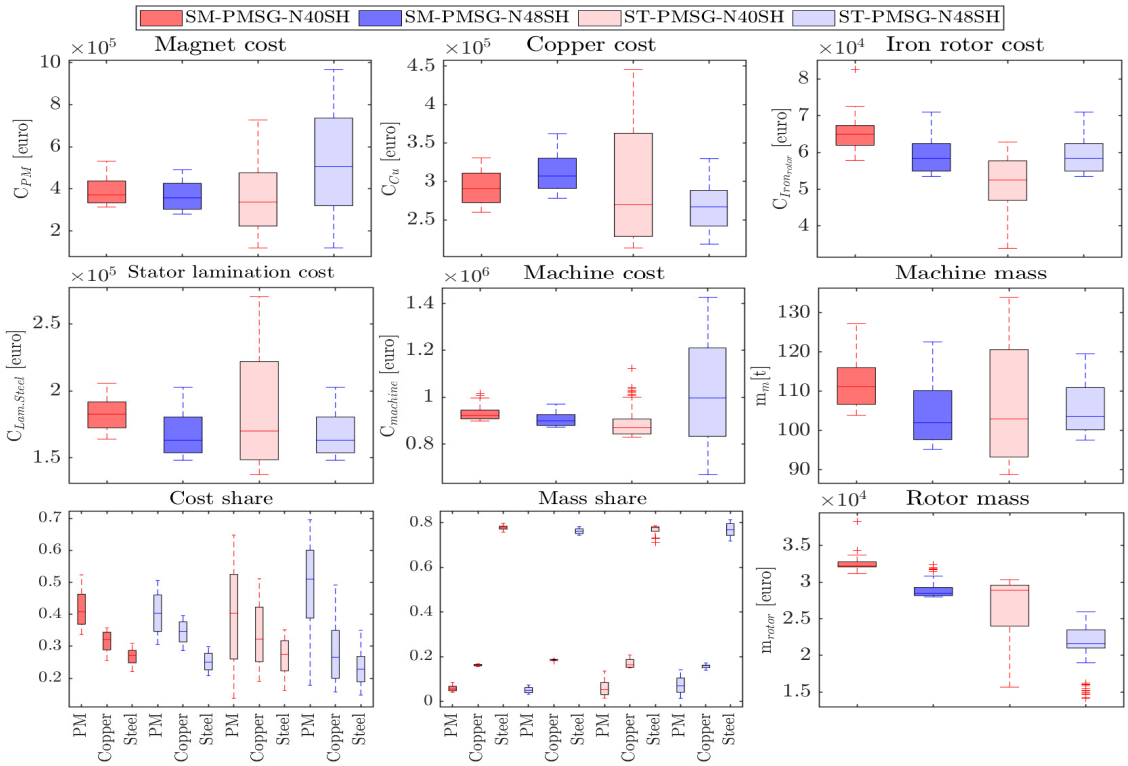

Figure 7.28: Statistical analysis of machine A -with NdFeB- characteristics II

B) **Machine A (with Ferrite)**

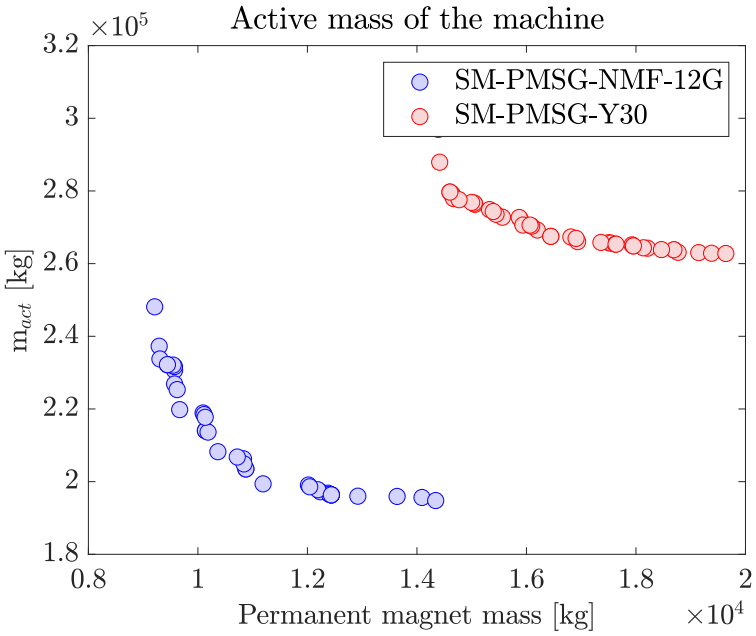

Figure 7.29: Pareto optimality (p=90 & N_s=648 with NMF-15G (B_r=0.5T)/Y30 (B_r=0.38T))

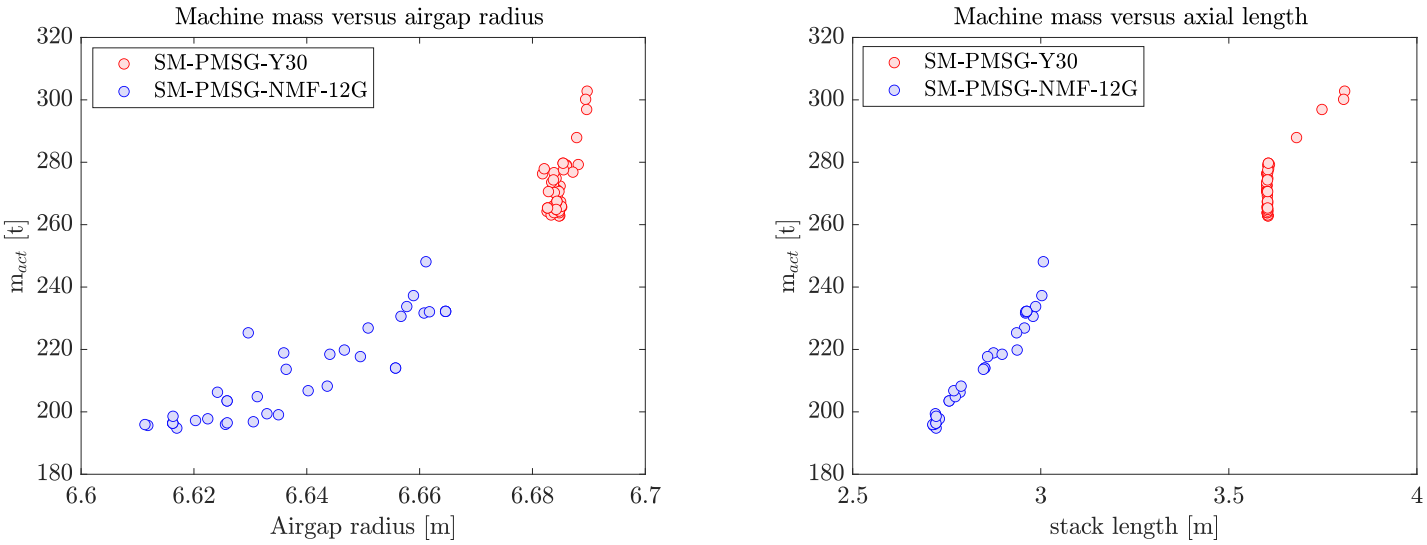

(a) Machine's mass versus airgap radius

(b) Machine's mass versus axial length

Figure 7.30: Mass of machine A versus its airgap radius and axial length

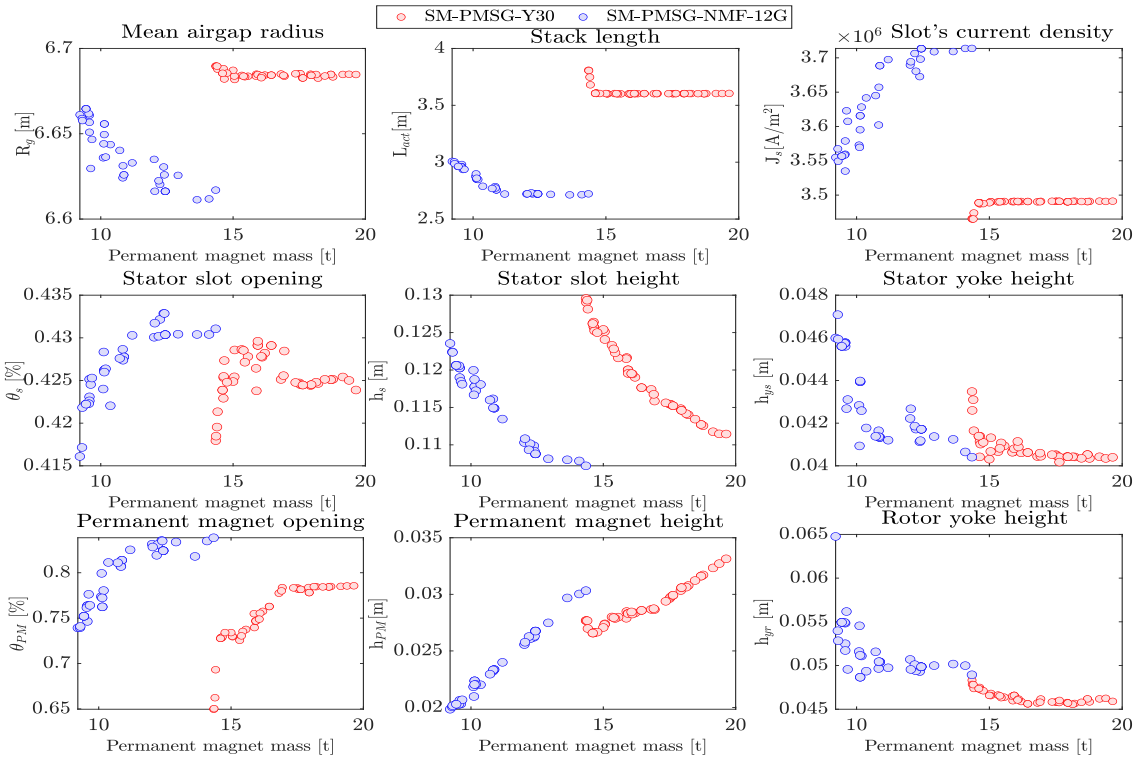

Figure 7.31: Variation trends of optimization parameters with respect to permanent magnet mass - machine A with Ferrite

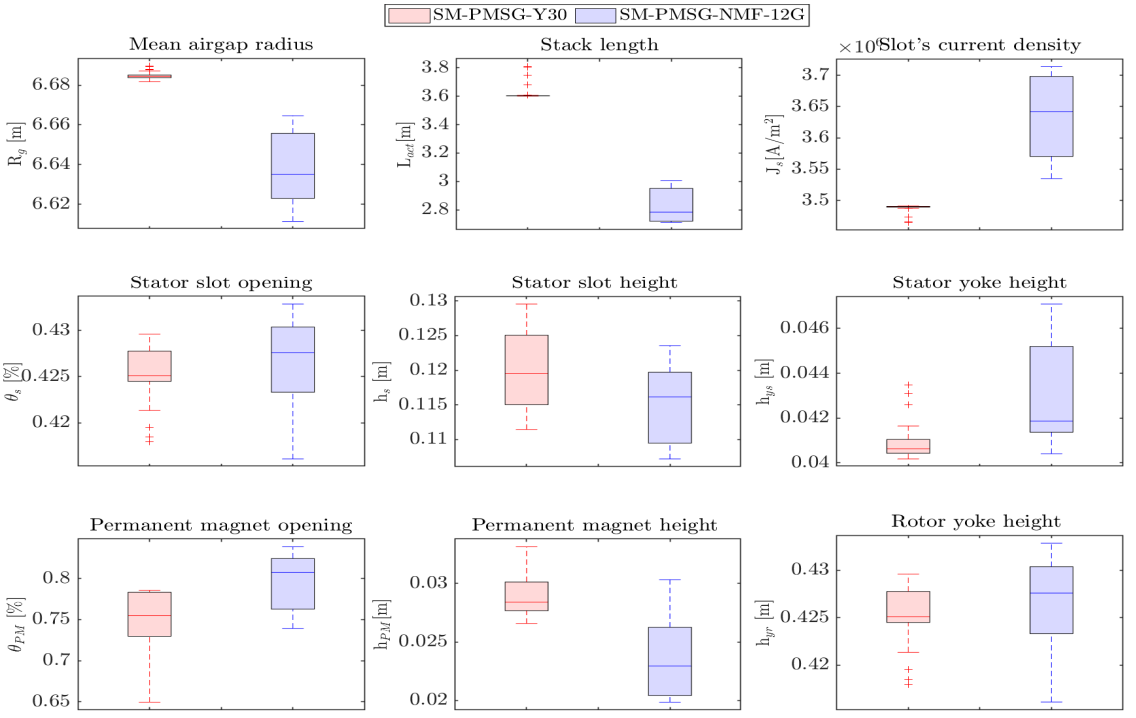

Figure 7.32: Statistical analysis of optimization parameters - machine A with Ferrite

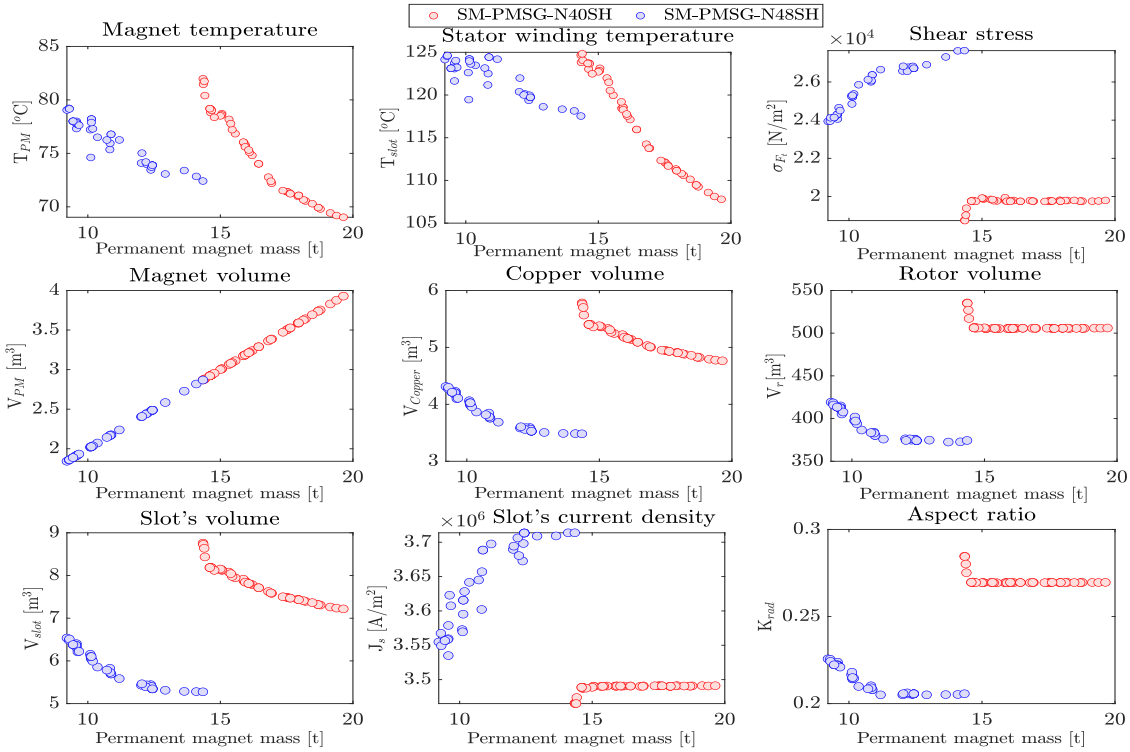

Figure 7.33: Comparative Analysis of machine A -with Ferrite- characteristics I

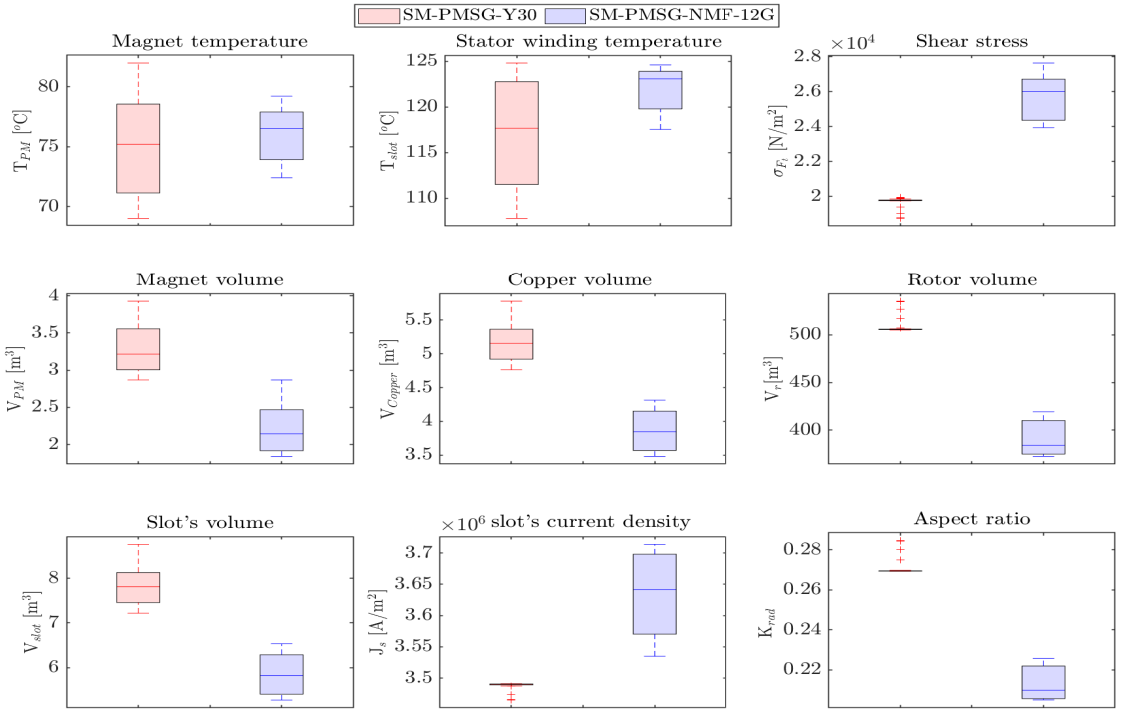

Figure 7.34: Statistical analysis of machine A -with NdFeB- characteristics I

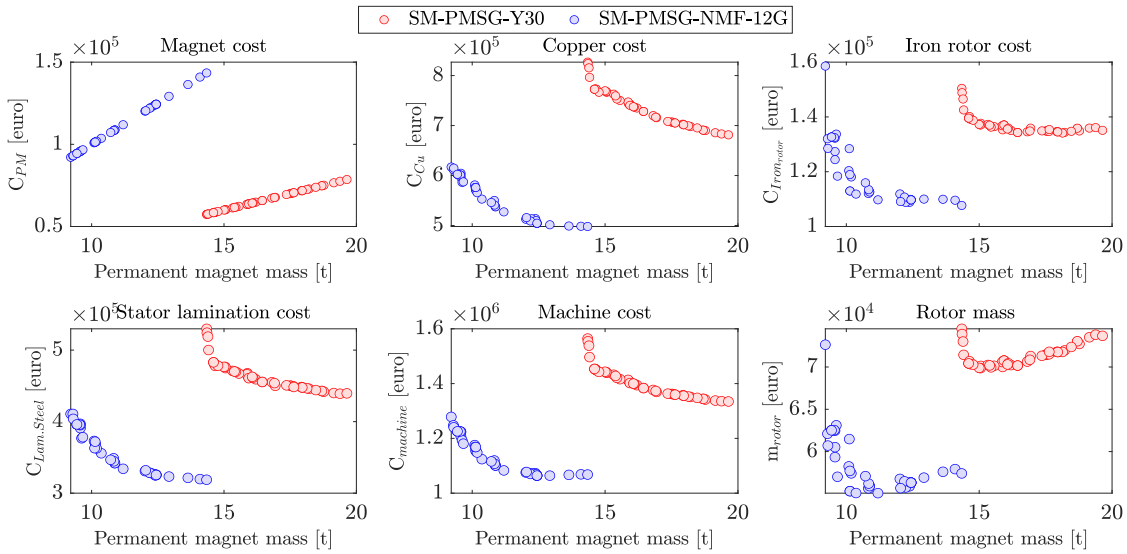

Figure 7.35: Comparative Analysis of machine A -with Ferrite- characteristics II

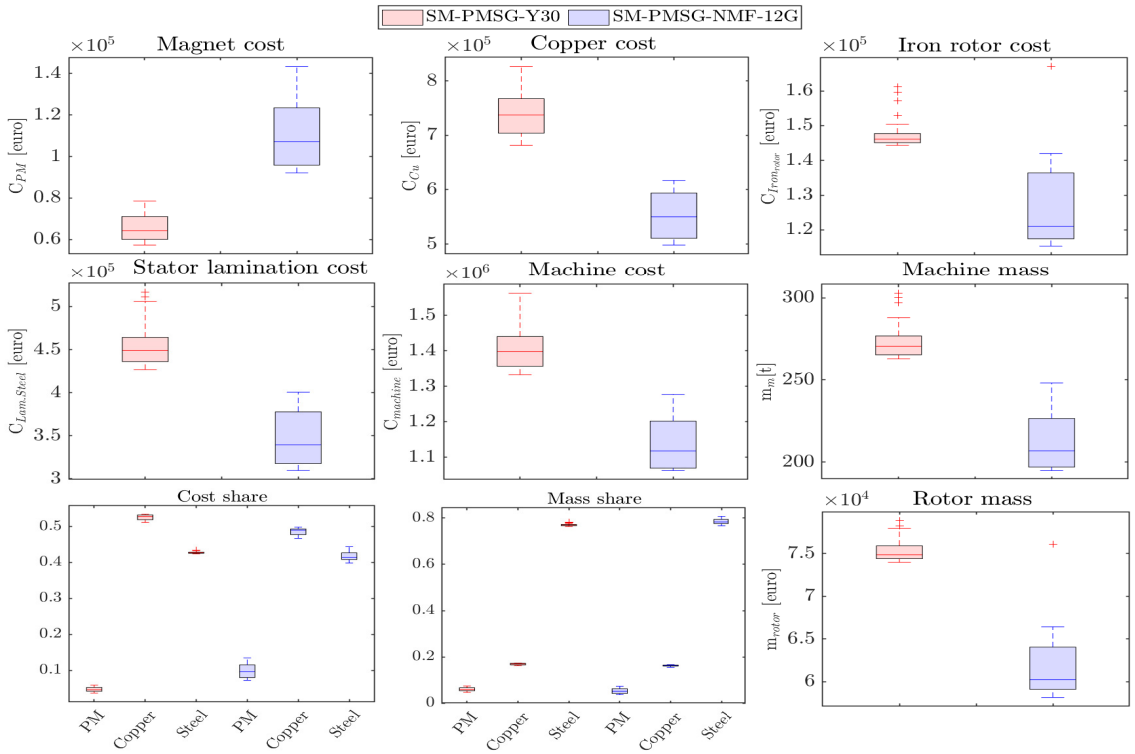

Figure 7.36: Statistical analysis of machine A -with Ferrite- characteristics II

7.4.2.2 Machine B (100 pole-pairs and 240 slots)

Table 7.11: Optimization problem of Machine B: key design parameters, bounds and constraints

<table>
<tr><td colspan="5">Fixed parameters</td><td>Constraints</td><td>Objective functions</td></tr>
<tr><td>PMSG</td><td colspan="2">ST-</td><td colspan="2">SM-</td><td rowspan="5">$T_{max} \leq 125\ ^{o}C$
$\Gamma_{max} \geq 20MNm$</td><td rowspan="5">$f_{Obj_1} = \min(m_{PM})$
$f_{Obj_2} = \min(m_{act})$</td></tr>
<tr><td>Nominal speed [rpm]</td><td colspan="2">7.5</td><td colspan="2">7.5</td></tr>
<tr><td>Winding topology</td><td colspan="4">3-phases 2-layers
Concentrated winding</td></tr>
<tr><td>Permanent magnet</td><td>N40SH</td><td>N48SH</td><td>Y30</td><td>NMF-15G</td></tr>
<tr><td>Airgap</td><td colspan="4">10.16</td></tr>
<tr><td colspan="7">Lower and upper bounds
LB/UB$_{ST-PMSG}$ =[R$_g$[m], L$_{act}$[m], θ_s[%], h$_s$[m], θ_{PM}[%], h$_{PM}$[m], J$_s$[A/m^2], h$_{ys}$[m]]
LB/UB$_{SM-PMSG}$ =[R$_g$[m], L$_{act}$[m], θ_s[%], h$_s$[m], θ_{PM}[%], h$_{PM}$[m], J$_s$[A/m^2], h$_{ys}$[m], h$_{yr}$[m]]</td></tr>
<tr><td>ST-PMSG$_{NdFeB}$</td><td colspan="6">LB = [3.0, 1.0, 0.30, 0.05, 0.15, 0.02, 2.5e6, 0.04]
UB = [7.0, 4.0, 0.55, 0.50, 0.50, 0.10, 5.5e6, 0.10]</td></tr>
<tr><td>ST-PMSG$_{Ferrite}$</td><td colspan="6">LB = [3.0, 1.0, 0.30, 0.05, 0.15, 0.02, 2.5e6, 0.04]
UB = [9.0, 5.0, 0.55, 0.50, 0.50, 0.10, 5.5e6, 0.10]</td></tr>
<tr><td>SM-PMSG$_{NdFeB}$</td><td colspan="6">LB = [2.7, 2.0, 0.30, 0.07, 0.50, 0.01, 2.5e6, 0.04, 0.045]
UB = [7.0, 4.0, 0.55, 0.50, 0.90, 0.10, 5.5e6, 0.30, 0.20]</td></tr>
<tr><td>SM-PMSG$_{Ferrite}$</td><td colspan="6">LB = [2.7, 2.0, 0.30, 0.07, 0.50, 0.01, 2.5e6, 0.04, 0.045]
UB = [9.0, 5.0, 0.55, 0.50, 0.90, 0.20, 5.5e6, 0.30, 0.20]</td></tr>
</table>

A) **Machine B (with NdFeB)**

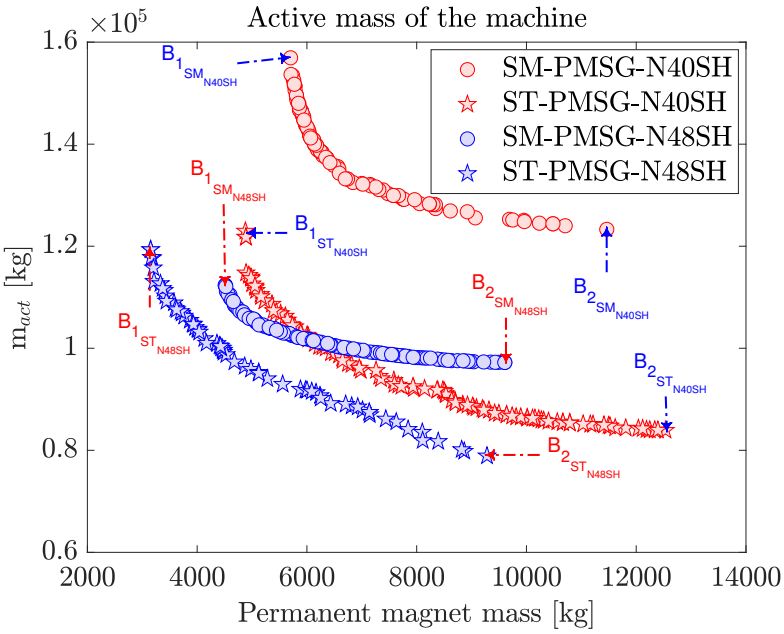

Figure 7.37: Pareto optimality of machine B (p=100 & N_s=240) with NdFeB N40SH (B_r = 1.21 T) & N48SH (B_r = 1.39 T)

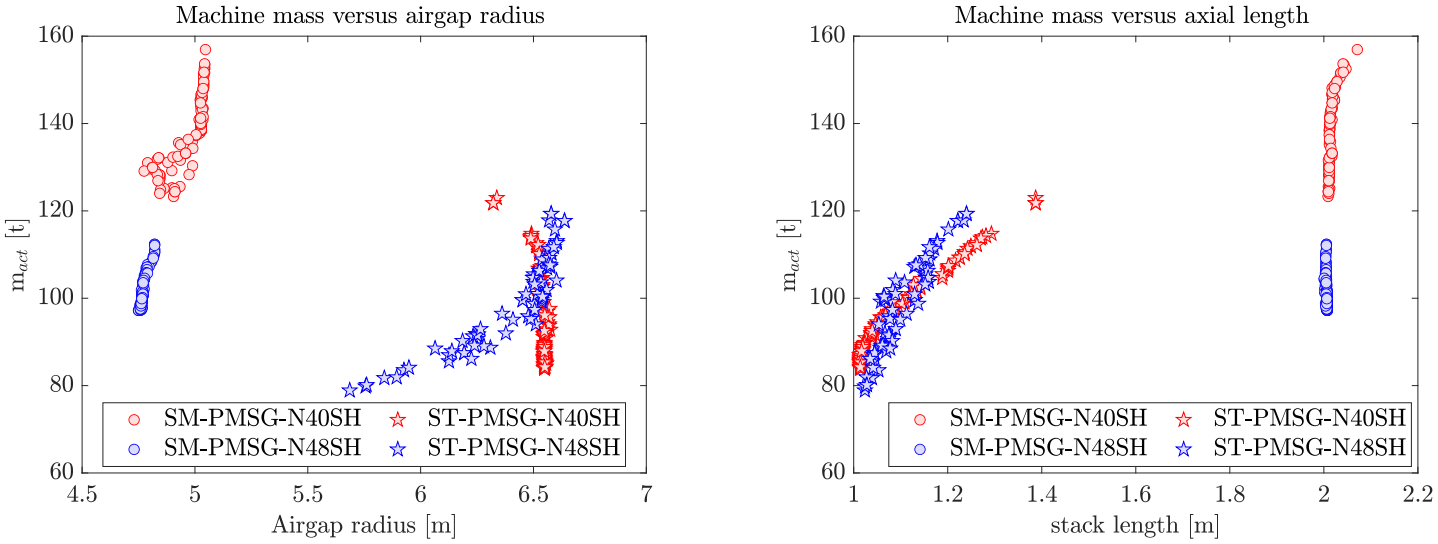

(a) Machine's mass versus airgap radius

(b) Machine's mass versus axial length

Figure 7.38: Mass of machine B versus its airgap radius and axial length

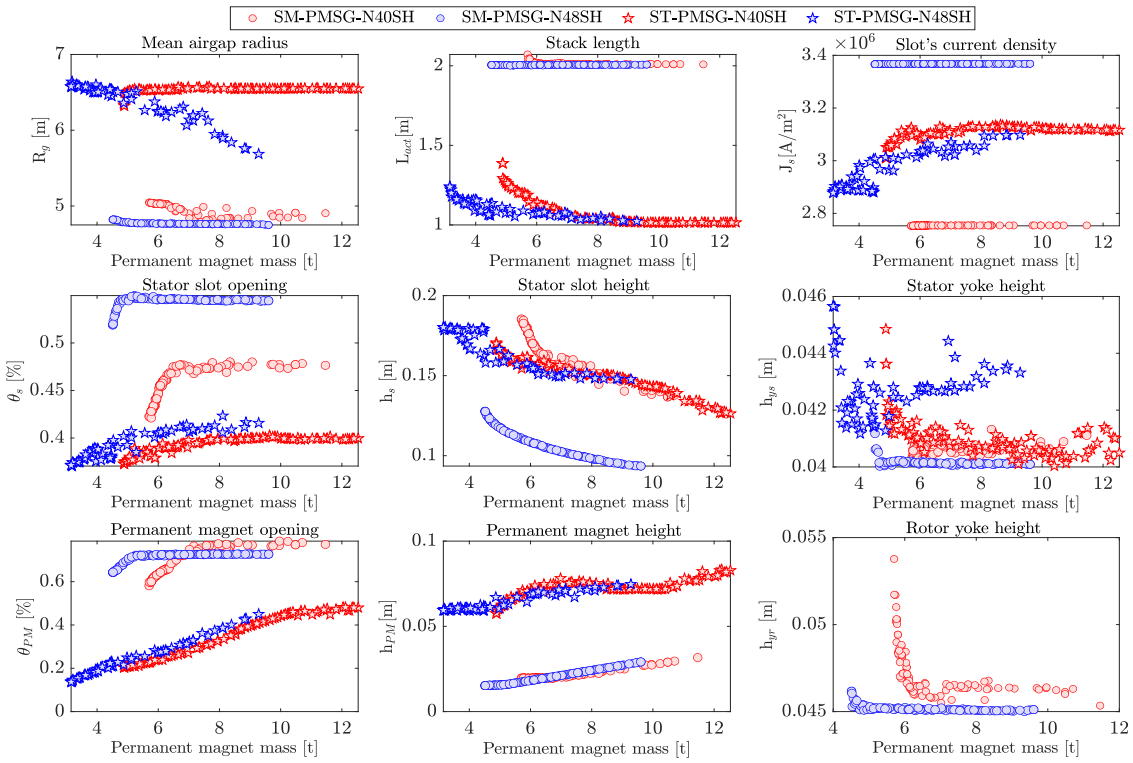

Figure 7.39: Variation trends of optimization parameters with respect to permanent magnet mass - machine B with NdFeB

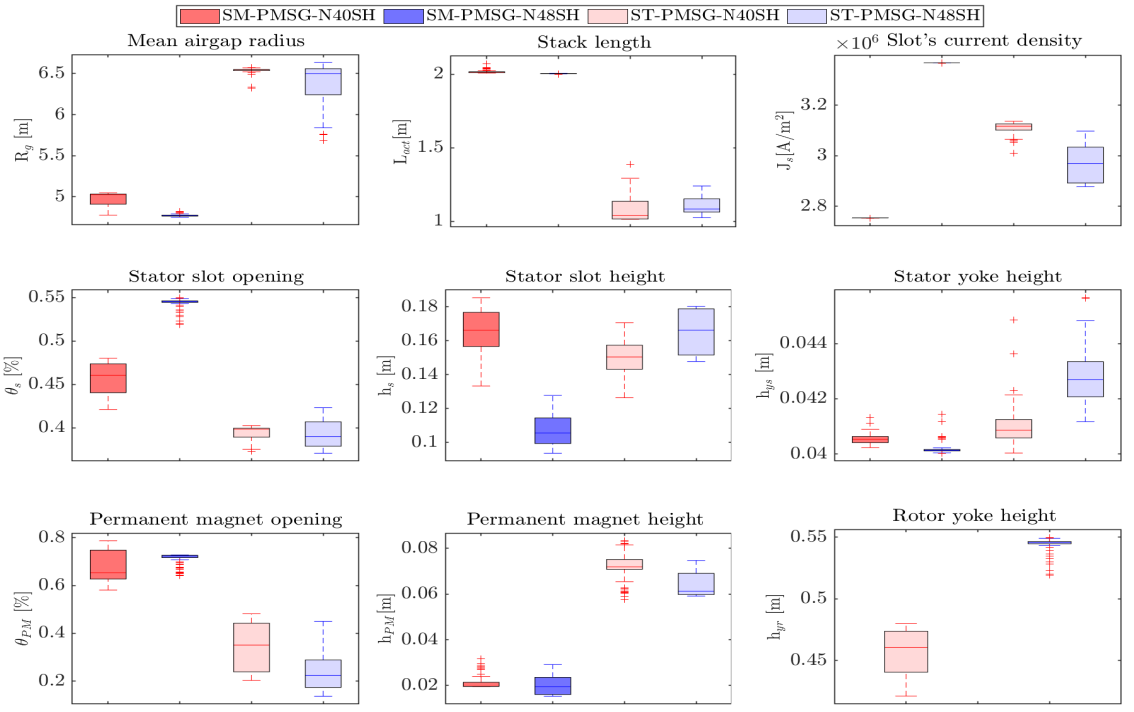

Figure 7.40: Statistical analysis of optimization parameters - machine B with NdFeB

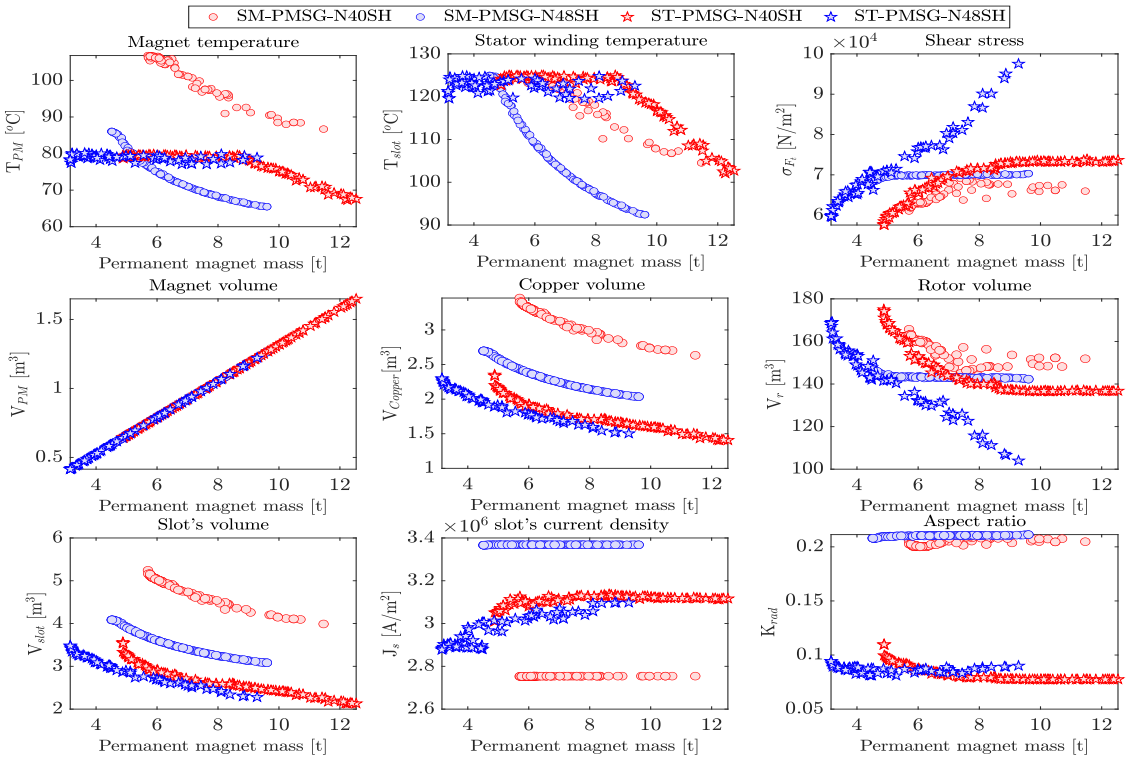

Figure 7.41: Comparative Analysis of machine B -with NdFeB- characteristics I

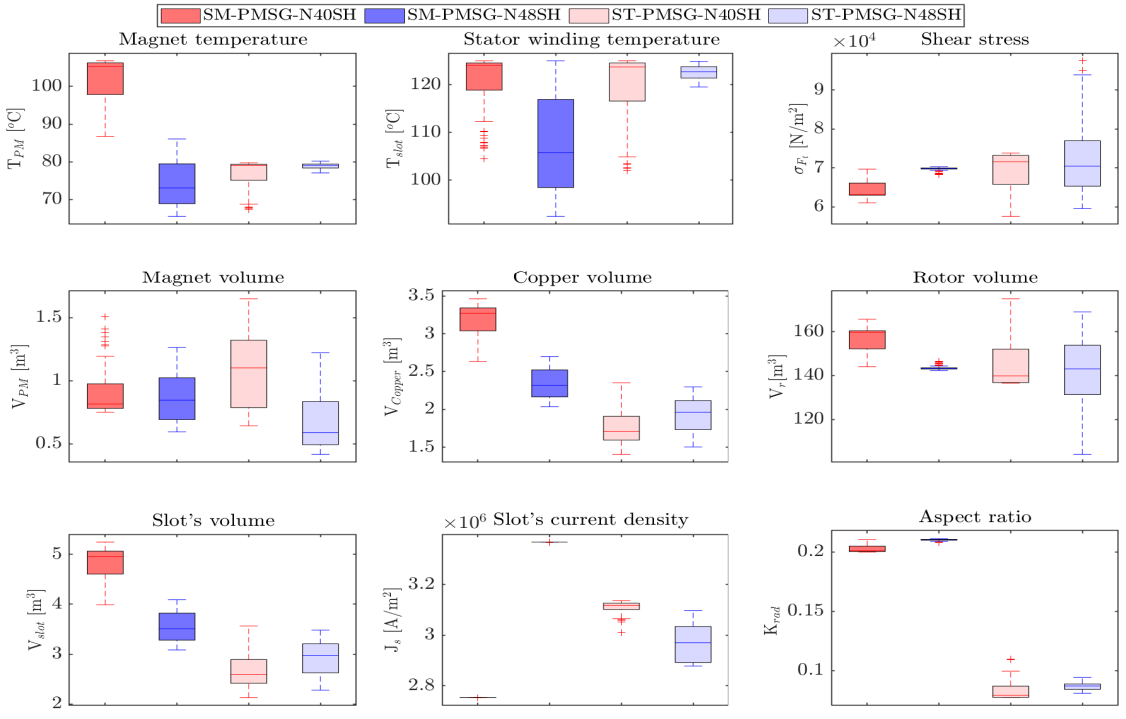

Figure 7.42: Statistical analysis of machine B -with NdFeB- characteristics I

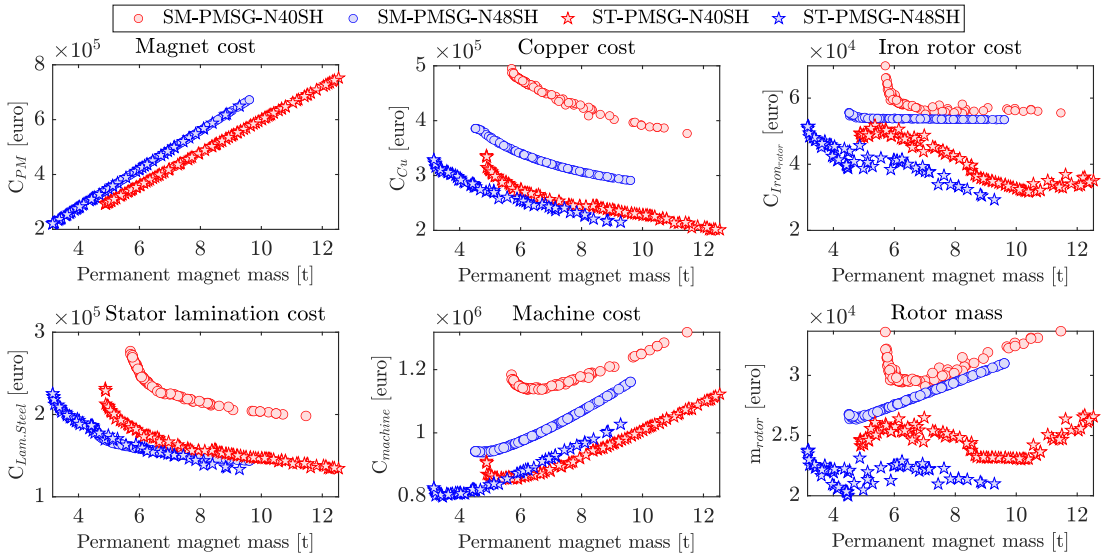

Figure 7.43: Comparative Analysis of machine B -with NdFeB- characteristics II

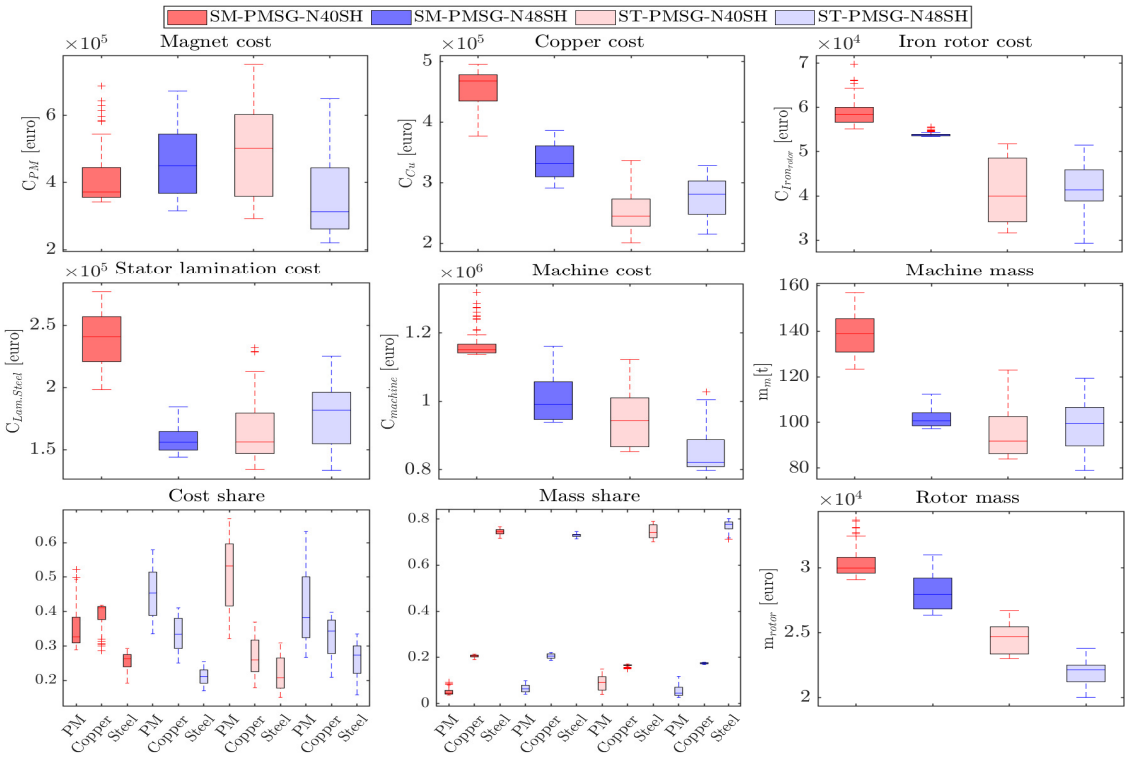

Figure 7.44: Statistical analysis of machine B -with NdFeB- characteristics II

B) **Machine B (with Ferrite)**

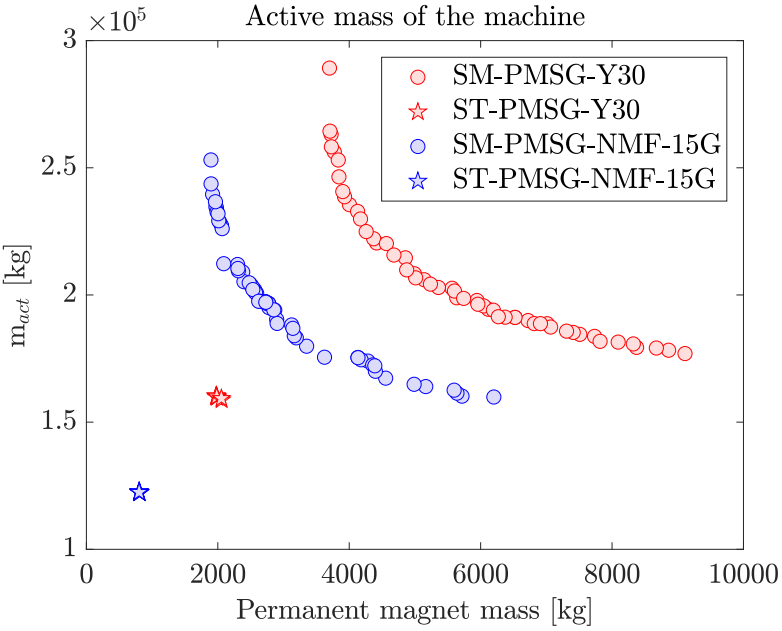

Figure 7.45: Pareto optimality (p=100 & N_s=240 with Ferrite NMF-15G (B_r = 0.50 T) and Y30 (B_r = 0.38 T))

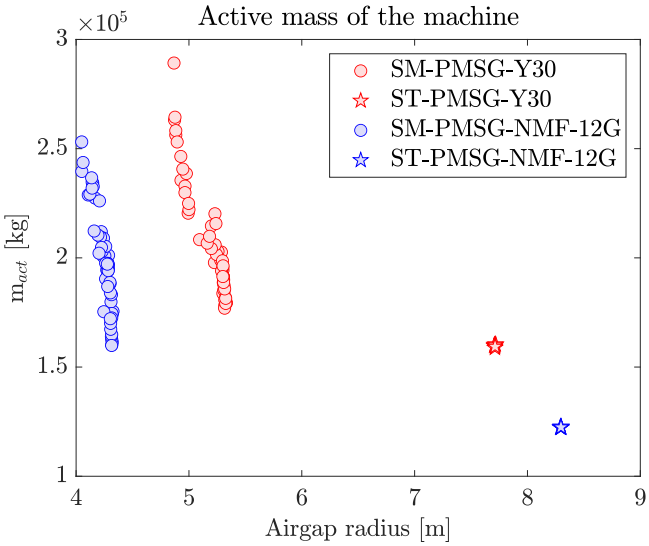

(a) Machine's mass versus airgap radius

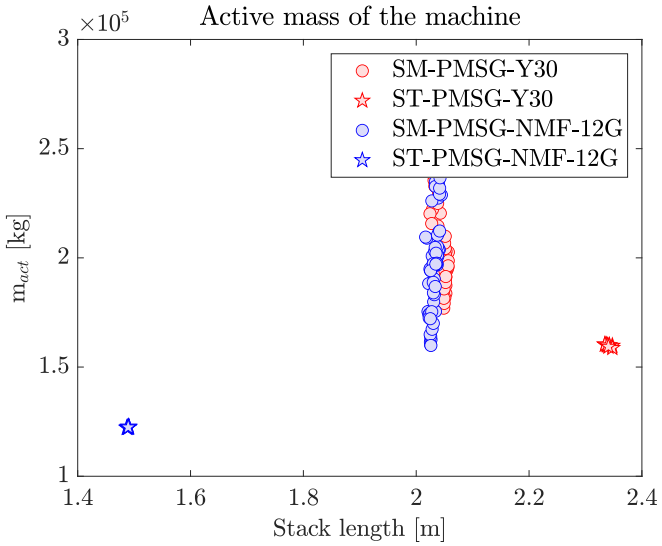

(b) Machine's mass versus axial length

Figure 7.46: Mass of machine B versus its airgap radius and axial length

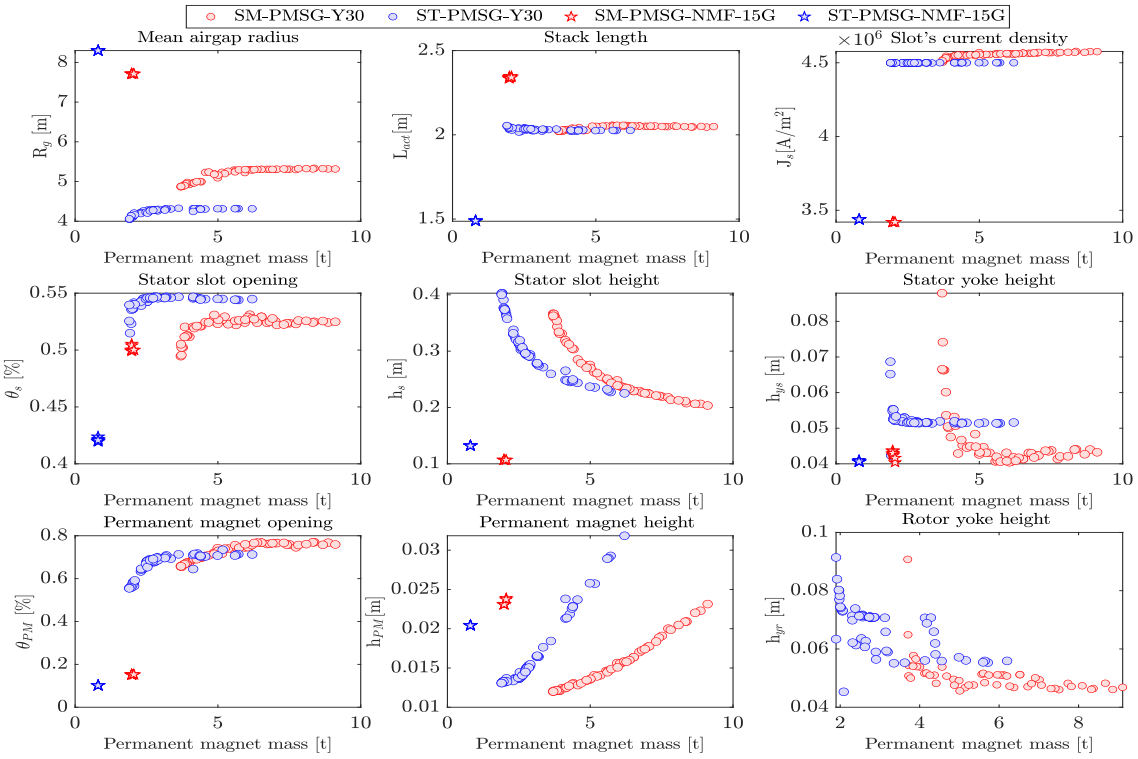

Figure 7.47: Variation trends of optimization parameters with respect to permanent magnet mass - machine B with Ferrite

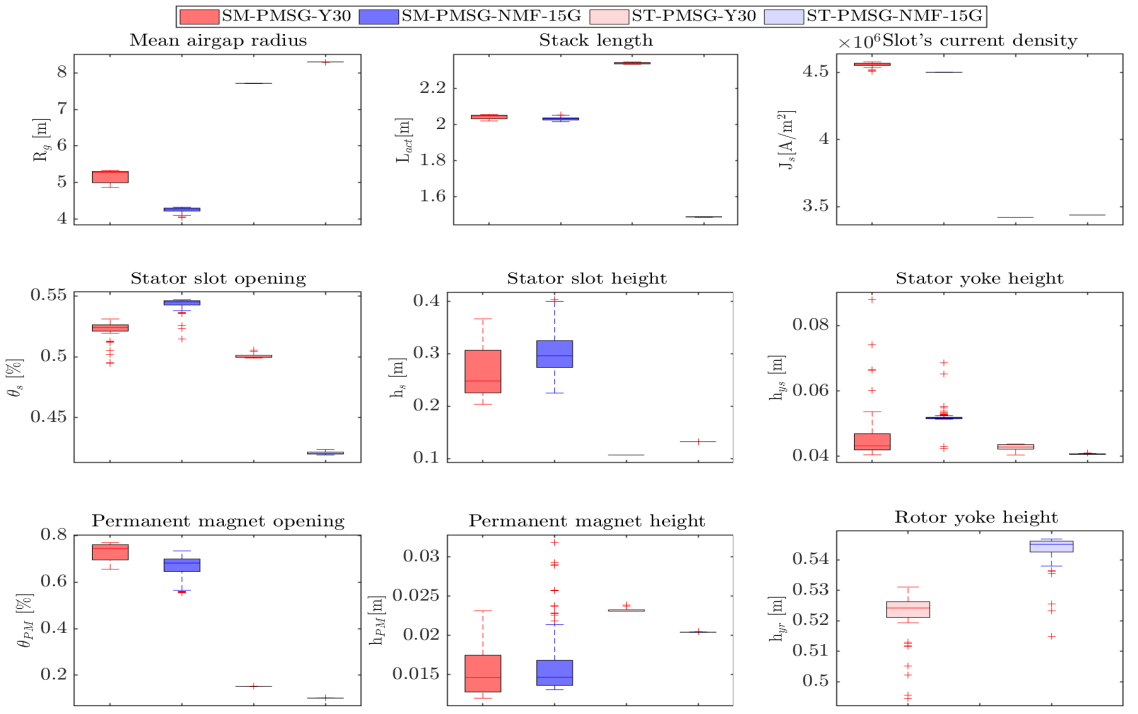

Figure 7.48: Statistical analysis of optimization parameters - machine B with Ferrite

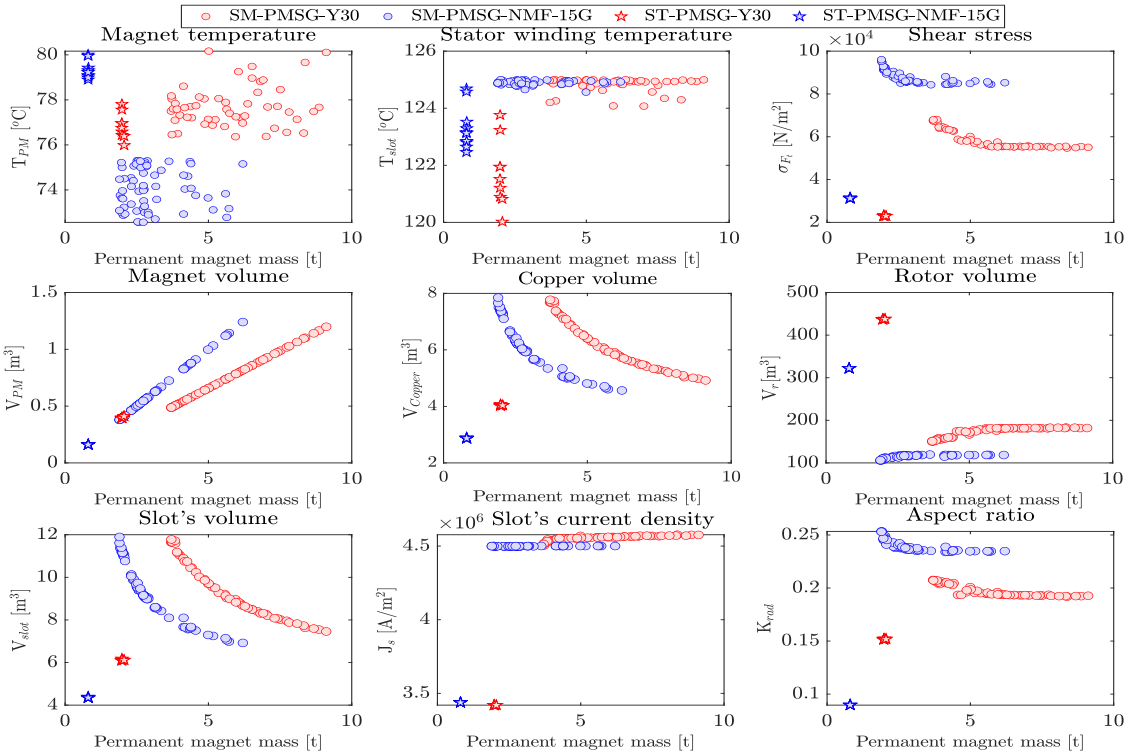

Figure 7.49: Comparative Analysis of machine B -with Ferrite- characteristics I

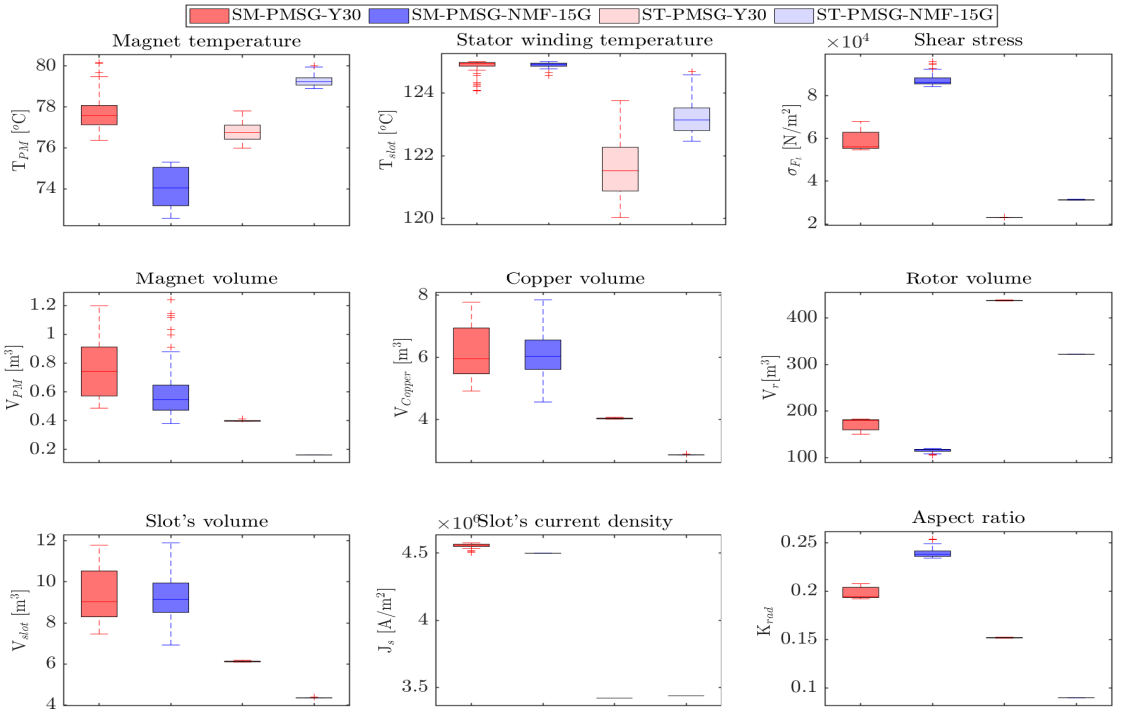

Figure 7.50: Statistical analysis of machine B -with Ferrite- characteristics I

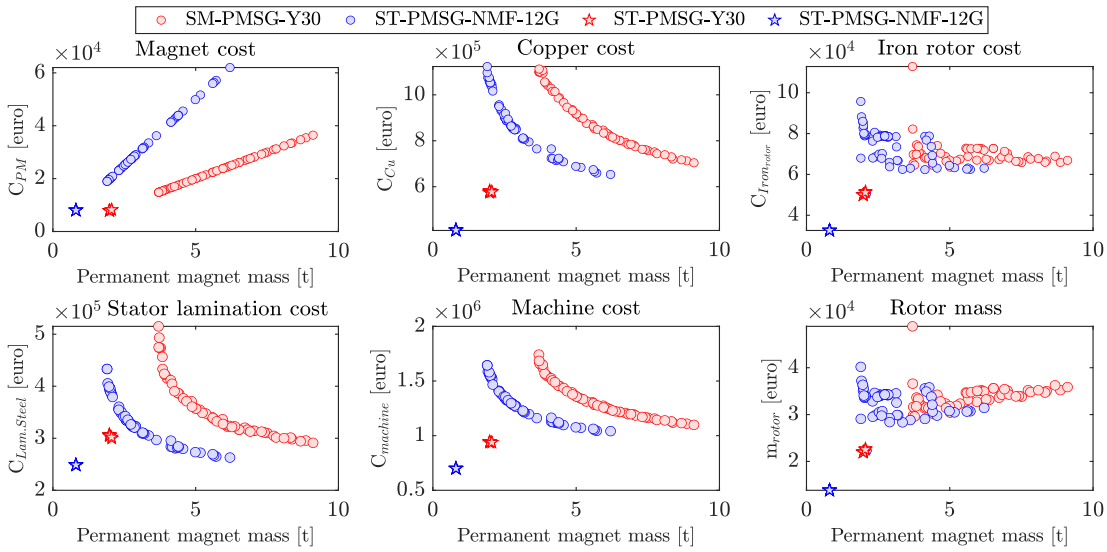

Figure 7.51: Comparative Analysis of machine B -with Ferrite- characteristics II

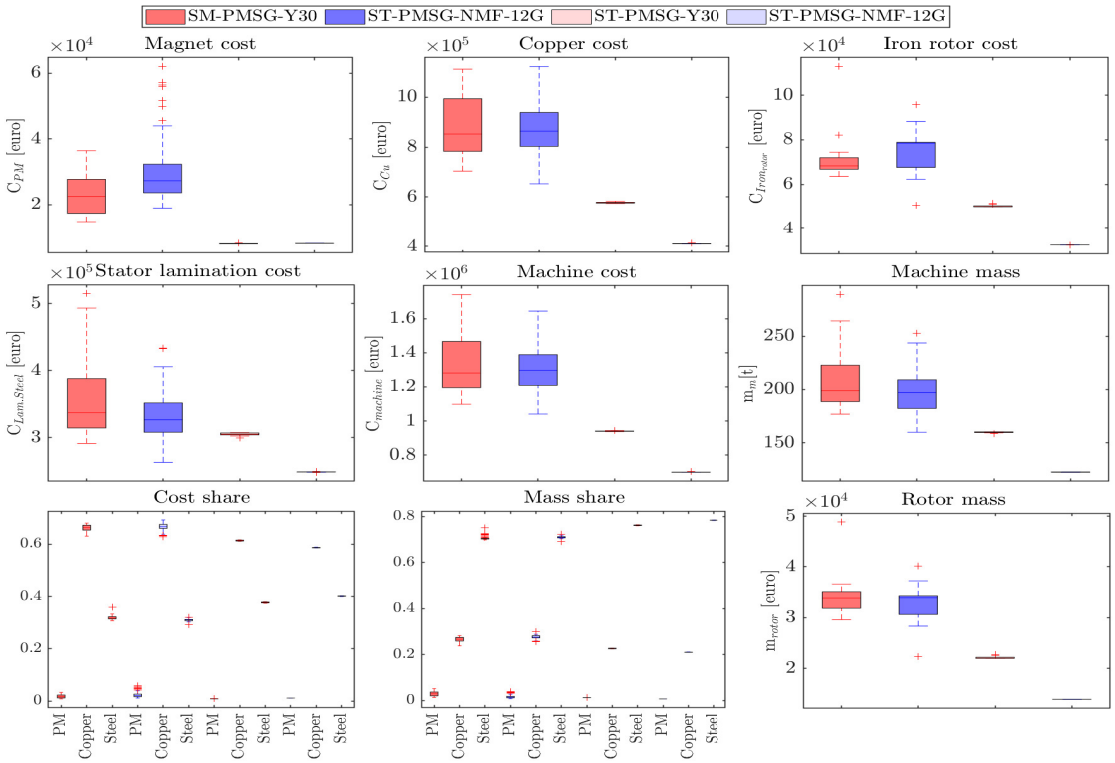

Figure 7.52: Statistical analysis of machine B -with Ferrite- characteristics II

7.4.2.3 Machine C (189 pole-pairs and 1134 slots)

Table 7.12: Optimization problem of Machine C: key design parameters, bounds and constraints

<table>
<tr><td colspan="5">Fixed parameters</td><td>Constraints</td><td>Objective functions</td></tr>
<tr><td>PMSG</td><td colspan="2">ST-</td><td colspan="2">SM-</td><td rowspan="5">$T_{max} \leq 125\ ^{o}$C
$\Gamma_{max} \geq 20$MNm</td><td rowspan="5">$f_{Obj_1} = \min(m_{PM})$
$f_{Obj_2} = \min(m_{act})$</td></tr>
<tr><td>Nominal speed [rpm]</td><td colspan="2">7.5</td><td colspan="2">7.5</td></tr>
<tr><td>Winding topology</td><td colspan="4">3-phases 1-layer
distributed winding</td></tr>
<tr><td>Permanent magnet</td><td>N40SH</td><td>N48SH</td><td>Y30</td><td>NMF-15G</td></tr>
<tr><td>Airgap</td><td colspan="4">16</td></tr>
<tr><td colspan="7">Lower and upper bounds
LB/UB$_{ST-PMSG}$ =[R_g[m], L_{act}[m], θ_s[%], h_s[m], θ_{PM}[%], h_{PM}[m], J_s[A/m^2], h_{ys}[m]]
LB/UB$_{SM-PMSG}$ =[R_g[m], L_{act}[m], θ_s[%], h_s[m], θ_{PM}[%], h_{PM}[m], J_s[A/m^2], h_{ys}[m], h_{yr}[m]]</td></tr>
<tr><td>ST-PMSG$_{NdFeB}$</td><td colspan="6">LB = [3.0, 1.0, 0.30, 0.05, 0.10, 0.01, 2.5e6, 0.04]
UB = [7.0, 4.0, 0.55, 0.50, 0.50, 0.70, 5.5e6, 0.10]</td></tr>
<tr><td>ST-PMSG$_{Ferrite}$</td><td colspan="6">LB = [3.0, 1.0, 0.30, 0.05, 0.10, 0.02, 2.5e6, 0.04]
UB = [9.0, 5.0, 0.55, 0.50, 0.50, 0.10, 5.5e6, 0.10]</td></tr>
<tr><td>SM-PMSG$_{NdFeB}$</td><td colspan="6">LB = [2.7, 1.5, 0.30, 0.07, 0.50, 0.01, 2.5e6, 0.04, 0.045]
UB = [7.0, 4.0, 0.55, 0.50, 0.90, 0.10, 5.5e6, 0.30, 0.20]</td></tr>
<tr><td>SM-PMSG$_{Ferrite}$</td><td colspan="6">LB = [2.7, 1.5, 0.30, 0.07, 0.50, 0.01, 2.5e6, 0.04, 0.045]
UB = [10.0, 5.5, 0.55, 0.50, 0.90, 0.20, 5.5e6, 0.30, 0.20]</td></tr>
</table>

A) **Machine C (with NdFeB)**

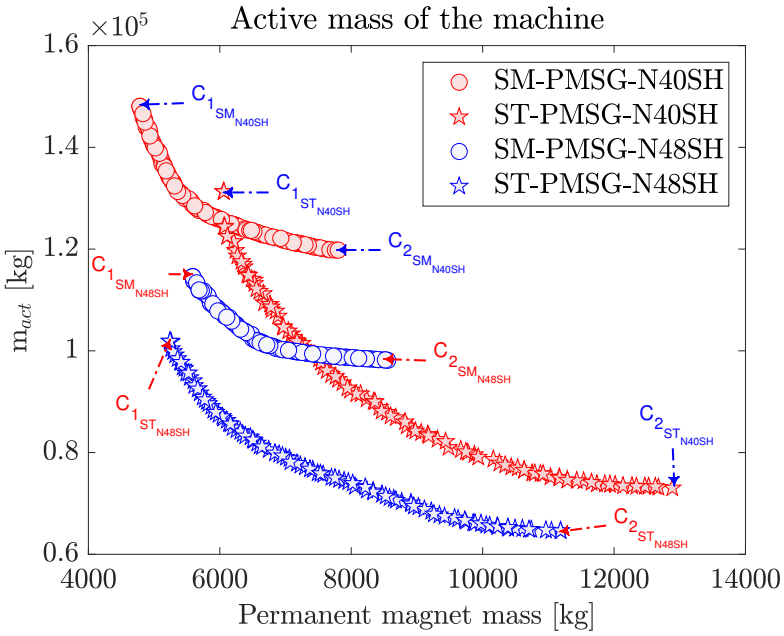

Figure 7.53: Pareto optimality of machine C (p=189 & N_s=1134) with NdFeB N40SH (B_r = 1.21 T) & N48SH (B_r = 1.39 T)

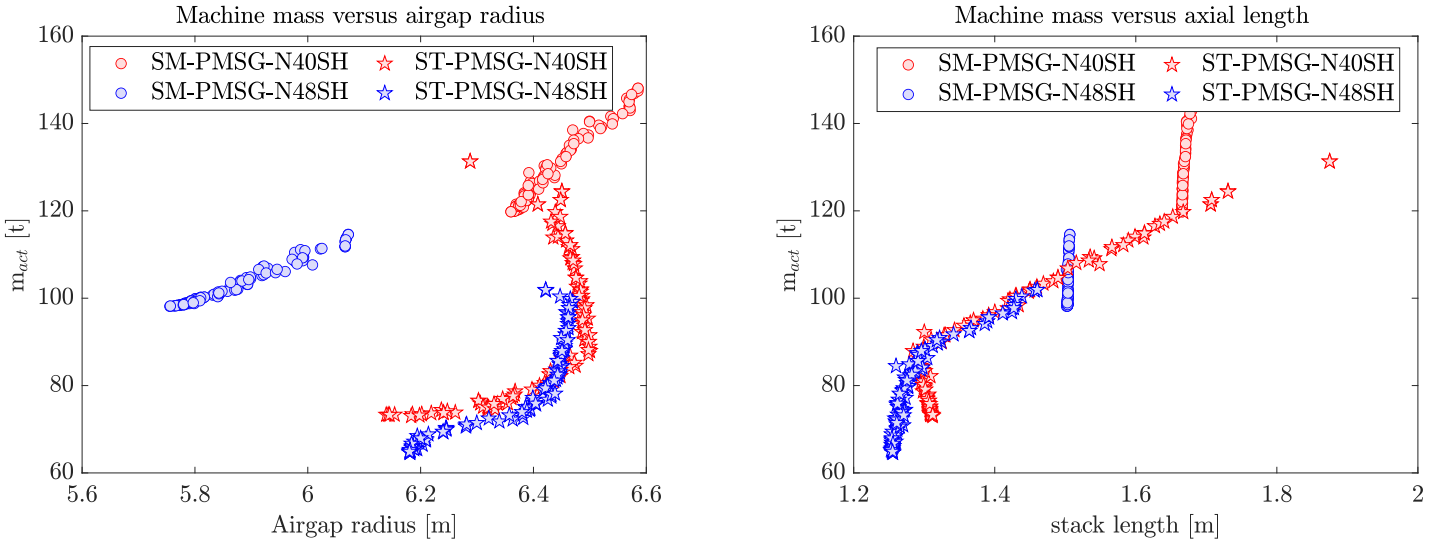

(a) Machine's mass versus airgap radius

(b) Machine's mass versus axial length

Figure 7.54: Mass of machine C versus its airgap radius and axial length

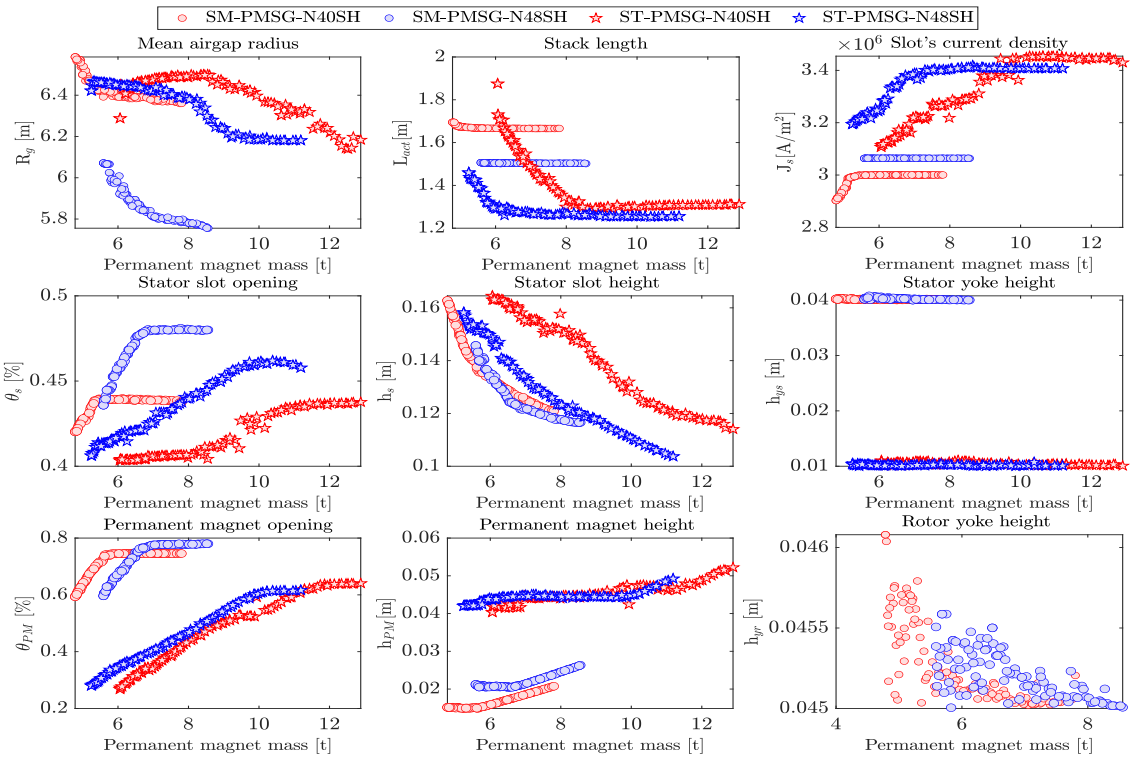

Figure 7.55: Variation trends of optimization parameters with respect to permanent magnet mass - machine C with NdFeB

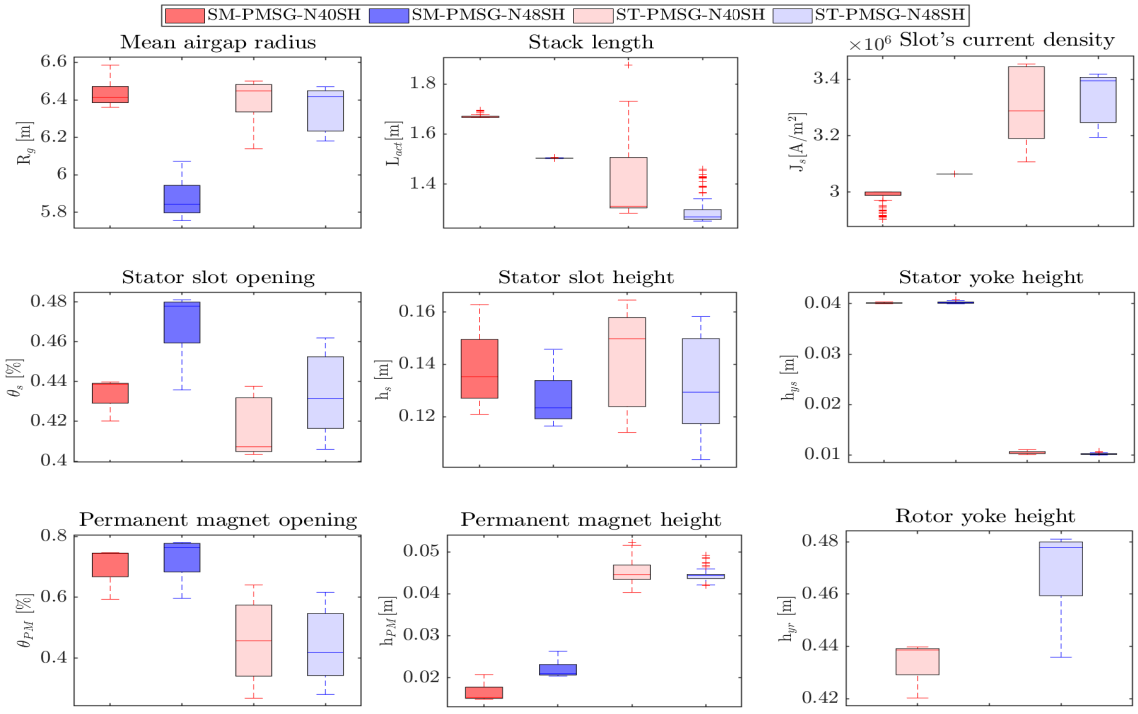

Figure 7.56: Statistical analysis of optimization parameters - machine C with NdFeB

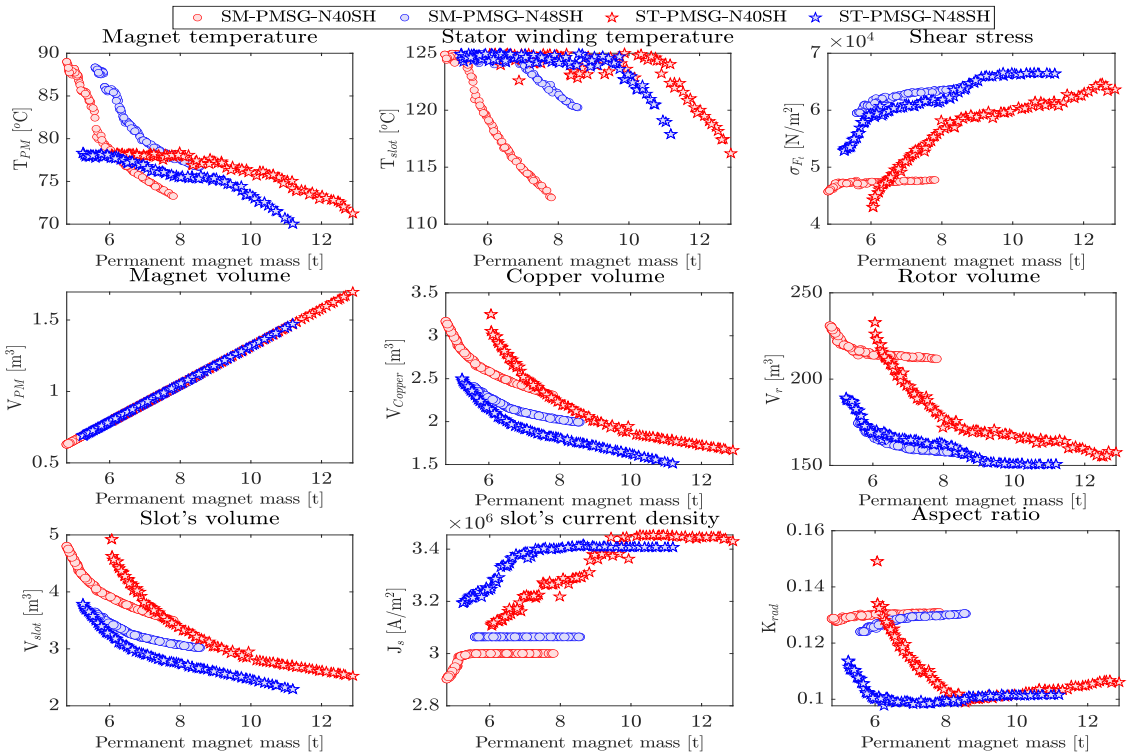

Figure 7.57: Comparative Analysis of machine C -with NdFeB- characteristics I

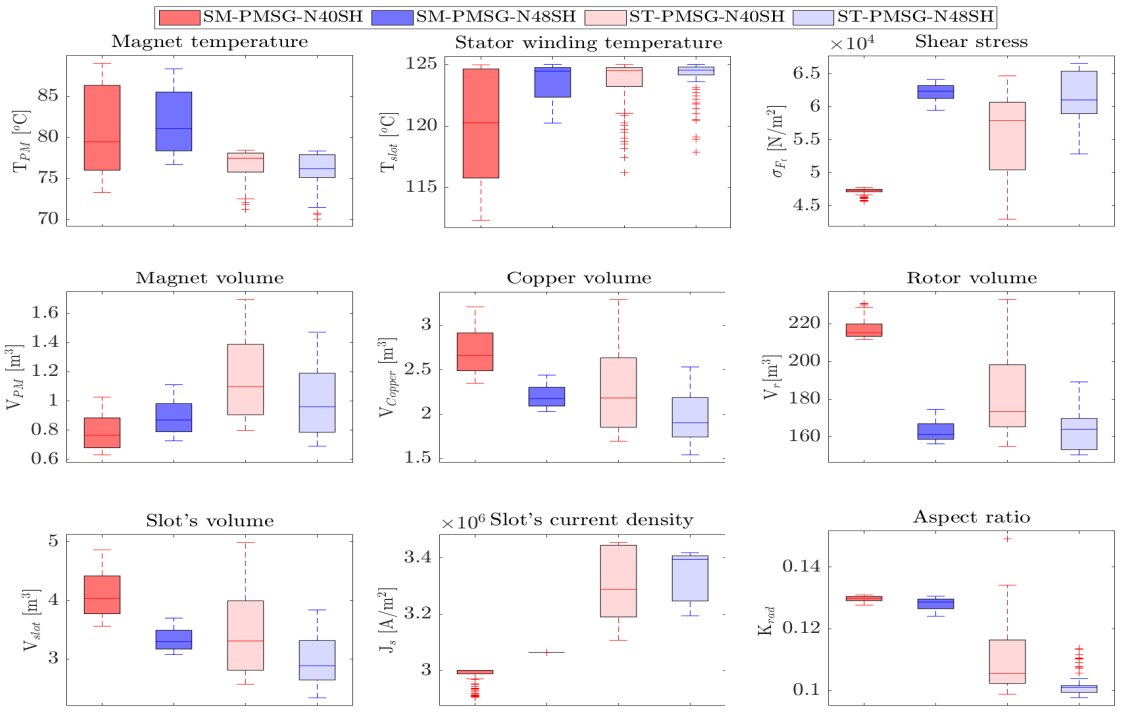

Figure 7.58: Statistical analysis of machine C -with NdFeB- characteristics I

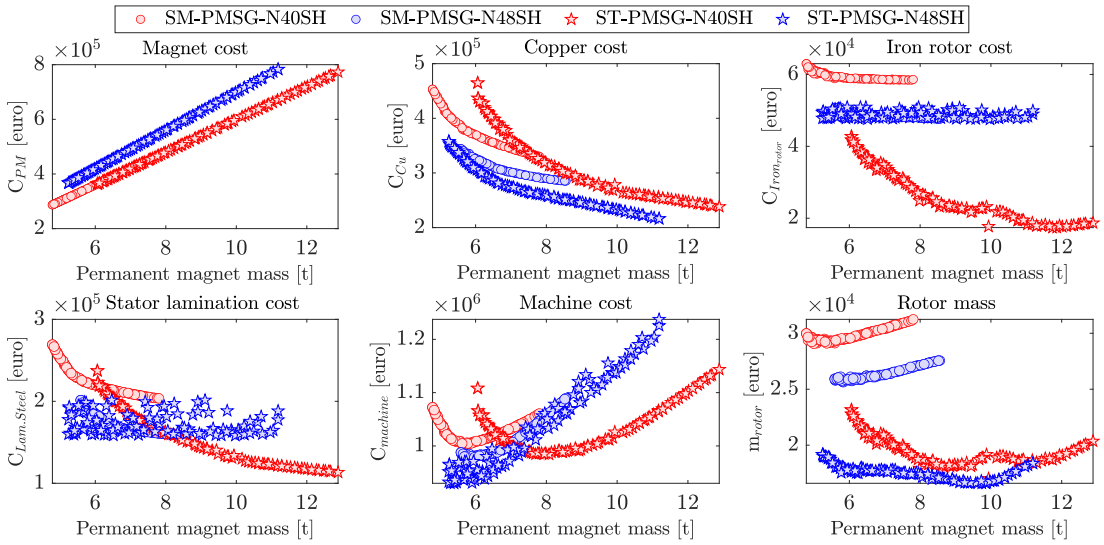

Figure 7.59: Comparative Analysis of machine C -with NdFeB- characteristics II

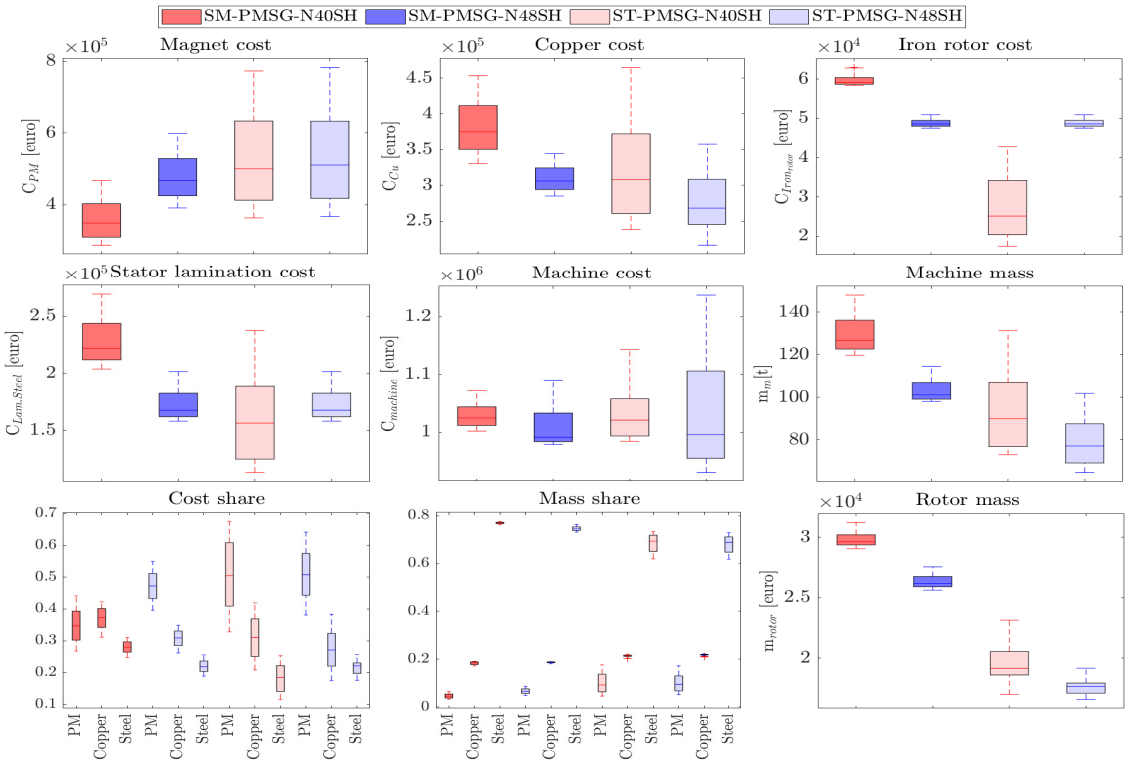

Figure 7.60: Statistical analysis of machine C -with NdFeB- characteristics II

B) **Machine C (with Ferrite)**

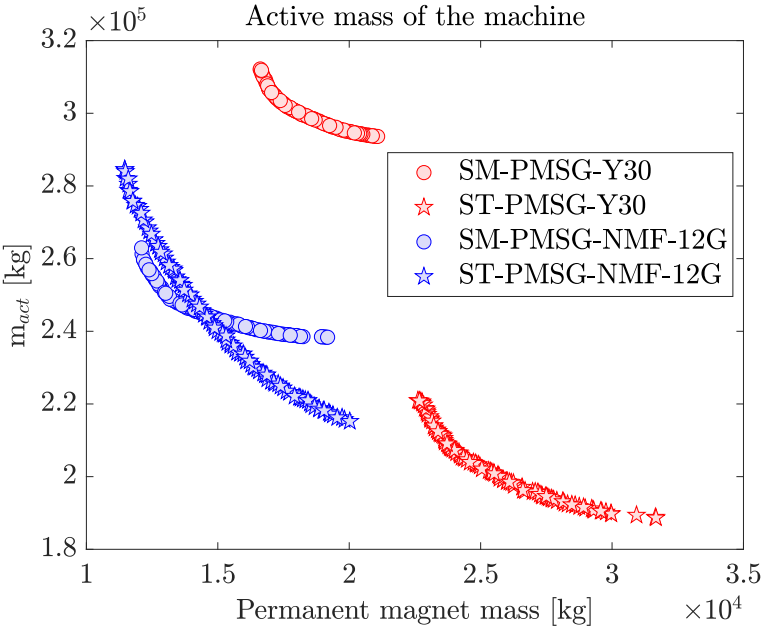

Figure 7.61: Pareto optimality (p=189 & N_s=1134 with NMF-15G (B_r=0.5T)/Y30 (B_r=0.38T))

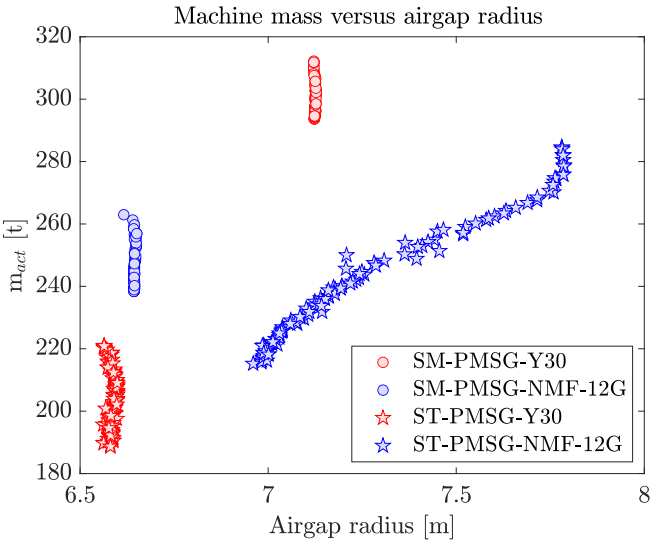

(a) Machine's mass versus airgap radius

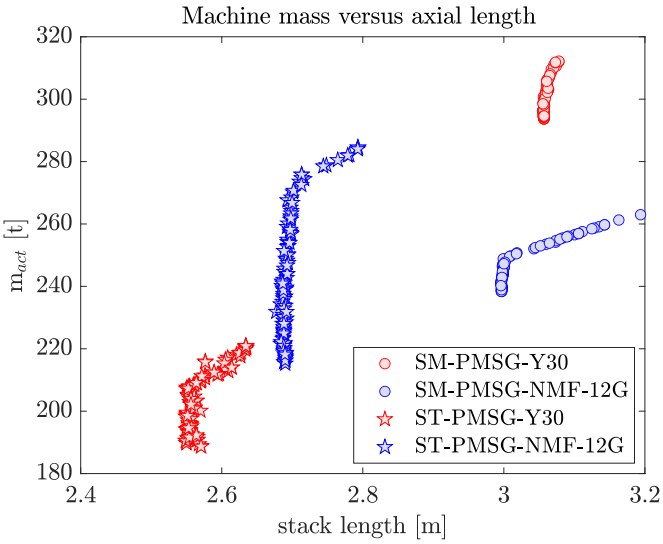

(b) Machine's mass versus axial length

Figure 7.62: Mass of machine C versus its airgap radius and axial length

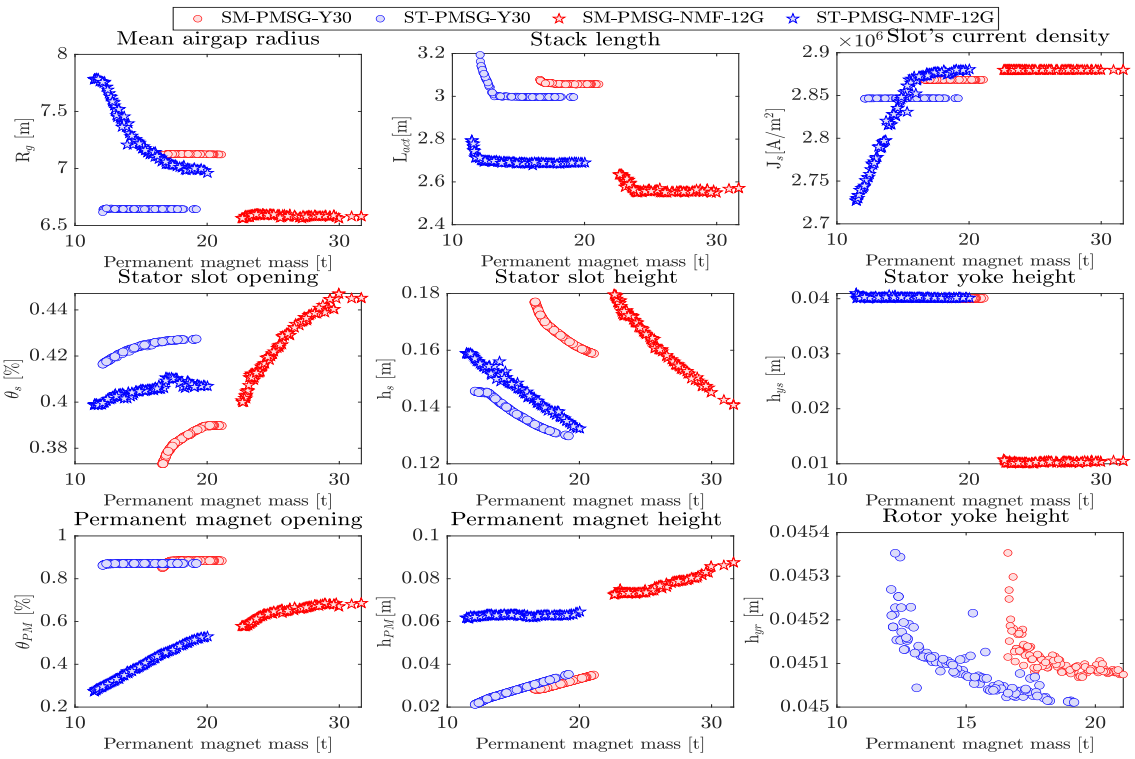

Figure 7.63: Variation trends of optimization parameters with respect to permanent magnet mass - machine C with Ferrite

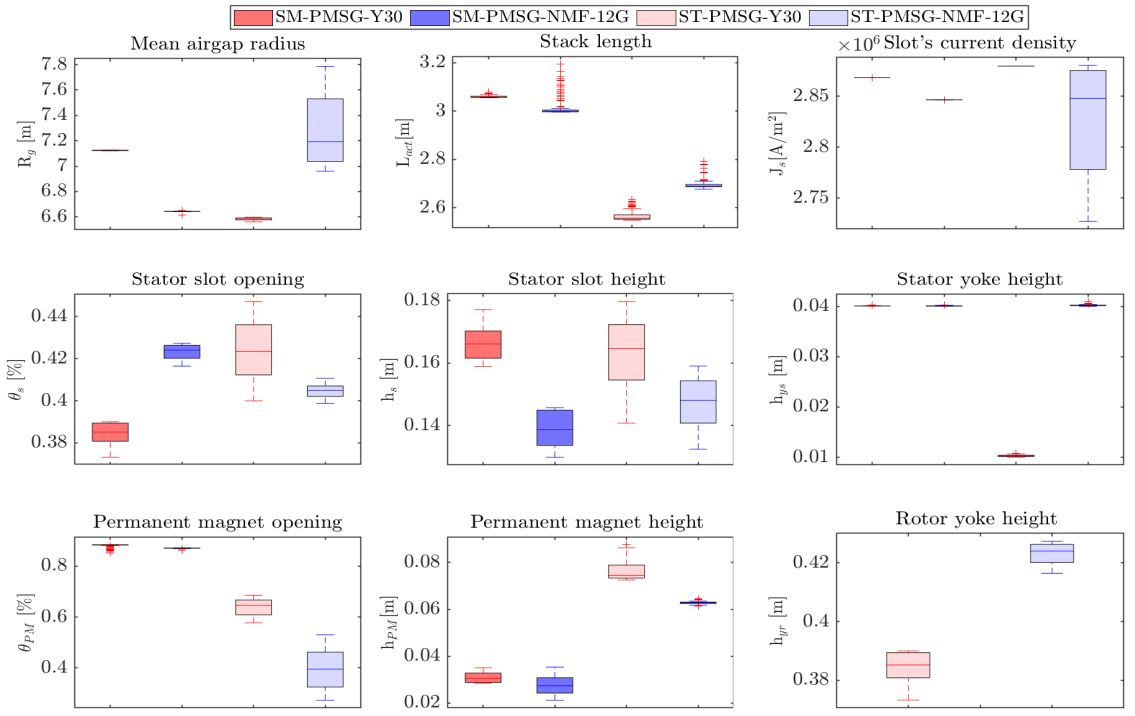

Figure 7.64: Statistical analysis of optimization parameters - machine C with Ferrite

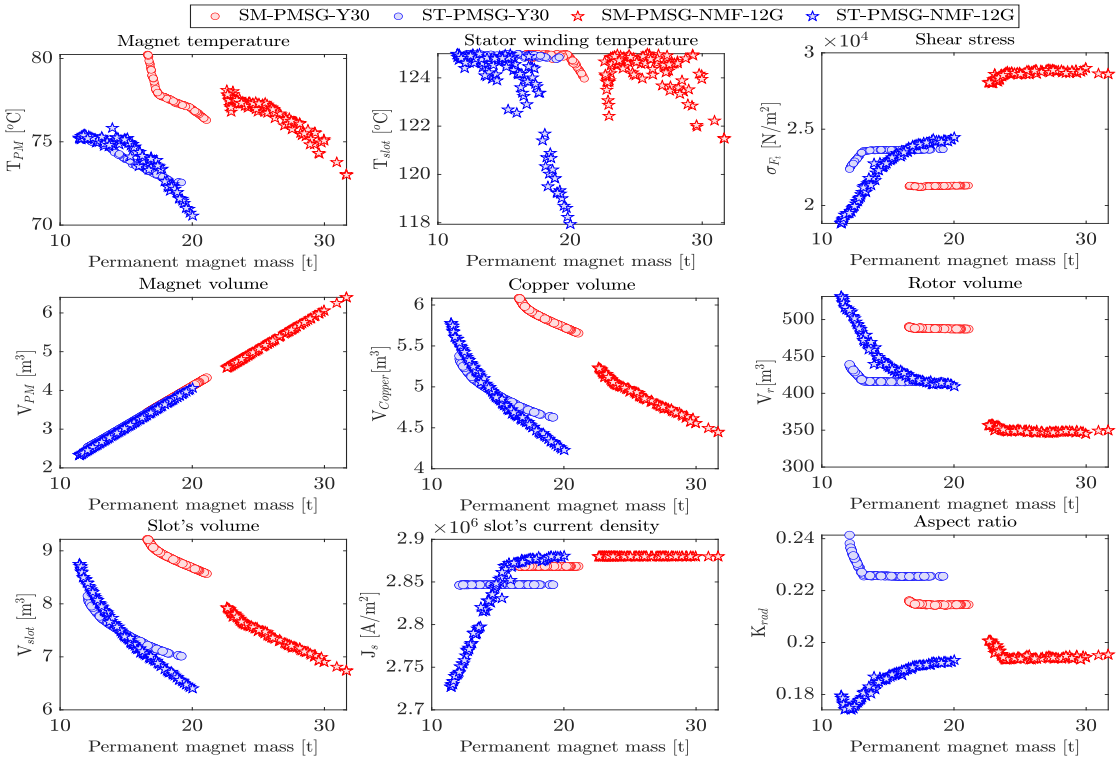

Figure 7.65: Comparative Analysis of machine C -with Ferrite- characteristics I

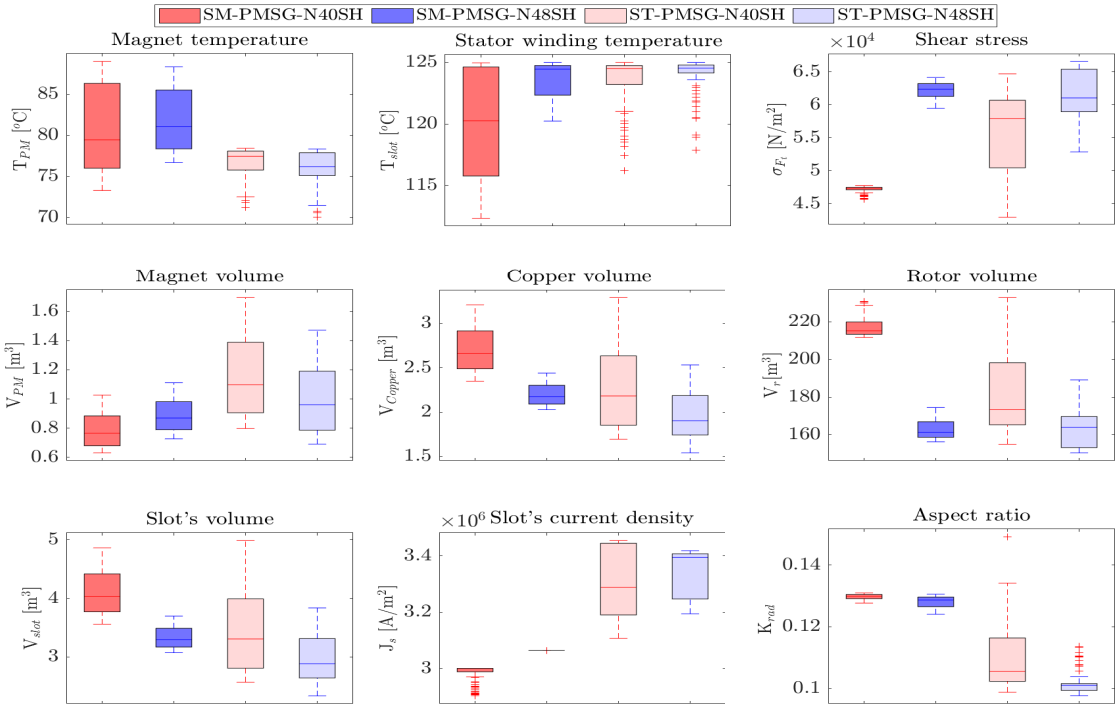

Figure 7.66: Statistical analysis of machine C -with Ferrite- characteristics I

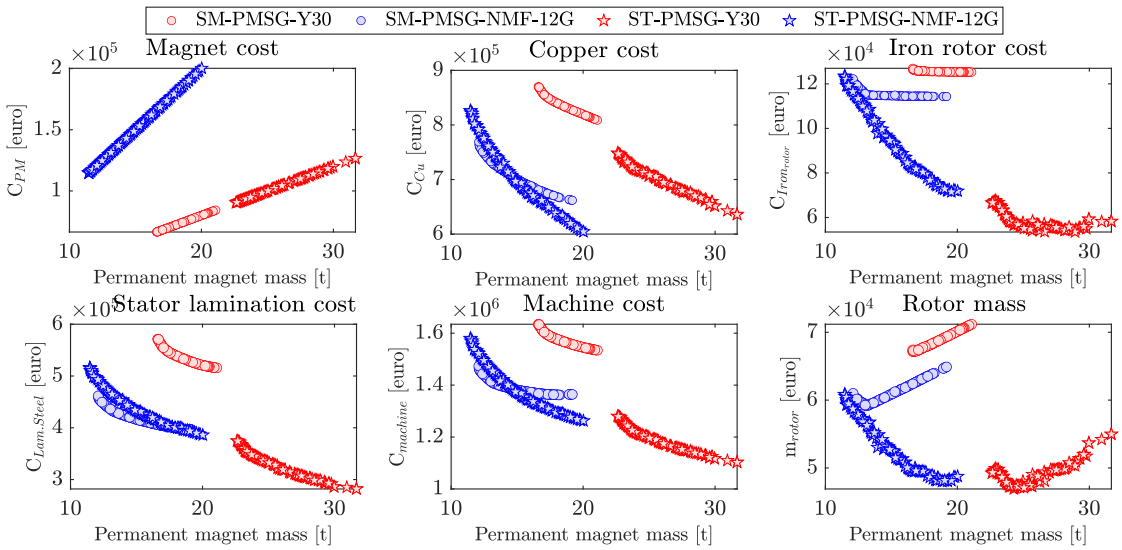

Figure 7.67: Comparative Analysis of machine C -with Ferrite- characteristics II

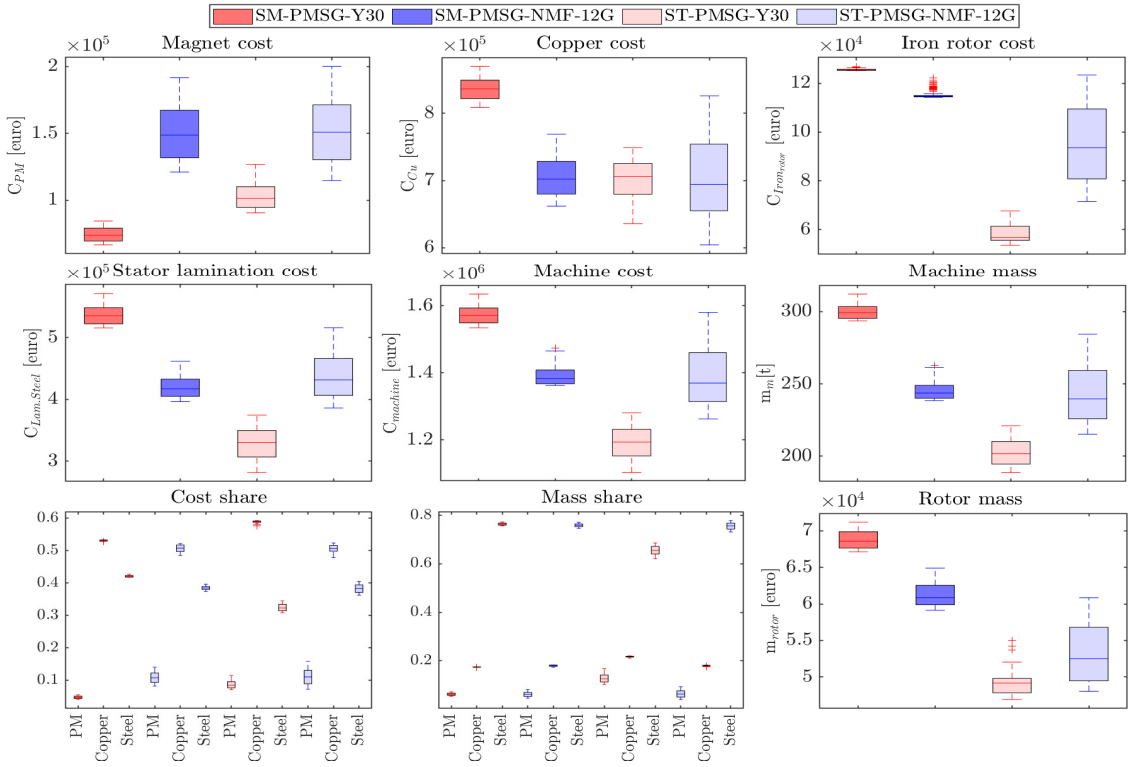

Figure 7.68: Statistical analysis of machine C -with Ferrite- characteristics II

7.4.3 Discussion

The design optimization presented in this chapter provides some interesting insight into the comparison along with highlighting the variables which have more influence on machine performances. Several conclusions can be drawn from the results obtained in this section:

1 **Technical comparison**

- It can be noticed that a compromise usually needs to be made between reducing permanent magnets mass and or machine mass. The machine's mass and the magnets mass are unambiguously conflicting objectives. Lighter machines consume magnets more than heavier ones. In order to balance the MMF in the machine, the reduction of the magnets mass must be compensated by increasing the copper volume. However, the mass density of copper is almost 15 per cent that of NdFeB which results in a significant increase of the machine's mass. For SM-PMSG machine A with NdFeB (See Fig. 7.21), reducing two fifths (3650 kg) of magnet mass induces a rise of one fifth (23400 kg) of the active materials mass. Then, to balance 3.650 t of magnet mass decrease, around 25 t of copper and steel is needed, and depending on the magnet grade the machine cost increase is between 5 % and 8 %. The same trends has been noticed for machines B and C with NdFeB (See Fig. 7.37 and Fig. 7.53).
- Considering the same magnet grade, spoke-type machines are found to be lighter than surface mounted radial flux machines. The only exception to this, was the results reported on the analysis on machine A with NdFeB N48SH. The ST-PMSG-N48SH is heavier than its equivalent SM-PMSG-N48SH over wide range of permanent magnet mass (above 4,2 t of PM). This could be explained by the high rotor volume of ST-PMSG (See Fig. 7.25 and Fig. 7.26).
- The performances of the machine may be reduced if the number of poles is too high, like in machine C with p = 189. While narrow magnets will have relatively high pole-to-pole leakage flux, narrow slots will have low filling factor especially in the case of bar coils; resulting in reduced torque density.
- **Magnet opening and thickness**

  For ST-PMSG, the magnet mass, m_{PM}, was found to increase linearly in general with increased magnet opening (See Fig. 7.23, Fig. 7.39 and Fig. 7.55), while above 5-8 t of magnet, the magnet thickness had a little effect on the increase in the magnet mass (See Fig. 7.24, Fig.

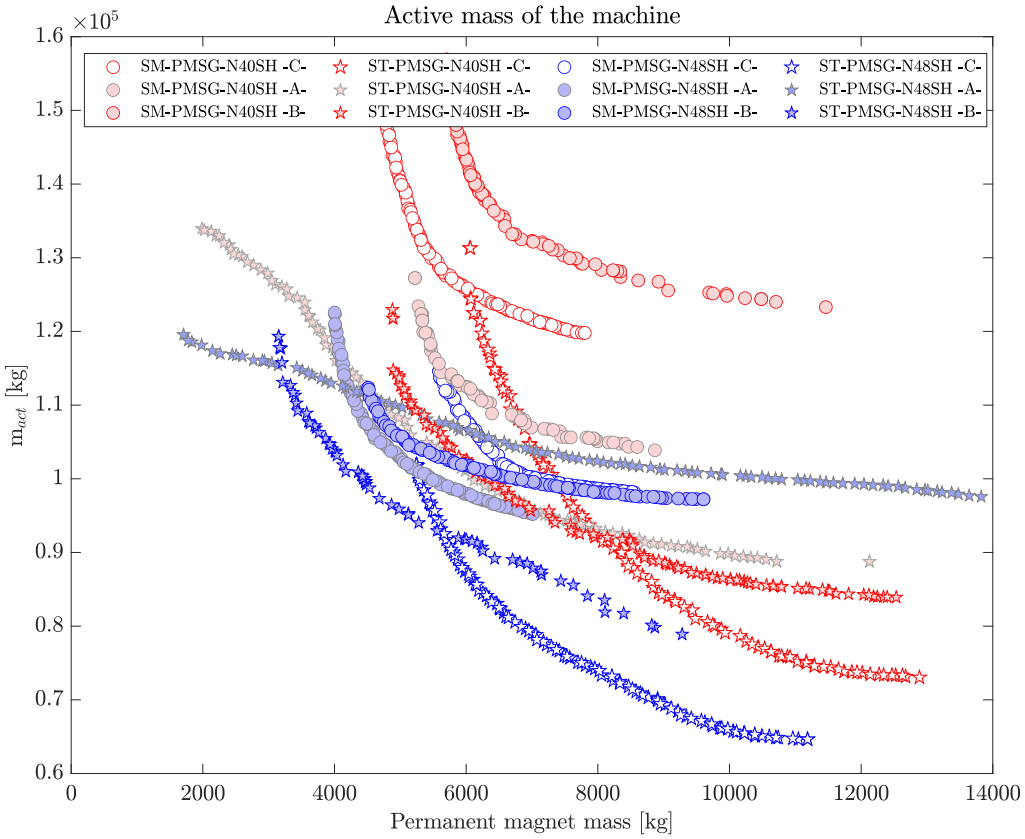

Figure 7.69: Mass comparison between NdFeB-based machines

7.40 and Fig. 7.56). Indeed, the magnetic field strength in the airgap will be weakened if the distance between the magnetic flux source in the rotor and the stator went up. In addition, these results were expected because in these intervals the airgap radius remained stable. The relationship between the mass (volume) of the magnet and its opening is then linear as expected in Eq. 7.4.

$$V_{PM} = \rho_{PM} m_{PM} = \pi \times \left[(R_g - e_g/2)^2 - (R_g - e_g/2 - h_{PM}) \right]^2 \times \theta_{PM} \quad (7.4)$$

where θ_{PM} is the magnet width to the pole pitch. This differs from the case of SM-PMSGs, where magnet opening had little impact compared to the magnet thickness in the reduction of the rotor volume. Additionally, the magnet thickness was found to moderately increase with magnet volume rise before eventually levelling off at around 20-30 mm. Although rising magnet height will automatically rise the magnet volume and then increase the magnetic flux density, it will also enlarge the gap between the rotor back-iron and the stator which might increase the

magnetic flux leakage. Therefore, above a certain threshold, increasing the magnet thickness is not beneficial. That is why it could be plainly viewed in Fig. 7.69 that the Pareto fronts representing SM-PMSG were very limited in term of magnet mass/volume increase. Further, increasing the volume of magnet in both cases reduces significantly the volume of the rotor, thereby reduces the mass of the machine. It is worth noticing that since the mass and torque of SM-PMSG are not greatly affected by the magnet opening, which remained fairly stable around 80 % of the pole pitch, it could be eliminated from the optimization variables in pre-design stages.

– **Rotor volume and shear stress**

The rotor volume was found to decease with increased magnet mass for relatively low magnet masses, while for significant magnet masses the rotor volume remained constant. In contrast, the machine's shear stress gradually grew in the first range of magnet mass, then reached a plateau of about 50-80 k.N/m^2. Often, the shear stress of ST-PMSGs was higher than that of SM-PMSGs for the same topology. The shear stress varied between 40 k.N/m^2 and 90 k.N/m^2.

– **Slot's dimensions and current density**

The copper volume (slot's volume) was found to decrease with magnet mass increase. It is interesting to note that, for all the investigated topologies the volume of the copper, permanent magnet and slots varied in the same manner and are within the same ranges respectively (See Fig. 7.25, Fig. 7.41 and Fig. 7.57). The slot's current density started to rise steadily over relatively low magnet masses, but flatted off at a fixed value (2.7 - 4.2 A/mm^2) for significant magnet mass. The low current density of 2.7 A/mm^2 was observed for SM-PMSG-N40SH (machine B), this is mainly due to the relatively low airgap radius, around 5 m, which constrains the thermal transfer and the machine's shear stress. In addition, the Joule losses need to be reduced since the slot's height is above 150 mm. As in the SM-PMSG-N48SH (machine B), with almost the same airgap radius, the slot's height was below 100 mm and the slot's current density reached 3.4 A/mm^2. Machine B with reduced slot number was found to have deep slots, then its design requires special attention. In fact, above a certain height limit, increasing the depth of the slot would not raise the torque density; however, it would only increase the inductance and then scale up the power converter.

– **Aspect ratio**

The aspect ratio remained more and less stable depending on the topology. It is worth noticing that, ST-PMSGs was found to have small aspect ratio, between 0.09 and 0.12, when compared with SM-PMSGs, between 0.14 and 0.2. According to the Fig. 7.23, Fig. 7.39 and Fig. 7.55, the spoke type machine has larger airgap diameters on average in comparison with SM-PMSGs. The airgap diameters average of spoke type PMSG had a medians between 6.2 m and 6.5 m, whereas for surface-mounted PMSG they were between 4.9 m and 6.4 m. On the other hand, the medians for the machine's axial lengths of spoke type PMSG were between 1.2 m and 2 m, whereas for surface mounted PMSG they were between 1.5 m and 2 m. Machines with short active length have an improved rotor dynamic behaviour and stator winding ventilation. The optimum mass and cost aspect ratio was in the range of 0.1 - 1.125 for ST-PMSGs while it was in the range of 0.135 - 0.21 for SM-PMSGs. It has been reported in [126] that, with an increase in the aspect ratio (The rated power of the investigated machines were between 2 MW and 20 MW), the mass and cost of electromagnetic materials increase, while the structural mass decreases rapidly. Therefore, the contribution of structural material to generator mass and cost increases need to be considered to make a final decision.

– **Stator winding & permanent magnet temperature**

It can be clearly observed that the thermal constraints were satisfied. Indeed, it is not difficult to remove heat since in large wind turbine generators the ambient temperature is relatively low and the cooling surface is large. Then, large diameter machines can be built with natural cooling. Nevertheless, reducing the size of megawatts generators is limited by the capacity to remove heat from the stator windings and thereby direct liquid cooling of the winding allows the electrical generators to operate at a higher output for a particular size as compared to an air-cooled generator of the same size.

– **Ferrite-based machines**

* The machine's active mass and the magnet mass are conflicting objectives.
* The Ferrite-based Pareto fronts reveal that the airgap radius was kept almost the same as in NdFeB-based optimization design, while the axial length was found to rise by more than 60 per cent, thereby the rotor volume grew considerably by more than two thirds. The shear stress fell significantly, between 20 k.N/m^2 and 28 k.N/m^2 compared to NdFeB-based

machines. In fact, it is not only necessary to have wider machine to achieve the same performances as with NdFeB machines, but also more magnetic and structural materials need to be used. For instance, when comparing rare-earth-based PMSGs with free-rare-earth-based ones, we noticed that the copper volume, iron volume and the magnet volume doubled to produce the same required torque. Then, the total mass of active part doubled (See Fig. 7.21 and Fig. 7.29). Although the ferrite is noticably cheaper than NdFeB, the price of the machine with ferrite was found more expensive than that of rare-earth material machines. The main drawback with this solution is that the generator construction losses the weight advantage compared to the conventional machines. Finally, the mass share was almost the same for both machines, whereas the cost share changed considerably. While the magnet cost share in the total price of the NdFeB-based machines was around 45 per cent, it was below 10 per cent for Ferrite-based machines. More than 80 per cent of cost of Ferrite machines was shared almost equally between steel and copper.

2 **Economical comparison**

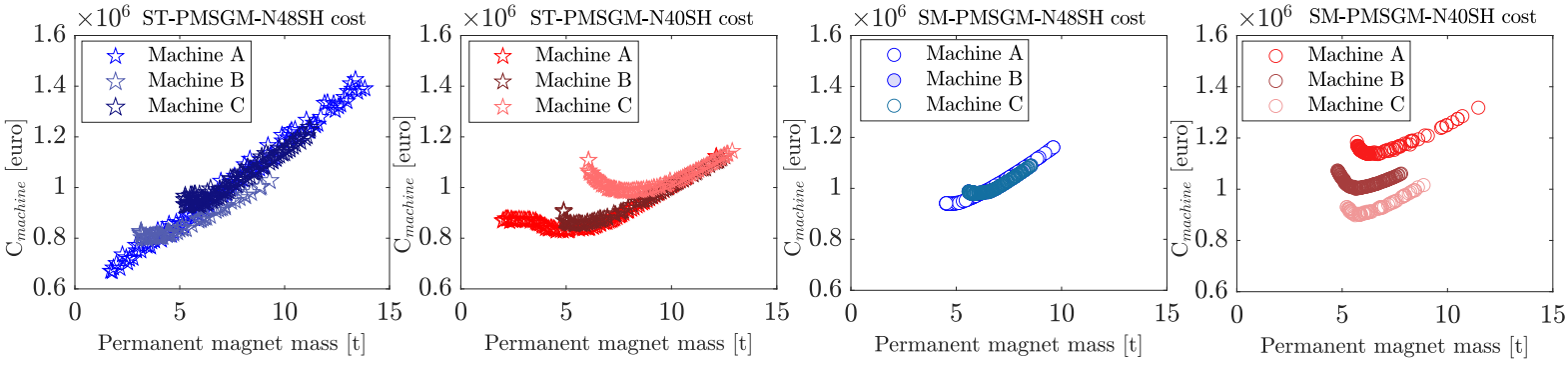

Figure 7.70: Cost comparison between NdFeB-based machines

– Figures Fig. 7.27, Fig. 7.43 and Fig. 7.59 depict the active materials cost of each studied topology. Overall, the machine's cost increase with the increase of the amount of permanent magnets used. In Fig. 7.70, it can be noticed that most of Pareto fronts representing the machine's cost versus the NdFeB magnet mass can be split into three parts. Fig. 7.71 illustrates these three parts (ST-PMSG-N40SH machine C will be taken as an example) :

1. Part I (Low PM mass): the machine's cost was found to decrease with permanent magnet mass increase. The interval representing this part is either extremely small or non-existent for machines based on N48SH NdFeB. In this part, the PM cost varies from 34 % to 44 %

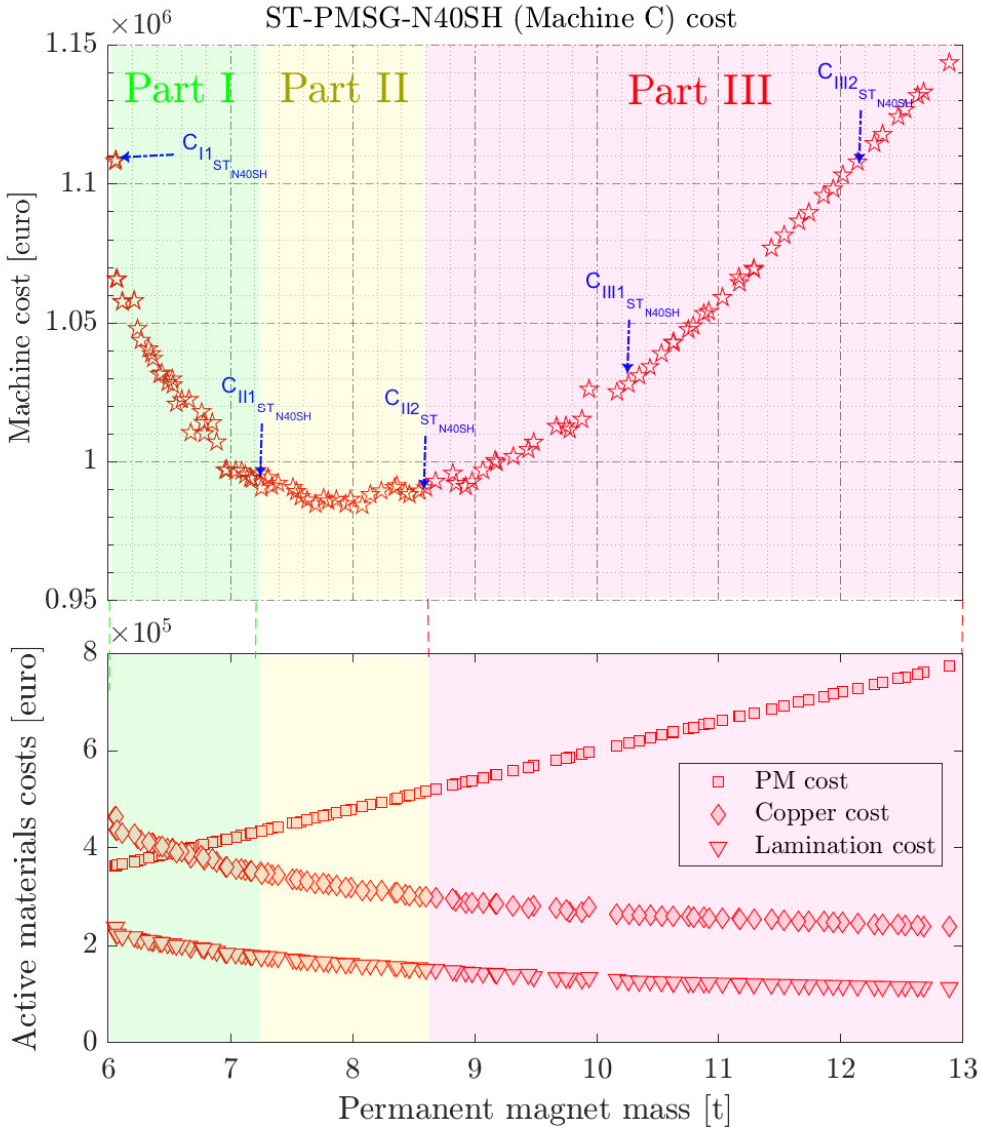

Figure 7.71: The ST-PMSG-N40SH cost versus the permanent magnet mass (Machine C)

of the machine total cost (See Fig. 7.72).

2. Part II (Middle PM mass part) : in this part, a plateau of machine's cost can be noticed, the cost fluctuates around fixed value over this range. Indeed, in this interval the increase in the magnet mass had little effect on the machine's cost. In this part, the PM cost varies from 44 % to 52 % of the machine total cost (See Fig. 7.72).

3. Part III (High PM mass part) : in the last part, the machine's cost is found to increase linearly with increase in the magnet mass. In this part, the PM cost represents a large proportion of the machine total cost (over half) (See Fig. 7.72). The PM in this part is the

main cost factor which drive the cost of the machine much higher.

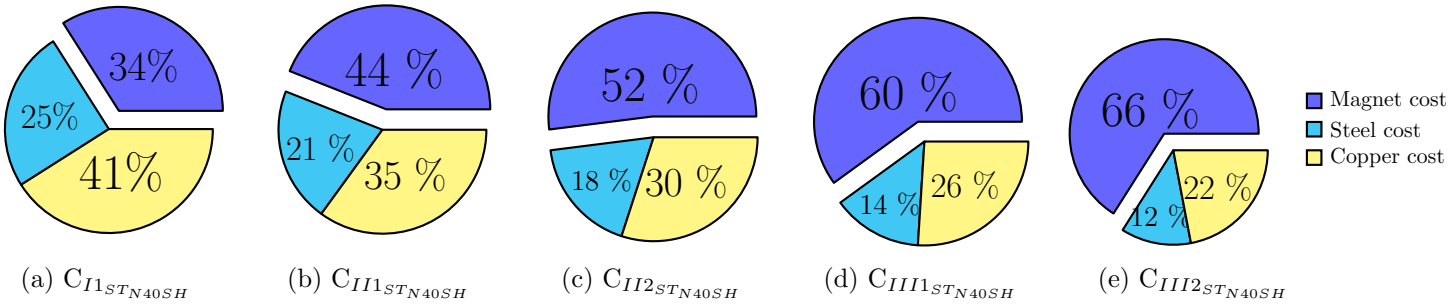

(a) $C_{I1_{ST_{N40SH}}}$ (b) $C_{II1_{ST_{N40SH}}}$ (c) $C_{II2_{ST_{N40SH}}}$ (d) $C_{III1_{ST_{N40SH}}}$ (e) $C_{III2_{ST_{N40SH}}}$

Figure 7.72: Cost shares distribution of some ST-PMSG-N40SH selected machines (machine C)

– Above a certain threshold, magnet mass and machine's cost are antagonistic goals (See Fig. 7.27, Fig. 7.43 and Fig. 7.59). The magnet mass reduction led to machine mass increase for all the investigated machines, that does not necessary imply a cheaper machines. This is mainly due to the cost share differences between light (A_2, B_2 and C_2[2]) and heavy machines (A_1, B_1 and C_1). Let's take machine C ST-PMSG-N40SH as an example. A diminution of 2 t in permanent magnet mass in the interval form [6-8] t helps to save almost 100 k€ of magnets. However, a large volume of copper is required to compensate the MMF which rises the machine's active mass by 32 t (copper and additional steel) and costs approximately 257 k€. The price of the new machine is higher by 125 k€, and then reducing the mass of permanent magnet in this range is not economically viable. Nevertheless, if the price of N40SH goes up to 128 €, the lighter machine become more cost-competitive. Furthermore, decreasing 2 t of magnet mass in the range of [8-10] t helps to save almost 100 k€ of magnet cost, while only 84 k€ of active materials are needed to counterbalance this reduction. Consequently, less copper volume and steel are necessary to offset the magnet mass decrease comparing to the previous study case. Considering fixed topology, the impact of the permanent magnet reduction depends on the chosen magnet mass range. Finally, when compromise should be found between the machine's mass and its cost, it would be interesting to select a machines from the plateau of the machine's cost.

– Figures Fig. 7.74, Fig. 7.76, Fig. 7.78 depicts the cost share distribution of the two selected machines in the Pareto fronts, for each investigated topology. With regards to PM cost share in the studied machines, it should be pointed out :

[2]As indicated in the respective Pareto fronts Fig. 7.21, Fig. 7.37 and Fig. 7.53

* The PM cost share depends on the position of the machine in the Pareto. Despite the fact that a maximum of 20 % of machine's mass is copper for all the investigated machines, the pie charts illustrate that for heavier machines (A_1,B_1 and C_1), with small PM masses, the copper cost accounted for the largest share of the total cost (between 35 % - 51 %).
* In lighter machines with high permanent magnet masses, magnet mass represents a very small portion of the machine's mass, less than 18 %, but its cost makes up more than half of the machine cost. Although ST-PMSGs are more reliant on magnet price than SM-PMSG, they could be an economically viable solution. For instance, in machine B ST-PMSG-N48SH, the magnet cost constitutes a large proportion of the cost and the price of the NdFeB N48SH is higher but the machine is cheaper than SM-PMSG over all the studied interval (PM masses).

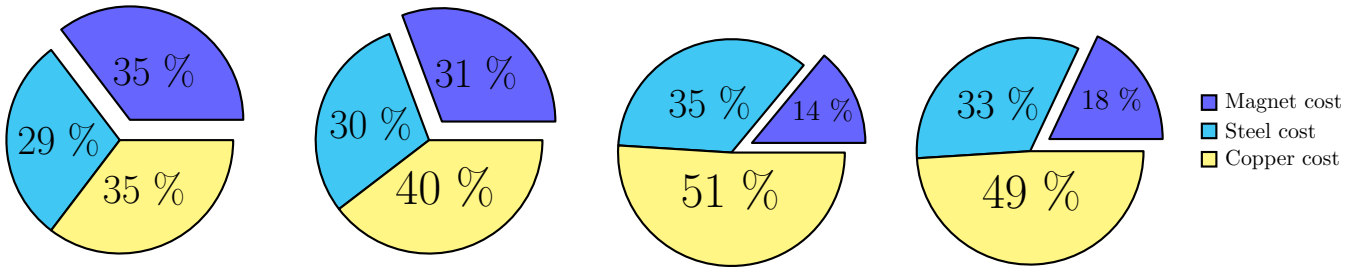

(a) $A_{1_{SM_{N40SH}}}$ (b) $A_{1_{SM_{N48SH}}}$ (c) $A_{1_{ST_{N40SH}}}$ (d) $A_{1_{ST_{N48SH}}}$

Figure 7.73: Cost shares distribution of machine A_1

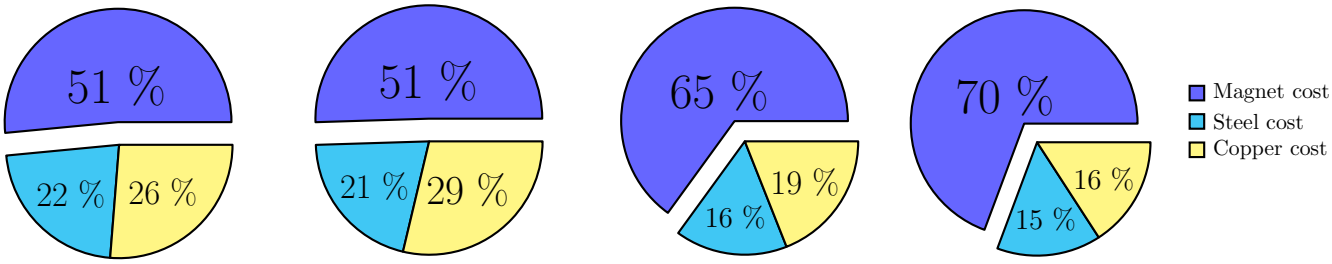

(a) $A_{2_{SM_{N40SH}}}$ (b) $A_{2_{SM_{N48SH}}}$ (c) $A_{2_{ST_{N40SH}}}$ (d) $A_{2_{ST_{N48SH}}}$

Figure 7.74: Cost shares distribution of machine A

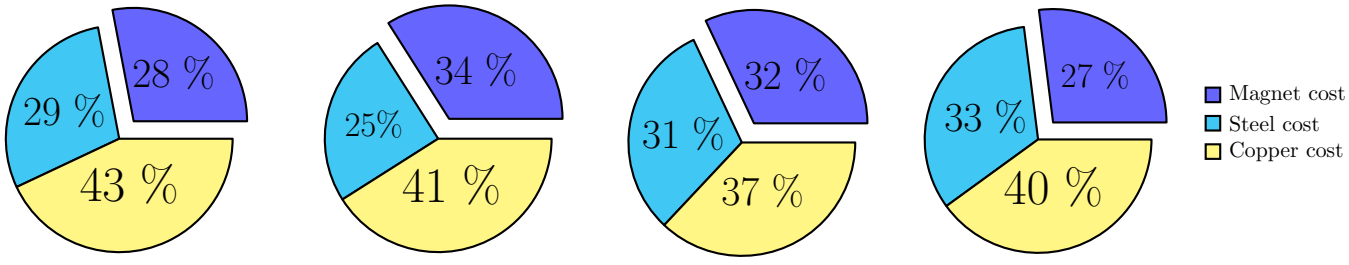

(a) $B_{1_{SM_{N40SH}}}$ (b) $B_{1_{SM_{N48SH}}}$ (c) $B_{1_{ST_{N40SH}}}$ (d) $B_{1_{ST_{N48SH}}}$

Figure 7.75: Cost shares distribution of machine B_1

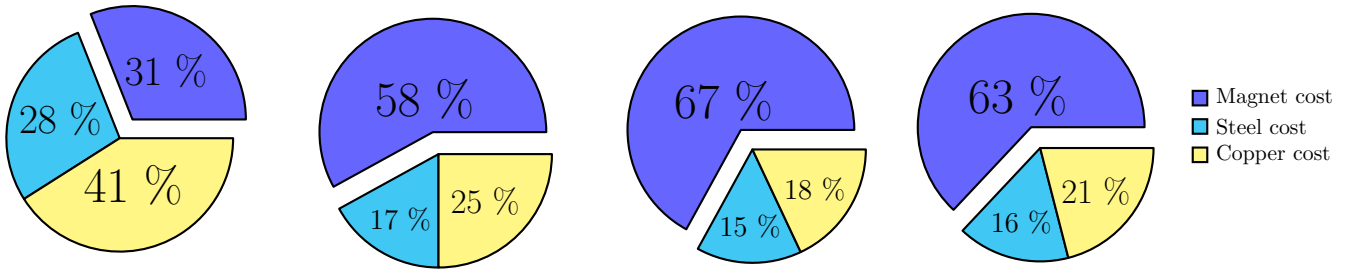

(a) $B_{2_{SM_{N40SH}}}$ (b) $B_{2_{SM_{N48SH}}}$ (c) $B_{2_{ST_{N40SH}}}$ (d) $B_{2_{ST_{N48SH}}}$

Figure 7.76: Cost shares distribution of machine B

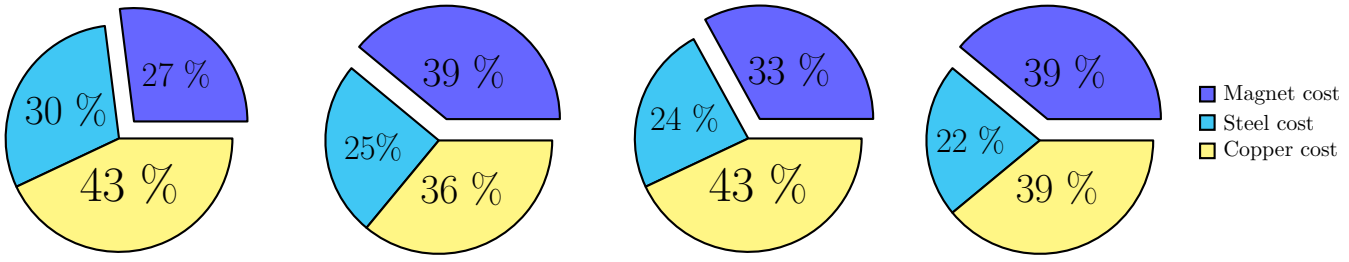

(a) $C_{1_{SM_{N40SH}}}$ (b) $C_{1_{SM_{N48SH}}}$ (c) $C_{1_{ST_{N40SH}}}$ (d) $C_{1_{ST_{N48SH}}}$

Figure 7.77: Cost shares distribution of machine C_1

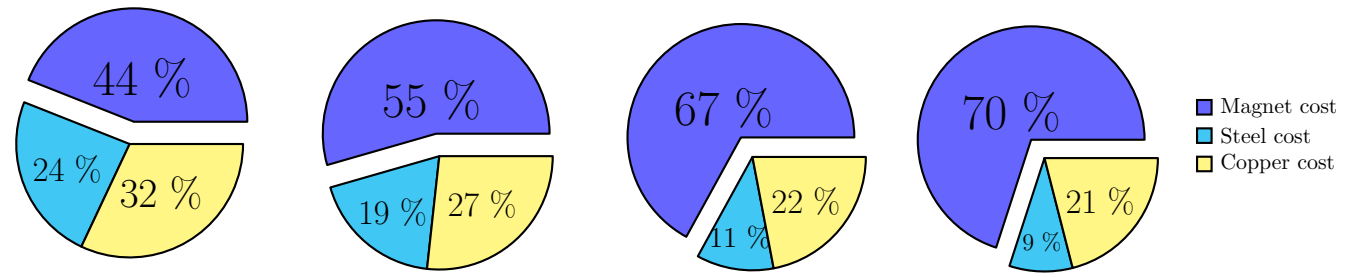

(a) $C_{2_{SM_{N40SH}}}$ (b) $C_{2_{SM_{N48SH}}}$ (c) $C_{2_{ST_{N40SH}}}$ (d) $C_{2_{ST_{N48SH}}}$

Figure 7.78: Cost shares distribution of machine C_2

7.5 Conclusion

In this chapter a comparative design of different radial-flux permanent magnet synchronous generators for 15 MW - 7.5 rpm direct-drive wind turbines was discussed. In order to design the optimum PMSG, it was necessary to study the effect of each parameter on the PMSG performances. The effect of stator, rotor, and permanent magnets dimensions on the generator mas and cost was studied. This chapter may be sub divided into two parts. In the first one a comparative study between two different optimization models was conducted, one based on linear AM and an other on nonlinear RNM for the magnetic design, both models are coupled with LPTM for the prediction of the thermal behaviour of the machine. The validity of the analytical model was confirmed by FEM. In the second part, the analytical model was used to assess several topologies of permanent magnet synchronous generators for 15 MW wind turbine. To allow a valuable comparison, the two sizing models were integrated in the same optimization problem with the same constraints and parameters. From the comparison in the first part, it is concluded that:

- The two optimization models share a common trend in the optimization variables.
- Both optimization methods results on similar sized machines with the parameters agreeing within 1.04 - 18 % on most variables.
- Optimization based on analytical sizing model was almost 18 times faster than that based on RNM.
- Analytical sizing model underestimate the overall dimensions of the machine. This is because it does not include the magnetic saturation.
- The machine resulting from AM-based optimization have lower volume but higher shear stress and larger slots compared with RN-based optimization. The main cause of this difference is the consideration of saturation on the nonlinear RNM.
- Despite the fact that RN-based optimization is time consuming but it has relatively high accuracy.

From the comparison in the second part, it is concluded that:

- It was found that it is possible to use lower grade magnets then NdFeB magnet but with this the mass and the cost of machine are rising.
- The ferrite-based Pareto fronts reveal that the airgap radius was kept almost the same as in NdFeB-based optimization design, while the axial length was found to rise by more than 60 per cent, thereby the rotor volume grew considerably by more than two thirds.

- The shear stress fell considerably when compared NdFeB-based with ferrite-based machines.
- It is not only necessary to have larger machines to achieve the same performances as with NdFeB machines, but also more magnetic and structural materials need to be used.
- When comparing rare-earth-based PMSGs with free-rare-earth-based ones, we noticed that the copper volume, iron volume and the magnet volume doubled to produce the same required torque thereby the total mass of active part doubled.
- In spite the fact that the ferrite is noticably cheaper than NdFeB, the price of the machine with ferrite was found more expensive than that of rare-earth material machines. The main drawback with this solution is that the generator construction losses the weight advantage compared to the conventional machines.
- The mass share was almost the same for both machines, whereas the cost share changed considerably. While the magnet cost share in the total price of the NdFeB-based machines was around 45 per cent, it was below 10 per cent for Ferrite-based machines. More than 80 per cent of cost of Ferrite machines was shared almost equally between steel and copper.
- Condensing the same magnet grade, ST-PMSG were found to be lighter conventional SM-PMSG.
- The rotor volume was found to decease with increased magnet mass for relatively low magnet masses, while for significant magnet masses the rotor volume remained constant. In contrast, the machine's shear stress gradually grew in the first range of magnet mass, then reached a plateau of about 50-80 k.N/m^2.
- ST-PMSGs was found to have small aspect ratio when compared with SM-PMSGs. Machines with short active length have an improved rotor dynamic behaviour and stator winding ventilation. With an increase in the aspect ratio, the mass and cost of electromagnetic materials increase, while the structural mass might decrease. Therefore, the contribution of structural material to generator mass and cost increases need to be considered to make a final decision.
- From the economical point of view, one can conclude that the impact of the permanent magnet reduction depends on the topology and the chosen magnet mass range. While increasing the magnet mass reduces systematically the mass of the machine, it does not often results on increase of the machine's cost. Then, compromise should be found between the machine's mass and its cost.
- In order to make the final choice, different points may be selected among the Pareto depending on the design criteria.

General Conclusion

Conclusions and Recommendations

Concluding Remarks

The main objective of this thesis was to find the permanent magnet synchronous generator machine with the highest torque density and the lowest possible cost for direct-drive 15 MW wind turbine. To identify the mass and the cost competitiveness of permanent magnet synchronous generators for 15 MW direct-drive wind turbine, several configurations and topologies of radial flux machines was investigated. The investigation was limited to electromagnetic part of the electrical generator.

A thorough literature review has been completed in the first two chapters, providing an overview of the different conversion systems in multi-megawatts wind turbines in order to help the reader to understand the features of those conversion systems. In the second chapter, a broader overview of electrical generators topologies used in direct-drive wind turbines was realized.

The third chapter introduced the electromagnetic design of 15 MW direct-drive generator. It aimed gain understanding of the assessment criteria and design requirement of such large electrical generator. It represented the practical part of this thesis by introducing the desired characteristics, the proposed topologies, and the materials selected for the machine design.

The fourth chapter dealt with magnetic design of electrical machines. The magnetic design was performed thanks to two types of 2-D models: a linear model based on the formal resolution of Maxwell's equation in the low permeability regions of the machine and a non-linear mesh-based reluctance network model. The fifth chapters developed two-dimensional steady state lumped parameters thermal network for large diameter permanent magnet synchronous generator.

The sixth chapter presented a review of electrical machine design optimization. Various optimization structures, models and algorithms were compared.

In the last chapter's outcome can be seen in the optimization of the geometries chosen in the third chapter. The first goal of this chapter was to validated the analytical model for further design optimizations. The second goal was to deeply analysed three different configurations of radial-flux permanent magnet synchronous generators for direct-drive wind turbines. Three permanent magnet synchronous generators was proposed and four magnets grades was used, including NdFeB N40SH, NdFeB N48SH, Ferrite Y30 and Ferrite NMF-15G.

According to the investigation, the following remarks can be made

- The devolved analytical-based design optimization allow fast inspecting of a large design space.
- The potential downsides of using ferrite magnets in high-power low-speed generators:
  - It was found that it is possible to use lower grade magnets then NdFeB magnet but significant increase was noticed on the machine mass and the cost.
  - The rotor volume rises substantially by more than two thirds, and the machine's mass doubled.
  - The force density declines sharply when compared NdFeB-based with ferrite-based machines. It is not only necessary to have larger machines to achieve the same performances as with NdFeB machines, but also more magnetic and structural materials need to be used.
  - The price of the active parts of the machine with ferrite was found more expensive than that of rare-earth material machines.
  - When evaluating the mass-competitiveness of rare-earth-based PMSGs and free-rare-earth-based ones, we noticed that the copper volume, iron volume and the magnet volume doubled to produce the same required torque thereby the total mass of active part doubled. It should be mentioned that the structural mass must be added, which may worsen the situation.
  - Although the ferrite machines was found to have twice the mass of the NdFeB machines, their cost was fairly similar.
  - Ferrite machines are more sensitive to the price of the copper and the stator lamination than to that of magnet. The cost of the ferrite magnet does not exceed 15 % of the machine total cost, while copper and steel together accounted for over 85 % of the total cost.
- NdFeB machines are more sensitive to the price of the magnets than that of stator lamination and copper. The NdFeB magnet accounted for more than 30 % of the machine total cost and it may reach a maximum of 70 % for some selected machines.

- Condensing the same magnet grade, ST-PMSG were found to be lighter conventional SM-PMSG. However, surface mounted NdFeB generators has a often better than spoke type ones.
- Compromise should be found between the machine's mass and its cost. The main objective of such investigation is reduce the cost of the energy production, through transport, material cost reduction. Hence, the obtained results are not final from the economical point of view.
- It was found that higher magnet grades produce a lower machines cost.
- In order to make the final choice, different points may be selected among the Pareto depending on the design criteria.

Outlook and Future Work

Future works may be focused on possible improvement for the developed models.

- High the fore densities was achieved with deep slots, which lead to high reactance. Machines with high shear stresses are expected to have relatively high stator. Increasing the stator inductance will considerable increase the cost of the machine frequency converter. Therefore, the reactance should be considered for further investigations.
- The sizing reduction of large generators is mainly limited by the temperature rise of the stator windings, thus it would be of great interest to investigated the impact of direct-cooling of the winding in the mass and the cost of the high-torque low-speed generator dedicated for wind turbines.
- The end windings of a large electrical generator constitute a considerable mass. The forces in the end windings caused by the current of individual conductors acting upon one another, and also vibration excited by the motion of the stator core should be investigated in further works.
- In a large diameter generator, the thermal distortion of the stator is relatively large, and when the stator support is not symmetrical, unbalanced thermal distortion may happen. The later may increase levels of vibration, which results on increased friction and, ultimately, to a turn-to-turn or ground fault. The mechanical performance of the such generator need to be integrated in the pre-design stage optimization.
- The analytical model used could be improved by integrating the saturation.
- It will be of interest to investigated other NdFeB regular grades (replacing of H and SH grades). The effective remanent flux density can be enhanced by using improved cooling system. Reducing

the magnet temperature allow to use cheaper grades of NdFeB with less percentages of critical materials.

Bibliography

[1] T. Andre and F. Guerra, *Renewables 2020: Global Status Report*. June 2020.

[2] FS-UNEP, "Global trends in renewable energy investment 2020," tech. rep., The Frankfurt School – UNEP Collaborating Centre for Climate Sustainable Energy Finance, 2020.

[3] GWEC, "Global wind report 2021," tech. rep., Global Wind Energy Council, 2021.

[4] B. I. WindEurope, "Wind energyin europe: 2020 statistics and the outlook for 2021-2025," tech. rep., Wind Europe, 2021.

[5] "Neodymium iron boron (ndfeb), https://www.arnoldmagnetics.com/products/neodymium-iron-boron-magnets/," 2021. Accessed Apr. 20, 2021.

[6] S. R. Joshua Earnest, *Wind Power Technology*. PHI Learning, Mar. 2020.

[7] GWEC, "Global offshore wind report 2020," tech. rep., Global Wind Energy Council, 2020.

[8] F. C. Energy, "Global wind market update, demand & supply 2016: Part one – supply side analysis," *FTI Intelligence*, Mar. 2017.

[9] A. Bensalah, G. Barakat, and Y. Amara, "Electrical generators for large wind turbine: Trends and challenges," *Energies*, vol. 15, no. 18, 2022.

[10] A. Parviainen, J. Pyrhonen, and P. Kontkanen, "Axial flux permanent magnet generator with concentrated winding for small wind power applications," in *IEEE International Conference on Electric Machines and Drives, 2005.*, pp. 1187–1191, 2005.

[11] A. S. McDonald, N. Al-Khayat, D. Belshaw, M. Ravilious, A. Kumaraperumal, A. M. Benatamane, M. Galbraith, D. Staton, K. Benoit, and M. Mueller, "1mw multi-stage air-cored permanent magnet

generator for wind turbines," in *6th IET International Conference on Power Electronics, Machines and Drives (PEMD 2012)*, pp. 1–6, 2012.

[12] B. E. Hasubek, *Analysis and design of passive rotor transverse fluxmachines with permanent magnets on the stator*. PhD thesis, University of Calgary, 2000.

[13] D. je Bang, H. Polinder, G. Shrestha, and J. A. Ferreira, "Comparative design of radial and transverse flux PM generators for direct-drive wind turbines," in *18th International Conference on Electrical Machines*, IEEE, sep 2008.

[14] R. Kumar, Z.-Q. Zhu, A. Duke, A. Thomas, R. Clark, Z. Azar, and Z.-Y. Wu, "A review on transverse flux permanent magnet machines for wind power applications," *IEEE Access*, vol. 8, pp. 216543–216565, 2020.

[15] G. Viktor, O. Dobzhanskyi, G. Rostislav, and R. Gouws, "Improvement of transverse-flux machine characteristics by finding an optimal air-gap diameter and coil cross-section at the given magnetomotive force of the PMs," *Energies*, vol. 14, p. 755, feb 2021.

[16] M. R. J. Dubois, *Optimized Permanent Magnet GeneratorTopologies for Direct-Drive Wind Turbines*. PhD thesis, Delft University of Technology, 2004.

[17] C. P. Maddison, *Transverse flux machines for high torque applications*. PhD thesis, Newcastle University, 1999.

[18] H. Weh, "Transverse-flux machines in drive and generator application," *Proceedings of the IEEE Symposium on Electric Power Engineering (Stockholm Power Tech), Strockholm, Sweden*, p. 75–80, 1995.

[19] W. AMSC, "Concepts for high power wind turbinesintroducing hts technology," *World Green Energy Forum 2010*, 2010.

[20] D. McGahn, "Direct drive generators: High temperature superconductor based machines," tech. rep., AMSC American Superconductor, Offshore Workshop, 2009.

[21] R. Fair, W. Stautner, M. Douglass, R. Rajput-Ghoshal, M. Moscinski, P.Riley, D. Wagner, J. Kim, S. Hou, F. Lopez, K. Haran, J. Bray, T. Laskaris, J. Rochford, and R. Duckworth, "Next gen-

eration drive train: Superconductivity for large-scale wind turbines," *Applied Superconductivity Conference*, Oct. 2012.

[22] E. Spooner, A. Williamson, and G. Catto, "Modular design of permanent-magnet generators for wind turbines," *IEE Proceedings - Electric Power Applications*, vol. 143, no. 5, p. 388, 1996.

[23] J. Le Besnerais, P. Pellerey, V. Lanfranchi, and M. Hecquet, "Bruit acoustique d'origine magnétique dans les machines synchrones," *Techniques Ingenieur*, 2013.

[24] M. Zakotnik and C. Tudor, "Commercial-scale recycling of ndfeb-type magnets with grain boundary modification yields products with 'designer properties' that exceed those of starting materials," *Waste Management*, vol. 44, pp. 48–54, 2015.

[25] Arnold, "The important role of dysprosium in modern permanent magnets," tech. rep., Arnold Magentic Technologies, 2017.

[26] G. C. Stone, I. Culbert, E. A. Boulter, and H. Dhirani, *Rotating Machine Insulation Systems*, pp. 1–46. 2014.

[27] E. Boulter and G. Stone, "Historical development of rotor and stator winding insulation materials and systems," *IEEE Electrical Insulation Magazine*, vol. 20, pp. 25–39, may 2004.

[28] G. D. Demetriades, H. Z. de la Parra, E. Andersson, and H. Olsson, "A real-time thermal model of a permanent-magnet synchronous motor," *IEEE Transactions on Power Electronics*, vol. 25, no. 2, pp. 463–474, 2010.

[29] A. Yulia, *Wind Turbine Direct-Drive Permanent-Magnet Generator with Direct LiquidCooling for Mass Reduction*. PhD thesis, Lappeenranta University of Technology, 2014.

[30] N. A. Bhuiyan and A. McDonald, "Optimization of offshore direct drive wind turbine generators with consideration of permanent magnet grade and temperature," *IEEE Transactions on Energy Conversion*, vol. 34, no. 2, pp. 1105–1114, 2019.

[31] Y. Lefèvre, S. E. Aabid, J.-F. Llibre, C. Henaux, and S. Touhami, "Performance assessment tool based on loadability concepts," *International Journal of Applied Electromagnetics and Mechanics*, vol. 59, no. 2, pp. 687–694, 2019.

[32] T. J. E. Miller, *Brushless Permanent-Magnet and Reluctance Motor Drives*. Oxford University Press, New York, 1989.

[33] "Neodymium iron boron (ndfeb), https://www.arnoldmagnetics.com/products/neodymium-iron-boron-magnets/," 2021. Accessed Apr. 02, 2021.

[34] ARNOLD, "Magnets." Accessed July 06, 2022.

[35] TDK, "Magnets, https://product.tdk.com/en/products/magnet/index.html." Accessed July 06, 2022.

[36] Cogent, "Electrical steel non orientedfully processed," tech. rep., Cogent Power Inc., 2006.

[37] W. Tong, "Rotor design," in *Mechanical Design of Electric Motors*, pp. 83–153, CRC Press, 2014.

[38] T. J. E. Hendershot, J. R. ; Miller, *Design of Brushless Permanent-magnet Motors*. Hillsboro, OH Oxford: Magna Pysics Pub. Clarendon Press, 1994.

[39] "Standard 60085 electrical insulation—thermal evaluation and designation," 2008.

[40] "Electrical insulation—thermal evaluation and designation. 4th edition," *IEC 60085, International Electrotechnical Commission (IEC)*, 2004.

[41] B. N. Azim and M. Alasdair, "Assessment of the suitability of ferrite magnet excited synchronous generators for offshore wind turbines," *EWEA OFFSHORE 2015*, Mar. 2015.

[42] L. D. Willey, *Design and development of megawatt wind turbines*, vol. Vol 44, ch. 6, pp. 187– 253. WIT Press, 2010.

[43] A. Bensalah, M. Benhamida, G. Barakat, and Y. Amara, "Large wind turbine generators: State-of-the-art review," in *2018 XIII International Conference on Electrical Machines (ICEM)*, pp. 2205–2211, 2018.

[44] A. McDonald and N. A. Bhuiyan, "On the optimization of generators for offshore direct drive wind turbines," *IEEE Transactions on Energy Conversion*, vol. 32, no. 1, pp. 348–358, 2017.

[45] A. Mcdonald, M. Mueller, and H. Polinder, "Structural mass in direct-drive permanent magnet electrical generators," *Renewable Power Generation, IET*, vol. 2, pp. 3 – 15, 04 2008.

[46] F. Spinato, P. Tavner, G. van Bussel, and E. Koutoulakos, "Reliability of wind turbine subassemblies," *IET Renewable Power Generation*, vol. 3, no. 4, p. 387, 2009.

[47] S. Faulstich, B. Hahn, and P. J. Tavner, "Wind turbine downtime and its importance for offshore deployment," *Wind Energy*, vol. 14, no. 3, pp. 327–337, 2011.

[48] J. Igba, K. Alemzadeh, C. Durugbo, and K. Henningsen, "Performance assessment of wind turbine gearboxes using in-service data: Current approaches and future trends," *Renewable and Sustainable Energy Reviews*, vol. 50, pp. 144–159, oct 2015.

[49] H. Tiegna, A. Bellara, Y. Amara, and G. Barakat, "Simumsap - an analytical design tool for permanent magnet electrical machines," in *ICEE 2012, Algiers, Algeria,*, 2012.

[50] IRENA, "Renewable capacity highlights," tech. rep., The International Renewable Energy Agency (IRENA), 2020.

[51] IRENA, "Renewable capacity statistics 2021," tech. rep., The International Renewable Energy Agency (IRENA), 2021.

[52] *A Review of the Development of Wind Turbine Generators Across the World*, vol. 4: Dynamics, Control and Uncertainty, Parts A and B of *ASME International Mechanical Engineering Congress and Exposition*, 11 2012.

[53] IRENA, "Renewable power generation costs in 2019," tech. rep., International Renewable Energy Agency, 2020.

[54] R. 2020, "Renewables 2021 global status report," tech. rep., REN21, 2020.

[55] H. Klinge Jacobsen, P. Hevia-Koch, and C. Wolter, "Nearshore and offshore wind development: Costs and competitive advantage exemplified by nearshore wind in denmark," *Energy for Sustainable Development*, vol. 50, pp. 91–100, 2019.

[56] B. Sovacool, P. Enevoldsen, C. Koch, and R. Barthelmie, "Cost performance and risk in the construction of offshore and onshore wind farms," *Wind Energy*, vol. 20, pp. 891–908, 2017.

[57] S. P. Neill and M. R. Hashemi, "Offshore wind," in *Fundamentals of Ocean Renewable Energy* (S. P. Neill and M. R. Hashemi, eds.), E-Business Solutions, pp. 83–106, Academic Press, 2018.

[58] W. Tong, "Fundamentals of wind energy," in *Wind power generation and wind turbine design*, p. 23, WIT Press Southampton, UK, 2010.

[59] A. G. Aissaoui and A. Tahour, eds., *Wind Turbines - Design, Control and Applications*. InTech, jul 2016.

[60] K. Dykes, A. Platt, Y. Guo, A. Ning, R. King, T. Parsons, D. Petch, and P. Veers, "Effect of tip-speed constraintson the optimized design of a wind turbine," tech. rep., National Renewable Energy Laboratory (NREL), 2014.

[61] L. J. Fingersh and K. Johnson, "Controls advanced research turbine (cart) commissioning and baseline data collection," in *National Renewable Energy Laboratory NREL*, 2002.

[62] K. Johnson, L. Fingersh, M. Balas, and L. Pao, "Methods for increasing region 2 power capture on a variable speed hawt," 01 2004.

[63] S. Mathew, G. S. Philip, and C. M. Lim, "Analysis of wind regimes and performance of wind turbines," in *Advances in Wind Energy Conversion Technology*, pp. 71–83, Springer Berlin Heidelberg, 2011.

[64] C. Vázquez-Hernández, J. Serrano-González, and G. Centeno, "A market-based analysis on the main characteristics of gearboxes used in onshore wind turbines," *Energies*, vol. 10, p. 1686, oct 2017.

[65] H. Polinder, S. W. H. de Haan, M. R. Dubois, and J. G. H. Slootweg, "Basic operation principles and electrical conversion systems of wind turbines," *EPE Journal*, vol. 15, pp. 43–50, dec 2005.

[66] E. Camm, M. R. Behnke, O. Bolado, M. Bollen, M. Bradt, C. Brooks, W. Dilling, M. Edds, W. J. Hejdak, D. Houseman, S. Klein, F. Li, J. Li, P. Maibach, T. Nicolai, J. Patino, S. V. Pasupulati, N. Samaan, S. Saylors, T. Siebert, T. Smith, M. Starke, and R. Walling, "Characteristics of wind turbine generators for wind power plants," in *2009 IEEE Power Energy Society General Meeting*, pp. 1–5, 2009.

[67] N. Madani, "Design of a permanent magnet synchronous generator for a vertical axis wind turbine," 2011.

[68] E. M. C. B. D. Handman, "Dual-speed windturbine generation," tech. rep., National Renewable Energy Laborator, 1996.

[69] A. Petersson, "Analysis, modeling and control of doubly-fed induction generators for wind turbines," 2005.

[70] P. Carlin, A. Laxson, and E. Muljadi, "The history and state of the art of variable-speed wind turbine technology," *Wind Energy*, vol. 6, pp. 129 – 159, 04 2003.

[71] M. Cheng and Y. Zhu, "The state of the art of wind energy conversion systems and technologies: A review," *Energy Conversion and Management*, vol. 88, pp. 332–347, 2014.

[72] F. Blaabjerg, F. Iov, Z. Chen, and K. Ma, "Power electronics and controls for wind turbine systems," in *2010 IEEE International Energy Conference*, pp. 333–344, 2010.

[73] M. R. Dubois, "Review of electromechanical conversion in wind turbines," tech. rep., Group Electrical Power Processing, TU Delft, 2000.

[74] M. S. S. Santoso, "Dynamic models for wind turbines and wind power plants," tech. rep., The University of Texas at Austin, Austin, Texas, 2008.

[75] A. D. Hansen and L. H. Hansen, "Wind turbine concept market penetration over 10 years (1995–2004)," *Wind Energy*, vol. 10, pp. 81–97, jan 2007.

[76] A. D. Hansen, "Generators and power electronics for wind turbines," apr 2012.

[77] Z. Chen, "Issues of connecting wind farms into power systems," in *2005 IEEE/PES Transmission &amp Distribution Conference &amp Exposition: Asia and Pacific*, IEEE, 2005.

[78] A. Ragheb and M. Ragheb, "Wind turbine gearbox technologies," in *2010 1st International Nuclear & Renewable Energy Conference (INREC)*, IEEE, mar 2010.

[79] W. Teng, X. Ding, S. Tang, J. Xu, B. Shi, and Y. Liu, "Vibration analysis for fault detection of wind turbine drivetrains—a comprehensive investigation," *Sensors*, vol. 21, p. 1686, mar 2021.

[80] H. Polinder, F. V. D. Pijl, G.-J. D. Vilder, and P. Tavner, "Comparison of direct-drive and geared generator concepts for wind turbines," *IEEE Transactions on Energy Conversion*, vol. 21, pp. 725–733, sep 2006.

[81] A. Grauers, *Design of Direct-drivenPermanent-magnet Generatorsfor Wind Turbines*. PhD thesis, Chalmers University of Technology, 1996.

[82] K. Touimi, *Design Optimization of a Gearbox Driven Tidal Stream Turbine.* PhD thesis, Université de Bretagne Occidentale, 2020.

[83] A. S. Mikhail, K. L. Cousineau, L. H. Howes, W. Erdman, and W. Holley, "Variable speed distributed drive train wind turbine system," 2005.

[84] R. Thresher and A. Laxson, "Advanced wind technology: Newchallenges for a new century," 2006.

[85] IEA, "Offshore windoutlook 2019," tech. rep., The International Energy Agency, 2019.

[86] WindEurope, "Wind energy in europe: Outlook to 2020," tech. rep., Wind Europe, 2017.

[87] WindEurope, "Offshore wind in europe – key trends and statistics 2020," tech. rep., Wind Europe, 2020.

[88] "Northwester 2, https://www.belgianoffshoreplatform.be/fr/projects/northwester-2/." Accessed Apr. 12, 2021.

[89] QFWE, "2020 global floating wind energymarket and forecast report2019 - 2034," tech. rep., Quest Floating Wind energy, 2020.

[90] "Le projet en bref, https://dieppe-le-treport.eoliennes-mer.fr/le-projet/le-projet-en-bref/." Accessed Apr. 12, 2021.

[91] "Le projet en bref, https://iles-yeu-noirmoutier.eoliennes-mer.fr/le-projet/le-projet-en-bref/." Accessed Apr. 12, 2021.

[92] "Hornsea two, https://hornseaprojects.co.uk/hornsea-project-two." Accessed Apr. 12, 2021.

[93] "Windpark estinnes, https://www.windvision.com/project/estinnes." Accessed Apr. 12, 2021.

[94] GE, "Haliade-x offshore wind turbine, https://www.ge.com/renewableenergy/wind-energy/offshore-wind/haliade-x-offshore-turbine." Accessed Apr. 10, 2021.

[95] SIEMENS, "Sg 11.0-200 dd offshore wind turbine, https://www.siemensgamesa.com/products-and-services/offshore/wind-turbine-sg-11-0-200-dd." Accessed Apr. 10, 2021.

[96] "Seawind's innovative high-performing turbine, https://seawindtechnology.com/solutions/." Accessed Apr. 10, 2021.

[97] T. Telsnig, *Wind energy Technology Development Report 2020*. Luxembourg: Publications Office of the European Union, 2020.

[98] EOLINK, "Eolink cost-effective floating wind farms, http://eolink.fr/en/about." Accessed Apr. 10, 2021.

[99] "Sem-rev presentation mission, https://sem-rev.ec-nantes.fr/english-version/sem-rev/sem-rev-presentation-mission." Accessed Apr. 10, 2021.

[100] EnBW, "Floating wind turbine: Nezzy², https://www.enbw.com/renewable-energy/wind-energy/our-offshore-wind-farms/nezzy2-floating-wind-turbine/." Accessed Apr. 10, 2021.

[101] INNWIND.EU, "Design of state of the art 10-20mw offshore wind turbines, http://www.innwind.eu/about-innwind." Accessed Apr. 10, 2021.

[102] SUMR, "Sumr segmented ultralight morphing rotor, https://sumrwind.com/." Accessed Apr. 10, 2021.

[103] "The hiprwind project, http://www.hiprwind.eu/?q=mission." Accessed Apr. 10, 2021.

[104] "Corewind project, http://corewind.eu/about/." Accessed Apr. 10, 2021.

[105] "The flotant project, https://flotantproject.eu/." Accessed Apr. 10, 2021.

[106] S. Sheng, "Gearbox typical failuremodes, detection andmitigation methods," tech. rep., National Renewable Energy Laboratory/National WindTechnology Center, 2014.

[107] A. M. Ragheb and M. Ragheb, *Fundamental and Advanced Topics in Wind Power*, ch. Wind Turbine Gearbox Technologies, pp. 189–206. IntechOpen, 2011.

[108] N. V. . A. Ukonsaari, J. Bennstedt, "Wind turbine gearboxes: Maintenance effect on present and future gearboxes for windturbines," tech. rep., ENERGIFORSK, 2016.

[109] R.-Z. Szász and L. Fuchs, *Wind turbine acoustics*, pp. 153–183. United Kingdom: WIT Press, 2010.

[110] S. Oerlemans, "Wind turbine noise: primary noise sources," tech. rep., National Aerospace Laboratory NLR, 2011.

[111] D. A. Spera, "Introduction to Modern Wind Turbines," in *Wind Turbine Technology: Fundamental Concepts in Wind Turbine Engineering, Second Edition*, ASME Press, 01 2009.

[112] D. je Bang, H. Polinder, G. Shrestha, and J. A. Ferreira, "Promising direct-drive generator system for large wind turbines," in *Wind Power to the Grid - EPE Wind Energy Chapter 1st Seminar*, IEEE, mar 2008.

[113] H. Li and Z. Chen, "Design optimization and site matching of direct-drive permanent magnet wind power generator systems," *Renewable Energy*, vol. 34, no. 4, pp. 1175–1184, 2009.

[114] Z. Chen and F. Blaabjerg, "Wind energy: The world's fastest growing energy source," *IEEE Power Electronics Society Newsletter*, vol. 18, no. 3, pp. 15–19, 2006.

[115] M. Chinchilla, S. Arnaltes, and J. C. Burgos, "Control of permanent-magnet generators applied to variable-speed wind-energy systems connected to the grid," *IEEE Transactions on Energy Conversion*, vol. 21, no. 1, pp. 130–135, 2006.

[116] Z. Chen, J. M. Guerrero, and F. Blaabjerg, "A review of the state of the art of power electronics for wind turbines," *IEEE Transactions on Power Electronics*, vol. 24, no. 8, pp. 1859–1875, 2009.

[117] E. Hamatwi, I. E. Davidson, and M. N. Gitau, "Rotor speed control of a direct-driven permanent magnet synchronous generator-based wind turbine using phase-lag compensators to optimize wind power extraction," *Journal of Control Science and Engineering*, vol. 2017, pp. 1–17, 2017.

[118] H. Geng, D. Xu, B. Wu, and G. Yang, "Active damping for pmsg-based wecs with dc-link current estimation," *IEEE Transactions on Industrial Electronics*, vol. 58, no. 4, pp. 1110–1119, 2011.

[119] O. Alizadeh and A. Yazdani, "A strategy for real power control in a direct-drive pmsg-based wind energy conversion system," *IEEE Transactions on Power Delivery*, vol. 28, no. 3, pp. 1297–1305, 2013.

[120] P. Novak, T. Ekelund, I. Jovik, and B. Schmidtbauer, "Modeling and control of variable-speed wind-turbine drive-system dynamics," *IEEE Control Systems Magazine*, vol. 15, no. 4, pp. 28–38, 1995.

[121] O. Keysan, "Future electrical generator technologies for offshore wind turbines," *Engineering Technology Reference*, vol. 1, 2015.

[122] G. Bywaters, V. John, J. Lynch, P. Mattila, G. Norton, J. Stowell, M. Salata, O. Labath, A. Chertok, and D. Hablanian, "Northern power systems windpact drive train alternative design study report; period of performance: April 12, 2001 to january 31, 2005," 10 2004.

[123] C. Stork, C. Butterfield, W. Holley, P. Madsen, and P. Jensen, "Wind conditions for wind turbine design proposals for revision of the iec 1400-1 standard," *Journal of Wind Engineering and Industrial Aerodynamics*, vol. 74-76, pp. 443–454, 1998.

[124] E. De Vries, "6 - wind turbine drive systems: a commercial overview," in *Electrical Drives for Direct Drive Renewable Energy Systems* (M. Mueller and H. Polinder, eds.), Woodhead Publishing Series in Energy, pp. 139–157, Woodhead Publishing, 2013.

[125] Y. C. Chong, *Thermal Analysis and Air Flow Modellingof Electrical Machines.* PhD thesis, The University of Edinburgh, 2015.

[126] G. Shrestha, *Structural Flexibility of Large Direct Drive Generators for Wind Turbines.* PhD thesis, Electrical Engineering, Mathematics and Computer Science, TU Delft, 2013.

[127] W. Cao, Y. Xie, and Z. Tan, "Wind turbine generator technologies," in *Advances in Wind Power*, InTech, nov 2012.

[128] P. Lampola, *Directly Driven, Low-Speed Permanent-Magnet Generators for Wind Power Applications.* PhD thesis, Helsinki University of Technology, 2000.

[129] E. Spooner, P. Gordon, and C. French, "Lightweight, ironless-stator, pm generators for direct-drive wind turbines," in *Second International Conference on Power Electronics, Machines and Drives (PEMD 2004).*, vol. 1, pp. 29–33 Vol.1, 2004.

[130] J. Coey, "Permanent magnet applications," *Journal of Magnetism and Magnetic Materials*, vol. 248, no. 3, pp. 441–456, 2002.

[131] P. Eklund and S. Eriksson, "The influence of permanent magnet material properties on generator rotor design," *Energies*, vol. 12, no. 7, 2019.

[132] Y. Liu, *Design of a superconducting DC wind generator*. PhD thesis, Karlsruher Institut für Technologie (KIT), 2018. 37.06.02; LK 01.

[133] E. Laithwaite, J. Eastham, H. Bolton, and T. Fellows, "Linear motors with transverse flux," *Proceedings of the Institution of Electrical Engineers*, vol. 118, no. 12, p. 1761, 1971.

[134] N. Dehlinger, *Étude des performances d'une machine à flux transverse à noyaux ferromagnétiques amorphes*. PhD thesis, Université Laval, 2007.

[135] E. Spooner, P. Gordon, J. Bumby, and C. French, "Lightweight ironless-stator PM generators for direct-drive wind turbines," *IEE Proceedings - Electric Power Applications*, vol. 152, no. 1, p. 17, 2005.

[136] D. Bang, H. Polinder, G. Shrestha, and J. A. Ferreira, "Review of generator systems for direct-drive wind turbines," 2008.

[137] M. Mueller and A. Zavvos, "Electrical generators for direct drive systems: a technology overview," in *Electrical Drives for Direct Drive Renewable Energy Systems* (M. Mueller and H. Polinder, eds.), Woodhead Publishing Series in Energy, pp. 3–29, Woodhead Publishing, 2013.

[138] E. Spooner and A. Williamson, "Direct coupled, permanent magnet generators for wind turbine applications," *Electric Power Applications, IEE Proceedings*, vol. 143, pp. 1 – 8, 02 1996.

[139] C. Zhao, D. Zhu, and Y. Yan, "The optimization of auxiliary poles of ipm synchronous machine," in *2005 International Conference on Electrical Machines and Systems*, vol. 1, pp. 344–349 Vol. 1, 2005.

[140] F. Libert, "Design, optimization and comparison of permanent magnet motors for a low-speed direct-driven mixer," 2004.

[141] K. Sitapati and R. Krishnan, "Performance comparisons of radial and axial field, permanent-magnet, brushless machines," *IEEE Transactions on Industry Applications*, vol. 37, pp. 1219–1226, Sep 2001.

[142] A. Cavagnino, M. Lazzari, F. Profumo, and A. Tenconi, "A comparison between the axial flux and the radial flux structures for pm synchronous motors," *IEEE Transactions on Industry Applications*, vol. 38, no. 6, pp. 1517–1524, 2002.

[143] S. Huang, J. Luo, F. Leonardi, and T. Lipo, "A comparison of power density for axial flux machines based on general purpose sizing equations," *IEEE Transactions on Energy Conversion*, vol. 14, no. 2, pp. 185–192, 1999.

[144] Z. Zhang, R. Nilssen, S. M. Muyeen, A. Nysveen, and A. Al-Durra, "Design optimization of ironless multi-stage axial-flux permanent magnet generators for offshore wind turbines," *Engineering Optimization*, vol. 49, no. 5, pp. 815–827, 2017.

[145] B. J. Chalmers and E. Spooner, "An axial-flux permanent-magnet generator for a gearless wind energy system," *IEEE Transactions on Energy Conversion*, vol. 14, pp. 251–257, Jun 1999.

[146] L. Soderlund, J. T. Eriksson, J. Salonen, H. Vihriala, and R. Perala, "A permanent-magnet generator for wind power applications," *IEEE Transactions on Magnetics*, vol. 32, pp. 2389–2392, Jul 1996.

[147] E. Muljadi, C. P. Butterfield, and Y.-H. Wan, "Axial-flux modular permanent-magnet generator with a toroidal winding for wind-turbine applications," *IEEE Transactions on Industry Applications*, vol. 35, pp. 831–836, Jul 1999.

[148] A. D. Gerlando, G. Foglia, M. F. Iacchetti, and R. Perini, "Axial flux pm machines with concentrated armature windings: Design analysis and test validation of wind energy generators," *IEEE Transactions on Industrial Electronics*, vol. 58, pp. 3795–3805, Sept 2011.

[149] W. Wu, E. Spooner, and B. Chalmers, "Design of slotless torus generators with reduced voltage regulation," 1995.

[150] Y. Chen and P. Pillay, "Axial-flux pm wind generator with a soft magnetic composite core," in *Fourtieth IAS Annual Meeting. Conference Record of the 2005 Industry Applications Conference, 2005.*, vol. 1, pp. 231–237 Vol. 1, 2005.

[151] Y. Chen, P. Pillay, and A. Khan, "Pm wind generator topologies," *IEEE Transactions on Industry Applications*, vol. 41, no. 6, pp. 1619–1626, 2005.

[152] M. Mueller, A. McDonald, and D. Macpherson, "Structural analysis of low-speed axial-flux permanent-magnet machines," *IEE Proceedings - Electric Power Applications*, vol. 152, no. 6, p. 1417, 2005.

[153] M. Rapin and J.-M. Noël, *Énergie éolienne : Du petit éolien à l'éolien offshore*. ADEME, 2 ed., 2016.

[154] M. Dubois and H. Polinder, "Study of tfpm machines with toothed rotor applied to direct-drive generators for wind turbines," 06 2004.

[155] J. Chang, D. Kang, J. Lee, and J. Hong, "Development of transverse flux linear motor with permanent-magnet excitation for direct drive applications," *IEEE Transactions on Magnetics*, vol. 41, no. 5, pp. 1936–1939, 2005.

[156] H. L. J. M. H. P. J. Weh, H.; Hoffmann, "Directly driven permanent magnet excited sychronous generator for varibale speed operation," *European Community Wind Energy Conference*, pp. pp. 566–72, 1988.

[157] Z. Wan, *Design of a Stator Permanent Magnet Transverse Flux Machine for Direct-drive Application*. PhD thesis, Carolina State University, 2018.

[158] B. H. C. Z. Henk, Polinder; Deok-JE, "Concept report on generator topologies, mechanical electromagnetic optimization," tech. rep., Delft University of Technology, 2007.

[159] M. Harris, G. Pajooman, and S. Abu Sharkh, "The problem of power factor in vrpm (transverse-flux) machines," in *Eighth International Conference on Electrical Machines and Drives (Conf. Publ. No. 444)*, pp. 386–390, 1997.

[160] J. R. Anglada and S. M. Sharkh, "An insight into torque production and power factor in transverse-flux machines," *IEEE Transactions on Industry Applications*, vol. 53, pp. 1971–1977, may 2017.

[161] J. Wang, K. T. Chau, J. Z. Jiang, and C. Yu, "Design and analysis of a transverse flux permanent-magnet machine using three-dimensional scalar magnetic potential finite element method," *Journal of Applied Physics*, vol. 103, p. 07F107, apr 2008.

[162] L. Matsch, *Electromagnetic and electromechanical machines*. New York: Harper & Row, 1986.

[163] J. R. Anglada and S. M. Sharkh, "Analysis of transverse flux machines using a virtual mutual inductance approach," *IEEE Transactions on Energy Conversion*, vol. 33, pp. 465–472, jun 2018.

[164] A. Ahmed and I. Husain, "Power factor improvement of a transverse flux machine with high torque density," *IEEE Transactions on Industry Applications*, vol. 54, pp. 4297–4305, sep 2018.

[165] M. Dubois, H. Polinder, and J. Ferreira, "Influence of air gap thickness in transverse flux permanent magnet (tfpm) generators for wind turbine application," 01 2002.

[166] B. Deok-JE, *Design of Transverse Flux Permanent Magnet Machines for Large Direct-DriveWind Turbines*. PhD thesis, Delft University of Technology, 2010.

[167] D. Svechkzrenko, *On Analytical Modeling and Design of a Novel Transverse Flux Generator for OffshoreWind Turbines*. PhD thesis, KTH Royal Institute of Technology, Stockholm, Sweden, May 2007.

[168] D. J. Bang, H. Polinder, G. Shrestha, and J. A. Ferreira, "Design of a lightweight transverse flux permanent magnet machine for direct-drive wind turbines," in *2008 IEEE Industry Applications Society Annual Meeting*, pp. 1–7, Oct 2008.

[169] M. Dubois, H. Polinder, and J. Ferreira, "Comparison of generator topologies for direct-drive wind turbines," *Nordic Countries Power and Industrial Electronics Conference (NORPIE)*, June 2000.

[170] none, "Advanced wind turbine drivetrain concepts. workshop report," tech. rep., dec 2010.

[171] G. Shrestha, H. Polinder, and J. Ferreira, "Scaling laws for direct drive generators in wind turbines," in *2009 IEEE International Electric Machines and Drives Conference*, pp. 797–803, 2009.

[172] A. Grauers and P. Kasinathan, "Force density limits in low-speed pm machines due to temperature and reactance," *IEEE Transactions on Energy Conversion*, vol. 19, no. 3, pp. 518–525, 2004.

[173] H. Polinder, "Principles of electrical design of permanent magnet generators for direct drive renewable energy systems," in *Electrical Drives for Direct Drive Renewable Energy Systems* (M. Mueller and H. Polinder, eds.), Woodhead Publishing Series in Energy, pp. 30–50, Woodhead Publishing, 2013.

[174] R. S. Semken, M. Polikarpova, P. Roytta, J. Alexandrova, J. Pyrhonen, J. Nerg, A. Mikkola, and J. Backman, "Direct-drive permanent magnet generators for high-power wind turbines: benefits and limiting factors," *IET Renewable Power Generation*, vol. 6, no. 1, p. 1, 2012.

[175] C. Kim, H.-J. Sung, B.-S. Go, K. Sim, G. D. Nam, S. Kim, and M. Park, "Design, fabrication, and testing of a full-scale hts coil for a 10 mw hts wind power generator," *IEEE Transactions on Applied Superconductivity*, vol. 31, no. 5, pp. 1–5, 2021.

[176] Y. Xu, L. An, B. Jia, and N. Maki, "Study on electrical design of large-capacity fully superconducting offshore wind turbine generators," *IEEE Transactions on Applied Superconductivity*, vol. 31, no. 5, pp. 1–5, 2021.

[177] Y. Cheng, Y. Zhang, R. Qu, D. Li, Y. Liu, and M. Noe, "Design and analysis of 10 mw hts double-stator flux-modulation generator for wind turbine," *IEEE Transactions on Applied Superconductivity*, vol. 31, no. 5, pp. 1–8, 2021.

[178] G. Seo, J. Mun, D. Kim, M. Park, and S. Kim, "Neon-helium hybrid cooling system for a 10 mw class superconducting wind power generator," *IEEE Transactions on Applied Superconductivity*, vol. 31, no. 5, pp. 1–5, 2021.

[179] Y. Terao, M. Sekino, and H. Ohsaki, "Comparison of conventional and superconducting generator concepts for offshore wind turbines," *IEEE Transactions on Applied Superconductivity*, vol. 23, no. 3, pp. 5200904–5200904, 2013.

[180] Y. Xu, N. Maki, and M. Izumi, "Performance comparison of 10-mw wind turbine generators with hts, copper, and pm excitation," *IEEE Transactions on Applied Superconductivity*, vol. 25, no. 6, pp. 1–6, 2015.

[181] I. Marino, A. Pujana, G. Sarmiento, S. Sanz, J. M. Merino, M. Tropeano, J. Sun, and T. Canosa, "Lightweight mgb 2 superconducting 10 mw wind generator," *Superconductor Science and Technology*, vol. 29, no. 2, p. 024005, 2016.

[182] R. Shafaie and M. Kalantar, "Design of a 10-mw-class wind turbine hts synchronous generator with optimized field winding," *IEEE Transactions on Applied Superconductivity*, vol. 23, pp. 5202307–5202307, Aug 2013.

[183] H. Karmaker, M. Ho, and D. Kulkarni, "Comparison between different design topologies for multi-megawatt direct drive wind generators using improved second generation high temperature superconductors," *IEEE Transactions on Applied Superconductivity*, vol. 25, pp. 1–5, June 2015.

[184] H. J. Sung, G. H. Kim, K. Kim, S. J. Jung, M. Park, I. K. Yu, Y. G. Kim, H. Lee, and A. R. Kim, "Practical design of a 10 mw superconducting wind power generator considering weight issue," *IEEE Transactions on Applied Superconductivity*, vol. 23, pp. 5201805–5201805, June 2013.

[185] J. Wang, R. Qu, Y. Tang, Y. Liu, B. Zhang, J. He, Z. Zhu, H. Fang, and L. Su, "Design of a superconducting synchronous generator with lts field windings for 12 mw offshore direct-drive wind turbines," *IEEE Transactions on Industrial Electronics*, vol. 63, pp. 1618–1628, March 2016.

[186] "Method and apparatus for a superconducting generator driven by wind turbine," 2008.

[187] "Superconducting generator driven by a wind turbine," 2020.

[188] V. Prince, "Large-scale wind energy systems: 10mw and beyond," *World Future Energy Summit 2015*, Jan. 2015.

[189] X. Song, C. Bührer, P. Brutsaert, A. Ammar, J. Krause, A. Bergen, T. Winkler, M. Dhalle, J. Hansen, A. V. Rebsdorf, S. Wessel, M. t. Brake, M. Bauer, J. Kellers, J. Wiezoreck, H. Pütz, H. Kyling, H. Boy, and E. Seitz, "Ground testing of the world's first mw-class direct-drive superconducting wind turbine generator," *IEEE Transactions on Energy Conversion*, vol. 35, no. 2, pp. 757–764, 2020.

[190] H. Li, Z. Chen, and H. Polinder, "Optimization of multibrid permanent-magnet wind generator systems," *IEEE Transactions on Energy Conversion*, vol. 24, no. 1, pp. 82–92, 2009.

[191] G. Shrestha, H. Polinder, D. J. Bang, and J. A. Ferreira, "Structural flexibility: A solution for weight reduction of large direct-drive wind-turbine generators," *IEEE Transactions on Energy Conversion*, vol. 25, pp. 732–740, Sept 2010.

[192] W. Miller, L. Zhuang, J. Bottema, A. Wittebrood, P. De Smet, A. Haszler, and A. Vieregge, "Recent development in aluminium alloys for the automotive industry," *Materials Science and Engineering: A*, vol. 280, no. 1, pp. 37–49, 2000.

[193] Z. Zhang, A. Matveev, R. Nilssen, and A. Nysveen, "Ironless permanent-magnet generators for offshore wind turbines," *IEEE Transactions on Industry Applications*, vol. 50, pp. 1835–1846, May 2014.

[194] M. A. Mueller and A. S. McDonald, "A lightweight low-speed permanent magnet electrical generator for direct-drive wind turbines," *Wind Energy*, vol. 12, no. 8, pp. 768–780, 2009.

[195] S. Engstrom and S. Lindgren, "Design of newgen direct drive generator for demonstration in a

3.5 mw wind turbine," in *EWEC (European Wind Energy Conference & Exhibition, Milan, Italy*, 2007.

[196] E. Spooner and A. Williamson, "Modular, permanent-magnet wind-turbine generators," in *IAS '96. Conference Record of the 1996 IEEE Industry Applications Conference Thirty-First IAS Annual Meeting*, vol. 1, pp. 497–502 vol.1, 1996.

[197] U. Shipurkar, H. Polinder, and J. A. Ferreira, "Modularity in wind türbine generator systems — opportunities and challenges," in *2016 18th European Conference on Power Electronics and Applications (EPE'16 ECCE Europe)*, pp. 1–10, 2016.

[198] Z. Chen and E. Spooner, "A modular, permanent-magnet generator for variable speed wind turbines," in *1995 Seventh International Conference on Electrical Machines and Drives (Conf. Publ. No. 412)*, pp. 453–457, 1995.

[199] C. C. Pavel, R. Lacal-Arántegui, A. Marmier, D. Schüler, E. Tzimas, M. Buchert, W. Jenseit, and D. Blagoeva, "Substitution strategies for reducing the use of rare earths in wind turbines," *Resources Policy*, vol. 52, pp. 349 – 357, 2017.

[200] S. Eriksson and H. Bernhoff, "Rotor design for pm generators reflecting the unstable neodymium price," in *2012 XXth International Conference on Electrical Machines*, pp. 1419–1423, Sept 2012.

[201] O. Danielsson, K. Thorburn, M. Eriksson, and M. Leijon, "Permanent magnet fixation concepts for linear generator," *Fifth European Wave Energy Conference*, 2007.

[202] H. A. Khazdozian, *Improved Design of Permanent Magnet Generators for Large Scale Wind Turbines*. PhD thesis, Iowa State University, 2016.

[203] J. Lutz and J. Ley, "Brushless pm machine construction enabling low coercivity magnets," 2015.

[204] M. Henriksen and B. B. Jensen, "Induction generators for direct-drive wind turbines," in *2011 IEEE International Electric Machines & Drives Conference (IEMDC)*, IEEE, may 2011.

[205] Z. Jiang, "Installation of offshore wind turbines: A technical review," *Renewable and Sustainable Energy Reviews*, vol. 139, p. 110576, 2021.

[206] Liebherr, "Heavy lift crane series - shaping tomorrows energy," tech. rep., Avialable: https://www.liebherr.com/en/int/products/maritime-cranes/offshore-cranes/heavy-lift-crane/heavy-lift-crane.html, 2021.

[207] E. Muljadi and J. Green, "Cogging torque reduction in a permanent magnet wind turbine generator," in *ASME 2002 Wind Energy Symposium*, ASMEDC, jan 2002.

[208] V. Ruuskanen, *Design Aspects of Megawatt-Range Direct-Driven Permanent Magnet Wind Generators*. PhD thesis, Lappeenranta University of Technology, 2011.

[209] F. Meier, *Permanent-magnet synchronous machines with non-overlapping concentrated windings for low- speed direct-drive applications*. Stockholm: School of Electrical Engineering, Electrical Machines and Power Electronics, 2008.

[210] A. McDonald, M. Mueller, and A. Zavvos, "Electrical, thermal and structural generator design and systems integration for direct drive renewable energy systems," in *Electrical Drives for Direct Drive Renewable Energy Systems*, pp. 51–79, Elsevier, 2013.

[211] P. Juha, J. Tapani, and H. Valeria, *Design Rotating Electrical Machine*. John Wiley Sons, Dec. 2013.

[212] E. Devillers, *Electromagnetic subdomain modeling technique for the fast prediction of radial and circumferential stress harmonics in electrical machines*. PhD thesis, Universite de Lille, 2018.

[213] P. L. Alger, "The acoustic behavior of induction motors," *The Journal of the Acoustical Society of America*, vol. 25, pp. 831–831, jul 1953.

[214] J. C. L. Jacek F. Gieras, Chong Wang, *Noise of Polyphase Electric Motors*. CRC/Taylor Francis, 2006.

[215] S. Garvey, "Tangential forces matter," in *9th International Conference on Electrical Machines and Drives*, IEE, 1999.

[216] T. Pyrhönen, Juha; Jokinen and V. Hrabovcová, "Design of magnetic circuits," in *Design of Rotating Electrical Machines*, pp. 155–228, John Wiley & Sons, Ltd, oct 2013.

[217] K. Overshott, "Magnetism: It is permanent," *IEE Proceedings*, vol. 138, pp. 22–30, 1991.

[218] L. Welzel, "End-of-life wind turbines in the eu:an estimation of the ndfeb-magnetsand containing rare earth elementsin the anthropogenic stockof germany and denmark," tech. rep., Uppsala University, Department of Earth Sciences, 2019.

[219] B. J. Smith and R. G. Eggert, "Costs, substitution, and material use: The case of rare earth magnets," *Environmental Science &amp Technology*, vol. 52, pp. 3803–3811, mar 2018.

[220] B. J. Smith and R. G. Eggert, "Multifaceted material substitution: The case of NdFeB magnets, 2010–2015," *JOM*, vol. 68, pp. 1964–1971, apr 2016.

[221] Arnold, "N40sh- sintered neodymium-iron-boron magnets," tech. rep., Arnold Magentic Technologies, 2017.

[222] Arnold, "N48sh- sintered neodymium-iron-boron magnets," tech. rep., Arnold Magentic Technologies, 2017.

[223] Eclipse, "Ferrite magnets/ceramic magnets datasheet," tech. rep., Eclipse Magnetics, 2022.

[224] Gooudsmith, "Products and services," tech. rep., GOUDSMIT UK, 2019.

[225] Hitachi, "High-energy ferrite magnet," tech. rep., Hitachi Metals, Ltd. Materials, 2008.

[226] "Grades of ferrite: The original online company, https://e-magnetsuk.com/ferrite-magnets/grades-of-ferrite/," 2022. Accessed Jul. 28, 2022.

[227] C. de Julian Fernandez, C. Sangregorio, J. de la Figuera, B. Belec, D. Makovec, and A. Quesada, "Progress and prospects of hard hexaferrites for permanent magnet applications," *Journal of Physics D: Applied Physics*, dec 2020.

[228] FRED, "Global price of copper, https://fred.stlouisfed.org/series/pcoppusdq." Accessed Oct. 12, 2021.

[229] L. Sethuraman and K. Dykes, "Generatorse: A sizing tool forvariable-speed wind turbinegenerators," tech. rep., National Renewable Energy Laboratory, 2017.

[230] B. Sneyers, D. W. Novotny, and T. A. Lipo, "Field weakening in buried permanent magnet ac motor drives," *IEEE Transactions on Industry Applications*, vol. IA-21, no. 2, pp. 398–407, 1985.

[231] T. M. Jahns, "Flux-weakening regime operation of an interior permanent-magnet synchronous motor drive," *IEEE Transactions on Industry Applications*, vol. IA-23, no. 4, pp. 681–689, 1987.

[232] G.-H. Kang, J. Hur, H.-G. Sung, and J.-P. Hong, "Optimal design of spoke type bldc motor considering irreversible demagnetization of permanent magnet," in *Sixth International Conference on Electrical Machines and Systems, 2003. ICEMS 2003.*, vol. 1, pp. 234–237 vol.1, 2003.

[233] B.-K. Lee, G.-H. Kang, J. Hur, and D.-W. You, "Design of spoke type bldc motors with high power density for traction applications," in *Conference Record of the 2004 IEEE Industry Applications Conference, 2004. 39th IAS Annual Meeting.*, vol. 2, pp. 1068–1074 vol.2, 2004.

[234] J. Bianchi, Nicols; T, "Design, analysis, and control of interior pm synchronous machines," in *IEEE Industrial Application Society*, 2004.

[235] A. Fasolo, L. Alberti, and N. Bianchi, "Performance comparison between switching-flux and ipm machine with rare earth and ferrite pms," in *2012 XXth International Conference on Electrical Machines*, pp. 731–737, 2012.

[236] W. Kakihara, M. Takemoto, and S. Ogasawara, "Rotor structure in 50 kw spoke-type interior permanent magnet synchronous motor with ferrite permanent magnets for automotive applications," in *2013 IEEE Energy Conversion Congress and Exposition*, pp. 606–613, 2013.

[237] W. Tong, *Mechanical Design of Electric Motors*. CRC Press, apr 2014.

[238] N. Bianchi and S. Bolognani, "Design techniques for reducing the cogging torque in surface-mounted pm motors," *IEEE Transactions on Industry Applications*, vol. 38, no. 5, pp. 1259–1265, 2002.

[239] S.-M. Hwang, J.-B. Eom, Y.-H. Jung, D.-W. Lee, and B.-S. Kang, "Various design techniques to reduce cogging torque by controlling energy variation in permanent magnet motors," *IEEE Transactions on Magnetics*, vol. 37, no. 4, pp. 2806–2809, 2001.

[240] C. Breton, J. Bartolome, J. Benito, G. Tassinario, I. Flotats, C. Lu, and B. Chalmers, "Influence of machine symmetry on reduction of cogging torque in permanent-magnet brushless motors," *IEEE Transactions on Magnetics*, vol. 36, no. 5, pp. 3819–3823, 2000.

[241] S. R. Pérez, "Analysis of a light permanent magnetin-wheel motor for an electric vehiclewith autonomous corner modules," Master's thesis, KTH Electrical Engineering, 2011.

[242] J. Chen, C. Nayar, and L. Xu, "Design and finite-element analysis of an outer-rotor permanent-magnet generator for directly coupled wind turbines," *IEEE Transactions on Magnetics*, vol. 36, no. 5, pp. 3802–3809, 2000.

[243] F. Libert and J. Soulard, "Design study of different direct-driven permanent-magnet motors for a low speed application," in *The Nordic Workshop on Power and Industrial Electronics (NORpie), Trondheim, Norway*, 2004.

[244] W. Wu, V. Ramsden, T. Crawford, and G. Hill, "A low speed, high-torque, direct-drive permanent magnet generator for wind turbines," in *Conference Record of the 2000 IEEE Industry Applications Conference. Thirty-Fifth IAS Annual Meeting and World Conference on Industrial Applications of Electrical Energy (Cat. No.00CH37129)*, vol. 1, pp. 147–154 vol.1, Oct 2000.

[245] H. Polinder, "Overview of and trends in wind turbine generator systems," in *2011 IEEE Power and Energy Society General Meeting*, pp. 1–8, 2011.

[246] G. L. Olson, "Bar-wound versus wire-wound alternators," tech. rep., Technical information from Cummins Power Generation, Power topic 9013, 2010.

[247] J. Haldemann, "Transpositions in stator bars of large turbogenerators," *IEEE Transactions on Energy Conversion*, vol. 19, no. 3, pp. 553–560, 2004.

[248] A. M. EL-Refaie, "Fractional-slot concentrated-windings synchronous permanent magnet machines: Opportunities and challenges," *IEEE Transactions on Industrial Electronics*, vol. 57, no. 1, pp. 107–121, 2010.

[249] F. Libert and J. Soulard, "Investigation on pole-slot combinations for permanent-magnet machines with concentrated windings," in *2004 International Conference on Electrical Machines (ICEM), pp. 5-8*, 2004.

[250] F. Magnussen and C. Sadarangani, "Winding factors and joule losses of permanent magnet machines with concentrated windings," in *IEEE International Electric Machines and Drives Conference, 2003. IEMDC'03.*, vol. 1, pp. 333–339 vol.1, 2003.

[251] H. Jussila, P. Salminen, M. Niemela, and J. Pyrhonen, "Guidelines for designing concentrated winding fractional slot permanent magnet machines," in *2007 International Conference on Power Engineering, Energy and Electrical Drives*, pp. 191–194, 2007.

[252] D. Ishak, Z. Zhu, and D. Howe, "Comparison of pm brushless motors, having either all teeth or alternate teeth wound," *IEEE Transactions on Energy Conversion*, vol. 21, no. 1, pp. 95–103, 2006.

[253] P. Kasinathan, A. Grauers, and E. Hamdi, "Force density limits in low-speed permanent-magnet machines due to saturation," *IEEE Transactions on Energy Conversion*, vol. 20, no. 1, pp. 37–44, 2005.

[254] H. Bang, D; Polinder, "On rough design of 10 and 20 mw direct-drive generators," tech. rep., Project Upwind, 2008.

[255] M. Curti, J. J. H. Paulides, and E. A. Lomonova, "An overview of analytical methods for magnetic field computation," in *2015 Tenth International Conference on Ecological Vehicles and Renewable Energies (EVER)*, pp. 1–7, March 2015.

[256] H. Tiegna, Y. Amara, and G. Barakat, "Overview of analytical models of permanent magnet electrical machines for analysis and design purposes," *Mathematics and Computers in Simulation*, vol. 90, pp. 162 – 177, 2013. ELECTRIMACS 2011- PART I.

[257] A. Bellara, Y. Amara, G. Barakat, and B. Dakyo, "Two-dimensional exact analytical solution of armature reaction field in slotted surface mounted pm radial flux synchronous machines," *IEEE Transactions on Magnetics*, vol. 45, pp. 4534–4538, Oct 2009.

[258] Z. Q. Zhu, D. Howe, and C. C. Chan, "Improved analytical model for predicting the magnetic field distribution in brushless permanent-magnet machines," *IEEE Transactions on Magnetics*, vol. 38, pp. 229–238, Jan 2002.

[259] M. A. Benhamida, H. Ennassiri, Y. Amara, G. Barakat, and N. Debbah, "Study of switching flux permanent magnet machines using interpolation based reluctance network model," in *2016 International Conference on Electrical Sciences and Technologies in Maghreb (CISTEM)*, pp. 1–7, Oct 2016.

[260] M. Amrhein and P. T. Krein, "3-d magnetic equivalent circuit framework for modeling electromechanical devices," *IEEE Transactions on Energy Conversion*, vol. 24, pp. 397–405, June 2009.

[261] S. A. Saied, K. Abbaszadeh, and M. Fadaie, "Reduced order model of developed magnetic equivalent circuit in electrical machine modeling," *IEEE Transactions on Magnetics*, vol. 46, pp. 2649–2655, July 2010.

[262] D. d. L. B. Olivier, *Modèles analytiques électromagnétiques bi et tri dimensionnels en vue de l'optimisation des actionneurs disques : étude théorique et expérimentale des pertes magnétiques dans les matériaux granulaires.* PhD thesis, École normale supérieure de Cachan, 2010.

[263] T. Lubin, "Contribution à la modélisation analytique des actionneurs électromécaniques," tech. rep., Habilitation à diriger des recherches, Université de Lorraine, 2016.

[264] Y. Amara, "Modélisation pour le dimensionnement des machinesélectriques. application à des machines spéciales.," tech. rep., Habilitation à diriger des recherches, Université Le Havre Normandie, 2012.

[265] M. Dhifli, *Contribution au développement de structures discoïdes de machines électriques à aimants permanents à commutation de flux pour l'éolien.* PhD thesis, Université Le Havre Normandie, 2016.

[266] J. Azzouzi, *Contribution à la modélisation et à l'optimisation des machines synchrones à aimants permanents à flux axial. Application au cas de l'aérogénérateur.* PhD thesis, Université Le Havre Normandie, 2007.

[267] N. Abdelkarim, *Optimisation multi-critères et multi-physique d'aérogénérateurs à aimants permanents à flux axial.* PhD thesis, Université Le Havre Normandie, 2008.

[268] G. Verez, *Contribution à l'étude des émissions vibro-acoustiques des machines électriques : cas des machines synchrones à aimants dans un contexte automobile.* PhD thesis, Université Le Havre Normandie, 2014.

[269] H. Tiegna, *Contribution à la modélisation analytique des machines synchrones à flux axial à aimants permanents à attaquedirecte en vue de leur dimensionnement. Application aux éoliennes.* PhD thesis, Université Le Havre Normandie, 2013.

[270] D. C. Hanselman, *Brushless Permanent-Magnet Motor Design.* The Writers' Collective, 1994.

[271] V. Ostovic, *Dynamics of Saturated Electric Machines.* Springer-Verlag GMBH, Dec. 1989.

[272] M.-F. Hsieh and Y.-C. Hsu, "A generalized magnetic circuit modeling approach for design of surface permanent-magnet machines," *IEEE Transactions on Industrial Electronics*, vol. 59, no. 2, pp. 779–792, 2012.

[273] S. D. Sudhoff, B. T. Kuhn, K. A. Corzine, and B. T. Branecky, "Magnetic equivalent circuit modeling of induction motors," *IEEE Transactions on Energy Conversion*, vol. 22, no. 2, pp. 259–270, 2007.

[274] H. W. Derbas, J. M. Williams, A. C. Koenig, and S. D. Pekarek, "A comparison of nodal- and mesh-based magnetic equivalent circuit models," *IEEE Transactions on Energy Conversion*, vol. 24, no. 2, pp. 388–396, 2009.

[275] M. Amrhein, *Induction Machine Performance Improvements: Design-Oriented Approaches*. PhD thesis, University of Illinois at Urbana-Champaign, 2007.

[276] B. Nedjar, *Modélisation basée sur la méthode des réseaux de perméances en vue de l'optimisation de machines synchrones à simple et à double excitation*. PhD thesis, Ecole normale supérieure de Cachan-ENS Cachan, 2011.

[277] S. Asfirane, *Développement d'un outil de génération automatique des réseaux de réluctances pour la modélisation de dispositifs électromécaniques*. PhD thesis, École Normale Supérieure Paris-Saclay, 2019.

[278] M. A. Benhamida, *Investigation of new generator technologies for offshore wind turbines*. PhD thesis, Normandie Université, 2018.

[279] H. Dogan, L. Garbuio, H. Nguyen-Xuan, B. Delinchant, A. Foggia, and F. Wurtz, "Multistatic reluctance network modeling for the design of permanent-magnet synchronous machines," *IEEE Transactions on Magnetics*, vol. 49, no. 5, pp. 2347–2350, 2013.

[280] M. A. Benhamida, H. Ennassiri, Y. Amara, G. Barakat, and N. Debbah, "Study of switching flux permanent magnet machines using interpolation based reluctance network model," in *2016 International Conference on Electrical Sciences and Technologies in Maghreb (CISTEM)*, pp. 1–7, 2016.

[281] G. Barakat and Y. Amara, "A simple and effective way to couple analytical formal solution of magnetic potential and reluctance network models," in *9th IET International Conference on Computation in Electromagnetics (CEM 2014)*, pp. 1–2, 2014.

[282] K. J. W. Pluk, J. W. Jansen, and E. A. Lomonova, "Hybrid analytical modeling: Fourier modeling combined with mesh-based magnetic equivalent circuits," *IEEE Transactions on Magnetics*, vol. 51, no. 8, pp. 1–12, 2015.

[283] Y. Laoubi, M. Dhifli, G. Verez, Y. Amara, and G. Barakat, "Open circuit performance analysis of a permanent magnet linear machine using a new hybrid analytical model," *IEEE Transactions on Magnetics*, vol. 51, no. 3, pp. 1–4, 2015.

[284] S. Ouagued, A. Aden Diriye, Y. Amara, and G. Barakat, "A general framework based on a hybrid analytical model for the analysis and design of permanent magnet machines," *IEEE Transactions on Magnetics*, vol. 51, no. 11, pp. 1–4, 2015.

[285] P. D. Sewell, K. J. Bradley, J. Clare, P. W. Wheeler, A. Ferrah, and R. Magill, "Efficient dynamic models for induction machines," *International Journal of Numerical Modelling-electronic Networks Devices and Fields*, vol. 12, pp. 449–464, 1999.

[286] D. Petrichenko, *Contribution à la modélisation et à la conception optimale des turbo-alternateurs de faible puissancepar.* PhD thesis, Ecole Centrale de Lille, 2007.

[287] A. . A. Y. Ouagued, Sofiane ; Aden-Diriye and G. Barakat, "Consideration of magnetic saturation in a new hybrid seminumerical model," in *Compumag, Montreal*, 2015.

[288] I. Hasan, T. Husain, M. W. Uddin, Y. Sozer, I. Husain, and E. Muljadi, "Analytical modeling of a novel transverse flux machine for direct drive wind turbine applications," in *2015 IEEE Energy Conversion Congress and Exposition (ECCE)*, pp. 2161–2168, 2015.

[289] J. Kokernak and D. Torrey, "Magnetic circuit model for the mutually coupled switched-reluctance machine," *IEEE Transactions on Magnetics*, vol. 36, pp. 500–507, March 2000.

[290] J. M. Williams, *Modeling and analysis of electric machines with asymmetric rotor poles using a reluctance based, magnetic equivalent circuit.* PhD thesis, University of Missouri–Rolla, 2004.

[291] J. P. Barton, "Empirical equations for the magnetization curve," *Transactions of the American Institute of Electrical Engineers*, vol. 52, no. 2, pp. 659–664, 1933.

[292] M. Dadić, M. Jurčević, and R. Malarić, "Approximation of the nonlinear b-h curve by complex exponential series," *IEEE Access*, vol. 8, pp. 49610–49616, 2020.

[293] S. Ruoho, E. Dlala, and A. Arkkio, "Comparison of demagnetization models for finite-element analysis of permanent-magnet synchronous machines," *IEEE Transactions on Magnetics*, vol. 43, no. 11, pp. 3964–3968, 2007.

[294] P. Diez and J. P. Webb, "A rational approach to $b - h$ curve representation," *IEEE Transactions on Magnetics*, vol. 52, no. 3, pp. 1–4, 2016.

[295] J. Brauer, "Simple equations for the magnetization and reluctivity curves of steel," *IEEE Transactions on Magnetics*, vol. 11, no. 1, pp. 81–81, 1975.

[296] C. Pechstein and B. Jüttler, "Monotonicity-preserving interproximation of b–h-curves," *Journal of Computational and Applied Mathematics*, vol. 196, no. 1, pp. 45–57, 2006.

[297] V. Sandeep, S. S. Murthy, and B. Singh, "A comparative study on approaches to curve fitting of magnetization characteristics for induction generators," in *2012 IEEE International Conference on Power Electronics, Drives and Energy Systems (PEDES)*, pp. 1–6, 2012.

[298] F. C. Trutt, E. A. Erdelyi, and R. F. Jackson, "The non-linear potential equation and its numerical solution for highly saturated electrical machines," *IEEE Transactions on Aerospace*, vol. 1, no. 2, pp. 430–440, 1963.

[299] J. Rivas, J. Zamarro, E. Martin, and C. Pereira, "Simple approximation for magnetization curves and hysteresis loops," *IEEE Transactions on Magnetics*, vol. 17, no. 4, pp. 1498–1502, 1981.

[300] M. El-Sherbiny, "Representation of the magnetization characteristic by a sum of exponentials," *IEEE Transactions on Magnetics*, vol. 9, no. 1, pp. 60–61, 1973.

[301] B. Forghani, E. Freeman, D. Lowther, and P. Silvester, "Interactive modelling of magnetisation curves," *IEEE Transactions on Magnetics*, vol. 18, no. 6, pp. 1070–1072, 1982.

[302] T. Hülsmann, "Nonlinear material curve modeling and sensitivity analysis for mqs-problems," Master's thesis, University of Wuppertal, 2012.

[303] P. Diez, "Symmetric invertible $b - h$ curves using piecewise linear rationals," *IEEE Transactions on Magnetics*, vol. 53, no. 6, pp. 1–3, 2017.

[304] G. Stone, "Advancements during the past quarter century in on-line monitoring of motor and generator winding insulation," *IEEE Transactions on Dielectrics and Electrical Insulation*, vol. 9, no. 5, pp. 746–751, 2002.

[305] S. Ruoho, J. Kolehmainen, J. Ikaheimo, and A. Arkkio, "Interdependence of demagnetization, loading, and temperature rise in a permanent-magnet synchronous motor," *IEEE Transactions on Magnetics*, vol. 46, no. 3, pp. 949–953, 2010.

[306] A. Boglietti, A. Cavagnino, D. Staton, M. Shanel, M. Mueller, and C. Mejuto, "Evolution and modern approaches for thermal analysis of electrical machines," *IEEE Transactions on Industrial Electronics*, vol. 56, no. 3, pp. 871–882, 2009.

[307] A. S. Bornschlegell, J. Pelle, S. Harmand, A. Fasquelle, and J.-P. Corriou, "Thermal optimization of a high-power salient-pole electrical machine," *IEEE Transactions on Industrial Electronics*, vol. 60, no. 5, pp. 1734–1746, 2013.

[308] J. Mugglestone, S. Pickering, and D. Lampard, "Effect of geometric changes on the flow and heat transfer in the end region of a tefc induction motor," in *1999. Ninth International Conference on Electrical Machines and Drives (Conf. Publ. No. 468)*, pp. 40–44, 1999.

[309] D. A. Staton and A. Cavagnino, "Convection heat transfer and flow calculations suitable for electric machines thermal models," *IEEE Transactions on Industrial Electronics*, vol. 55, no. 10, pp. 3509–3516, 2008.

[310] Y. Yang, B. Bilgin, M. Kasprzak, S. Nalakath, H. Sadek, M. Preindl, J. Cotton, N. Schofield, and A. Emadi, "Thermal management of electric machines," *IET Electrical Systems in Transportation*, vol. 7, pp. 104–116, jun 2017.

[311] N. Lancial, F. Torriano, F. Beaubert, S. Harmand, and G. Rolland, "Taylor-couette-poiseuille flow and heat transfer in an annular channel with a slotted rotor," *International Journal of Thermal Sciences*, vol. 112, pp. 92–103, 2017.

[312] A. Bousbaine, "Thermal modelling of induction motors based on accurate loss density distribution," *Electric Machines & Power Systems*, vol. 27, no. 3, pp. 311–324, 1999.

[313] J. Nerg, M. Rilla, and J. Pyrhonen, "Thermal analysis of radial-flux electrical machines with a high power density," *IEEE Transactions on Industrial Electronics*, vol. 55, no. 10, pp. 3543–3554, 2008.

[314] S. Henneberger, *Design and Development of a Permanent Magnet Synchronous Motor for a Hybrid Electric Vehicle Drive*. PhD thesis, Katholieke Universiteit Leuven, 1998.

[315] V. James E, "Prediction of windage power loss in alternators," tech. rep., Lewis Research Center, Ohio, 1968.

[316] J. Saari, *Thermal analysis of high-speed induction machines*. Doctoral thesis, 1998.

[317] G. Bertotti, "General properties of power losses in soft ferromagnetic materials," *IEEE Transactions on Magnetics*, vol. 24, no. 1, pp. 621–630, 1988.

[318] G. Stone, E. A. Boulter, I. Culbert, and H. Dhirani, *Stator Failure Mechanisms and Repair*, pp. 137–180. 2004.

[319] M. Istad, M. Runde, and A. Nysveen, "A review of results from thermal cycling tests of hydrogenerator stator windings," *IEEE Transactions on Energy Conversion*, vol. 26, no. 3, pp. 890–903, 2011.

[320] R. Brütsch and M. Chapman, "Insulating systems for high voltage rotating machines and reliability considerations," in *2010 IEEE International Symposium on Electrical Insulation*, pp. 1–5, 2010.

[321] I. P. Girsang, J. S. Dhupia, E. Muljadi, M. Singh, and J. Jonkman, "Modeling and control to mitigate resonant load in variable-speed wind turbine drivetrain," *IEEE Journal of Emerging and Selected Topics in Power Electronics*, vol. 1, no. 4, pp. 277–286, 2013.

[322] P. David James, *Modelling of high power density electrical machines for aerospace*. PhD thesis, University of Sheffield, 2003.

[323] D. Staton, A. Boglietti, and A. Cavagnino, "Solving the more difficult aspects of electric motor thermal analysis in small and medium size industrial induction motors," *IEEE Transactions on Energy Conversion*, vol. 20, pp. 620–628, Sep. 2005.

[324] A. Boglietti, A. Cavagnino, M. Lazzari, and M. Pastorelli, "A simplified thermal model for variable-speed self-cooled industrial induction motor," *IEEE Transactions on Industry Applications*, vol. 39, no. 4, pp. 945–952, 2003.

[325] N. Simpson, R. Wrobel, and P. H. Mellor, "Estimation of equivalent thermal parameters of impregnated electrical windings," *IEEE Transactions on Industry Applications*, vol. 49, no. 6, pp. 2505–2515, 2013.

[326] J. Bai, Y. Liu, Y. Sui, C. Tong, Q. Zhao, and J. Zhang, "Investigation of the cooling and thermal-measuring system of a compound-structure permanent-magnet synchronous machine," *Energies*, vol. 7, no. 3, pp. 1393–1426, 2014.

[327] L. Idoughi, X. Mininger, F. Bouillault, L. Bernard, and E. Hoang, "Thermal model with winding homogenization and fit discretization for stator slot," *IEEE Transactions on Magnetics*, vol. 47, no. 12, pp. 4822–4826, 2011.

[328] Z. Hashin and S. Shtrikman, "A variational approach to the theory of the elastic behaviour of multiphase materials," *Journal of the Mechanics and Physics of Solids*, vol. 11, no. 2, pp. 127–140, 1963.

[329] S. Nategh, O. Wallmark, M. Leksell, and S. Zhao, "Thermal analysis of a pmasrm using partial fea and lumped parameter modeling," *IEEE Transactions on Energy Conversion*, vol. 27, no. 2, pp. 477–488, 2012.

[330] M. A. Benhamida, H. Ennassiri, and Y. Amara, "Reluctance network lumped mechanical thermal models for the modeling and predesign of concentrated flux synchronous machine," *Open Physics*, vol. 16, no. 1, pp. 692–705, 2018.

[331] A. Boglietti, A. Cavagnino, and D. Staton, "Determination of critical parameters in electrical machine thermal models," in *2007 IEEE Industry Applications Annual Meeting*, pp. 73–80, 2007.

[332] R. A. Matula, "Electrical resistivity of copper, gold, palladium, and silver," *Journal of Physical and Chemical Reference Data*, 2009.

[333] G. Lei, J. Zhu, Y. Guo, C. Liu, and B. Ma, "A review of design optimization methods for electrical machines," *Energies*, vol. 10, p. 1962, nov 2017.

[334] Y. Okamoto, Y. Matsubayashi, S. Wakao, and S. Sato, "Material-density-based topology optimization with magnetic nonlinearity by means of stabilized sequential linear programming: Slpstab," *IEEE Transactions on Magnetics*, vol. 51, no. 3, pp. 1–4, 2015.

[335] J. S. Choi and J. Yoo, "Simultaneous structural topology optimization of electromagnetic sources and ferromagnetic materials," *Computer Methods in Applied Mechanics and Engineering*, vol. 198, no. 27, pp. 2111–2121, 2009.

[336] J. kyu Byun, I. han Park, and S. yop Hahn, "Topology optimization of electrostatic actuator using design sensitivity," *IEEE Transactions on Magnetics*, vol. 38, no. 2, pp. 1053–1056, 2002.

[337] Y.-S. Chung, J. Ryu, C. Cheon, I.-H. Park, and S.-Y. Hahn, "Optimal design method for microwave device using time domain method and design sensitivity analysis. i. fetd case," *IEEE Transactions on Magnetics*, vol. 37, no. 5, pp. 3289–3293, 2001.

[338] T. Labbé and B. Dehez, "Convexity-oriented method for the topology optimization of ferromagnetic moving parts in electromagnetic actuators using magnetic energy," *IEEE Transactions on Magnetics*, vol. 46, no. 12, pp. 4016–4022, 2010.

[339] B. B. S. Mohamodhosen, F. Gillon, M. Tounzi, and L. Chevallier, "Topology optimisation using nonlinear behaviour of ferromagnetic materials," *COMPEL - The international journal for computation and mathematics in electrical and electronic engineering*, vol. 37, pp. 2211–2223, sep 2018.

[340] H. Lian, A. N. Christiansen, D. A. Tortorelli, O. Sigmund, and N. Aage, "Combined shape and topology optimization for minimization of maximal von mises stress," *Structural and Multidisciplinary Optimization*, vol. 55, pp. 1541–1557, jan 2017.

[341] F. Guo, *Topology Optimization of Synchronous Electric Machines*. PhD thesis, Illinois Institute of Technology, 2021.

[342] I. H. Park, "Hole and dot sensitivity for topology optimization," in *Design Sensitivity Analysis and Optimization of Electromagnetic Systems*, pp. 265–301, Springer Singapore, aug 2018.

[343] M. P. Bendsøe and O. Sigmund, "Topology optimization by distribution of isotropic material," in *Topology Optimization*, pp. 1–69, Springer Berlin Heidelberg, 2004.

[344] G. Bramerdorfer, J. A. Tapia, J. J. Pyrhönen, and A. Cavagnino, "Modern electrical machine design optimization: Techniques, trends, and best practices," *IEEE Transactions on Industrial Electronics*, vol. 65, no. 10, pp. 7672–7684, 2018.

[345] J. Aubry, H. Ben Ahmed, and B. Multon, "Sizing optimization methodology of a surface permanent magnet machine-converter system over a torque-speed operating profile: Application to a wave energy converter," *IEEE Transactions on Industrial Electronics*, vol. 59, no. 5, pp. 2116–2125, 2012.

[346] P. Gangl, "Sensitivity-based topology and shape optimization with application to electrical machines," 2017.

[347] M. H. Imam, "Three-dimensional shape optimization," *International Journal for Numerical Methods in Engineering*, vol. 18, pp. 661–673, may 1982.

[348] R. Meske, J. Sauter, and E. Schnack, "Nonparametric gradient-less shape optimization for real-world applications," *Structural and Multidisciplinary Optimization*, vol. 30, pp. 201–218, may 2005.

[349] V. Braibant and C. Fleury, "An approximation-concepts approach to shape optimal design," *Computer Methods in Applied Mechanics and Engineering*, vol. 53, pp. 119–148, nov 1985.

[350] V. Braibant and C. Fleury, "Shape optimal design using b-splines," *Computer Methods in Applied Mechanics and Engineering*, vol. 44, pp. 247–267, aug 1984.

[351] P. Beckers, "Recent developments in shape sensitivity analysis: the physical approach," *Engineering Optimization*, vol. 18, pp. 67–78, nov 1991.

[352] J. Chen, V. Shapiro, K. Suresh, and I. Tsukanov, "Shape optimization with topological changes and parametric control," *International Journal for Numerical Methods in Engineering*, vol. 71, no. 3, pp. 313–346, 2007.

[353] M. Ashabani and Y. A.-R. I. Mohamed, "Multiobjective shape optimization of segmented pole permanent-magnet synchronous machines with improved torque characteristics," *IEEE Transactions on Magnetics*, vol. 47, no. 4, pp. 795–804, 2011.

[354] F. Scuiller, "Magnet shape optimization to reduce pulsating torque for a five-phase permanent-magnet low-speed machine," *IEEE Transactions on Magnetics*, vol. 50, no. 4, pp. 1–9, 2014.

[355] K. Yamazaki and H. Ishigami, "Rotor-shape optimization of interior-permanent-magnet motors to reduce harmonic iron losses," *IEEE Transactions on Industrial Electronics*, vol. 57, no. 1, pp. 61–69, 2010.

[356] E. Tyflopoulos and M. Steinert, "Topology and parametric optimization-based design processes for lightweight structures," *Applied Sciences*, vol. 10, p. 4496, jun 2020.

[357] I. G. Ion, Z. Bontinck, D. Loukrezis, U. Römer, O. Lass, S. Ulbrich, S. Schöps, and H. D. Gersem, "Robust shape optimization of electric devices based on deterministic optimization methods and finite-element analysis with affine parametrization and design elements," *Electrical Engineering*, vol. 100, pp. 2635–2647, aug 2018.

[358] A. Schleupen, K. Maute, and E. Ramm, "Adaptive FE-procedures in shape optimization," *Structural and Multidisciplinary Optimization*, vol. 19, pp. 282–302, jul 2000.

[359] B. D. Upadhyay, S. S. Sonigra, and S. D. Daxini, "Numerical analysis perspective in structural shape optimization: A review post 2000," *Advances in Engineering Software*, vol. 155, p. 102992, may 2021.

[360] P. Gangl, U. Langer, A. Laurain, H. Meftahi, and K. Sturm, "Shape optimization of an electric motor subject to nonlinear magnetostatics," *SIAM Journal on Scientific Computing*, vol. 37, pp. B1002–B1025, jan 2015.

[361] Y. Hahn and J. I. Cofer, "Study of parametric and non-parametric optimization of a rotor-bearing system," in *Volume 7A: Structures and Dynamics*, American Society of Mechanical Engineers, jun 2014.

[362] M. P. Bendsøe and N. Kikuchi, "Generating optimal topologies in structural design using a homogenization method," *Computer Methods in Applied Mechanics and Engineering*, vol. 71, pp. 197–224, nov 1988.

[363] J. Yoo and N. Kikuchi, "Topology optimization in magnetic fields using the homogenization design method," *International Journal for Numerical Methods in Engineering*, vol. 48, no. 10, pp. 1463–1479, 2000.

[364] M. Burger and R. Stainko, "Phase-field relaxation of topology optimization with local stress constraints," *SIAM Journal on Control and Optimization*, vol. 45, pp. 1447–1466, jan 2006.

[365] H. Garcke, C. Hecht, M. Hinze, and C. Kahle, "Numerical approximation of phase field based shape and topology optimization for fluids," *SIAM Journal on Scientific Computing*, vol. 37, pp. A1846–A1871, jan 2015.

[366] O. Sigmund and K. Maute, "Topology optimization approaches," *Structural and Multidisciplinary Optimization*, vol. 48, pp. 1031–1055, aug 2013.

[367] M. Burger and S. Osher, "A survey on level set methods for inverse problems and optimal design," *European Journal of Applied Mathematics*, vol. 16, pp. 263–301, jun 2005.

[368] H. A. Eschenauer, V. V. Kobelev, and A. Schumacher, "Bubble method for topology and shape optimization of structures," *Structural Optimization*, vol. 8, pp. 42–51, aug 1994.

[369] X.-S. Yang, "Nature-inspired optimization algorithms: Challenges and open problems," *Journal of Computational Science*, vol. 46, p. 101104, oct 2020.

[370] G. Allaire and F. Jouve, "Coupling the level set method and the topological gradient in structural optimization," in *Solid Mechanics and Its Applications*, pp. 3–12, Springer Netherlands, 2006.

[371] Y. Okamoto, M. Ohtake, and N. Takahashi, "Magnetic shield design of perpendicular magnetic recording head by using topology optimization technique," *IEEE Transactions on Magnetics*, vol. 41, no. 5, pp. 1788–1791, 2005.

[372] F. Moussouni, *Multi-level and multi-objective design optimization tools for handling complex systems*. PhD thesis, Ecole Centrale de Lille, 2009.

[373] H. T. Reiner Horst, *Global Optimization*. Springer Berlin Heidelberg, Nov. 2013.

[374] H. Adeli, ed., *Advances in Design Optimization*. CRC Press, feb 1994.

[375] P. Venkataraman, *Applied Optimization with MATLAB Programming*. John Wiley Sons, Mar. 2009.

[376] U. M. Diwekar, "Multiobjective optimization," in *Introduction to Applied Optimization*, pp. 217–257, Springer International Publishing, 2020.

[377] Y. Collette and P. Siarry, "Interactive methods," in *Multiobjective Optimization*, pp. 77–98, Springer Berlin Heidelberg, 2004.

[378] A. Bonilla-Petriciolet and G. P. Rangaiah, "Introduction," in *Multi-Objective Optimization in Chemical Engineering*, pp. 1–16, John Wiley & Sons Ltd, apr 2013.

[379] C.-L. Hwang and A. S. M. Masud, *Multiple Objective Decision Making—Methods and Applications: a state-of-the-art survey*, vol. 164. Springer Science & Business Media, 2012.

[380] K. Miettinen, *Nonlinear Multiobjective Optimization*. Springer US, Dec. 1999.

[381] C. L. Hwang and A. S. M. Masud, *Multiple Objective Decision Making - Methods and Applications*. Springer Berlin Heidelberg, Dec. 2012.

[382] J. L. Cohon, R. L. Church, and D. P. Sheer, "Generating multiobjective trade-offs: An algorithm for bicriterion problems," *Water Resources Research*, vol. 15, pp. 1001–1010, oct 1979.

[383] I. Kim and O. de Weck, "Adaptive weighted-sum method for bi-objective optimization: Pareto front generation," *Structural and Multidisciplinary Optimization*, vol. 29, pp. 149–158, sep 2004.

[384] O. Grodzevich, I. Halevy, Z. Kava, O. Romanko, and T. Seeman, "Normalization and other topics in multiobjective optimization," 2006.

[385] K. Deb, K. Miettinen, and S. Chaudhuri, "Toward an estimation of nadir objective vector using a hybrid of evolutionary and local search approaches," *IEEE Transactions on Evolutionary Computation*, vol. 14, no. 6, pp. 821–841, 2010.

[386] Y. Y. Haimes, L. S. Lasdon, and D. A. Wismer, "On a bicriterion formulation of the problems of integrated system identification and system optimization," *IEEE Transactions on Systems, Man, and Cybernetics*, vol. SMC-1, no. 3, pp. 296–297, 1971.

[387] J. Sobieszczanski-Sobieski, "A linear decomposition method for large optimization problems. blueprint for development," tech. rep., NASA National Aeronautics and Space Administration, 1982.

[388] B. Delinchant, F. Wurtz, and E. Atienza, "Reducing sensitivity analysis time-cost of compound model," *IEEE Transactions on Magnetics*, vol. 40, no. 2, pp. 1216–1219, 2004.

[389] G. Lei, C. Liu, J. Zhu, and Y. Guo, "Techniques for multilevel design optimization of permanent magnet motors," *IEEE Transactions on Energy Conversion*, vol. 30, no. 4, pp. 1574–1584, 2015.

[390] L. Brevault and M. Balesdent, "Multidisciplinary system modeling and optimization," in *Springer Optimization and Its Applications*, pp. 3–30, Springer International Publishing, 2020.

[391] R. J. Balling and J. Sobieszczanski-Sobieski, "Optimization of coupled systems - a critical overview of approaches," *AIAA Journal*, vol. 34, pp. 6–17, jan 1996.

[392] J. T. Allison, *Complex System Optimization: A Reviewof Analytical Target Cascading, Collaborative Optimization, and Other Formulations*. PhD thesis, The University of Michigan, 2004.

[393] S. Kodiyalam, "Evaluation of methods for multidisciplinary design optimization (mdo), part ii," *National Aeronautics andSpace Administration NASA*, 2000.

[394] E. J. Cramer, J. J. E. Dennis, P. D. Frank, R. M. Lewis, and G. R. Shubin, "Problem formulation for multidisciplinary optimization," *SIAM Journal on Optimization*, vol. 4, pp. 754–776, nov 1994.

[395] T. de Paula Machado Bazzo, J. F. Kölzer, R. Carlson, F. Wurtz, and L. Gerbaud, "Multiphysics design optimization of a permanent magnet synchronous generator," *IEEE Transactions on Industrial Electronics*, vol. 64, no. 12, pp. 9815–9823, 2017.

[396] S. Brisset, D. Vizireanu, and P. Brochet, "Design and optimization of a nine-phase axial-flux pm synchronous generator with concentrated winding for direct-drive wind turbine," *IEEE Transactions on Industry Applications*, vol. 44, no. 3, pp. 707–715, 2008.

[397] J. A. Reyer and P. Y. Papalambros, "Combined optimal design and control with application to an electric DC motor," *Journal of Mechanical Design*, vol. 124, pp. 183–191, may 2002.

[398] F. Messine, B. Nogarede, and J.-L. Lagouanelle, "Optimal design of electromechanical actuators: a new method based on global optimization," *IEEE Transactions on Magnetics*, vol. 34, no. 1, pp. 299–308, 1998.

[399] J. Fontchastagner, F. Messine, and Y. Lefevre, "Design of electrical rotating machines by associating deterministic global optimization algorithm with combinatorial analytical and numerical models," *IEEE Transactions on Magnetics*, vol. 43, no. 8, pp. 3411–3419, 2007.

[400] N. Bianchi and F. Dughiero, "Optimal design techniques applied to transverse-flux induction heating systems," *IEEE Transactions on Magnetics*, vol. 31, no. 3, pp. 1992–1995, 1995.

[401] N. Boules, "Design optimization of permanent magnet dc motors," *IEEE Transactions on Industry Applications*, vol. 26, pp. 786–792, July 1990.

[402] B. Singh, B. P. Singh, S. S. Murthy, and C. S. Jha, "Experience in design optimization of induction motor using 'sumt' algorithm," *IEEE Transactions on Power Apparatus and Systems*, vol. PAS-102, no. 10, pp. 3379–3384, 1983.

[403] P. Putek, R. Pulch, A. Bartel, E. J. W. ter Maten, M. Günther, and K. M. Gawrylczyk, "Shape and topology optimization of a permanent-magnet machine under uncertainties," *Journal of Mathematics in Industry*, vol. 6, nov 2016.

[404] X. Ge and Z. Q. Zhu, "Influence of manufacturing tolerances on cogging torque in interior permanent magnet machines with eccentric and sinusoidal rotor contours," *IEEE Transactions on Industry Applications*, vol. 53, no. 4, pp. 3568–3578, 2017.

[405] A. Tessarolo, F. Luise, S. Pieri, A. Benedetti, M. Bortolozzi, and M. De Martin, "Design for manufacturability of an off-shore direct-drive wind generator: An insight into additional loss prediction and mitigation," *IEEE Transactions on Industry Applications*, vol. 53, no. 5, pp. 4831–4842, 2017.

[406] R. Ramarotafika, A. Benabou, and S. Clenet, "Stochastic modeling of soft magnetic properties of electrical steels: Application to stators of electrical machines," *IEEE Transactions on Magnetics*, vol. 48, no. 10, pp. 2573–2584, 2012.

[407] P. Offermann, H. Mac, T. T. Nguyen, S. Clénet, H. De Gersem, and K. Hameyer, "Uncertainty quantification and sensitivity analysis in electrical machines with stochastically varying machine parameters," *IEEE Transactions on Magnetics*, vol. 51, no. 3, pp. 1–4, 2015.

[408] K. Deb and H. Gupta, "Introducing robustness in multi-objective optimization," *Evolutionary Computation*, vol. 14, pp. 463–494, dec 2006.

[409] J. Dréo, P. Siarry, A. Pétrowski, and E. Taillard, *Metaheuristics for Hard Optimization*. Springer-Verlag GmbH, Jan. 2006.

[410] X.-S. Yang, *Engineering Optimization*. John Wiley Sons, June 2010.

[411] J. J. Grefenstette, "Optimization of control parameters for genetic algorithms," *IEEE Transactions on Systems, Man, and Cybernetics*, vol. 16, no. 1, pp. 122–128, 1986.

[412] D. E. Goldberg and J. H. Holland, "Genetic algorithms and machine learning," *Machine Learning*, vol. 3, pp. 95–99, oct 1988.

[413] Y.-W. Leung and Y. Wang, "Multiobjective programming using uniform design and genetic algorithm," *IEEE Transactions on Systems, Man, and Cybernetics, Part C (Applications and Reviews)*, vol. 30, no. 3, pp. 293–304, 2000.

[414] X.-B. Hu and E. Di Paolo, "Binary-representation-based genetic algorithm for aircraft arrival sequencing and scheduling," *IEEE Transactions on Intelligent Transportation Systems*, vol. 9, no. 2, pp. 301–310, 2008.

[415] C. W. Ahn and R. Ramakrishna, "Elitism-based compact genetic algorithms," *IEEE Transactions on Evolutionary Computation*, vol. 7, no. 4, pp. 367–385, 2003.

[416] J. H. Holland, *Adaptation in Natural and Artificial Systems: An Introductory Analysis with Applications to Biology, Control, and Artificial Intelligence*. The MIT Press, 1992.

[417] N. Bianchi and S. Bolognani, "Brushless dc motor design: an optimisation procedure based on genetic algorithms," in *1997 Eighth International Conference on Electrical Machines and Drives (Conf. Publ. No. 444)*, pp. 16–20, 1997.

[418] N. Bianchi and S. Bolognani, "Design optimisation of electric motors by genetic algorithms," *IEE Proceedings - Electric Power Applications*, vol. 145, no. 5, p. 475, 1998.

[419] D.-J. Sim, D.-H. Cho, J.-S. Chun, H.-K. Jung, and T.-K. Chung, "Efficiency optimization of interior permanent magnet synchronous motor using genetic algorithms," *IEEE Transactions on Magnetics*, vol. 33, no. 2, pp. 1880–1883, 1997.

[420] N. Rostami, M. R. Feyzi, J. Pyrhonen, A. Parviainen, and V. Behjat, "Genetic algorithm approach for improved design of a variable speed axial-flux permanent-magnet synchronous generator," *IEEE Transactions on Magnetics*, vol. 48, no. 12, pp. 4860–4865, 2012.

[421] K.-J. Han, H.-S. Cho, D.-H. Cho, and H.-K. Jung, "Optimal core shape design for cogging torque reduction of brushless dc motor using genetic algorithm," *IEEE Transactions on Magnetics*, vol. 36, no. 4, pp. 1927–1931, 2000.

[422] M. Lukaniszyn, M. JagieLa, and R. Wrobel, "Optimization of permanent magnet shape for minimum cogging torque using a genetic algorithm," *IEEE Transactions on Magnetics*, vol. 40, no. 2, pp. 1228–1231, 2004.

[423] R. Eberhart and J. Kennedy, "A new optimizer using particle swarm theory," in *MHS'95. Proceedings of the Sixth International Symposium on Micro Machine and Human Science*, pp. 39–43, 1995.

[424] J. Kennedy and R. Eberhart, "Particle swarm optimization," in *Proceedings of ICNN'95 - International Conference on Neural Networks*, vol. 4, pp. 1942–1948 vol.4, 1995.

[425] D. Bratton and J. Kennedy, "Defining a standard for particle swarm optimization," in *2007 IEEE Swarm Intelligence Symposium*, pp. 120–127, 2007.

[426] S. Ho, S. Yang, G. Ni, and H. Wong, "A particle swarm optimization method with enhanced global search ability for design optimizations of electromagnetic devices," *IEEE Transactions on Magnetics*, vol. 42, no. 4, pp. 1107–1110, 2006.

[427] A. Zare Bazghaleh, M. R. Naghashan, and M. R. Meshkatoddini, "Optimum design of single-sided linear induction motors for improved motor performance," *IEEE Transactions on Magnetics*, vol. 46, no. 11, pp. 3939–3947, 2010.

[428] J.-H. Seo, S.-M. Kim, and H.-K. Jung, "Rotor-design strategy of ipmsm for 42 v integrated starter generator," *IEEE Transactions on Magnetics*, vol. 46, no. 6, pp. 2458–2461, 2010.

[429] J. H. Lee, J.-Y. Song, D.-W. Kim, J.-W. Kim, Y.-J. Kim, and S.-Y. Jung, "Particle swarm optimization algorithm with intelligent particle number control for optimal design of electric machines," *IEEE Transactions on Industrial Electronics*, vol. 65, no. 2, pp. 1791–1798, 2018.

[430] J. H. Lee, J.-W. Kim, J.-Y. Song, D.-W. Kim, Y.-J. Kim, and S.-Y. Jung, "Distance-based intelligent particle swarm optimization for optimal design of permanent magnet synchronous machine," *IEEE Transactions on Magnetics*, vol. 53, no. 6, pp. 1–4, 2017.

[431] A. A. Arkadan, M. N. ElBsat, and M. A. Mneimneh, "Particle swarm design optimization of ala rotor synrm for traction applications," *IEEE Transactions on Magnetics*, vol. 45, no. 3, pp. 956–959, 2009.

[432] M. Dorigo and L. Gambardella, "Ant colony system: a cooperative learning approach to the traveling salesman problem," *IEEE Transactions on Evolutionary Computation*, vol. 1, no. 1, pp. 53–66, 1997.

[433] M. Dorigo, V. Maniezzo, and A. Colorni, "Ant system: Optimization by a colony of cooperating agents," *IEEE Transactions on Systems, Man, and Cybernetics, Part B (Cybernetics)*, vol. 26, no. 1, pp. 29–41, 1996.

[434] M. Dorigo and C. Blum, "Ant colony optimization theory: A survey," *Theoretical Computer Science*, vol. 344, no. 2, pp. 243–278, 2005.

[435] M. Dorigo and T. Stützle, *Ant colony optimization*. Cambridge, Mass: MIT Press, 2004.

[436] A. YILDIZ, M. POLAT, and M. T. Özdemir, "Design optimization of inverted switched reluctance motor using ant colony optimization algorithm," in *International Conference on Artificial Intelligence and Data Processing (IDAP)*, pp. 1–6, 2018.

[437] P. Prakash and P. Aravindhababu, "Multiobjective design of induction motor using ant colony optimization," *International Research Journal of Engineering and Technology (IRJET)*, 2017.

[438] A. Ajith and J. Lakhmi, "Evolutionary multiobjective optimization," in *Advanced Information and Knowledge Processing*, pp. 1–6, Springer-Verlag, 2005.

[439] C. Coello, D. Veldhuizen, and G. Lamont, *Evolutionary Algorithms for Solving Multi-Objective Problems*. Springer, 01 2007.

[440] J. D. Schaffer, *Multiple Objective Optimization with Vector Evaluated Genetic Algorithms*. PhD thesis, Vanderbilt University, Nashville, Tennesse, 1984.

[441] J. D. Schaffer, "Multiple objective optimization with vector evaluated genetic algorithms," in *Proceedings of the 1st International Conference on Genetic Algorithms*, 1985.

[442] C. Fonseca and P. Fleming, "Multiobjective genetic algorithms," in *IEE Colloquium on Genetic Algorithms for Control Systems Engineering*, pp. 6/1–6/5, 1993.

[443] J. Horn, N. Nafpliotis, and D. Goldberg, "A niched pareto genetic algorithm for multiobjective optimization," in *Proceedings of the First IEEE Conference on Evolutionary Computation. IEEE World Congress on Computational Intelligence*, pp. 82–87 vol.1, 1994.

[444] M. Abido, "A niched pareto genetic algorithm for multiobjective environmental/economic dispatch," *International Journal of Electrical Power Energy Systems*, vol. 25, no. 2, pp. 97–105, 2003.

[445] N. Srinivas and K. Deb, "Muiltiobjective optimization using nondominated sorting in genetic algorithms," *Evolutionary Computation*, vol. 2, no. 3, pp. 221–248, 1994.

[446] J. Knowles and D. Corne, "The pareto archived evolution strategy: a new baseline algorithm for pareto multiobjective optimisation," in *Proceedings of the 1999 Congress on Evolutionary Computation-CEC99 (Cat. No. 99TH8406)*, vol. 1, pp. 98–105 Vol. 1, 1999.

[447] J. D. Knowles and D. W. Corne, "Approximating the nondominated front using the pareto archived evolution strategy," *Evolutionary Computation*, vol. 8, pp. 149–172, jun 2000.

[448] K. Deb, A. Pratap, S. Agarwal, and T. Meyarivan, "A fast and elitist multiobjective genetic algorithm: Nsga-ii," *IEEE Transactions on Evolutionary Computation*, vol. 6, no. 2, pp. 182–197, 2002.

[449] E. Zitzler, M. Laumanns, and L. Thiele, "Spea2: Improving the strength pareto evolutionary algorithm," 2001.

[450] D. A. Van Veldhuizen and G. B. Lamont, "Multiobjective optimization with messy genetic algorithms," in *Proceedings of the 2000 ACM symposium on Applied computing - SAC '00*, ACM Press, 2000.

[451] K. Deb, "Multi-objective genetic algorithms: Problem difficulties and construction of test problems," *Evolutionary Computation*, vol. 7, pp. 205–230, sep 1999.

[452] C. C. Coello, G. B. Lamont, and D. A. van Veldhuizen, "MOP evolutionary algorithm approaches," in *Genetic and Evolutionary Computation Series*, pp. 61–130, Springer US, 2007.

[453] D. A. Van Veldhuizen and G. B. Lamont, "Multiobjective evolutionary algorithms: Analyzing the state-of-the-art," *Evolutionary Computation*, vol. 8, pp. 125–147, jun 2000.

[454] K. M. Cisse, S. Hlioui, M. Belhadi, G. Mermaz Rollet, M. Gabsi, and Y. Cheng, "Design optimization of multi-layer permanent magnet synchronous machines for electric vehicle applications," *Energies*, vol. 14, no. 21, 2021.

[455] A. H. Isfahani, A. H.-S. Boroujerdi, and S. Hasanzadeh, "Multi-objective design optimization of a large-scale directdrive permanent magnet generator for wind energy conversion systems," *Frontiers in Energy*, vol. 8, pp. 182–191, may 2014.

[456] S. Meo, A. Zohoori, and A. Vahedi, "Optimal design of permanent magnet flux switching generator for wind applications via artificial neural network and multi-objective particle swarm optimization hybrid approach," *Energy Conversion and Management*, vol. 110, pp. 230–239, 2016.

[457] E.-G. Talbi, *Metaheuristics : from design to implementation.* Hoboken, N.J: John Wiley & Sons, 2009.

[458] C. M. Fonseca and P. J. Fleming, "Genetic algorithms for multiobjective optimization: Formulationdiscussion and generalization," in *ICGA*, 1993.

[459] Y. Collette and P. Siarry, *Multiobjective Optimization.* Springer Berlin Heidelberg, June 2013.

[460] R. Purshouse and P. Fleming, "Why use elitism and sharing in a multi-objective genetic algorithm?," in *GECCO 2002: Proceedings of the Genetic and Evolutionary Computation Conference, New York, USA, 9-13 July 2002*, 2002.

[461] S. G. Min, G. Bramerdorfer, and B. Sarlioglu, "Analytical modeling and optimization for electromagnetic performances of fractional-slot pm brushless machines," *IEEE Transactions on Industrial Electronics*, vol. 65, no. 5, pp. 4017–4027, 2018.

[462] Z. Xue, H. Li, Y. Zhou, N. Ren, and W. Wen, "Analytical prediction and optimization of cogging torque in surface-mounted permanent magnet machines with modified particle swarm optimization," *IEEE Transactions on Industrial Electronics*, vol. 64, no. 12, pp. 9795–9805, 2017.

[463] S. Mohammadi and M. Mirsalim, "Analytical design framework for torque and back-emf optimization, and inductance calculation in double-rotor radial-flux air-cored permanent-magnet synchronous machines," *IEEE Transactions on Magnetics*, vol. 50, no. 1, pp. 1–16, 2014.

[464] N. Bracikowski, M. Hecquet, P. Brochet, and S. V. Shirinskii, "Multiphysics modeling of a permanent magnet synchronous machine by using lumped models," *IEEE Transactions on Industrial Electronics*, vol. 59, no. 6, pp. 2426–2437, 2012.

[465] Y. Hua, H. Zhu, M. Gao, and Z. Ji, "Multiobjective optimization design of permanent magnet assisted bearingless synchronous reluctance motor using nsga-," *IEEE Transactions on Industrial Electronics*, vol. 68, no. 11, pp. 10477–10487, 2021.

[466] A. S. Mohammadi and J. P. F. Trovão, "System-level optimization of hybrid excitation synchronous machines for a three-wheel electric vehicle," *IEEE Transactions on Transportation Electrification*, vol. 6, no. 2, pp. 690–702, 2020.

[467] H. Zhao, C. Liu, Z. Song, and W. Wang, "Exact modeling and multiobjective optimization of vernier machines," *IEEE Transactions on Industrial Electronics*, vol. 68, no. 12, pp. 11740–11751, 2021.

[468] J. Wu, X. Zhu, D. Fan, Z. Xiang, L. Xu, and L. Quan, "Robust optimization design for permanent magnet machine considering magnet material uncertainties," *IEEE Transactions on Magnetics*, vol. 58, no. 2, pp. 1–7, 2022.

[469] J. Zhang, H. Wang, L. Chen, C. Tan, and Y. Wang, "Multi-objective optimal design of bearingless switched reluctance motor based on multi-objective genetic particle swarm optimizer," *IEEE Transactions on Magnetics*, vol. 54, no. 1, pp. 1–13, 2018.

[470] S. G. Min and B. Sarlioglu, "3-d performance analysis and multiobjective optimization of coreless-type pm linear synchronous motors," *IEEE Transactions on Industrial Electronics*, vol. 65, no. 2, pp. 1855–1864, 2018.

[471] M. Mooney and G. Maclaurin, "Transportation of large windcomponents: A review ofexisting geospatial data," tech. rep., NREL National Renewable Energy Laboratory, 2016.

[472] "Motors and generators," *NEMA MG 1-2011, National Electric Manufacturers Association NEMA*, 2011.

[473] "Rare earth element prices, https://strategicmetalsinvest.com/current-strategic-metals-prices/," 2022. Accessed Jul. 28, 2022.

[474] A. Røkke, *Permanent magnet generators for marine current tidal turbines: Analysis and optimisation of low-to medium-speed machines featuring various winding layouts.* PhD thesis, Department of Electric Power Engineering at Norwegian University of Science and Technology, 2017.

ARNOLD® MAGNETIC TECHNOLOGIES

N40SH

Sintered Neodymium-Iron-Boron Magnets

These are also referred to as "Neo" or NdFeB magnets. They offer a combination of high magnetic output at moderate cost. Please contact Arnold for additional grade information and recommendations for protective coating. Assemblies using these magnets can also be provided.

	Characteristic	Units	min.	nominal	max.
Magnetic Properties	**Br**, Residual Induction	Gauss	12,500	12,700	12,900
		mT	1250	1270	1290
	H_{cB}, Coercivity	Oersteds	11,800	12,050	12,300
		kA/m	939	959	979
	H_{cJ}, Intrinsic Coercivity	Oersteds	20,000		
		kA/m	1,592		
	BHmax, Maximum Energy Product	MGOe	38	41	43
		kJ/m³	302	322	342

	Characteristic	Units	C //	C ⊥
Thermal Properties	Reversible Temperature Coefficients (1)			
	of Induction, α(Br)	%/ºC	-0.12	
	of Coercivity, α(Hcj)	%/ºC	-0.55	
	Coefficient of Thermal Expansion (2)	ΔL/L per ºCx10⁻⁶	7	-1
	Thermal Conductivity	kcal/mhrºC	5.3	5.8
	Specific Heat (3)	cal/gºC	0.11	
	Curie Temperature, Tc	ºC	310	
Other Properties	Flexural Strength	psi	41,300	
		MPa	285	
	Density	g/cm³	7.6	
	Hardness, Vickers	Hv	620	
	Electrical Resistivity, ρ	μΩ • cm	150 // 130 ⊥	

Notes: (1) Coefficients measured between 20 and 150 ºC
(2) Between 20 and 200 ºC. Values are typical and can vary.
(3) Between 20 and 140 ºC

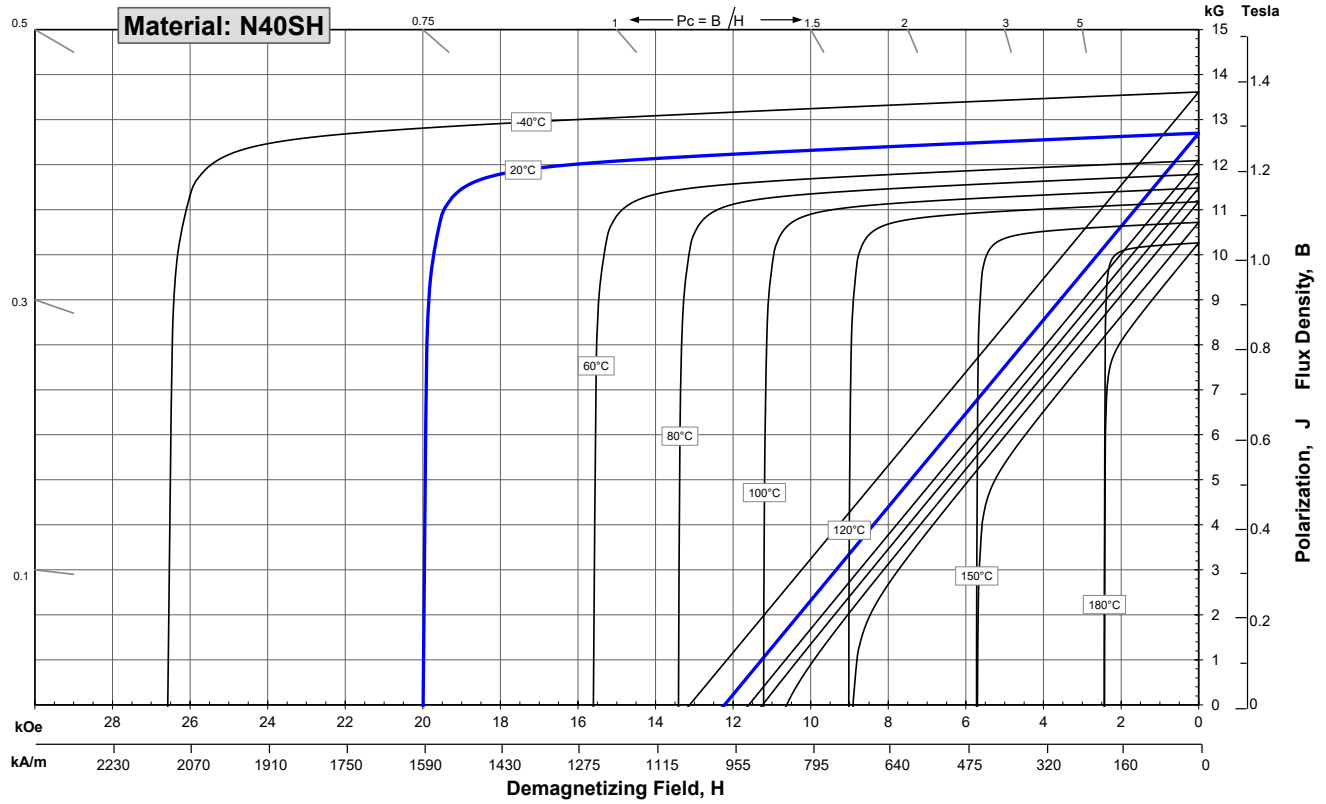

1 kA/m = 12.566 Oe 1 kOe = 79.577 kA/m

Notes The material data and demagnetization curves shown above represent typical properties that may vary due to product shape and size.
Demagnetization curves show nominal Br and minimum Hci.
Magnets can be supplied thermally stabilized or magnetically calibrated to customer specifications.
Additional grades are available. Please contact the factory for information.

ARNOLD® MAGNETIC TECHNOLOGIES

N48SH

Sintered Neodymium-Iron-Boron Magnets

These are also referred to as "Neo" or NdFeB magnets. They offer a combination of high magnetic output at moderate cost. Please contact Arnold for additional grade information and recommendations for protective coating. Assemblies using these magnets can also be provided.

	Characteristic	Units	min.	nominal	max.
Magnetic Properties	**Br**, Residual Induction	Gauss	13,600	13,900	14,200
		mT	1360	1390	1420
	H_{cB}, Coercivity	Oersteds	12,500	13,050	13,600
		kA/m	995	1039	1082
	H_{cJ}, Intrinsic Coercivity	Oersteds	19,000		
		kA/m	1,512		
	BHmax, Maximum Energy Product	MGOe	45	48	50
		kJ/m³	358	378	398

	Characteristic	Units	C //	C ⊥
Thermal Properties	Reversible Temperature Coefficients (1)			
	of Induction, α(Br)	%/ºC	-0.12	
	of Coercivity, α(Hcj)	%/ºC	-0.57	
	Coefficient of Thermal Expansion (2)	ΔL/L per ºCx10⁻⁶	7	-1
	Thermal Conductivity	kcal/mhrºC	5.3	5.8
	Specific Heat (3)	cal/gºC	0.11	
	Curie Temperature, Tc	ºC	310	
Other Properties	Flexural Strength	psi	41,300	
		MPa	285	
	Density	g/cm³	7.6	
	Hardness, Vickers	Hv	620	
	Electrical Resistivity, ρ	μΩ • cm	150 // 130 ⊥	

Notes: (1) Coefficients measured between 20 and 150 ºC
(2) Between 20 and 200 ºC. Values are typical and can vary.
(3) Between 20 and 140 ºC

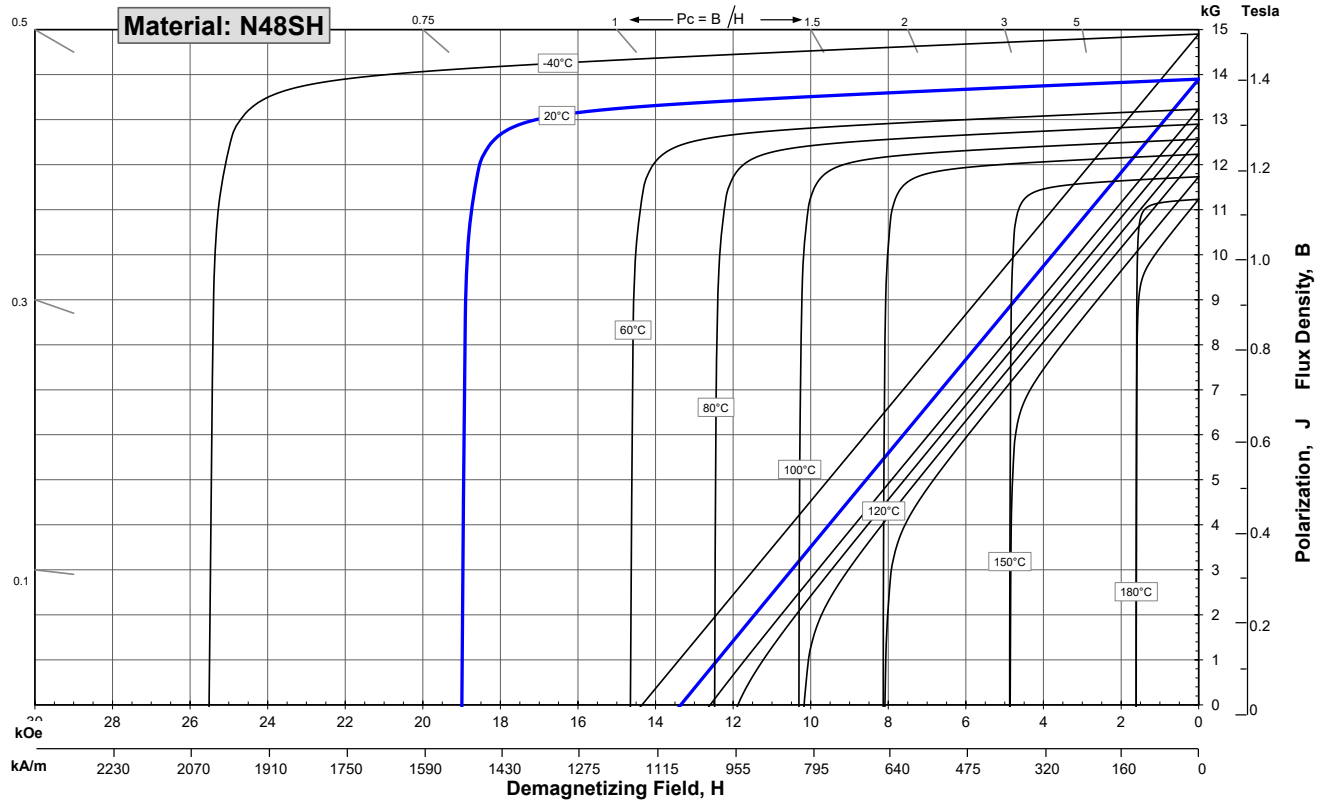

1 kA/m = 12.566 Oe 1 kOe = 79.577 kA/m

Notes The material data and demagnetization curves shown above represent typical properties that may vary due to product shape and size.
Demagnetization curves show nominal Br and minimum Hci.
Magnets can be supplied thermally stabilized or magnetically calibrated to customer specifications.
Additional grades are available. Please contact the factory for information.

Design Optimization of 15 MW Electric Generator for Offshore Wind Turbine: Sizing and Optimization

Abstract

The aim of this work is to find the suitable electrical generator for 15 MW direct-drive wind turbine with high-energy yield and low cost. In order to achieve that, the suitability assessment of some topologies and configurations was conducted. The different proposed generators were compared with a conventional surface mounted permanent magnet synchronous generator using NdFeb for the same power rating in terms of permanent magnet mass, machine mass, machine cost, torque density and efficiency. These criteria of evaluation should make it possible for the designers to know whether the electrical generator is technically feasible and economically viable for high-power low-speed wind turbines. Further, in order to investigate a very broad spectrum of synchronous generators through magneto-thermal design, inspecting a large design space with fast method is required. Magneto-thermal models for preliminary analysis of high-power low-speed permanent magnet synchronous generator was developed, which when integrated in optimization process provides the different optimal performances with reasonable computation time while keeping acceptable accuracy. These models were combined with multi-objective genetic algorithm in order to optimize the mass of the generator and that of permanent magnet without overtaking the imposed limits. The investigated theoretical designs suitable for the application were compared and their advantages and drawbacks were emphasized.

Keywords: Offshore wind turbine, Radial flux machine, Direct-drive, Analytical model, Reluctance network model, Multi-megawatt, Permanent magnet.

Étude et Conception de Structures de Génératrices Électriques de 15 MW pour l'Éolien Offshore : Dimensionnement et Optimisation

Résumé

L'objectif de ce travail est de trouver la génératrice électrique approprié, avec un rendement énergétique élevé et un faible coût, destinée à une éolienne offshore de 15 MW à entraînement direct. Les critères les plus importants qui guident la conception des aérogénérateurs de forte puissance ont étés discutés à travers une analyse bibliographique des technologies existantes. Les différentes génératrices proposés été comparés avec la structure conventionnelle de machine synchrone à flux radial à aimant NdFeB monté en surface pour une même puissance nominale en termes de masse de l'aimant permanent, de masse de la machine, de coût de la machine, de densité de couple et d'efficacité. Ces critères d'évaluation devraient permettre aux concepteurs de décider si la génératrice est techniquement faisable et économiquement viable pour des éoliennes offshores. La phase de pré-dimensionnement des machines électriques nécessite l'utilisation des modèles rapides afin d'explorer rapidement l'espace des solutions. Des modèles magnéto-thermiques pour l'analyse préliminaire des génératrices de forte puissance synchrone à aimants permanents ont été développés, qui, lorsqu'ils sont intégrés dans le processus d'optimisation, fournissent les différentes performances optimales avec un temps de calcul raisonnable tout en conservant une précision acceptable. Ces modèles ont été combinés à des algorithmes génétiques multi-objectifs afin d'optimiser la masse du générateur et celle de l'aimant permanent toute en respectant les limites physiques imposées. Ce travail d'optimisation a abouti à une comparaison et une analyse approfondie des caractéristiques et des performances des nouvelles structures en regard des génératrices actuelles à base d'aimants terres rares.

Mots clés: Éolien offshore, Machine a flux axial, Entraînement direct, Modélisation analytique, méthode des constantes localisées, Multimégawatt, Aimant permanent.